Relative Intensity Noise in the LISA Pathfinder Interferometer - Experiments on ground and in space

Von der Fakultät für Mathematik und Physik
der Gottfried Wilhelm Leibniz Universität Hannover

zur Erlangung des akademischen Grades
Doktor der Naturwissenschaften
Dr. rer. nat.

genehmigte Dissertation von

M.Sc., Andreas Michael Wittchen

2021

Abstract

In recent years big progress was made on the measurement of gravitational waves; after the direct measurement had been unsuccessful for many years the Laser Interferometer Gravitational-Wave Observatory (LIGO) measured a first gravitational wave signal in 2015. To measure GWs in a lower frequency band the LISA mission is being developed, and scheduled to launch in 2034. This detector features a long arm interferometric displacement measurement between six free-falling test masses on three satellites in a triangular configuration, 2.5 million kilometres apart.

To demonstrate the necessary performance the technology demonstrator mission LISA Pathfinder was designed and successfully operated. It was launched in December of 2015 and operated until July of 2017. Here, the residual acceleration noise between a pair of test masses was measured with heterodyne interferometry. Two beams with a frequency difference f_{het} are interfered, from the phase change of the resulting heterodyne signal the relative displacement is calculated.

The main subject of this thesis is the coupling of Relative Intensity Noise (RIN) at f_{het} and $2f_{het}$ to the phase measurement. The contribution of RIN to the sensing noise depends on the position of the TM. With optimal TM placement this phase noise is subtracted while in other circumstances this phase noise can be the main contribution. Due to this TM dependency understanding the noise coupling is an important part in the successful operation of the LPF interferometer, and others similar to it.

In this thesis the engineering model of the LPF optical metrology system is used to verify the derived coupling equations with an injection of RIN and a measurement of the resulting phase noise. To enable these experiments the previous analog setup is upgraded to a digital setup, and additional components are introduced to inject and measure RIN and move the position of the TM.

In experiments during the operations phase of LPF the RIN level is calculated from the measured phase noise using the same method as is used in the laboratory. Here, no RIN is injected. In these experiments RIN at $1f_{het}$ does not contribute to the measured phase noise. The calculated noise level for correlated RIN at $2f_{het}$ over the mission duration is between $\hat{r}^{(2)} = (1.27 \pm 0.01)\frac{10^{-6}}{\sqrt{\text{Hz}}}$ and $\hat{r}^{(2)} = (1.828 \pm 0.008)\frac{10^{-6}}{\sqrt{\text{Hz}}}$.

Contents

List of Figures

List of Tables

Acronyms

AEI Albert-Einstein-Institute

ASD Astrium Deutschland

AO Analysis Object

BS Beamsplitter

CDS AdvLigo Control and Data System. recent version is called advligorts.

DAQ Data acquisition

DWS Differential Wavefront Sensing

DPS Differential Power Sensing

ESA European Space Agency

FST model model of the CDS, sampling frequency of 64 kHz. Also called fast model.

GRS Gravitational Reference Sensor

GUI General User Interface

GW Gravitational Wave

IGR Institute for Gravitational Research, University of Glasgow

NASA National Aeronautics and Space Administration

LISA Laser Interferometer Space Antenna

LTP LISA Technology Package

LTPDA LISA Technology Package Data Analysis

LPF LISA Pathfinder

LPSD Logarithmic Power Spectral Density

LO Local Oszillator

LTP model model of the CDS, sampling frequency of 2 kHz. Also called slow model.

MB Modulation Bench

NoP Noise over Position. Changing phase noise for different TM offset positions

OB Optical Bench

OMS Optical Metrology System

OPD Optical Pathlength Difference

PD Photo Diode

PM Phasemeter

PMI Phasemeter Interface

QPD Quadrant Photodiode

RIN Relative Intensity Noise

SNR Signal to Noise Ratio

SVN Small Vector Noise

TM Test Mass

TM1 Test Mass 1

TM2 Test Mass 2

$\mathbf{X_1}$ Measurement interferometer for displacement of TM1 relative to the OB

$\mathbf{X_{12}}$ Measurement interferometer for relative displacement between TM1 and TM2

$\mathbf{X_F}$ Frequency interferometer

$\mathbf{X_R}$ Reference interferometer

φ_1 Signal of measurement interferometer X_1 in phase radian, balanced signal of both diodes

φ_1_A Signal of the A diode measurement interferometer X_1, in phase radian

x1 Signal of measurement interferometer X_1 in meter, balanced signal of both diodes

x1_A Signal of the A diode of measurement interferometer X_1, in metre

o1 Signal of x1 with the reference interferometer signal xR subtracted, in metre

o1_A Signal of x1_A with the reference interferometer signal xR_A subtracted, in metre

1

Introduction

1.1. Black holes, gravitational waves and LISA

Gravitational waves are one consequence of the general theory of relativity [1]. The change in the gravitational field due to change in the mass distribution is limited by the speed of light [1]. To emit gravitational waves the system of masses in motion must not have radial symmetry, these perturbations in space time travel outward from the event which caused them [2]. One example of such a system would be a binary system of heavy objects orbiting each other. This radiation of GWs lead to an energy loss of the orbiting system [2]. Over time the distance between the orbiting objects decreases, the first measurement of this effect could be made on the binary pulsar PSR1913 + 16, see [3][4].

Due to the weak interaction of these gravitational waves with other matter they can be detected far from their source. Only GWs caused by very heavy objects strain the space-time continuum to a level which is detectable by current technology [5]. One such source are pairs of black holes (BHs). Two BHs in orbit around each other change the gravitational field in a sinusoidal pattern, the frequency of which depends on their orbital period [5].

When the orbital distance of two black holes decreases the two objects spiral into each other, the current data suggests that they then merge to a bigger black hole. The maximum orbital frequency before the merger depends on the masses of the BHs involved. Due to their smaller size lighter black holes have a higher merger frequency [6].

In recent years the scientific progress on gravitational waves and black holes has been remarkable. In 2015 the first gravitational wave from two BHs in an inspiral, and their final merger, has been detected by the Advanced Laser Interferometer Gravitational-Wave Observatory (aLIGO) [7][5], with many detections following the first. At the time of writing, the measurement results of 10 stellar-mass binary black hole mergers have been published [8], leading to a first understanding of the distribution of black holes in the part of the universe observable by LIGO. These discoveries are one part of the larger puzzle of the evolution of the universe after the big bang, since black holes are an integral part of the formation of galaxies.

As the name suggests, LIGO measures gravitational waves via laser interferometry. Two Michelson interferometers with an armlength of $4\,\mathrm{km}$ are placed $3000\,\mathrm{km}$ apart. By interfering the laser beams from the two arms, variations in the light travel times along the arms can be measured. These measured variations are caused by noise in the system, and in some exciting instances by deformations of spacetime due to gravitational waves.

Due to seismic noise and gravity gradient noise the measurement of GWs on Earth is limited towards frequencies below of $50\,\mathrm{Hz}$ with aLIGO [9], and to frequencies of $\approx 1\,\mathrm{Hz}$ with the upcoming generation of detectors. The detection of BH inspirals is limited to sources with a high orbital frequency towards the merger. To measure the merger of black holes with slower

orbital frequencies, in the mHz range, this measurement has to be performed away from the disturbances related to the environment on Earth.

With this motivation the gravitational universe was proposed as a theme to ESA in 2013 [6] for the next large missions L2 and L3, which are expected to launch in 2028 and 2034. This theme was accepted for the L3 mission.[1] In this theme questions such as "What is the role of black hole mergers?" (in the formation of galaxies), "Does gravity travel at the speed of light?" and "Does the graviton have mass?" are raised. As a method to find answers to these questions, and more, the measurement of gravitational waves from Galactic Binaries (GBs), massive black hole binaries (MBHBs) and extreme mass ratio inspirals (EMRIs) is motivated; and as a detector for these GWs the Laser Interferometry Space Antenna (LISA) is proposed. This observatory consists of three satellites in an orbit around the sun in a triangular formation, with an armlength of 2.5 million kilometres.[2]

The design of the mission underwent changes over time, a recent description of the LISA design can be found in the proposal in response to the ESA call for L3 mission concepts [11]. This proposed mission was adopted by ESA, with a launch scheduled in 2034.
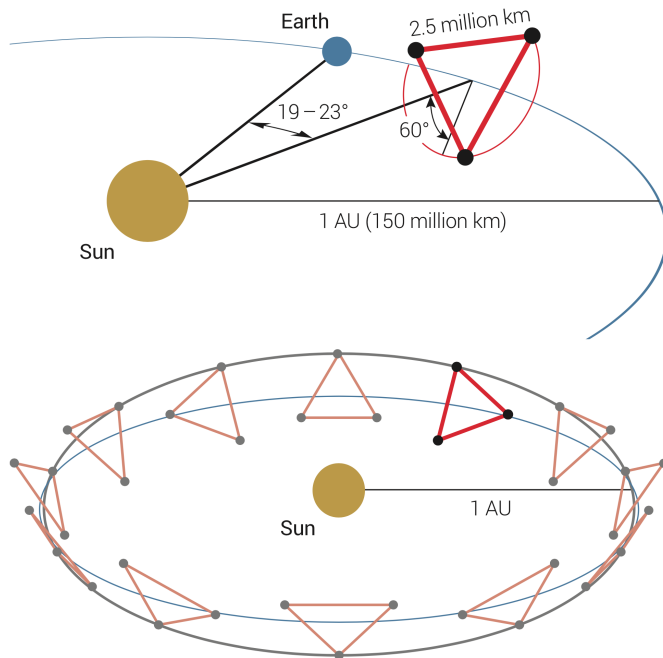
Figure 1.1.
This figure is a reprint from [6]. The top part shows the orbit of the LISA constellation, it travels behind the earth around the Sun. The bottom part shows the orbit of one individual satellite of the constellation. To achieve a stable triangular configuration, which rotates around its centre, the orbits of the individual satellites are tilted with respect to the orbital plane of the Earth-Sun system.

---

[1]Selected for L2 was the Athena mission, which observes X-ray signals. Joint operations of these two detectors would enable more areas of research than possible for each mission individually [10].

[2]To put this armlength into context, the Sun has a diameter of ≈ 1.4 million kilometres.

1.2. LISA Pathfinder

One necessary component for the success of the LISA mission is the precise measurement of the relative displacement of the local TM.

To demonstrate that the acceleration of the local TM can be kept below the requirements necessary for LISA, the technology demonstrator mission LISA Pathfinder (LPF) was designed. A description of the mission concept can be found in [12], details on the development process can be found in [13][14][15]. For LPF the measurement requirements are relaxed by a factor ≈ 7, and limited to frequencies above $1\,\mathrm{mHz}$, compared to the target sensitivity of LISA, to save on the cost and construction time.

The TM displacement is measured with a heterodyne interferometer. To accurately measure this displacement, a quiet reference test mass to the first is placed in the same satellite. The differential displacement between the two is the main science measurement. This measurement is made by the Optical Metrology System (OMS). For the analysis of force noise acting on the TMs the differential acceleration is used as a more natural unit. An overview of the components can be found in Figure 1.2.

Figure 1.2.: Shown here is an overview of the LPF satellite. This picture is a reprint from informational material by the European Space Agency ESA [16].

This overview shows the two test masses with the OMS at the heart of the LPF satellite. Around the OMS the other components, such as the laser, the on-board computer and the fuel tanks, are placed carefully to balance the gravitational influence on the two TMs.

A description of the system as-built, and a short summary of the operations time and first results, can be found in [17]. LISA Pathfinder was launched in December of 2015, and operated in a Lissajous orbit around the Lagrange point L1. On the way to its final orbit the commissioning of the subsystems was started, during which the individual units on board are switched on and tested. From March of 2016 until July of 2017 investigations to explain and improve the sensitivity of the optical measurement were performed.

This mission showed that a system can be build where the residual acceleration between two local test masses is at the requirements necessary for the targeted sensitivity of the LISA mission. At mHz frequencies this acceleration noise was shown to be $(1.74 \pm 0.05)\frac{\mathrm{fm\,s^{-2}}}{\sqrt{\mathrm{Hz}}}$ [18]. The sensor noise of the displacement measurement could be shown to be between $27.8\frac{\mathrm{fm}}{\sqrt{\mathrm{Hz}}}$ and $45.1\frac{\mathrm{fm}}{\sqrt{\mathrm{Hz}}}$ for frequencies between $200\,\mathrm{mHz}$ and $5\,\mathrm{Hz}$ [19]. This performance far exceeds the requirements of LPF of

$$S_{\delta x}^{1/2} \leq 9\frac{\mathrm{pm}}{\sqrt{\mathrm{Hz}}}\sqrt{1+\left(\frac{3\,\mathrm{mHz}}{f}\right)^4} \tag{1.1}$$

and even passes the LISA requirements [18].

To set these measurements into context, one E.coli bacterium with a weight of 1pg dropping on the TM surface with $a = 9.81\frac{\mathrm{m}}{\mathrm{s}^2}$, and then sticking there, would accelerate the 2kg TM by $\approx 5\frac{\mathrm{fm}}{\mathrm{s}^2}$. With the precision of the displacement sensor in the specified frequency band a sinusoidal TM motion at, for example, $0.5\,\mathrm{Hz}$ by the diameter of the hydrogen atom of $0.1\,\mathrm{nm}$ would be measurable.

1.3. Data Analysis

In this thesis, spectra and spectral densities are frequently calculated from a time series, using the Discrete Fourier Transform (DFT) [20]. These are very useful to describe noise, or signals in that noise, and are a standard tool in data analysis [21]. The calculation of spectra and spectral densities is implemented in LTPDA [22], using the Fast Fourier Transform algorithm (FFT). For averaging purposes a longer time series is cut into shorter segments, for each the spectrum or spectral density is calculated. Longer timespans increase the frequency resolution, and more averages increase the accuracy of the calculated values. To optimise the number of averages, a calculation of spectra based on [23] is used frequently. This logarithmic power spectral density (lpsd) sets the number of averages, meaning the number of smaller segments the longer timespan is cut into, according to the frequency which is calculated. Using this tool the given time series is divided in larger segments to provide more data points towards lower frequencies, and a higher number of segments to provide more accurate results towards higher frequencies. For some calculations, a linear fit is subtracted from each of the time segments, in LPTDA this is called a 'detrend of order 1'.

The DFT assumes an infinite timespan in the calculation of the spectra, therefore the shorter time segment under analysis are assumed to be repeated to ensure the periodicity of the signals and noise contained. To prevent effects from the edges of the segments to influence the calculated spectra a window function is applied. These functions are zero at the edges, and one in the centre of the timespan.

In most practical applications the shorter timespans from which the spectra are calculated overlap, since otherwise the parts where the amplitude is reduced by the window function are not used. In this thesis a Blackman-Harris window BH92 is used to calculate power spectral densities [24]. The optimal overlap of this window function is 66.1% [25], to reduce the correlation between the frequency bins an overlap of 50% is chosen in most cases. For the calculation of amplitude spectra, and the amplitude at a single frequency, a HFT70 flat-top window is used. In the calculation of amplitude spectra the individual segments of the timespan have an overlap of 50%. More details on these windows can be found in [25].

To make a fit with a given function to measured data points the Marcov Chain Monte Carlo (MCMC) method implemented in LTPDA is used. Used for the fit is a model, with a set of parameters, to explain the measured data. This model is derived from the physical understanding of the system under analysis.

In this thesis the model consists of the description of the expected phase noise contributions. The noise power of these individual contributions are used as parameters. Compared to the analysis of the complete noise model of the in-flight measurements the models used here are more simple [26]. They consist of noise contributions with a sinusoidal dependency on the measured phase and a constant noise floor.

The MCMC method optimises these parameters so that the difference between the model of the noise to the measured data is minimised. A Marcov Chain is a sequence of steps of a random walker, the probability of the direction of the next step of this walker is only dependent on the previous step. Using this method the available parameter space is explored. The aim is to find the parameters of the implemented model with the highest probability of explaining the measured data.

In this algorithm it is assumed that the noise model with fitted parameters that best describe the measured data is a good description of the true noise of the system. A necessary component from a physicists point of view is the careful selection of the model used, which must have a good foundation in the known properties of the system under analysis. More information can be found in the thesis of Nikolaos Karnesis [27], see also [28].

1.4. This thesis

In this thesis experiments on the optical metrology system (OMS) of LPF of the laboratory setup, and of the in-flight system are shown. A more detailed description of the optical measurement can be found in Chapter 2. Shown there is the measurement principle of heterodyne interferometry, and its implementation in both setups.

This thesis is concerned with the sensor noise of the optical measurement, the most relevant components are explained in Chapter 3. The focus of the experiments lies on Relative Intensity Noise (RIN), the derivation of the coupling of this noise to the phase measurement is shown in detail.

In preparation of the in-flight experiments the previous laboratory OMS with analog control loops is improved to a setup with digital control loops. Details on these are shown in Chapter 4. For the planned experiments of the RIN coupling additional components are needed, a digital control loop on the longitudinal and angular degrees of freedom on the test masses is added to the existing control scheme. Also included is a method to inject and measure RIN. Using these components, predicted properties of the RIN coupling are confirmed in the laboratory setup. These experiments are shown in Chapter 5. First, an experiment where RIN is injected as a sinusoidal RIN equivalent intensity modulation at a fixed frequency, and different amplitudes, to measure the transfer coefficient from RIN to phase is shown. In a similar experiment, the amplitude of the injected RIN is kept constant, and the frequency of the injection is changed. Then, the subtraction of RIN from the measured phase with a reference signal is demonstrated.

In Chapter 6 the planning and analysis of the RIN experiments performed during the LPF mission is shown. With two similar experiments to the RIN subtraction experiment presented in the previous chapter, the measured phase noise is used to calculate the RIN level of the flight OMS. Then, the RIN level of the flight OMS is measured directly, using channels intended for the phase measurement.

With the methods and results of the earlier experiments the RIN coupling of the free-flight experiments and during noise runs is explored. The results of the in-flight experiments are summarised in Section 6.8.

A summary of the whole thesis can be found in Chapter 7, and a conclusion can be found in Chapter 8.

2

OMS introduction and laboratory setup

The differential acceleration between two test masses was monitored on the LISA Pathfinder satellite at the first Lagrange point L1, between sun and earth. To measure the TM position with picometre and orientation with microradian accuracy an Optical Metrology System (OMS) was designed. These measurements are used in the Drag Free Attitude Control System (DFACS) to keep one test mass in free fall along the longitudinal degree of freedom, and control the other degrees. As a reference, a second test mass is kept at a stable position with respect to the first, and the satellite, with low actuation force. The displacement between the two TMs is the main science measurement.

The OMS consists of four heterodyne interferometers. The signal for heterodyne interferometry is created with two frequency shifted laser beams, which are interfered at a recombination beamsplitter. The resulting signal is measured with a photodiode.

In Section 2.1 heterodyne interferometry is briefly explained. The two laser beams are provided by the modulation bench (MB), see Section 2.2, which are fed to the optical bench (OB) via optical fibres. Four interferometers are bonded on the optical bench, which will be explained in Section 2.3.

To measure the interferometer signals two Quadrant photodiodes (QPDs) are used per interferometer. The phase from these signals is measured by the phasemeter; the phasemeter processing is explained in Section 2.6.

To reduce noise the interferometer signals of both ports of the recombination beamsplitter are measured. These signals are used for balanced detection. For further reduction of the noise the signal of a reference interferometer is subtracted from the signals of the other interferometers; details for both can be found in Section 2.6.2.

Quadrant photodiodes allow not only the measurement of the test mass longitudinal motion, but also of the angular motion through a process called differential wavefront sensing (DWS), which is explained in Section 2.6.3.

In this thesis measurements taken on-board the LPF satellite and on ground in the AEI laboratory with the engineering model are analysed. The processing of the measured phasemeter data is explained for both setups.

The LISA Technology Package Data Analysis (LTPDA toolbox [22]) for MATLAB® is used for the analysis, both for flight data and laboratory data.

2.1. Heterodyne interferometry

The interferometers of LISA Pathfinder are heterodyne interferometers. Two beams with a frequency difference of f_{het} are interfered on a recombination beamsplitter to create the heterodyne signal. A change in the optical pathlength between the beams results in a phase change of the heterodyne signal. From this measured phase the pathlength change is calculated. A simplified way to describe the two beams, here named measurement beam and reference beam, is

$$\vec{E}_r(\vec{r},t) = E_{r_0}(t)e^{-i(\vec{k}\vec{r}-2\pi f_r t-\varphi_r)}, \tag{2.1}$$

$$\vec{E}_m(\vec{r},t) = E_{m_0}(t)e^{-i(\vec{k}\vec{r}-2\pi f_m t-\varphi_m(t))}. \tag{2.2}$$

Where f_r and f_m are the frequencies of the individual beams, with $f_{het} = f_m - f_r$. The phase of the reference beam φ_r will be assumed to be static here, while the phase of the measurement beam $\varphi_m(t)$ is time dependant. These two beams are interfered on a recombination beamsplitter with the transmission coefficient τ, and reflective coefficient ρ. If losses due to stray light and heating of the component are disregarded, conservation of energy yields:

$$\tau^2 + \rho^2 = 1, \tag{2.3}$$

since the properties of the recombination beamsplitter relate to the amplitude of the electric field. Implemented for LPF are beamsplitters with a 50/50 splitting ratio, where

$$|\tau| = |\rho| = \frac{1}{\sqrt{2}}. \tag{2.4}$$

The recombination beamsplitter has two output ports, see Figure 2.1, where one quadrant photodiode per port is used to measure the beam power. These two ports are named symmetric and asymmetric port. The photodiode of the symmetric port is called A-diode, of the asymmetric port B-diode.
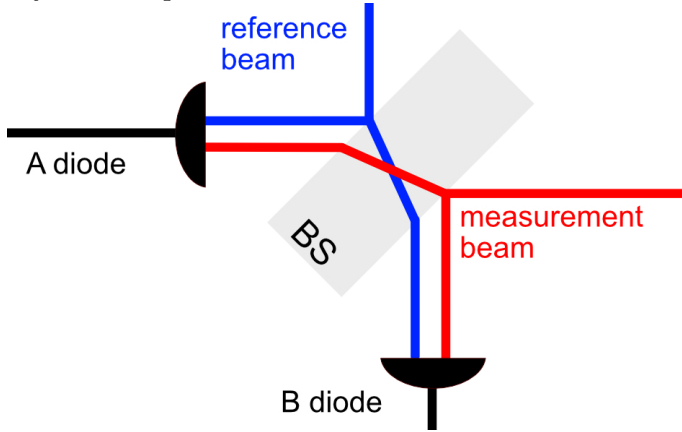
Figure 2.1.
A recombination beamsplitter (BS) interferes two laser beams (red and blue). The interferometric signal is measured by two photodiodes A and B on the symmetric and asymmetric port. In an ideal setup the two beams hit the centre of the diodes, the size of the BS is exaggerated in this depiction.

The photocurrent $I_{symm}(t)$ of the symmetric port is measured as:

$$I_{symm}(t) \propto |i\tau E_r + \rho E_m(t)|^2, \tag{2.5}$$

$$\propto (i\tau E_r + \rho E_m(t))(i\tau E_r + \rho E_m(t))^*, \tag{2.6}$$

$$\propto \tau^2 E_r^2 + \rho^2 E_m(t)^2 + i\tau\rho(E_m(t)E_r^* - E_r E_m(t)^*), \tag{2.7}$$

$$\propto \tau^2 E_r^2 + \rho^2 E_m(t)^2 + 2\tau\rho E_m(t)E_r \sin(2\pi f_{het}t + \varphi_m(t) - \varphi_r). \tag{2.8}$$

Due to the reflection of the measurement beam on the recombination beamsplitter the signal on the asymmetric port is phase shifted by π, therefore

$$I_{asymm}(t) \propto \rho^2 E_r^2 + \tau^2 E_m^2 - 2\rho\tau E_m E_r \sin(2\pi f_{het}t + \varphi_m(t) - \varphi_r). \tag{2.9}$$

The phase $\Delta\varphi(t) = \varphi_{\mathrm{m}}(t) - \varphi_{\mathrm{r}}$ is the pathlength difference of the two beam paths. In this simplified description, the phase of the measurement beam $\varphi_{\mathrm{m}}(t)$ contains the motion of the test mass, while the phase φ_{r} of the reference beam is constant. Since quadrant photodiodes are used there are four signals per port. This phase difference is measured in the phasemeter. The heterodyne signal is demodulated to measure the sine and cosine component, which is used to calculate the phase. Initially, the calculated phase signal has the unit radian, the calibration to the longitudinal and angular motion of the test mass is shown in Section 2.6. A number of different noise sources, which will disrupt the accurate phase measurement, are the subject of this thesis.

A more detailed description can be found in [29][30], see also [31].

2.2. The modulation bench

On the modulation bench the output of a single laser is split into two beams called the measurement and reference beam. On ground, the laser is a Mephisto 500 with a wavelength of 1064 nm. The laser current is set to achieve a beam power of $\approx 400\,\mathrm{mW}$. After a polarisation filter, a faraday isolator and one fibre, $\approx 150\,\mathrm{mW}$ arrive at the modulation bench. A 50-50 beamsplitter divides the single beam of the laser. The two resulting beams travel through one acousto-optic modulator (AOM) per beam to change the frequency of the laser light via Bragg diffraction.

Theoretical descriptions of heterodyne interferometry often describe the frequencies of the interfering beams as $\mathrm{f} = \mathrm{f_{Laser}} \pm \frac{\mathrm{f_{het}}}{2}$. For the LPF setup the desired heterodyne frequency is in the kHz range. Since the diffraction to a negative frequency difference is not very efficient, and the operation frequency of the AOMs is in the range of MHz, the implementation is different. Both beams are frequency shifted with the nominal frequency of $\mathrm{f_{AOM}} = 80\,\mathrm{MHz}$, from which half the heterodyne frequency is added or subtracted [32]. This leads to the final frequencies

$$\mathrm{f_{meas}} = \mathrm{f_{Laser}} + \mathrm{f_{AOM}} + \frac{\mathrm{f_{het}}}{2}, \tag{2.10}$$

$$\mathrm{f_{ref}} = \mathrm{f_{Laser}} + \mathrm{f_{AOM}} - \frac{\mathrm{f_{het}}}{2}. \tag{2.11}$$

The LPF laser frequency is $\mathrm{f_{Laser}} = \frac{1064\,\mathrm{nm}}{c} \approx 282\,\mathrm{THz}$. The heterodyne frequency in the ground setup is $\mathrm{f_{het}} \approx 1623.37\,\mathrm{Hz}$, while for the flight setup the heterodyne frequency is $\mathrm{f_{het}} = 1\,\mathrm{kHz}$.

Both beams are then coupled into optical fibres and fed to the optical bench, which is placed in a vacuum tank. The beam paths of the ground setup can be seen in Figure 2.2. In front
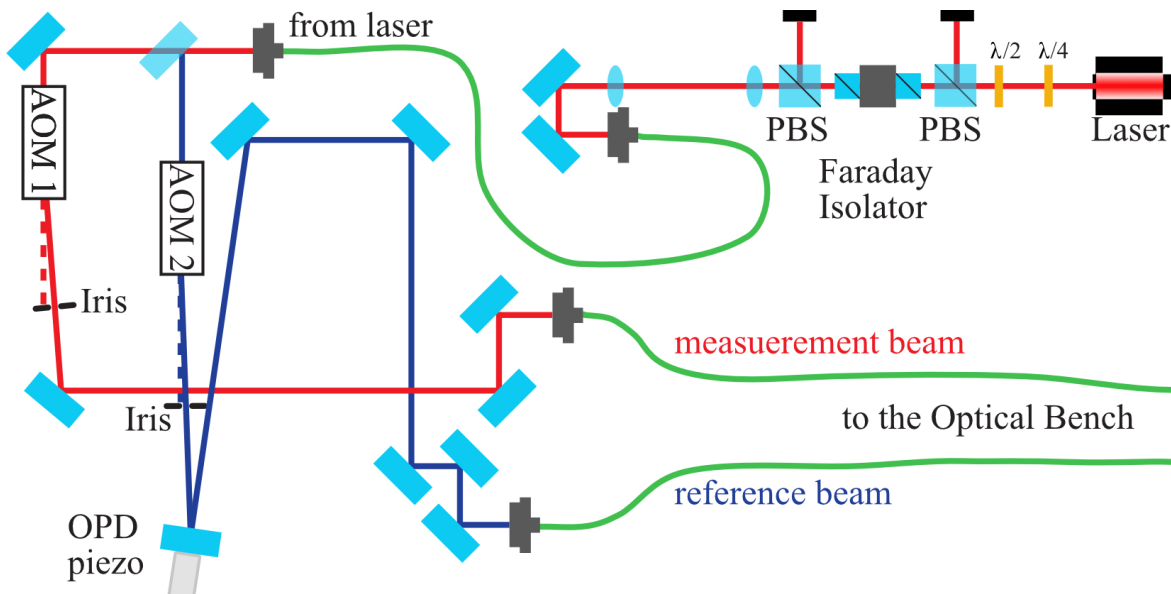
Figure 2.2.: The laser in the top right corner produces the beam, the polarisation is cleaned with $\frac{\lambda}{2}$ and $\frac{\lambda}{4}$ waveplates. Two polarising beamsplitters (PBS) and a faraday isolator are placed in the beampaths to prevent back-reflection.
Via an optical fibre, shown in green, the beam is sent to the main part of the modulation bench. The beam is divided into measurement and reference beam, one AOM per beam is used to frequency shift the laser light to create the heterodyne frequency difference between the two. On the bottom left a piezo is attached to one mirror to change the pathlength of the reference beam. This piezo functions as actuator for a control loop on the optical pathlength difference between the two beams, see Section 4.1.

of the fibres the beams have a power of $\approx 20\,\mathrm{mW}$; around $4\,\mathrm{mW}$ arrive on the optical bench. Routine alignment is necessary to maintain these power levels

For later experiments the electronics to create the frequency input to the AOMs are switched, a result of this is that the positive and negative frequency change $\frac{f_{\mathrm{het}}}{2}$ is also switched between the beams, see Section 4.5.

2.3. The optical bench
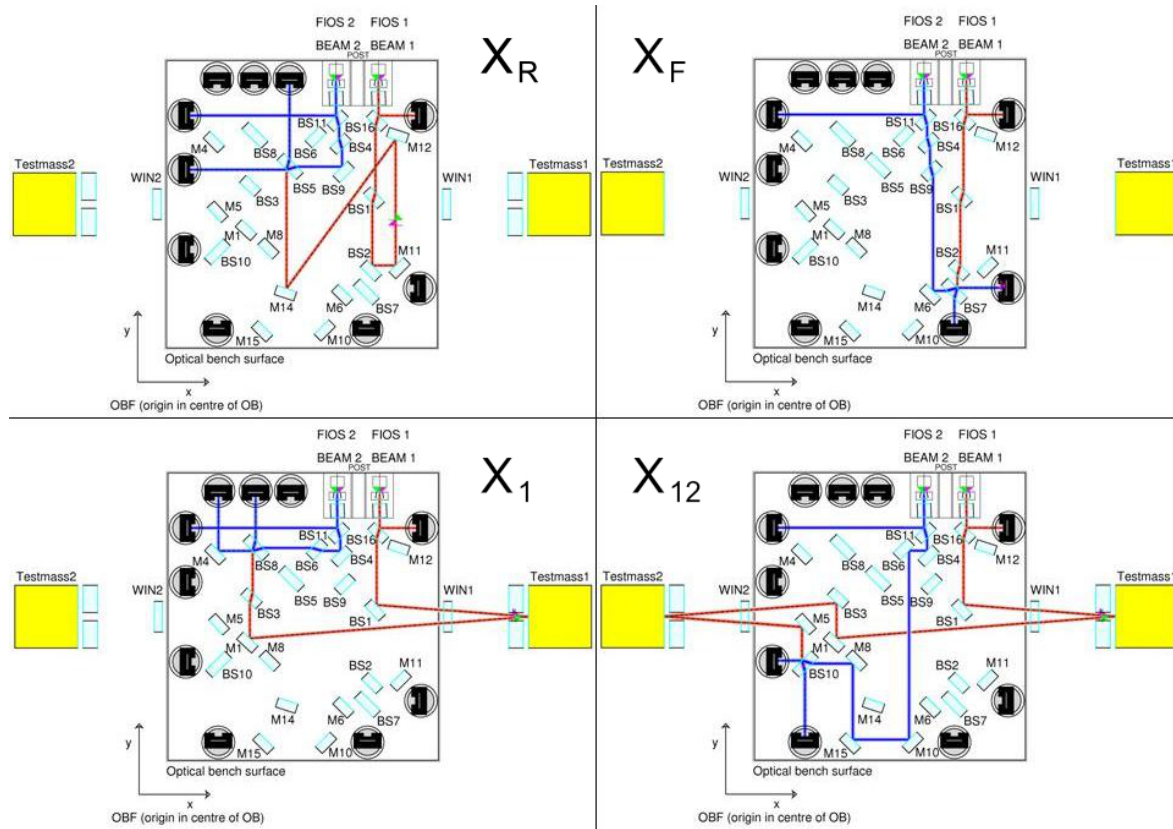
Figure 2.3.: This is the LISA Pathfinder optical bench flight model. The measurement beam (red) is interfered with the reference beam (blue). The motion of two test masses (yellow) is measured by the X_1 interferometer (bottom left) and the X_{12} interferometer (bottom right). On the top right the frequency interferometer X_F is shown, the reference interferometer X_R can be seen on the top left. The optical fibres have different length, such that the frequency interferometer has a total path length difference of ≈ 38 cm, and the other three interferometers have a path length difference close to zero. Picture courtesy of ASD and IGR.

The optical bench (OB) is the key component of the optical metrology system. It was designed at the AEI in Hannover, and constructed at the Rutherford Appelton Laboratories, with support from the AEI and the University of Glasgow. The OB design of the flight model (FM) can be seen in Figure 2.3, the engineering model (EM) of the OB used in the ground setup can be seen in Figure 2.4. See also [33].

The subject of the laboratory investigations is the engineering model of the optical bench. From the results of experiments done by Felipe Guzmán Cervantes [34] the design of flight model was modified to avoid beam clipping. For example, the beamsplitter BS1 in front of TM1 was moved. The functionality of the two benches, FM and EM, is the same, such that investigations on the engineering model in preparation for the mission are applicable for the flight model. More design details and some of the experiments on the engineering model can be found in [35][29][36][37][38][39][40].

Four heterodyne Mach-Zehnder interferometers are bonded on the optical bench. The ground plate is made out of Zerodur, a material with high thermal stability. Unlike glue, bonding forms atomic bonds between the component and the baseplate, which leads to high stability. The two beams from the modulation bench with a frequency difference of f_{het} are sent to the optical bench. The beam hitting the test masses is called the measurement beam; it is
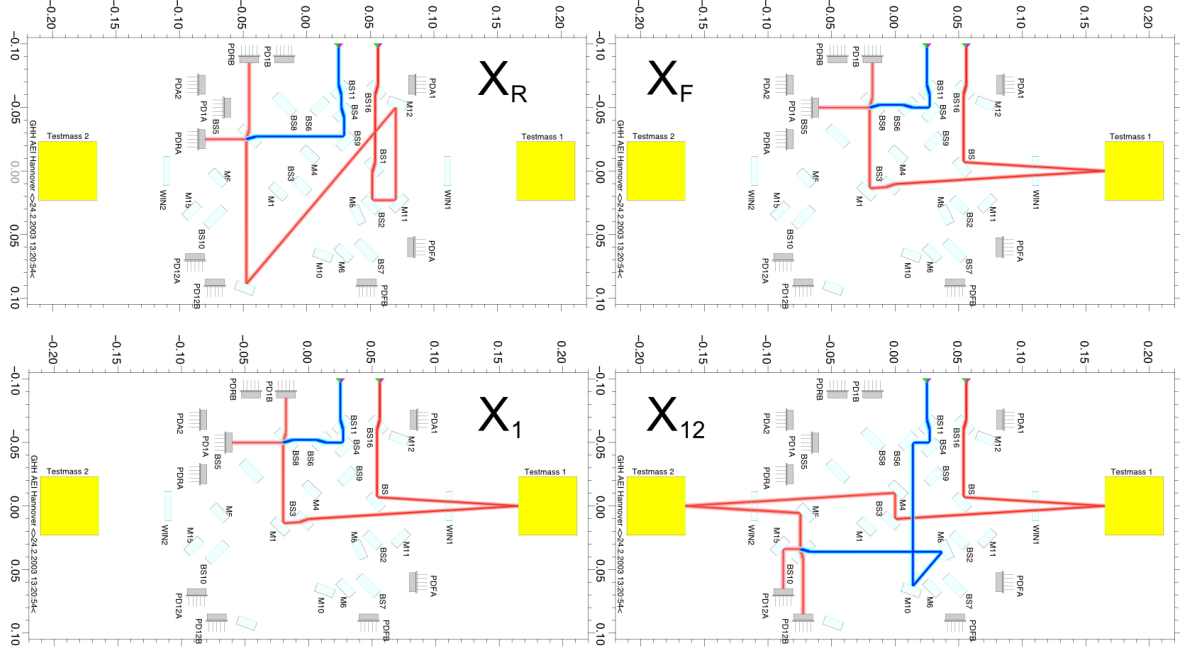
Figure 2.4.: This is the engineering model of the optical bench, it is used in the laboratory at the AEI for ground experiments. The flight model OB was designed from the lessons learned of this bench [34]. This picture was made by Gerhard Heinzel, and copied from [29]. To adapt this depiction to the others in this thesis the reference beam colour is changed to blue.

interfered at a recombination beamsplitter with the reference beam to create the heterodyne signal.

The interferometer used to measure motion of TM1 relative to the optical bench is named X_1. Relative movement of TM2 to TM1 is measured with the X_{12} interferometer, via $x_{12} = x_1 - x_2$ the motion of TM2 can be calculated.

The measurement beam and reference beam have the same optical path length when the TMs are in their nominal position at zero phase difference. Movement from the zero position leads to a pathlength change of the measurement beam, thus giving a phase difference between the two beams. This phase difference leads to a phase change in the heterodyne signal, which is recorded by the phasemeter. With this information the phase difference is calculated in post-processing, see Section 2.6. Both the symmetric and asymmetric port of the beamsplitters are used to measure the phase, see Section 2.1. The signals of both ports are combined to form the signal of one interferometer via balanced detection, see Sections 2.6.1 and 2.6.2.

The two outputs of the beam splitter are measured on quadrant photodiodes (QPD). The use of QPDs allows computation of the relative angle between the beams via a method called Differential Wavefront Sensing (DWS), which is used to calculate the angular orientation of the test mass, see Section 2.6.3. A graph of the test masses and the coordinate frame which defines the longitudinal axis and angular orientations can be found in Figure 2.5.

To suppress any phase changes not generated from motion of the test masses, two more interferometers are bonded on the optical bench. Like the measurement interferometers the reference interferometer X_R has no macroscopic path length difference. Its signal is used as input to the Optical Pathlength Difference loop (OPD loop), and to subtract remaining noise from the signals of the other interferometers.

To account for instabilities of the laser the frequency interferometer is included. An intentional arm length difference of $\approx 38 \, \mathrm{cm}$ allows a measurement of frequency noise. The signal of this interferometer is used as input to the frequency control loop. Amplitude fluctuations are measured with one single element photo diode per beam, these two signals are used as

input to a fast amplitude stabilisation control loop.

These components are best explained in context: in Chapter 4 more details about the control loops in the laboratory are shown. The OPD loop of the ground setup is shown in Section 4.1, the frequency loop of the ground setup is explained in Section 4.2. Experiments with the control loop of the flight OMS were performed during the mission, and analysed by colleagues [41][42].

On the ground, instead of free falling test masses mirrors mounted on piezoelectric actuators are used. These piezos allow longitudinal and angular motion. These two specific mirrors will be called test mass mirrors, TM mirrors or TM1 and TM2.
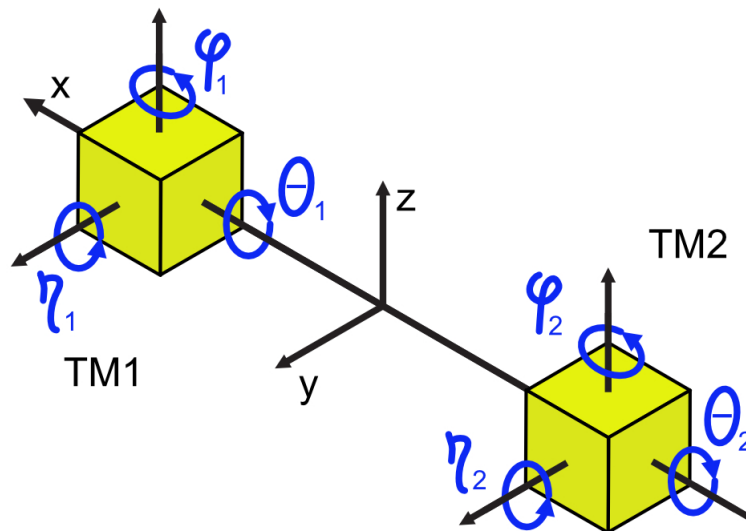
Figure 2.5.: Shown here are the two test masses, TM1 and TM2, together with the coordinate frame relative to the centre of the optical bench. Test mass motion is measured by the OMS, relative to this coordinate frame. In the flight model the position and orientation of the TM is also measured by capacitive sensing [43].

2.4. The laboratory setup - from an analog to a digital system

The previous laboratory setup used a vacuum tank with feedthroughs in the base. To open the tank the lid on the top had to be lifted with a crane. A scroll pump was used to pump the tank down. To keep the tank under vacuum, it was then connected to the house vacuum. This setup was used during the initial tests of the EM OB and the development of the analog control loops, and for the experiments during my master thesis [31].
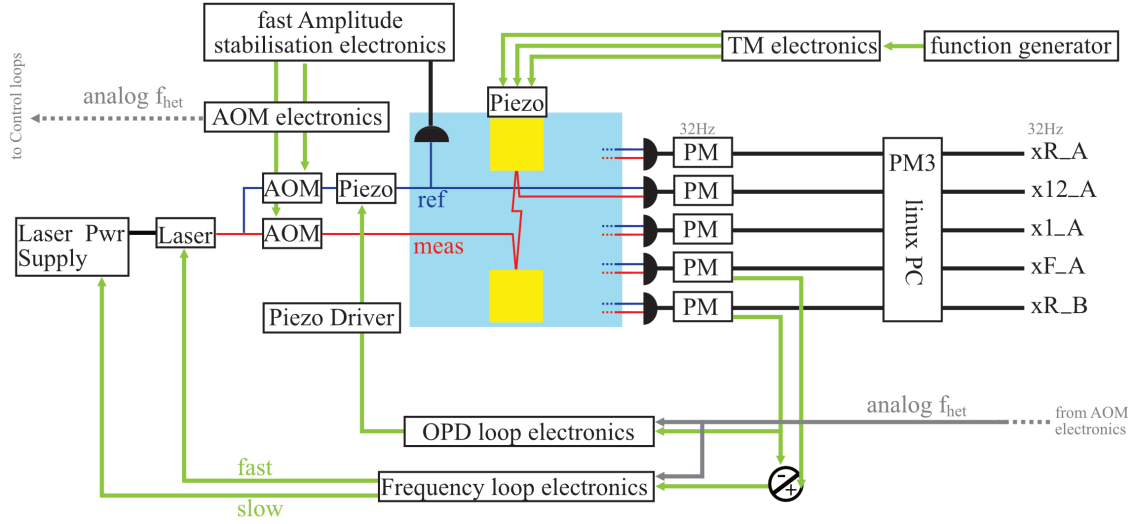
Figure 2.6.: This overview shows the analog control loops present in the old setup. The OPD, frequency and fast amplitude control loops each had their own electronics. The phasemeter has a voltage output from one reference interferometer diode and from one frequency interferometer diode, these are used as inputs for the OPD and Frequency control loop electronics. In addition to the depicted fast amplitude amplitude control loop on the reference beam the same was build on the measurement beam. The heterodyne frequency is generated by the AOM control and distributed to the control loops and the AOM electronics. The PM data is processed and saved by a Linux PC running the PM3 code.

One change in the setup is the use of a smaller and more convenient vacuum tank. The new tank was previously used for flight hardware, it is smaller, has more feed-throughs and a front-opening door. With a long vacuum tube a setup of a turbo pump and a scroll pump are connected, the pump setup is placed further away to reduce the vibrations on the optical setup. With the optical bench and all the cables inside, pressures of $\approx 10^{-5}$ mbar could be achieved.

Since the new tank already had feed-throughs installed, some of the cables were changed. The feed-through connectors are changed from two 50-pin connectors to two Allectra 37-pin sub-D connectors, making the external components easier to solder since these connectors have only two rows of pins, and not three. The inside components are vacuum compatible, with the cables of the OB photodiodes connected with crimp contacts. The connection to the Photodiodes on the bench uses a micro sub-D connector with 9 pins; two for each quadrant, and a connection to the shield.

The grounds of all quadrants are combined in the outgoing cable, and the signal of each quadrant is connected individually to the corresponding phasemeter channel. The cables from the tank to the phasemeter use the same round 5 pin connectors as before, and connect to the phasemeter in the same way. The shield of the diode is fed out of the tank in its own cable and connects to the shield of the phasemeter, therefore the connection between the shields of the diodes is through the phasemeter. In the connection from the PM to the
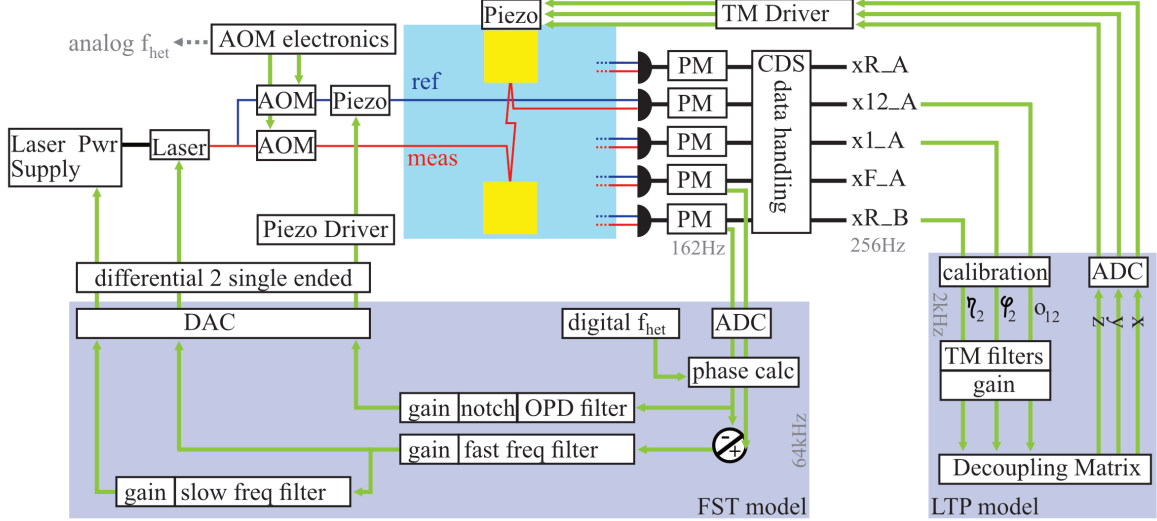
Figure 2.7.: This graph shows a part of the OMS Ground Setup, with almost all implemented digital control loops. The test mass control loops are implemented LTP model of CDS. Only the control loop for TM2 is shown, the control loop for TM1 is similar, and uses the same TM driver.
The OPD loop and frequency loop are implemented in the FST model. As input the same voltage output of the phasemeter as before is used. The heterodyne frequency as generated by the AOM electronics is recorded by the CDS, and is compared with the digital heterodyne frequency of the fast model, see also Section 2.6.4.

CDS the ground of the two are separated. The shields of all the diodes on the optical bench were connected with each other with wires, see Appendix A.1. These are removed, since these connections lead to ground loops when the amplitude stabilisation diodes (PDA) are connected. These PDA diodes are connected via transimpedance amplifiers to the CDS, while the other diodes are connected to the phasemeter.

Instead of a Linux computer to record the phasemeter measurement a Control and Data System (CDS) is used [44], this data acquisition and control system is used in advanced LIGO and also at the AEI in other experiments. The switch to CDS is described in Section 2.5. To process the data, the CDS runs models designed with the Simulink® GUI by MathWorks®, see Section 2.6.

While the laser and the modulation bench are placed on an optical table to suppress ground vibrations, the tank which contains the optical bench is not shielded from ground vibrations. Vibrations can lead to jitter of the TM mirrors. Some vibration suppression was achieved when the optical bench was placed on a baseplate, which rests on rubber feet. The best measurements were done over night, or over the weekend in a more quiet environment.

Reaching the required picometer precision is a challenging task, and control elements are needed to suppress various noise sources. The noise suppression methods through control loops will be explained in the following subsections; the three loops which were already present on the analog setup were mentioned when the optical bench was explained, see Section 2.3; further explanation can be found in Sections 4.2 and 4.1. The control loops on the test mass mirrors are explained in Section 4.3. An overview of all loops which were implemented in the analog setup is given by Figure 2.6, the digital loops can be found in Figure 2.7. With the digital setup the distribution of the 10 MHz reference frequency and of the heterodyne frequency needed to be changed, an overview of the frequency distribution can be found in Figure 2.8.
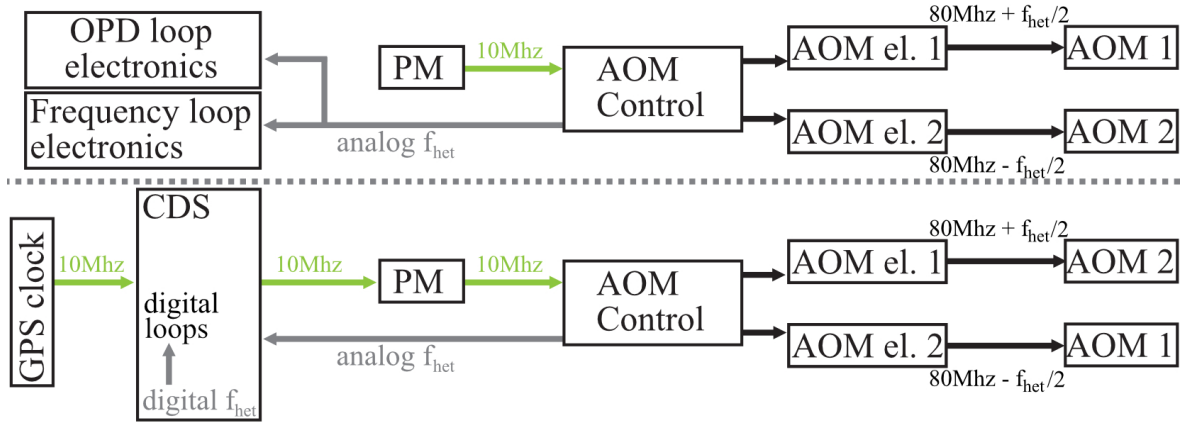
Figure 2.8.: This overview shows the frequency distribution of the analog (top) and digital setup (bottom). A 10 MHz signal is used as a reference clock. In the analog setup this signal is generated by the phasemeter and used as input to the AOM control to create the heterodyne frequency. The AOM Control sends an 80 MHz signal, a 5 MHz and $\frac{f_{het}}{2}$ to each of the AOM electronics.

In the digital setup the frequency distribution of the AOMs remains unchanged. To reduce the impact of sidebands on later RIN experiments the AOMs are switched, see Section 4.5. The phasemeter is switched from the origin of the 10 MHz reference signal, to receive this signal through CDS from a GPS reference clock. To calculate phase signals in CDS a digital heterodyne frequency is introduced. As verification this frequency is compared to the analog heterodyne frequency, see Section 2.6.4

2.4.1. Control loops – motivation for the change to digital

The AEI laboratory setup was successfully used for hardware development of the LPF mission, but the development and testing of in-flight experiments requires a better control and measurement.

This new digital system enables timed injections, with the same signal durations and frequencies as in the planned in-flight experiments. The data measured is not representative of the results expected in orbit, but functions as a testing ground for the data analysis, in addition to experiments from the simulator.

The planned injection frequencies of experiments on OPD and Frequency control loops could be tested with real data. With the new control loops on the TM mirrors planned experiments on the system identification of the test mass and its control loops could be tested in a safe environment.

Not only the experiments were tested, but a safe shut-down procedure of the OPD loop was tested in the laboratory and could be improved upon. Just turning the loop off would lead to a step back to the zero position of the OPD actuator. This step looks like rapid test mass motion to the TM control loops, and led to a fast counteraction to the end of the test mass mirror actuator range. This experiment carries no risk in a safe laboratory environment, unintended large and fast test mass motions could lead to unintended consequences if performed in flight. Most experiments presented in this thesis are performed with injection scripts, which enable long experiments where the test mass performs steps, or the amplitude or frequency of an injection are changed in regular intervals, see Sections 5.1, 5.2 and 5.3.

Not only would it have been very time consuming to do this by hand, but scripted injections also enabled repeated experiments, and the re-use of the same analysis scripts for the new data; and are especially helpful in experiments where data is recorded at a high sampling frequency, to keep the experiment timeline short. The scripts and experiments can be gradually improved upon and easily adapted to new ideas.

2.5. CDS and Simulink$^{\circledR}$ - data recording and processing

In the previous setup the data was recorded with a linux computer, which runs the PM3 code[1]. This C-code takes the data from the phasemeter output, and calculates the longitudinal and angular signals for each interferometer. For each measurement this code had to be started manually, and it could record data for a maximum of 48 hours.

As a new computer system for the LPF laboratory a small scale version of the AdvLigo Control and Data System (CDS) is used [44], with a code generator version RCG 2.8.3. This system was developed for Advanced LIGO [45]; the most recent version is named advligorts [46]. The CDS is able to acquire data, save it, and also to provide real-time output dependant on measured values and external inputs. An additional phasemeter interface (PMI) developed at the AEI is used to record the data from the phasemeter [47].

CDS is chosen as a base for our digital setup since people familiar with the system already work at the AEI, and can help with the implementation. Specifically GEO600 and the 10m-prototype also use a CDS system [48][49]. This system is able to handle the larger amount of data compared to the previous setup. This is necessary since more interferometer channels, not only the phase and DWS, are recorded, but also power and contrast, and also monitoring data for the digital control loops.

Using the PM3 code and available documentation the calculation of the longitudinal and DWS signals from the individual quadrant data is implemented in Simulink$^{\circledR}$ by MathWorks$^{\circledR}$. Simulink$^{\circledR}$ is a program with a simple graphical user interface (GUI) to model and simulate complex systems, the models build can be compiled to C-code and run on CDS. The possibilities to record and process data with the new CDS is a big improvement from the previous setup. Data can be recorded for arbitrary timespans, which enabled longterm stability experiments and experiments with more setup changes.

The LPF laboratory CDS consists of three models.

The LTP model (slow model) records and handles data at a sampling frequency of 2 kHz, and records the data of the phasemeter. The processing of the PM output, namely the calculation of the phase from the sine and cosine components of each quadrant and further processing to the longitudinal and angular channels, can be found in Section 2.6. To confirm the calibration of the new implementation a sine wave was injected into the OPD control loop, the longitudinal signal was recorded on the old linux setup and the new CDS setup. The measured amplitudes are the same, which confirms that the calibration is done the correct way. With this direct access to the calculation it was possible to de-bug the DWS calculation to remove phase jumps in the angular test mass signal. Also recorded with the CDS are the power and contrast of the diodes, which previously were only displayed in a live feed to adjust the system. Environmental channels, like the temperature and the pressure in the vacuum tank, are now also recorded. In this model the test mass control loops are implemented, see Section 4.3. This data is typically saved with a sampling frequency of 256 Hz.

The FST model (fast model) records data at 64 kHz. This model is used for the OPD and Frequency control loops. This model is also used to measure the power of the amplitude stabilisation diodes PDA to calculate the RIN, see Section 4.5. With the transition to CDS the data of the digital control loops, like loop input and output, as well as injected signals or noise, can now also be recorded and used to measure the transfer functions. In the FST model the control loop data is typically also saved with a sampling frequency of 256 Hz. Data for RIN experiments is saved with 16 kHz, or in demodulated form also with 256 Hz. The saved data has to be corrected for the lowpass filter of the downsampling, see Section 4.5.2 and [50].

A top level view of the OPD and Frequency control loop can be found in Figure 2.9. Shown

---

[1]This code was developed in-house, and ran on a Linux PC with a data acquisition board. Some details can be found in Chapter 6 of [34].
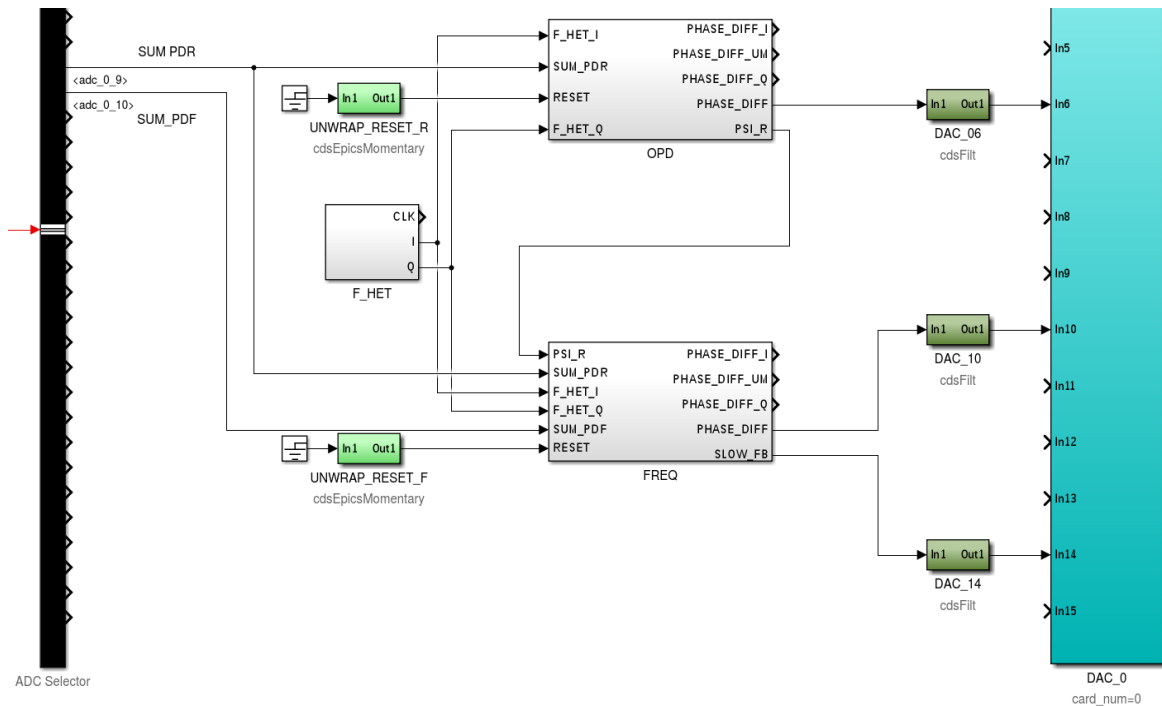
Figure 2.9.: Shown here is a screenshot of CDS FST model in Simulink®. Voltage signals of PD_R and PD_F from the phasemeter are measured by the ADC, shown on the left in black. The digital representation of these voltages are used as input to the OPD and frequency control loops, where the phase is calculated with the digital representation of the heterodyne frequency. The signal of the reference diode as computed by the OPD loop is also used as input to the frequency loop. The control output of these loops is fed as a differential voltage via the DAC, shown on the right in blue, out of CDS.

on the left is the ADC input to the fast model. Here the voltage output of one X_R diode and one X_F diode and the digital representation of the heterodyne frequency are used to calculate the phase signals PSI_R and PSI_F, which are used as input to the OPD and Frequency control loops. Inside the boxes with the labels OPD and FREQ the processing of the loops is placed. Details can be found in the respective sections. The output of the control loops is fed out of CDS via the DAC as a differential voltage, shown on the right hand side. These differential voltages are transformed to single-ended voltage signals, with electronics also placed in the CDS rack, and then used as input to the respective actuators.

The third model is the IOP model, it handles the communication of the other two models with the ADC and the DAC. This model has a sampling frequency of 64 kHz.
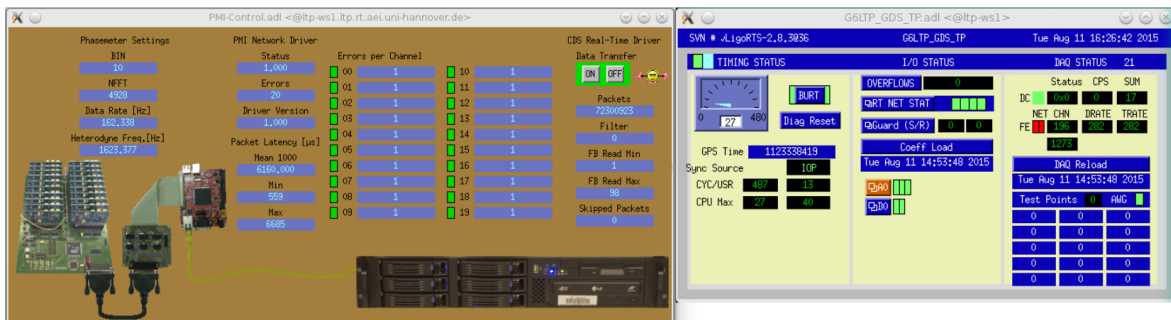
Figure 2.10.: These screenshots show part of the user interface of the LPF CDS setup. The left screen shows the status of the phasemeter: displayed on the left are the PM settings, like the sampling frequency and the heterodyne frequency. The right side of this display shows the status of the data transfer to the data recording with the phasemeter interface (PMI).

As an example the status display of the LTP model is shown on the right. The model interfaces for the FST model and the IOP model are similar. The left side of this display shows the status of the delay and synchronisation with the rest of the system. In the middle the status of the filters within is shown. Interesting in the day-to-day operations is the overflow counter, since it displays if any of the control loops has run out of range. Shown as green light with the labels AO and DO is the status of the ADC and the DAC. The right side shows the status of the data transfer to the storage system at the top, and the status of the signals created by the CDS and fed out by the DAC. Here, these signals are called test points. Each excitation receives an unique ID, which is shown in the overview that currently displays zeros. Via this ID individual signals can be terminated, if a problem occurs.

Similar displays show the status of the control loops, of the TM alignment and power distribution.

2.6. The phasemeter

The photocurrent from each QPD of the optical bench is transformed to a voltage by one transimpedance amplifier per quadrant. This voltage is then anti-alias filtered and recorded by one ADC channel per quadrant. In the flight PM the ADC has 16-bit, while the laboratory has an 18-bit ADC. One Field Programmable Gate Array (FPGA) is used to process the 4 signals from each QPD, it contains a digital signal processor which calculates the DFT at the heterodyne frequency. Since this frequency is known only one bin needs to be calculated. The result of this Single Bin DFT (SBDFT) is one complex vector $y_{i,\hat{j},k} + i \cdot z_{i,\hat{j},k}$ per quadrant, with these vectors the complex phase is calculated, see Section 2.6.1. The algorithm to calculate the longitudinal phase and angular signals from these complex values, for both the laboratory and flight setup, can be found in Sections 2.6.2 and 2.6.3. More information on the flight phasemeter can be found in [51].

The DC bin of the FFT is also calculated, this measurement can be calibrated to a measurement of the optical power. With the power measurement of the individual quadrants the spot positions of the beams on the QPD are calculated. This so-called Differential Power Sensing (DPS) signal is used to calculate the orientation of the test masses, this signal is used for initial alignment. The calculation of this signal is similar to the calculation of the TM orientation from the phase signals; more details can be found in [40].

The heterodyne frequency f_{het} in the laboratory is created by the AOM driver electronics from a $10\,\mathrm{MHz}$ reference signal. When the digital system was build the value for f_{het} from system documentation was used in the processing, a short explanation of the experiments performed to improve the precision can be found in Section 2.6.4.

To improve the phase signal at higher frequencies the transfer function of the window function of the phasemeter measurement can be corrected for, this phase correction is shown in Section 2.6.5.

2.6.1. Longitudinal phase measurement

In-flight processing

The processing of the flight data is described in different internal technical documents produced during satellite development, the phasemeter processing is described in [52]. A public description with a nice overview graph can be found in the thesis of Heather Audley [40], who got her doctorate at the AEI.

The photocurrents of the individual quadrants are converted to a voltage $V_{i,\hat{j},k}(t)$ with a transimpedance amplifier, these voltages contain the heterodyne signal. They are digitised by an ADC with a sampling frequency of $f_{sampling} = 50\,kHz$ to a digital representation $x_{i,\hat{j},k}(m)$. With a Single-Bin Discrete Fourier Transform (SBDFT) the real and complex amplitudes $y_{i,\hat{j},k}$ and $z_{i,\hat{j},k}$ of the $x_{i,\hat{j},k}(m)$ signal are computed by the phasemeter.

Here i is the label for the interferometer 1, 12, R or F; and $\hat{j}$ is the label for the quadrant of the diode, either A, B, C or D. The hat ˆ in the subscript $\hat{j}$ describes that the quadrants of the diodes have been re-labeled prior to the calculation of the balanced detection signal. The initial labeling of the quadrants is with respect to the front-view on the diodes. To account for the left-right switch in the beam walk of the measurement beam on the diode between the symmetric and asymmetric port the A-side diodes have their quadrant labels switched between left and right side. Due to the additional mirror placed after the recombination beamsplitter on the X_1 interferometer of the flight optical bench these labels are not switched, see [52] Chapter 4. For the laboratory setup no such re-labeling is done, since no balanced DWS signals are calculated.

The SBDFT calculates these components from the digitized voltage $x_{i,\hat{j},k}(m)$ with

$$y_{i,\hat{j},k} = \sum_{m=0}^{n-1} x_{i,\hat{j},k}(m) \cdot s_m, \tag{2.12}$$

$$z_{i,\hat{j},k} = \sum_{m=0}^{n-1} x_{i,\hat{j},k}(m) \cdot c_m, \tag{2.13}$$

$$d_{i,\hat{j},k} = \sum_{m=0}^{n-1} x_{i,\hat{j},k}(m). \tag{2.14}$$

The value $d_{i,\hat{j},k}$ of the DC bin is computed as well. The integer n is the length of the DFT $n = \frac{f_{sampling}}{f_{PM}}$. For the flight phasemeter the output sampling frequency is $f_{PM} = 100\,Hz$. Used here are sine and cosine parameters s_m and c_m, which were pre-computed on ground and are stored in a Look-Up-Table (LUT). These are calculated with

$$s_m = \sin\left(\frac{2\pi m k}{n}\right), \tag{2.15}$$

$$c_m = \cos\left(\frac{2\pi m k}{n}\right). \tag{2.16}$$

Where $k = \frac{f_{het} n}{f_{sampling}}$ is the number of the bin which would be used in a full FFT calculation. Relevant for the phase calculation is only the single bin which contains the heterodyne signal, therefore the complex amplitudes are only calculated for this bin, for each of the QPD quadrants. More information on the design of the phasemeter can be found in [51][53], see also [34].

From the SBDFT output the calibrated DC bin value $DC_{i,\hat{j},k}$ and the complex phase com-

ponents are calculated with

$$DC_{i,\hat{j},k} = c_{i,\hat{j},k}^{dc} \, d_{i,\hat{j},k} - c_{i,\hat{j},k}^{offset}, \tag{2.17}$$

$$Re\{F_{i,\hat{j},k}\} = c_{i,\hat{j},k}^{Ry} \, y_{i,\hat{j},k} + c_{i,\hat{j},k}^{Rz} \, z_{i,\hat{j},k} + c_{i,\hat{j},k}^{Rd} \, d_{i,\hat{j},k}, \tag{2.18}$$

$$Im\{F_{i,\hat{j},k}\} = c_{i,\hat{j},k}^{Iy} \, y_{i,\hat{j},k} + c_{i,\hat{j},k}^{Iz} \, z_{i,\hat{j},k} + c_{i,\hat{j},k}^{Id} \, d_{i,\hat{j},k}. \tag{2.19}$$

The $c_{i,\hat{j},k}$ coefficients were precomputed on ground: a total of $32\mathrm{x}8 = 256$ numbers with 32bit. Important for this discussion is the definition of the complex phase signals $F_{i,\hat{j},k}$ produced by the phasemeter outputs,

$$F_{i,\hat{j},k} = Re\{F_{i,\hat{j},k}\} + i Im\{F_{i,\hat{j},k}\}. \tag{2.20}$$

this digitised phase signal is used for further processing. The calculation of the real longitudinal phase in metres which is used for most of the analysis and the balanced detection signal calculation is shown Section 2.6.2. The definition and calculation of the real DWS signal from the complex phase of the individual quadrants can be found in Section 2.6.3.

Laboratory processing

The phasemeter was developed at the AEI, the laboratory unit functioned as a prototype for the development of the flight phasemeter [53]. It samples the photodiode signal with $f_{sampling} = 800\,\mathrm{kHz}$. This laboratory phasemeter only has 20 channels. Traditionally these were used to measure the phase signal of one quadrant photodiode per interferometer, with 4 spare channels to measure one additional QPD signal.

In the analog setup the 10 MHz reference signal was generated by the phasemeter and the AOM electronics used the PM output to generate the heterodyne signal. The old analog setup had a sampling frequency of the phase signal of $f_{PM} = 32.468\,\mathrm{Hz}$, with a heterodyne frequency of $\frac{10\,\mathrm{MHz}}{6160} \approx 1623.377\,\mathrm{Hz}$. Since the heterodyne frequency was generated electronically, and the resulting beatnote from the interfered beams was in the correct phasemeter SBDFT bin, it was not necessary to know the frequency with high precision.

After the switch to the CDS setup the sampling frequency output of the PM is increased to $f_{PM} = 162.33766234\,\mathrm{Hz}$, and after an investigation of the electronics the digital heterodyne frequency is set to $1623.37662338\,\mathrm{Hz}$. The 10 MHz reference signal is now generated by a GPS clock, and distributed to the 10 MHz input on the PM, the CDS and the AOM control electronics.

When the digital OPD control loop was implemented a drift in the reference interferometer was found, this drift is caused by a difference between the analog and digital heterodyne frequencies. After series of experiments with different heterodyne frequencies the digital heterodyne frequency is set to $1623.37658691\,\mathrm{Hz}$. In most plot labels and descriptions this value is shortened to $1.6\,\mathrm{kHz}$. A short description of this experiment can be found in Section 2.6.4.

The phasemeter gives the sine, cosine and dc component of each quadrant as output and the CDS records these outputs at 2 kHz and saves specific channels at 256 Hz. The phase and all following parameters are calculated in the LTP model.

The imaginary component of the phase signal of one diode is calculated from the sum of the sine components of the four quadrants. The sum of all four cosine values is used to calculate the real component of the phase signal. With the atan2 algorithm the real phase, φ_i, of interferometer X_i is calculated from the complex amplitude. This signal is then phase-tracked and saved. The calculated phase can only take values between between 0 and 2π, the phase-tracking algorithm accounts for phase changes bigger than 2π and smaller than zero

by counting the number of fringes traversed. This algorithm also removes sudden jumps of 2π.

The full calculations for one diode can be seen in Figure A.2, this calculation is implemented for each of the PM channels. The implementation of this processing in Simulink® can be seen in Figure A.3, both figures are in Appendix A.2.

The data is saved and used for further processing, with a name similar to G6:LTP-PM_1_PHASE_QPD_DQ. Where G6 is name of the CDS system, LTP the name of the model run in CDS and PM stands for signals from the phasemeter. The labels on the phasemeter output are mirrored in the name in Simulink®, namely 1, 12, R, F and X. All CDS channels saved are labelled with _DQ.

In the next sections the processing of the DWS signals and the subtraction of the reference signal is shown.

2.6.2. Balanced detection and subtraction of the reference phase

The LPF OMS is designed to allow subtraction of noise sources which were not suppressed. The processing for the laboratory and flight data is described in the following subsections. All interferometers measure both ports of the recombination beamsplitter, with the symmetric and asymmetric port of each interferometer named A side and B side. These two diodes are used for balanced detection, a short description of balanced detection can be found in [54]. The measured complex phase signal has a sign difference between A and B, whereas amplitude noise at the heterodyne frequency has the same sign on both diodes. With balanced detection the B port is subtracted from the A port and the signal adds linearly, while the amplitude noise is subtracted. Other uncorrelated noise sources add quadratically, which increases the signal-to-noise ratio by a factor $\sqrt{2}$.

The reference interferometer is not only used as input for the OPD loop, but also to subtract remaining noise common to all interferometers from the measurement signals and the frequency interferometer signal. Relative Intensity Noise (RIN) is not as easily subtracted with this processing, and calculations and experiments related to this are the main part of this thesis.

In-flight processing

In the flight unit the signals of both ports are subtracted from each other. The inherent sign difference of the signal in A and B doubles the signal strength while removing amplitude noise. The resulting signal has to be divided by two to recover the original phase measurement. During the calculation of the complex phase $F_{i,\hat{j},k}$ the so-called c-coefficients are used to account for the π phase difference between between A and B side, which is why the complex amplitudes are added here, and not subtracted [52]. The complex phase of the balanced signal is calculated with

$$F_{i,j} = \frac{1}{2}\left(F_{i,A,\hat{j}} + F_{i,B,\hat{j}}\right), \tag{2.21}$$

where the subscripts are defined the same way as described above. The label i denotes the interferometer, $\hat{j}$ the re-labeled quadrants and j the quadrant combined from the A and B port after re-labeling. The signal $F_{i,j}$ is often called a logical segment.

For the longitudinal signal of one interferometer the logical segments are summed, and then divided by the number of quadrants used. The resulting signal is called F_i. Noise which remains in the measurement signal is further reduced by subtracting the reference signal; both interferometers have balanced detection. To remove phase jumps of 2π, and to account for larger phase changes, a phasetracking algorithm (PT) is used. The final signals are calculated with

$$o1 = \frac{\lambda}{4\pi\cos(\alpha)}\text{PT}\left(\arg\left(\frac{F_1}{F_R}\right)\right), \qquad \text{[m]} \qquad (2.22)$$

$$o12 = \frac{\lambda}{4\pi\cos(\alpha)}\text{PT}\left(\arg\left(\frac{F_{12}}{F_R}\right)\right), \qquad \text{[m]} \qquad (2.23)$$

$$xF = \frac{c}{2\pi\delta L}\text{PT}\left(\arg\left(\frac{F_F}{F_R}\right)\right), \qquad \text{[Hz]} \qquad (2.24)$$

$$\varphi_R = \text{PT}\left(\arg\left(F_R\right)\right). \qquad \text{[rad]} \qquad (2.25)$$

Where $\frac{\lambda}{2\pi}$ converts the optical pathlength change from radian to metres. Due to the reflection at the test mass, double the motion is measured and an additional factor $\frac{1}{2}$ accounts for this. λ is the wavelength of the laser. The angle α is the angle of incidence of the measurement beam on the test mass. For the flight optical bench this angle is $\alpha \approx 4.5°$[34].

The frequency interferometer signal xF is scaled from the raw measurement in radian φ_F to the frequency noise measurement of the laser in Hz with the parameter $\frac{c}{2\pi\delta L}$, where $\delta L = 38\,\text{cm}$ is the pathlength difference of X_F.

A nice summary of the phasemeter processing can be found in Heather Audley's thesis [40] and the official description can be found in a technical note [52].

The data from the in-flight experiments almost always is the o12 or o1 signal, as well as the reference signal φ_R. Available on ground are the real signals at a sampling frequency of either $10\,\text{Hz}$ or $1\,\text{Hz}$. Since the subtraction is performed at the original $100\,\text{Hz}$ sampling frequency and in the complex domain, it is not possible to recover the x1 and x12 signals, or individual A and B diodes, with the data available.

Laboratory processing

The laboratory setup does not natively feature balanced detection since the phasemeter only has 5 ports, one for each of the interferometers and a spare channel. For each diode the phase signal is calculated individually from the complex values. Since this algorithm is independent of the diode chosen the phase signal of A and B port computed from the heterodyne signal have the same sign, and the amplitude noise at the heterodyne frequency has a sign difference. In this case the two signals have to be added for balanced detection.

Any of the interferometer diodes can be connected to any of the PM inputs. In later experiments the X_{12} interferometer is disconnected in favour of both X_1 interferometer channels to enable comparison of the A and B sides, for most of the later RIN experiments the diodes chosen can be found in Table 2.1. For X_1 and X_R both the A and B side phase signal are calculated, and recorded in CDS with a sampling frequency of $256\,\text{Hz}$. The calibration to metres, the balanced signal, and the subtraction of the reference signal is calculated in MATLAB® using LTPDA [22].

$$x1[\text{m}] = \frac{\lambda}{4\pi\cos(\alpha)}\varphi_1[\text{rad}], \tag{2.26}$$

$$x12[\text{m}] = \frac{\lambda}{4\pi\cos(\alpha)}\varphi_{12}[\text{rad}], \tag{2.27}$$

$$xR[\text{m}] = \frac{\lambda}{4\pi}\varphi_R[\text{rad}] \tag{2.28}$$

$$o1[\text{m}] = \frac{\lambda}{4\pi\cos(\alpha)}(\varphi_1[\text{rad}] - \varphi_R[\text{rad}]), \tag{2.29}$$

$$o12[\text{m}] = \frac{\lambda}{4\pi\cos(\alpha)}(\varphi_{12}[\text{rad}] - \varphi_R[\text{rad}]), \tag{2.30}$$

$$xF[\text{Hz}] = \frac{c}{2\pi\delta L}(\varphi_F[\text{rad}] - \varphi_R[\text{rad}]). \tag{2.31}$$

The angle of incidence on the test mass of the optical bench in the laboratory is $\alpha \approx 3.6°$, due to it being the engineering model of the optical bench and not the flight model [34]. To make comparisons with the other interferometers signals easier the reference interferometer phase φ_R is calibrated to displacement using the parameter where the measurement beam is reflected on the TM, and not with the correct calibration parameter $\frac{\lambda}{2\pi}$. This processing is the same for the phase of a single port, $\varphi_{i,A}$ or $\varphi_{i,B}$, and the balanced signal φ_i.

PM port	QPD
1	PD1_A
12	PD1_B
R	PDR_B
F	PDF_A
X	PDR_A

Table 2.1.: This table shows the connected diodes for most of the experiment shown in this thesis. The laboratory phasemeter only has 5 channels, the X_{12} interferometer is not connected to enable balanced detection for X_1.

The processing in the laboratory is different from the flight data. The balanced and subtracted signals are calculated from the real phase φ_i, whereas in the flight processing this subtraction is done with the complex phases $F_{i,\hat{j},k}$. The whole calculation for the laboratory version of the o1 signal is

$$\mathrm{o1} = \frac{1}{2}\Big(\mathrm{PT}\left(\arg\left(F_{1,\ \mathrm{A}}\right)\right) + \mathrm{PT}\left(\arg\left(F_{1,\ \mathrm{B}}\right)\right)\Big) - \frac{1}{2}\Big(\mathrm{PT}\left(\arg\left(F_{\mathrm{R},\ \mathrm{A}}\right)\right) + \mathrm{PT}\left(\arg\left(F_{\mathrm{R},\ \mathrm{B}}\right)\right)\Big). \quad (2.32)$$

Analytically, this calculation is the same as for the in-flight processing.[1] In practise, the aliased noise level will be higher in the laboratory than in flight, as noise at higher frequencies is not subtracted before the signal is downsampled to $10\,\mathrm{Hz}$ from the recorded frequency. This problem could be avoided: the data of the laboratory setup is analysed at the initial sampling frequency of $256\,\mathrm{Hz}$, and does not include aliased noise.

---

[1]For small DWS offsets. For bigger DWS offsets the A and B port are not equal, and the two processing types will yield different results.

2.6.3. DWS measurement
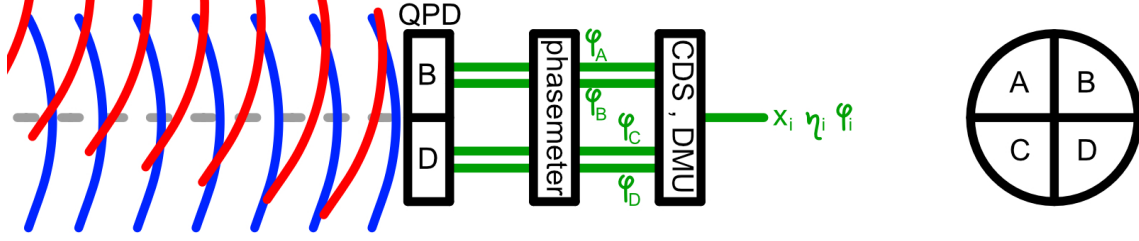
Figure 2.11.: Shown here is an illustration of Differential Wavefront Sensing (DWS). The measured phase on the four quadrants A, B, C, D differs depending on the angle between the two beams. Using this phase difference the angle between the incoming beams can be calculated.

The angular jitter of the test mass is important information during flight for the Drag Free and Attitude Control System (DFACS), and can also be used to subtract cross-coupling from angular jitter to longitudinal phase in post processing. From the signals of the individual quadrants of the QPD the orientation of the test masses can be calculated. Each quadrant measures a phase $\varphi_{i,j,k}$. If the two beams are not parallel when they reach the diode the quadrants will measure different phases. With this information the angle between the two beams can be calculated. Since the measurement beam is reflected of the test masses, their orientation with respect to the optical bench can be calculated [29][55]. The angles of the TM measured by DWS are called φ_i and η_i, see also Figure 2.5. In this overview of the PM processing this creates confusion with the longitudinal phase signals φ_i, due to additional labels the distinction between the two in the implemented processing is clear.

In-flight processing

In flight the DWS signals are calculated from the complex amplitudes $F_{i,j}$, which are already the balanced signals of quadrant j of interferometer X_i. The left, right, up and down components of DWS are calculated for each interferometer. For example the left component is calculated as $F_i^{\text{Left}} = F_{i,A} + F_{i,C}$, the calculation of the other component is obvious. As the reference beam hits the diodes with normal incidence the DWS_i signals represent the orientation of the measurement beam on the diodes of one interferometer, with

$$\text{DWS}_i^{\varphi} = \arg\left(\frac{F_i^{\text{Left}}}{F_i^{\text{Right}}}\right), \tag{2.33}$$

$$\text{DWS}_i^{\eta} = \arg\left(\frac{F_i^{\text{Up}}}{F_i^{\text{Down}}}\right). \tag{2.34}$$

The calibration to calculate the orientation of the test mass from the measurement beam angle measured on the QPDs was done in Glasgow. The calibration parameters g_j are different for the engineering model and flight model optical bench and were measured on ground [52]. In flight the test mass orientation DWS signals are calculated with:

$$\varphi_1 = g_1 \cdot \text{DWS}_1^{\varphi}, \tag{2.35}$$

$$\eta_1 = g_2 \cdot \text{DWS}_1^{\eta}, \tag{2.36}$$

$$\varphi_2 = g_3 \cdot \text{DWS}_1^{\phi} + g_4 \cdot \text{DWS}_{12}^{\phi}, \tag{2.37}$$

$$\eta_2 = g_5 \cdot \text{DWS}_1^{\eta} + g_6 \cdot \text{DWS}_{12}^{\eta}. \tag{2.38}$$

Laboratory

The laboratory OMS does not use balanced detection for the individual quadrants, the DWS signal is calculated for individual diodes [34]. The complex phasemeter output of the individual quadrants is used for the DWS calculation, with

$$\text{DWS}_i^{\varphi} = \arg\left(\frac{\zeta_A + \zeta_C}{\zeta_B + \zeta_D}\right), \tag{2.39}$$

$$\text{DWS}_i^{\eta} = \arg\left(\frac{\zeta_A + \zeta_B}{\zeta_C + \zeta_D}\right), \tag{2.40}$$

where ζ_i is the complex phase of quadrant i. This signal is then phasetracked, and used for further analysis. The orientation of the TMs is calculated from the DWS signals in the same way as in the flight OMS, the g_j coefficients are different for the EM OB.

This calculation has been implemented using Simulink® in the LTP model, screenshots can be found in Appendix A.2. A screenshot of the processing of the DWS signal can be seen in Figure A.4. The old DWS calculation with occasional phase jumps described in [34] is marked in green, the implemented improved calculation is marked in red. The calculation of the TM orientation from the DWS signal can be found in Figure A.5.

Similar to the calculation of the DWS signal the Differential Power Sensing (DPS) is implemented. From the distribution of power on the quadrants the spot position of the measurement beam can be derived. This DPS signal can be calibrated to a measurement of the test mass orientation. The implementation of this calculation in the LTP model can be found in Figure A.6.

2.6.4. Phasemeter heterodyne frequency change

To calculate the phase signal of the reference and frequency interferometer from the voltage output of the phasemeter for the input signal to the digital control loops a digital version of the heterodyne frequency is implemented. To create the frequency difference of the two beams the (analog) heterodyne frequency of the AOM electronics is used, this analog frequency is also used for the phasemeter processing.

In the initial phase after the switch from the analog setup to the digital setup the digital heterodyne frequency in CDS was set to 1623.377 Hz, and the data output of the phasemeter was still set on 32 Hz. Shortly after this initial setup the heterodyne frequency of old lab reports was used, $f_{het} = 1623.37662338$ Hz, together with an increased data output rate of the phasemeter of 162.33766234 Hz. When the OPD loop was implemented and turned on, a slow drift in the reference interferometer signal was found. This drift was a beatnote between the digitally implemented heterodyne frequency and the analog heterodyne frequency of the AOM. The cause for this difference was not found, the first heterodyne frequency matches the expectation from the implemented electronics, where the frequency is generated from a 10 MHz signal which is reduced in frequency by a factor 6160. A reason might be a problem in CDS with the generation of the signals using the fractional phase algorithm. To match the analog heterodyne frequency the digital heterodyne frequency needs to be changed.

An extra channel was created, which compared the analog and digital signal against each other, see Figure 2.12. Initial analysis revealed a signal at $3.762 \cdot 10^{-5}$ Hz. To match the analog and digital f_{het} the digital heterodyne frequency needs to be changed by $3.762 \cdot 10^{-5}$ Hz, not known from this measurement is if this frequency offset has to be added or subtracted.
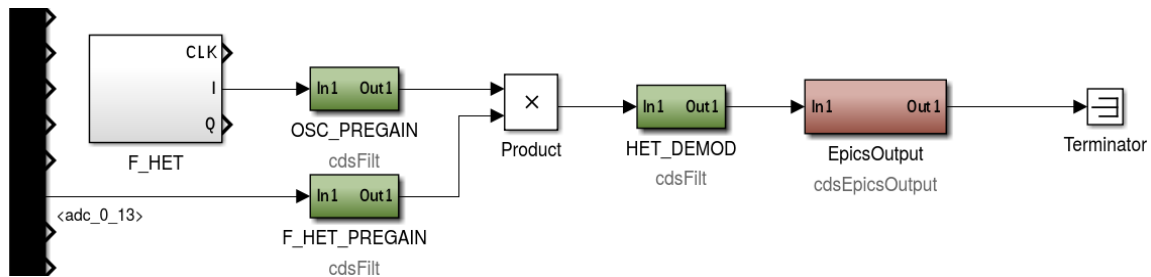
Figure 2.12.: Shown here is the circuit to create the beatnote between the analog heterodyne frequency, implemented via Simulink® in the FST model. The digital f_{het} is connected to the channel OSC_PREGAIN, the analog f_{het} is measured with and ADC channel of the FST model, and the handed to F_HET_PREGAIN. The beatnote between the two is the channel HET_DEMOD, this signal is used in the following analysis.

An experiment was performed to change this offset, at first the step size was small for safety reasons. With these conservative step sizes it was obvious that the frequency change needed to be positive one.

As a test, the heterodyne frequency is changed by $+3 \cdot 10^{-5}$ Hz and after an hour to $+4 \cdot 10^{-5}$ Hz for another hour. On 2018-01-08 16:56 UTC the heterodyne frequency is set to the new value. With the data available from 2016-01-08 17:00 UTC till 2016-01-18 17:00 UTC a new estimate for the error between analog and digital heterodyne frequency was made, the first two zero-crossings happened on 2016-01-09 09:06 and 2016-01-14 09:34, which is a timespan of 120,5 hours, or a frequency of $1.15 \cdot 10^{-6}$ Hz.

The beginning of this measurement can be seen in Figure 2.13, together with the previous measurements.
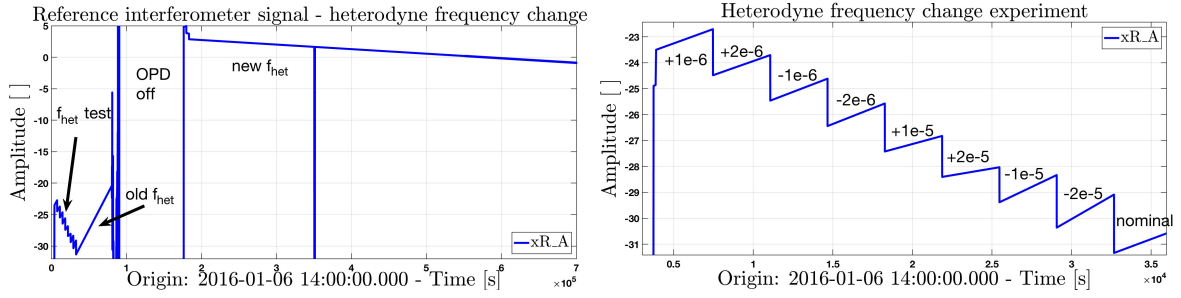
Figure 2.13.: Shown here is the time series of the xR_A signal during the heterodyne frequency change experiments. The left plot shows the experiment where f_{het} is changed. After this experiment f_{het} is returned to the original value. During the data analysis the OPD loop was turned off, and the xR_A signal is out of frame. Then f_{het} is changed to the new value. A closer look at the frequency change experiment is shown on the right.

As there was still a drift after the correction, a 20 day stretch of data of the beatnote between analog and the initial digital heterodyne frequency was to calculate the frequency. A plot of this spectrum can be seen in Figure 2.14. The beatnote was measured at $3.646 \cdot 10^{-5}$ Hz, this frequency difference was used to correct the heterodyne frequency with $f_{het\,new} = f_{het\,old} + 3.646 \cdot 10^{-5}$ Hz $= 1623.376\,586\,91$ Hz. This change was made on 2018-01-18.
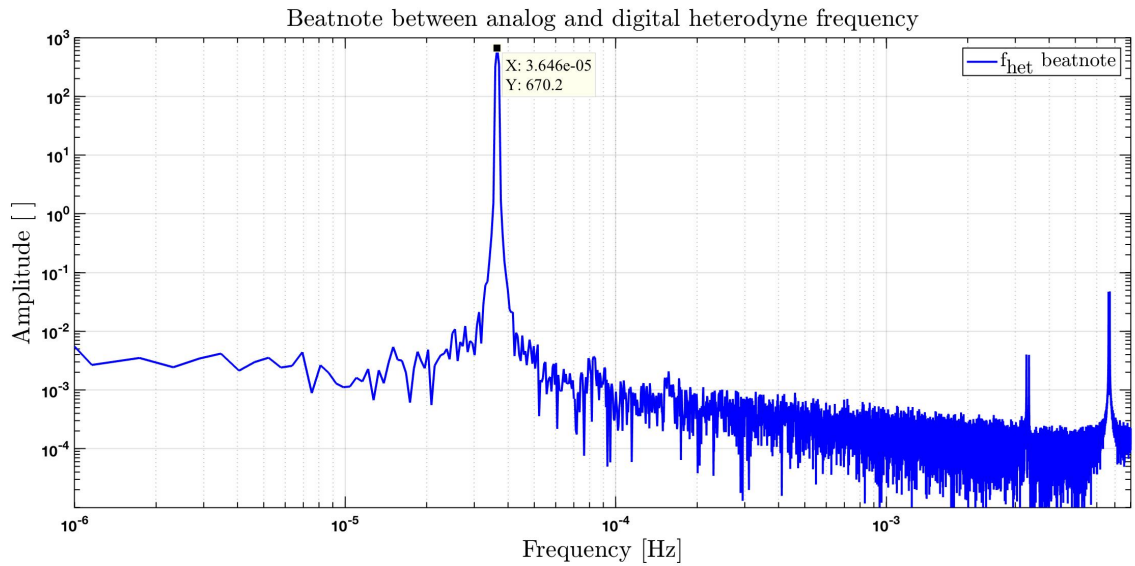
Figure 2.14.: This is the amplitude spectrum of a 20 day measurement of the demodulation signal. The spectrum is calculated over the whole timespan to get the frequency with the highest precision. The peak amplitude is of no concern here.

2.6.5. Phasemeter sinc filter correction
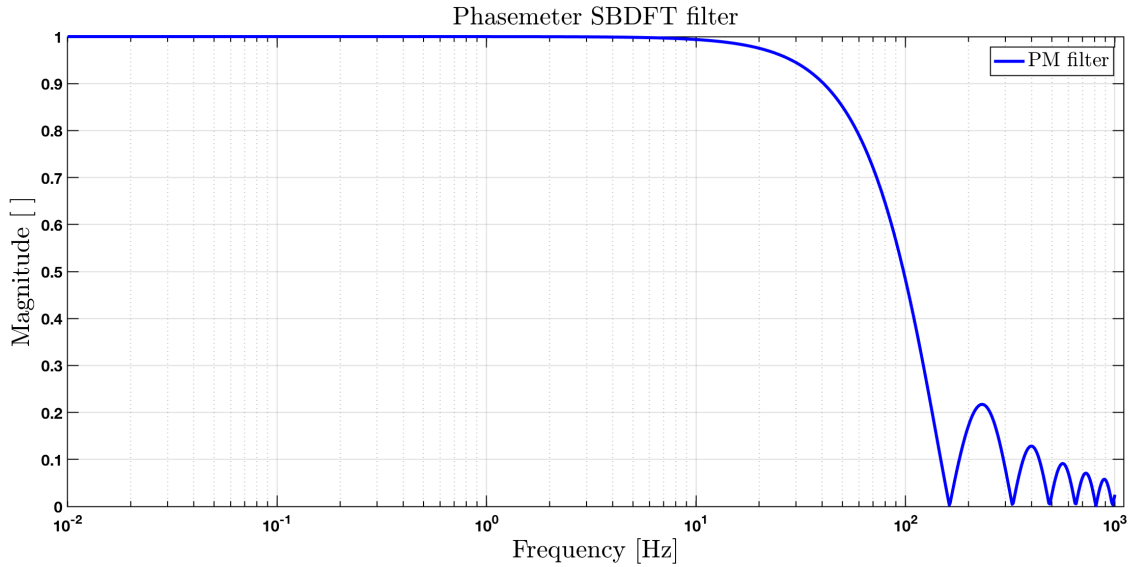
Figure 2.15.: This is a plot of the transfer function of the phasemeter single bin DFT filter. The value of this transfer function at 10 Hz is ≈ 0.994, the value at 20 Hz is ≈ 0.975. The highest frequency under analysis is 60 Hz in the RIN frequency experiment, see Section 5.2. The filter at this frequency has a value of ≈ 0.789.

The phasemeter data is corrected in post-processing for the transfer function of the single bin DFT. The frequency response of the DFT window can be described as:

$$\mathrm{PM\_filter(f)} = \mathrm{abs}\left(\frac{\sin(\mathrm{N}\,\pi\,\mathrm{f}\;\mathrm{fs})}{\mathrm{N}\,\sin(\pi\,\mathrm{f}\;\;\mathrm{fs})}\right). \tag{2.41}$$

Where N = 4928, and the sampling frequency is fs = 800 kHz, for the laboratory setup. This correction is not necessary for most measurements, as the frequency range of interest in traditional pathfinder experiments is in the milihertz range, where the error made due to the PM is negligible.

In experiments presented in this thesis signals are often above 10 Hz, and the correction should be taken into account. The amplitude spectral density $\mathrm{a_{asd}(f)}$ of the interferometer signal will be corrected with

$$\mathrm{a_{asd,\,corrected}(f)} = \frac{\mathrm{a_{asd}(f)}}{\mathrm{PM\_filter(f)}}. \tag{2.42}$$

Any results of a DFT calculation at a frequency $\mathrm{f_{DFT}}$ will be corrected with $\mathrm{PM\_filter(f_{DFT})}$. For the correction of power spectral densities $\mathrm{a_{psd}(f)}$ the filter function must be squared.

3   OMS phase noise contributions

This chapter gives a short explanation of the most relevant noise sources of the Optical Metrology System (OMS). Most of these were well known before the in-flight operations, and the work to describe and mitigate them was done by others. These noise sources are mentioned for context and completeness sake, see also [32][36][29][34][37][40][56].

First, the noise contributions which can be suppressed by control loops are shown. The coupling of OPD noise, Section 3.1, and Frequency noise, Section 3.2, to the phase is well understood.

Amplitude noise near the heterodyne frequency f_{het} and radiation pressure noise are briefly mentioned in Section 3.3. In the laboratory, amplitude noise was suppressed with a control loop in the analog setup, but not in the current digital setup. In the flight OMS this amplitude noise is suppressed with the fast amplitude control loops. New is the description of Relative Intensity Noise (RIN) near $1f_{het}$ and $2f_{het}$, with more detailed calculations for coupling and suppression in Section 3.4. This analysis was done together with Lennart Wissel (AEI), who has the initial findings for RIN in the DWS measurement in his masters thesis [57].

The sensing noise of the phase measurement is explained in Section 3.5. The coupling of ADC noise, the noise of the transimpedance amplifier electronics of the photodiodes and shot noise to the phase measurement are known, the difficulty lies in adapting the formulas to the system at hand.

To create a more complete overview of the noise contributions to the LPF optical measurement, additional noise sources are mentioned briefly in Section 3.6; these contributions were analysed by other members of the LPF team. An overview of the LPF OMS sensor noise of the in-flight measurement can be found in [19].

3.1. Optical Pathlength Difference noise

The interferometers measure pathlength fluctuations between the measurement beam and the reference beam, the intended measurement is the motion of the test masses. However, the pathlength difference between the two beams might also change due to environmental reasons. Both beams have the same origin and are split on the modulation bench, pass through their own AOM and are sent to the optical bench via optical fibres. Any pathlength fluctuations on the beams before they reach the stable optical bench are measured in all interferometers. This phase noise is called Optical Pathlength Difference noise (OPD noise). These fluctuations are measured in the φ_R signal by the reference interferometer X_R, this signal is used as input to the OPD control loop. A description of this loop can be found in Section 4.1.

Since X_R has a macroscopic pathlength difference of zero, like the measurement interferometers X_1 and X_{12}, remaining OPD noise can be subtracted. This reference measurement is also subtracted from the frequency interferometer signal. This noise subtraction is part of the processing as shown in Section 2.6.2.

3.1.1. Small Vector Noise

Small Vector Noise (SVN) is different from the optical pathlength changes mentioned earlier. This noise source was long known and is well studied. In the LISA project this noise source was first described in a meeting by D. Robertson, it had been seen in the AEI and Glasgow optical setups as early as 2002. This effect was studied further at the AEI together with Glasgow scientists, and was the topic in technical notes, see [32][58], and PhD theses at the AEI [29][36][34][37].

This noise source originates from sidebands on the light introduced by electrical cross-coupling from the AOM driving signal, a description of this coupling process can be found in S2-AEI-TN-3028 [32]. The coupling of this noise source to the phase signal depends on the pathlength difference between measurement beam and reference beam. The OPD loop, see Section 4.1, stabilises this pathlength and reduces the impact of this noise source on the phase measurement.

It should be noted that the coupling formulas of this noise source are of a similar type as for Relative Intensity Noise (RIN), the phase difference of interest in the latter is between measurement and reference interferometer. The source for both noise sources are sidebands on the light, but the coupling to the phase is different. As this noise source is well studied, it was also well suppressed for the flight unit. In a dedicated experiments where the OPD actuator is moved to create a phase difference this contribution was measured. The design and analysis of these flight experiments were lead by Dr. Michael Born, AEI; results of these experiments will be published in an upcoming paper [59].

In laboratory experiments, where the AOMs are used to inject RIN via the amplitude stabilisation, an additional SVN component is created. More details can be found in Section 5.1.4.

3.2. Frequency noise

In the LPF OMS laser frequency noise $\delta\nu$ couples to pathlength noise with

$$\delta x_{\text{freq}} = \frac{\delta\nu}{\nu}\delta L. \qquad\qquad \left[\frac{\text{m}}{\sqrt{\text{Hz}}}\right] \qquad\qquad (3.1)$$

The displacement noise δx_{freq} caused by frequency noise $\delta\nu$ depends on the path length difference δL between the measurement and reference beam, see also [32] Chapter 12 and [36].

To reduce the coupling of frequency noise to the measurement interferometers X_1, X_{12} and the reference interferometer X_R they were designed to have no path length difference.

The actual path length difference between the two beam paths is caused by alignment and construction errors. The frequency stability requirements were calculated with a worst-case value of $1\,\text{cm}$ difference. From in-flight experiments the pathlength difference between the measurement interferometers and X_R was measured to $\approx 350\,\mu\text{m}$ for o_{12} and $\approx 140\,\mu\text{m}$ for o_1 [41], which is much better than the worst case assumption.

With the frequency interferometer X_F frequency noise is measured, it has an intentionally large path length difference of $\delta L \approx 38\,\text{cm}$ between measurement and reference beam to increase the noise coupling. From the signal φ_F the reference signal φ_R is subtracted, the resulting signal xF is used as input to the frequency control loops.

The laser in the laboratory setup is a `Mephisto 500` from `Innolight` [60], it has two inputs to change the frequency of the light. The frequency control loop has a fast and a slow component, it is described in more detail in Section 4.2.

A description of the flight frequency control loops and the characterisation experiments performed can be found in the PhD thesis of Sarah Paczkowski (AEI) [41].

3.2.1. Subtraction of frequency noise

With the measurement of remaining frequency noise in X_F its contribution to the science measurements can be further reduced, in most cases the change is little and only in a small frequency range. The transfer function from frequency noise in the xF signal to o1 and o12 can be calculated with the `ltfe` function. This function is part of LTPDA and estimates the transfer function on a logarithmic frequency axis, the calculation is based on [23].

The mean value C of this transfer function in the frequency range where frequency noise contributes is calculated. For laboratory measurements this region falls typically between $0.2\,\text{Hz}$ and $0.9\,\text{Hz}$.

This coupling coefficient, C, can be used to calculate the time series of frequency contribution to the science measurement. Remaining frequency noise can be then be removed by subtracting the noise time series from the measurement with

$$\text{o12}_{\text{f}}(\text{t}) = \text{o12}(\text{t}) - C \cdot \text{xF}(\text{t}). \qquad\qquad (3.2)$$

In a sensing noise overview a spectrum of the frequency noise contribution $C \cdot \text{xF}$ can be shown along with the phasemeter noise. This contribution to the sensing noise in the laboratory OMS is shown in Section 4.4. In Section 6.4.2 the frequency noise contribution of one flight experiment is shown.

3.3. Amplitude noise

In the previous chapter the laser power on one photodiode was calculated, see Section 2.1. For this calculation the beam amplitudes E_m and E_r were assumed to be constant. An important aspect of the OMS noise is the noise on the laser amplitude

$$E_i(t) = E_i + \delta E_i(t). \qquad\qquad i = \{\text{m, r}\} \qquad\qquad (3.3)$$

Amplitude noise around the heterodyne frequency f_{het} couples into the phase measurement as it is present in the same phasemeter FFT bin used to calculate the phase signal. This noise coupling is best described as a Relative Intensity Noise (RIN). The coupling from RIN near $1f_{\text{het}}$ was known previously, however RIN near $2f_{\text{het}}$ also couples to the phase signal. A description of the coupling of both can be found in Section 3.4.

A control loop was designed to suppress amplitude noise around the heterodyne frequency. Two single element photodiodes PDA_1 and PDA_2 are placed on the optical bench to measure the amplitude noise. These diodes are placed as the first components after the fibre output couplers, see Figures 2.3 and 2.4. The previous analog setup of the ground setup had one fast amplitude control loop per beam. The photocurrent

$$I(t) = \text{R}_{\text{PD}} \cdot E_i(t)^2 \qquad\qquad = I_{\text{DC}} + \delta I(t) \qquad\qquad (3.4)$$

of both PDAs was sent to one control circuit per beam, where it is transformed to a voltage $U(t)$ with a transimpedance amplifier. The photodiode responsivity R_{PD} is the parameter to calculate the photocurrent from the laser power on the diode.

With the subtraction of the DC offset and a bandpass around the heterodyne frequency the input signal to the control loop was created. This voltage $\delta U(t)$ was then amplified and connected to the amplitude control input of the AOMs [32][61].

A very small loop delay is critical for this control loop to work. The accumulated delay when this loop was implemented in the digital setup was too large; the design and build of additional electronics was abandoned due to higher priority mission operation tasks. Therefore the electronics from the previous analog setup are used.

With the parts implemented the voltage from the amplitude stabilisation diodes can be recorded. With a transimpedance amplifier the photocurrent of the two PDA diodes are converted to voltage and connected to one ADC per beam of the CDS FST model. The input of the AOM driver electronics formerly used for the amplitude stabilisation can be used for noise and signal injections on the laser amplitude. These inputs are used for Relative Intensity Noise experiments, further discussed in Chapter 5.

For the flight setup a fiber-coupled Nd:YAG non-planar ring oscillator (NPRO) laser at a wavelength of 1064 nm with an output power of $\approx 35\,\text{mW}$ was used [40]. In the flight OMS the amplitude noise had to be reduced by careful selection of the laser operating point. The laser settings were scanned over temperature and injection current in search for a setting with low noise.

The laser itself has an amplitude stabilisation implemented, the details of this control loop are proprietary manufacturer information. To suppress noise around the heterodyne frequency the fast amplitude stabilisation was implemented in the flight setup. The slow amplitude control loop acts on the laser current, and the slow frequency control loop acts on the laser crystal temperature. Since actuation of these changes the RIN of the flight laser these loops were not used.

3.3.1. Radiation pressure noise

One of the forces acting on the free-falling test masses of the flight setup is the radiation pressure of the laser beam.

The laser pressure acts as a force that pushes the test mass away from the centre of the optical bench, noise in the laser power acts as a force noise on the test masses.

This force change on the test mass due to laser power changes was used by Brigitte Kaune (AEI) to calculate the reflectivity of the test masses [62].

In the in-flight measurement radiation pressure noise is a minor contribution to the noise below $1\,\mathrm{mHz}$, the acceleration noise caused is in the order of $2\,\frac{\mathrm{fm\,s^{-2}}}{\sqrt{\mathrm{Hz}}}$ [18].

Radiation pressure noise is not a problem in the ground setup, since the test mass mirrors are fixed to the housing of the optical bench.

3.4. Relative Intensity Noise

Relative Intensity Noise (RIN) is a property of the laser. This amplitude noise on the light is frequency dependent, and leads to an amplitude noise on the photodiode current, and then to fluctuations on the voltage from the transimpedance amplifier.

The phasemeter processing calculates the phase signal from the voltage in the FFT bin at the heterodyne frequency, the voltage in this bin contains the heterodyne signal and noise. RIN at the heterodyne frequency f_{het} and at twice the heterodyne frequency $2f_{het}$ couples into the phase measurement. The resulting noise is a white noise, if RIN is flat around the frequency range which couples to the phase.

Each interferometers consists of two photodiodes, the phase difference of the signals between the two ports is π. At the recombination beamsplitter each beam is divided in two, one half send to each photodiode to interfere with half of the other beam. The phase signal of one diode is subtracted from the other, this process is called balanced detection [54]. The resulting phase signal xi is the signal of interferometer X_i, see Section 2.6.2. Since the signals have a sign difference the signal strength doubles, while phase noise from RIN near $1f_{het}$ is subtracted. Phase noise from RIN near $2f_{het}$ remains in the interferometer signal. Other noise on the phase signal, for example ADC noise or electronic noise, add non-coherently and are increased by a factor $\sqrt{2}$ in the resulting phase signal.

The reference interferometer signal xR is subtracted from the other interferometer signals x1, x12 and φ_F to remove noise common to both interferometers. With this subtraction pathlength noise common to both interferometers is reduced, phase noise from RIN near $2f_{het}$ can be reduced as well. The efficiency of this subtraction depends on the phase difference between the two signals, and as such on the test mass position. The coupling from RIN to the phase and the subtraction with the reference interferometer is calculated in Section 3.4.1. For a test mass position at the interferometric zero the phase difference between the reference signal and the measurement signal is zero, and RIN is removed from the signals o1 = x1 − xR and o12 = x12 − xR. Therefore the test mass was positioned at, or close to, the interferometric zero for most in-flight experiments. The pathlength difference between φ_R and φ_F is fixed since both are bonded completely on the optical bench.

To confirm the predicted coupling from RIN to phase the coupling from a sinusoidal RIN equivalent intensity modulation to the phase of a single diode signal is calculated in Section 3.4.2. These equations are tested in the laboratory with a sinusoidal RIN injection in Section 5.1.

Experiments where the test mass is moved on purpose can be found in Section 5.3 for the ground setup. Since $1f_{het}$ RIN is subtracted with balanced detection only the A or B port are used in these experiments.

The in-flight experiments where the test mass is moved in steps are shown in Sections 6.2 and 6.3. An analysis of the RIN contribution during noise runs on the flight model can be seen in Section 6.6, and for free-fall experiments in Section 6.7.

The coupling of $2f_{het}$ RIN on the LPF OMS was first observed in 2009 [63], at the time the source of this noise was not known. After the noise source was found an earlier paper was discovered [54], a different description where this $2f_{het}$ amplitude noise is described as a phase noise can be found in [64]. The initial calculations of the subtraction of phase noise due to correlated RIN were a joined activity lead by Gerhard Heinzel; further work with the calculation of the coupling of uncorrelated RIN and of a sinusoidal RIN injection to the length measurement and the coupling to DWS was led by Lennart Wissel (AEI). The coupling from RIN to the DWS measurement can be found in [57], and is briefly mentioned in Section 3.4.3. See also [65].

3.4.1. Coupling of RIN to the longitudinal signal and RIN subtraction

In Section 2.1 the heterodyne signal on one photodiode from the interference of two beams was derived, now Relative Intensity Noise (RIN) is added to the light. The coupling of this noise to the phase measurement will be calculated in this section for RIN which is correlated between the measurement and reference beam, and at the same noise level. The RIN for one photodiode signal, for the interferometer signal after balanced detection, and for the final signal with the reference signal subtracted will be calculated.

One simplified way to represent the laser signal from the interference of two beams, here named measurement beam and reference beam, on one photodiode is:

$$|E_{\mathrm{m}} + E_{\mathrm{r}} e^{i(\omega_{\mathrm{het}} t + \phi)}|_{\mathrm{A/B}}^2 = |E_{\mathrm{m}}|^2 + |E_{\mathrm{r}}|^2 \pm 2\sqrt{\eta_{\mathrm{het}}} E_{\mathrm{m}} E_{\mathrm{r}} \cos(\omega_{\mathrm{het}} t + \varphi) \tag{3.5}$$

$$= (|E_{\mathrm{m}}|^2 + |E_{\mathrm{r}}|^2)(1 \pm c \cos(\omega_{\mathrm{het}} t + \varphi)). \tag{3.6}$$

With $\omega_{\mathrm{het}} = 2\pi \mathrm{f}_{\mathrm{het}}$. This describes the symmetric and antisymmetric interferometer port with index A and B, where the heterodyne signal is either added or subtracted from the DC component. The contrast is defined as

$$c = \frac{2\sqrt{\eta_{\mathrm{het}}} E_{\mathrm{m}} E_{\mathrm{r}}}{|E_{\mathrm{m}}|^2 + |E_{\mathrm{r}}|^2} \qquad = \frac{2\sqrt{\eta_{\mathrm{het}} \mathrm{P_m P_r}}}{\mathrm{P_m} + \mathrm{P_r}}. \tag{3.7}$$

With the the heterodyne efficiency η_{het}.

Instead of the individual beam powers the time dependent power on one output port $P(t)$ will be used, the average power on one output port is $P_0 = \frac{1}{2}(|E_1|^2 + |E_2|^2)$. The power on one port can be described as

$$P(t) = P_0(1 + r(t)), \tag{3.8}$$

where $r(t)$ is Relative Intensity Noise and the intensity noise is $P_0 r(t)$. Typically the RIN is small compared to the total power, $r(t) \ll 1$. Here it will be assumed that RIN is common to both beams. Since the two photodiodes per interferometer are named PD_A and PD_B the two output ports will be differentiated with the same index A and B.

$$P_{\mathrm{A/B}}(t) = P_0(1 + r(t))(1 \pm c \cos(\omega_{\mathrm{het}} t - \varphi)). \tag{3.9}$$

To calculate the normalised photodiode signal $y_{\mathrm{A/B}}(t)$ the power per port is divided by the average power P_0, which leads to

$$y_{\mathrm{A/B}}(\mathrm{t}) = \frac{P_{\mathrm{A/B}}}{P_0} = (1 + r(t))(1 \pm c \cos(\omega_{\mathrm{het}} t - \varphi)). \tag{3.10}$$

The coupling of RIN to the phase signal is frequency dependent. The noise can be written in a sinusoidal form to calculate the coupling for different frequencies ω_{RIN}

$$r(t) = \hat{r} \cos(\omega_{\mathrm{RIN}} t + \alpha). \tag{3.11}$$

Again the amplitude of the noise is small compared to the signal, $\hat{r} \ll 1$. The phase offset α is arbitrary, and will be disregarded in the following calculations. To calculate the coupling for noise at different frequencies ω_{RIN} the resulting signal will be expanded into additive components, which can be inspected individually:

$$y_{\mathrm{A/B}}(\mathrm{t}) = (1 + r(t))(1 \pm c \cos(\omega_{\mathrm{het}} t - \varphi)) \tag{3.12}$$

$$= (1 + \hat{r} \cos(\omega_{\mathrm{RIN}} t))(1 \pm c \cos(\omega_{\mathrm{het}} t - \varphi)) \tag{3.13}$$

$$= 1 \pm c \cos(\omega_{\mathrm{het}} t - \varphi) + \hat{r} \cos(\omega_{\mathrm{RIN}} t) \tag{3.14}$$

$$\pm \hat{r} c \cos(\omega_{\mathrm{het}} t - \varphi) \cos(\omega_{\mathrm{RIN}} t) \tag{3.15}$$

$$= 1 \pm c \cos(\omega_{\mathrm{het}} t - \varphi) \tag{3.16}$$

$$+ \hat{r} \cos(\omega_{\mathrm{RIN}} t) \tag{3.17}$$

$$\pm \frac{1}{2} \hat{r} c (\cos((\omega_{\mathrm{het}} + \omega_{\mathrm{RIN}}) t - \varphi) + \cos((\omega_{\mathrm{het}} - \omega_{\mathrm{RIN}}) t - \varphi)). \tag{3.18}$$

The phasemeter filters out signals at the heterodyne frequency, this removes the constant first term in line 3.16 of the equation above. The second term is the normal beatnote of the heterodyne signal. The third term, see line 3.17, produces relevant noise with an amplitude of $P_0 \hat{r}$ if $\omega_{\mathrm{RIN}} \approx \omega_{\mathrm{het}}$.

The last term, line 3.18, has two components. One produces relevant noise if $\omega_{\mathrm{RIN}} \approx 0$. The other couples to the phase measurement if $\omega_{\mathrm{RIN}} \approx 2\omega_{\mathrm{het}}$. Since the cosine is an even function, $\cos(x) = \cos(-x)$, this also causes the sign of the phase φ to change.

For each of those terms the coupling can be further analysed using

$$\omega_{\mathrm{RIN}} \;=\; n\omega_{\mathrm{het}} + \epsilon, \tag{3.19}$$

$$r(t) \;=\; \hat{r}\cos((n\omega_{\mathrm{het}} + \epsilon)t + \alpha), \tag{3.20}$$

where $n = \{0, 1, 2\}$. With $\epsilon \ll \omega_{\mathrm{het}}$ a small frequency offset from the harmonic of the heterodyne frequency currently under analysis will be described. Bigger offsets can be excluded since the phasemeter only processes frequencies in the FFT bin of the heterodyne frequency ω_{het}.

RIN couples to the phase measurement from only a small band around $n\omega_{\mathrm{het}}$. In this frequency range the noise can be regarded as flat and therefore contributes as a white noise to the sensing noise floor, see also Figure 3.1.
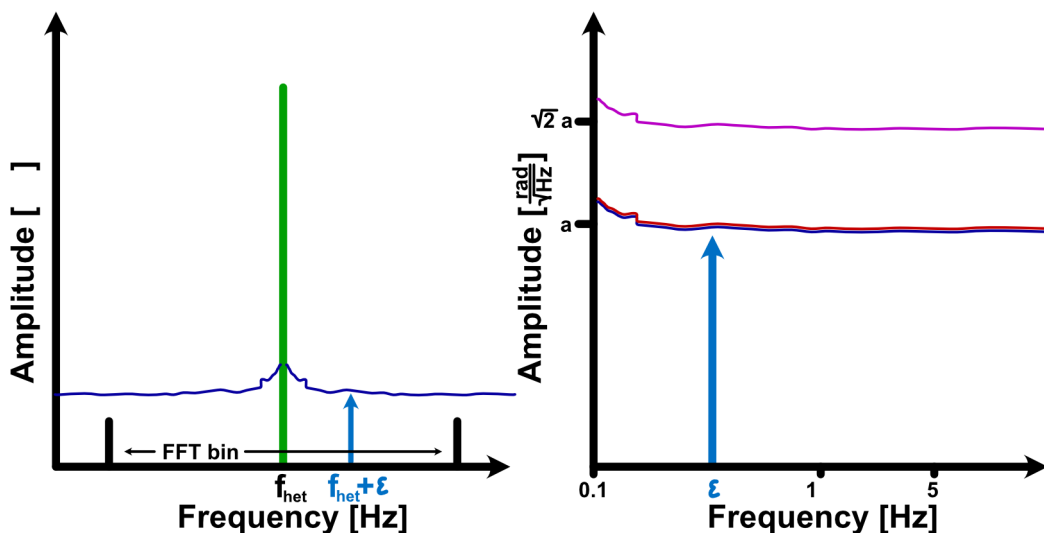
Figure 3.1.: Shown in this graph is the coupling from RIN around the heterodyne frequency, shown on the left, to the phase signal, which is shown on the right. Here, RIN is symmetric around the carrier (green). RIN with an offset of $\pm\epsilon$ of f_{het} couples to a frequency ϵ on the phase signal. Since the positive and negative side are uncorrelated they add quadratically in the phase signal to the final $1f_{\mathrm{het}}$ noise level.

For RIN near DC, $n = 0$, the following terms can be calculated

$$y_{\mathrm{A}}^{(0)}(t) \;=\; 1 + c\cos(\omega_{\mathrm{het}}\,t - \varphi) + \hat{r}\cos(\epsilon t) \tag{3.21}$$

$$+ \frac{1}{2}\hat{r}c\,(\cos((\omega_{\mathrm{het}} + \epsilon)\,t - \varphi) + \cos((\omega_{\mathrm{het}} - \epsilon)\,t - \varphi)) \tag{3.22}$$

$$=\; c\,(1 + \hat{r}\cos(\epsilon t))\cos(\omega_{\mathrm{het}}t - \varphi) + ..., \tag{3.23}$$

$$y_{\mathrm{B}}^{(0)}(t) \;=\; 1 - c\cos(\omega_{\mathrm{het}}\,t - \varphi) + \hat{r}\cos(\epsilon t) \tag{3.24}$$

$$- \frac{1}{2}\hat{r}c\,(\cos((\omega_{\mathrm{het}} + \epsilon)\,t - \varphi) + \cos((\omega_{\mathrm{het}} - \epsilon)\,t - \varphi)) \tag{3.25}$$

$$=\; -c\,(1 + \hat{r}\cos(\epsilon t))\cos(\omega_{\mathrm{het}}t - \varphi) + ... \tag{3.26}$$

Shown in grey are the terms that do not contribute since they are filterered by the phaseme-
ter. For $n = 0$ two symmetric sidebands remain at the frequencies $\omega_{\mathrm{het}} + \epsilon$ and $\omega_{\mathrm{het}} - \epsilon$.
With $\cos(a)\cos(b) = \frac{1}{2}\cos(a+b)\cos(a-b)$ it can be seen that this noise source is pure
amplitude noise at a frequency ϵ. This term covers the power fluctuations at low frequencies
ϵ. To first order this noise source does not couple into the phase measurement.

For RIN near the heterodyne frequency ω_{het}, $n = 1$, the following terms can be calculated,
again shown in grey are the terms that do not contribute:

$$y_{\mathrm{A}}^{(1)}(t) = c\cos(\omega_{\mathrm{het}}\,t - \varphi) + \hat{r}\cos((\omega_{\mathrm{het}} + \epsilon)\,t) \tag{3.27}$$

$$+ \frac{1}{2}\hat{r}c(\cos((2\,\omega_{\mathrm{het}} + \epsilon)\,t - \varphi) + \cos(\epsilon\,t - \varphi)), \tag{3.28}$$

$$y_{\mathrm{B}}^{(1)}(t) = -c\cos(\omega_{\mathrm{het}}\,t - \varphi) + \hat{r}\cos((\omega_{\mathrm{het}} + \epsilon)\,t) \tag{3.29}$$

$$- \frac{1}{2}\hat{r}c(\cos((2\,\omega_{\mathrm{het}} + \epsilon)\,t - \varphi) + \cos(\epsilon\,t - \varphi)). \tag{3.30}$$

The beatnote of the RIN component $\hat{r}\cos((\omega_{\mathrm{het}} + \epsilon)\,t)$ has an opposite sign in the A and B
photodiodes to the carrier. In balanced detection these signals are subtracted. So RIN for
$n = 1$, in the future called $1f_{\mathrm{het}}$ RIN, is removed from the interferometer signal while the
signal strength is increased. The efficiency of this subtraction is limited by the imbalance
in the interferometer arms. This imbalance is caused by differences in the signal processing
chain, which includes photodiodes and phasemeter electronics, as well as irregularities in the
recombination beamsplitter.
The $\mathrm{signal}_{\mathrm{rms}}$ and $\mathrm{noise}_{\mathrm{rms}}$ for one interferometer output port are:

$$\mathrm{signal}_{\mathrm{rms}} = \frac{c}{\sqrt{2}}, \tag{3.31}$$

$$\mathrm{noise}_{\mathrm{rms}} = \frac{\hat{r}^{(1)}}{\sqrt{2}}, \tag{3.32}$$

$$\hat{\varphi}^{(1)} = \frac{\mathrm{noise}_{\mathrm{rms}}}{\mathrm{signal}_{\mathrm{rms}}} = \frac{\hat{r}^{(1)}}{c}, \tag{3.33}$$

where $\hat{\varphi}^{(1)}$ is the error on the phase for one photodiode. The noise power $\hat{r}^{(1)}$ was normalised
with the light power P_0 earlier, see Equation 3.8. The noise level in the phase is still accurate
since the signal level is normalised with the same constant. This noise power is calculated
from the ratio of the RIN noise floor and the amplitude of the heterodyne signal, see Figure
3.1. The derivation of this calculation can be found in [66].

RIN near twice the heterodyne frequency $2\omega_{\mathrm{het}}$, or $n = 2$, consists of the following terms:

$$y_{\mathrm{A}}^{(2)}(t) = c\cos(\omega_{\mathrm{het}}\,t - \varphi) + \hat{r}(\cos((2\,\omega_{\mathrm{het}} + \epsilon)\,t - \varphi) \tag{3.34}$$

$$+ \frac{1}{2}\hat{r}c\cos((\omega_{\mathrm{het}} + \epsilon)\,t + \varphi) + \frac{1}{2}\hat{r}c\cos((3\,\omega_{\mathrm{het}} + \epsilon)\,t - \varphi), \tag{3.35}$$

$$y_{\mathrm{B}}^{(2)}(t) = -c\cos(\omega_{\mathrm{het}}\,t - \varphi) + \hat{r}(\cos((2\,\omega_{\mathrm{het}} + \epsilon)\,t - \varphi) \tag{3.36}$$

$$- \frac{1}{2}\hat{r}c\cos((\omega_{\mathrm{het}} + \epsilon)\,t + \varphi) - \frac{1}{2}\hat{r}c\cos((3\,\omega_{\mathrm{het}} + \epsilon)\,t - \varphi). \tag{3.37}$$

Again shown in grey are the therms which do not contribute.
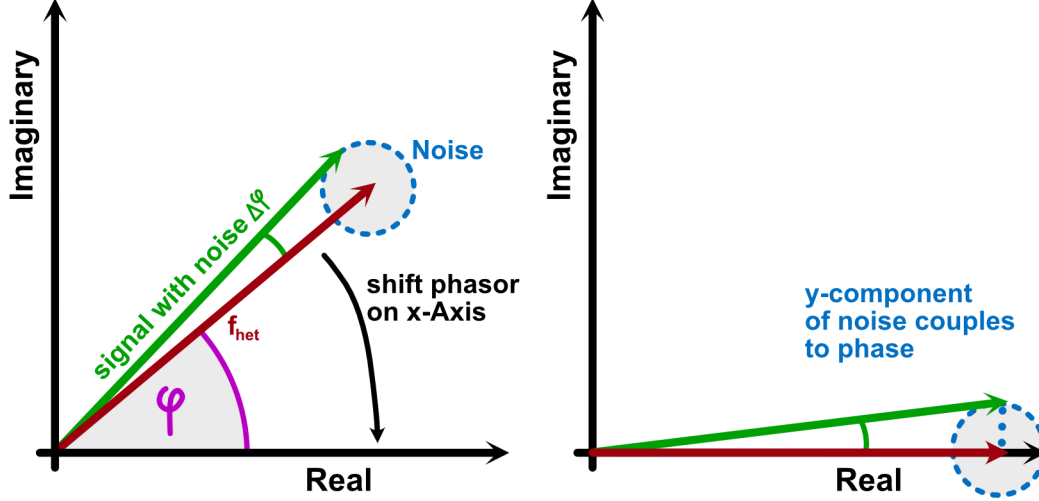
Figure 3.2.: Shown in these overviews in red is the phaser which can be constructed from the real and imaginary components of the heterodyne signal. Due to phase noise the measured phasor is different, an example phasor with noise is shown in green. To simplify the analysis the phasor is shifted from its arbitrary offset φ to the real axis. This allows the approximation of the phase noise caused by Relative Intensity Noise with the imaginary component. This approximation holds if the noise is small compared to the phasor amplitude.

The signal$_{\text{rms}}$ and noise$_{\text{rms}}$ for one interferometer output port are:

$$\text{signal}_{\text{rms}} = \frac{c}{\sqrt{2}}, \tag{3.38}$$

$$\text{noise}_{\text{rms}} = \frac{\hat{r}^{(2)}c}{2\sqrt{2}}, \tag{3.39}$$

$$\hat{\varphi}^{(2)} = \frac{\text{noise}_{\text{rms}}}{\text{signal}_{\text{rms}}} = \frac{\hat{r}^{(2)}}{2}. \tag{3.40}$$

In the following the propagation of RIN through the phasemeter will be calculated. From the real and imaginary part of the electric signal a phasor can be constructed, from which the phase with its noise can be calculated. To simplify the analysis the phase vector will be turned by the phase φ, so that it lies on the real axis. Figure 3.2 shows an illustration of this shift.

The phase change due to noise can now be calculated from the imaginary component. As one would expect, the phase noise $\Delta\varphi$ is calculated with the tangens, the approximation for small angles $\frac{Im(y)}{Re(y)} = \tan(\Delta\varphi) \approx \Delta\varphi$ is used. The real part $Re(y)$ is 1, since the signal was normalised with the power P_0 and contrast c.

RIN at ω_{het} or $2\omega_{\text{het}}$ is approximated with the imaginary component $Im(y)$

$$\Delta\varphi^{(1)} = \frac{\hat{r}^{(1)}}{c}\sin(\epsilon t - \varphi), \tag{3.41}$$

$$\Delta\varphi^{(2)} = \frac{1}{2}\hat{r}^{(2)}\sin(\epsilon t - 2\varphi). \tag{3.42}$$

Since the phasor is turned by $-\varphi$ the phase signal has an additional offset of φ, this leads to a total phase offset of φ for RIN at $1f_{\text{het}}$ and an offset of 2φ for RIN at $2f_{\text{het}}$.

Since the reference interferometer uses the same light as the measurement interferometers RIN is common to both signals, and it can be subtracted. To calculate the subtraction of $1f_{\text{het}}$ RIN it is assumed that balanced detection is not active.

The efficiency of the subtraction depends on the phase difference between measurement signal and reference signal, the phase dependency of this subtraction will be calculated in the following. The phase of the two unbalanced interferometer signals will be called ψ_{M} and ψ_{R}, where the M stands for both measurement interferometers and the frequency interferometer. These contain the phase signals φ_{M} and φ_{R}, as well as the RIN $\Delta\varphi_{\mathrm{M,R}}^{(1,2)}$ calculated earlier. Since these signals are in the unit radian the variables names o1 and o12 will not be used. It follows

$$\psi_{\mathrm{M,R}} = \varphi_{\mathrm{M,R}} + \Delta\varphi_{\mathrm{M,R}}^{(1)} + \Delta\varphi_{\mathrm{M,R}}^{(2)}, \tag{3.43}$$

$$\Psi_{\mathrm{M}} = \psi_{\mathrm{M}} - \psi_{\mathrm{R}}, \tag{3.44}$$

$$= \varphi_{\mathrm{M}} - \varphi_{\mathrm{R}} + \Delta\varphi_{\mathrm{M}}^{(1)} - \Delta\varphi_{\mathrm{R}}^{(1)} + \Delta\varphi_{\mathrm{M}}^{(2)} - \Delta\varphi_{\mathrm{R}}^{(2)}. \tag{3.45}$$

First, the subtraction for RIN at $1\omega_{\mathrm{het}}$ will be calculated, with

$$\Psi_{\mathrm{M}}^{(1)} = \varphi_{\mathrm{M}} + \varphi_{\mathrm{R}} + \frac{\hat{r}^{(1)}}{c}[\sin(\epsilon t + \varphi_{\mathrm{M}}) - \sin(\epsilon t + \varphi_{\mathrm{R}})] \tag{3.46}$$

$$= ... + \frac{\hat{r}^{(1)}}{c}[\sin(\epsilon t)\cos(\varphi_{\mathrm{M}}) + \cos(\epsilon t)\sin(\varphi_{\mathrm{M}}) - \sin(\epsilon t)\cos(\varphi_{\mathrm{R}}) - \cos(\epsilon t)\sin(\varphi_{\mathrm{R}})] \tag{3.47}$$

$$= ... + \frac{\hat{r}^{(1)}}{c}[\sin(\epsilon t)(\cos(\varphi_{\mathrm{M}}) - \cos(\varphi_{\mathrm{R}})) + \cos(\epsilon t)(\sin(\varphi_{\mathrm{M}}) - \sin(\varphi_{\mathrm{R}}))] \tag{3.48}$$

$$= ... + \frac{\hat{r}^{(1)}}{c}[\sin(\epsilon t)(-2\sin(\frac{\varphi_{\mathrm{M}} + \varphi_{\mathrm{R}}}{2})\sin(\frac{\varphi_{\mathrm{M}} - \varphi_{\mathrm{R}}}{2})) \tag{3.49}$$

$$- \cos(\epsilon t)(2\cos(\frac{\varphi_{\mathrm{M}} + \varphi_{\mathrm{R}}}{2})\sin(\frac{\varphi_{\mathrm{M}} - \varphi_{\mathrm{R}}}{2}))] \tag{3.50}$$

$$= ... - \frac{\hat{r}^{(1)}}{c}2\sin(\frac{\varphi_{\mathrm{M}} - \varphi_{\mathrm{R}}}{2})[\cos(\epsilon t)\cos(\frac{\varphi_{\mathrm{M}} + \varphi_{\mathrm{R}}}{2}) + \sin(\epsilon t)\sin(\frac{\varphi_{\mathrm{M}} + \varphi_{\mathrm{R}}}{2})] \tag{3.51}$$

$$= \varphi_{\mathrm{M}} - \varphi_{\mathrm{R}} - \frac{\hat{r}^{(1)}}{c}2\sin(\frac{\varphi_{\mathrm{M}} - \varphi_{\mathrm{R}}}{2})\cos(\epsilon t - \frac{\varphi_{\mathrm{M}} + \varphi_{\mathrm{R}}}{2}). \tag{3.52}$$

In the cosine component of line 3.52 in the equation above it can be seen that RIN from the frequency $\omega_{\mathrm{het}} + \epsilon$ or $\omega_{\mathrm{het}} - \epsilon$ couples into the measured phase at a frequency of ϵ. The phase offset in the noise component can be disregarded. The noise calculated shows a dependency on the phase difference between the measurement and reference interferometer of $\sin(\frac{\varphi_{\mathrm{M}} - \varphi_{\mathrm{R}}}{2})$.

Now, the subtraction for RIN at $2\omega_{\mathrm{het}}$, or $n = 2$, will be calculated. This noise is still present after balanced detection, in the nominal processing it is subtracted from the measurement signal with the reference signal. The derivation is similar to $n = 1$, the main difference is a static phase offset of $2\varphi_{\mathrm{i}}$ instead of φ_{i} in the RIN contribution of one interferomer $\mathrm{X_i}$. It follows

$$\Psi_{\mathrm{M}}^{(2)} = \varphi_{\mathrm{M}} - \varphi_{\mathrm{R}} + \frac{1}{2}\hat{r}^{(2)}[\sin(\epsilon t + 2\varphi_{\mathrm{M}}) - \sin(\epsilon t + 2\varphi_{\mathrm{R}})] \tag{3.53}$$

$$= ... \tag{3.54}$$

$$= \varphi_{\mathrm{M}} - \varphi_{\mathrm{R}} - \frac{1}{2}\hat{r}^{(2)}2\sin(\varphi_{\mathrm{M}} - \varphi_{\mathrm{R}})\cos(\epsilon t - (\varphi_{\mathrm{M}} + \varphi_{\mathrm{R}})) \tag{3.55}$$

In the cosine component it can be seen that RIN from the frequency $2\omega_{\mathrm{het}} + \epsilon$ or $2\omega_{\mathrm{het}} - \epsilon$ couples into the measured phase at a frequency of ϵ, the phase offset in this noise component can be disregarded as well. Here, the dependency on the phase difference between the measurement and reference interferometer of the noise measured is $\sin(\varphi_{\mathrm{M}} - \varphi_{\mathrm{R}})$.

Since the mean of the noise contributions is zero the phase error can be calculated from the root mean square value to predict the noise actually measured for different test mass positions. This rms noise is calculated over a frequency band B. The rms value of the time dependent sine and cosine noise components is $\frac{1}{\sqrt{2}}$, these components contain the frequency ϵ. It has also be taken into account that RIN with the same frequency offset, one for $+\epsilon$ and one for $-\epsilon$, causes uncorrelated noise at the same frequency in the phase signal. The noise calculated is multiplied with $\sqrt{2}$ to reflect this. Since the coupling is the same for all ϵ the noise level calculated is the white noise level in the phase spectrum.

The rms noise of the final signal follows from the subtracted signals as:

$$\mathrm{RMS}(\Psi_\mathrm{M}^{(1)}) = \sqrt{2}\frac{2\hat{r}^{(1)}}{c}|\sin(\frac{\varphi_\mathrm{M}-\varphi_\mathrm{R}}{2})|\frac{1}{\sqrt{2}}\sqrt{\mathrm{B}} \tag{3.56}$$

$$= \frac{2\hat{r}^{(1)}}{c}|\sin(\frac{\varphi_\mathrm{M}-\varphi_\mathrm{R}}{2})|\sqrt{\mathrm{B}} \tag{3.57}$$

$$\mathrm{RMS}(\Psi_\mathrm{M}^{(2)}) = \sqrt{2}\hat{r}^{(2)}|\sin(\varphi_\mathrm{M}-\varphi_\mathrm{R})|\frac{1}{\sqrt{2}}\sqrt{\mathrm{B}} \tag{3.58}$$

$$= \hat{r}^{(2)}|\sin(\varphi_\mathrm{M}-\varphi_\mathrm{R})|\sqrt{\mathrm{B}} \tag{3.59}$$

For the measured band B.

The noise as measured on the phase signals is therefore

$$\Psi_\mathrm{M}^{(1)} = \sqrt{2}\frac{\mathrm{RMS}(\Psi_\mathrm{M}^{(1)})}{\sqrt{\mathrm{B}}} = \sqrt{2}\frac{2\hat{r}^{(1)}}{c}|\sin(\frac{\varphi_\mathrm{M}-\varphi_\mathrm{R}}{2})| \tag{3.60}$$

$$\Psi_\mathrm{M}^{(2)} = \sqrt{2}\frac{\mathrm{RMS}(\Psi_\mathrm{M}^{(2)})}{\sqrt{\mathrm{B}}} = \sqrt{2}\hat{r}^{(2)}|\sin(\varphi_\mathrm{M}-\varphi_\mathrm{R})| \tag{3.61}$$

Where the additional factor $\sqrt{2}$ reflects the change from an rms amplitude noise to an amplitude noise. The contribution of the RIN for different test mass positions is added quadratically to other noise already present in the interferometer signal.

Laboratory experiments to confirm the coupling from a frequency offset $1\omega_\mathrm{het} + \epsilon$ and $2\omega_\mathrm{het} - \epsilon$ to ϵ in the length measurement can be found in 5.1 and 5.2. Experiments to test the noise over position are performed in the AEI laboratory, see Section 5.3, and in orbit, see Sections 6.2 and 6.3.

So far the calculations used the phase difference $\varphi_\mathrm{M} - \varphi_\mathrm{R}$ in radian and phase noise in $\left[\frac{\mathrm{rad}}{\sqrt{\mathrm{Hz}}}\right]$. However, in a typical experiment this phase difference is the measurement of either o1 or o12, which is in the unit nanometre. Typically, the noise level calculated from this is in $\left[\frac{\mathrm{fm}}{\sqrt{\mathrm{Hz}}}\right]$.

For the RIN subtractions measurements the functions

$$\hat{\mathrm{o}}12^{(1)^2} = \left(\frac{\lambda}{4\pi\cos\alpha}\cdot 2\sqrt{2}\,\frac{\hat{r}^{(1)}}{c}\sin\left(\frac{4\pi\cos\alpha}{\lambda}\frac{\mathrm{o}12}{2}\right)\right)^2, \qquad \left[\frac{\mathrm{fm}^2}{\mathrm{Hz}}\right] \tag{3.62}$$

$$\hat{\mathrm{o}}12^{(2)^2} = \left(\frac{\lambda}{4\pi\cos\alpha}\cdot\sqrt{2}\,\hat{r}^{(2)}\sin\left(\frac{4\pi\cos\alpha}{\lambda}\mathrm{o}12\right)\right)^2, \qquad \left[\frac{\mathrm{fm}^2}{\mathrm{Hz}}\right] \tag{3.63}$$

$$\hat{\mathrm{o}}12 = \sqrt{\hat{\mathrm{o}}12^{(1)^2} + \hat{\mathrm{o}}12^{(2)^2} + \mathrm{noisefloor}^2}, \qquad \left[\frac{\mathrm{fm}}{\sqrt{\mathrm{Hz}}}\right] \tag{3.64}$$

are used. The phase noise contributions from RIN are added quadratically to the sensing noise floor, which consists of contributions also described in this chapter.

These functions are used in the laboratory experiment shown in Section 5.3 to calculate the phase noise from the measured RIN.
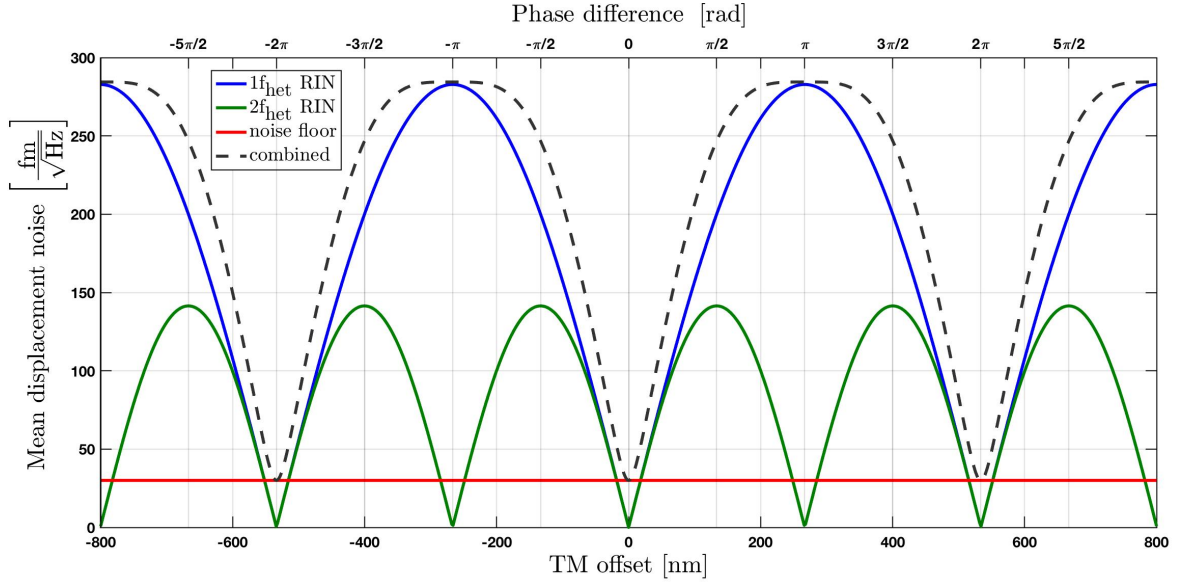
Figure 3.3.: This plot shows the calculated phase noise due to RIN, for changing phase difference between the two interferometers. Here this phase change is achieved by moving the test mass, the resulting phase difference is shown on the top x-axis. Shown are the individual noise contributions, $1f_{het}$ RIN in blue, $2f_{het}$ RIN in green and the noise floor in red. The noise floor is at $30 \frac{fm}{\sqrt{Hz}}$, both RIN contributions have a noise amplitude of $100 \frac{fm}{\sqrt{Hz}}$, with a contrast of 1. The individual noise components are added quadratically to produce the combined noise.

In the flight-experiments this function is used as a fit function to the measured phase noise for a changing TM position. From the fit results of the phase measurement in $\left[\frac{fm}{\sqrt{Hz}} \right]$ the RIN levels $\hat{r}^{(1)}$ and $\hat{r}^{(1)}$ in $\left[\frac{1}{\sqrt{Hz}} \right]$ can be calculated.

uncorrelated RIN

To calculate the phase noise for uncorrelated RIN the two beams have to be treated separately. In the previous derivation of the RIN coupling equations it was assumed that the beam powers P_r or P_m are the same for the two interferometers, and that the beamsplitters divide the beam power equally between the two ports.

In Section 3.4.2 the coupling from RIN at one frequency offset ϵ on the reference beam to the phase of one interferometer is calculated. These equations, see 3.93, are already used here to calculate the phase noise for uncorrelated RIN in a subtraction experiment. In the following, the phase difference will again be in radian, and the noise level in $\left[\frac{1}{\sqrt{Hz}} \right]$; but these can easily calibrated to a phase difference in nm and a noise level in $\left[\frac{fm}{\sqrt{Hz}} \right]$. For consistency, the signal names calibrated to metre are used.

Since the RIN of the two beams is uncorrelated the phase noise of the measurement beam and reference beam as calculated with Equation 3.93 is added quadratically. These equations are calculated for a white noise RIN, which couples from a positive and negative frequency offset ϵ instead of a single frequency. An additional factor $\sqrt{2}$ is multiplied on the derived

equations. It follows

$$\hat{x}1\_A^{(1)} = \sqrt{2} \left(\frac{\sqrt{\tau_r^4 P_r^2 \hat{r}_r^{(1)2} + \rho_m^4 P_m^2 \hat{r}_m^{(1)2}}}{\sqrt{4\eta_{\text{het,A}} \tau_r^2 \rho_m^2 P_r P_m}} \right), \qquad \left[\frac{\text{rad}}{\sqrt{\text{Hz}}} \right] \qquad (3.65)$$

$$\hat{x}1\_B^{(1)} = \sqrt{2} \left(\frac{\sqrt{\rho_r^4 P_r^2 \hat{r}_r^{(1)2} + \tau_m^4 P_m^2 \hat{r}_m^{(1)2}}}{\sqrt{4\eta_{\text{het,B}} \rho_r^2 \tau_m^2 P_r P_m}} \right), \qquad \left[\frac{\text{rad}}{\sqrt{\text{Hz}}} \right] \qquad (3.66)$$

$$\hat{x}1\_A,B^{(2)} = \sqrt{2} \left(\frac{1}{4} \sqrt{\hat{r}_r^{(2)2} + \hat{r}_m^{(2)2}} \right). \qquad \left[\frac{\text{rad}}{\sqrt{\text{Hz}}} \right] \qquad (3.67)$$

Here $\hat{r}_r^{(1)}$ is the amplitude spectral density of $1f_{\text{het}}$ RIN on the reference beam, the amplitude spectral density of RIN at $2f_{\text{het}}$ on the reference beam is $\hat{r}_r^{(2)}$. The RIN of the measurement beam is labelled with the subscript m.

The same calculation can be done for the reference signal, these two are now subtracted to calculate the signal o1. For this subtraction it will be assumed that the beamsplitter parameters ρ and τ and the beam powers P_r and P_m are the same on the two interferometers. The maximum noise of the subtracted signal can be calculated by linear addition of the noise of the individual interferometers. With the previously calculated subtraction properties the final equations are:

$$\hat{o}1\_A^{(1)} = 2 \cdot \hat{x}1\_A^{(1)} \left| \sin \left(\frac{\varphi_M - \varphi_R}{2} \right) \right|, \qquad \left[\frac{\text{rad}}{\sqrt{\text{Hz}}} \right] \qquad (3.68)$$

$$\hat{o}1\_B^{(1)} = 2 \cdot \hat{x}1\_B^{(1)} \left| \sin \left(\frac{\varphi_M - \varphi_R}{2} \right) \right|, \qquad \left[\frac{\text{rad}}{\sqrt{\text{Hz}}} \right] \qquad (3.69)$$

$$\hat{o}1\_A,B^{(2)} = 2 \cdot \hat{x}1\_A,B^{(2)} |\sin(\varphi_M - \varphi_R)|. \qquad \left[\frac{\text{rad}}{\sqrt{\text{Hz}}} \right] \qquad (3.70)$$

Which yields finally for the coupling of uncorrelated RIN

$$\hat{o}1\_A^{(1)} = \sqrt{\frac{2 \left(\tau_r^4 P_r^2 \hat{r}_r^{(1)2} + \rho_m^4 P_m^2 \hat{r}_m^{(1)2} \right)}{\eta_{\text{het,A}} \tau_r^2 \rho_m^2 P_r P_m}} \left| \sin \left(\frac{\varphi_M - \varphi_R}{2} \right) \right|, \qquad \left[\frac{\text{rad}}{\sqrt{\text{Hz}}} \right] \qquad (3.71)$$

$$\hat{o}1\_B^{(1)} = \sqrt{\frac{2 \left(\rho_r^4 P_r^2 \hat{r}_r^{(1)2} + \tau_m^4 P_m^2 \hat{r}_m^{(1)2} \right)}{\eta_{\text{het,B}} \rho_r^2 \tau_m^2 P_r P_m}} \left| \sin \left(\frac{\varphi_M - \varphi_R}{2} \right) \right|, \qquad \left[\frac{\text{rad}}{\sqrt{\text{Hz}}} \right] \qquad (3.72)$$

$$\hat{o}1\_A,B^{(2)} = \sqrt{\frac{\hat{r}_r^{(2)2} + \hat{r}_m^{(2)2}}{2}} |\sin(\varphi_M - \varphi_R)|. \qquad \left[\frac{\text{rad}}{\sqrt{\text{Hz}}} \right] \qquad (3.73)$$

uncorrelated RIN, with interferometers nearly matched

When the two interferometers are not well matched the phase noise for each interferometer has to be calculated individually with their respective beam powers and beamsplitter parameters. Depending on the correlation between the beams the contributions are added quadratically or linearly, with their respective RIN level and interferometer phase.

An estimate of the noise shape for nearly-matched interferometers, which use the same beams with the same RIN level, can be made. The phase noise due to RIN of the two interferometers is added, the result is multiplied with the expected subtraction noise shape. The peak noise of the subtraction can again be calculated by linear addition of the RIN of the individual interferometers X_1 and X_R. The minimum remaining noise after the subtraction can be calculated by linear subtraction of the two contributions.

Initially, for the calculation of the coupling of $1f_{het}$ RIN to the phase the individual beam powers in front of the beamsplitter and the beamsplitter parameters τ and ρ to calculate the beam powers on the A and B port were used. To also directly account for a possible beam power difference in front of the beamsplitters of the two interferometers the powers $P_{ij,m}$ and $P_{ij,r}$ as measured on interferometer X_i on diode $j = \{A,B\}$ are used now.

This equation is used in the calculation of the phase noise of the subtracted signals o1_A and o1_B in the laboratory experiment with injected RIN in Section 5.3. The resulting phase noise due to $1f_{het}$ RIN on the A side can be estimated with

$$
\hat{o}1\_A^{(1)} \approx \left[\frac{\sqrt{P_{1A,r}^2 \hat{r}_r^{(1)2} + P_{1A,m}^2 \hat{r}_m^{(1)2}}}{\sqrt{2}\,\eta_{het,1A} P_{1A,r} P_{1A,m}} + \frac{\sqrt{P_{RA,r}^2 \hat{r}_r^{(1)2} + P_{RA,m}^2 \hat{r}_m^{(1)2}}}{\sqrt{2}\,\eta_{het,RA} P_{RA,r} P_{RA,m}} \right] \cdots
$$

$$
\cdot \left| \sin\left(\frac{\varphi_M - \varphi_R}{2} \right) \right|. \qquad\qquad\qquad \left[\frac{rad}{\sqrt{Hz}} \right] \quad (3.74)
$$

This calculation does not account for the remaining noise at the minima of the noise shape; due to the high sensing noise in the laboratory measurements this remaining noise is not a significant contribution.

3.4.2. Coupling of RIN on one beam to the phase

The coupling coefficients calculated in the previous section will be confirmed experimentally in Chapter 5. Part of the claim is the coupling from RIN at kilohertz frequencies down to a phase noise in the LPF sensing noise frequency range. This claim will be confirmed with a sine wave injection on the laser amplitude, with fixed frequency and amplitude, on only one of the beams.

This RIN equivalent sinusoidal intensity modulation is injected at a fixed frequency offset ϵ of either $1f_{\text{het}}$ or $2f_{\text{het}}$, which couples down to the measurement band at a frequency of ϵ. The amplitude of this injection on the beam is traced to the amplitude on the phase signal of an individual diode, both $1f_{\text{het}} \pm \epsilon$ and $2f_{\text{het}} \pm \epsilon$ couple to a frequency of ϵ in the phase signal. The results of these experiments can be found in Sections 5.1 and 5.2.

In the equations derived previously symmetric white noise RIN around $1f_{\text{het}}$ or $2f_{\text{het}}$ was assumed, where positive and negative offsets ϵ couple down to the same frequency and add quadratically. Since the injection is at either a positive or negative frequency offset the expected coupling parameters are smaller by a factor of $\sqrt{2}$.

The beam powers of the individual beams on the diodes of interest are recorded before and after the experiment. It was found that the measured power is not the same between A and B side of the same diode. The measured power of the reference beam on the PD1A diode can be calculated with

$$P_{1A,r} = \tau^2 \, P_r \, R_{\text{PD1A}}, \tag{3.75}$$

where τ is the transmission coefficient of the beamsplitter, P_r is the power of the reference beam in front of the beamsplitter, and R_{PD1A} is the photodiode responsivity of PD1A. The BS coefficient of the reflected beam is called ρ. The effective beamsplitter ratios, τ_{im}/ρ_{im} and τ_{ir}/ρ_{ir}, can be calculated from the measured powers on the A and B diode. For both beams the values for the interferometer X_i can be calculated as

$$\tau_{im} = \sqrt{\frac{P_{iB,m}}{P_{iA,m} + P_{iB,m}}} \qquad\qquad \rho_{im} = \sqrt{\frac{P_{iA,m}}{P_{iA,m} + P_{iB,m}}} \tag{3.76}$$

$$\tau_{ir} = \sqrt{\frac{P_{iA,r}}{P_{iA,r} + P_{iB,r}}} \qquad\qquad \rho_{ir} = \sqrt{\frac{P_{iB,r}}{P_{iA,r} + P_{iB,r}}} \tag{3.77}$$

where the subscript m and r denote the measurement and reference beam. These splitting ratios include differences in the photodiode responsivity R_{PD} of the A and B side. These coefficients are a measure of the difference between A and B side, in other contexts this difference is often expressed with a parameter b. The splitting rations calculated from the individual beam powers on the diodes of interest can be found in Table 3.1.

X_1	τ^2	ρ^2	X_R	τ^2	ρ^2
M	$0.556 \pm 8 \cdot 10^{-5}$	$0.444 \pm 7 \cdot 10^{-5}$	M	$0.520 \pm 8 \cdot 10^{-5}$	$0.480 \pm 7 \cdot 10^{-5}$
R	$0.497 \pm 7 \cdot 10^{-5}$	$0.503 \pm 8 \cdot 10^{-5}$	R	$0.549 \pm 8 \cdot 10^{-5}$	$0.451 \pm 7 \cdot 10^{-5}$

Table 3.1.: These are the measured beamsplitter properties, calculated from the power of the individual beams measured on the A and B diodes. These parameters are a combination of the splitting ratios of the beamsplitter and differences in the photodiode responsivity. This measurement was repeated for other experiments over the course of a few months, the values remained the same. The errors are the result of the averaging of the beam powers over a timespan of ≈ 5 minutes, and do not include systematic errors.

The polarisation of the light on the optical bench was measured with a polarising beamsplitter for the X_1 and X_R diodes, for both the measurement and reference beam. The beams were found to be $\approx 99\%$ s-pol light. As an additional test the polarisation of the light was changed on the modulation bench and also on the optical bench, yet the splitting ratio between symmetric and asymmetric port remained the same. Therefore the calculated beamsplitter parameters must be a property of the beamsplitters and the diodes and not of the light. In the experiments shown later the RIN signal is injected on the reference beam, because the split-ratio is nearly 50-50 for the X_1 interferometer. The AOM electronics initially connected to the measurement beam were found to have fewer sidebands. These were switched to drive the reference beam instead for the experiments shown in Chapter 5.

In the derivation in Section 3.4 it was assumed that the beam powers were split 50/50 between A and B, and that the PD responsivity was the same for A and B. The mean power was removed from both the carrier and the RIN component since it was assumed that the RIN is correlated between measurement and reference beam, and only their combination was relevant for the final phase noise.

To measure the transfer coefficient from RIN to the phase a RIN equivalent intensity modulation is injected on the reference beam. Now the differences between the two beams are relevant for the calculation of the coupling. The RIN amplitude on the diode for $1f_{het}$ RIN of the reference beam, when it is not normalised for the power, can be described with

$$\tilde{v}_A^{(1)} = P_r \, \tau_r^2 \, \tilde{r}^{(1)}, \tag{3.78}$$

$$\tilde{v}_B^{(1)} = P_r \, \rho_r^2 \, \tilde{r}^{(1)}. \tag{3.79}$$

The powers P_r and P_m are the powers of the two beams before the beamsplitters. The different splitting ratios and photodiode responsivity are accounted for with the effective splitting rations ρ_r and τ_r. See also line 3.17 in the initial calculation of the RIN coupling.

The expected phase noise can be calculated from the ratio to the carrier amplitude, which is

$$S_A = 2\tau_m\rho_r\sqrt{\eta_{het,A}P_mP_r}, \tag{3.80}$$

$$S_B = 2\tau_r\rho_m\sqrt{\eta_{het,B}P_mP_r}. \tag{3.81}$$

Compared to the previously calculated Equation 3.6 this description includes the effective beamsplitter parameters, and is not normalised with the mean power. The heterodyne efficiencies $\eta_{het,A}$ and $\eta_{het,B}$ depend on the contrast, and can be calculated with

$$\eta_{het,j} = \left(c\frac{P_{j,r}+P_{j,m}}{2\sqrt{P_{j,r}\cdot P_{j,m}}} \right)^2. \qquad\qquad j = A,B \tag{3.82}$$

These values depend on beam alignment, and typically are in the order of ≈ 0.7.

From injected RIN amplitude and the carrier amplitude the final phase amplitude of the A side can be calculated with

$$\tilde{x}1\_A^{(1)} = \frac{\tilde{v}_A^{(1)}}{S_A} \qquad\qquad \text{[rad]} \tag{3.83}$$

$$= \frac{P_r\tau_r^2\tilde{r}^{(1)}}{2\tau_m\rho_r\sqrt{\eta_{het,A}P_mP_r}} \qquad\qquad \text{[rad]} \tag{3.84}$$

$$= \frac{P_r}{\sqrt{4\,\eta_{het,A}P_rP_m}}\frac{\tau_r}{\rho_m}\,\tilde{r}^{(1)}. \qquad\qquad \text{[rad]} \tag{3.85}$$

To calculate the phase rms amplitude the ratio $\hat{x}1\_A^{(1)} = \frac{\tilde{v}_A}{\sqrt{2}S_A}$ can be used. The calculation for the B side is similar.

For sinusoidal $2f_{het}$ RIN the signal on the diode from the injection on the reference beam can be described with

$$\tilde{v}_A^{(2)} = \frac{1}{2}\rho_r\tau_m\sqrt{\eta_{het,A}P_rP_r}\,\tilde{r}^{(2)}, \tag{3.86}$$

$$\tilde{v}_B^{(2)} = \frac{1}{2}\rho_m\tau_r\sqrt{\eta_{het,B}P_rP_r}\,\tilde{r}^{(2)}. \tag{3.87}$$

See also line 3.18 in the initial calculation of the RIN coupling. The expected phase amplitude is calculated in the same way with

$$\tilde{x}1\_A^{(2)} = \frac{\tilde{v}_A^{(2)}}{S_A} \qquad\qquad [\text{rad}] \tag{3.88}$$

$$= \frac{\frac{1}{2}\rho_r\tau_m\sqrt{\eta_{het,A}P_mP_r}\tilde{r}^{(2)}}{2\tau_m\rho_r\sqrt{\eta_{het,A}P_mP_r}} \qquad [\text{rad}] \tag{3.89}$$

$$= \frac{1}{4}\tilde{r}^{(2)}. \qquad\qquad [\text{rad}] \tag{3.90}$$

The coupling of $2f_{het}$ RIN is the same for A and B side.

The phase amplitude on the x1 signals for the RIN injected can be calculated with

$$\tilde{x}1\_A^{(1)} = \sqrt{\text{noisefloor}^2 + \left(\frac{P_r}{\sqrt{4\eta_{het,A}\,P_rP_m}}\,\frac{\tau_r}{\rho_m}\,\tilde{r}^{(1)}\right)^2}, \qquad [\text{rad}] \tag{3.91}$$

$$\tilde{x}1\_B^{(1)} = \sqrt{\text{noisefloor}^2 + \left(\frac{P_r}{\sqrt{4\eta_{het,B}\,P_rP_m}}\,\frac{\rho_r}{\tau_m}\,\tilde{r}^{(1)}\right)^2}, \qquad [\text{rad}] \tag{3.92}$$

$$\tilde{x}1\_A,B^{(2)} = \sqrt{\text{noisefloor}^2 + \left(\frac{1}{4}\,\tilde{r}^{(2)}\right)^2}, \qquad [\text{rad}] \tag{3.93}$$

where $\tilde{r}^{(1)}$ and $\tilde{r}^{(2)}$ are the amplitudes of the RIN injected, and $\tilde{x}1\_A^{(1)}$, $\tilde{x}1\_B^{(1)}$ and $\tilde{x}1\_A,B^{(2)}$ are the resulting amplitude on the phase signal. The same calculation applies for the xR signals, with the beamsplitter parameters and powers of the X_R interferometer. A description of the measurement of the RIN levels $\tilde{r}^{(1)}$ and $\tilde{r}^{(2)}$ in the laboratory can be found in Section 4.5.

For the calculation of $1f_{het}$ RIN to the phase signal the individual beam powers of the two beams on the individual interferometer diodes are needed; the beam powers P_m and P_r are the powers of the measurement beam and reference beam in the interferometer under analysis. In most practical applications the beam powers on the diodes are measured directly on the diode, and not in front of the beamsplitter. In this case the beam power in front of the diode in this formula can be replaced with this measured value multiplied with either the transmission of reflection coefficient, which effectively removes the BS ratio from this equation.

In the first RIN transfer function experiment in the ground setup, see Section 5.1, the two beam powers are measured with the phasemeter before the measurement by subsequent blocking of one of the beams on the modulation bench. The dark current is subtracted.

In the second RIN transfer function experiment the duration of the experiment is longer; to calculate the powers of the individual beams on the interferometer diodes the signal from the amplitude stabilisation is used, see Section 4.5.5.

In the experiments shown in Section 5.1 the injected RIN level is measured. From this RIN amplitude the phase amplitude is predicted with the equations derived here, and compared with the measured phase amplitude. The error of the prediction consists of the errors of the individual components. To calculate the error of the $1f_{het}$ RIN prediction the error of the mean laser powers of the individual laser beams and of the mean contrast are used. The

heterodyne efficiency η_het is calculated from these values. These measured values and their errors can be found in the discussion of the experiment results in Chapter 5. Since in the phase noise predictions for $2f_\text{het}$ RIN the only input is the RIN level no error is calculated.

RIN coupling to the phase of a single diode, $i = \{1,12,\mathrm{R,F}\}$		
$1f_{\mathrm{het}}$	sinusoidal	$\tilde{\mathrm{x}}i\_\mathrm{A}(\tilde{r}_\mathrm{r}) = \dfrac{\mathrm{P_r}}{\sqrt{4\eta_{\mathrm{het,A}}\,\mathrm{P_rP_m}}}\,\dfrac{\tau_\mathrm{r}}{\rho_\mathrm{m}}\,\tilde{r}_\mathrm{r} = \dfrac{\mathrm{P_{iA,r}}}{\sqrt{4\eta_{\mathrm{het,A}}\,\mathrm{P_{iA,r}P_{iA,m)}}}}\,\tilde{r}_\mathrm{r}$ $\tilde{\mathrm{x}}i\_\mathrm{B}(\tilde{r}_\mathrm{r}) = \dfrac{\mathrm{P_r}}{\sqrt{4\eta_{\mathrm{het,B}}\,\mathrm{P_rP_m}}}\,\dfrac{\rho_\mathrm{r}}{\tau_\mathrm{m}}\,\tilde{r}_\mathrm{r} = \dfrac{\mathrm{P_{iB,r}}}{\sqrt{4\eta_{\mathrm{het,B}}\,\mathrm{P_{iB,r}P_{iB,m}}}}\,\tilde{r}_\mathrm{r}$
	white noise	$\hat{\mathrm{x}}i\_\mathrm{A,B}(\hat{r}_\mathrm{r}) = \sqrt{2}\cdot\tilde{\mathrm{x}}i\_\mathrm{A,B}(\tilde{r}_\mathrm{r})$ $\hat{\mathrm{x}}i\_\mathrm{A,B}(\hat{r}_\mathrm{r},\hat{r}_\mathrm{m})_{\mathrm{corr.}} = \hat{\mathrm{x}}i\_\mathrm{A,B}(\hat{r}_\mathrm{r}) + \hat{\mathrm{x}}i\_\mathrm{A,B}(\hat{r}_\mathrm{m})$ $\hat{\mathrm{x}}\_\mathrm{A,B}(\hat{r}_\mathrm{r},\hat{r}_\mathrm{m})_{\mathrm{uncorr.}} = \sqrt{\hat{\mathrm{x}}i\_\mathrm{A,B}(\hat{r}_\mathrm{r})^2 + \hat{\mathrm{x}}i\_\mathrm{A,B}(\hat{r}_\mathrm{m})^2}$
$2f_{\mathrm{het}}$	sinusoidal	$\tilde{\mathrm{x}}i\_\mathrm{A,B,AB}(\tilde{r}_\mathrm{r}) = \frac{1}{4}\,\tilde{r}$
	white noise	$\hat{\mathrm{x}}i\_\mathrm{A},B,AB(\hat{r}_\mathrm{r}) = \sqrt{2}\cdot\tilde{\mathrm{x}}i\_\mathrm{A},B(\tilde{r}_\mathrm{r})$ $\hat{\mathrm{x}}i\_\mathrm{A,B,AB}(\hat{r}_\mathrm{r},\hat{r}_\mathrm{m})_{\mathrm{corr.}} = \frac{\sqrt{2}}{4}\cdot\frac{\hat{r}_\mathrm{r}+\hat{r}_\mathrm{m}}{2}$ $\hat{\mathrm{x}}i\_\mathrm{A,B,AB}(\hat{r}_\mathrm{r},\hat{r}_\mathrm{m})_{\mathrm{uncorr.}} = \frac{\sqrt{2}}{4}\cdot\sqrt{\hat{r}_\mathrm{r}^2 + \hat{r}_\mathrm{m}^2}$
RIN subtraction, $i = \{1,12,\mathrm{F}\}$		
$1f_{\mathrm{het}}$	sinusoidal	$\tilde{\mathrm{o}}i\_\mathrm{A,B}(\tilde{r}_\mathrm{r},\tilde{r}_\mathrm{m}) = \left(\tilde{\mathrm{x}}i\_\mathrm{A,B}(\tilde{r}_\mathrm{r},\tilde{r}_\mathrm{m}) + \tilde{\mathrm{x}}\mathrm{R}\_\mathrm{A,B}(\tilde{r}_\mathrm{r},\tilde{r}_\mathrm{m})\right)\left|\sin\left(\frac{\varphi_i-\varphi_\mathrm{R}}{2}\right)\right|$ $= \sqrt{\dfrac{\tau_\mathrm{r}^4\mathrm{P_r^2}\tilde{r}_\mathrm{r}^2 + \rho_\mathrm{m}^4\mathrm{P_m^2}\tilde{r}_\mathrm{m}^2}{\eta_{\mathrm{het,A}}\,\tau_\mathrm{r}^2\rho_\mathrm{m}^2\mathrm{P_rP_m}}}\left|\sin\left(\frac{\varphi_i-\varphi_\mathrm{R}}{2}\right)\right|$ with $\rho_\mathrm{m}^2\mathrm{P_m} = \mathrm{P}_{i,\mathrm{m}} = \mathrm{P_{R,m}}$ and $\tau_\mathrm{r}^2\mathrm{P_r} = \mathrm{P}_{i,\mathrm{r}} = \mathrm{P_{R,r}}$
	white noise	$\hat{\mathrm{o}}i\_\mathrm{A,B}(\hat{r}_\mathrm{r},\hat{r}_\mathrm{m})_{\mathrm{corr.}} = \frac{2\sqrt{2}}{c}\,\frac{\hat{r}_\mathrm{r}+\hat{r}_\mathrm{m}}{2}\left|\sin\left(\frac{\varphi_i-\varphi_\mathrm{R}}{2}\right)\right|,$ with $\mathrm{P}_{i,\mathrm{m}} = \mathrm{P}_{i,\mathrm{r}} = \mathrm{P_{R,m}} = \mathrm{P_{R,r}}$ $\hat{\mathrm{o}}i\_\mathrm{A}(\hat{r}_\mathrm{r},\hat{r}_\mathrm{m})_{\mathrm{uncorr.}} = \sqrt{\dfrac{2\left(\tau_\mathrm{r}^4\mathrm{P_r^2}\hat{r}_\mathrm{r}^2 + \rho_\mathrm{m}^4\mathrm{P_m^2}\hat{r}_\mathrm{m}^2\right)}{\eta_{\mathrm{het,A}}\,\tau_\mathrm{r}^2\rho_\mathrm{m}^2\mathrm{P_rP_m}}}\left|\sin\left(\frac{\varphi_i-\varphi_\mathrm{R}}{2}\right)\right|,$ with $\rho_\mathrm{m}^2\mathrm{P_m} = \mathrm{P}_{i,\mathrm{m}} = \mathrm{P_{R,m}}$ and $\tau_\mathrm{r}^2\mathrm{P_r} = \mathrm{P}_{i,\mathrm{r}} = \mathrm{P_{R,r}}$
$2f_{\mathrm{het}}$	sinusoidal	$\tilde{\mathrm{o}}i\_\mathrm{A,B,AB}(\hat{r}_\mathrm{r},\hat{r}_\mathrm{m}) = \sqrt{\dfrac{\tilde{r}_\mathrm{r}^2+\tilde{r}_\mathrm{m}^2}{4}}\left|\sin\left(\varphi_i - \varphi_\mathrm{R}\right)\right|$
	white noise	$\hat{\mathrm{o}}i\_\mathrm{A,B,AB}(\hat{r}_\mathrm{r},\hat{r}_\mathrm{m})_{\mathrm{corr.}} = \sqrt{2}\,\frac{\hat{r}_\mathrm{r}+\hat{r}_\mathrm{m}}{2}\left|\sin\left(\varphi_i - \varphi_\mathrm{R}\right)\right|$ $\hat{\mathrm{o}}i\_\mathrm{A,B,AB}(\hat{r}_\mathrm{r},\hat{r}_\mathrm{m})_{\mathrm{uncorr.}} = \sqrt{\dfrac{\hat{r}_\mathrm{r}^2+\hat{r}_\mathrm{m}^2}{2}}\left|\sin\left(\varphi_i - \varphi_\mathrm{R}\right)\right|$

Table 3.2.: Summarised here are the derived coupling coefficients from RIN to the phase signal. To show the coupling for one and two beams the frequency and beam is now indicated in brackets. All equations are either in [rad] or $\left[\frac{\mathrm{rad}}{\sqrt{\mathrm{Hz}}}\right]$. The subtraction of phase noise due to $1f_{\mathrm{het}}$ RIN when the beam powers are all different is more complicated, an example can be found in Equation 3.74. To increase readability the $^{(1)}$ and $^{(2)}$, which indicated the RIN frequency at either $1f_{\mathrm{het}}$ or $2f_{\mathrm{het}}$, are dropped, since the RIN frequency is already indicated in the first column.

3.4.3. Coupling of RIN to the DWS measurement

RIN not only couples to the length measurement, but also to the DWS measurement. The contribution of RIN to the sensing noise floor increases for bigger DWS offsets. As was explained in Subsection 2.6.3, the DWS signal is calculated by a subtraction of quadrant pairs. The pitch angles η are calculated by a subtraction of the lower two quadrants from the top two; and the yaw angles φ are calculated with a subtraction of the right side quadrants from the left side. The DWS signal is generated by the phase difference between the two pairs, if the two beams are parallel this phase difference is zero. Since RIN is present on the individual quadrants it is automatically subtracted in a similar fashion as in the longitudinal case; the remaining RIN follows a similar dependency on the phase difference.

Two experiments were performed during operations with the in-flight OMS. In the first the DWS offsets were increased by motion of TM2, an increase in noise could be found which followed the expected pattern for RIN. In the second experiment both test masses were moved to compensate for the beam motion associated with TM angular offsets.
The range of motion of both experiments is limited by the available range of test mass angular offsets. After a risk-assessment experiment to ensure the safety of bigger DWS offsets the range could be increased for the second DWS experiment. There, a decrease in noise for bigger offsets could be seen as is expected for the sinusoidal nature of RIN coupling.
The design and analysis of RIN DWS experiments for the LPF mission was done by Lennart Wissel, the analysis of the first DWS experiment can be found in his masters thesis [57]. The analysis of the second experiment will be shown in his PhD thesis.

3.5. Sensing noise

This section contains a short overview of the noise sources commonly summarised as phasemeter noise, namely electronic noise and ADC noise. In addition, the contribution of shot noise is shown. These noise sources are well known and the main difficulty lies in finding or measuring the relevant parameters. Of interest here is a technical note [66], also shown there are the calculations to estimate the noise on the phase from the signal-to-noise ratio between the carrier and the noise floor on the photocurrent. These are derived as

$$\hat{\varphi}_\mathrm{q} = \frac{1}{\mathrm{C/N_0}} = \frac{\hat{\mathrm{x}}}{\mathrm{x_{signal,\ rms}}}, \tag{3.94}$$

where x is a time domain signal and $\mathrm{C/N_0}$ is the signal-to-noise ratio. The amplitude of the phase signal to be measured is $\mathrm{x_{signal,\ rms}}$, with $\hat{\mathrm{x}}$ the amplitude spectral density of x near the carrier frequency. $\hat{\varphi}_\mathrm{q}$ is the resulting linear spectral density of the measured phase noise of one quadrant.

This noise level is calculated for one QPD quadrant, these contributions need to be added up according to the quadrants used. The signal on these quadrant diodes adds linearly while the noise is added quadratically. When the balanced signal of one quadrant pair of one interferometer is calculated the noise floor of the resulting phase signal decreases by $\sqrt{2}$. The signal strength of the whole interferometer, so all four quadrant pairs, adds linearly and therefore increases by a factor 4, while the noise adds quadratically and increases by a factor 2. The noise floor $\hat{\varphi}_i$ of one interferometer X_i can therefore to be calculated as

$$\hat{\varphi}_i = \frac{1}{2} \cdot \hat{\varphi}_\mathrm{q,\ balanced} \qquad \left[\frac{\mathrm{rad}}{\sqrt{\mathrm{Hz}}}\right], \tag{3.95}$$

$$= \frac{1}{2} \cdot \frac{1}{\sqrt{2}} \cdot \hat{\varphi}_\mathrm{q} \qquad \left[\frac{\mathrm{rad}}{\sqrt{\mathrm{Hz}}}\right]. \tag{3.96}$$

When the noise floor for o1, o12 or xF is calculated differences in the measurement interferometer signal, either x1, x12 or φ_F, and the reference signal φ_R have to be taken into account. The signals of the individual interferometers are obviously not the same, therefore do not add linearly, and the noise floor increases by $\sqrt{2}$ when o1, o12 and xF are calculated.[1]

$$\hat{\mathrm{o}}(1,12) = \frac{\lambda}{4\pi\cos\alpha}\sqrt{2} \cdot \hat{\varphi}_{1,12}, \qquad \left[\frac{\mathrm{m}}{\sqrt{\mathrm{Hz}}}\right], \tag{3.97}$$

$$\hat{\mathrm{xF}} = \frac{c}{2\pi\delta L}\sqrt{2} \cdot \hat{\varphi}_\mathrm{F}, \qquad \left[\frac{\mathrm{Hz}}{\sqrt{\mathrm{Hz}}}\right], \tag{3.98}$$

$$\hat{\mathrm{xR}} = \frac{\lambda}{4\pi\cos\alpha} \cdot \hat{\varphi}_\mathrm{R}, \qquad \left[\frac{\mathrm{m}}{\sqrt{\mathrm{Hz}}}\right]. \tag{3.99}$$

The contribution of the sensing noise floor and shot noise in flight is calculated from known and measured values. The laser wavelength λ, the photodiode responsivity $\mathrm{R_{PD}}$, the voltage range of the ADC $\mathrm{U_{ADC}}$ and the resistance of the transimpedance amplifier R are design properties of the system. The contrast C is measured for each interferometer, its mean value over the duration of the timespan under analysis is used in the calculation of the noise floor. Typical values for the measurement interferometers in the flight setup are 0.98% for X_{12} and 0.955% for X_1. During commissioning contrast values of 99% could be reached with careful test mass orientation, this test mass position however is not optimal for the performance

---

[1]Technically the calibration of the reference interferometer signal φ_R to nanometre is not correct, since its measurement beam is not reflected of the test mass. However, here the φ_R signal is calibrated in the same way as the measurement interferometer signals to compare the noise contributions.

variable	value	description
λ	$1064\,\mathrm{nm}$	Laser wavelength
$\mathrm{R_{PD}}$	$0.855 \pm 0.02\,\frac{\mathrm{A}}{\mathrm{W}}$	Photodiode responsivity (pre flight)[67]
$\mathrm{R_{PD}}$	$0.821 \pm 0.01\,\frac{\mathrm{A}}{\mathrm{W}}$	Photodiode responsivity (flight)[62]
$\mathrm{G_{flight}}$	$0.923 \pm 0.005 \cdot \frac{\mathrm{mW}}{\mathrm{AU}}$	Calibration factor for the power, flight setup [62]
$\mathrm{G_{lab}}$	$1.58 \pm 0.19\,\frac{\mathrm{mW}}{\mathrm{CDS\ units}}$	Calibration factor for the power, laboratory setup
$\mathrm{U_{ADC}}$	$5\,\mathrm{V}$	Voltage range of the ADC
$\mathrm{R_{TI}}$	$6640\,\Omega$	Transimpedance amplifier resistance

Table 3.3.: This table shows the necessary coefficients to calculate the sensing noise from measured values.

of the OMS. The power of the flight setup can be calculated from the measured sigma parameter. This parameter is calculated from the DC bins of the phasemeter measurement of the individual diodes, for each QPD quadrant the A and B diode measurement are added and multiplied by $\frac{1}{2}$. These four average DC values are then summed to create a measurement of the average power of both diodes of one interferometer [52]. The calibration factor $\mathrm{G_{flight}}$ from this DC bin measurement in arbitrary units to the laser power was measured for each diode, here their average value is used; see also [62].

The noise floor of the individual interferometer signals will be different for special circumstances, as was the case when the test masses were grabbed and the contrast in the measurement interferometers was very low. The noise floor model for the in-flight measurements holds in these circumstances when the noise floor is calculated for each interferometer individually and then added quadratically. A paper with a comparison of these is in preparation [59].

For the laboratory the contrast of all interferometers is typically around 85%. The DC bin of the phasemeter measurement of each photodiode input is recorded by the CDS; this value can be calibrated to power with the measured factor $\mathrm{G_{lab}}$, see Section 4.4.

The photocurrent I_i of the interferometer X_i can be calculated from the beam power on both photodiodes with

$$\mathrm{I}_i = \mathrm{R_{PD}}\left(\mathrm{P_m} + \mathrm{P_r}\right), \qquad \text{(laboratory)} \qquad (3.100)$$

$$\mathrm{I}_i = 2\,\mathrm{sigma} \cdot \frac{\mathrm{U_{ADC}}}{R}. \qquad \text{(flight)} \qquad (3.101)$$

For the calculation of the noise contributions shown later of the in-flight measurement the photocurrent is calculated as in Formula 3.101, for the laboratory measurement the photocurrent is calculated as in Formula 3.100.

The power can be calibrated from the measured value with

$$\mathrm{P}_{i,k} = \mathrm{G_{lab}} \cdot \mathrm{DC\_SUM} \qquad \text{(laboratory)}, \qquad (3.102)$$

$$\mathrm{P}_i = \mathrm{G_{flight}} \cdot \mathrm{sigma} \qquad \text{(flight)}. \qquad (3.103)$$

Where P_i is the average power of both diodes of one interferometer X_i of the flight setup, and $\mathrm{P}_{i,k}$ is the power of one diode of the laboratory setup. DC_SUM is the output of the DC bin of the laboratory phasemeter FFT of one interferometer.

3.5.1. Electronic noise

The noise contribution of the transimpedance circuit of one interferometer with balanced detection is calculated with:

$$\hat{x}_{i,\text{elec}} = \frac{\lambda}{4\pi \cos\alpha} \cdot \frac{4 I_{\text{q, elec}}}{R_{\text{PD}} C (P_{\text{m}} + P_{\text{r}})}, \qquad \left[\frac{\text{m}}{\sqrt{\text{Hz}}}\right] \qquad (3.104)$$

where $I_{\text{q, elec}}$ is the equivalent input current noise of the electronic circuit in $\left[\frac{\text{A}}{\sqrt{\text{Hz}}}\right]$ of one QPD quadrant, calculated in preparation of the mission. It was estimated via simulations of the electronic circuit and flight components used using LISO [68] and yields a value for the equivalent input current noise of $I_{\text{q, elec}} = 17.2 \frac{\text{pA}}{\sqrt{\text{Hz}}}$.

The contribution of electronic noise to the length measurement is calculated from the measured contrast and photocurrent, both values are the mean of the measured data of the experiment under analysis.

3.5.2. ADC noise

ADC noise is the main contribution to the sensing noise floor. The expected noise level of one interferometer with balanced detection can be calculated as

$$\hat{x}_{i,\text{ADC}} = \frac{\lambda}{4\pi \cos\alpha} \cdot \frac{4 I_{\text{q, ADC}}}{R_{\text{PD}} C (P_{\text{m}} + P_{\text{r}})}, \qquad \left[\frac{\text{m}}{\sqrt{\text{Hz}}}\right] \qquad (3.105)$$

where $I_{\text{q, ADC}}$ is the equivalent input current noise associated with the digitisation and number of effective bits in the ADC. The measured mean contrast and photocurrent are used to calculate the ADC quantisation noise. The noise is lower for higher contrast and bigger photocurrent as more of the ADC range is used.

The ADC current noise $I_{\text{q, ADC}}$ can be calculated from known values with

$$I_{\text{q, ADC}} = \frac{U_{\text{q, ADC}}}{R_{\text{TI}}}, \qquad \left[\frac{\text{A}}{\sqrt{\text{Hz}}}\right] \qquad (3.106)$$

$$= \frac{1}{R_{\text{TI}}} \cdot \frac{2^{-Nbits} U_{\text{ADC range}}}{\sqrt{6 f_{\text{ADC}}}}. \qquad \left[\frac{\text{A}}{\sqrt{\text{Hz}}}\right] \qquad (3.107)$$

Implemented in flight is a 16-bit ADC. Known from the data sheet is the number of effective bits for a sampling frequency of 333 kHz of 14.8 bits. The sampling frequency used however is 50 kHz. With this frequency and 14.8 effective bits the equivalent input current noise of $I_{\text{q, ADC}} = 48.5 \frac{\text{pA}}{\sqrt{\text{Hz}}}$ can be calculated.

From measurements in preparation of the mission, made with the ADC settings chosen for LPF and other flight hardware, the phase noise of two subtracted channels was measured to $\approx 650 \frac{\text{nrad}}{\sqrt{\text{Hz}}}$. From this the equivalent ADC input current noise was calculated to be $I_{\text{q, ADC}} = 102.4 \frac{\text{pA}}{\sqrt{\text{Hz}}}$ [66][69]. This value is used in the calculation of the ADC noise contribution of flight data in Section 6.5, and in [19].

For noise measurements where the test masses were grabbed this calculation is very interesting, as the noise contribution to o12 is very different between the X_{12} and X_{R} interferometers since the contrast on the PD12 diodes is very low and the contrast on the PDR diodes is in nominal range.

In the laboratory phasemeter an 18-bit ADC is implemented. With an effective number of 16 bits, and a sampling frequency of 800 kHz the equivalent ADC input current noise is $I_{\text{q, ADC}} = 5.2 \frac{\text{pA}}{\sqrt{\text{Hz}}}$.

3.5.3. Shot noise

The phase noise contribution of shot noise is calculated from the shot noise of the DC current and the rms value of the heterodyne signal level on the photocurrent with

$$\hat{x}_{i,\text{shot}} \quad = \frac{\lambda}{4\pi\cos\alpha} \frac{4}{C} \sqrt{\frac{e}{2R_{\text{PD}}(P_m+P_r)}} \cdot \quad \left[\frac{m}{\sqrt{Hz}}\right] \tag{3.108}$$

This noise scales with the laser power and is independent of the number of quadrants used.

3.6. Other noise sources

Relevant for the sensing noise measured are also other noise contributions which are not the focus of this thesis, but are often part of the error discussion of the results. This section contains a short overview of these other effects and references where more information can be found.

3.6.1. Tilt-to-length coupling

Visible in almost all spectra of the longitudinal measurement is the contribution of the pickup of space craft motion, this noise is visible as a 'bump' in the frequency range between $20\,\mathrm{mHz}$ and $200\,\mathrm{mHz}$. Space craft motion couples to the length measurement through various effects related to the tilt and offsets of the test masses, and the misalignment between the spacecraft and the optical bench. Via tilt-to-length coupling this noise contributes to the longitudinal measurement. Its impact was reduced by careful re-alignment of the test masses by adjusting the angular control setpoints.
This noise can be subtracted by a linear combination of the measurement of the spacecraft acceleration. However, through this process the sensing noise of the channels used is added to the sensing noise already present. During operations this process was called "de-bumping". In the first LPF paper this noise source is already mentioned, a noise spectrum with and without the bump are shown in [70]. Further details can be found in [42]; dedicated papers are in preparation [71][72].

3.6.2. Polarisation noise

In longterm monitoring experiments of the TM reflectivity and photodiode responsivity of the in-flight OMS an unexpected low frequency power noise was found. This noise is caused by an unstable polarisation state due to a degradation in the Polarising Beam Splitter (PBS) used to clean the light. At low frequencies this power noise causes radiation pressure noise on the test masses, more details can be found in [62].

3.6.3. Glitches and vibrations

In the laboratory setup vibrations have an effect on the measurement; the source are mainly other people near the laboratory, and construction work around the institute.
Measurements of the laboratory setup are cut around such disturbances, and noise measurements are often done over night or over the weekend.

In the flight data various glitches are present. Efforts were made to model and characterize the glitches and remove them from the data. These glitches appear in the signal after high frequency noise is removed with a lowpass filter, they can be categorized as one sided and two sided glitches which average back to zero.
The most likely cause for one sided glitches are sudden bursts of outgassing, which bounce multiple times between the test mass and the electrode housing. This spurious force signal ends when the gas is re-absorbed, or exits the vacuum tank which contains the test mass. A possible source for two sided glitches might be sudden steps in the pathlength difference, the second derivative of which would look like some of the glitches observed.
A first look at the nature and removal of glitches can be found in the supplemental material of the second big performance paper [18]. A longer and more detailed investigation of glitches can be found in [73][74].

3.6.4. Aliasing and windowing effects

When time series data is downsampled noise from higher frequencies can be transferred to noise at lower frequencies in the data at lower sampling frequency. This process is called aliasing, and is commonly mitigated with a lowpass filter before downsampling. Any sensing noise floor measured, and the contributions calculated from it, only function as a higher bound. The 'real' noise level might be lower, but is increased due to aliasing. A nice general explanation of aliasing can be found in [21], a description of the filters and frequencies of LPF can be found in [57].

On-board LISA Pathfinder the recorded $100\,\mathrm{Hz}$ is sampled to either $10\,\mathrm{Hz}$, $1\,\mathrm{Hz}$ or a lower frequency for housekeeping data, which is then send to ground. The sensing noise at higher frequencies was measured during the in-flight RIN step experiments, a comparison of $100\,\mathrm{Hz}$ with the $10\,\mathrm{Hz}$ counterpart can be found in Section 6.4.

The sampling frequency in the laboratory is higher than in flight, the phasemeter provides data at a sampling frequency of $\approx 162\,\mathrm{Hz}$, which is then recorded at a sampling frequency of $2\,\mathrm{kHz}$ in CDS and saved with $256\,\mathrm{Hz}$. Since the phasemeter data of the laboratory experiments is oversampled aliasing is not an issue. The effect of the window of the phasemeter on the spectrum can be removed, as was shown in Section 2.6.5.
RIN is recorded with the CDS FST model with an ADC, the effect of the the anti-aliasing filter of the ADC on the data is removed in post processing, as shown in Section 4.5. The sampling frequency of RIN data with $16\,\mathrm{kHz}$ is chosen so that the influence of the standard CDS downsampling lowpass filter will have a negligible influence on the highest frequencies of interest with $2\mathrm{f}_{\mathrm{het}} = 3.2\,\mathrm{kHz}$. RIN from $1\mathrm{f}_{\mathrm{het}}$ and $2\mathrm{f}_{\mathrm{het}}$ is also demodulated, and recorded at a sampling frequency of $256\,\mathrm{Hz}$, see Section 4.5.3. This data has to be corrected for the lowpass filter, more details can be found in Section 4.5.2.

3.7. Difference between laboratory and flight unit

The most obvious difference between the laboratory unit and the flight unit is the environment in which the measurements are made. One sits in a vacuum tank on earth, and the other 1.5 million kilometres away at Lagrange point 1 in the vacuum of space.

On earth the system experiences vibrations and temperature changes, a noise increase in the laboratory due to ground vibrations, worse vacuum and temperature changes is expected. The environment in space is more stable in this regard, the loss of the protective atmosphere however leads to an increase in radiation from the sun, and a gradual increase in the electric charge on the test masses. Experiments to characterize the charge rate and the discharge of the test masses were an important part of LPF operations, details can be found in [75].

The optical bench in the laboratory is the engineering model, the flight model optical bench was improved with the experience made in the laboratory. On the flight model some mirrors were moved to reduce beam clipping, and the angle between incoming and outgoing beam on the test masses was increased from 3.6° to 4.5° on the flight model. A documentation of the design improvements of the optical bench can be found in the thesis of Felipe Guzmán Cervantes (AEI) [34].

In the laboratory the test masses are glued on three-axis piezo actuators, which are mounted on the housing of the optical bench. The test mass mirrors can be expected to vibrate similarly to the optical bench and can be considered as reasonably stable. However the thermal expansion of the piezo and metal mounds is different than the thermally stable optical bench, the resulting test mass motion can be suppressed by a control loop. A description of this loop can be found in Section 4.3.

In flight the test masses are controlled with the Drag Free and Attitude Control System (DFACS) [76]. This control system uses the measurement of the position and orientation of the test masses, as well as star tracker data, as input and computes the actuation on the test masses and on the space craft thrusters to ensure the stability of the free-falling test masses. The cross-coupling from angular TM motion and space craft motion to the longitudinal TM measurement is an important aspect of the noise floor between 20 mHz and 200 mHz. This noise contribution was briefly mentioned in Section 3.6.1, a description can be found in [70]. The many kinds of forces acting on the free-falling flight test masses are subject of most papers about the performance of the LPF OMS in orbit, a first overview can be found in the two main LPF performance papers [70] and [18].

The ground setup has the obvious advantage that more channels can be read out, and that the practical maximum of the sampling frequency is at 64 kHz, whereas the typical downlink sampling frequency of the flight data is either 1 Hz or 10 Hz and can only be increased to 100 Hz for short periods of time.

The overall design of the LPF satellite is more careful than the laboratory, since the ground setup is an engineering model all the electronics and optics are less precise and all electric and optical noise sources can be expected to be higher.

4 Application to the laboratory

In the earlier chapters the noise sources of interest were explained, this knowledge is now applied to the laboratory setup.

In this chapter the design and performance of the laboratory control loops is shown. The transformation from analog to digital control loops of the OPD loop and frequency loop can be found in Sections 4.1 and 4.2. The newly designed control loop on the position and orientation of the test mass mirrors is shown in Section 4.3. In Section 4.4 the noise floor of the laboratory measurement is calculated.

In Chapter 5 the laboratory experiments to measure the properties of RIN are shown, this RIN is injected with the input on the AOM electronics intended to be used for the fast amplitude stabilisation. In these experiments the OPD loop is needed to stabilise the injected RIN in frequency, and to move the phase difference between the two beams to measure the contribution of small vector noise. The subtraction properties of RIN are tested in experiments where the test mass is moved with the TM control loop. An explanation of the laboratory setup to measure and inject RIN can be found in Section 4.5.

4.1. OPD control loop implementation

When the OPD loop was designed its aim was to suppress Small Vector Noise (SVN), a noise term caused by sidebands on the light. The source of these sidebands is an EM cross-coupling in the AOM electronics; in the setup at the AEI EM-shielding on the circuits was included to reduce this noise coupling. Remaining SVN is suppressed with a control loop. The coupling of this noise depends on the phase difference between the measurement beam and reference beam. The reference interferometer signal φ_R is used as input to the OPD loop, which stabilises this difference to zero.

A description of this noise source, and the initial investigations related to it, can be found in the technical note S2-AEI-TN-3028 [32]; further description of the loop design can be found in later technical notes [77][78] and in some of the PhD theses already mentioned in the introduction to Chapter 3 [29][36][37][40].

Since SVN was identified as a serious problem, extra care was taken for the flight unit to mitigate this noise source. Extra EM-shielding on the flight electronics as well as the OPD loop managed to reduce this noise.

The reference interferometer X_R has no armlength difference between measurement and reference beam, like the measurement interferometers X_1 and X_{12}, but does not reflect off the TMs. Any phase changes measured by X_R are not due to TM motion and are considered as noise. The signal of this interferometer is the input to the control loop. The phase measurement of X_R is used to control a piezo-actuated mirror on the modulation bench. In the laboratory the piezo acts on the reference beam; the flight model has piezos on both beams. When phase changes between the reference and measurement beams are measured the mirror is moved in the opposite direction to adjust the optical path length. This control loop is called the Optical Pathlength Difference loop, or OPD loop for short. Since this loop suppresses phase changes measured by the reference interferometer, it suppresses not only SVN but also other differential phase changes, such as vibrations and optical pathlength changes in the fibres.

The OPD loop only suppresses path length difference noise between the measurement and reference beams. Any phase changes present in both beams (common mode phase noise), can not be suppressed. Since X_R, X_1 and X_{12} have the same macroscopic path length difference between measurement and reference beam this common mode noise can be mostly removed by subtracting the reference interferometer phase from the other measurements [78]. In the laboratory OMS this subtraction is performed with the calculated phase signals, either with the balanced signals of one interferometer or with matched A and B ports between the measurement interferometers and the reference interferometer,

$$\text{xR[m]} = \frac{\lambda}{4\pi}\varphi_R[\text{rad}], \tag{4.1}$$

$$\text{o1[m]} = \frac{\lambda}{4\pi\cos(\alpha)}(\varphi_1[\text{rad}] - \varphi_R[\text{rad}]), \tag{4.2}$$

$$\text{o12[m]} = \frac{\lambda}{4\pi\cos(\alpha)}(\varphi_{12}[\text{rad}] - \varphi_R[\text{rad}]), \tag{4.3}$$

$$\text{xF[Hz]} = \frac{c}{2\pi\delta\text{L}}(\varphi_F[\text{rad}] - \varphi_R[\text{rad}]), \tag{4.4}$$

whereas in the flight processing this subtraction is done with the complex phase [52], see also Section 2.6. The efficiency of this subtraction depends on the phase difference between the reference and measurement signal, and on the source of the noise.

Relative Intensity Noise is the most interesting in this subtraction, as shown in Section 3.4.

4.1.1. Design of the loop

The phasemeter in the AEI laboratory only has 20 channels. In the nominal setup the phase of one quadrant photodiode per interferometer is measured, with an additional channel for one of the remaining diodes. In most of the experiments performed both of the X_R diodes, one of the X_F diodes as well as both of the diodes of either the X_1 or X_{12} interferometer are used.

The OPD loop in the laboratory uses only one of the reference interferometer diodes as input, and does not use balanced detection. With a balanced reference signal the OPD loop would not suppress antiphase noise in the system, which is noise common to the A and B diodes and removed when the balanced signal is calculated. Since for most laboratory experiments the signal of individual diodes is used, the noise of individual diode signals must be minimized. The setup of this, however, means that for noise sources which have a different sign for the symmetric and antisymmetric port of the recombination beamsplitter the noise suppression increases the noise in the port not used as loop input. This sign difference between A and B port is the case for RIN around $1f_{het}$, see Section 3.4.1.

For the control signal the same output of the phasemeter as in the analog setup is used; within the phasemeter the voltage output of all four quadrants of one of the reference interferometer diodes are summed and fed to an additional output. This voltage output is connected to an ADC of the CDS FST model where the data is recorded with a sampling frequency of 64 kHz. In the digital setup the reference interferometer output voltage is used to calculate the phase with the digital representation of the heterodyne signal.

The measurement of this input voltage is bandpassed around the heterodyne frequency. The implemented filter is a butterworth bandpass filter of order 8, with a lower frequency of 1 kHz
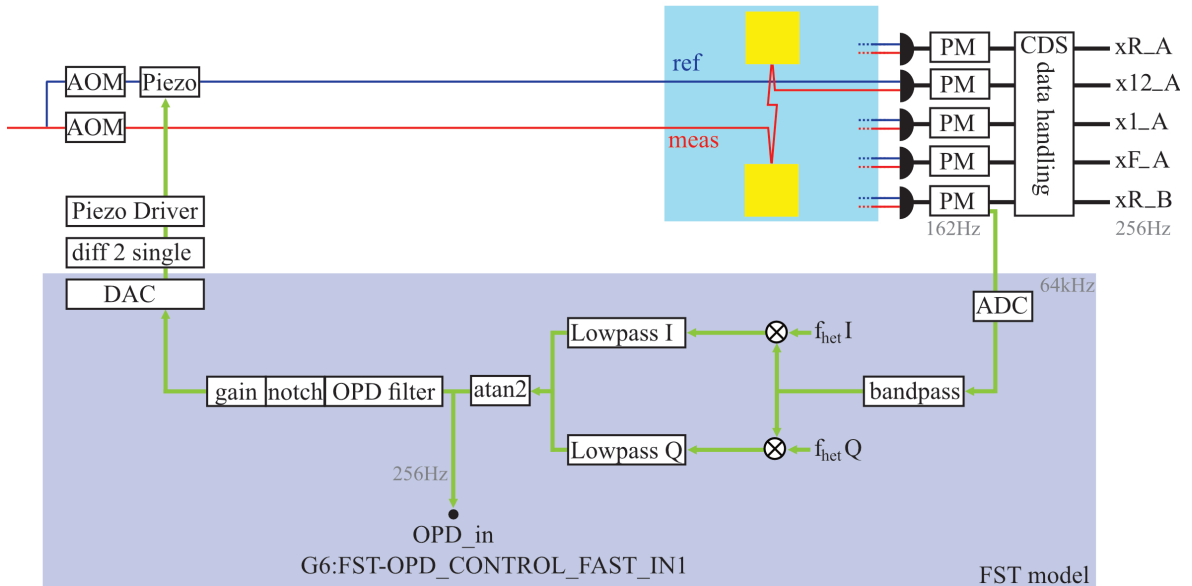
Figure 4.1.: This diagram shows the components of the OPD loop. From the interfered signal of the individual beams the phase signal is calculated, the reference beam is shown in blue and the measurement beam in red. Relevant here is the diode used as input to the OPD loop PDR_B. The phasemeter calculates the standard signal $\varphi_{R\_}B$ and also gives the summed voltage of all four quadrants of PDR_B. From the voltage and the digital heterodyne frequency the phase is calculated in the FST model, which is then used as input to the OPD loop. The PM and CDS phase signals are not the same, due to their different paths the delay of the PM signal is higher. The DAC output of the digital OPD loop is converted from a differential voltage signal to a single-ended voltage. This voltage is then used as input to the driver, which moves the OPD piezo on the modulation bench.

and an upper frequency of 2.1 kHz. By creating a beatnote with the I and Q component of the digital representation of the heterodyne signal the real and imaginary component of the phase are calculated. To remove noise these signals are lowpassed, with an additional notch filter at $2f_{het}$. The phase is calculated with an atan2 function from its real and imaginary components. The calculated phase signal $\varphi_{R,FST}$ is used as input to the OPD loop, digital filters are then applied to calculate the desired actuation.

The differential voltage output from the DAC of the CDS is fed into a self-built differential-to-single ended converter. Via the DAC this actuation is applied to the piezo actuator on the modulation bench, which changes the pathlength of the reference beam to suppress the measured noise.

An overview of the whole control loop can be found in Figure 4.1, the Simulink® implementation of the processing in the FST model can be found in Figure A.4, in the appendix.

In the previous analog setup the same voltage output of the phasemeter was used, but the loop electronics calculated the phase by creating a beatnote with the analog heterodyne signal. The phase error derived from this electric signal was used as input to the analog OPD controller, which moves the previously mentioned piezo actuated mirror on the modulation bench. The same actuator and its electronics are still in use.

The OPD loop must be turned on for experiments where RIN is injected as a sine wave; the reasoning can be found in Section 4.5.1. The loop, however, changes the amplitude of the injected signal. This amplitude needs to be restored for the experimental confirmation of the predicted RIN transfer functions, the correction which needs to be applied to remove the effect of the OPD loop can be found in Section 4.1.3.

4.1.2. Transfer function

A measurement of the transfer function of the whole closed loop can be found in Figure 4.2. The transfer function measured is $\mathrm{CLG}_2 = |\frac{\mathrm{G}}{1-\mathrm{G}}|$, where G is the open loop gain. The transfer function was measured with the `diaggui` tool of the CDS, for both PDR_A and PDR_B as input to the OPD loop, and exported to MATLAB® as complex values. From the measured closed loop transfer function the open loop transfer function G of the loop can be calculated with

$$\mathrm{G} = \frac{\mathrm{CLG}_2}{1+\mathrm{CLG}_2} = \frac{\mathrm{CLG}_{\mathrm{measured}}}{1-\mathrm{CLG}_{\mathrm{measured}}}, \tag{4.5}$$

where the sign difference between theoretical and measured transfer function is due to the way the loop output is used to correct the measured phase noise. The measured transfer function CLG_2 is plotted together with the open loop gain G and the closed loop transfer function $\mathrm{CLG}_1 = \frac{1}{1-\mathrm{G}}$ in Figure 4.2. The individual components of the OPD loop are implemented in MATLAB® to correct the measured phase for the actuation of the OPD loop.
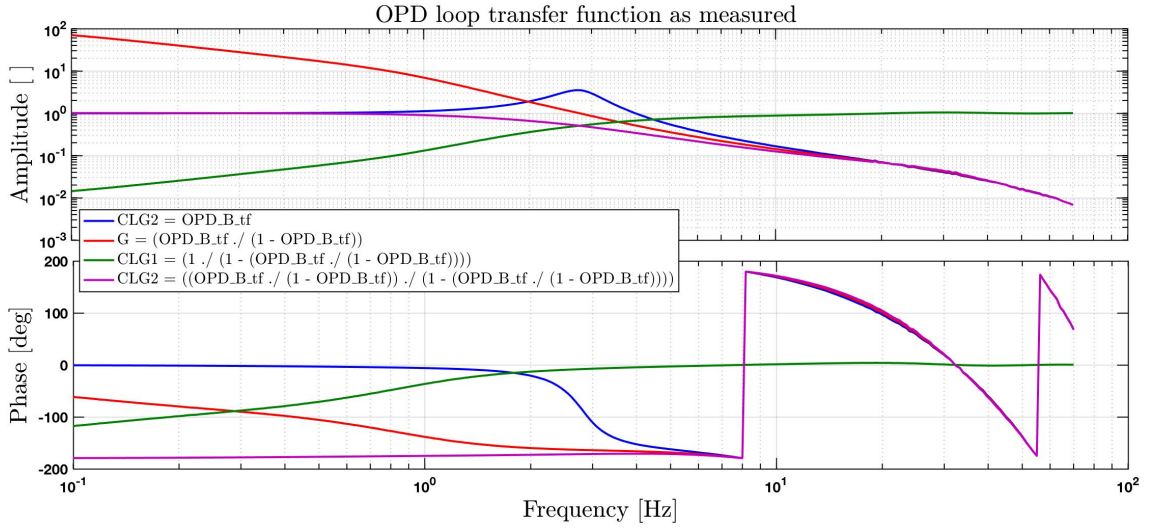
Figure 4.2.: Shown here is the result of a closed loop transfer function measurement of the OPD loop, in blue, with PDR_B as input to the loop. From this measurement the loop gain (red) and the loop noise suppression (green) is calculated.

The AA filter of the ADC and the lowpass filters of the phase calculation can be ignored for the calculation of the OPD loop transfer function, since these are applied to the voltage, and not to the phase calculated from it. Only the accumulated delay of these components is relevant for the model of the whole loop.

To calculate the desired loop output digital filters are applied to the calculated phase, a plot of the implemented digital filter can be found in Figure 4.3. The filter implemented in CDS has poles at [1e-2, 1e-2, 0.5, 50] Hz and zeros at [1, 5, 15] Hz, with a gain of -0.02. With an additional notch filter at $1\mathrm{f}_{\mathrm{het}}$ residual high frequency signals are removed. The same filter is implemented in the loop model for the phase correction.

The phase signal measured is in the mrad range, and is scaled with a gain of $10^9 \frac{\mathrm{Count}}{\mathrm{rad}}$ to fit to the desired range for the output voltage of the DAC. The 16-bit DAC calculates the output voltage of $\mathrm{V}_{\mathrm{DAC\ range}} = \pm 10\,\mathrm{V}$ per pin from the internal unit Counts, which have a range between $\mathrm{DAC}_{\mathrm{out}} = \pm 2^{15}\,\mathrm{Count} \approx \pm 32\,\mathrm{kCount}$.

The differential output voltage is converted to a single-ended signal with self-build electronics. To reduce quantisation noise the output voltage of the DAC is increased above the needed
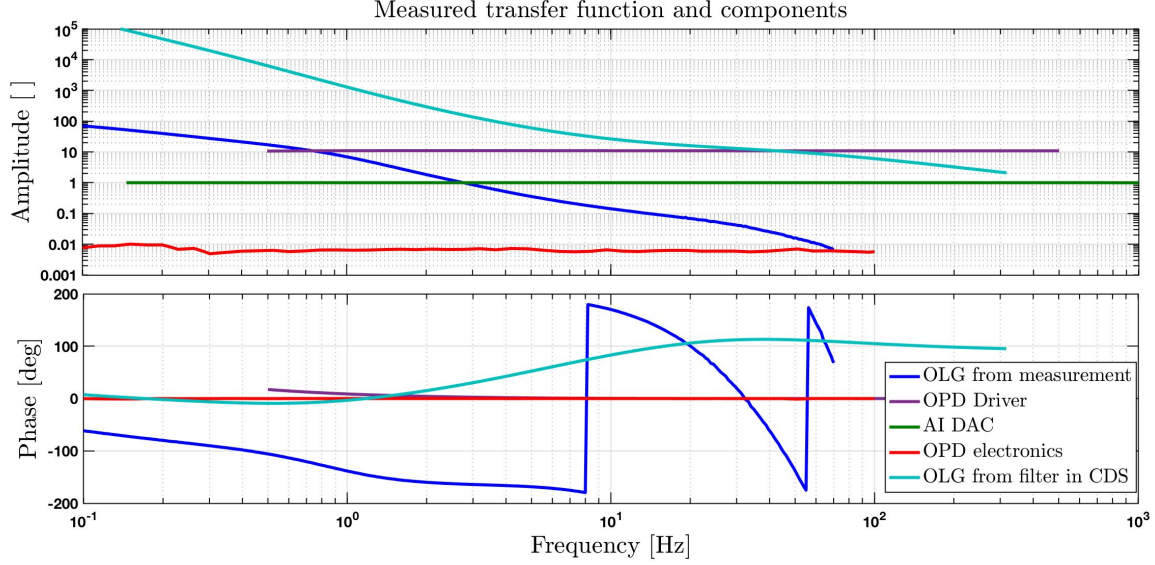
Figure 4.3.: Shown here is a measurement of the transfer function of individual hardware components of the OPD loop. The transfer function of the OPD electronics, which convert the voltage signal from differential voltage to single-ended, and the OPD driver electronics are measured with a spectrum analyser. The transfer function of the Anti-Imaging filter of the DAC is measured with CDS. In the frequency range of interest the hardware transfer functions are flat and have an effective delay of zero. In the model of the loop they are therefore represented as a gain.

The open-loop-gain of the digital filter as implemented in CDS is shown in turquoise. This filter bank includes a Notch filter at $2f_{het}$, which is flat at lower frequencies. The input to this filter is the phase signal calculated from the voltage of one of the X_R diodes with the digital representation of the heterodyne frequency. The output of this filter is sent out of the DAC to the OPD piezo on the modulation bench.

level, this converter also contains a gain stage to reduce the voltage to the level needed as input to the OPD piezo driver. A monitor output with a buffer is included to readout applied signals with an oscilloscope. The measured transfer function of this converter with a single-ended voltage input is almost flat with a gain of $G_{\text{OPD el}} = 0.006$ in the frequency range of the OPD loop, with a negligible phase delay. As the nominal input is a differential voltage the factor between input and output voltage is expected to be around 0.012; see Figure 4.3 for a measurement of the transfer function.

The transfer function of the piezo is unknown, though it is expected to consist only of a gain in the frequency range of interest. This gain, which effectively converts the input voltage to a pathlength change, is combined with the DAC gain of $G_{\text{DAC}} = \frac{10\,\text{V}}{2^{15}\,\text{Count}}$. Their combined gain is determined to be $G_{\text{act}} = G_{\text{piezo}}G_{\text{DAC}} = 0.06\,\frac{\text{rad}}{\text{Count}}$ in the confines of the model.

Also of interest for this correction is the delay between the phasemeter measurement and the CDS measurement in the FST model. To correct the impact of the OPD loop correctly from the phase measurement the measured input value has to include an additional delay. This delay is measured to $d_{\text{PM-CDS}} \approx 0.015\,\text{s}$ by a calculation of the transfer function between a phasemeter measurement and a CDS FST model measurement of the same signal. A plot of this measurement can be found in Section 4.1.3 in Figure 4.6.

The transfer function of the DAC, the differential-to-single-ended electronics and the piezo with its electronics are flat in the frequency band of the OPD loop, they can be approximated by a gain for the model of the loop.

This model is used to correct for the phase change due to the OPD loop actuation, the MATLAB® implementation can be found in Appendix A.3. A comparison of the measured

transfer function with the transfer function of the model of the OPD loop can be found in Figure 4.4. The motion of the OPD piezo is calculated from the recorded OPD loop input with the open loop gain of the OPD loop. This motion is then used to correct the measured phase amplitudes in RIN experiments in Sections 5.1 and 5.2; a description of this correction can be found in Section 4.1.3.
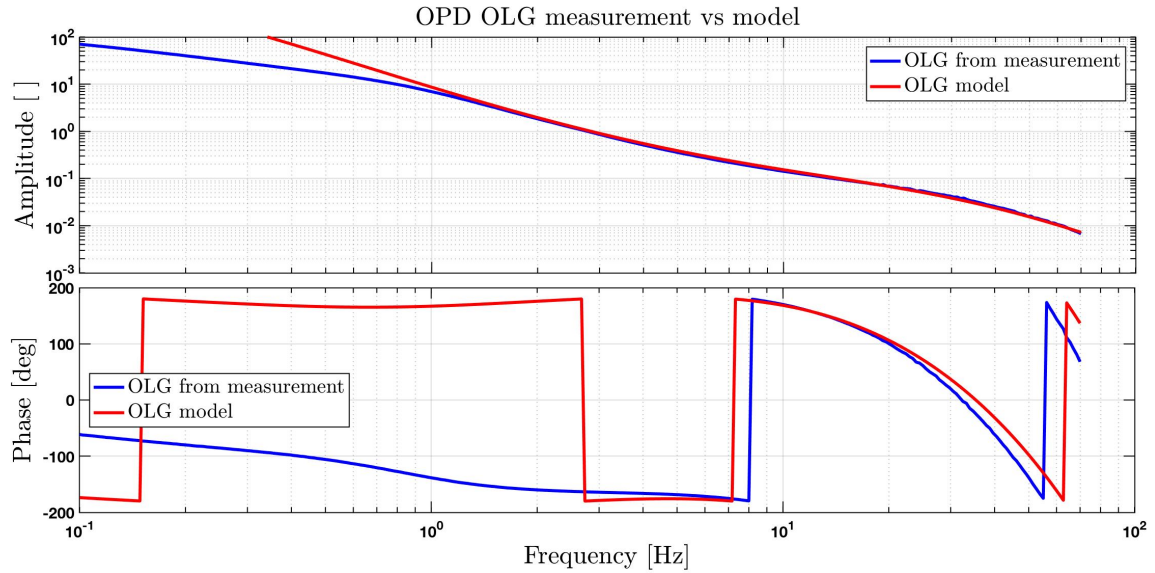
Figure 4.4.: Shown here is the complete model of the OPD loop in a comparison with the measured transfer function. For the correction of the measurements presented in this thesis the model only needs to be accurate above 1 Hz, the reason for the discrepancy at lower frequencies could not be found. The delay of the OPD loop model is accurate around 12 Hz, which is a frequency of interest in the experiments shown in Section 5.1.

4.1.3. Correction of the phase signal

A main part of this thesis is the experimental confirmation of the theoretical prediction of the behaviour of RIN in our interferometer. During the setup of these experiments it became clear that the OPD loop needs to be turned on for the experiments to work; an explanation can be found in Section 4.5.1.

In the RIN experiments shown in Sections 5.1 and 5.2 a sinusoidal signal is injected on the laser amplitude, which leads to a sinusoidal response on the phase signal. However, the amplitude of this phase signal is influenced by the OPD loop, and the impact of the OPD loop needs to be corrected. The input signal to the OPD loop $\varphi_{\mathrm{R,FST}} = \mathrm{OPD}_{\mathrm{in}}$ is recorded and can be used to correct the measured phase. The input is recorded as G6:FST-OPD_CONTROL_FAST_IN1_DQ and it is saved with a sampling frequency of 256 Hz. This data was originally recorded at a sampling frequency of 64 kHz, and needs to be corrected for the downsampling filter $\mathrm{tf}_{\mathrm{DAQ}}$. See also Section 4.5.2.

From the time series of $\mathrm{OPD}_{\mathrm{in}}$ the motion of the OPD piezo is calculated by using the `fftfilt` function with the open loop gain of the OPD loop components after the input. With the `fftfilt` function of LTPDA a filter can be applied to a time series object. The motion of the OPD piezo $\mathrm{OPD}_{\mathrm{piezo}}(t)$ is calculated with the modelled OPD loop gain G(f) from the recorded input to the loop with

$$\mathrm{OPD}_{\mathrm{piezo}}(t) = \mathtt{fftfilt}\left(\mathrm{OPD}_{\mathrm{in}}(t), \mathrm{G(f)}\right). \tag{4.6}$$

Shown in Figure 4.5 is the time series of the PDR_B diode, as measured by the phasemeter in the signal xR_B and as input to the OPD loop calculated from the QPD voltage output and the digital representation of the heterodyne frequency, OPD_in. The control signal of the OPD loop moves a piezo on the modulation bench, its motion is calculated as in Equation 4.6, and is labelled as OPD actuation in the plot. The time series are bandpassed around 12 Hz, since this is the frequency of the RIN injection of this experiment. For this injection frequency the closed-loop gain is less than 1.
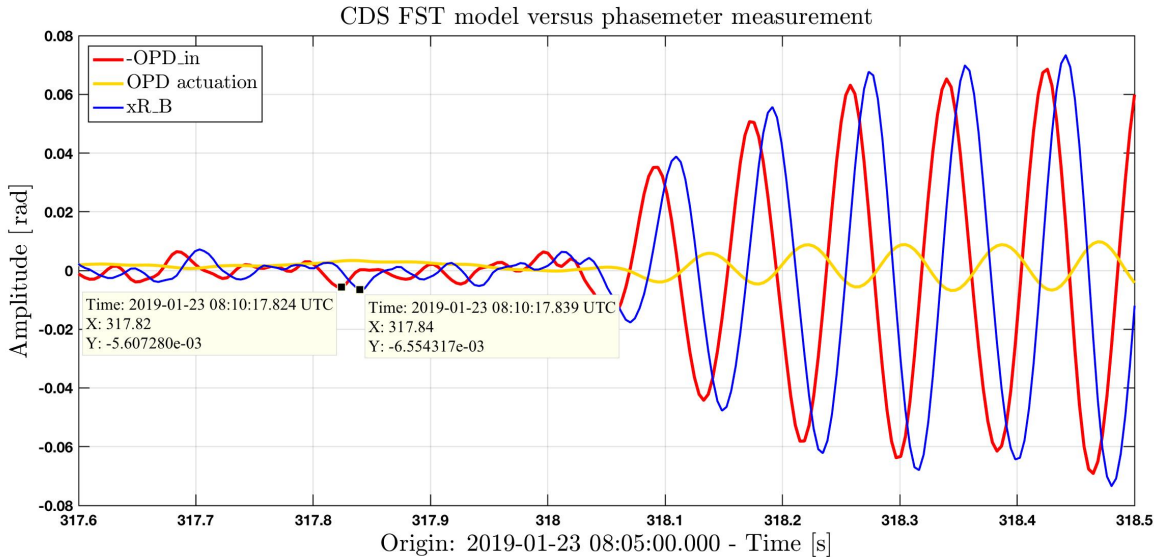
Figure 4.5.: Shown in this plot is the start of a RIN injection at $1\mathrm{f}_{\mathrm{het}} + 12\,\mathrm{Hz}$, the data is bandpassed around 12 Hz. The signal of the PDR_B diode is measured by the phasemeter as xR_B (blue), and by the CDS FST model as input to the OPD loop as OPD_in (red). From the OPD input the actuation of the OPD piezo on the modulation bench is calculated, shown in yellow. The phasemeter measurement xR_B accumulated a bigger delay in its measurement chain than the CDS measurement by $\mathrm{d}_{\mathrm{PM\text{-}CDS}} \approx 0.015\,\mathrm{seconds}$.

The amplitudes of the phase due to the injected RIN, and of the OPD loop reaction to it, are calculated with a DFT. In the following calculations the measured signal on the phase as calculated by the DFT is named $a_{measured}$, and the motion of the piezo is named $a_{OPD\ piezo}$. The impact of the OPD loop on the measured amplitude is restored with

$$a_{corrected} = abs(a_{measured} - a_{OPD\ piezo}).\qquad(4.7)$$

This correction removes the motion of the OPD piezo from the phase signal. The sign of the correction is the same for the A and B diodes. Since the DFT calculates a complex value the delay of the OPD loop, meaning here the delayed response of the OPD piezo motion on the modulation bench to the signal on the phase, is accounted for. The phase difference between symmetric and asymmetric port for RIN injections near $1f_{het}$, as calculated in Section 3.4.1, is also accounted for by the phase of the complex DFT.

This corrected measured phase signal $a_{corrected}$ is then used for further analysis.

An important part of this correction is the delay in the measurement of the phasemeter and of the CDS FST model. The control loops function with voltage inputs to the DAC, which are processed within the CDS. The standard phase signals of the interferometer are calculated by the phasemeter and then recorded in the CDS. Since the phase signal xR_B and the OPD loop input OPD_in are recorded from the same diode PDR_B with different measurement chains the delay between the two can be measured. This is achieved with the calculation of the transfer function from OPD_in to xR_B, a plot of which is shown in Figure 4.6. Visible here is that the measured amplitude is the same at frequencies below 1 Hz, but the sensing noise at higher frequencies is different. In the phase difference of the two signals the delay between the two measurement chains can be calculated to $d_{PM\text{-}CDS} \approx 0.015s$.

This delay is accounted for in the calculation of the OPD loop model, since this model is used to calculate the correction on measurements made by the phasemeter.
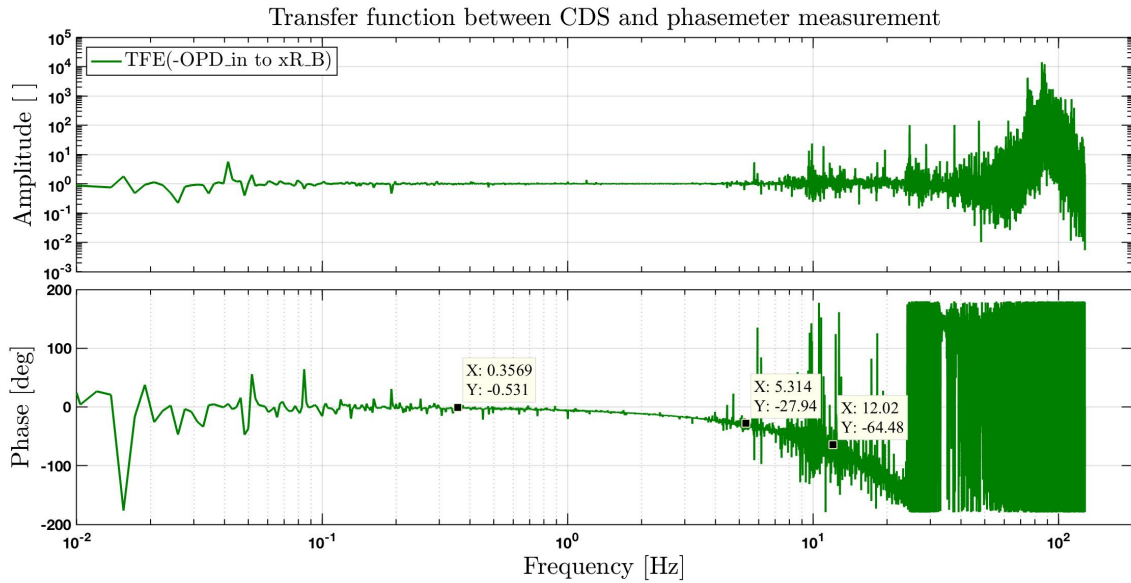
Figure 4.6.: With the transfer function calculated between the phasemeter channel xR_B and the CDS channel OPD_in the delay between the two is estimated to $d_{PM\text{-}CDS} \approx 0.015s$. For lower frequencies this delay is a smaller percentage of the wavelength and for higher frequencies a bigger percentage, which is why the phase shift is frequency dependant.

4.2. Frequency control loop implementation

Frequency noise couples to the length measurement as explained in Section 3.2. The coupling to the phase depends on the pathlength difference between reference and measurement beam. Frequency noise is measured with the frequency interferometer X_F, with an intentional arm length difference of 38 cm; this measurement is used as input to the frequency control loop. It is implemented in the digital setup in a similar way to the OPD loop.

The frequency control consists of two nested control loops. Fast changes of the laser frequency can be achieved by putting strain on the laser crystal with a piezo [60]. To increase stability the output of the fast loop is also the input to the filter banks of the slow loop. The signal of the slow loop changes the temperature of the laser crystal to counteract longterm drifts and bigger offsets in the laser frequency [78][32][79].

For the main experiments shown in this thesis the frequency control loop was not turned on, therefore it will not be described with a high level of detail.

4.2.1. Design of the loop

The fast and slow frequency control loop are part of the FST model of the CDS. For the frequency control loop the sum of the voltages of all four quadrants of one diode of the frequency interferometer is used as input, the same voltage output of the phasemeter as in the analog setup is used. This voltage is recorded by a DAC channel of the CDS FST model. The digital implementation is similar to the OPD loop. The phase signal of the frequency interferometer $\varphi_{F,FST}$ is calculated from the real and imaginary components I and Q from the beatnote between the voltage output of one X_F diode and the digital representation of the heterodyne frequency.

To remove common noise, and uncover the frequency noise, the reference interferometer signal as calculated by the OPD loop is subtracted from this frequency interferometer signal. Other
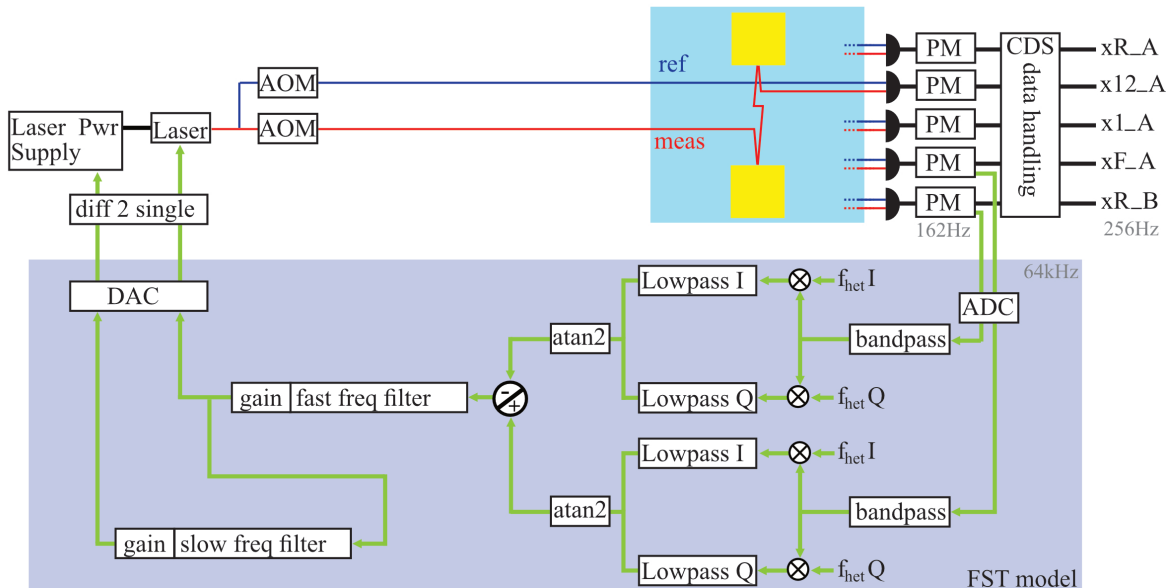
Figure 4.7.: Shown here is the implementation of the Frequency control loop in CDS. The phase signal for both X_F and X_R are calculated from the voltage output of the phasemeter with the digital representation of the heterodyne frequency. The frequency noise is isolated by a subtraction of the reference. From this the two loop outputs are calculated by the filter banks and send to the DAC. This differential voltage signal is transformed to a single-ended voltage signal, and send to the laser temperature control on the laser power supply and the piezo input on the laser.

noise common to all interferometers should not be part of the input to the loop, since it is not desired to counteract phase noise from other sources with a change in laser frequency. The resulting signal $\text{FREQ}_{\text{in}} = \varphi_{\text{F,FST}} - \varphi_{\text{R,FST}}$ is then used as input to the digital control filters.

In the previous analog setup the same voltages from the phasemeter were used as input. The phase φ_{F} was calculated from a beatnote with the analog heterodyne frequency, the control loop outputs were calculated by dedicated electronics. Different to the previous analog setup the complexity of the loop now resides in software, while the hardware is only used to adapt the output voltage of the CDS to the desired inputs on the laser system. A screenshot of the implementation in Simulink® can be found in the Appendix in Figure A.6. A simplified diagram of the whole control loop can be found in Figure 4.7. The connection from this model to the reference phase from the OPD loop and the DAC can be seen in Figure 2.9 where an overview of the CDS FST model was shown.

In preparation of control loop experiments of the in-flight setup the frequency loop in the laboratory was adapted to be closer to the flight model. Instead of the digital transfer functions which are similar to the transfer functions of the previous analog setup, the same parameters as in the flight control loop were implemented. The same filters were used during the OSTT campaign, a description of these measurements can be found in the technical note [80] and in [40].

The in-flight experiments consist of short sinusoidal injections at an increasing frequency to characterise the loop response. With scripted injections the planned in-flight experiments could be tested in the laboratory. The analysis of the in-flight measurements can be found in the thesis of Sarah Paczkowski [41] and [19].

4.3. Test mass control loop implementations

Due to temperature changes the piezo mounted test mass mirrors move relative to the optical bench, over the course of a day-night cycle this motion is typically around 500 nm. Other temperature changes, for example due to weather effects, also influence the measured TM position.

For some of the experiments it is necessary to keep the TMs stable, or move them in a controlled manner. If the TM is kept at its zero position the noise contributions from RIN in the subtracted signal can be minimised, and the coupling of angular noise to the length measurement can be kept at a constant value. To this end, a control loop for each relevant degree of freedom is implemented. The length and angular changes measured by the phasemeter are used as input. As actuator a three-axis piezo is used. It is able to move the TM mirrors longitudinally, as well as in pitch and yaw angles. The TM control loops hold the measured phase and DWS offset near optical zero, and enable experiments where the TM mirrors are moved in steps or with sinusoidal injections. The possible motion range is fixed by the voltage output of the DAC, faster motion of the TM can be achieved by an increased gain.

In the initial version of this loop the single-diode signals x1_A and x12_B were used as input to the TM control loops. For later experiments the input is changed to A-side signals with the reference signal subtracted. It was found that the OPD loop works better with the PDR_B diode, so the diodes were switched on the phasemeter. The input to the loop was not changed, however it still functions as desired since the noise sources relevant for the TM control are the same on the A and B side.

In flight the TMs are controlled with the Drag Free Attitude Control System (DFACS). Since the TMs are free-falling the force is applied with capacitive actuators [76][43].

4.3.1. Design of the loops
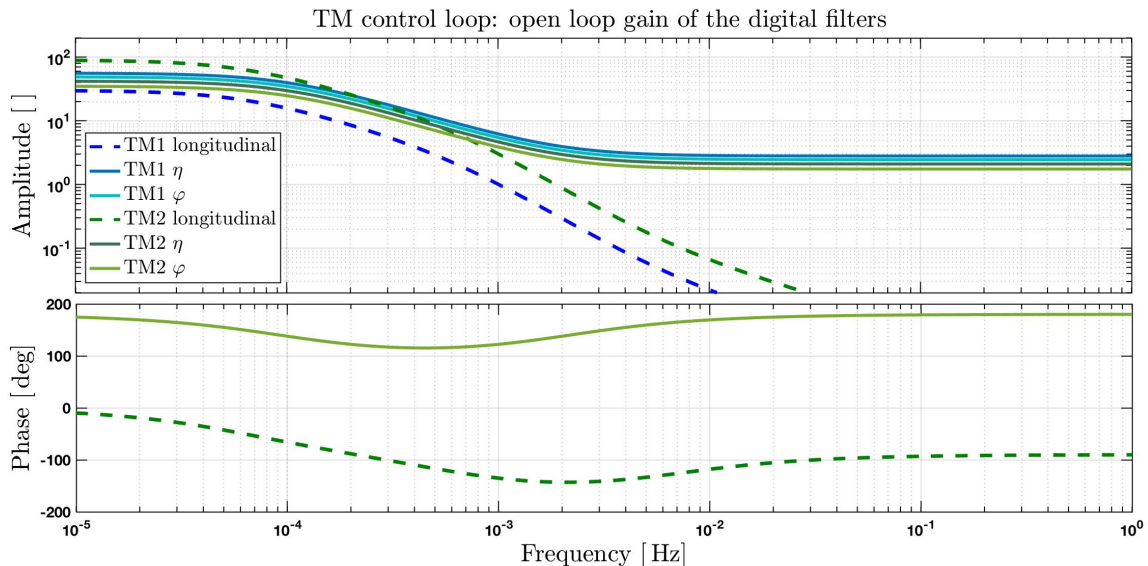
Figure 4.8.: This is a plot of the digital implementation of the loop filter. Not included here is the transfer function of the matrix to calculate the voltage on the piezos and the gain applied to each DoF. Shown in blue colours are the transfer functions on TM1, in green the transfer functions on TM2. The longitudinal axis is plotted with dashed lines. The delay of the two longitudinal filters is the same, as are the delays of the angular filters.

A first design of the TM control loops had the gain set so that the control loops would act

pole zero model		DOF	Gain
longitudinal		x1	1
poles	$6.28 \cdot 10^{-5}\,\mathrm{Hz}$, $6.28 \cdot 10^{-4}\,\mathrm{Hz}$	$\eta 1$	0.08
zeroes	$6.28 \cdot 10^{-3}\,\mathrm{Hz}$	$\varphi 1$	0.07
angular		x2	3
poles	$1 \cdot 10^{-4}\,\mathrm{Hz}$, $1 \cdot 10^{-5}\,\mathrm{Hz}$	$\eta 2$	0.06
zeroes	$2 \cdot 10^{-3}\,\mathrm{Hz}$, $4 \cdot 10^{-4}\,\mathrm{Hz}$	$\varphi 2$	0.05

Table 4.1.: Shown here are the filters and gains of the TM control loops as implemented in the laboratory. Not shown is an initial gain of 30 for both linear degrees of freedom, and a gain of 700 for the angular DoFs. These filters were improved from initial values over the course of the in-orbit operations in long-term performance experiments.

at very low frequencies, below the measurement band. An increase in quantisation noise near unity gain of these control loops was found, this additional noise was present in the measurement band and could not be removed. Therefore the gain of the TM control loops was increased, so that unity gain is above the interesting frequency range. This design change led to a suppression of regular noise and to an undesired reduction of the noise floor. The input to the control loops is recorded and can be restored to the measured phase signal, see Section 4.3.4. The phasemeter output of the pathlength change and the DWS signal is measured in (optical) radian, for these control loops these signals are then calibrated to meter and (angular) radian in CDS.

To reduce numerical noise in the filters, and since it is a more natural unit to the scale of motion of the Pathfinder setup, the input is calibrated to nanometre and microradian for length and angular measurement, respectively. This signal is then passed through a filter bank to suppress high frequency fluctuations.

The transfer function implemented for the linear control loops of the two TMs are the same, as are the transfer functions for all angular degrees of freedom. A gain is implemented after each transfer function. Some amount of actuation crosstalk from one loop to the other degrees of freedom is expected, setting the control loops at different strengths removes the risk of oscillations between the loops of one TM. The poles and zeroes of the longitudinal and angular transfer functions, as well as the gains to separate the loops, can be found in Table 4.1. The transfer functions are implemented as a pole-zero model in `foton`. `Foton` is the program within CDS to create filters, which can applied in filter banks implemented in Simulink®.

To prepare for the RIN step investigations during the mission, laboratory experiments were performed. For a test run of the planned experiments TM2 was moved in steps over a large parameter space. The gain of the x2-loop was lower during setup of the initial control system than the gain on x1, so that TM2 loosely follows the motion of TM1. For these experiments the gain on the longitudinal control of TM2 was increased from the initial value 0.8 to 3.

The improved laboratory experiments where TM1 is moved in steps to measure the RIN subtraction can be found in Section 5.3. For these experiments the gain on the TM1 longitudinal control is reduced to 0.5. In these experiments the x12 signal is not measured to enable balanced detection.

The voltage input on the three axis piezos must be calculated from the desired actuation on the degrees of freedom of the TM mirrors. For this a matrix that calculates the needed voltage output from the DAC to each of the three piezos of the TM mirror for a given TM actuation is calculated from a decoupling experiment. A short description can be found in Section 4.3.3.

With three differential DAC channels per TM the voltage is fed through the TM driver circuit
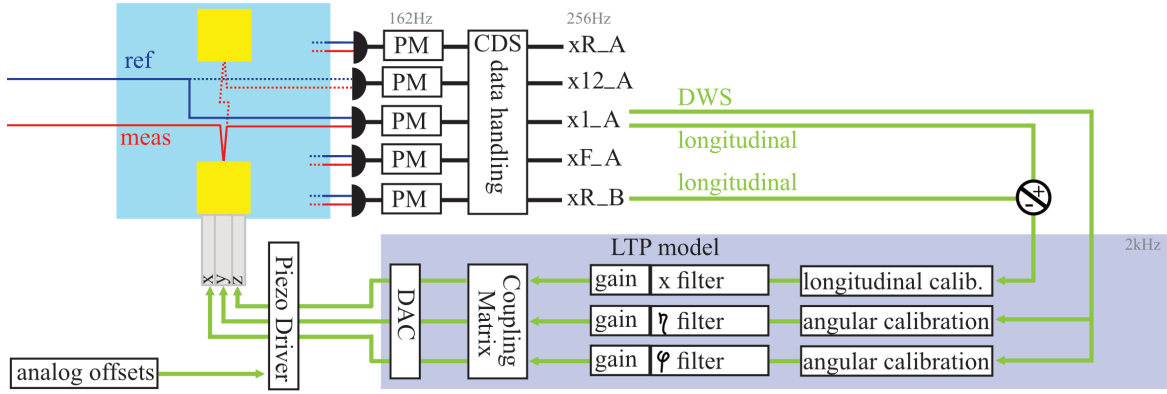
Figure 4.9.: This diagram shows the longitudinal and angular control loops on TM1. For the longitudinal control loop the x1_A signal with the reference signal subtracted is used as input. For the angular control loops the DWS signal measured by the phasemeter is calibrated to the TM angular offset, which is then used as input to the digital filters. Digital filters are applied to the phasemeter signals to calculate the desired TM actuation; the filters implemented for all degrees of freedom can be found in Table 4.1. These signals are fed out of the CDS via the DAC, with three channels per TM. This differential voltage output is transformed to a single-ended signal in the TM driver, see Section 4.3.2, this voltage is then applied on the piezo actuator on the TM mirrors.

to the three-axis piezo on the optical bench. This circuit converts the differential voltage to a single-ended signal, and includes a lowpass to reduce quantisation noise. An analog voltage offset can be added to the actuation voltage to align the TMs, a description of the electronics can be found in Section 4.3.2. The implementation of the digital components in Simulink® can be found in Appendix A.8; a diagram of the whole control loop of TM1 can be found in Figure 4.9. The control loop on TM2 is similar. For this control loop the x12 signal with the reference signal subtracted is used for the longitudinal loop, and the DWS angles φ_2 and η_2 calculated as shown in Section 2.6.3 are used as input for the angular control. This loop could already be seen in Figure 2.7.

A measurement of the closed loop transfer function of the longitudinal control loop on TM1 can be found in Figure 4.10; this plot also shows the model of the transfer function of this control loop. The LTPDA implementation of this control loop model can be found in the Appendix A.7.
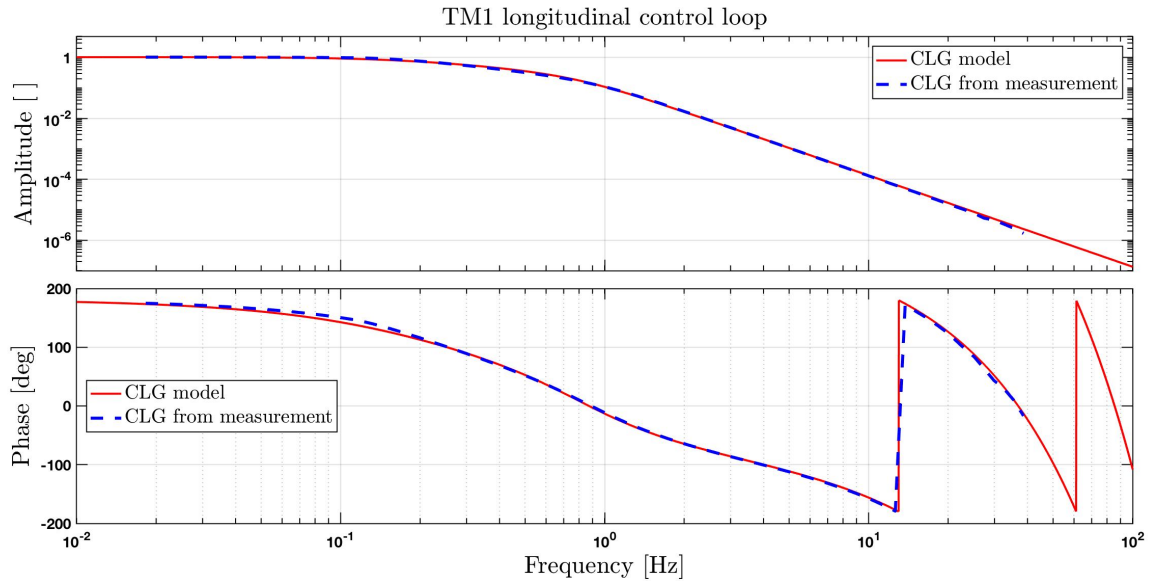
Figure 4.10.: This plot shows the measured closed loop gain of the longitudinal control loop of TM1, this transfer function is measured with the `diaggui` tool of CDS. Also shown in this plot is the modelled transfer function of the control loop. Implemented are the known components of the loop, with the gain of the piezo actuator as the only unknown piece. This gain was derived from the measured transfer function.

4.3.2. Electronics

In the previous analog setup the piezos were moved with one driver circuit per TM. This old driver has an input for injections along the x, η and φ degrees of freedom. With an additional high voltage input the range of piezo motion could be extended. The electronics divide voltages according to a fixed orientation of the TM mirror. Fine adjustments can be achieved by observation of the cross-coupling between x, η and φ, and manual decoupling by turning a trimmer.

In the new setup, the CDS is used to control the TM piezos. The intricate circuit design of the previous setup is replace with a simpler circuit. The complicated decoupling of the degrees of freedom is performed in software, the driver circuit translates the differential output from the CDS to a voltage with ground reference. The influence of digital noise on TM motion is reduced with a 2nd order active lowpass filter with a 1Hz corner frequency. The circuit was designed with LISO. In Appendix A.12 a measurement of the transfer function, together with the modelled transfer function can be found.

After experiments with the prototype electronics it was decided that a voltage offset on all piezos is necessary for rough alignment of the TM, before the control loops are turned on. Due to the limited range of only $\pm 10\,\mathrm{V}$ per pin of the DAC, analog voltage offsets and a voltage adder are included on the circuit, instead of digital offsets in CDS. The final driver circuit for one piezo axis can be found in Appendix A.8. This circuit is implemented for all 6 piezo channels; it was build with EAGLE©.

4.3.3. Calibration of the TM mirror actuator
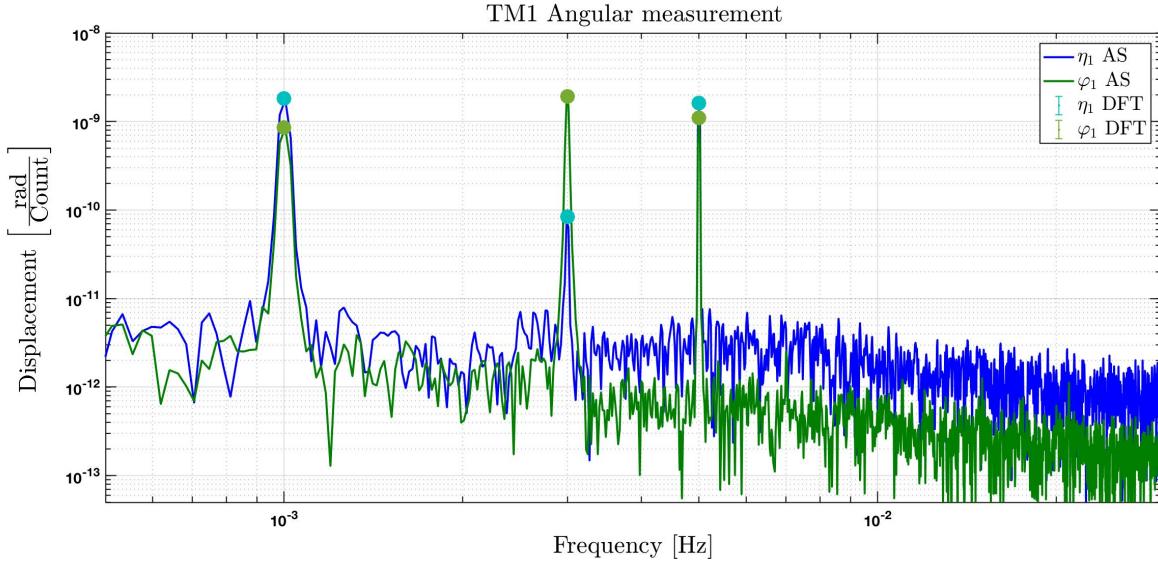
Figure 4.11.: Shown here is the peak amplitude as calculated by the DFT with a Hanning window, shown as well is the Amplitude spectrum of the same data. A sinusoidal signal is injected, on both of the three-axis piezos. Each signal has a different frequency, but the same amplitude. Dependant on the orientation of the piezo this injection couples to the measured TM degrees of freedom. The inverse of this coupling is used to control the TM piezos along the axis of the OMS.

This section describes the experiment to measure the coupling from the actuation axis of the piezo to the different degrees of freedom of the TM in the reference frame of the OMS. This coupling can be described as a coupling matrix P_i:

$$\begin{pmatrix} \mathrm{x}(t)\,[\mu m] \\ \eta(t)\,[\mu rad] \\ \varphi(t)\,[\mu rad] \end{pmatrix} = P_i \cdot \begin{pmatrix} x(t)\,[\mathrm{Count}] \\ y(t)\,[\mathrm{Count}] \\ z(t)\,[\mathrm{Count}] \end{pmatrix} = \begin{pmatrix} p_{x,\mathrm{x}} & p_{y,\mathrm{x}} & p_{z,\mathrm{x}} \\ p_{x,\eta} & p_{y,\eta} & p_{z,\eta} \\ p_{x,\varphi} & p_{y,\varphi} & p_{z,\varphi} \end{pmatrix} \cdot \begin{pmatrix} x(t) \\ y(t) \\ z(t) \end{pmatrix}, i = \{1,2\}. \quad (4.8)$$

Where $\mathrm{x}(t)$, $\eta(t)$ and $\varphi(t)$ are the test mass degrees of freedom, and $x(t)$, $y(t)$ and $z(t)$ are the three axis of the piezo. To move the TM longitudinally the input to all three piezos should be roughly the same, for motion in φ and η the signal is different for each piezo. The transfer matrix from the three piezos to the three degrees of freedom can be measured. Each piezo receives a sinusoidal input ($x(t)$, $y(t)$ and $z(t)$), where the frequencies and their harmonics do not overlap. Used are $1\,\mathrm{mHz}$, $3\,\mathrm{mHz}$ and $5\,\mathrm{mHz}$ with an amplitude of $50\,\mathrm{Count} = 15.3\,\mathrm{mV}$ on TM1. And on TM2 $7\,\mathrm{mHz}$, $11\,\mathrm{mHz}$ and $13\,\mathrm{mHz}$, also with an amplitude of $50\,\mathrm{Count}$, are used.

The response of this injection is measured on the longitudinal axis x and along the angular degrees of freedom η and φ. The amplitude in the phase signal is calculated with the absolute value of a DFT, an example plot for the measurement of the angular degrees of freedom on TM1 can be found in Figure 4.11. In this plot the measurement of the coupling matrix values $p_{\eta,x}$, $p_{\eta,y}$ and $p_{\eta,z}$ can be seen, together with an amplitude spectrum of η. The measurement for φ is shown in the same plot. The other degrees of freedom are measured in the same way. With the measured amplitudes from to the injected signals the coupling matrix A_i, from each piezo channel to the 3 degrees of freedom of the TM, can be constructed to

$$
\begin{pmatrix} x(t)\,[\text{Count}] \\ y(t)\,[\text{Count}] \\ z(t)\,[\text{Count}] \end{pmatrix} = A_i \cdot \begin{pmatrix} \text{x}(t)\,[\mu\text{m}] \\ \eta(t)\,[\mu\text{rad}] \\ \phi(t)\,[\mu\text{rad}] \end{pmatrix} = \begin{pmatrix} \text{p}_{\text{x},x} & \text{p}_{\eta,x} & \text{p}_{\varphi,x} \\ \text{p}_{\text{x},y} & \text{p}_{\eta,y} & \text{p}_{\varphi,y} \\ \text{p}_{\text{x},z} & \text{p}_{\eta,z} & \text{p}_{\varphi,z} \end{pmatrix} \cdot \begin{pmatrix} \text{x}(t) \\ \eta(t) \\ \phi(t) \end{pmatrix}, i = \{1,2\}. \quad (4.9)
$$

The inverse of the matrix $A_i^{-1} = P_i$ is used to calculate the desired output of the three piezos $x(t), y(t)$ and $z(t)$ to achieve a given motion in $\text{x}(t), \eta(t)$ and $\varphi(t)$. The calculated amplitude is always positive and does not display if the piezo needs to be moved forwards or backwards to achieve the desired actuation. The direction could be found in the sign of the phase of the complex DFT result. The coupling matrices calculated from the measurement which are implemented in CDS are:

$$
P_1 = 38307.484 \cdot \begin{vmatrix} 1 & 0.00252982 & -0.00545245 \\ 1.072031 & -0.00664728 & 0.000577357 \\ 1.061590 & 0.00319911 & 0.00532163 \end{vmatrix}
$$

$$
P_2 = 43262.495 \cdot \begin{vmatrix} 1 & 0.00257407 & 0.00374945 \\ 0.999484 & -0.00621464 & 0.00105287 \\ 0.981178 & 0.00073549 & -0.00572462 \end{vmatrix}
$$

The first column has the units $\left[\frac{\text{Count}}{\mu\text{m}}\right]$, the second and third columns are in the units $\left[\frac{\text{Count}}{\mu\text{rad}}\right]$. This matrix is then tested by a similar sinusoidal input to x, η and φ and a measurement of the cross-coupling to the other channels. This coupling matrix depends on the orientation of the piezo in the optical bench housing, when the piezo is adjusted in its housing the calibration experiment has to be redone.

4.3.4. Correction of the phase signal
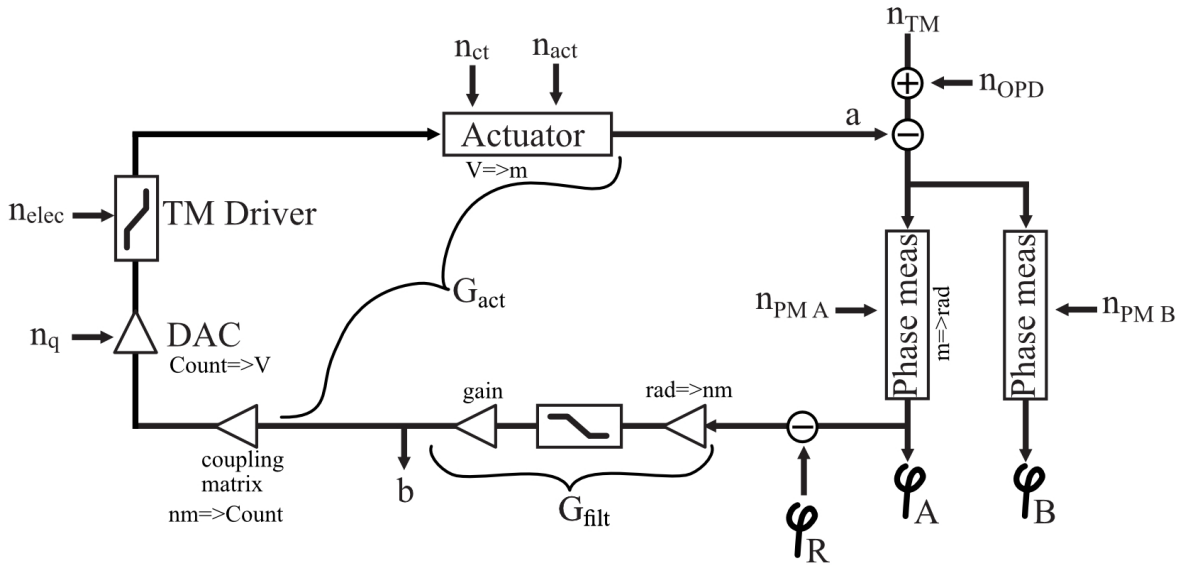
Figure 4.12.: Shown here is the control diagram of one longitudinal TM control loop. In an open loop measurement the phase changes due to TM motion n_{TM} and OPD noise n_{OPD} would be measured. The combined transfer function of the phase measurement system is described by X_{PM}, with the sensing noise n_{PM}. The phase in radian φ_A of the phasemeter is used as input to the longitudinal control loop, the reference interferometer phase is subtracted and it is then calibrated to nanometre. Applied to this signal is the digital transfer function to calculate the desired TM actuation. This digital signal is send via the DAC and the TM driver to the piezo actuator on the TM mirror. The actuation signal from the loop on the TM results in a phase change a, with the intend to counteract TM drifts n_{TM}. Since other phase changes are also suppressed by the TM control loop they need to be restored to the signal.

The performance is measured with the longitudinal and angular control on both TMs, the TMs are effectively stabilised near the optical zero. The control loops suppress the noise in the measurement band as well, which is an undesired influence on the performance characterisation. The suppressed noise is restored to the spectrum, as the desired effect of the control loops is a stable TM position, and not a reduction of noise sources unrelated to position dependent effects.

The measured phase φ_A in-loop is

$$\varphi_A = X_{PM}(n_{TM} + n_{OPD} - a) + n_{PM}. \tag{4.10}$$

Here, the noise due to TM motion is n_{TM} and the noise due to OPD noise is n_{OPD}, the actuation of the TM control loop is in the variable a. These length variations are measured with the photodiode and the phasemeter, their transfer function X_{PM} gives the interferometer signal in radian. The sensing noise and both RIN contributions are summarised in n_{PM}, see Section 3.5. Since the actuation commanded to the TM mirrors is measured it can be added back to the spectrum. The loop output of the digital filters is saved with a sampling frequency of 256 Hz at the point indicated with b in the loop diagram shown in Figure 4.12, where $b = G_{filt}\varphi_A$. The filter G_{filt} consists of the digital transfer functions implemented in CDS: the gain necessary to calculate the PM signal in nanometre, the lowpass filter shown in Section 4.3.1, and the gain to set the strength of the control loop. To calculate the actuation

a of the TM mirrors this output b is filtered through the transfer function G_{act}; where

$$a = G_{piezo}\left(G_{Driver}\left(G_{DAC}G_{CM}b + n_q\right) + n_{elec}\right) + n_{ct} + n_{act}, \tag{4.11}$$

$$= G_{piezo}G_{Driver}G_{DAC}G_{CM}b + G_{piezo}G_{Driver}n_q + G_{piezo}n_{elec} + n_{ct} + n_{act}, \tag{4.12}$$

$$= G_{act}b + n_{loop}, \tag{4.13}$$

$$= G_{act}G_{filt}\varphi_A + n_{loop}. \tag{4.14}$$

The transfer function G_{act} consists of the individual transfer functions of the components after the digital loop output. Here, this output is transformed to three signal chains for the individual piezos by the coupling matrix, and then fed out of the three DAC channels through the driver electronics to the piezos; therefore $G_{act} = G_{piezo}G_{Driver}G_{DAC}G_{CM}$.

All the noise contributions are summarised in n_{loop}. The quantisation noise of the DAC n_q is filtered through the transfer function of the later components. This is similar for the electronic noise of the TM driver n_{elec}. For both of these noise sources the contributions of the three channels per TM must be added up.

When the DWS control loops are also turned on, actuation crosstalk n_{ct} has also to be taken into account; though this is suppressed by the longitudinal control, since this DoF has the highest gain. The actuation noise n_{act} of the piezo also adds to the overall noise of the measured in-loop signal.

With the `fftfilt` function in LTPDA filters can be applied to a time series; this is used to to calculate the motion of the TM a from the digital loop output b with the transfer function G_{act}. This applied motion contains the suppressed noise, by adding it to the measured phase the open-loop longitudinal signal is restored:

$$a' = \text{fftfilt}(b, G_{act}), \tag{4.15}$$

$$\varphi_{A,\,corrected} = \varphi_A + X_{PM}a', \tag{4.16}$$

$$= X_{PM}\left(n_{TM} + n_{OPD} - a\right) + n_{PM} + X_{PM}a', \tag{4.17}$$

$$= X_{PM}\left(n_{TM} + n_{OPD} - n_{loop}\right) + n_{PM}. \tag{4.18}$$

Experiments to show the restoration of the original noise were performed with the first version of the TM loop where the single-diode signals were used as input. In Figure 4.13 the noise restoration with x12_B as input to the TM loop is shown. The restored noise level is compared with a measurement from the next day, where the loop TM loops are turned off and all other settings are kept the same.

The phase noise suppressed by the TM1 longitudinal control loop with the o1 signal as input can be seen in Figure 4.15. In the experiment presented in Section 5.3 the suppressed noise of the loop is not restored, since the frequency range of interest is above the corner frequency.
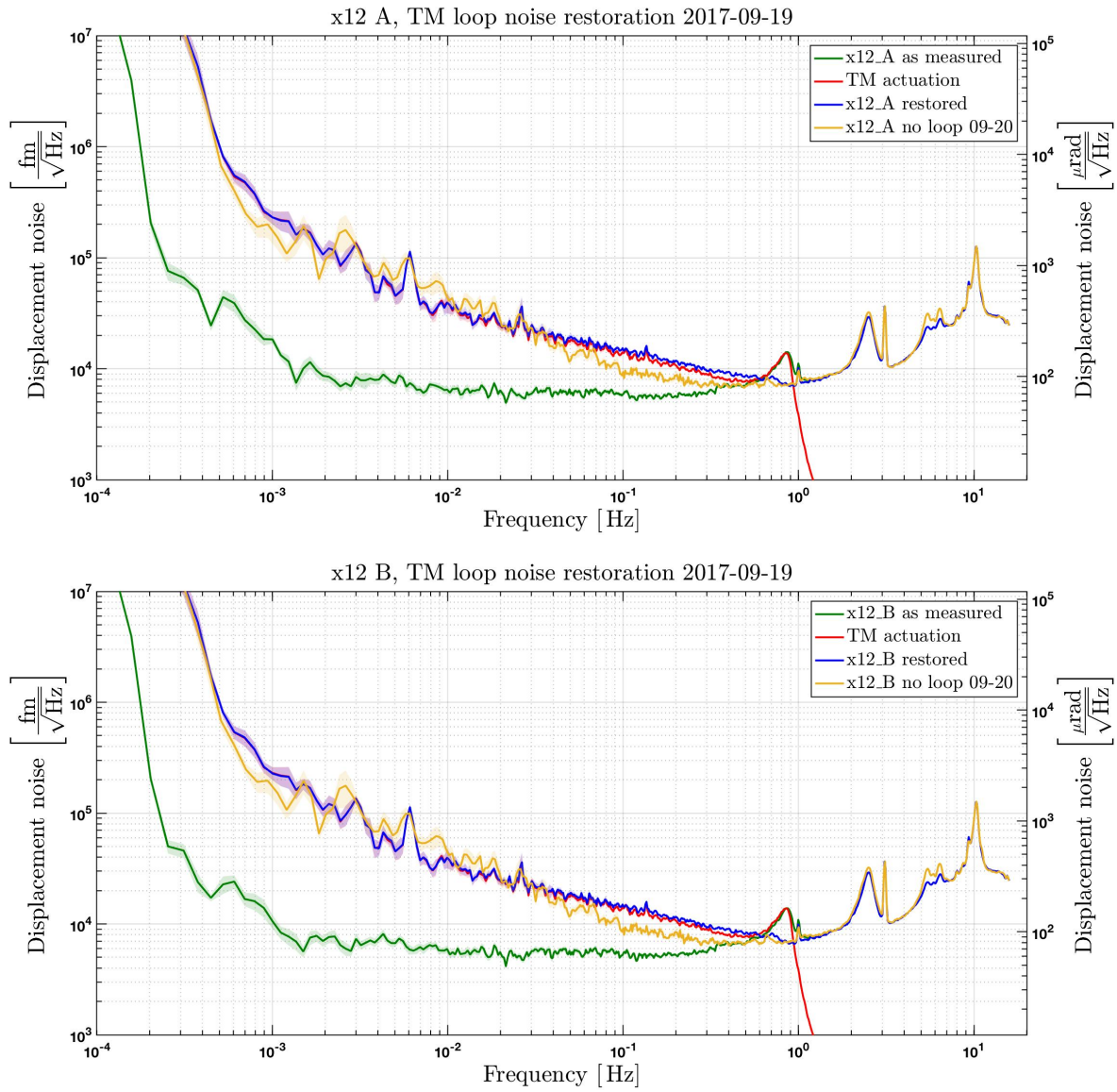
Figure 4.13.: These plots show a noise measurement with the TM control loops turned on. The spectra are calculated with the `lpsd` function, with a BH92 window and 50% overlap. Shown in green is the spectrum of x12_A and x12_B as measured. The actuation on the TM is shown in red, the actuation signal is calculated by the TM control loop from the measurement of the x12_B signal. The noise suppressed by the longitudinal TM control loop can be restored to the measurement with the output of the CDS, and the known transfer function of the electronics and TM piezo. The noise of both x12 signals with the noise restored is shown in dark blue. As a comparison a noise measurement without the TM loops active is shown in yellow. The TM longitudinal loop only suppresses noise up to $\approx 1\,\mathrm{Hz}$. Since the x12_B signal is used as input to the loop the sensing noise on this port is partly suppressed by TM actuation. Since the sensing noise of the two ports is uncorrelated, the suppressed noise from the B side is added to the A side measurement.

4.4. Sensing noise floor in the laboratory OMS

Now the sensing noise floor contributions as shown in Section 3.5 are calculated for the laboratory OMS. The main contributions of the sensing noise floor is the electronic noise of the transimpedance amplifier, shot noise plays a smaller role. ADC noise is only a minor contribution due to the high sampling frequency of the laboratory phasemeter of 800 kHz, contrary to the sampling frequency of the in-flight phasemeter of 50 kHz.

The noise floor contributions in Section 3.5 were calculated for 8 quadrants for an interferometer with balanced detection. There are only 4 quadrants in use for one interferometer; the electronic noise and ADC noise are reduced by a factor $\sqrt{2}$, but the signal strength is also only half. The noise floor is effectively bigger by a factor $\sqrt{2}$. Shot noise is calculated with the same equation, since it depends on the total laser power irrespective of the division in quadrants. The noise is calculated from the power on one QPD. The processing of the data is different between laboratory and flight units. In the laboratory the phase of the individual diodes is calculated, then the balanced and subtracted signals are calculated. In the flight processing these calculations are done with complex values, the phase is calculated from the resulting signals. For the sensing noise components this processing difference leads to the same noise functions in the final signal. In addition, the factor $\frac{\lambda}{4\pi \cos\alpha}$ is removed to make the comparison with other measurement setups easier; with $1\frac{\mu\text{rad}}{\sqrt{\text{Hz}}} \approx 84.8\frac{\text{fm}}{\sqrt{\text{Hz}}}$ the noise contributions can be converted between units.

For the calculation of the noise contributions the measurement of the laser power is needed. However, the phasemeter only outputs the sum of the DC bin measurements of one QPD, which is not calibrated to mW. With the vacuum tank open the laser power in front of the photodiodes was measured with a handheld powermeter, this measurement is used to calibrate the laser power as measured by the phasemeter and displayed by CDS in unknown units.

The values calculated can be found in Table 4.2. Due to the way the optical bench is secured in its container not all diodes are equally accessible, and the calibration was not done for the PDR_B diode. Since the power was measured with a handheld device a bigger error has to be assumed. For each diode the calibration is calculated for both beams and the beams individually, the average is used as parameter for this diode. Under the assumption that all diodes are the same the average calibration factor from CDS units to mW can be calculated to $C_{Pwr} \approx 1.58 \pm 0.19 \frac{\text{mW}}{\text{CDS units}}$. Typical total beam powers on one diode are in the order of 0.5 mW.

For the experiment presented in Section 5.1.1 these sensing noise contributions are calculated, and shown together with the measured phase noise in Figure 4.14. This experiment has the OPD loop turned on, and the frequency loop and the TM control loops turned off. The amplitude spectral density of the sensing noise floor calculated for this measurement can be

Diode	both		meas		ref		calibration
PD1_A	0.52 mW	0.307	0.29 mW	0.179	0.22 mW	0.143	$\approx 1.6 \left[\frac{\text{mW}}{\text{CDS units}}\right]$
PD1_B	0.51 mW	0.362	0.29 mW	0.229	0.18 mW	0.148	$\approx 1.3 \left[\frac{\text{mW}}{\text{CDS units}}\right]$
PD12_A	0.4 mW	0.289	0.21 mW	0.154	0.18 mW	0.147	$\approx 1.3 \left[\frac{\text{mW}}{\text{CDS units}}\right]$
PD12_B	0.4 mW	0.175	0.21 mW	0.087	0.17 mW	0.103	$\approx 2.3 \left[\frac{\text{mW}}{\text{CDS units}}\right]$
PDR_A	0.48 mW	0.336	0.26 mW	0.193	0.21 mW	0.162	$\approx 1.4 \left[\frac{\text{mW}}{\text{CDS units}}\right]$

Table 4.2.: Shown here are the power on the diodes as measured by the PM and recorded by the CDS, and by a powermeter in mW. With these measurements the diode measurement from the phasemeter can be calibrated to mW. The PDR_B diode was not calibrated since it is not possible to place the power meter in front of the diode due to the OB case.

Signal	shot noise $\left[\frac{\mu\text{rad}}{\sqrt{\text{Hz}}}\right]$	ADC noise $\left[\frac{\mu\text{rad}}{\sqrt{\text{Hz}}}\right]$	el. noise $\left[\frac{\mu\text{rad}}{\sqrt{\text{Hz}}}\right]$	noise floor $\left[\frac{\mu\text{rad}}{\sqrt{\text{Hz}}}\right]$
x1_A	$0.143 \pm 2 \cdot 10^{-6}$	$0.097 \pm 7 \cdot 10^{-5}$	$0.317 \pm 6 \cdot 10^{-5}$	$0.361 \pm 5 \cdot 10^{-5}$
xR_A	$0.134 \pm 2 \cdot 10^{-6}$	$0.084 \pm 6 \cdot 10^{-5}$	$0.275 \pm 5 \cdot 10^{-5}$	$0.317 \pm 5 \cdot 10^{-5}$
o1_A	$0.196 \pm 2 \cdot 10^{-6}$	$0.131 \pm 7 \cdot 10^{-5}$	$0.429 \pm 5 \cdot 10^{-5}$	$0.490 \pm 5 \cdot 10^{-5}$
o1	$0.139 \pm 1 \cdot 10^{-6}$	$0.084 \pm 3 \cdot 10^{-5}$	$0.276 \pm 2 \cdot 10^{-5}$	$0.320 \pm 2 \cdot 10^{-5}$

Signal	shot noise $\left[\frac{\text{fm}}{\sqrt{\text{Hz}}}\right]$	ADC noise $\left[\frac{\text{fm}}{\sqrt{\text{Hz}}}\right]$	el. noise $\left[\frac{\text{fm}}{\sqrt{\text{Hz}}}\right]$	noise floor $\left[\frac{\text{fm}}{\sqrt{\text{Hz}}}\right]$
x1_A	$12.2 \pm 19 \cdot 10^{-5}$	$8.2 \pm 6 \cdot 10^{-3}$	$26.9 \pm 5 \cdot 10^{-3}$	$30.6 \pm 4 \cdot 10^{-3}$
xR_A	$11.3 \pm 18 \cdot 10^{-5}$	$7.1 \pm 5 \cdot 10^{-3}$	$23.3 \pm 4 \cdot 10^{-3}$	$26.9 \pm 4 \cdot 10^{-3}$
o1_A	$16.7 \pm 19 \cdot 10^{-5}$	$11.10 \pm 6 \cdot 10^{-3}$	$36.4 \pm 5 \cdot 10^{-3}$	$41.6 \pm 4 \cdot 10^{-3}$
o1	$11.8 \pm 9 \cdot 10^{-5}$	$7.13 \pm 3 \cdot 10^{-3}$	$23.4 \pm 2 \cdot 10^{-3}$	$27.1 \pm 2 \cdot 10^{-3}$

Table 4.3.: This table shows the noise floor components calculated for a measurement in the laboratory, see Figure 4.14. The top table shows the amplitude spectral density of the noise floor components in $\left[\frac{\mu\text{rad}}{\sqrt{\text{Hz}}}\right]$, the bottom shows the same results calibrated to $\left[\frac{\text{fm}}{\sqrt{\text{Hz}}}\right]$. The ADC and electronic noise of the single diode signals are added quadratically to produce the noise of o1_A. In the balanced signal o1 the total noise is effectively reduced by a factor $\sqrt{2}$. The errors are calculated from the errors on the power calibration, and the measured laser power and contrast. The power and contrast are averaged over a long duration, and their error is small.

found in Table 4.3.

The frequency noise contribution is shown in the noise overview, it is calculated from the xF signal and the transfer function to o1, and shows the frequency noise level without the control loop on. To show the OPD noise, which is suppressed by the OPD control loop, the actuation of the piezo on the modulation bench is calculated in the same way as shown in Section 4.1.3. The spectrum of this actuation is shown in the same noise overview.

The contribution of RIN to the sensing noise was measured in the setup of the RIN subtraction measurements, see Section 5.3. The TM was moved in steps without an additional RIN injection. From the measured noise shape the RIN already present in the system was calculated to $781.2 \pm 6.7 \frac{\text{fm}}{\sqrt{\text{Hz}}}$ for 1f_{het} RIN and $1037.2.4 \pm 6.9 \frac{\text{fm}}{\sqrt{\text{Hz}}}$ for 2f_{het} RIN. Since the noise measurement shown here is from a later date the RIN levels $800 \pm 20 \frac{\text{fm}}{\sqrt{\text{Hz}}}$ for 1f_{het} RIN and $1050 \pm 20 \frac{\text{fm}}{\sqrt{\text{Hz}}}$ for 2f_{het} RIN are used. Here it is assumed that this RIN is equally distributed on the two interferometers and correlated. The phase noise power due to RIN on one interferometer is divided by a factor 2 as a result. In the subtracted signal o1 the mean TM offsets are used to calculate the RIN contributions to the sensing noise.

The noise floor calculated from the components does not represent the noise as measured. The difference in the single diode signals compared with the subtracted noise is probably due to small vector noise and ground loops, which are common to all interferometers.
Environmental electromagnetic noise couples to the measurement via magnetic fields that pass in the surface area encircled by cables, these then couple to the electric current in the cable and disturb the measurement. Components which are connected with each other are grouped on the same power supply to minimize the area between the cables, and if possible air-gaps in the cable shields are introduced. When the amplitude stabilisation diodes on the optical bench were connected to the CDS it was found that the shield of these were connected to the shields of the other diodes, thus creating a ground loop between the phasemeter and the CDS power supplies. This could easily be repaired, see Appendix A.1.
However, not all ground loops could be removed. The removal of potential ground loops in the distribution of the $10\,\text{MHz}$ reference frequency and the heterodyne frequency f_{het} is

not possible, since the measurement does not work without these connections. This noise is higher in the ground setup, since the components of the experiment are further apart and are connected with longer cables than the flight model in the satellite. In addition, in the laboratory environment many sources of EM radiation are present. An analysis of the EM environment during the LPF mission can be found in [81].

To improve the measurement of the RIN transfer function the setup of the AOM driver electronics was optimised and the impact of SVN on the measurement could be reduced. Another measurement of the noise floor can be seen in Figure 4.15, this measurement was done in a previous version of the experiment shown in Section 5.3. In this measurement the longitudinal TM1 control loop keeps the phase difference at a TM offset of 266 nm, which reduces the coupling of $2f_{het}$ RIN and has maximum coupling for $1f_{het}$ RIN. During this measurement the vacuum pump is not turned on and not connected to power, due to an earlier malfunction. This leads to a reduction of ground vibrations. This experiment shows a lower measured noise floor than previous measurements, but is still higher than the calculated contributions. However, this difference indicates that the additional noise above the sensing noise floor consists of vibrations, ground loops and SVN. From a comparison with the flight model it is also likely that temperature fluctuations and the worse vacuum in the ground setup also contribute to this difference.

The sampling frequency of the laboratory data is with $256\,Hz$ significantly higher than the sampling frequency of either $1\,Hz$ or $10\,Hz$, while the frequency range of interest is similar. Since the laboratory phasemeter has an output sampling frequency of $\approx 162\,Hz$ the data analysed is oversampled, the sensing noise therefore does not contain aliased noise.
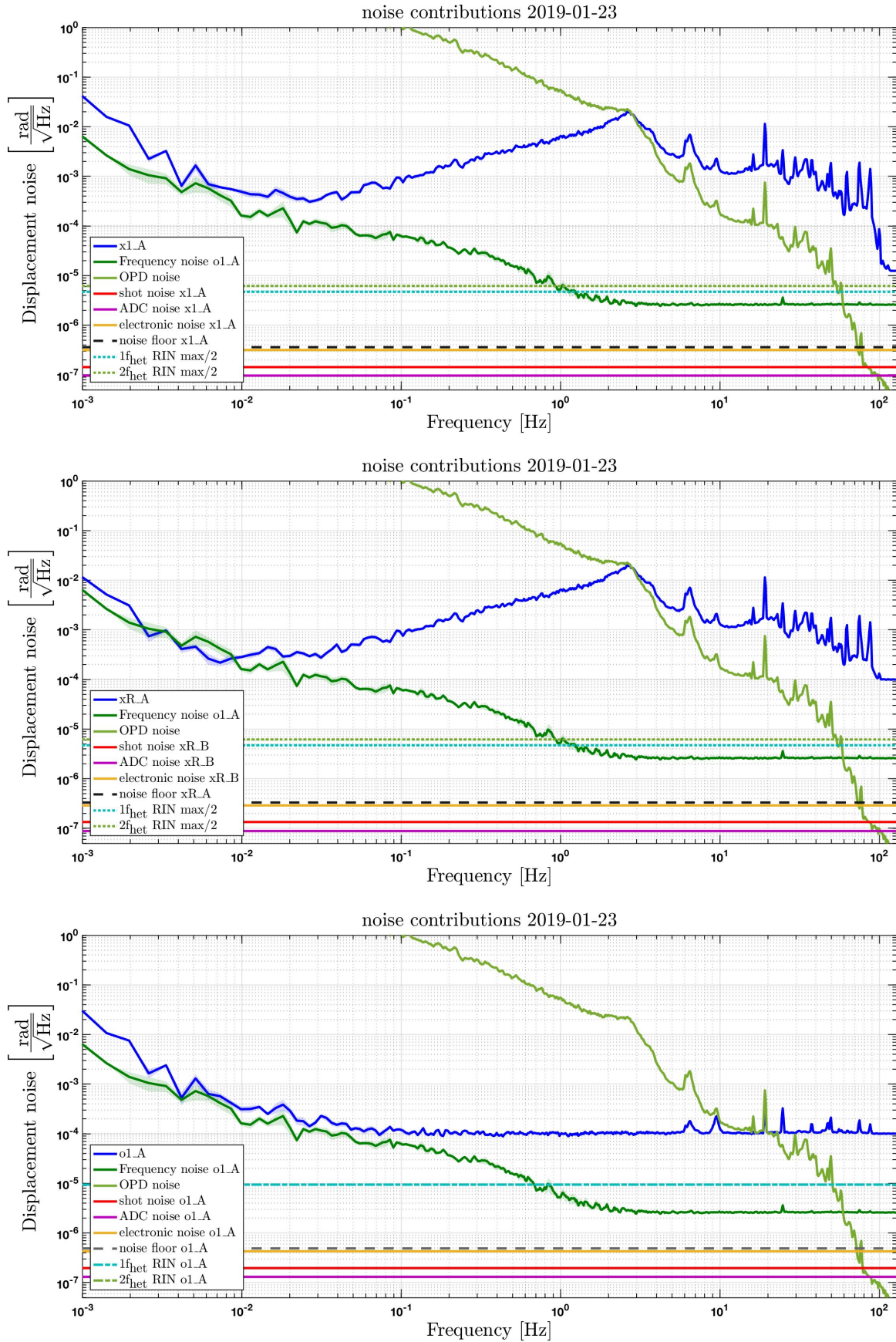
Figure 4.14.: Shown here are the noise floor components as calculated for a typical noise measurement. This noise floor was calculated for both x1_A and xR_A, the third plot shows o1_A signal with the noise contributions combined from the first two measurements. During this measurement the OPD loop is on, the frequency and TM control loops are turned off.
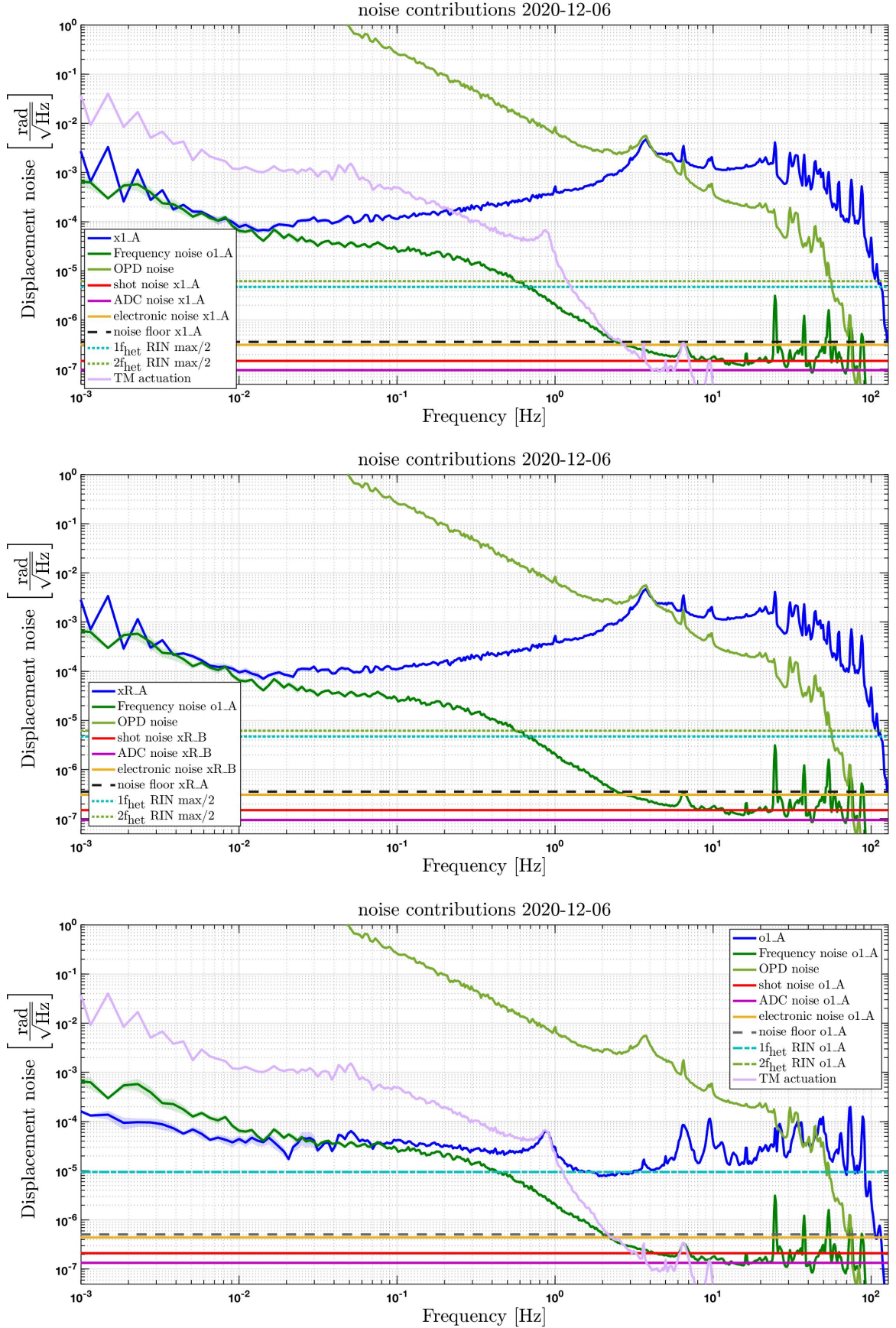
Figure 4.15.: In this later noise measurement the vacuum pump is disconnected, additionally the coupling of small vector noise is reduced. The OPD loop and the TM control loops are on, the frequency control loop is off. At lower frequencies the TM control loop suppresses the frequency noise, the actuation of the TM loop is shown in lilac. With this TM actuation measurement the non-suppressed phase noise can be restored, see also 4.3.4.

4.5. RIN Injection and RIN measurement
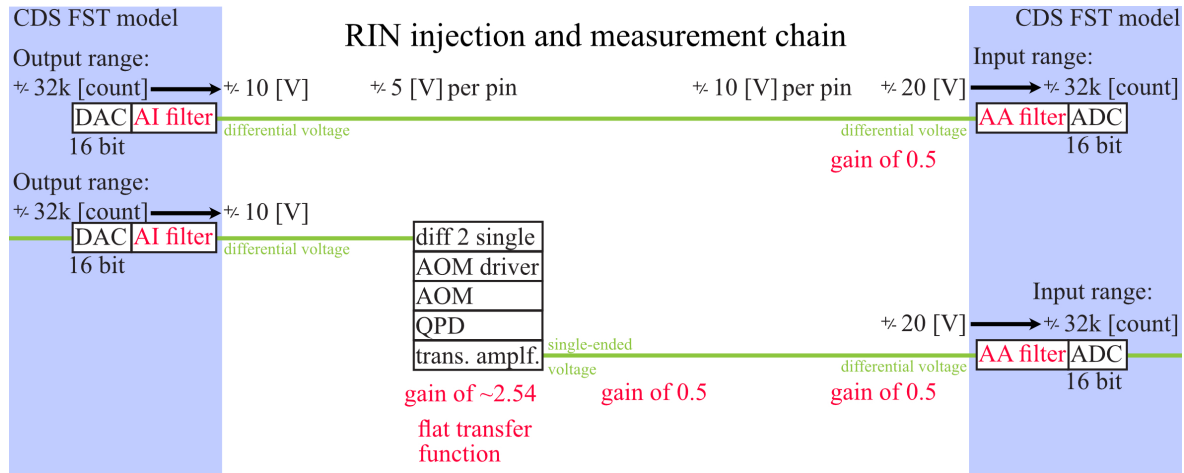
Figure 4.16.: This graph shows two measurement chains. The top chain just connects the DAC to the ADC, and is used to measure the DAC-to-ADC transfer function. The second chain shows the injection and measurement of RIN. In CDS the RIN signal is created and fed out via the DAC and the differential-to-single-ended electronics to the amplitude stabilisation input of the AOM. The RIN injected is measured by the QPDs as a photocurrent, which is converted to a voltage, digitised by the ADC and recorded by CDS. From a comparison of the transfer function of the DAC-ADC measurement and the measurement of the whole chain the transfer function of the components in between is found to be flat in the frequency range of interest, see Figure 4.17. The measured RIN is corrected for the anti-alias filter of the ADC.

The top graph in Figure 4.16 shows the measurement chain of the DAC-ADC transfer function. This transfer function consists of the anti-aliasing filter of the ADC and the anti-imaging filter of the DAC.
The transfer function as measured is

$$\text{tf}_{\text{DAC-ADC}} = 0.5 \cdot \text{tf}_{\text{AI}} \cdot \text{tf}_{\text{AA}}. \qquad \text{[mag]} \qquad (4.19)$$

Since the DAC has an output range of $\pm 10\,\text{V}$ and the ADC a measurement range of $\pm 20\,\text{V}$ the gain between the two components is $\text{gain}_{\text{DAC-ADC}} = 0.5$, or $\text{gain}_{\text{DAC-ADC}} \approx -6\,\text{dB}$.
The electronics of the AA and AI filter are the same, therefore

$$\text{tf}_{\text{AI}} = \text{tf}_{\text{AA}} = \sqrt{2 \cdot \text{tf}_{\text{DAC-ADC}}}, \qquad \text{[mag]} \qquad (4.20)$$

where the measured transfer function $\text{tf}_{\text{DAC-ADC}}$ is scaled to magnitude, and not decibel.
The second chain in Figure 4.16 shows the injection and measurement chain of the RIN experiments. Intentionally injected RIN is created in CDS as a digital signal; the differential output of the DAC is passed through a differential-to-single-ended box, which is a standard component from the electronics workshop of the AEI. The AOM drivers have an input to modulate the laser light amplitude, which is intended as an input for the fast amplitude control loop, but is used here as an input for RIN or RIN equivalent intensity modulations. The RIN injected is measured on the optical bench by the quadrant photodiodes. The photocurrent of the QPD is converted to a voltage with a transimpedance amplifier, and then digitised by the ADC of the CDS FST model. From a comparison of the two measurement chains, the transfer function from DAC to ADC and the whole chain with the optics included, it can be seen that the transfer function of the additional components is mostly flat, see Figure 4.17. The DC gain affects the mean power and the injection amplitude the same way and cancels in the calculation of RIN. Since the anti-aliasing filter of the ADC is frequency

dependent it needs to be corrected for. An example correction of the AA filter on RIN can be seen in Figure 4.22. The dark current is measured and subtracted from the power measurement before the AA filter correction.

The main interest in the experiments presented here is the correction around the heterodyne frequency and twice the heterodyne frequency. The amplitudes of the AA filter at these frequencies are $\mathrm{tf_{AA}(f_{het})} \approx 0.9896$ and $\mathrm{tf_{AA}(2f_{het})} \approx 0.9624$. The DC power is not changed by the filter.
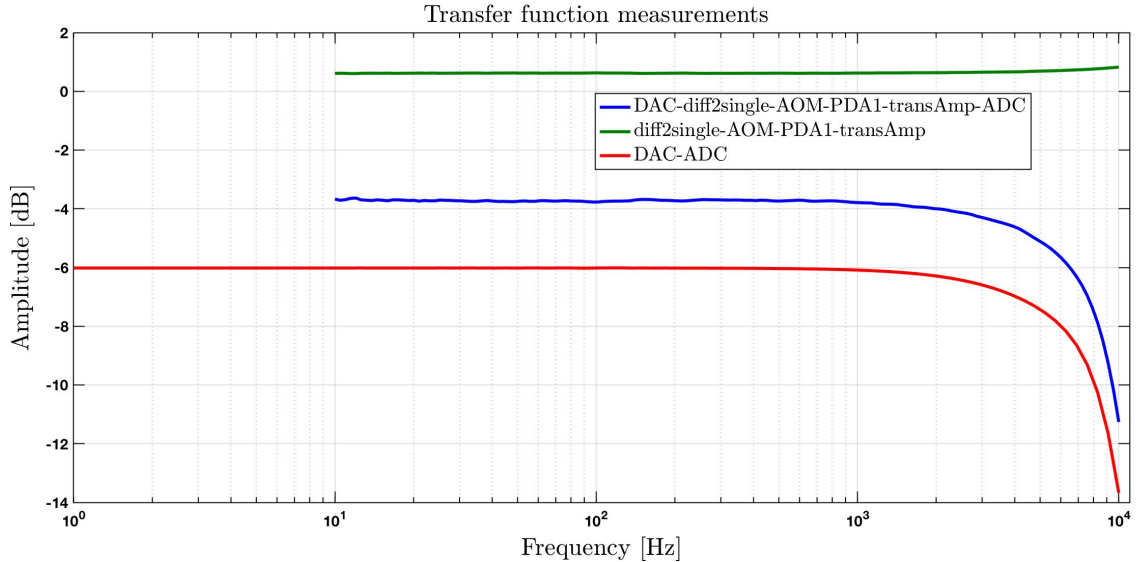
Figure 4.17.: Shown in red is the transfer function measurement from the ADC to the DAC, which includes the Anti-Aliasing filter and the Anti-Imaging filter. Shown in blue is the the transfer function with the same ADC and DAC channels, but with all the components of the RIN measurement in between. The DAC output is used as input to the AOM amplitude control, the power fluctuations are measured with PDA1 connected to the transimpedance amplifier, the voltage is measured by the ADC. From these two measurements the transfer function of the additional components is computed, shown in green here. The gain of these is flat, as expected.

A given amplitude injection in the CDS unit Count produces similar RIN levels. The transfer function from DAC output in Volt to laser power change in mW shows a slow drift, which is the reason why it is not sufficient to know the injection amplitude in Count to calculate the RIN level.

One of the difficulties of the experiment were sidebands on the light. A sinusoidal injection on the AOM amplitude input of one beam would not only lead to amplitude changes at the desired frequency, but also to strong sidebands. As an example, an injection with a frequency of $1\mathrm{f_{het}} + \epsilon$ on the measurement beam would lead to sidebands not only at $1\mathrm{f_{het}} - \epsilon$ and at $2\mathrm{f_{het}} \pm \epsilon$ on the same beam, but also on the other beam at the same frequencies with smaller amplitudes. All of these sidebands cause a phase signal at ϵ. The phase relation between these signals is unclear, and the measured phase amplitude at ϵ is a combination of all of them.

Experiments were performed where a signal is injected on one beam, and the power of both beams is measured individually. Repeated injections with different configurations of the output voltage and position of the AOM drivers could reduce the sidebands to a manageable level. In the initial setup the AOM drivers and the AOM frequency distribution were vertically placed next to each other. Now the AOM drivers are further apart and horizontal. Additionally, the cables and connectors were exchanged to improve shielding. After these adjustments the AOM electronics of the measurement beam were found to have fewer side-

bands and will be used for injections, see Figure 4.18. The exact cause for the sidebands was not found, from the efforts to reduce their impact it is clear that they are caused both by electrical crosstalk as well as through EM radiation.
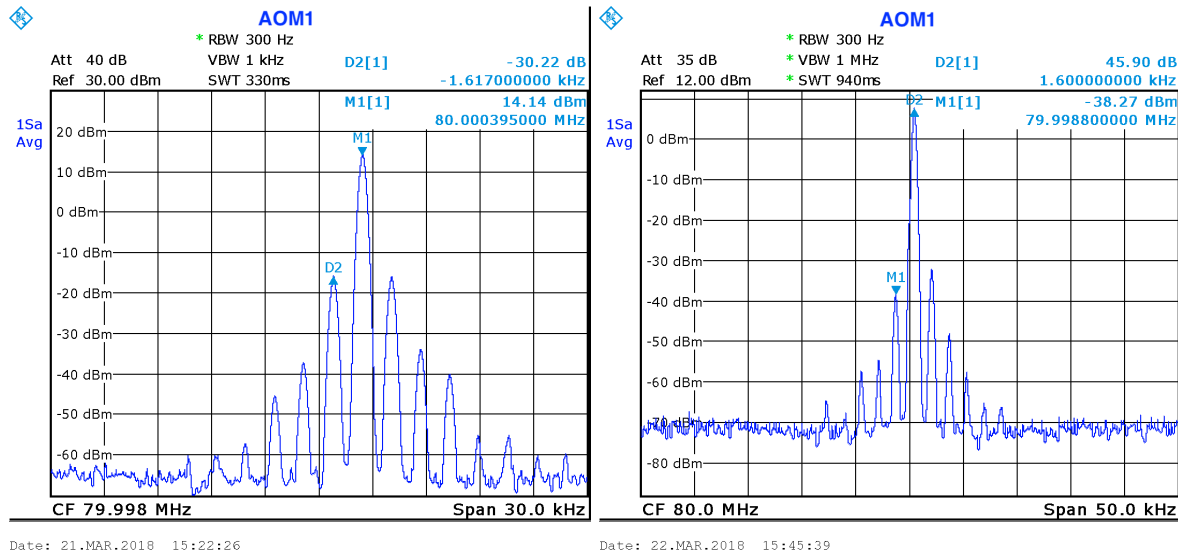
Figure 4.18.: The sidebands on the voltage output from the AOM driver electronics to the AOM were measured with a network analyser during a sinusoidal RIN injection. The top left plot shows the sidebands after initial improvements. The top right plot shows the sidebands after the AOM drivers were moved, and the output voltage was reduced. The two bottom plots show the two placements of the AOM drivers. In the initial setup the two drivers are placed left and right of the frequency distribution, but were then moved away and positioned horizontally.

The power of the reference beam is split almost 50/50 at the X_1 interferometer recombination beamsplitter, whereas the power of the measurement beam is split about 44/56, with more power on the B side. RIN is injected on one beam, and the RIN level should be equally strong on both ports, so that the RIN on the A and B side is of a similar level. Therefore the injection was changed to the reference beam with the AOM driver initially connected to the measurement beam. Example spectra of the reference beam with an injection and the interfered signal can be found in Figure 4.19.
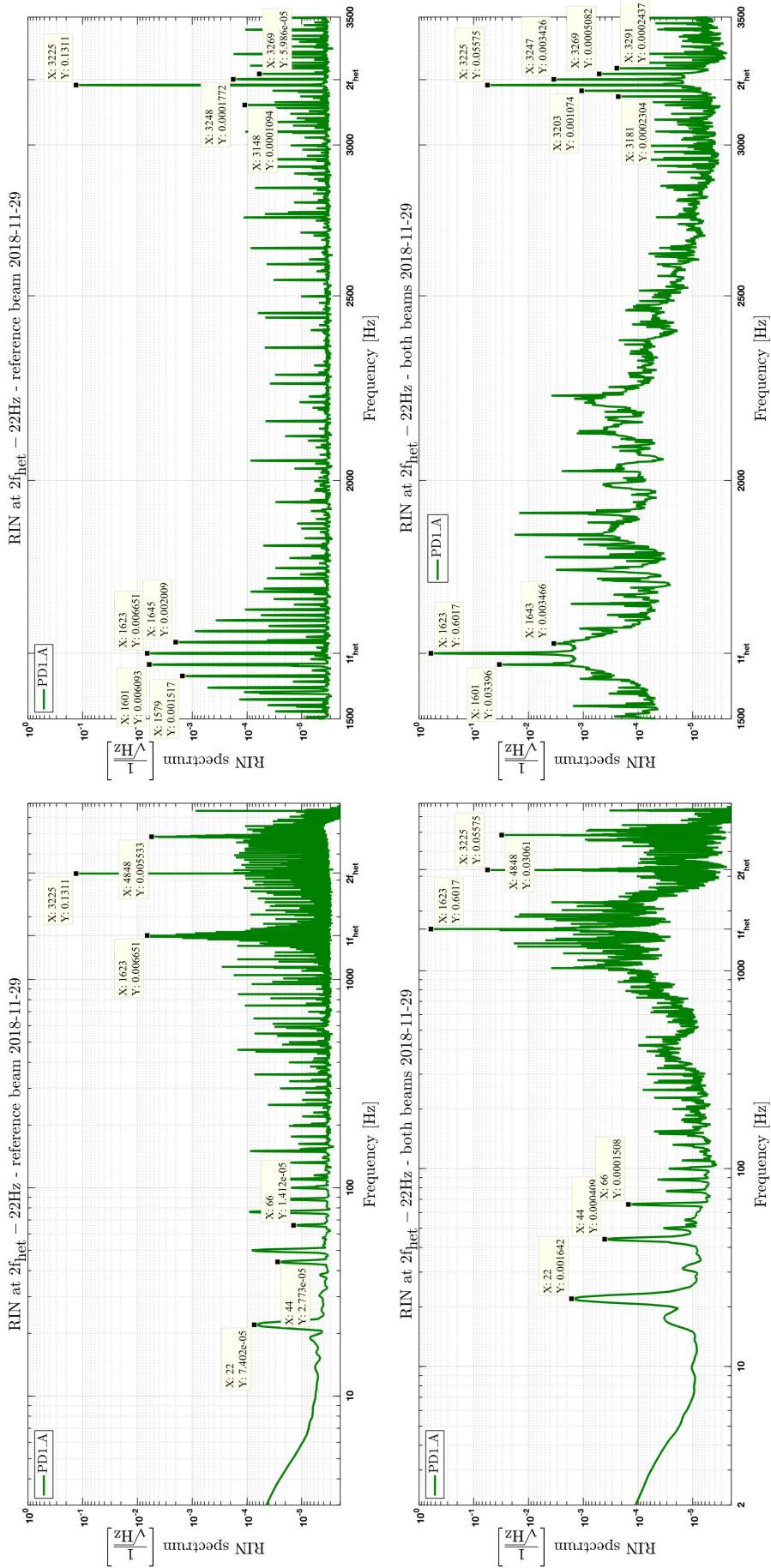
Figure 4.19.:: These plots show the amplitude spectral density of the RIN of the reference beam (top) and of the interfered signal (bottom), with an injection on the reference beam at $2f_{het} - 22\,\mathrm{Hz} \approx 3226\,\mathrm{Hz}$ with an Amplitude of 3000 Count. This injection equals $0.916\,\mathrm{V}$ or a RIN of ≈ 0.13. Also visible is the structure of RIN in the interfered signal caused by the interference of both beams. The two plots on the right show the spectrum around $1f_{het}$ and $2f_{het}$. Visible here are the sidebands caused by this injection, both around $2f_{het}$ and $1f_{het}$. For smaller injection voltages the sideband amplitudes are smaller, see Section 5.1.4. These amplitude spectral densities are calculated from 60 seconds of data sampled at $16\,\mathrm{kHz}$, using the lpsd function with a BH92 window, and 66.1% overlap.

4.5.1. RIN injection stability
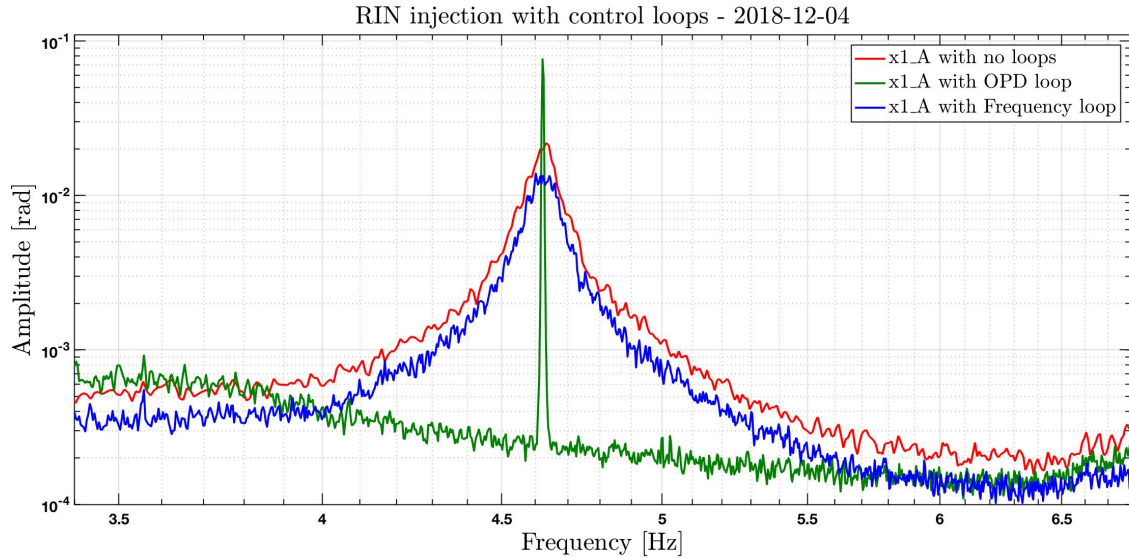
Figure 4.20.: This plot shows the amplitude spectrum of the x1_A phase signal with a sinusoidal RIN injection on the reference beam, at a frequency of 4.6 Hz with an amplitude of 3500 counts. During this injection the spectra with no control loop on (red), frequency loop on (blue), and OPD loop on (green) are compared. This plot shows the amplitude spectrum, calculated with a Hanning window with 50% overlap and 30 averages. The amplitude spectrum with the OPD loop on shows a clear peak, the other two do not, and it's not possible to calculate the peak height.

In the RIN experiments shown in Section 5.1 initially all control loops were turned off, since the aim is the measurement of the coupling parameter from a RIN equivalent intensity modulation to the phase signal. The phase change due to the injected RIN is also measured by the reference interferometer, and will be suppressed by the OPD loop, which was therefore initially turned off. For these experiments frequency noise could be ignored, because the phase amplitude of the RIN injections made is well above the noise floor. Therefore the frequency control loop is also turned off. Since the reference interferometer signal is not subtracted from the measurement signal the phase difference between the two is not relevant for this experiment, and the test mass control loops are turned off as well.

However, during stability experiments, where the same amplitude modulation at a fixed frequency was injected for multiple hours, fluctuations in the phase amplitude of about $\pm 15\%$ were measured. The calculated amplitude of the phase signal changed with the chosen segment length, which indicated that the signal behaves more like a noise. The amplitude spectral density around the intended signal frequency also changed depending on segment length, this lead to the conclusion that the sine wave measured by the phasemeter changes in frequency. Without a stabilisation of the phase difference between the two beams, the heterodyne signal drifts in frequency by small amounts. The phase still can be calculated, since the signal does not drift out of the FFT bin of the phasemeter. However, the frequency difference ϵ between the sinusoidal injection on the laser amplitude and the heterodyne signal is not constant. Therefore, the frequency ϵ of the phase signal due to the injected RIN is not constant.

In both the calculated spectrum and the spectral density this results in a signal smeared over a small frequency range with unclear amplitude. With the OPD loop the phase difference between the beams can be stabilised, this additional stability is required and the OPD loop needs to be on for these RIN injection experiments.

A comparison plot of the measured phase for the same RIN equivalent intensity modulation injection with and without the OPD loop can be found in Figure 4.20.

The OPD loop uses either PDR_A or PDR_B as input. Noise or signals common to both ports are suppressed by the loop as intended, noise or signals with a sign difference or amplitude difference between the two ports have to be investigated more carefully. The frequency of the RIN injections in in Section 5.1 are chosen to be above the resonance frequency of the OPD loop. In experiments shown in Section 5.2 RIN is injected at many frequency offsets $\pm\epsilon$, and the effect of the OPD loop is removed.

4.5.2. Sampling frequency and filter corrections
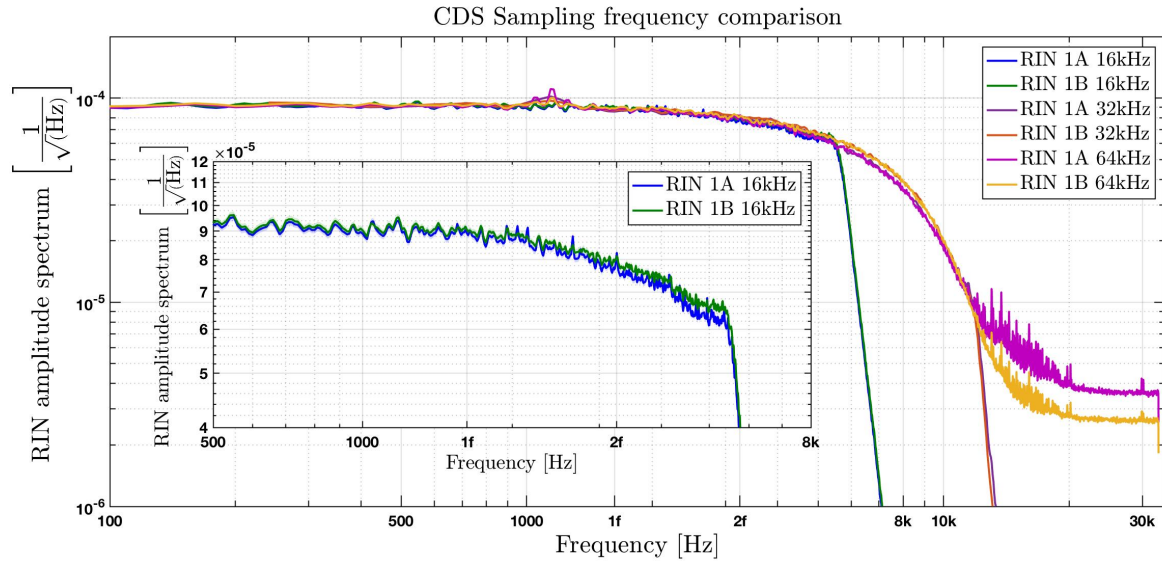
Figure 4.21.: Shown here are noise spectra of the RIN measurement for different sampling frequencies, at 16 kHz, 32 kHz and 64 kHz. The injection is performed via CDS with a noise amplitude of 600 Count, between 0 Hz and 15 kHz on the measurement beam. The reference beam is blocked during these experiments. These spectra show the RIN as measured and are not corrected for the anti-aliasing filter of the ADC. The amplitude spectral densities are calculated with a BH92 window, with an overlap of 50%.

A spectrum of a RIN injection measured at different sampling frequencies can be found in Figure 4.21. Noise between 0 Hz and 15 kHz is injected on the measurement beam with AOM1, the reference beam is blocked during these experiments. In this plot the sharp drop in measured noise due to the lowpass of the downsampling to a sampling frequency of either 16 kHz or 32 kHz is visible, together with the slower decrease of the injected noise to higher frequencies due to the selected injection range. The sampling frequency of the RIN measurement is chosen to be 16 kHz, so that the lowpass filter of the downsampling in CDS does not change the recorded amplitudes at our injection frequencies. These spectra are not yet corrected for the transfer function of the anti-aliasing filter of the ADC.

RIN measured with a sampling frequency of 16 kHz is corrected for the AA filter in postprocessing. This correction is shown in Figure 4.22. Injected on the reference beam is a white noise RIN between 0 Hz and 32 kHz. Contrary to the measurement in Figure 4.21 a higher end-frequency for this noise is chosen to avoid the noise-decrease in the frequency range of interest. Visible is the increase in the measured noise due to the correction of the AA filter, and a sharp drop in the spectrum of the lowpass filter due to the downsampling from the original sampling frequency of 64 kHz to 16 kHz.

Also shown is the correction for the Anti-Imaging filter of the DAC. Due to this filter the injected RIN towards higher frequencies is reduced. This filter is not corrected for in the calculation of the RIN level since the actual RIN in the heterodyne signal is of interest, and not the noise amplitude in software.

The correction at $1f_{het}$ is $tf_{AA}(1 \cdot f_{het}) \approx 0.9896$, for the measurement of $2f_{het}$ the correction is $tf_{AA}(2 \cdot f_{het}) \approx 0.9624$.
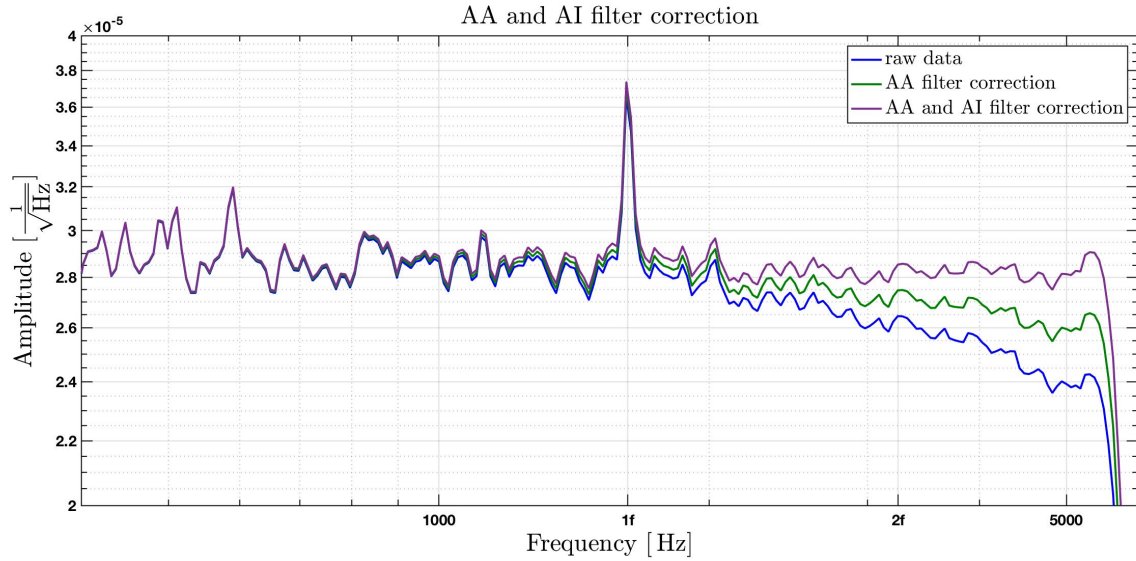
Figure 4.22.: Shown here is the AA and AI filter correction of the RIN measurement of the reference beam, sampled at 16 kHz. Shown is the RIN as measured (blue) and corrected for the AA filter of the ADC (green), only this correction is used on the measured data. When the AI filter of the DAC is also corrected for the flat noise shape of the injection as created in CDS as a digital signal is revealed (purple).

Downsampling lowpass filter

The data in the CDS FST model is measured at the sampling frequency of 64 kHz. When this data is saved at the sampling frequency of 256 Hz a downsampling filter tf_{DAQ} is applied. Since the sampling frequency is reduced by a big factor of 256 this reduction creates a band-pass ripple [50]. The influence of this filter is removed from the data, here this is relevant for the measurement of the demodulated RIN signals, see Section 4.5.3, and for the correction of the influence of the OPD loop, see Section 4.1.3. When the data is saved at a sampling frequency of 16 kHz this ripple is not as pronounced, and the frequency range of interest for the RIN analysis is further away from the Nyquist frequency. The normal PM data is not affected by this since it is recorded in the LTP model with a sampling frequency of 2 kHz, and the reduction in sampling frequency to the saved data is only a factor 4. In Figure 4.23 the measured power with and without this correction can be seen, the filter coefficients and a plot of the transfer function can be found in Appendix A.12.
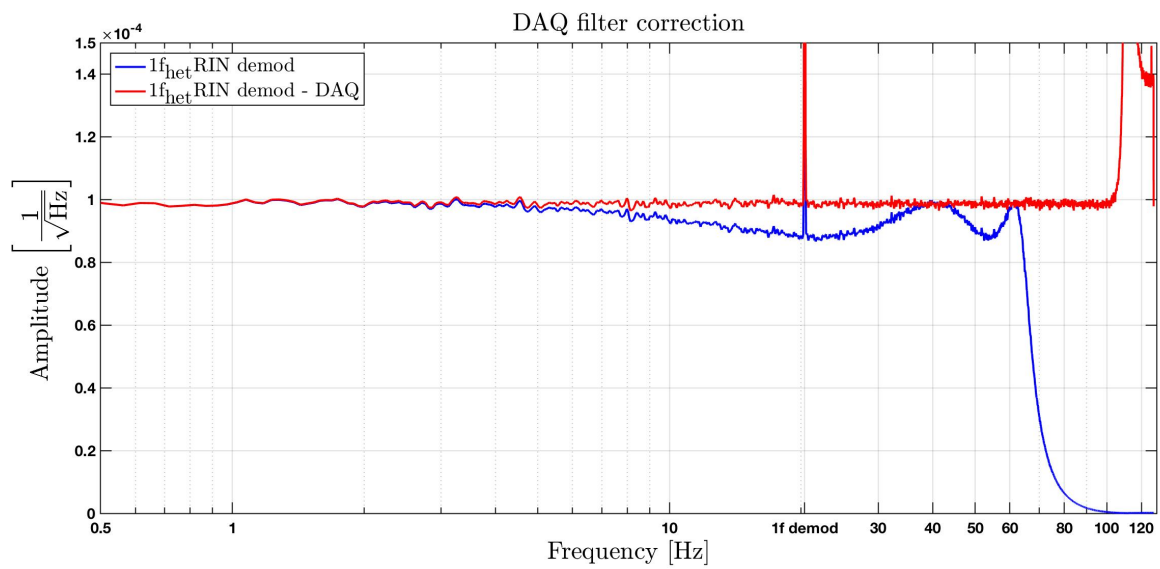
Figure 4.23.: This plot shows the effect of the downsampling filter on the 256 Hz data, plotted in blue. This effect is corrected for in post-processing (red). These spectra are produced from $1f_{het}$ RIN demodulated data, see Section 4.5.3, with a measurement duration of 12 hours. For each FFT 5000 samples are used, with a BH92 window and 50% overlap; this equals 4423 averages.

4.5.3. RIN demodulation
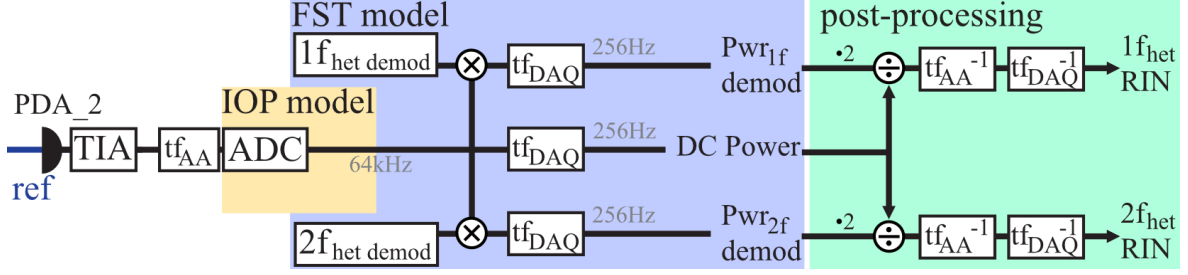
Figure 4.24.: The measured power of the amplitude stabilisation diodes is multiplied with demodulation signals to measure the injected RIN at a lower sampling frequency. Shown here is the design of the reference beam measurement, the measurement beam setup is the same. The power signal is multiplied with a sinusoidal demodulation signal with an amplitude of 1, the frequency chosen for the $1f_{\text{het}}$ RIN measurement is $1603\,\text{Hz}$ and $3226\,\text{Hz}$ for $2f_{\text{het}}$. The demodulated signals as well as the DC power are recorded with $256\,\text{Hz}$ by the CDS FST model, downsampled from the sampling frequency of $64\,\text{kHz}$. RIN is calculated in post-processing from these channels as shown on the right. The correction for the transfer function of the AA filter tf_{AA} on the demodulated signal has to be at the frequency the ADC initially recorded the signal under analysis. Then the RIN is corrected for the low-pass filter of the downsampling tf_{DAQ}.

The powers of the measurement beam and reference beam are measured with the amplitude stabilisation diodes, and recorded by the CDS FST model. RIN measured on these diodes can be used for the calculation of the predicted phase amplitude on the interferometer diodes from a RIN injection. To measure the RIN amplitude for injections near $1f_{\text{het}}$ and $2f_{\text{het}}$ for longer timespans these powers are multiplied with a sinusoidal signal with an amplitude of 1. The resulting signals contain the injected RIN at lower frequencies since

$$
\sin(2\pi\,f_{\text{RIN}}\,t) \cdot \sin(2\pi\,f_{\text{demod}}\,t) = \frac{1}{2}\cos(2\pi(f_{\text{RIN}} - f_{\text{demod}}) \cdot t)
$$
$$
- \frac{1}{2}\cos(2\pi(f_{\text{RIN}} + f_{\text{demod}}) \cdot t). \tag{4.21}
$$

To restore the amplitude of the original signal the time series of the demodulated signal has to be multiplied by a factor 2. With an additional 4th-order Butterworth lowpass filter with a corner frequency of $500\,\text{Hz}$ to remove the high-frequency component the injected RIN can be recorded at a lower sampling frequency. A representation of the implemented power demodulation can be seen in Figure 4.24, a screenshot of the implementation in Simulink® can be found in Appendix A.13. For the measurement of RIN near $1f_{\text{het}}$ a sinusoidal signal with a frequency of $1603\,\text{Hz}$ is used, to measure RIN near $2f_{\text{het}}$ a frequency of $3226\,\text{Hz}$ is chosen. These frequencies are chosen to avoid beatnotes between the demodulation signal and $1f_{\text{het}}$, $2f_{\text{het}}$ and all the $50\,\text{Hz}$ lines. With this setup the amplitude of RIN equivalent intensity modulations and white noise RIN is measured.

RIN equivalent sinusoidal intensity modulation

In the experiments shown in Section 5.1.5 RIN is injected as a RIN equivalent sinusoidal intensity modulation, a measurement of this RIN measured with higher sampling frequency and the demodulated signal can be seen in Figure 4.25. These plots show the RIN measured on the reference beam. Even though this measurement contains only a single beam, a small peak at the heterodyne frequency can be seen. This peak was also present in previous single-beam power measurements and is probably caused by ghost beams or electrical cross-coupling

Figure 4.25.: These plots show a comparison of the RIN spectra as measured with a sampling frequency of 16 kHz and as computed from the demodulated signal. Of interest for the analysis is the amplitude of the RIN equivalent intensity modulation signal, here this signal is visible at the original RIN at $1f_{het} + 12\,Hz$ in the top plot and $2f_{het} + 12\,Hz$ in the bottom plot. These injections are measured in the demodulated signals at a frequency of $1f_{het\,demod} + 12\,Hz$ and $2f_{het\,demod} + 12\,Hz$, respectively.

in the AOMs so that each beam also has a small modulation at the frequency of the other. Injected RIN with an offset ϵ from either $1f_{het}$ and $2f_{het}$ has the same offset in the demodulated signal. In the experiments shown in this section the frequency offset of these injections is typically $\epsilon = 12\,Hz$. These RIN injections are visible at $32.37658691\,Hz$ and $32.75317382\,Hz$ in their demodulated signals[2]. The RIN is calculated from the modulated power signal by division with the mean power of the unmodulated signal; the amplitudes of the demodulated signals as calculated with a DFT are corrected for the transfer function of the AA filter at the frequency they were initially recorded at. Since the demodulated data is recorded at 256 Hz the influence of the downsampling filter from the data recorded at 64 kHz is also corrected for.

---

[2]As a reminder: $1f_{het} = 1623.37658691\,Hz$ and $2f_{het} = 3246.75317382\,Hz$.

So, in summary, the amplitude of the injected sinusoidal RIN is calculated from the demodulated power measurement as

$$a_{\text{RIN}} = \frac{\sqrt{2}}{\text{tf}_{\text{AA}}\,\text{tf}_{\text{DAQ}}} \cdot \text{DFT}\left(\frac{2\cdot\text{P}_{\text{demod}}(t)}{\text{P}_{\text{DC}}}\right), \qquad [\ ] \qquad (4.22)$$

where the factor 2 inside the DFT function accounts for the factor $\frac{1}{2}$ in the creation of the demodulated signal. With the factor $\sqrt{2}$ the DFT result is converted from an rms amplitude to an amplitude.

RIN

In the experiments shown in Section 5.3 the subtraction properties of RIN for different test mass positions are investigated. RIN is injected as one would typically expect as a white noise, which is bandpassed around either $1f_{\text{het}}$ or $2f_{\text{het}}$. A butterworth bandpass filter of order 6 is placed around either $1.6\,\text{kHz}$ or $3.2\,\text{kHz}$. The noise amplitudes of these injections are also measured with the demodulated signals. A measurement of the high frequency RIN together with the demodulated RIN for a noise injection can be seen in Figure 4.26. The mean noise is measured in two ways:

- The input time series is cut into segments, for each the power spectral density is calculated. From each spectrum the mean noise power in a given frequency band is calculated. The final mean noise power is calculated by calculating the average.

- The mean noise in a given frequency band is calculated from the standard power spectral density. The individual spectra are averaged prior to the calculation of the mean noise in the given frequency band.

The first version is used for shorter timespans. For the calculation of the mean phase noise a Gaussian distribution can be assumed, due to the lower number of segments this can not be assumed for the mean noise values. Calculating the mean noise this way gives a better error estimate of the final value. The second version is used for longer timespans with more segments, where a Gaussian distribution can be assumed for both. It is significantly faster to compute.

One of the frequency ranges of the phase signal selected for analysis in Section 5.3 is between $14\,\text{Hz}$ and $15.5\,\text{Hz}$. Therefore, the mean noise level of the measured RIN should be calculated at kHz frequencies in the band from $1f_{\text{het}} + 14\,\text{Hz}$ to $1f_{\text{het}} + 15.5\,\text{Hz}$ and $1f_{\text{het}} - 15.5\,\text{Hz}$ to $1f_{\text{het}} - 14\,\text{Hz}$, since this noise couples to the phase signal from $14\,\text{Hz}$ to $15.5\,\text{Hz}$.
In the $1f_{\text{het}}$ demodulated RIN measurement the heterodyne frequency is down-converted to $20.371\,\text{Hz}$. The desired RIN can be measured in the frequency bands from $34.371\,\text{Hz}$ to $35.871\,\text{Hz}$ and from $4.87\,\text{Hz}$ to $6.37\,\text{Hz}$. The lower frequency range is not ideal to calculate the mean noise for shorter measurement durations, so instead of taking the quadratic mean of the two noise amplitudes the RIN level is just calculated from the higher band.
In addition to the desired RIN the negative offsets from the demodulation frequency couple to the same frequency band in the demodulated RIN. Here, this concerns the frequency range from $1567.123\,\text{Hz}$ to $1568.623\,\text{Hz}$, which also couples in the demodulated signal from $1f_{\text{het, demod}} + 14\,\text{Hz}$ to $1f_{\text{het,demod}} + 15.5\,\text{Hz}$. Since RIN is injected as a white noise these two uncorrelated noise contributions add quadratically. The demodulated RIN amplitude spectral density in the band $34.371\,\text{Hz}$ to $35.871\,\text{Hz}$ is a factor $\sqrt{2}$ higher than the actual RIN, if the two contributions have the same noise level. The measured RIN amplitude from the demodulated power signal has to be divided by a factor $\sqrt{2}$. The mean noise level in this band can be used to predict the phase noise, if the RIN is sufficiently white. Which means, it should have
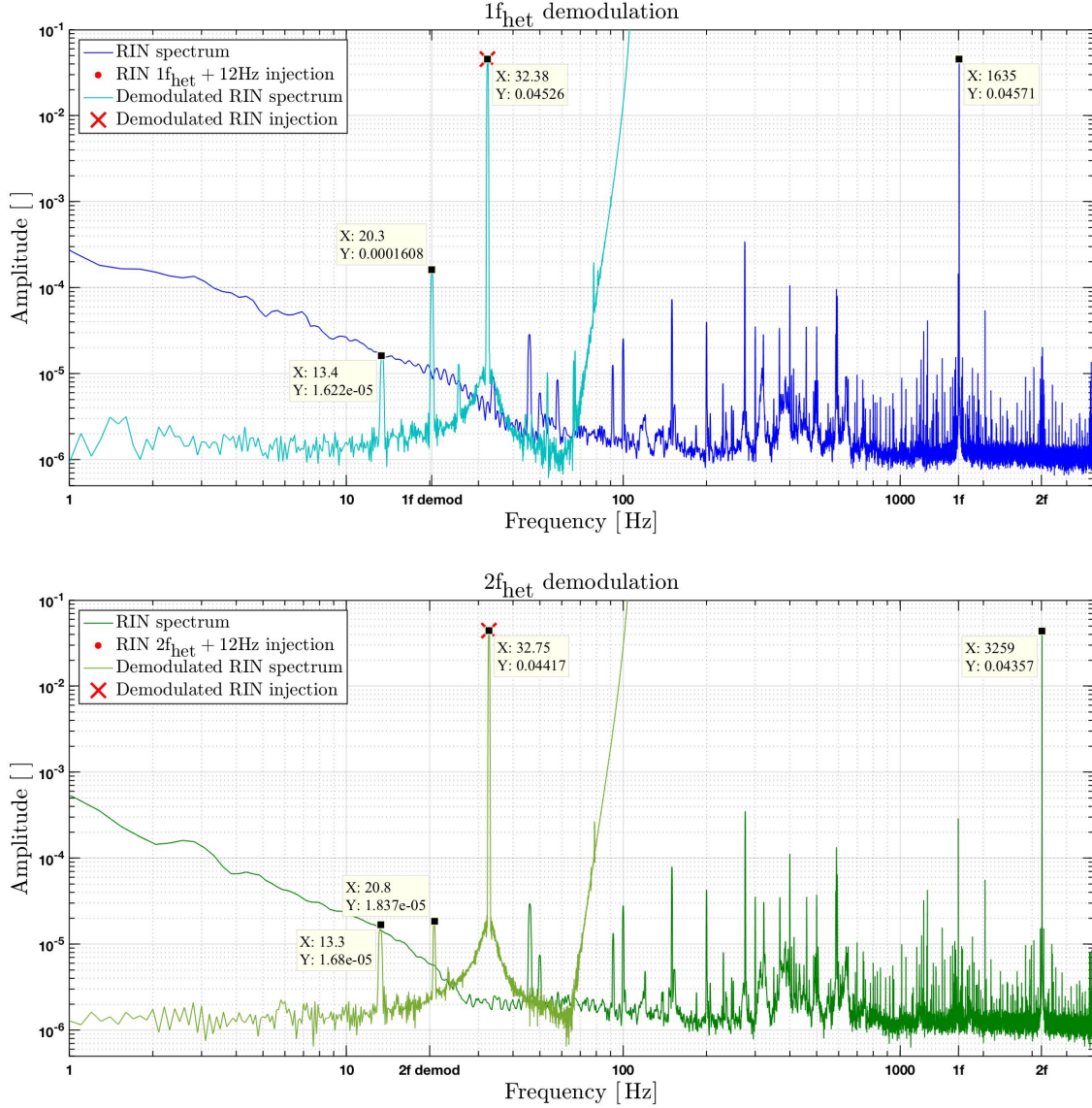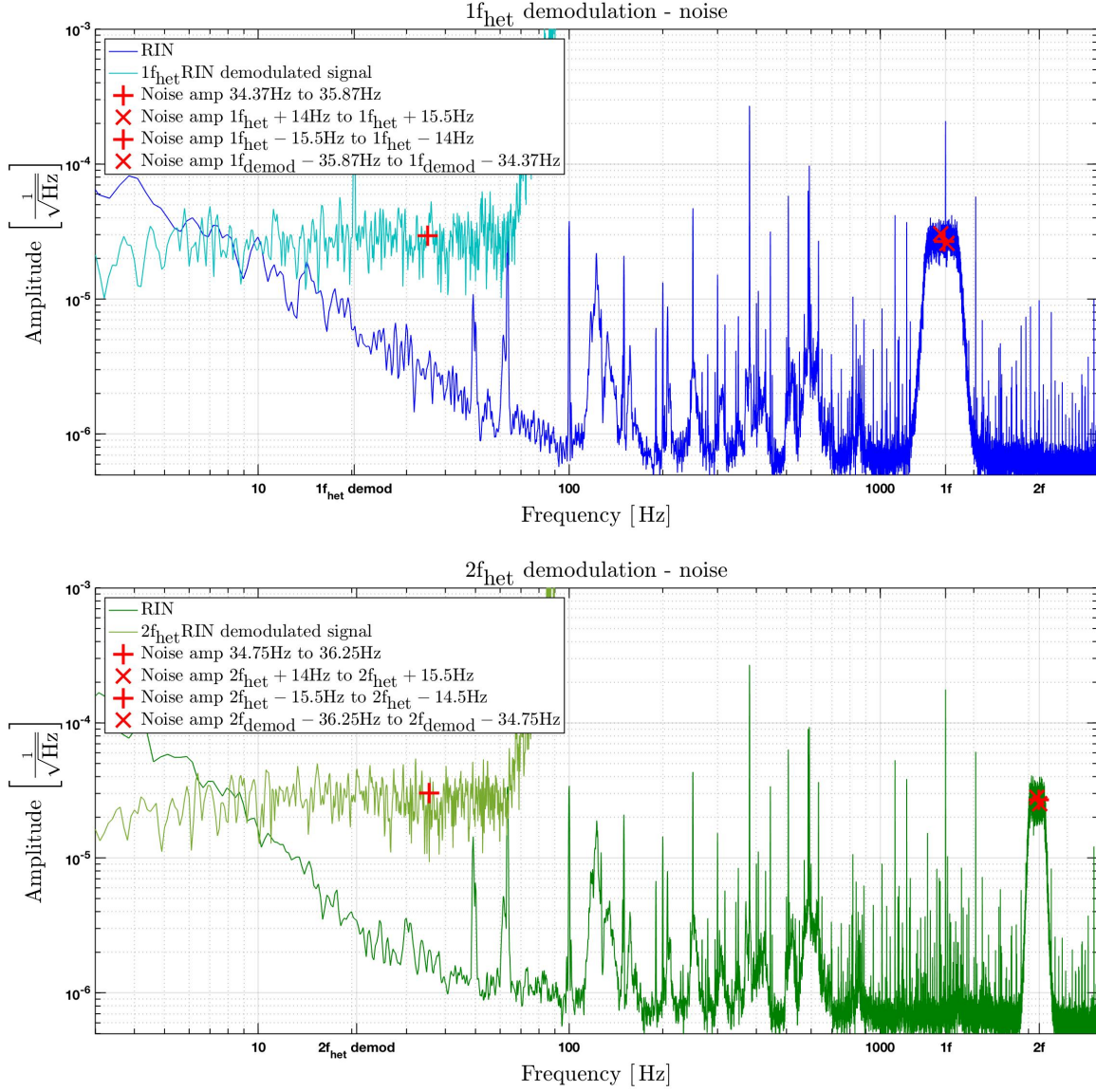
Figure 4.26.: These plots also show a comparison of the RIN spectra as measured with a sampling frequency of 16 kHz and as calculated from the demodulated signal. Shown here is a RIN injection where the noise is centred around $1f_{het}$ (top) and $2f_{het}$ (bottom). This noise was injected via CDS, an amplitude of 200 Count was chosen for both. The same injection is used in the experiments described in Section 5.3. Shown in red markers is the square root of the noise power calculated in the stated frequency band, the frequency band in RIN couples from 14 Hz to 15.5 Hz in the phase signal. The amplitude spectral density in the demodulated signal is a factor $\sqrt{2}$ higher than the original RIN since both the positive and negative frequency offset $\pm\epsilon$ from the demodulation frequency couple down to ϵ in the demodulated signal, the spectra shown are corrected for this additional noise.

the same spectral density in the three relevant frequency bands; a comparison can be found in Figure 4.27. The RIN spectrum is shown together with the mean noise calculated for the relevant frequency bands.

The same reasoning can be applied to the measurement of $2f_{\text{het}}$ RIN. The frequency $2f_{\text{het}}$ is down converted to $20.753\,\text{Hz}$; the mean noise level is calculated in the band between $34.753\,\text{Hz}$ and $36.253\,\text{Hz}$.

In this measurement the noise level in the three high frequency bands is not the same. A comparison of the three amplitude noise levels measured at $16\,\text{kHz}$ added quadratically shows a difference of $\approx 7.5\%$ for $1f_{\text{het}}$ RIN and $\approx 2.1\%$ for $2f_{\text{het}}$ RIN in noise power in the measurement presented here. In other measurements the $2f_{\text{het}}$ RIN error was bigger. This difference is smaller for bigger frequency ranges, and probably smaller for longer measurement durations possible with the demodulated signals.

The errors on the measured noise amplitudes of RIN in later experiments are calculated from the distribution of measured noise over the measurement duration, this white-noise error in the noise measurement will be considered in the discussion of the results.

So, in summary, the amplitude spectral density of the injected RIN is calculated from the demodulated power measurement as

$$
a_{\text{RIN}} = \frac{1}{\text{tf}_{\text{AA}}\,\text{tf}_{\text{DAQ}}} \sqrt{\frac{1}{2}\text{psd}\left(\frac{2 \cdot \text{P}_{\text{demod}}(t)}{\text{P}_{\text{DC}}}\right)}, \qquad \left[\frac{1}{\sqrt{\text{Hz}}}\right] \qquad (4.23)
$$

where the factor 2 inside the psd function accounts for the factor $\frac{1}{2}$ in the creation of the demodulated signal. With the factor $\frac{1}{2}$ the power spectral density of the undesired frequency band is removed.

An overview of the complete chain, from the source of the injected RIN to the measured amplitude noise and sinusoidal amplitude can be found in Figure 4.5.3.
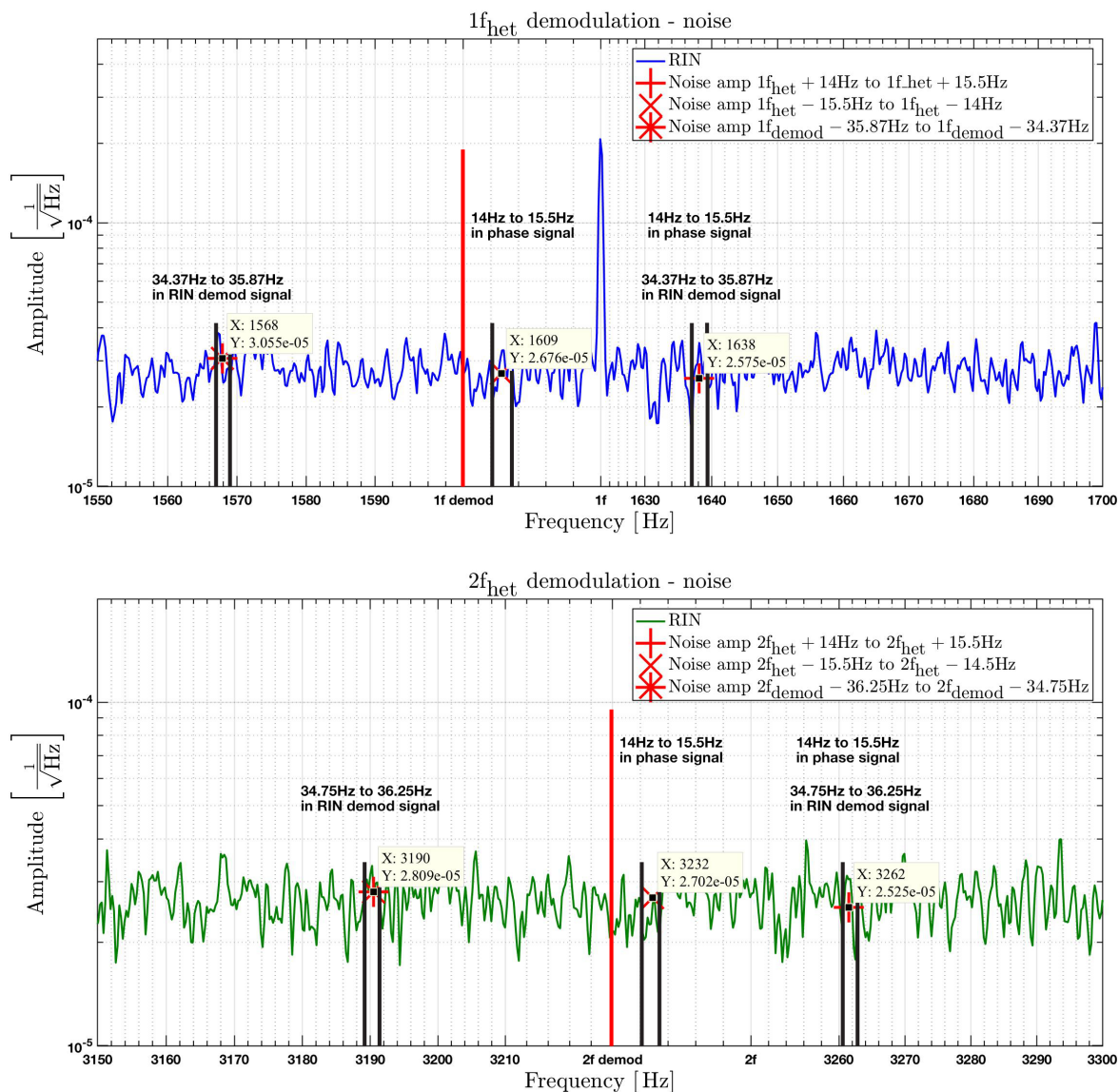
Figure 4.27.: Shown here is a noise amplitude comparison of the injected white noise RIN of the three frequency ranges on the reference beam RIN measurement, recorded with a sampling frequency of 16 kHz. This single beam spectrum shows a peak at the heterodyne frequency due to cross-coupling.

The frequency of the demodulation signal is marked with a red line. Marked in black are the two RIN frequency ranges which couple to the phase noise between 14 Hz and 15.5 Hz. When this noise is measured in the demodulated signal the noise from another frequency range is folded into the same band, this range is also shown with black markers. The noise level measured in the demodulated RIN signals are $\approx 38.1 \frac{10^{-6}}{\sqrt{\text{Hz}}}$ for $1f_{\text{het}}$ RIN and $\approx 36,1 \frac{10^{-6}}{\sqrt{\text{Hz}}}$ for $2f_{\text{het}}$ RIN.
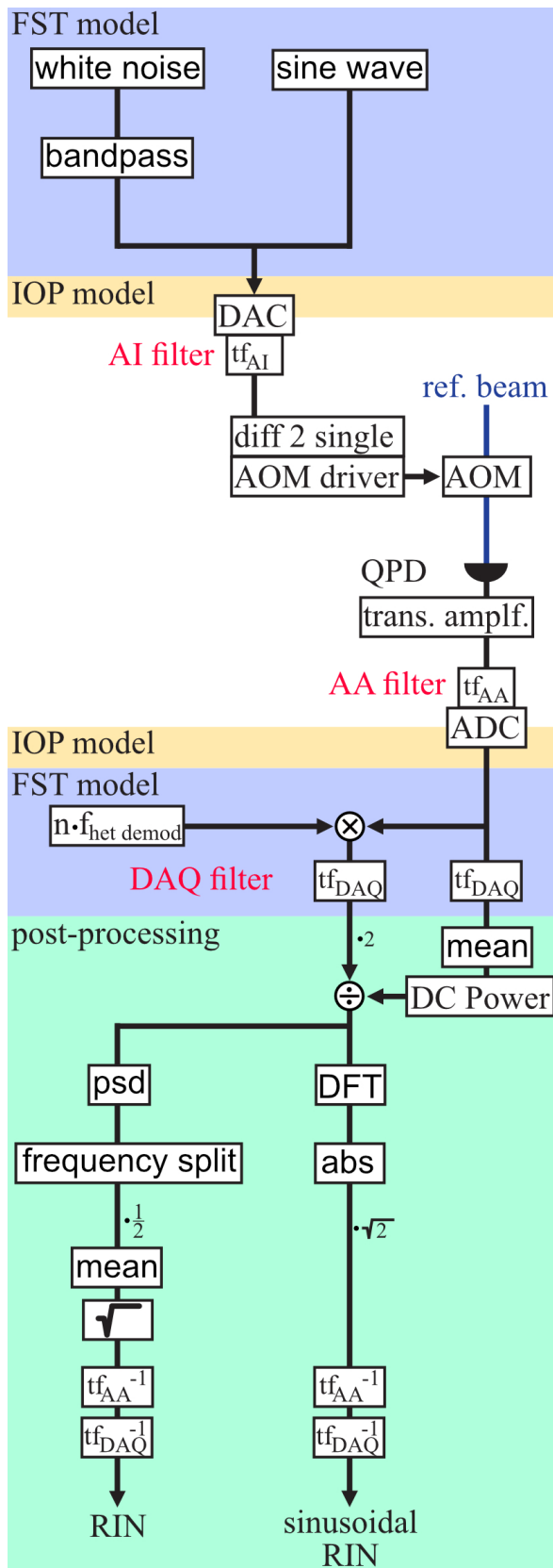
Figure 4.28.: Shown here is the complete chain of the injection and measurement of RIN, this graph should be read from top to bottom. The injected RIN is created in the FST model of CDS, either as a white noise which is then bandpassed, or as a sinusoidal signal. This signal is then injected on the light with the fast amplitude control loop input via the AOM driver electronics, and measured with the PDA diodes previously used for the fast amplitude control loop. This data is recorded with one ADC channel per beam with a sampling frequency of $64\,\mathrm{kHz}$. In the initial experiments this data is saved with a sampling frequency of $16\,\mathrm{kHz}$.

In later experiments this power measurement is demodulated near $1\mathrm{f}_{\mathrm{het}}$ and $2\mathrm{f}_{\mathrm{het}}$, and recorded at $256\,\mathrm{Hz}$. The DC power is recorded in a separate channel. These signals are then used to calculate the injected RIN, either the mean amplitude spectral density in a given band, or the amplitude of the sinusoidal injection. The injection of RIN via the DAC is shown at the start of Section 4.5. More details on the correction of the $\mathrm{tf}_{\mathrm{AA}}$ filter and $\mathrm{tf}_{\mathrm{DAQ}}$ filter can be found in Section 4.5.2.

4.5.4. RIN correlation

RIN couples differently to the phase signal dependent on the correlation of the noise between measurement and reference beam. In normal circumstances the RIN is correlated between the two beams since they have the same source, the noise adds linearly when the two beams are interfered. In the experiments shown here the RIN is only injected on one of the beams. Injected are sinusoidal RIN equivalent intensity modulations and white noise RIN. This injected RIN adds quadratically to the RIN already present. Relevant for the calculation of the RIN coupling to the phase is the correlation of the noise in the two beams.

To estimate these beam properties the coherence between the two is calculated during a noise measurement and for all types of RIN injection. Plots of the coherence in the relevant frequency band for a measurement with a sampling frequency of $16\,\mathrm{kHz}$ can be found in Figure 4.29. Due to the higher sampling frequency the measurement is short, and the frequency resolution is low. Interesting of course is the coherence at $1\mathrm{f}_{\mathrm{het}}$ and $2\mathrm{f}_{\mathrm{het}}$. If no injection at these frequencies is present the coherence between the two beams is ≈ 1. Due to the low frequency resolution in the calculation with the higher sampling frequency it is not possible to decouple these coherent signals due to the heterodyne beat from the injected RIN.

For a greater frequency resolution the coherence is also calculated from the demodulated RIN measurement. In Figure 4.30 the coherence of the two beams during the experiment shown in Section 5.3 is shown, here white noise RIN is injected. Due to the longer measurement duration of the coherence calculation from the demodulated signals the frequency resolution is better. For a noise injection the coherence between the two beams drops from ≈ 0.3 to ≈ 0.2. As a rule of thumb, with a calculated coherence in this range the two input objects can be treated as uncorrelated.

Therefore, in the experiment shown in Section 5.3 the injected RIN on the reference beam can be treated as uncorrelated to the RIN on the measurement beam. In addition, the two RIN levels are different, with the RIN on the measurement beam a factor ≈ 40 smaller. With these values the expected change in phase noise when both beams and their correlation are respected compared to a measurement on just the reference beam can be estimated with

$$\frac{\mathrm{RIN}_{\mathrm{m\ and\ r}}}{\mathrm{RIN}_{\mathrm{r}}} \approx \frac{\sqrt{(0.8\,\hat{r}_{\mathrm{r}})^2 + (0.8\,\hat{r}_{\mathrm{m}})^2 + (0.2\,\hat{r}_{\mathrm{r}} + 0.2\,\hat{r}_{\mathrm{m}})^2}}{\sqrt{\hat{r}_{\mathrm{r}}^2}}, \tag{4.24}$$

$$\approx \frac{\sqrt{(0.8 \cdot 40)^2 + 0.8^2 + (0.2 \cdot 40 + 0.2)^2}\,\hat{r}_{\mathrm{m}}}{\sqrt{40^2}\,\hat{r}_{\mathrm{m}}}, \tag{4.25}$$

$$\approx 1.005. \tag{4.26}$$

The measured injected reference beam RIN can be used as a good estimate for the total RIN at this frequency, since the difference to a more correct calculation with measured correlation is small. The amplitude spectral density for both beams can be found in Figure 4.31. A comparison of the noise amplitudes in the relevant frequency range of both beams for this experiment can be found in Figure 5.29. The RIN in the measurement beam is at a similar level to the non-injected RIN in the reference beam. The difference in total noise if this additional RIN is added linearly or quadratically is small.

In experiments where RIN is injected as a RIN equivalent intensity modulation at a fixed frequency the difference is even smaller, since the amplitude of these injections are significantly higher than the noise floor, and the amplitude of the sidebands created during this injection is small for the improved version of this experiment. The amplitudes of the sidebands for the improved sinusoidal RIN injection can be found in Figure 5.16. The injected RIN compared to other phase noise can be found in Figure 5.4.

For the analysis of the in-flight measurements the correlation of the RIN between the beams is not known, the RIN level is calculated from the measured phase noise for both cases. The
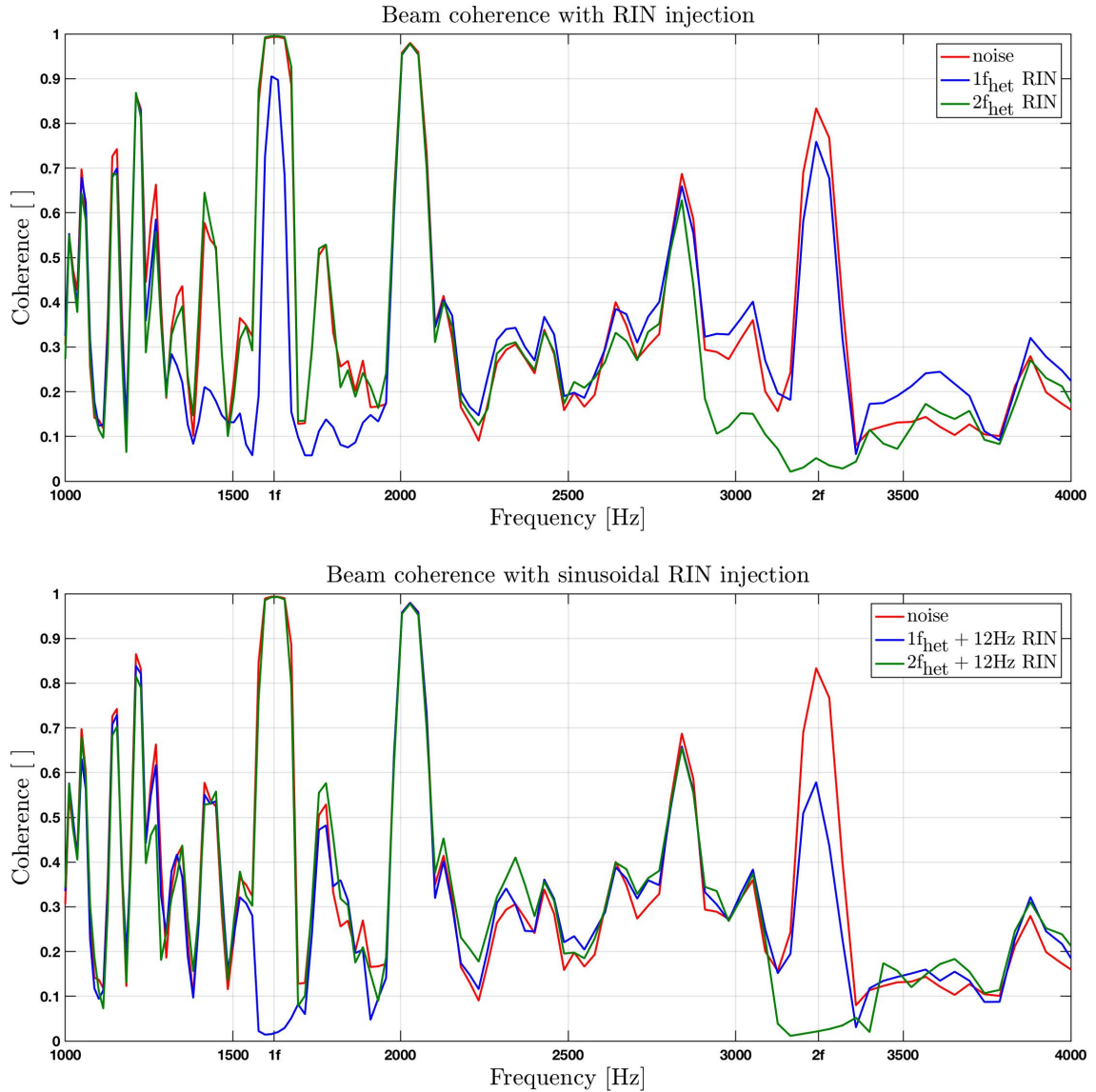
Figure 4.29.: These plots show the coherence between the two beams. Similar to the calculation of spectra using the lpsd function the correlation is calculated with higher number of averages at higher frequencies, see [23]. Plotted in red is the coherence during a noise measurement, the blue data shows the same channels with a RIN injection at $1f_{het}$ and in green with an injection at $2f_{het}$. The top plot shows the coherence for a sinusoidal RIN equivalent intensity modulation, the bottom plot shows the coherence with a bandpassed white-noise RIN injection. The power data is recorded with a sampling frequency of $16\,kHz$. Due to the short duration of the measurement the frequency resolution is not as good as needed.

real RIN level is most likely between the two calculated values, a high percentage of correlated RIN is likely since the two beams originate from the same laser. Uncorrelated RIN might be caused by the AOMs and fibres. In these experiments no RIN was injected.
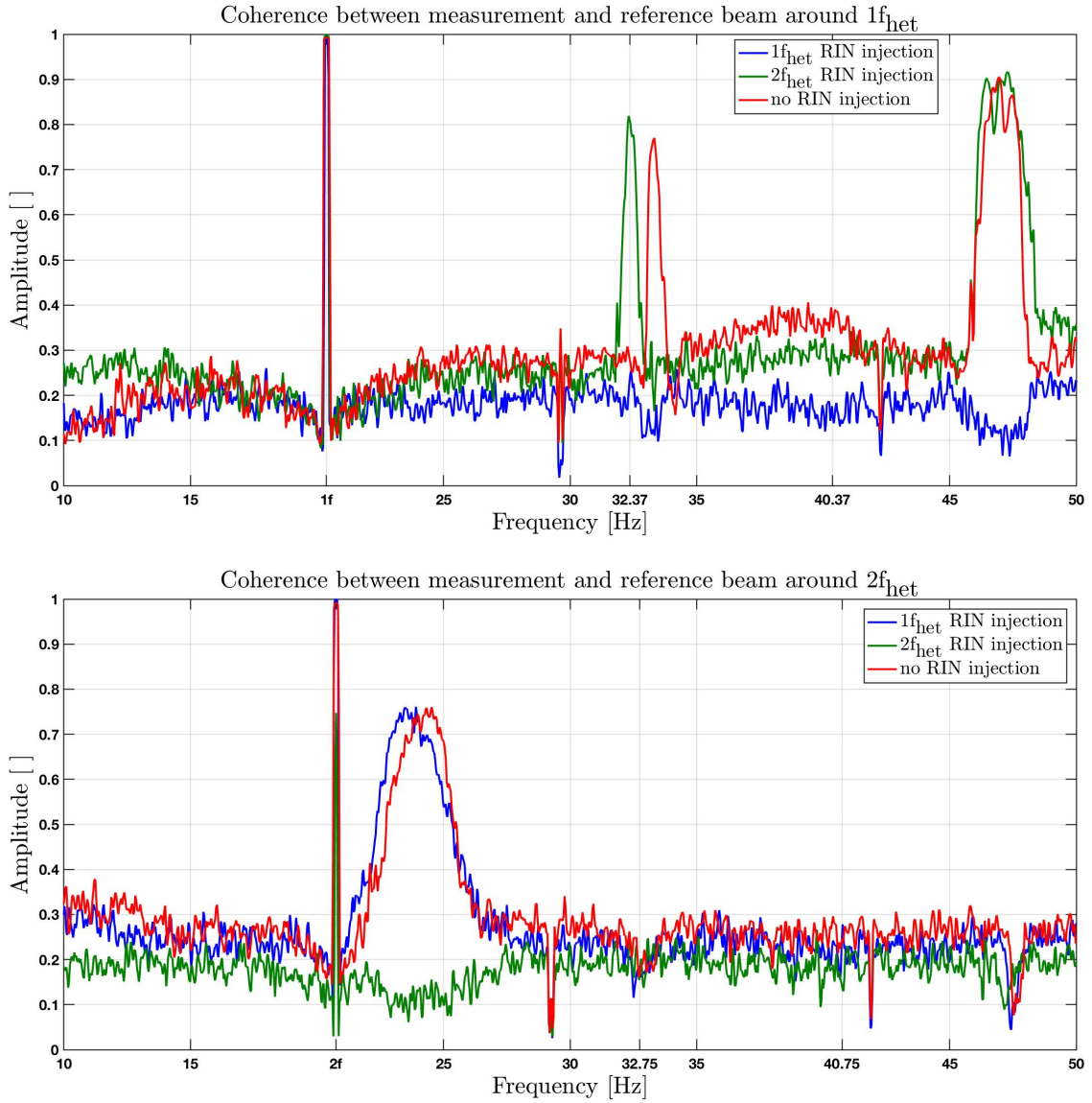
Figure 4.30.: These plots show the coherence between the two beams, calculated from the demodulated power signals. These are calculated from ≈ 2.7h of data measured during the experiment shown in Section 5.3, with 1000 averages, and a detrend of order 2 and a BH92 window with 66.1% overlap. The top plot shows the coherence of the demodulated power signal around $1f_{het}$ and the bottom plot around $2f_{het}$. Plotted in red is the coherence during a noise measurement, the blue data shows the same channels with a RIN injection at $1f_{het}$ and in green with an injection at $2f_{het}$. The coherence of the RIN between the two beams in the relevant frequency range for the experiment in Section 5.3 is between 0.2 and 0.3. The RIN between the two beams can be treated as uncorrelated. Due to the high correlation at $1f_{het}$ and $2f_{het}$ the calculated correlation with a lower frequency resolution, see Figure 4.29, is skewed towards higher values in the frequency range of interest. The reason for the features in the correlation is not known.
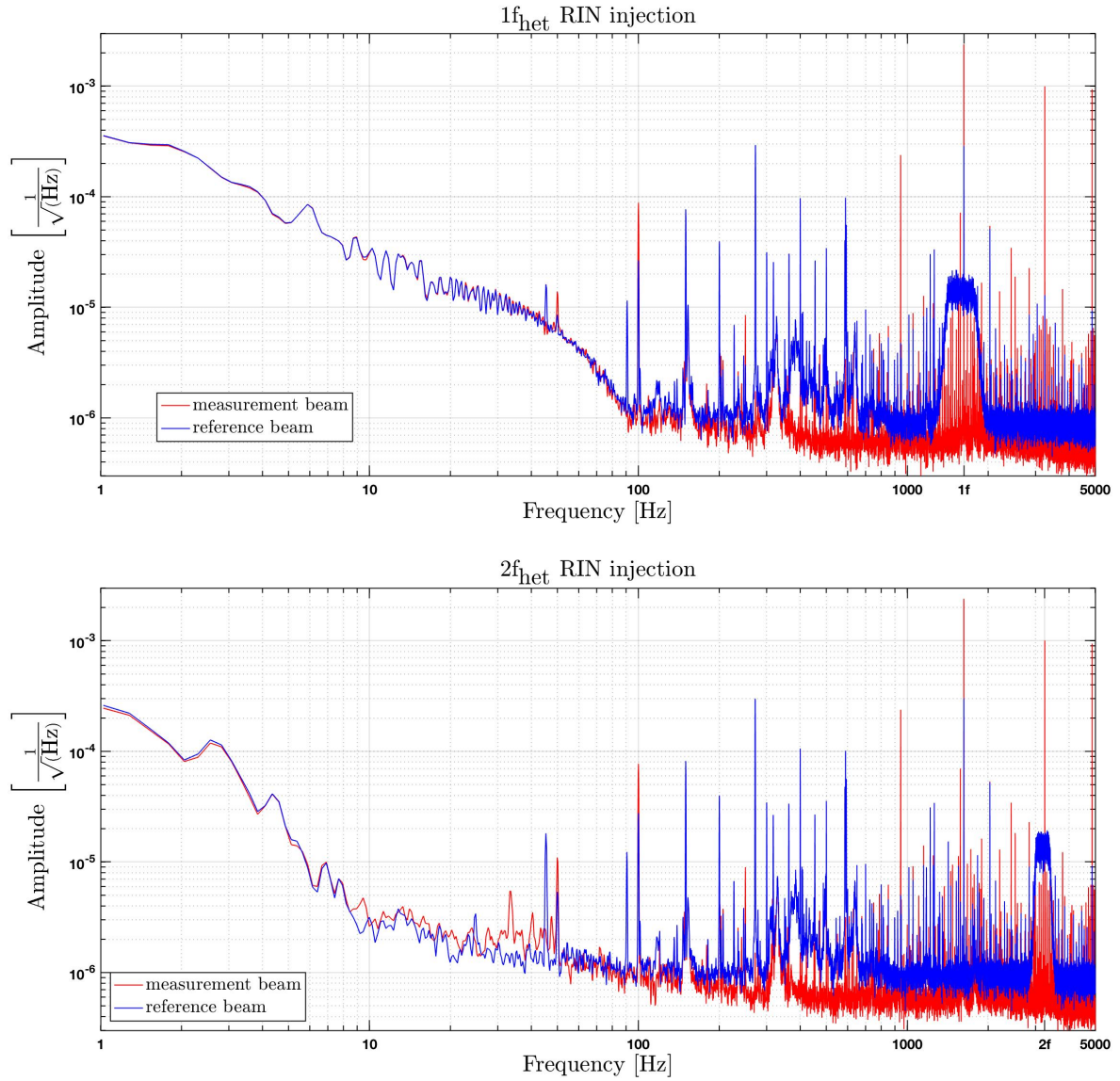
Figure 4.31.: Shown here are spectra of the measurement beam (red) and reference beam (blue) with a RIN injection around $1f_{het}$ (top) and $2f_{het}$ (bottom), recorded at a sampling frequency of 16 kHz. The data of the reference beam was already shown together with its demodulated signal. The interference of the two beams shown here produces the heterodyne signal used to calculate the phase. The injected RIN has an amplitude of 100 Count, for later experiments this amplitude is increased to 600 Count. Due to the lower voltages in the noise injection than in the sinusoidal injection the crosstalk between the beams for noise injections is lower. The noise of the reference beam is also higher than of the measurement beam if no injection is present, the reason is not known.

4.5.5. Beam power measurement

During longer experiments the power drifts over the measurement duration, which changes the coupling of $1f_{\text{het}}$ RIN. To calculate the individual beam powers of the interfered signal on the interferometer diodes the powers as measured by the amplitude stabilisation diodes are calibrated to the relevant interferometers.

This beam power calibration is done for most measurements. The beams are blocked in turn and the powers are recorded on the PDA diodes by the CDS and the interferometer diodes by the phasemeter. The transfer coefficient from the measurement of the individual beam powers P_k to the power of the same beam on the other diodes $P_{ij,k}$ is calculated by dividing the two measured powers, both with their dark currents subtracted

$$c_{\text{Pwr}} = \frac{\overline{P}_{ij,k} - P_{\text{dark ifo}}}{\overline{P}_k - P_{\text{dark PDA}}}. \qquad i = \{1,12,\text{F,R}\}, j = \{\text{A,B}\}, k = \{\text{m,r}\} \qquad (4.27)$$

To test the accuracy of this calibration the calculated individual beam powers can be added and compared with the total beam power as measured by the phasemeter. Two example plots of the calibrated beam powers and the total power can be found in Figure 4.32.

At the start of the top plot the calibration experiment can be seen, for the calculation of the reference beam power calibration 321 seconds of data are used. For the measurement beam 385 seconds are used. In this timespan the powers are stable, and the calibration parameters derived have small errors. Small changes in these parameters over longer timespans are expected since the gain of the transimpedance amplifier of the amplitude stabilisation diodes is temperature dependent.

The calibration parameters from the DAC measurement of the PDA diodes to the PM power measurements of the experiments shown in Section 5.1.5 and 5.3 can be found in Table 4.4. To calculate the power in mW from these values they need to be multiplied with the power calibration shown in Section 4.4 in Table 4.2, however in the phase noise calculation this calibration parameter cancels since only the power ratio is of interest.

Diode	reference beam calibration $\left[\frac{1}{\text{Count}}\right]$	measurement beam calibration $\left[\frac{1}{\text{Count}}\right]$
PD1_A	$7.6387\cdot 10^{-6} \pm 2\cdot 10^{-10}$	$10.9919\cdot 10^{-6} \pm 3\cdot 10^{-10}$
PD1_B	$7.9110\cdot 10^{-6} \pm 2\cdot 10^{-10}$	$13.8601\cdot 10^{-6} \pm 3\cdot 10^{-10}$
PDR_A	$8.7101\cdot 10^{-6} \pm 2\cdot 10^{-10}$	$11.4042\cdot 10^{-6} \pm 3\cdot 10^{-10}$
PDR_B	$7.0391\cdot 10^{-6} \pm 2\cdot 10^{-10}$	$12.2103\cdot 10^{-6} \pm 3\cdot 10^{-10}$

Diode	reference beam calibration $\left[\frac{1}{\text{Count}}\right]$	measurement beam calibration $\left[\frac{1}{\text{Count}}\right]$
PD1_A	$7.6384\cdot 10^{-6} \pm 8\cdot 10^{-11}$	$11.0350\cdot 10^{-6} \pm 1\cdot 10^{-10}$
PD1_B	$7.9059\cdot 10^{-6} \pm 8\cdot 10^{-11}$	$13.8431\cdot 10^{-6} \pm 1\cdot 10^{-10}$
PDR_A	$8.6995\cdot 10^{-6} \pm 9\cdot 10^{-11}$	$11.4340\cdot 10^{-6} \pm 1\cdot 10^{-10}$
PDR_B	$6.9833\cdot 10^{-6} \pm 7\cdot 10^{-11}$	$12.0401\cdot 10^{-6} \pm 1\cdot 10^{-10}$

Table 4.4.: These are the parameters used to calculate the beam powers on the interferometer diodes from the measurement of the amplitude stabilsation diodes. The power from these PDA diodes is recorded with one DAC channel each of the CDS FST model; the same measurement is used to measure RIN. This calibration depends on the gain of the transimpedance amplifier of the PDA electronics. The top table shows the calibration of the experiment shown in Section 5.1.5 in November 2020 and the bottom table shows the calibration used in Section 5.3 in March of 2021.
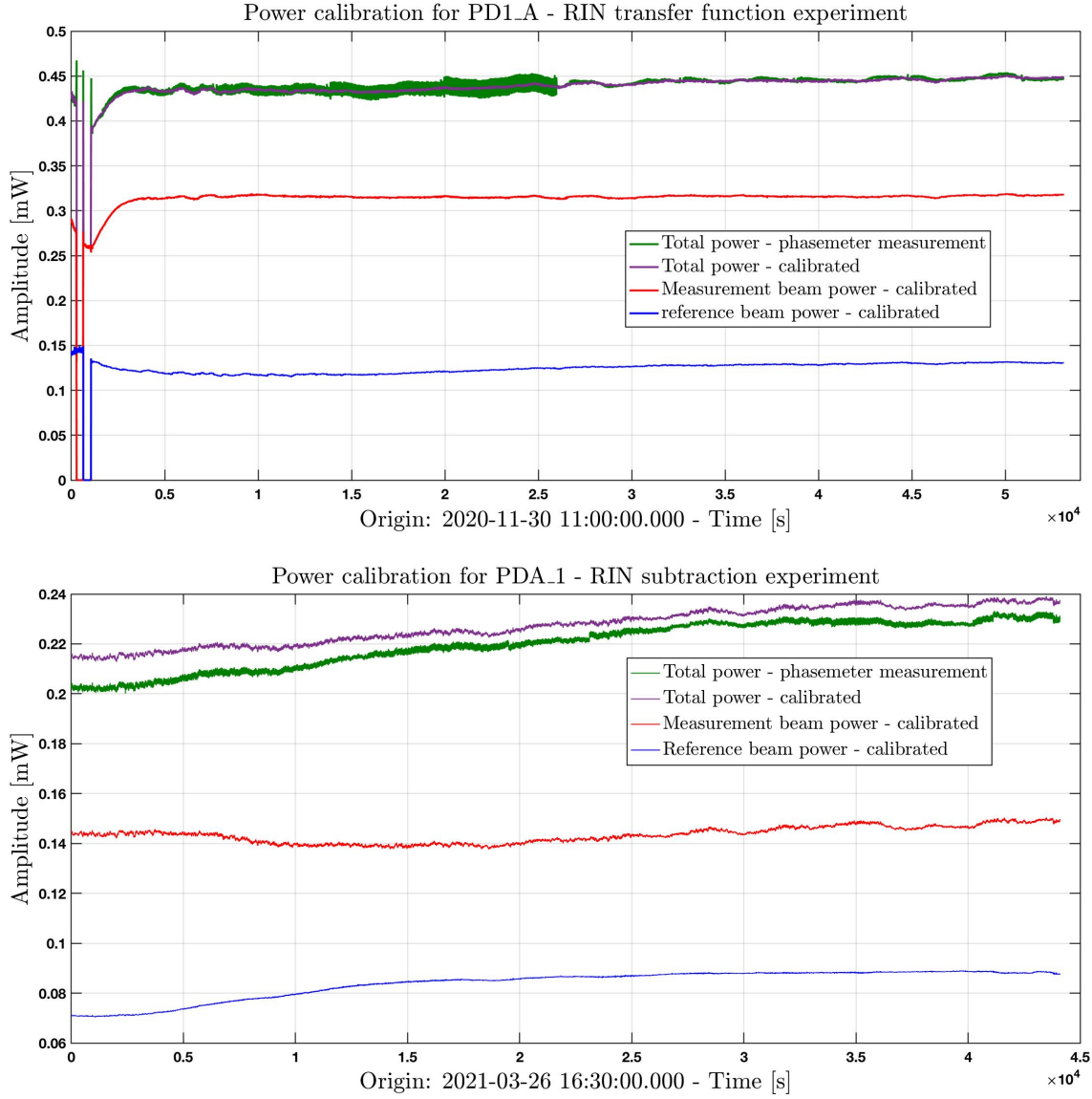
Figure 4.32.: Shown in the top plot are the beam powers on PD1_A during an injection of sinusoidal RIN during the experiment shown in Section 5.1.5. At the start of the measurement the calibration is done by blocking the beams individually. The bigger power fluctuations in the phasemeter measurement correspond to the $1f_{het}$ RIN injection. The mean beam power values over the measurement duration and the difference to the PM measurement can be found in Table A.1.

Shown in the bottom plot are the beam powers during the $1f_{het}$ RIN injection from Section 5.3, the calibration is done a few hours after this measurement. The mean beam power values over the measurement duration, and the difference to the PM measured power can be found in Table 5.5.

5   RIN laboratory experiments

The coupling of Relative Intensity Noise (RIN) was first measured in the laboratory during the initial OMS experiment runs [63]. A test mass position dependent noise was found and then attributed to amplitude noise coupling into the phase measurement.

Compared to other noise sources its contribution to the noise floor was minor. The coupling was not further investigated after it was discovered that it could be suppressed well enough by the fast amplitude control loop and balanced detection.

The measurements of the coupling from RIN to phase noise were improved during my master thesis at the AEI [31].

At the time of these experiments (2013) the LPF laboratory setup still had analog control loops. Actuation on the test masses with the fully analog driver was too noisy for controlled experiments, and did not include a control loop to keep the TMs at a fixed position and orientation. In these experiments TM motion due to temperature changes was used to measure noise at different TM offsets, the range of which was entirely dependent on environmental factors. A white noise around $1f_{het}$ and $2f_{het}$ was injected at the AOM amplitude control loop inputs to produce RIN, the predicted subtraction properties of the RIN injected for different test mass positions could be demonstrated.

The current OMS setup (after 2014) features digital control loops, with the option to move the TMs and hold them at a fixed position. The digital setup also allows for an improved injection of noise and signals via the CDS, instead of a function generator. The injection and measurement of RIN was explained in Section 4.5.

In this Chapter the laboratory experiments performed to confirm the calculated RIN couplings are shown. With one set of experiments the coupling parameters from RIN to the phase signal are confirmed; the first version of this experiment and an improved version can be found in Section 5.1. The frequency dependency of the RIN coupling is shown, see Section 5.2. With another set of experiments the dependency of the RIN subtraction on the phase difference between measurement and reference interferometer is confirmed, see Section 5.3.

The laboratory setup has a different heterodyne frequency than the flight setup, $f_{het\ ground} = 1.6\,\mathrm{kHz}$ on the ground versus $f_{het\ space} = 1\,\mathrm{kHz}$ in the flight setup. For the experiments in the LPF laboratory RIN and RIN equivalent intensity fluctuations around 1.6 kHz and 3.2 kHz are injected into the input of the fast amplitude control loops of the AOM. Sanity check experiments with injections at other frequencies were performed. As expected these did not couple to the phase measurement.

RIN coupling to the phase measurement could also be observed in experiments with the LISA phasemeter on the hexagon interferometer, a short description can be found in [82].

5.1. RIN coupling to the phase

Interesting for the description of the noise floor of the phase signal is the contribution of Relative Intensity Noise (RIN) around $1f_{het}$ and $2f_{het}$. This noise at kilohertz frequencies couples down to the measurement band, as described in Section 3.4. The theory predicts that RIN with an offset of $\pm\epsilon$ from either $1f_{het}$ or $2f_{het}$ will result in a phase noise at the frequency ϵ. With an injection of white noise on the laser power it is impossible to ascertain if this is true, or if there is some other frequency dependency.

With a sinusoidal injection near $1f_{het}$ or $2f_{het}$ the frequency behaviour can be tested, and the measured transfer coefficient can be compared with the theoretical predictions. In this section a RIN equivalent sinusoidal intensity modulation at a fixed frequency $1f_{het} \pm \epsilon$ or $2f_{het} \pm \epsilon$ with changing amplitude is injected, and traced to the phase signal as measured by the phasemeter. For this transfer function measurement a frequency offset $\epsilon = +12\,\text{Hz}$ is chosen, the description of an experiment with a wider range of positive and negative offsets ϵ can be found in Section 5.2.

Presented are two experiment designs to measure the transfer function from RIN to phase. The first experiment is designed to be a minimal test; the RIN signal is injected on one beam and the phase signal on the individual diodes of X_1 and X_R is observed. This experiment is shown in Section 5.1.2, additional results of this experiment are shown in Section 5.1.3. However, in the analysis of this experiment it was found that an injection of RIN produces an additional Small Vector Noise (SVN) component; this coupling is explained in Section 5.1.4. With this knowledge a new experiment is designed to create a fit to this SVN, and subtract it. Effectively, this new experiment repeats the first version for different OPD loop setpoints to scan the coupling of SVN noise; the description of the results of this experiment can be found in Section 5.1.5.

The coupling coefficients for these experiments are different from the coefficients for a noise injection. In this experiment the sinusoidal signal appears only on one side of either $1f_{het}$ or $2f_{het}$, so ϵ either has a positive or a negative offset. Whereas the noise of course couples from both $+\epsilon$ and $-\epsilon$ offsets in RIN to ϵ in phase. Therefore, the predicted amplitude for sinusoidal injections is a factor $\sqrt{2}$ lower than for noise injections.

5.1.1. Design and data analysis of the first experiment

In this experiment RIN and phase are measured on the same diode. Since the phasemeter cannot record kHz signals it was necessary to measure the power and the phase independently of each other.

The diodes are connected to the phasemeter for the phase measurement. For this experiment PD1_A and PD1_B are connected to the x1 channel and x12 channel of the PM, their phase signals are recorded at 256 Hz. To measure the power these QPDs are connected to one transimpedance amplifier per quadrant. With a voltage summer the four signals are combined and recorded with the CDS at a sampling frequency of 64 kHz. The data is saved with a sampling frequency of 16 kHz. Due to this high sampling frequency, the RIN measurement is only one minute long. The phase measurement is 10 minutes long to record more cycles at the lower frequency ϵ. In these experiments RIN is injected on the reference beam, as explained in Section 4.5. To measure the RIN on the reference beam the measurement beam is blocked.

The aim of this experiment is a measurement of the simplest and most direct coupling from RIN to phase, which is why the minimum number of control loops and complications are chosen. The OPD loop is necessary during this experiment, as explained in Section 4.5.1. The amplitude of the phase signal is restored as explained in Section 4.1.3, which will be confirmed in Section 5.2. The expected phase signal for the RIN injected was calculated in Section 3.4.2, the measured data will be compared with this prediction.

RIN measurement

The injection frequency of the RIN injection is chosen so that the resulting phase signal is above the gain increase around the resonance frequency of the OPD loop at $\approx 3\,\mathrm{Hz}$, but the frequency is low enough not to be affected by the phasemeter window or the Doppler effect [37][34]. An offset of $\epsilon = 12\,\mathrm{Hz}$ is chosen because the phase spectrum is flat around this frequency, and the RIN spectrum is also flat for $1\mathrm{f_{het}} + 12\,\mathrm{Hz} \approx 1635.376\,\mathrm{Hz}$ and $2\mathrm{f_{het}} + 12\,\mathrm{Hz} \approx 3258.753\,\mathrm{Hz}$.

The experiment is performed at decreasing injection voltages to measure the linearity of the coupling and to allow for a fit through the data points. The timeline of these injections is performed with a script run on CDS. A short part of the shell script used to inject RIN can be found in Appendix A.14. The time series of the measured power can be found in Figure 5.1. This time series is split into segments for each injection amplitude, amplitude spectra of these segments can be found in Figure 5.2. Visible is the decreasing peak height of the injected RIN; the stronger sidebands at 12 Hz offsets are from the RIN injections with the biggest amplitudes, see also Figure 5.11. Also visible in these spectra are the peaks at multiples of 50 Hz due to electrical cross-coupling.

The injection amplitudes from the CDS in the internal unit Count and the resulting output voltage of the DAC are shown in Table 5.1, together with the approximate amplitude of the RIN equivalent intensity modulation.

The amplitude of the RIN equivalent signal injection is calculated as

$$\tilde{r}_{\mathrm{r}}^{(1,2)} = \frac{\sqrt{2}}{\mathrm{tf_{AA}}} \cdot \mathrm{abs}\left(\frac{\mathrm{P_{DFT}}}{\mathrm{P_{DC}}}\right). \tag{5.1}$$

Where $\mathrm{P_{DFT}}$ is the DFT at the injection frequency, calculated with the flat top window HFT70, and calibrated to amplitude from the rms output of the DFT with a factor $\sqrt{2}$. To calculate the RIN amplitude $\tilde{r}_{\mathrm{r}}^{(1,2)}$ the power value is divided by the DC power $\mathrm{P_{DC}}$ of the segment under analysis. The measured peak height is adjusted for the transfer function of the anti aliasing filter $\mathrm{tf_{AA}}$ of the ADC, which was calculated from the measured DAC-ADC transfer function as shown in Section 4.5. Its value is 1 for lower frequencies and
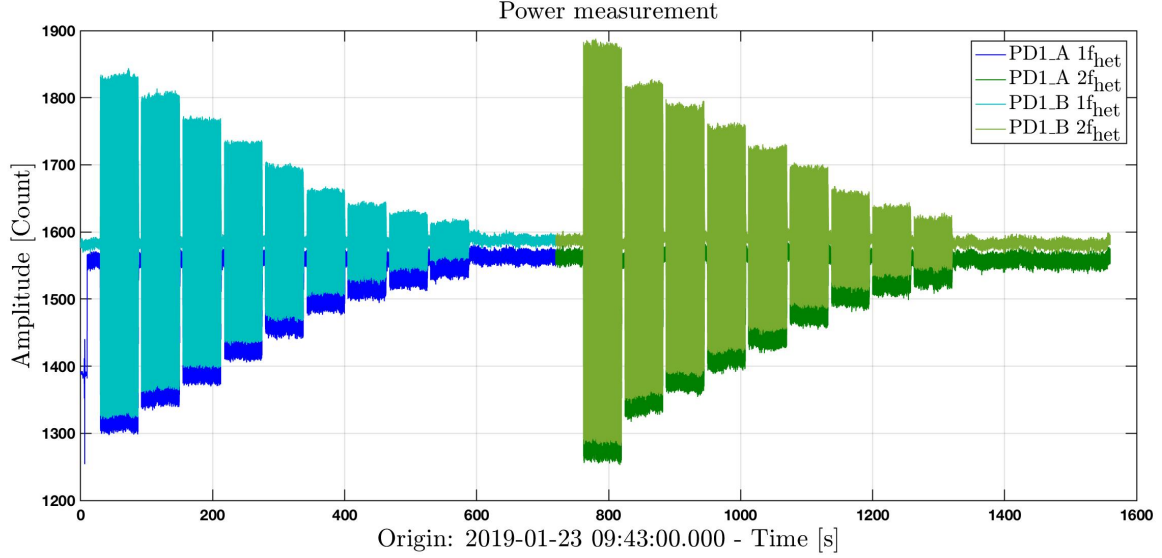
Figure 5.1.: This is the time series of the power measurement of the two QPDs of X_1, with sinusoidal actuation on the laser amplitude by the AOM amplitude control. The first injection is at $1f_{het} + 12\,Hz$ and the second at $2f_{het} + 12\,Hz$. Each injection is 58 seconds long with a 2 second gap between the different amplitudes. From this power measurement the RIN amplitudes are calculated.

Injection [Count]	Injection [V]	RIN $\tilde{r}_r^{(1)}$ [ ]	RIN $\tilde{r}_r^{(2)}$ [ ]
4500	1.373	-	0.19
3500	1.068	0.16	0.15
3000	0.916	0.14	0.13
2500	0.763	0.12	0.11
2000	0.610	0.09	0.09
1500	0.456	0.07	0.07
1000	0.305	0.05	0.04
700	0.214	0.03	0.03
500	0.152	0.02	0.02
300	0.092	0.01	-

Table 5.1.: This table shows the amplitude of the RIN equivalent intensity modulation injections in the internal CDS unit Count, and the resulting output voltage of the DAC. The RIN associated with this injection is shown for typical laser powers for injections near $1f_{het}$ and $2f_{het}$.

decreases above $1\,kHz$, the measured signals are attenuated by a factor $tf_{AA}(f_{het}) \approx 0.9896$ and $tf_{AA}(2f_{het}) \approx 0.9624$. Here, the gain between DAC and ADC, and of the components in between, is of no interest since it affects the peak height calculated with the DFT and the DC power the same way.

Figure 5.2.: The time series shown in Figure 5.1 is cut into one segment per injection. For each segment the amplitude spectrum is calculated, with a HFT70 window and 50% overlap of the FFT segments. The number of samples per FFT are chosen so that the injection frequency is in the middle of an FFT bin.

Shown in the top plot are the segments of the RIN injection at $1f_{het} + 12\,\mathrm{Hz}$, the signals of PD1_A are plotted in blue and PD1_B in green. In the bottom plot the spectra for a RIN injection at $2f_{het} + 12\,\mathrm{Hz}$ are shown. Visible here is the decreasing amplitude of the injected RIN.

Phase measurement

To calculate the coupling parameters the amplitude on the phase signal is also measured, Figure 5.3 shows the time series of the X_1 diodes with a bandpass around $12\,\mathrm{Hz}$. First, the signal near $1f_{het}$ is injected. Then the PD cables are connected to the transimpedance amplifier to measure the RIN. During this time the phasemeter measures only noise. After the RIN measurement the cables are reconnected to the phasemeter, and the phase response for RIN injected near $2f_{het}$ is measured. Clearly visible is the decrease in the amplitude of the phase signal as the RIN injection amplitude decreases.

Shown in Figure 5.4 is the amplitude spectrum of the phase for the injected signals at
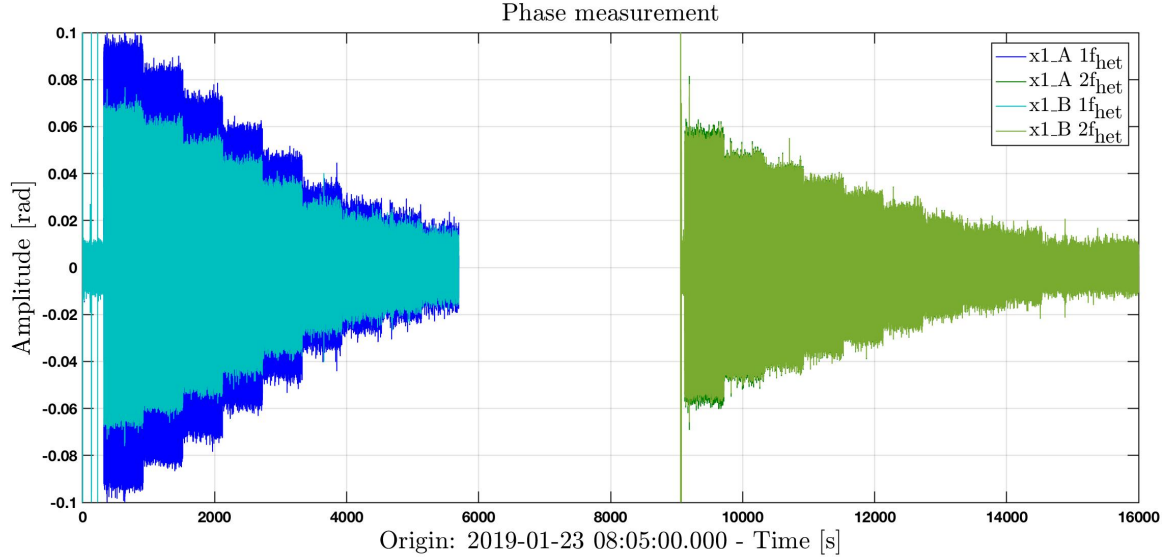
Figure 5.3.: This is the time series of the phase measurement; the signal is bandpassed between 11.5 Hz and 12.5 Hz. Seen here is the phase signal due to the injected RIN; first RIN at $1f_{het} + 12$ Hz is injected, visible is the decreasing amplitude of the injection. The second set shows the phase signal due to the RIN injected at $2f_{het} + 12$ Hz. Each injection is 598 seconds long, with a 2 second gap between RIN amplitudes. Between these two measurements the photodiode cables are connected to the CDS to record the RIN, see Figure 5.1.

$1f_{het} + 12$ Hz and $2f_{het} + 12$ Hz of the X_1 interferometer. The phase response to the injected RIN equivalent intensity modulation is clearly visible at 12 Hz. Also visible in the phase measurement are peaks at 24 Hz with decreasing amplitude, these are most likely caused by the second-order sidebands on the laser amplitude.

With the DFT function the amplitude φ_{RIN} of these peaks on the phase signal is calculated, again the flat top window HFT70 is used. This amplitude is later corrected for the sinc filter of the phasemeter, see Section 2.6.5. The error is calculated from the ratio of the peak height to the noise floor around it. Since most of the injected RIN signals are large compared to the sensing noise floor the error on these values is small, however it does not include systematic errors.
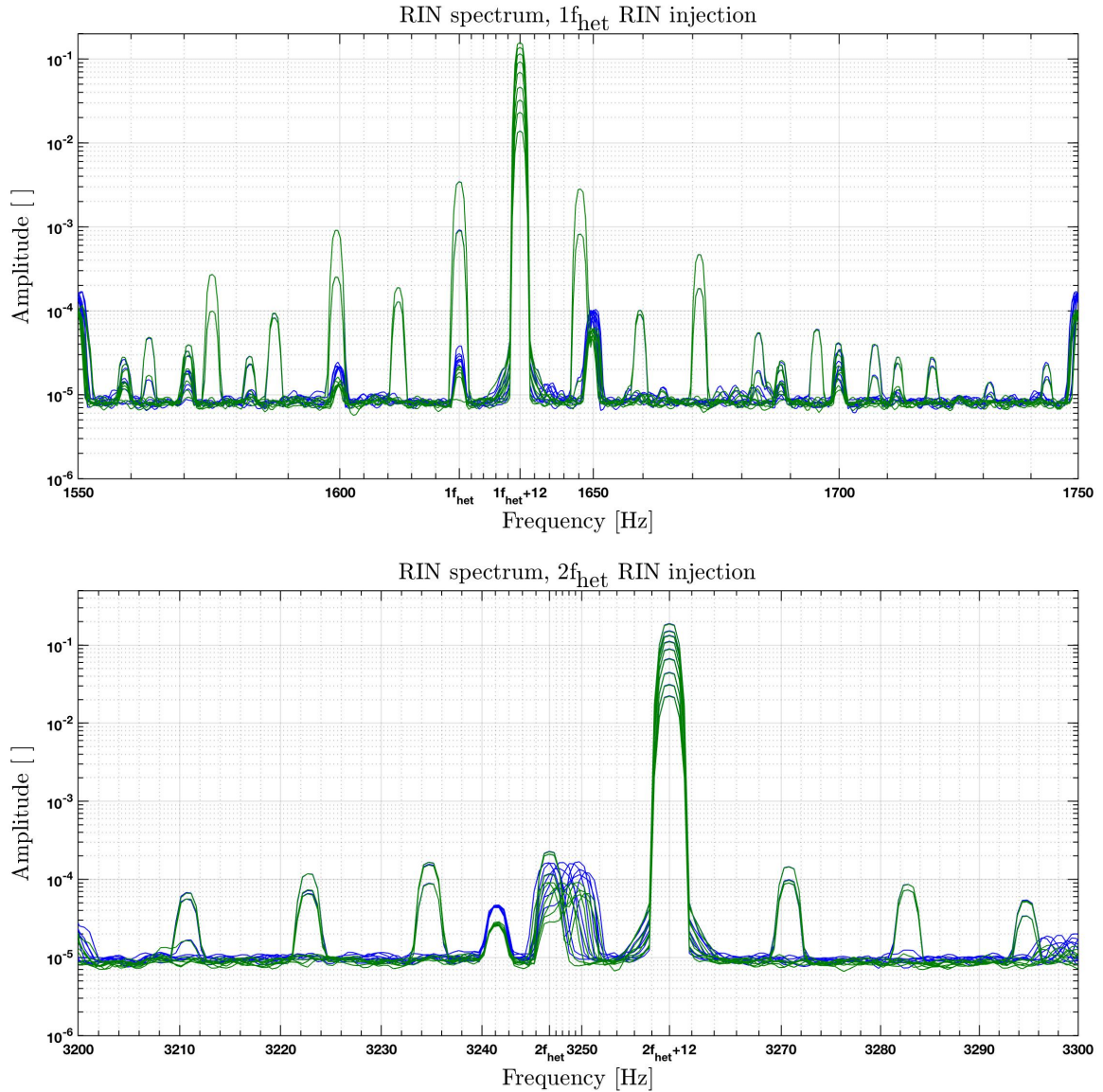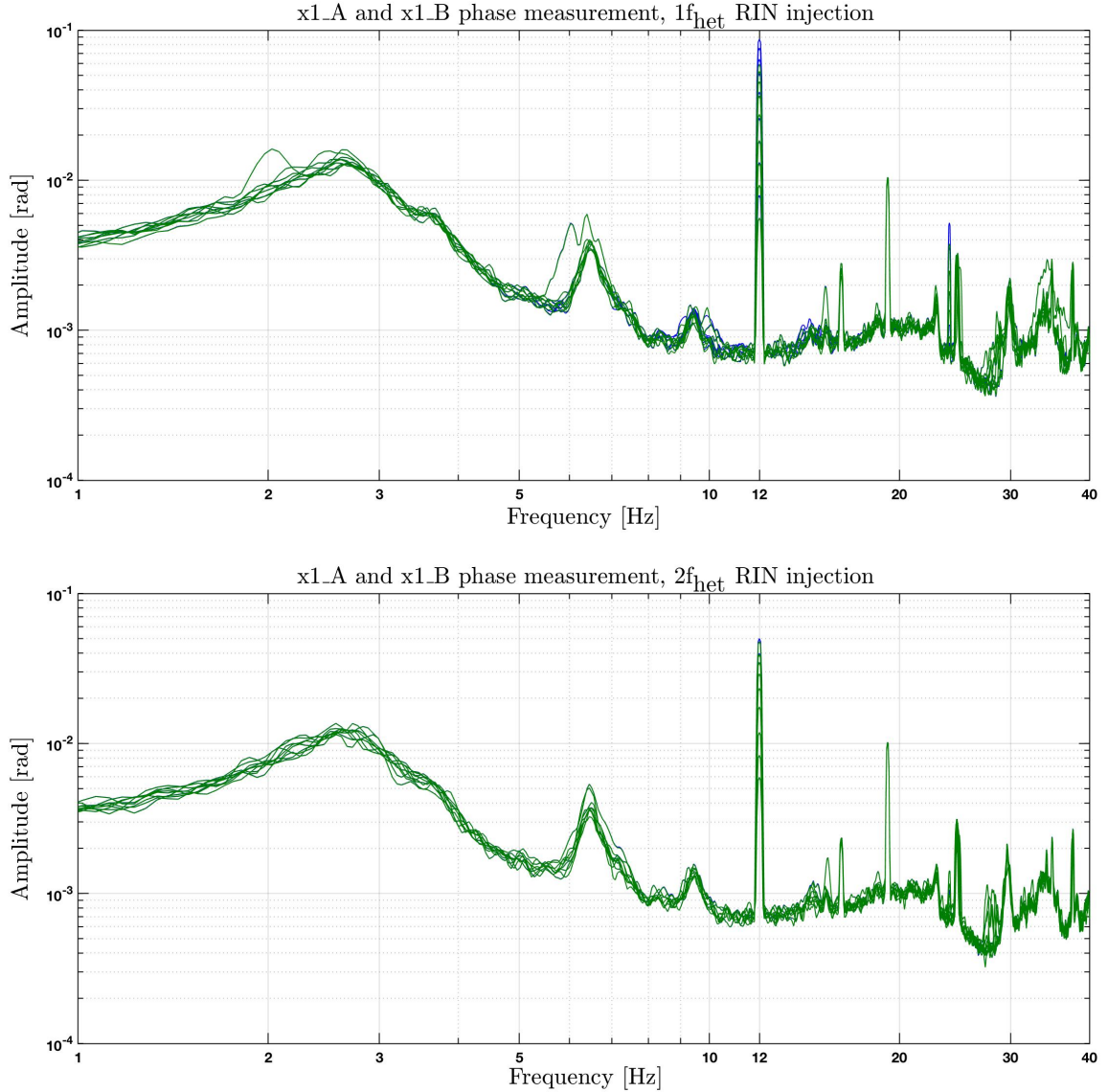
Figure 5.4.: The time series of the phase signal as shown in Figure 5.3 is cut into one segment per injection. For each segment the amplitude spectrum is calculated. In each FFT 4800 samples are used, with an HFT70 window. Shown in the top plot is the resulting phase signal on x1_A (blue) and x1_B (green) of the RIN injection at $1f_{het} + 12\,Hz$. The spectrum for the $2f_{het} + 12\,Hz$ RIN injection is similar, shown in the bottom plot. The intended phase signal of the injection is at $12\,Hz$, also visible are the second-order peaks at $24\,Hz$ and the bump in the spectrum around $3\,Hz$ caused by the OPD loop.

Phase response to RIN injection

The measured amplitudes $\tilde{r}_r^{(1,2)}$ of the injected RIN and the amplitude of the corresponding phase signal φ_{RIN} are combined; this object is built for both diodes of the X_1 and X_R interferometers for injections near both $1f_{het}$ and $2f_{het}$.

The analysis objects calculated here are used for further analysis. These phase amplitudes are corrected for the change due to the OPD loop. This corrected data can then be compared to the values expected for the RIN transfer coefficient from the calculations in Section 3.4.2, where the predicted phase amplitude for a sinusoidal RIN equivalent intensity modulation on only one of the beams was derived.

As a sanity check the same object is created with the peak height of amplitude spectra

Diode	Power both	Power meas.	Power ref.	Contrast	η_{het}
PD1_A	0.2877	0.17255	0.1343	$0.809 \pm 5 \cdot 10^{-6}$	0.668 ± 0.03
PD1_B	0.3336	0.2162	0.1361	$0.810 \pm 3 \cdot 10^{-6}$	0.702 ± 0.03
PDR_A	0.3089	0.1775	0.1514	$0.851 \pm 6 \cdot 10^{-6}$	0.730 ± 0.03
PDR_B	0.30275	0.1925	0.12454	$0.844 \pm 5 \cdot 10^{-6}$	0.756 ± 0.03

Table 5.2.: The beam powers are measured before the experiment by blocking one of the beams, they represent a snapshot of the system at this time. The error on these values is estimated to $\approx 2\%$ from the beam power drift over the experiment duration. The contrast is measured over the whole experiment duration, from this time series the mean value during the $1f_{\text{het}}$ RIN experiment is calculated. Also shown is the heterodyne efficiency η_{het}.

as calculated by the psd function of LTPDA for both RIN and phase measurement. The number of samples is chosen carefully, so that the peak is in the middle of the FFT bin. The amplitudes calculated from the amplitude spectrum are consistent with the amplitudes calculated by DFT.

In the derivation of the coupling the power on the individual diodes was calculated from the power in front of the beamsplitter with the BS splitting parameters τ and ρ, see Equation 3.93. However, since the individual beam powers are measured on the diodes it is more convenient to use these directly, with

$$\tilde{x}1\_A^{(1)} = \sqrt{\text{noisefloor}^2 + \left(\frac{P_{1A,r}}{\sqrt{4\eta_{\text{het,A}} P_{1A,r} P_{1A,m}}} \, \tilde{r}_r^{(1)} \right)^2}, \qquad [\text{rad}] \qquad (5.2)$$

$$\tilde{x}1\_B^{(1)} = \sqrt{\text{noisefloor}^2 + \left(\frac{P_{1B,r}}{\sqrt{4\eta_{\text{het,B}} P_{1B,r} P_{1B,m}}} \, \tilde{r}_r^{(1)} \right)^2}, \qquad [\text{rad}] \qquad (5.3)$$

$$\tilde{x}1\_A,B^{(2)} = \sqrt{\text{noisefloor}^2 + \left(\frac{1}{4} \, \tilde{r}_r^{(2)} \right)^2}. \qquad [\text{rad}] \qquad (5.4)$$

The contrast is measured by the phasemeter, the mean value over the $1f_{\text{het}}$ measurement duration time is used for this prediction. Its error is calculated from the distribution of data points, see Appendix A.10.

The individual beam powers on the diodes are recorded from the CDS interface before the experiment by blocking the beams individually. These do not need to be calibrated to actual power from the PM unit they are recorded in, since only the ratio between them is of interest for the coupling coefficient. With the parameters in Section 4.4 the beam powers in mW can be calculated from these values. The error on the power was estimated from the power drift over the course of the measurement, in the experiment under analysis the power of the combined beams changes $\approx 4\%$. The error on the individual beam power is set to $\pm 2\%$ of the measured value.

From the measured beam powers and the contrast the heterodyne efficiencies η_{het} are calculated. The measured values for this experiment can be found in Table 5.2.

The errors on the predicted values for $1f_{\text{het}}$ RIN coupling are calculated from the errors of its contributions, they are shown as error bars around the predicted phase amplitudes.

5.1.2. Results of the first experiment

Shown here are the results of the first experiment design, an improved version of this experiment to account for the impact of small vector noise can be found in Section 5.1.5. In Figure 5.5 the short segment of time when the RIN injection starts is shown, visible are both diodes of X_1 and X_R for both $1f_{het}$ and $2f_{het}$ RIN injections. The difference in coupling to the phase is easy to see in this plot. The sinusoidal signal due to the RIN injection near $1f_{het}$ shows a phase difference of π between A and B side, while the signal due to the $2f_{het}$ RIN injection shown no such phase difference.

Also shown is the input to the OPD loop, the xR_B signal is used as input and the response of the loop to it will either add to or subtract from the RIN signal. Also visible in the comparison between the loop input and the phasemeter measurement is the delay between CDS FST model and PM measurement chain, which was accounted for in the model of the OPD loop transfer function, see Section 4.1.
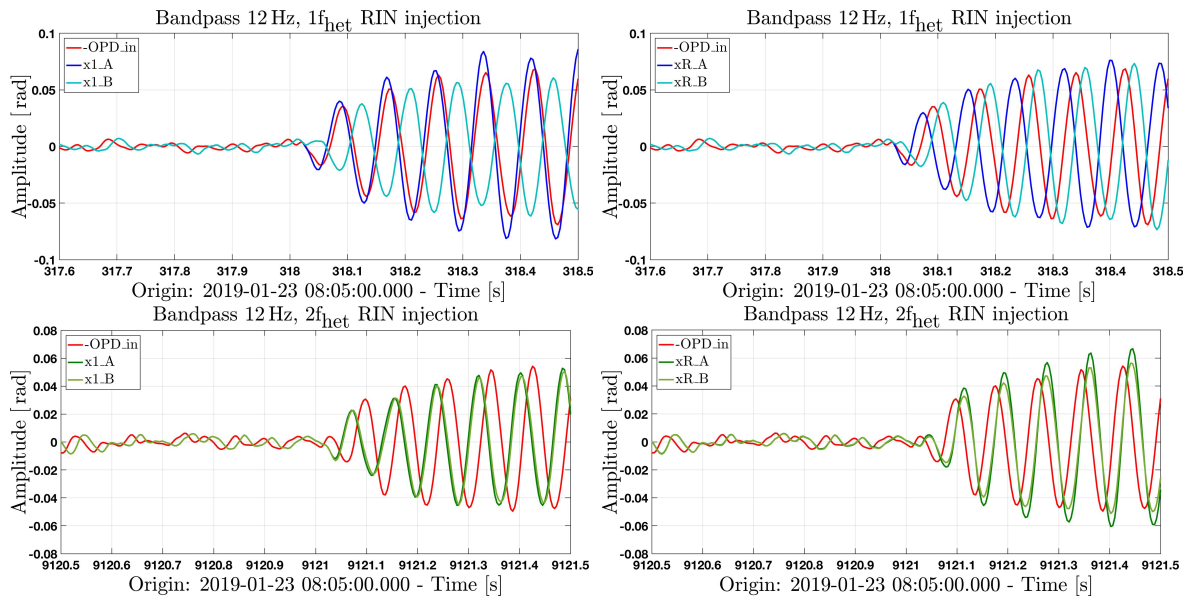
Figure 5.5.: The top plots show the bandpassed phase signal at the start of a $1f_{het}$ RIN injection, the lower two for $2f_{het}$ RIN. Here the difference between the two couplings is visible, for $1f_{het}$ injections the sine wave shows a phase shift of π between A and B port, while the $2f_{het}$ signals show the same sign.

$1f_{het}$ RIN Results

The phase noise predictions for RIN near $1f_{het}$ are calculated from measured values of individual beam powers and contrast.

In a repeated experiment one beam power experienced a strong drift, both the predicted and the measured coupling parameters were non-linear in the same way. The result of this experiment is shown with other plausibility checks in Section 5.1.3.

As mentioned before, the OPD loop has to be turned on during this experiment, and the effect of the loop has to be corrected as shown in Section 4.1.3. The predictions were calculated under the assumption that no OPD loop is on and therefore are not corrected.

The phase amplitude for each RIN injection amplitude of this first coupling parameter measurement can be found in Figure 5.6, both the $1f_{het}$ RIN and $2f_{het}$ RIN results are shown together with the predictions. The results for the X_1 and X_R interferometers are shown, the amplitudes are not yet corrected for the impact of to the OPD loop. In this experiment the RIN of the reference beam is measured on the diodes of the X_1 interferometer, this value should be the same on the X_R interferometer.

117
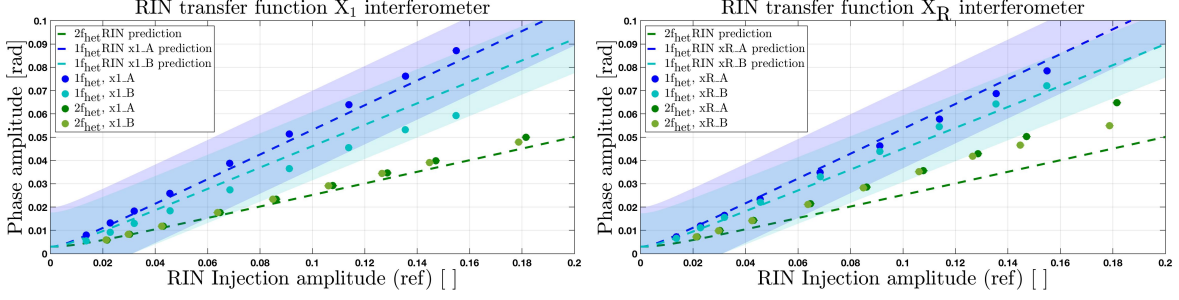
Figure 5.6.: The results for the RIN transfer coefficient as measured of the X_1 interferometer are shown on the left, of the X_R interferometer on the right. The x-axis shows the RIN amplitude, and the y-axis shows the corresponding phase amplitude in radian. The phase is not yet corrected for the impact of the OPD loop. The corrections for the sinc filter on the phase amplitude and the AA filter on the RIN amplitude are applied.

In Figure 5.7 the results with the correction for the OPD loop are shown. The measured phase amplitudes for X_1 and X_R are very similar. The measurement on the X_R interferometer is within a few percent to the predicted values of the predictions for both A and B side, while for the X_1 interferometer only the A side fits to the prediction. On the B side the difference is about 10% for the highest and lowest injection amplitudes, and about 5% inbetween. All $1f_{het}$ measurements moved closer to the predicted values with the correction for the OPD loop. With small variations on gain and delay of the transfer function of the OPD loop the amplitudes did not change significantly, and it can be assumed that the results are robust against small errors in the model of the OPD loop transfer function.

$2f_{het}$ RIN Results

The prediction for $2f_{het}$ does not use measured data, and therefore does not have an error bar. The distance between measured transfer function and predicted transfer function increased with the correction of the OPD loop. Also visible is the bigger difference in the results of the two interferometers, which can't be explained by a difference in the beam powers.

In the investigation of these differences to the predicted values the impact of small vector noise (SVN) became clear. In Section 5.1.4 this will be explained further and a measurement of SVN is shown; with this knowledge a new experiment is designed to reduce the impact of this noise source.

In this first experiment the phase offsets for the reference interferometer are $\approx -0.2\,\mathrm{rad}$ for xR_B and $\approx 2.9\,\mathrm{rad}$ for xR_A for both RIN injections. For the X_1 interferometer the phase offsets for the $1f_{het}$ RIN measurement are $\approx -1.57\,\mathrm{rad}$ and $\approx 1.56\,\mathrm{rad}$ for x1_A and x1_B, respectively. At the start of the $2f_{het}$ RIN measurement the TM has drifted, the phase offsets are $\approx -1.81\,\mathrm{rad}$ and $\approx 1.31\,\mathrm{rad}$ for x1_A and x1_B. Here, a different small vector noise contribution can be expected, see Section 5.1.4.

In this experiment the RIN was measured on the X_1 interferometer diodes, while in the experiment shown in Section 5.1.3 RIN was measured on the reference interferometer diodes. In both a bigger $2f_{het}$ RIN amplitude is measured on the A-side. To investigate this the TIA electronics and DAC readout were switched, but the difference between A and B side remained. The injected RIN is on the reference beam, which means that the A side measures the transmitted beam and the B side measures the reflected beam. Since this difference is not present on the $1f_{het}$ RIN injection, and the light on the diodes was measured to be $\approx 99\%$ s-polarised, this difference is most likely not due to polarisation. In later experiments the RIN of both beams is measured via the power stabilisation diodes, and used to calculate the predicted phase amplitude for both interferometers. This issue was not investigated further.
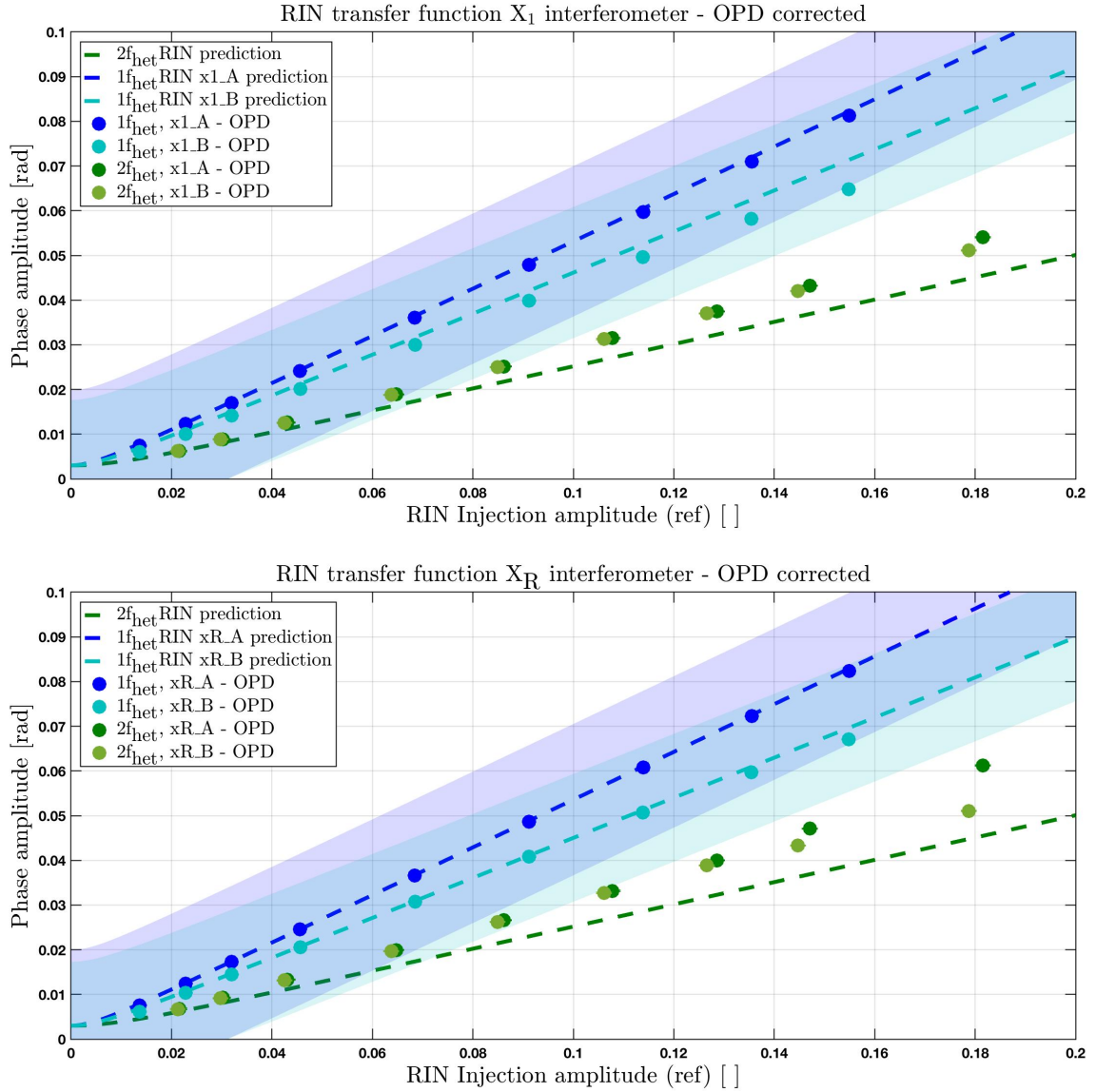
Figure 5.7.: Shown here is the result of the first RIN transfer function experiment, $1f_{het}$ is shown in blue, and $2f_{het}$ in green. The measured phase amplitudes are corrected for the impact of the OPD loop, for the $1f_{het}$ the correction moves the amplitudes close to the predicted values. However, the OPD correction moves the measured $2f_{het}$ phase further away from the predicted values, which indicates that the measured amplitude is not completely caused by the $2f_{het}$ RIN injection.

5.1.3. Plausibility checks

The experiment shown in this section was also performed with the A diode of the reference interferometer as input to the OPD loop, the results are similar to the ones presented. During the design of the experiment other frequency offsets $1f_{het} \pm \epsilon$ and $2f_{het} \pm \epsilon$ were tried, while the analysis was not done with the same level of detail the increase of the amplitudes on the phase signal is also linear with increasing RIN injection amplitude.

Phase difference of the RIN signal
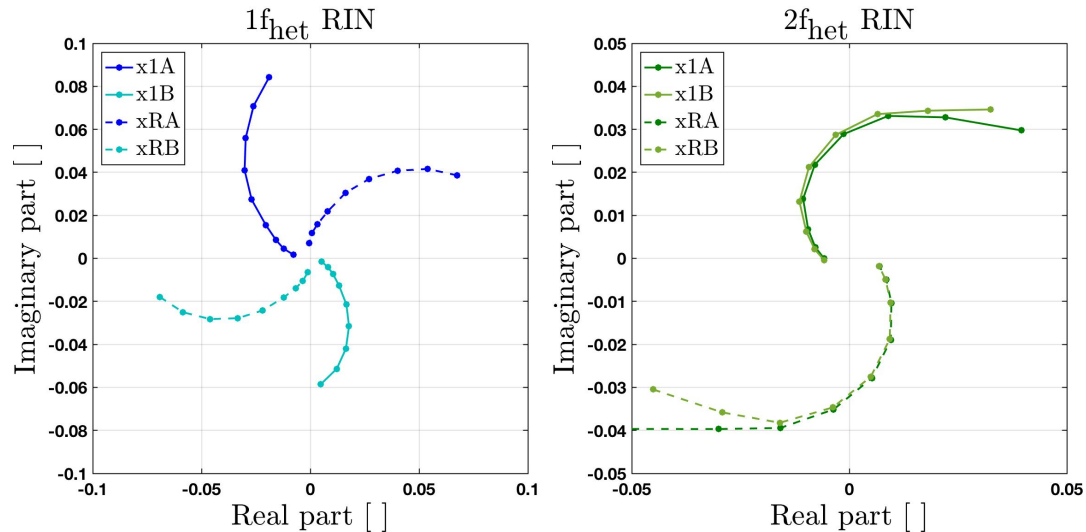
Figure 5.8.: Shown here is the result of the complex DFT of the phase signal. Their absolute value can be seen in Figure 5.6, the colours for $1f_{het}$ and $2f_{het}$ are the same. The phase offset is arbitrary and depends on the start point of the time series selected for analysis. Due to a small regular shift in start time for different DFT calculations the data points curl.

To show the phase difference between $1f_{het}$ and $2f_{het}$ on the A and B ports in an intuitive way the complex result of the DFT is shown with the imaginary part on the y-axis and the real part on the x-axis in Figure 5.8. As shown in the theoretical description of the RIN coupling in Section 3.4, for $1f_{het}$ RIN the phase difference between A and B is π, whereas the phase difference for $2f_{het}$ RIN is almost zero. This difference is the reason why $1f_{het}$ RIN can be removed with balanced detection and $2f_{het}$ cannot. At higher injection amplitudes the $2f_{het}$ phase difference between A and B increases, which indicates additional effects for bigger injections. The phase difference between the x1 and xR signal depends on the TM position, and is interesting for the noise subtraction with o1 = x1 - xR.

RIN at other frequencies

It was also tested if RIN equivalent intensity modulations at frequencies not around either $1f_{het}$ or $2f_{het}$ would couple to the measured phase in a hands-on-experiment, where the result can directly be observed on the CDS live-feed. No coupling at other frequencies was found. An additional test with noise injected around 2.2 kHz was performed in the design phase of the RIN subtraction experiment, see Section 5.3. In this experiment no coupling from this RIN to the phase was visible.

In a similar hands-on-experiment the linearity of the injection on the measurement beam was tested, a linear increase in the phase amplitude for increasing RIN injection could be seen. However, the amplitude and observable number of sidebands in the RIN measurement was also visibly higher for bigger injections.

Power drift

In a repeated experiment of the transfer function measurement shown earlier the power of the measurement beam drifted while the reference beam remained stable. This lead to a slight change in the coupling parameter for $1f_{het}$ RIN over the duration of the measurement, a plot of the results of this measurement can be found in Figure 5.9.

The left plot shows the drift of the power on the interferometer diodes calculated from the measurement of the individual beam powers on the amplitude stabilisation diodes PDA. For each of the segments of RIN injection the predicted phase response is calculated with the beam powers of this segment, the predicted phase amplitude is therefore only calculated for the RIN which is injected and not for smaller or bigger RIN amplitudes. The right plot shows the measured RIN coupling together with their predicted values. The $1f_{het}$ RIN measurements and their prediction show a slight trend upward, while the $2f_{het}$ RIN is independent of this power drift and linear. The contribution of SVN is visible in both. For $1f_{het}$ RIN SVN causes the phase offset to the prediction, and for $2f_{het}$ RIN in the phase difference of the A and B side values.
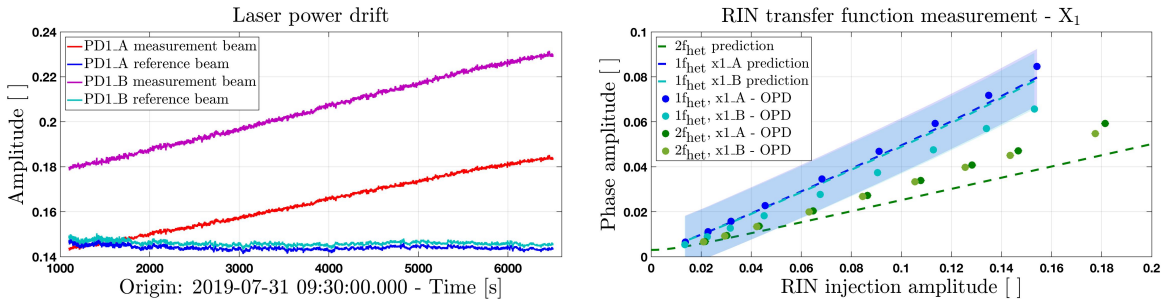
Figure 5.9.: This plot shows a repeated measurement of the first experiment shown in this Section, during this experiment the measurement beam experienced a strong power drift.

Balanced detection

RIN around $1f_{het}$ is removed with balanced detection in the nominal setup. As mentioned in Section 3.4.2, the recombination beamsplitters do not divide the beams exactly 50/50 on the two ports. This imperfect balancing leads to different RIN levels for $1f_{het}$ RIN and prevents a complete removal in the laboratory measurements with standard balanced detection. In principle this imbalance could be fixed with a different gain on the A and B port phase signal in post-processing. However, this gain would also apply to the phase change due to TM motion, which is not desired. The two signals can not be balanced with a different gain on the diode signal, either the photocurrent or the voltage after the TIA, since this gain applies to both signal and noise. For balanced detection it is important to balance the two signals by careful construction of the optical setup.

Shown in Figure 5.10 are two spectra for the RIN injection at $1f_{het} + 12\,\mathrm{Hz}$ and one spectrum for $2f_{het} + 12\,\mathrm{Hz}$ RIN. In the $1f_{het}$ plots the amplitude difference in A and B port can be seen, also shown is the balanced signal where the RIN level is reduced but is not removed completely. Also shown are the two ports and the balanced signal for a $2f_{het}$ injection, the amplitude between the three changes only very little.

In the flight OMS the contribution of RIN around $1f_{het}$ could not be seen, which can be attributed to a better optical bench and the fast amplitude stabilisation.
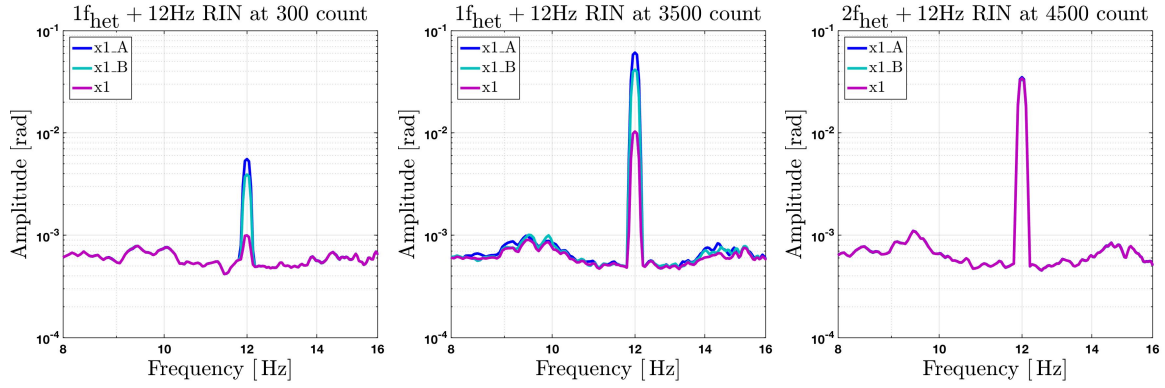
Figure 5.10.: Shown here are the spectra for the individual signals x1_A and x1_B, as well as the balanced signal x1. These amplitude spectra are calculated with an HFT70 window with 50% overlap. The amplitude of the peak at 12 Hz was shown on the y-axis in Figure 5.7. Due to non-perfect balancing between the two ports the amplitudes of x1_A (blue) and x1_B (cyan) of the $1f_{het} + 12\,Hz$ injection are different. The injected RIN can't be removed completely with balanced detection, as visible in the spectrum of x1 (purple). The RIN injection at $2f_{het} + 12\,Hz$ is not subtracted with balanced detection.

Subtraction of the reference

Since in this experiment the test mass control loop is turned off the phase difference between x1 and xR is not stabilised. For the measurement of $1f_{het} + 12\,Hz$ the TM offset is $\approx 58\,nm$, the phase noise from this RIN would be removed for a TM offset of $0\,nm$, and reaches its maximum for $266\,nm$.

During the $2f_{het} + 12\,Hz$ RIN injection the TM offset is $\approx 381\,nm$. In the subtracted signal $2f_{het}$ RIN has minima at TM offsets of $0\,nm$, $266\,nm$ and $532\,nm$ and maxima at $133\,nm$ and $399\,nm$.

5.1.4. RIN Sidebands and Small Vector Noise

When sinusoidal RIN equivalent intensity modulation signals are injected on the light via the AOM inputs this modulation is not only present at the intended frequency $nf_{het} + \epsilon$, but also at offsets ϵ from both $1f_{het}$ and $2f_{het}$ on both beams due to electrical crosstalk. During the setup of the experiment the amplitude of sidebands of the injected sinusoidal amplitude modulation could be reduced.

All of these sidebands lead to a phase change at ϵ, the phase difference between the resulting phase signals is unknown. The amplitude of the sidebands is recorded in a dedicated experiment. In this experiment RIN is injected on the reference beam; the sideband amplitudes on both the reference beam and measurement beam are measured. The sideband amplitudes are recorded as a percentage of the intended signal, the measured values can be found in Table 5.3. In Figure 5.11 the measured sideband amplitudes of the measurement shown in Section 5.1.2 for an increasing injection strength can be seen, visible is a non-linear increase in the amplitude. A RIN spectrum where the sidebands are visible for an injection of RIN at $2f_{het} - 22\,\text{Hz}$ with an Amplitude of 3000 Count can be seen in Figure 4.19. RIN injections at $1f_{het} + 12\,\text{Hz}$ produce mainly sidebands around $2f_{het}$, and vice versa.

RIN sidebands

As a first assumption the sidebands are treated as additional RIN at the same offset ϵ from $1f_{het}$ and $2f_{het}$. From the measured sideband amplitudes the expected total phase change is calculated. In a realistic best case scenario these contributions are not correlated and add quadratically, however this is unlikely since they all originate from the same injected RIN. In a worst case scenario these phases add linearly with zero phase difference, and cause a bigger change in the expected amplitude.

With all the sidebands the new predicted phase amplitudes are calculated for linear and quadratic addition, and compared with the predicted amplitude of the RIN at the intended injection frequency:

$$\text{prediction}_{\text{linear}} = \sqrt{\text{noise floor}^2 + \left(\varphi_{\text{injected}} + \sum \varphi_{\text{sidebands}}\right)^2} \tag{5.5}$$

$$\text{prediction}_{\text{quadratic}} = \sqrt{\text{noise floor}^2 + \varphi_{\text{injected}}^2 + \sum \varphi_{\text{sidebands}}^2} \tag{5.6}$$

The slope of the predicted RIN coupling increases with the addition of the sidebands. The difference amounts to an increase of $\approx 10\,\%$ in the $2f_{het}$ case and $\approx 5\,\%$ in the $1f_{het}$ case in the worst case scenario of linear addition.

Sideband frequency	$1f_{het} + 12\,\text{Hz}$ injection [%]	$2f_{het} + 12\,\text{Hz}$ injection [%]
r, $1f_{het} - 12\,\text{Hz}$	0.11	5.8
r, $1f_{het} + 12\,\text{Hz}$	100 (injected)	1
m, $1f_{het} - 12\,\text{Hz}$	0.063	0.01
m, $1f_{het} + 12\,\text{Hz}$	0.061	0.01
r, $2f_{het} - 12\,\text{Hz}$	0.62	1
r, $2f_{het} + 12\,\text{Hz}$	1.9	100 (injected)
m, $2f_{het} - 12\,\text{Hz}$	0.038	0.06
m, $2f_{het} + 12\,\text{Hz}$	0.061	0.004

Table 5.3.: Shown here are the measured sidebands for an injection at $1f_{het} + 12\,\text{Hz}$ or $2f_{het} + 12\,\text{Hz}$ with 3500 counts, the sideband amplitude is shown as a percentage of the injected signal amplitude. A sideband on the measurement beam is labelled with m, on the reference beam with r.
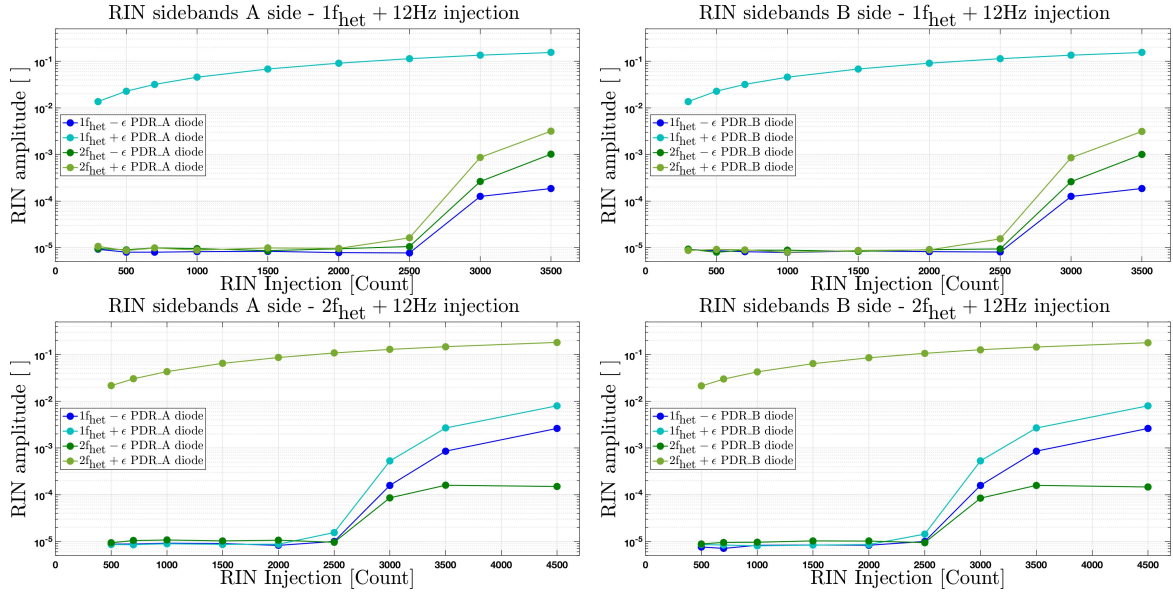
Figure 5.11.: Shown here are the sidebands as measured during the experiment shown in Section 5.1.1, the amplitude of the sideband is plotted for increasing RIN injection amplitude. The measurement with amplitudes higher than 10^{-2} shows the injected RIN amplitudes, these are used for the measurement of the RIN amplitude. The lower three measurements show the amplitude of the sidebands, calculated with a DFT from the same RIN measured with a sampling frequency of $16\,\text{kHz}$. The amplitude of these sidebands rises for injections with an amplitude of bigger than $2500\,\text{Counts}$.

The theory that the sidebands also couple like RIN had to be discarded after a dependency on the phase difference between the two interfered beams was found. These sidebands are a small vector noise (SVN), since RIN shows no such dependency.

Small Vector Noise

RIN and SVN couple differently to the phase. The coupling of small vector noise to the phase has a dependency on the phase difference between the two beams, while the amplitude of RIN is independent of this phase difference. The properties of this noise were a main reason for the creation OPD loop, which stabilises this phase difference. The coupling of SVN to the phase is described in [34] in Chapter 9.4.2; more details can be found in a technical note [32]. Shown there are the experiments which were performed to characterise SVN during a noise measurement, coupling parameters were fitted to the expected dependency on the phase difference. In these experiments the signal under analysis had the reference phase subtracted to reduce the impact of other noise. The remaining noise shape was fitted using the function

$$\Delta\Psi_i^{\mathrm{OPD}} = \mathbf{k}_i' \cdot \mathbf{OPD}(\varphi_i, \varphi_R),\tag{5.7}$$

with

$$\mathbf{k}_i' = (k_{ia}' \; k_{ib} \; k_{ic}' \; k_{id}'),\tag{5.8}$$

$$\mathbf{OPD}(\varphi_i, \varphi_R) = \begin{pmatrix} \sin(\frac{\varphi_i+\varphi_R}{2})\sin(\frac{\varphi_i-\varphi_R}{2}) \\ \cos(\frac{\varphi_i+\varphi_R}{2})\sin(\frac{\varphi_i-\varphi_R}{2}) \\ \sin(\varphi_i+\varphi_R)\sin(\varphi_i-\varphi_R) \\ \cos(\varphi_i+\varphi_R)\sin(\varphi_i-\varphi_R) \end{pmatrix}.\tag{5.9}$$

The first two SVN components describe the coupling of first-order sidebands, the second two components of second-order sidebands; with the amplitudes $\mathbf{k}_i'$.

To characterise the SVN caused by the RIN injection the OPD setpoint is moved in steps while a sinusoidal RIN equivalent intensity modulation is injected. The time series of these OPD steps is shown in Figure 5.12. For each of these setpoints the amplitude on the phase due to the injected RIN is measured. This amplitude is calculated in the same way as shown earlier in this section, and is also corrected for the transfer function of the phasemeter and the impact of the OPD loop. During these steps the amplitude of the injected RIN is constant, and the amplitude of the phase signal caused by the injection changes with the phase difference between the two beams. This phase difference is measured by the phasemeter, the phase change due to the injected RIN is only a small fluctuation on the larger phase steps.

Since in this experiment the SVN is at such a high level that the reference interferometer must not be subtracted to uncover the pattern the fit formulas are separated in their interferometer components with $\sin(x)\sin(y) = \frac{1}{2}(\cos(x-y) - \cos(x+y))$ and $\cos(x)\sin(y) = \frac{1}{2}(\sin(y-x) + \sin(x+y))$. Small vector noise couples to one interferometer with

$$\Delta\Psi_i^{\mathrm{OPD}} = \mathbf{k}_i \cdot \mathbf{OPD}(\varphi_i) + \varphi_{\mathrm{RIN}},\tag{5.10}$$

$$\mathbf{k}_i = (k_{ia} \; k_{ib} \; k_{ic} \; k_{id}),\tag{5.11}$$

$$\mathbf{OPD}(\varphi_i) = \begin{pmatrix} \sin(\varphi_i) \\ \cos(\varphi_i) \\ \sin(2\varphi_i) \\ \cos(2\varphi_i) \end{pmatrix}.\tag{5.12}$$

With the single diode SVN amplitudes $\mathbf{k}_i = \frac{1}{2}\mathbf{k}_i'$. These individual SVN contributions add to a final noise on the phase signal of one diode. In the subtracted signal the peak SVN contribution is twice as big as on one diode, with a dependency on the phase difference between the diodes.

In Figure 5.13 the phase amplitude due to the RIN injection is shown over the mean phase offset, a dependency on the phase difference is clearly visible. In this experiment RIN is injected with an amplitude of 2000 counts, which leads to a RIN level of ≈ 0.09. For RIN injected at an offset to $1\mathrm{f}_{\mathrm{het}}$ the sidebands mainly lead to a SVN with a φ dependency,
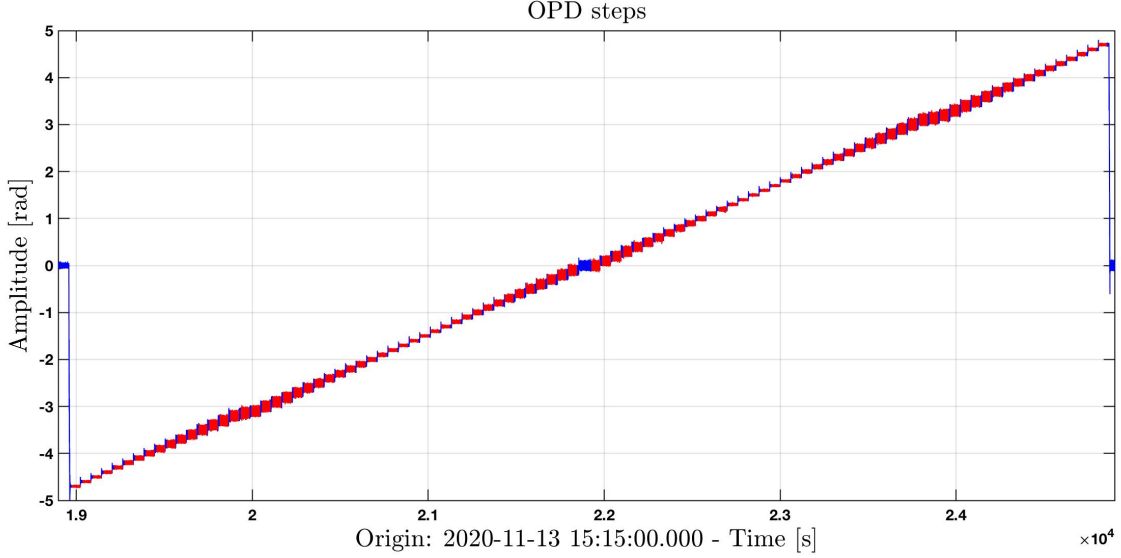
Figure 5.12.: Shown here is the time series of the input to the OPD loop (blue) and the segments selected for analysis (red). This data is computed from the voltage of the PDR_B diode and the digital heterodyne frequency. The setpoint of the OPD loop is changed in steps with a stepsize of 0.1 rad to scan the phase difference between reference and measurement beam. In addition to the regular 0.1 rad steps additional offsets at $-\pi$ and π are included. These resulting phase change due to the OPD loop setpoint steps are measured by the regular interferometers.

while $2f_{\mathrm{het}}$ RIN leads to SVN with a 2φ dependency. The addition of the sine and cosine component with different amplitudes lead to a final sinusoidal SVN pattern with a combined amplitude, which has a phase offset from 0 rad. In this laboratory setup the SVN is created due to an injection, and is therefore correlated to the injected RIN. To remove SVN from the measurement the SVN components are added linearly to the RIN amplitude. In the following laboratory experiments the fit function

$$f_{\mathrm{RIN}}(\varphi_i) = \varphi_{\mathrm{RIN}} + k_{ia}\sin(\varphi_i) + k_{ib}\cos(\varphi_i) + k_{ic}\sin(2\varphi_i) + k_{id}\cos(2\varphi_i) \qquad (5.13)$$

is used. Again the phase amplitude due to the injected RIN is φ_{RIN}. This value is independent of the phase difference φ_i between the two beams. For a more realistic calculation of the error of the phase amplitude the value as calculated by the fit is not used, instead the SVN components are subtracted from the data. For the phase amplitude for the injected RIN level the mean value from the residuals of this subtraction, one data point per OPD setpoint, is calculated.

It can be concluded that small vector noise is a significant part of the amplitude of the phase signal. As far as is known this coupling is time dependant. The results of the experiment shown in Section 5.1.2 can not be corrected for SVN since the amplitude and zero point of the SVN at this time are not known. This experiment is therefore redesigned; for all RIN injections the OPD setpoint is moved in steps to show the contribution of small vector noise. From this measured noise pattern the amplitude of RIN can be determined with a fit. This experiment is described further in Section 5.1.5

As a sanity check the RIN level as measured by the amplitude stabilisation diodes was compared for different OPD setpoints. The RIN shows no dependency on the OPD loop setpoint.

In the flight setup the coupling of SVN is expected to be different; SVN is most likely uncorrelated to the other noise floor components. RIN is a property of the laser, while SVN enters the system due to electrical cross-coupling in the AOMs. SVN should also be
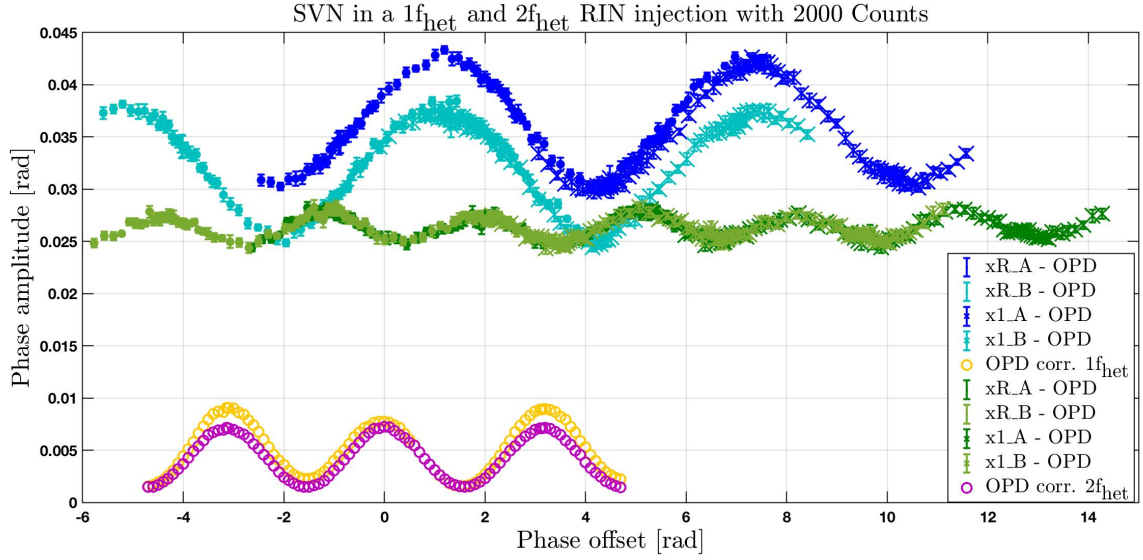
Figure 5.13.: RIN is injected at either $1f_{het} + 12\,\text{Hz}$ (blue) or $2f_{het} + 12\,\text{Hz}$ (green) with an amplitude of $2000\,\text{Count}$. For each of the phase offsets as seen in 5.12 the amplitude on the phase signal at $12\,\text{Hz}$ is shown; as always this amplitude is corrected for the OPD loop. Amplitudes from the X_1 interferometer are shown with an x, amplitudes from the X_R interferometer with a dot. For the correction the x values of the OPD loop actuation are shifted to the phase offsets of the respective diode. If the measured phase amplitude was caused purely by RIN it would be constant for all phase offsets. The modulation on the constant RIN is caused by small vector noise (SVN). This contribution can be fitted and subtracted from the data to recover the RIN level.

uncorrelated to electrical noise, ADC noise and shot noise. Therefore, the expectation for this noise is quadratic addition to the RIN contributions and the sensing noise floor. More details on the in-flight sensing noise can be found in [19], and in an upcoming paper [59].

5.1.5. Design and data analysis of the second experiment

In the analysis of the first experiment the impact of small vector noise on the measured phase amplitude became clear. This improved experiment design aims to remove SVN from the measurement with a fit. In the first transfer function experiment the timeline was intentionally kept short since the amplitude of the injected RIN drifts. The individual beam powers also have a drift, which changes the coupling to the phase. The measurement of RIN over longer experiments is limited due to the necessary higher sampling frequency, to monitor the amplitude of the injected RIN over this longer duration the measured power is demodulated and recorded at $256\,\mathrm{Hz}$. A description of this measurement of RIN can be found in Section 4.5.3.

RIN measurement

As in the first experiment RIN is injected with different amplitudes; the RIN frequency offset ϵ from either $1\mathrm{f}_\mathrm{het}$ or $2\mathrm{f}_\mathrm{het}$ is kept constant at $\epsilon = 12\,\mathrm{Hz}$. For this experiment the OPD setpoint is moved in steps for each RIN injection amplitude, at each OPD setpoint the phase amplitude at this offset frequency ϵ is measured. To reduce the impact of sidebands the maximum injection amplitude is reduced to $2000\,\mathrm{Count}$. At the maximum RIN injection the amplitude is $\approx 3\%$ of the carrier amplitude. For this ratio the approximation for small angles in Section 3.4 still holds. In Figure 5.17 a time series plot of the injected RIN amplitude together with the steps on the OPD setpoint are shown. At each of these OPD setpoints the RIN amplitude and phase amplitude are calculated with the same processing as in the first experiment. Both amplitudes are measured with a DFT. The phase amplitude is corrected for the sinc filter of the phasemeter and the actuation of the OPD loop. The RIN amplitudes are corrected for the AA filter of the ADC and the lowpass filter of the data downsampling. Since the injected RIN amplitude is constant for each set of steps, the final RIN level of one step is calculated by taking the mean. A time series plot of the RIN in both beams at an
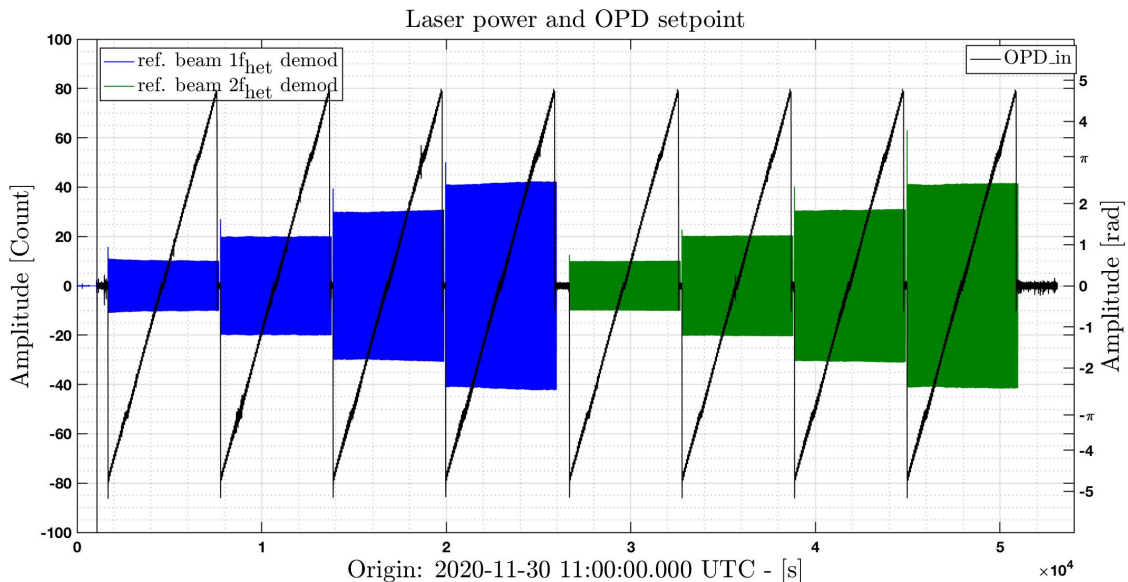
Figure 5.14.: This plot shows the setpoint steps of the OPD loop input (black) together with the measured amplitude of the demodulated power signal, bandpassed around the RIN injection. The RIN injected with an offset to $1\mathrm{f}_\mathrm{het}$ is shown in blue, $2\mathrm{f}_\mathrm{het}$ in green. For each set of OPD setpoint steps the RIN injection amplitude is increased. The time series of the OPD input looks like it has higher noise around offsets of $-\pi$ and π because an additional offset for these two values is included to the otherwise uniform OPD step size of $0.1\,\mathrm{rad}$.

offset of 12 Hz can be found in Figure 5.15; the measured RIN amplitude can be found in Table A.2 in the Appendix. As in the discussion of the first experiment a cross-coupling from the intended injection to a RIN in the other beam is visible. Here, the biggest cross-coupling for the reference beam injection is to the measurement beam at the same frequency, with a factor $\approx 8 \cdot 10^{-4}$ for both $1f_{het}$ RIN and $2f_{het}$ RIN.

The amplitudes of the sidebands with a -12 Hz frequency offset are even lower with a factor of less than $\approx 3.5 \cdot 10^{-4}$ for the $1f_{het} + 12$ Hz RIN injection, and less than $\approx 1 \cdot 10^{-4}$ for the injected RIN at $2f_{het} + 12$ Hz. Plots of the sideband amplitudes over the measurement duration can be found in Figure 5.16. These sideband amplitudes are significantly lower than in the first experiment, probably due to the non-linear increase of the sideband amplitude for bigger injection voltages. The maximum voltage in this experiment is 0.61 V. The sidebands contributions in the first experiment were measured with a voltage of 1.068 V, and could be seen increasing rapidly for voltages bigger than 0.763 V.
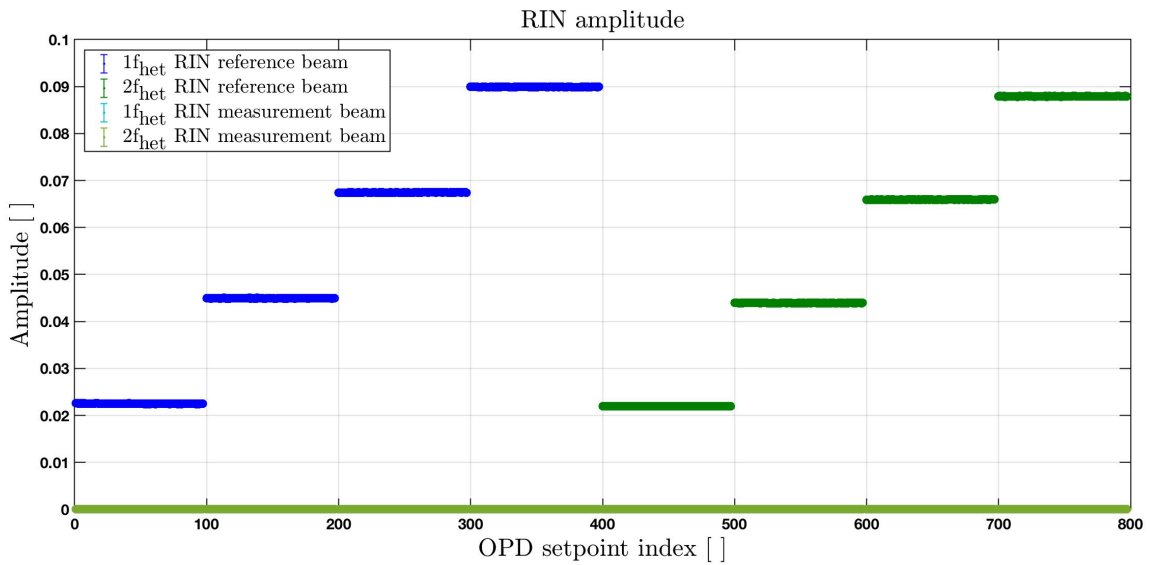
Figure 5.15.: This plots show the amplitudes of the RIN as measured with the demodulated power signals. The increase in injected RIN is visible, for each OPD setpoint the RIN amplitude is calculated with a DFT. The mean RIN of one injection amplitude is used in the following analysis. Here, the $1f_{het} + 12$ Hz RIN of the measurement beam is plotted below the $2f_{het} + 12$ Hz RIN of the measurement beam. The sideband amplitudes for $+12$ Hz and -12 Hz offsets of both beams can be found in Figure 5.16, in this plot both measurement beam RIN levels are visible.

Phase measurement

The coupling from SVN to the phase for changing OPD setpoints could already be seen in Section 5.1.4 for one RIN injection amplitude measured on all diodes. Here this measurement is repeated for more RIN amplitudes. The result of this measurement for the x1_A signal with increasing RIN can be seen in Figures 5.17 and 5.18. The data shown is already corrected for the impact of the OPD loop. In these experiments the phase amplitude due to the injected RIN and due to SVN add linearly, since they originate from the same voltage input these noise contributions are correlated. In other circumstances with uncorrelated noise these contributions would add quadratically. The measurements of the other signals x1_B, xR_A and xR_B can be found in Appendix A.17.

At each RIN injection amplitude the noise pattern due to the SVN contribution can be seen. For each of these measurements a fit is done using Equation 5.13, with the RIN level added
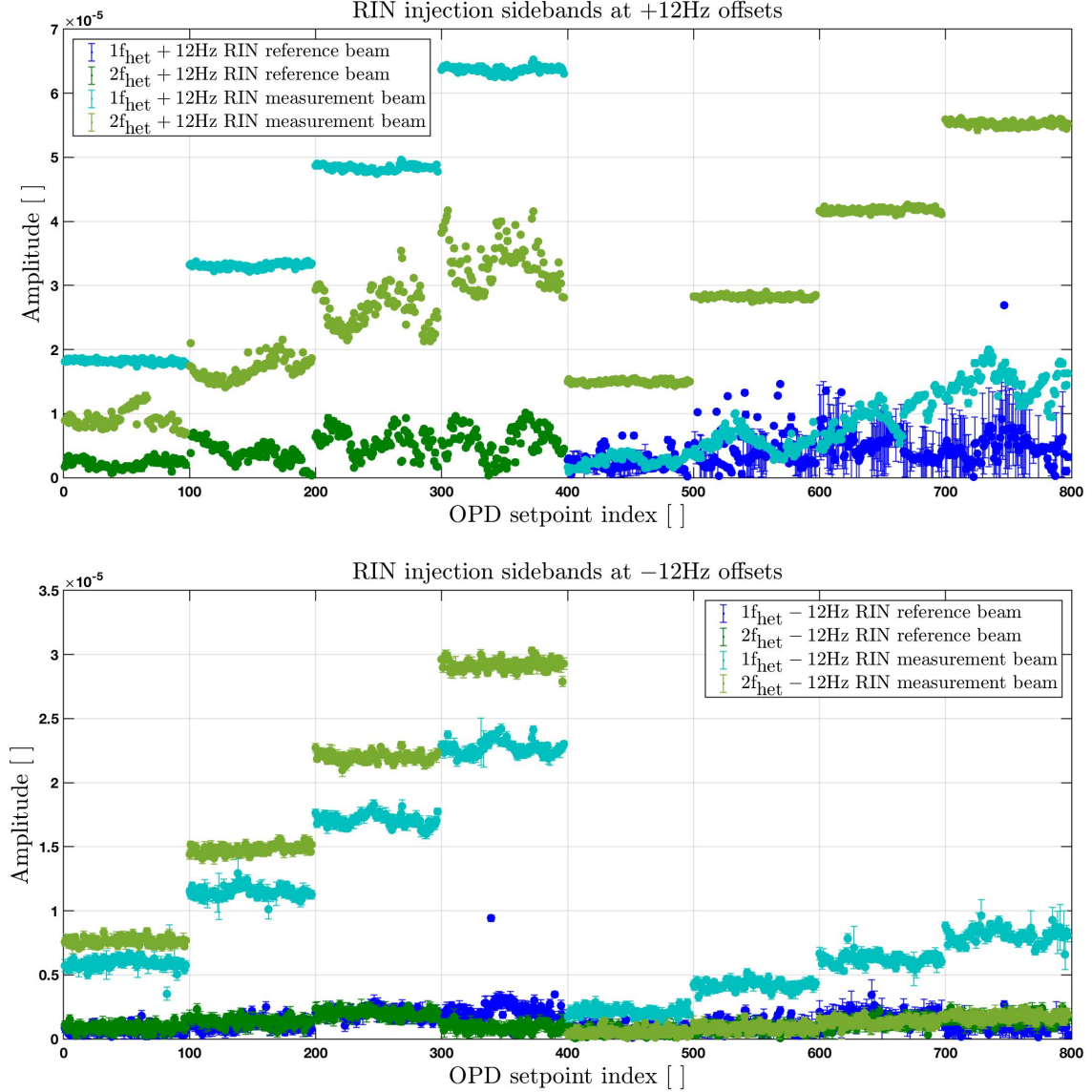
Figure 5.16.: These plots show the amplitudes of the sidebands of the injected RIN as measured with the demodulated power signals. For some sidebands the amplitude increases with an increase in the amplitude of the injected RIN. The biggest sideband amplitude is on the measurement beam at the injection frequency, this can be seen in the top plot.

to it as an offset. In this single-diode measurement the fit results to the SVN pattern with the amplitudes k_{ia}, k_{ib}, k_{ic} and k_{id}, for both $1\mathrm{f_{het}}$ and $2\mathrm{f_{het}}$ RIN can be found in Tables A.4 and A.5 in Appendix A.17. For these RIN injections the amplitude of the combined SVN contributions depend linearly on the amplitude of the injected RIN. From the fitted SVN component and the measured RIN level for the biggest three injections the SVN contribution can be estimated with

$$k_{iab} = \sqrt{k_{ia}^2 + k_{ib}^2} \qquad\qquad = (0.0669 \pm 4 \cdot 10^{-5}) \cdot \tilde{r}_{\mathrm{r}}^{(1)}, \qquad (5.14)$$

$$k_{icd} = \sqrt{k_{ic}^2 + k_{id}^2} \qquad\qquad = (0.0221 \pm 3 \cdot 10^{-4}) \cdot \tilde{r}_{\mathrm{r}}^{(2)}. \qquad (5.15)$$

For the biggest $1\mathrm{f_{het}}$ RIN injection in this experiment this equals a maximum SVN contribution of $k_{iab} \approx 0.0060\,\mathrm{rad}$, for a RIN amplitude of $\tilde{r}_{\mathrm{r}}^{(1)} \approx 0.0899$. The biggest $2\mathrm{f_{het}}$ RIN amplitude is $\tilde{r}_{\mathrm{r}}^{(2)} \approx 0.0868$, with a maximum SVN amplitude of $k_{icd} \approx 0.0019\,\mathrm{rad}$.

For the bigger RIN injections seen in the first experiment, see Figure 5.11 in Section 5.1.4, the sidebands increase faster than linear for injection amplitudes bigger than 2500 Count. This equals a RIN amplitudes of $\tilde{r}_r^{(1)} \approx 0.12$ and $\tilde{r}_r^{(2)} \approx 0.11$. A bigger contribution of SVN to the measured phase can be expected for bigger RIN injections.

The fitted SVN contribution is subtracted from the measured noise shape, the residuals after the SVN subtraction are a measurement of the phase response to the injected RIN. A plot of the residuals of this subtraction can also be found in Figures 5.17 and 5.18. An example of the covariance of the fit parameters can be found in Appendix A.21.

For the comparison of this measured phase amplitude with the predicted phase amplitude due to the RIN injected the mean value of the residuals is calculated. Any effects not subtracted with the SVN fit are visible in the distribution of the residuals, and contribute to the error of the result. Since the OPD setpoint is moved to 97 different positions other effects can be reduced by averaging. The mean value of this phase amplitude has a small error; this error is computed as shown in Appendix A.10. These mean phase amplitudes are computed for all four diodes, for both an injection at $1f_{het} + 12\,Hz$ and $2f_{het} + 12\,Hz$. In Figure 5.19 the results of these mean RIN phase amplitudes are shown together with the predicted values, with the amplitude of the injected RIN on the x-axis. This is the same kind of plot as in Figure 5.7 in Section 5.1.1, where the first experiment was shown. However, the RIN and phase amplitudes are measured differently. As described, the amplitude of the RIN is measured by the demodulated power channels, and the amplitude of the phase is the mean value of a DFT measurement with the OPD loop actuation and the SVN contribution subtracted.

The predictions are calculated with the same equation as in the first transfer function experiment, which were derived in Section 3.4.2. In these experiments the powers on the individual diodes are calculated directly from the measured power of the individual beams on the amplitude stabilisation diodes; in the derivation this power is calculated from the power in front of the beamsplitter with the effective beamsplitter parameters.

Since the duration of this measurement is significantly longer the prediction for each mean value is calculated from the mean beam power during the related set of OPD steps. To measure the individual beam powers on the interferometer diodes the beam power as measured by the PDA diodes and recorded by the CDS is calibrated to the power on the interferometers. The calibration parameters can be found in Table 4.4 in Section 4.5.5, these are measured before this experiment. Since only the ratio of the powers is relevant these are not calibrated to mW. The mean powers and contrast during this experiment can be found in Table A.1 in the Appendix. Again, the error on this prediction is small due to the long measurement duration of the beam powers and RIN level used to calculate it; this error does not include any systematic problems. Since the beam powers are calculated with the previously measured calibration parameters an error of 1% is set on each. The difference of the mean value of the combined powers with the measurement by the phasemeter can also be found in the same table. This difference of the total powers is less than 1% for all diodes.

From the mean beam powers per segment and the mean contrast the heterodyne efficiencies are calculated for each set of OPD steps, also see Table A.1 in the Appendix. Again, due to the long averaging times the calculated errors on these values are small.
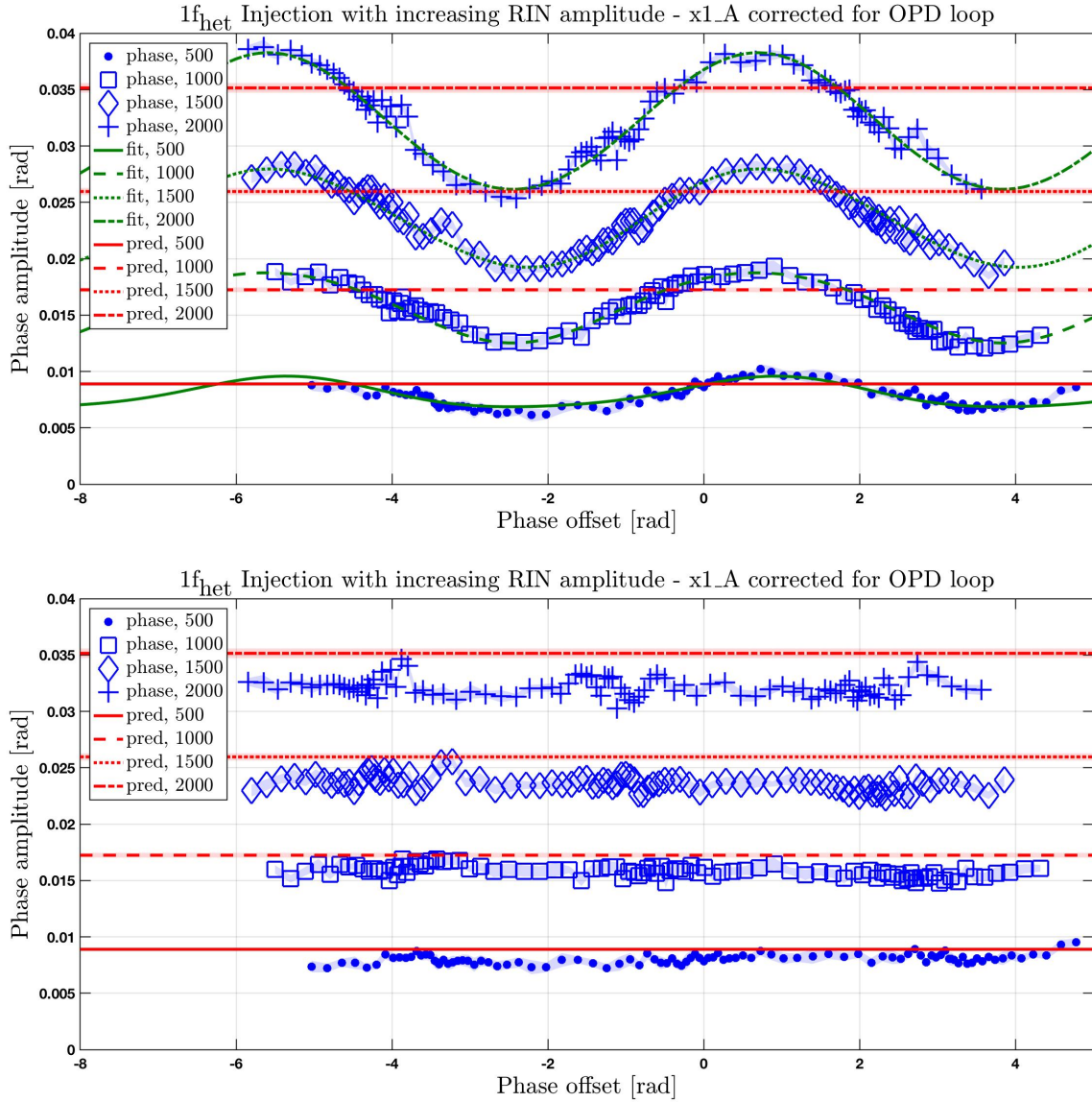
Figure 5.17.: Shown here is the measured 1f$_{\text{het}}$ RIN amplitude of the x1_A signal, the amplitude of the injected RIN is increased. The injection amplitude in the CDS unit Count can be found in the legend. At each RIN injection amplitude the OPD setpoint is moved in steps; which moves the phase difference between the two beams. This phase difference is shown on the x-axis. The top plot shows the data after the OPD loop correction, the noise shape is caused by small vector noise. Each of these sets of data is fit with Equation 5.13 to describe the constant phase amplitude due to the RIN coupling with an additional SVN amplitude. The SVN depends on the phase difference while the RIN level is constant.
The bottom plot shows the residuals after the SVN component is subtracted. Plotted in red is the phase amplitude as predicted from the measured RIN amplitude.
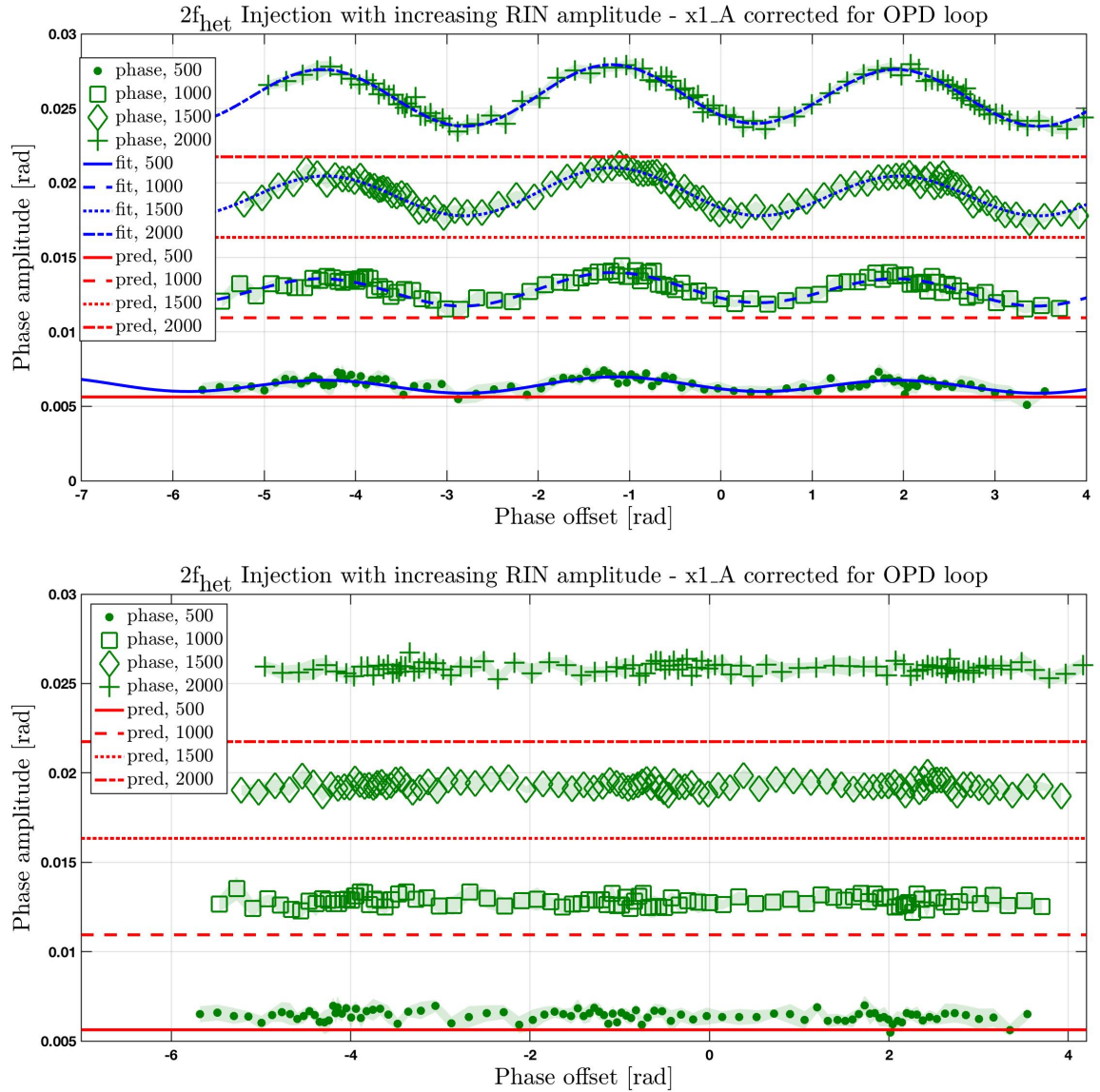
Figure 5.18.: In these plots the phase amplitudes for a $2f_{het}$ RIN injection are shown. The top plot shows the measured amplitudes corrected for the OPD loop in green and the fit to the SVN components in blue. The coupling of SVN ot the phase has only half the wavelength compared to the SVN in the $1f_{het}$ RIN measurement. The phase amplitude as predicted from the RIN amplitude is shown in red. These predictions only depend on the RIN level. The bottom plot shows the residuals after the subtraction of the fitted SVN contribution, from these the mean phase amplitude for the injected RIN is calculated.

5.1.6. Results of the second experiment

The measured phase amplitude and the predicted phase amplitude from the injected RIN can be found in Figure 5.19. An overview of the measured and predicted values can be found in Table A.3 in the Appendix; the factor between the two values can be found in Table 5.4. For the $1f_{het}$ RIN measurement the predicted and calculated phase amplitude are within a few percent for all but the x1_A signal, where the difference is $\approx 9\%$. An error from the calculation of the beam powers on the interferometer diodes with the measured powers due to drift can be expected. In the calculation of the phase amplitude prediction an error of 1% on the beam powers is used, these errors are derived from a comparison of the mean power of both calibrated beams with the mean total power as measured by the phasemeter. A plot of the beam powers on PD1_A can be found in Figure 4.32 in Section 4.5.5.

These beam powers are used together with the measured contrast to calculate the heterodyne efficiency. Another contribution to this difference could be the cumulative effect of the sidebands shown in Figure 5.16.

In the comparison of the measured and predicted phase amplitude of the $2f_{het}$ RIN injection the measured values are too high by $\approx 19\%$ for the X_1 interferometer and by $\approx 18\%$ for the X_R interferometer. This difference looks like it is caused by a systematic error; since it is not clear if this error is on the phase or the RIN measurement an ellipse displays a 15% error around both values. This discrepancy is similar to the difference in the first experiment design, however, this seems to be a coincidence. The measured $2f_{het}$ amplitudes and phase offsets there do not fit on the SVN pattern shown here.

An early idea for the consistent difference for the $2f_{het}$ RIN transfer function measurement were $1f_{het}$ sidebands due to electrical cross-coupling. In Section 5.1.4 the difference in phase amplitude with the sidebands measured could be estimated to a worst case of 10%. However, the measured amplitudes do not change in a significant way with balanced detection, which would be expected for $1f_{het}$ RIN sidebands. The balanced signal for the $2f_{het}$ RIN injection is shown in the same plot with a purple marker. Additionally, the amplitude of the measured sidebands is smaller than in the previous experiment due to the smaller RIN injection amplitude, see Figure 5.16. Which makes this contribution of additional RIN unlikely to be the cause for the discrepancy.

Another likely candidate for this difference is a filter somewhere in the measurement chain, which influences $1f_{het}$ RIN different to $2f_{het}$ RIN. In the RIN measurement the frequency difference of the two injections is accounted for in the correction of the AA filter tf_{AA} and the

RIN inj. amp. [Count]	x1A	x1B	xRA	xRB
$1f_{het}$ RIN: 500	0.903	1.002	0.977	0.958
$1f_{het}$ RIN: 1000	0.917	1.001	0.983	0.973
$1f_{het}$ RIN: 1500	0.909	1.018	0.990	0.969
$1f_{het}$ RIN: 2000	0.914	1.014	0.990	0.974
RIN inj. amp. [Count]	x1A	x1B	xRA	xRB
$2f_{het}$ RIN: 500	1.139	1.139	1.159	1.133
$2f_{het}$ RIN: 1000	1.172	1.173	1.177	1.150
$2f_{het}$ RIN: 1500	1.181	1.183	1.184	1.162
$2f_{het}$ RIN: 2000	1.189	1.191	1.183	1.161

Table 5.4.: Shown here is the ratio of the measured and predicted phase amplitude for the injected RIN. The first column shows the amplitude of the injected RIN in the CDS unit Count, the ratio between the measured and predicted phase amplitude is listed for all diodes.
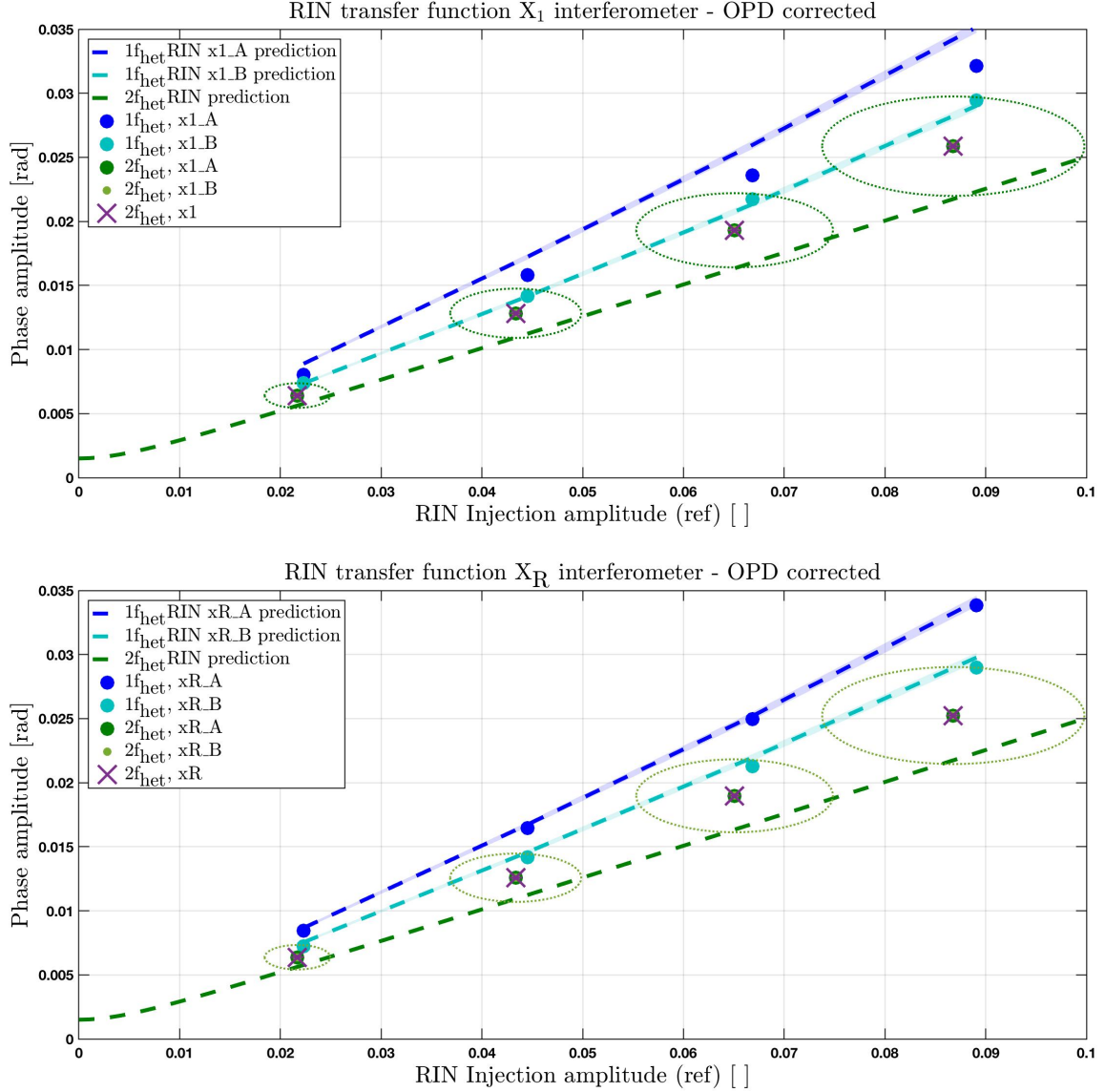
Figure 5.19.: Shown here is the result of the second design of the RIN transfer function experiment, the top plot shows the results of the X_1 interferometer and the bottom plot the X_R interferometer. On the x-axis the injected RIN amplitude is shown, this amplitude is measured with the demodulated power channels. The amplitude of the phase response is shown on the y-axis. This value is computed from the residuals of the measured amplitudes with the OPD loop actuation and SVN contribution subtracted. In addition to the previous single-diode signals the balanced detection signal for the $2f_{het}$ RIN measurement is shown, around this value an ellipse displays an 15% error area on phase and RIN amplitude. The prediction for the coupling of $1f_{het}$ RIN is calculated from the individual beam powers on the interferometer diode calculated from the power on the amplitude stabilisation diodes.

downsampling filter tf_{DAQ}. Both injections are close in frequency in the demodulated signal, which makes an amplitude difference there unlikely. The AI filter of the DAC, and any filters in the AOM electronics, only influence the RIN before it is modulated on the light, and are not relevant here.

In the phasemeter processing both RIN injections cause a phase change at the same frequency. The phase error due to the injected $2f_{het}$ RIN is measured in the same FFT bin as for the $1f_{het}$ RIN injection. An effect of a window or similar in the phasemeter processing is unlikely. SVN is often a candidate for unexplained noise contributions, in this experiment this noise

is measured, and subtracted.

For both RIN injections the phase offsets from zero of the SVN pattern changes between the different injection amplitudes, but seems to be stable during the timespan of one injection. This offset is a result of the combination of the sine and cosine component of SVN, a change in this offset is caused by a change in the amplitude ratio between the two components.

This offset changes in the same direction between one injection amplitude to the next for all four phase signals for both injections. For the $2f_{het}$ RIN injection the offset even changes by a similar amount. In the $1f_{het}$ RIN injection the offset changes by different values from one injection amplitude to the next, even for A and B side of the same interferometer. This could be the result of different splitting of the sidebands of the measurement beam and reference beam on the recombination beamsplitters, which changes the ratios between the sidebands. Plots of the SVN contribution and the fit not shown in this Section can be found in Appendix A.17. Since this difference is part of the fit, and subtracted, it is unlikely that this changes the amplitude in a significant way. Therefore, the cause for different coupling of this SVN created by the RIN injection to the phase of the different diodes was not explored further.

5.2. RIN frequency dependency

The aim of this experiment is twofold, the initial reason was a test of the theoretical claim that the transfer coefficient from RIN to phase noise is independent of the offset, within a reasonable band around either $1f_{het}$ or $2f_{het}$.

This experiment also serves as a test of the OPD loop correction as described in Section 4.1.3, and already applied in Section 5.1. During stability experiments in the development of the transfer function measurement it was found that the OPD loop needs to be turned on during RIN experiments, in Section 4.5.1 a short description of this stability experiment can be found.

It is expected that an injection at different frequencies, but with the same amplitude, initially has a frequency dependent phase amplitude due to the frequency dependant gain of the OPD loop. After the correction for the contribution of the OPD loop, the phase amplitudes should be constant within the expected errors.

When these experiments were performed the error due to small vector noise was not yet known. Since the aim of this experiment is a test of the frequency dependency of the RIN coupling the results still apply, as long as the contribution of SVN is constant over the measurement duration.

5.2.1. Design and data analysis

In this experiment a RIN equivalent intensity modulation is injected at different frequencies. All injections have the same injection amplitude of 1500 Count, which creates a RIN with an amplitude of $\tilde{r}_r^{(1,2)} \approx 0.07$. The set of frequencies includes both negative and positive frequency offsets ϵ from either $1\mathrm{f}_{\mathrm{het}}$ or $2\mathrm{f}_{\mathrm{het}}$. The offsets ϵ, in Hz, as injected are:

```
0.7,  −0.7,  1.5,  −1.5,  2,  −2,  2.5,  −2.5,  3.5,  −3.5,  4.7,  −4.7,
7,  −7,  9,  −9,  12,  −12,  14,  −14,  15,  −15,  17,  −17,  22,  −22,
27,  −27,  32,  −32,  42.5,  −42.5,  51,  −51,  60,  −60
```

for both $1\mathrm{f}_{\mathrm{het}}$ and $2\mathrm{f}_{\mathrm{het}}$. Due to a typo the $[17\,\mathrm{Hz}, -17\,\mathrm{Hz}]$ frequency pair of the $1\mathrm{f}_{\mathrm{het}}$ injection is $[17\,\mathrm{Hz}, -16\,\mathrm{Hz}]$.

The frequencies are chosen so that in both the RIN spectrum and the phase spectrum the region around the injection is mostly flat. For the lower frequencies, namely offsets of $\epsilon = \pm 0.7\,\mathrm{Hz}$ and $\epsilon = \pm 1.5\,\mathrm{Hz}$, the signal is injected for 20 minutes. For all other frequencies the duration is 10 minutes. The highest injection frequency is at $60\,\mathrm{Hz}$, since the Nyquist frequency of the PM measurement is $\approx 81\,\mathrm{Hz}$. A code snippet of the first few injections can be found in the Appendix A.15. The phase signal is recorded with a sampling frequency of $256\,\mathrm{Hz}$. The RIN is not measured at a sampling frequency of $16\,\mathrm{kHz}$ for this experiment since this experiment is part of a longer series where the same injections are repeated for different OPD loop gain settings back-to-back. At the time these experiments were run the demodulated power channels to measure RIN over longer timespans did not exist yet.

The measured time series is split according to the injections, and the amplitude of each injection is calculated via DFT. This amplitude can be plotted together with the amplitude spectrum, in Figure 5.20 both DFT results and the amplitude spectrum of a set of injections around $1\mathrm{f}_{\mathrm{het}}$ can be found.
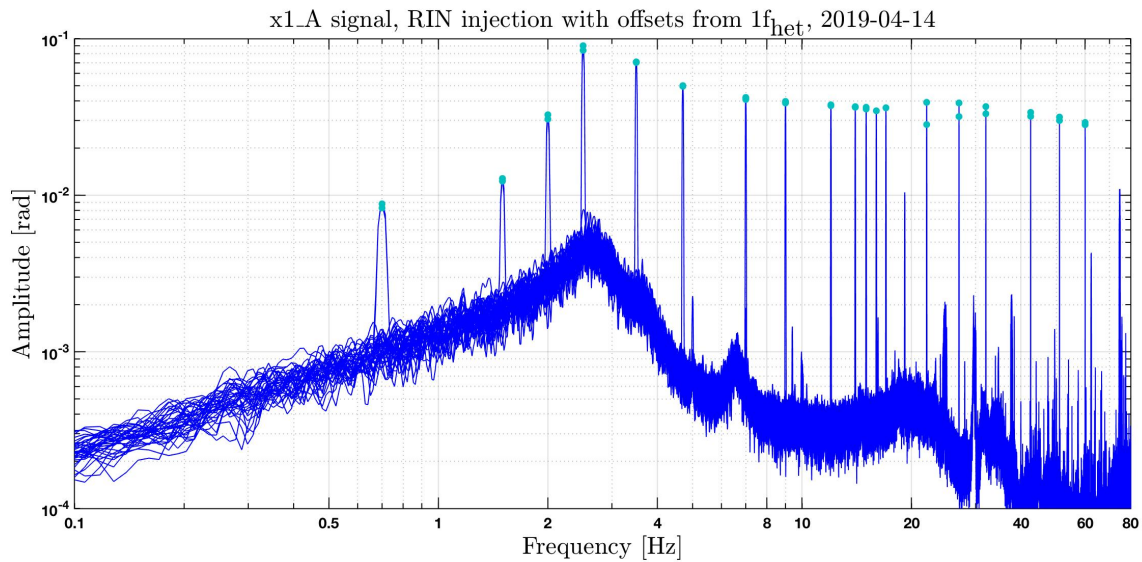
Figure 5.20.: Shown here is the amplitude spectrum of the phase. The spikes in the spectrum are due to RIN injections at different offset frequencies. Their amplitudes are calculated with a DFT, and shown with a light blue dot. The window used for both is HFT70. To increase the frequency resolution the amplitude spectra are not averaged, the full ≈ 94 seconds of phase data for each injection frequency are used.

The analysis continues with the amplitudes calculated by the DFT, this allows for easy comparison between the different interferometer channels and injection frequencies. One such set of experiments can be seen in Figure 5.21 for the X_1 interferometer and in Figure

5.22 for the reference interferometer X_R. Clearly visible as a bump in the measured spectrum and DFT values is the resonance frequency of the OPD loop transfer function around $3\,\mathrm{Hz}$. Around this frequency the gain of the OPD loop is above 1, and the phase noise and phase amplitude due to the injected RIN are increased. Below this bump the gain is 1, and the suppression of the loop is visible. Above the bump the suppression drops off, and the difference in measured amplitudes and corrected amplitudes is smaller. This measurement was repeated for different OPD loop gains, the amplitude increase moves with the resonance frequency of the OPD loop.

With the OPD loop corrections calculated in Section 4.1.3 the phase amplitudes can be corrected. The input to the OPD loop is filtered with the OPD open loop transfer function to calculate the time series of the motion of the OPD piezo. From this calculated piezo motion the amplitude is calculated for the same segments as before, which is then added to the measured amplitudes. To account for the delay between the phasemeter and CDS measurements, and sign differences between A and B port, the absolute value of the complex DFT result is calculated after the correction:

$$\varphi_{\mathrm{RIN}}(\epsilon) = \mathrm{abs}\Big(\varphi_{\mathrm{measured}}(\epsilon) - \varphi_{\mathrm{OPD\ piezo}}(\epsilon)\Big). \tag{5.16}$$

The absolute value of this corrected signal is then compared with the predicted amplitude for the RIN injected. After a successful OPD correction the amplitude should be similar at all injection frequencies.

5.2.2. Results

For this experiment both X_1 diodes and both X_R diodes are connected to the phasemeter. The phase amplitude in this section is calculated with a DFT for all four diodes, with both positive and negative offset frequencies ϵ of either $1f_{\text{het}}$ or $2f_{\text{het}}$. The results for injections near $1f_{\text{het}}$ are shown in blue, results near $2f_{\text{het}}$ are shown in green, as in Section 5.1. All amplitudes are corrected for the contribution of the OPD loop, the measured and corrected signals due to the injected RIN are shown next to each other in Figures 5.21 and 5.22.

Again clearly visible is the increase in signal amplitude around the resonance frequency in the OPD loop around $3\,\text{Hz}$, at lower frequencies the OPD loop suppresses the phase noise caused by the injected RIN. In this experiment the OPD loop uses the PDR_A diode as input, see Section 4.1. In the other experiments shown in this section the B-diode of the reference interferometer is used. This RIN frequency dependency experiment was done for both input diodes and for different OPD loop gains.

For the RIN around $1f_{\text{het}}$ the sign of the resulting phase signal between A and B side is different. Since the OPD loop uses the A side as input the amplitude of the x1_A and xR_A signals is reduced; due to this sign difference the measured amplitude for the B-side is increased by the OPD piezo actuation.

The predicted RIN is calculated for the RIN level expected for the injection voltage chosen. To compare the results of this experiment with the results of the first transfer function measurement the predictions of this experiment are copied into the plots where the measured amplitudes are corrected for the OPD loop actuation. Even though the predictions are not calculated from data recorded during this experiment, the predicted phase amplitude from the previous experiment is used as a first estimate for the expected amplitudes, since the settings are similar.

Not known for this measurement is the impact of small vector noise. Since the phase difference between the two beams is relatively stable over the course of the measurement the offset due to SVN should have a similar value for all data points measured, and the phase amplitudes should show a similar value for all injection frequencies when corrected for the OPD loop. Since the OPD loop is turned on the result for the X_R interferometer has the same phase difference for the whole measurement, the SVN level is expected to be constant.

Since the TM control loop is not turned on the measured amplitude on x1_A and x1_B could change due to changing SVN contribution. During this measurement the TM drifted by $0.46\,\text{rad}$ from an offset of $2.98\,\text{rad}$ to $2.65\,\text{rad}$ during the 1_{het} RIN injection, and from there to an offset of $2.52\,\text{rad}$ at the end of the 2_{het} RIN injection, as measured by the x1_A signal. In the experiment shown in Section 5.1.5 this corresponds to an amplitude change of $\approx 6\%$ for 1_{het} RIN and $\approx 2\%$ for 2_{het} RIN. In the measured amplitudes no consistent drift in amplitude is visible. The decrease of the amplitude at higher frequencies can also be seen in repeats of the same experiment and is most likely not caused by SVN. Since the amplitude decreases for both positive and negative frequency offset it is not due to the AI filter of the DAC.

For both interferometers the measured phase amplitude for the $2f_{\text{het}}$ RIN injection is closer to the predicted amplitude than in the transfer function experiments. This might be due to a SVN contribution, which changed the measured amplitude in this direction by coincidence. In the RIN transfer function experiment in the previous section the contribution of SVN changed between injections due to a changing ratio in the sine and cosine component, which leads to a shift in the offset of the SVN pattern from a phase difference of $0\,\text{rad}$. A change in the measured amplitude due to this effect could not be observed here.

These results overall show that the correction for the impact of the OPD loop is successful.

For the lower injection frequencies the corrected amplitudes are flat within a reasonable error band. These results also show that the coupling of RIN to the phase measurement is independent of the frequency offset ϵ. A difference in the observed amplitudes of the $1f_{het}$ RIN injection between the A and B diode above $21\,\mathrm{Hz}$ can be seen, this anomaly can be attributed to the delay of the OPD loop. More details can be found in Section 5.2.3.
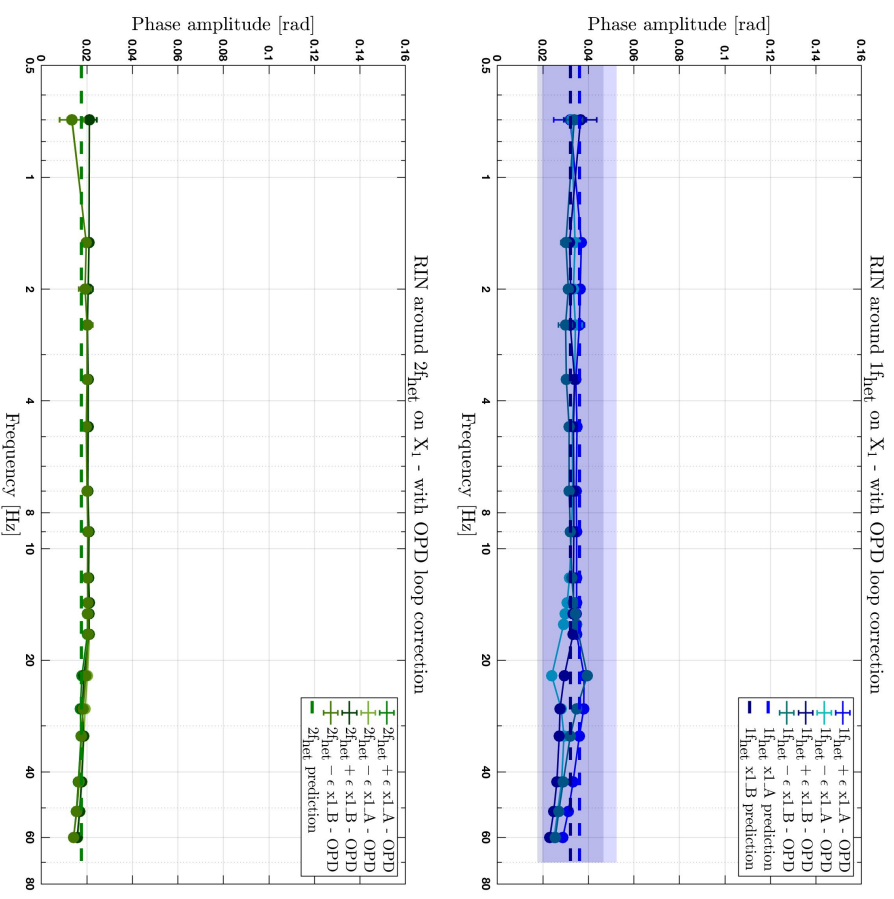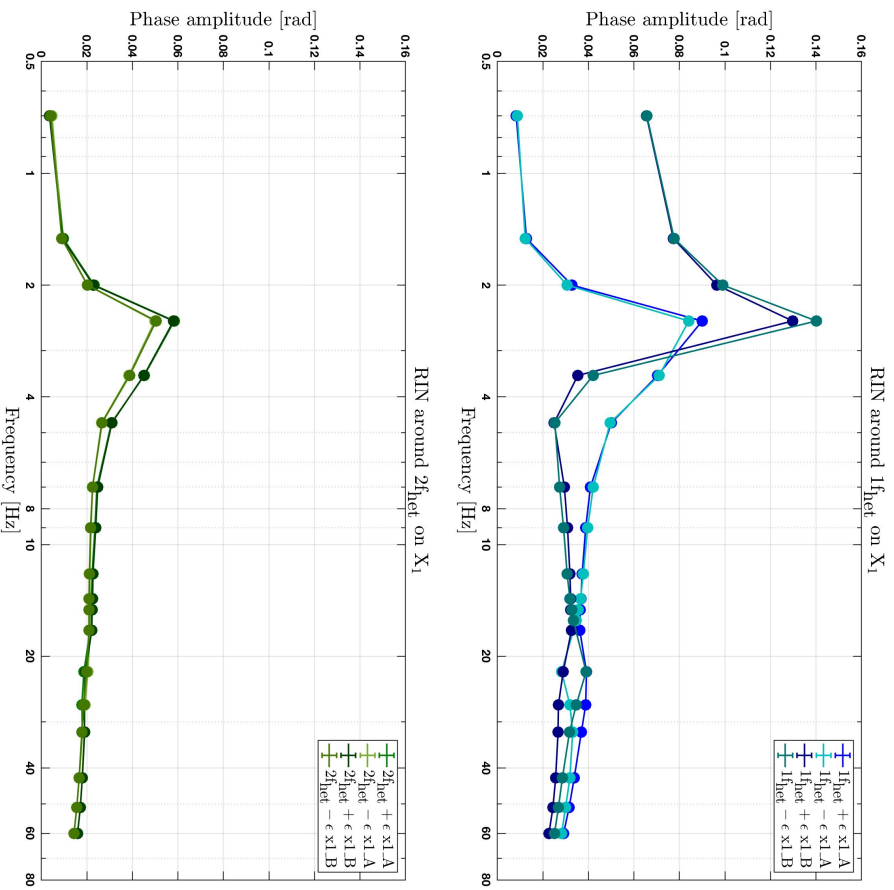
Figure 5.21.: Shown here are the phase amplitudes due to the injected RIN equivalent intensity modulations at different frequencies with the same amplitude of the A and B diode of the X_1 interferometer. The x-axis shows the frequency offset ϵ of the injection, both the positive and negative offset. On the y-axis the corresponding phase amplitude is shown. The amplitude is calculated with a DFT with a flat-top HFT70 window. The left plot shows the amplitudes as measured, the right plot shows the amplitudes corrected for the OPD loop contribution, together with the predicted amplitude. This prediction is calculated in the same way as in Section 5.1. The top plots show the injection with offsets from $1f_{het}$, the bottom plots show offsets of $2f_{het}$.
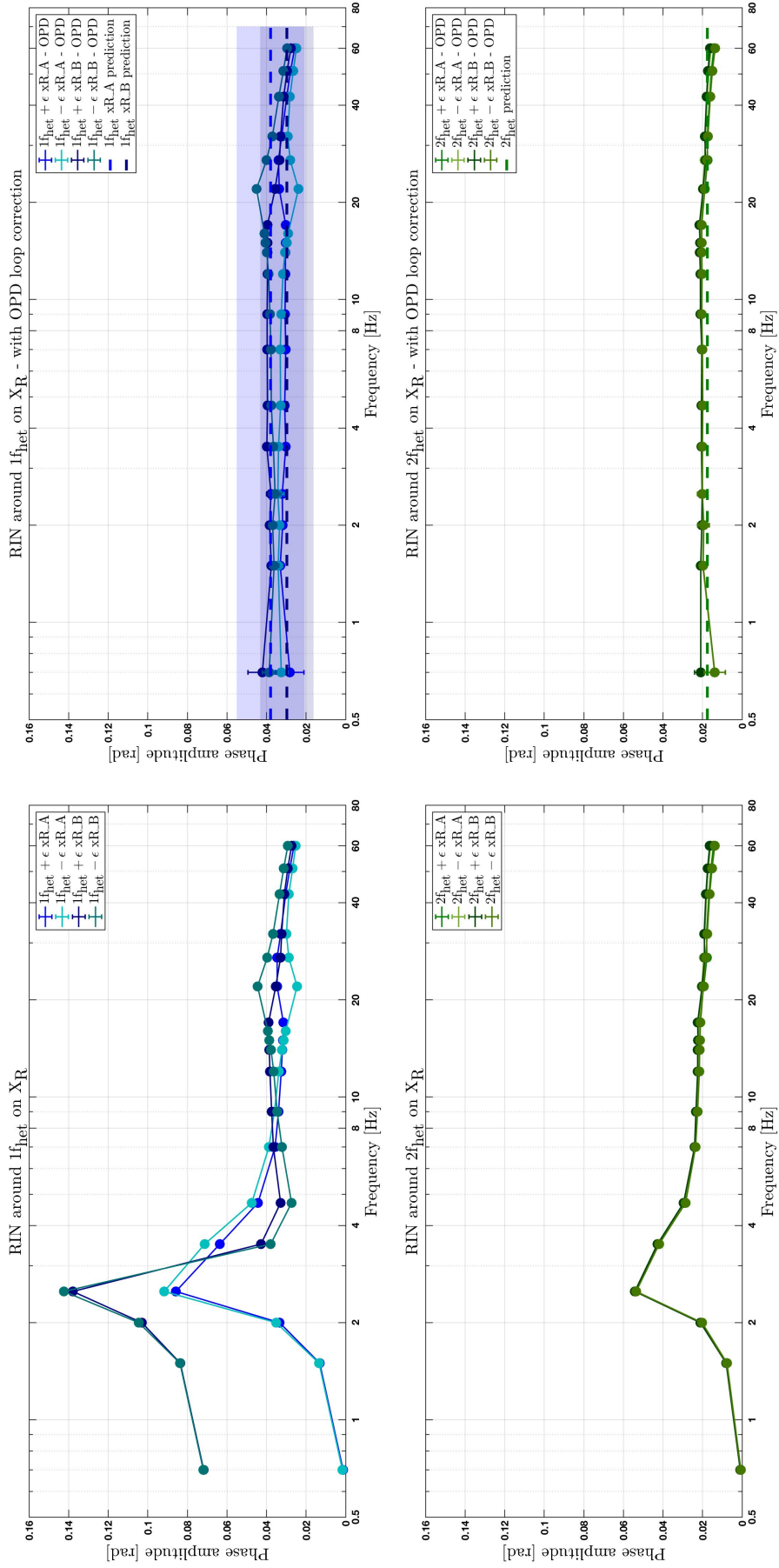
Figure 5.22.: The same injection as in Figure 5.21 is also recorded on the X_R diodes. Shown here are the measurements with injection frequencies around $1f_{het}$ and $2f_{het}$, together with the measured amplitudes corrected for the OPD loop.

5.2.3. 21 Hz anomaly

Some differences in the measured phase amplitudes can be found. For frequency offsets ϵ above 21 Hz the phase amplitude is different for positive and negative offsets for $1f_{het}$ injections.

One possible reason might be the window function of the FFT. If the heterodyne signal is not placed in the middle of the FFT bin the amplitude for positive and negative offsets might be affected differently by the window. However, this effect is different for offsets from $1f_{het}$ and $2f_{het}$, and any window effects should only depend on the frequency offset ϵ.

Another possibility are different sidebands due to different coupling of the injection in the AOM for higher frequencies, however the sidebands for injections below and above 21 Hz on the RIN are also the same. Compared were injections at $f_{het} - 12$ Hz and $f_{het} + 12$ Hz with the sidebands of injections at $f_{het} - 22$ Hz and $f_{het} + 32$ Hz, and no difference could be found.
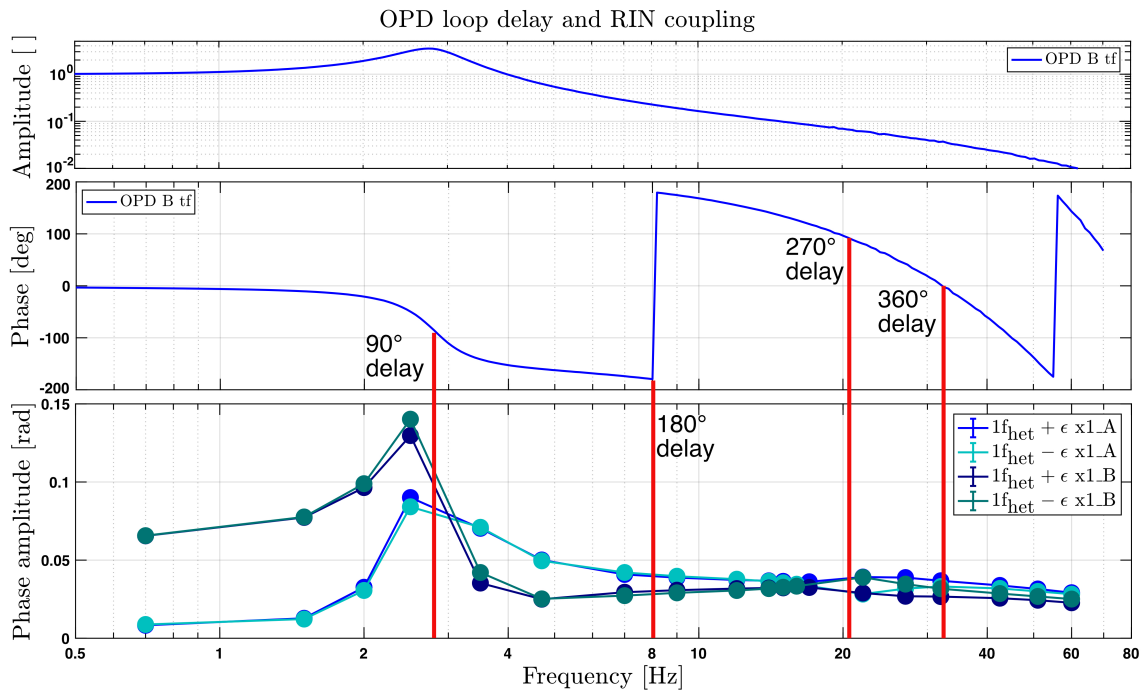
Figure 5.23.: These plots show the delay of the OPD loop versus the measured amplitudes of RIN injection at different frequencies. From the delay of the OPD loop it is obvious which way the measured amplitudes should move when corrected for. At 21 Hz the delay of the loop is 270°, above this frequency the coupling of positive and negative frequency offset changes.

The most likely cause is the OPD control loop. In this experiment the PDR_A diode signal is used as input. The delay of the loop at ≈ 8 Hz is 180°, at ≈ 21 Hz the delay is 270°, and at ≈ 30 Hz the delay is 360°. This delay is the phase difference between the signal of the injected RIN and the reaction of the OPD loop. A comparison of the results of this experiment with the transfer function of the control loop can be found in Figure 5.23.

Due to the gain of the OPD loop higher than 1 the amplitude shows an increase around 2.5 Hz. Due to a loop delay of more than 90° above ≈ 2.8 Hz the actuation of the loop corrects in the wrong direction; on the A side the signal amplitude is increased and decreased on the B side. Since the gain is smaller than 1 the difference between A and B side is smaller than at lower frequencies. Between 8 Hz and 21 Hz, with a delay of more than 180°, the loop corrects again in the correct direction, with a gain smaller than 0.22. Above 21 Hz the delay of the loop is bigger than 270°. Due to the phase difference in A and B port in the coupling of $1f_{het}$ RIN this delay effects the two measurements differently, while the coupling of $2f_{het}$ RIN has no phase difference between A and B.

While at lower frequencies the injected signal on the individual ports has a similar amplitude for injections with positive and negative frequency offsets, these amplitudes now seems to be switched. The A port with $-\epsilon$ is at a similar amplitude as the B port with $+\epsilon$, and vice versa. This apparent flip of the coupling parameter is a coincidence. In Figure 5.24 two plots of this type of experiment with different OPD loop gain are shown. Visible in these measurements is the dependency of the coupling on the gain of the OPD loop.

The transfer function of the OPD at these gains was not measured, but the delay is the same. In these measurements for RIN injections with a frequency offset bigger than a threshold of $\approx 21\,\mathrm{Hz}$ the coupling with a negative frequency offset also differs from the positive frequency offset injection. The difference between positive and negative frequency offset is larger for higher OPD loop gain. In this measurement this difference is also visible at lower frequencies, a reason might be a different interaction of the SVN caused by the RIN injection and the suppression of the loop.

This issue was not investigated further. In the experiment shown in the next section RIN is injected as a white noise. To calculate the mean amplitude spectral density frequencies below $20\,\mathrm{Hz}$ are chosen to avoid this effect. In the initial design of this experiment the gain of the OPD loop was set to the standard -0.02, in the experiment shown the gain was reduced to -0.008 to enable a RIN coupling measurement at lower frequencies.
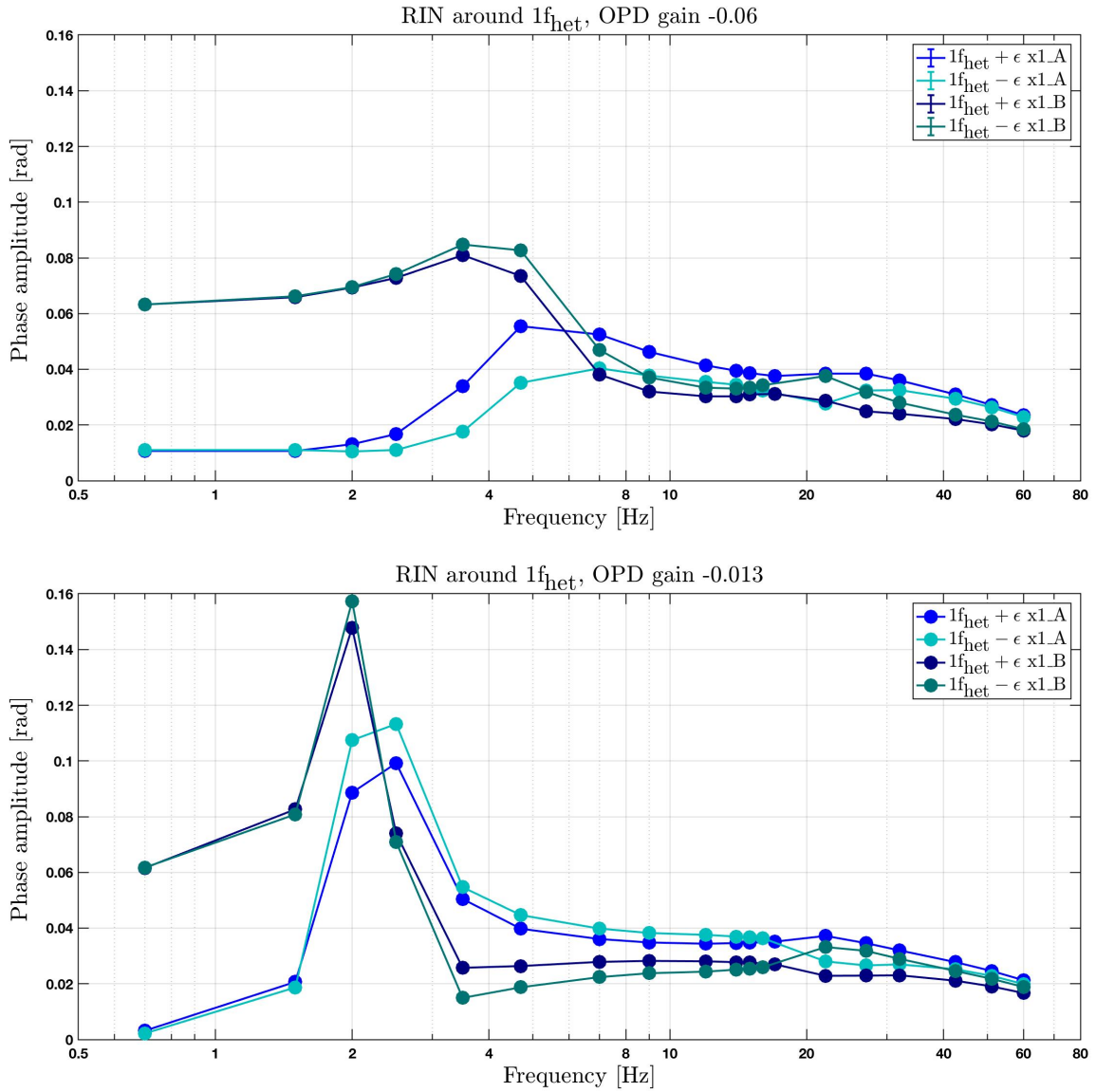
Figure 5.24.: Shown here are the measured amplitudes of the same experiment design, but with OPD loop gains of -0.06 and -0.013. The standard gain is -0.02. This data is not corrected for the OPD loop actuation.

The measured amplitudes here differ for positive and negative offsets as well, this difference is bigger for higher OPD loop gain. In this setting the difference between A and B side is smaller than in the lower gain setting. With lower loop gain the smaller influence of the loop is more visible in the flatter phase amplitude towards higher frequencies, up to 20 Hz.

Also visible is the higher resonance frequency with lower peak amplitude for the higher OPD loop gain.

5.2.4. Balanced detection

From the signals of the A and B diodes of the X_1 and X_R interferometers the balanced detection signal can be calculated. As shown in Section 2.6.2 the signals of the two ports of one interferometer are added, and then divided by two. This process removes RIN near $1f_{het}$, but does not remove RIN near $2f_{het}$, as calculated in Section 3.4 and already seen in Section 5.1.3.

To account for the sign difference in the A and B diodes this calculation is done with the complex DFTs, before the absolute value is calculated. Used here are the results already corrected for the effect of the OPD loop.

In Figure 5.25 the balanced signals of the X_1 and X_R interferometer can be seen. For both, the amplitudes of the RIN injected around $1f_{het}$ is reduced by $\approx 90\%$. In the balanced signals the anomaly around $21\,Hz$ can also be seen, there the subtraction of $1f_{het}$ RIN does not work as well as in other frequency areas.

The phase amplitude of RIN injected around $2f_{het}$ is at a similar amplitude as in the individual diodes. The balanced signal differs from the single diode measurement by less than 2% for RIN injections with a frequency offset ϵ smaller than $21\,Hz$, and by less than 7% for bigger frequency offsets.

For this experiment the subtraction of the reference signal from the measurement signal o1 = x1 - xR is not useful to calculate. At the start of the frequency injections the phase difference between x1 and xR is $\approx 20\,nm$, over the duration of the measurement the test masses drift to an offset of $\approx 9\,nm$, and then back to $\approx 19\,nm$. The expected change in the noise subtraction for a phase change between x1 and xR can be found in Section 5.3, where the test mass is moved on purpose.
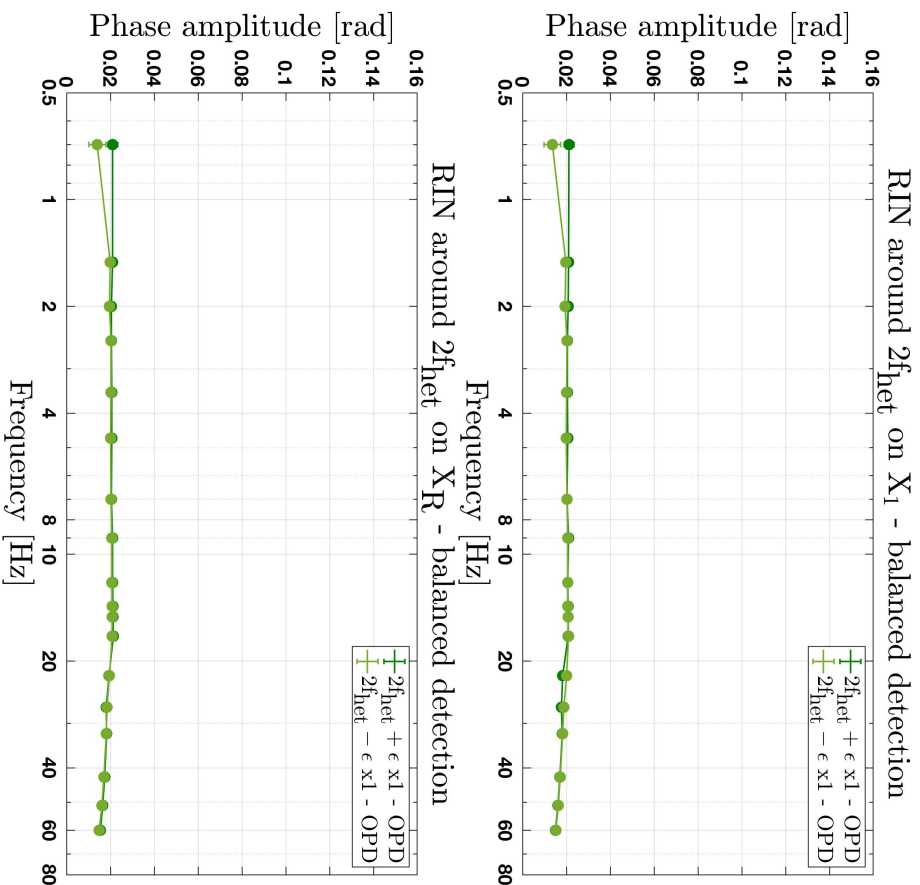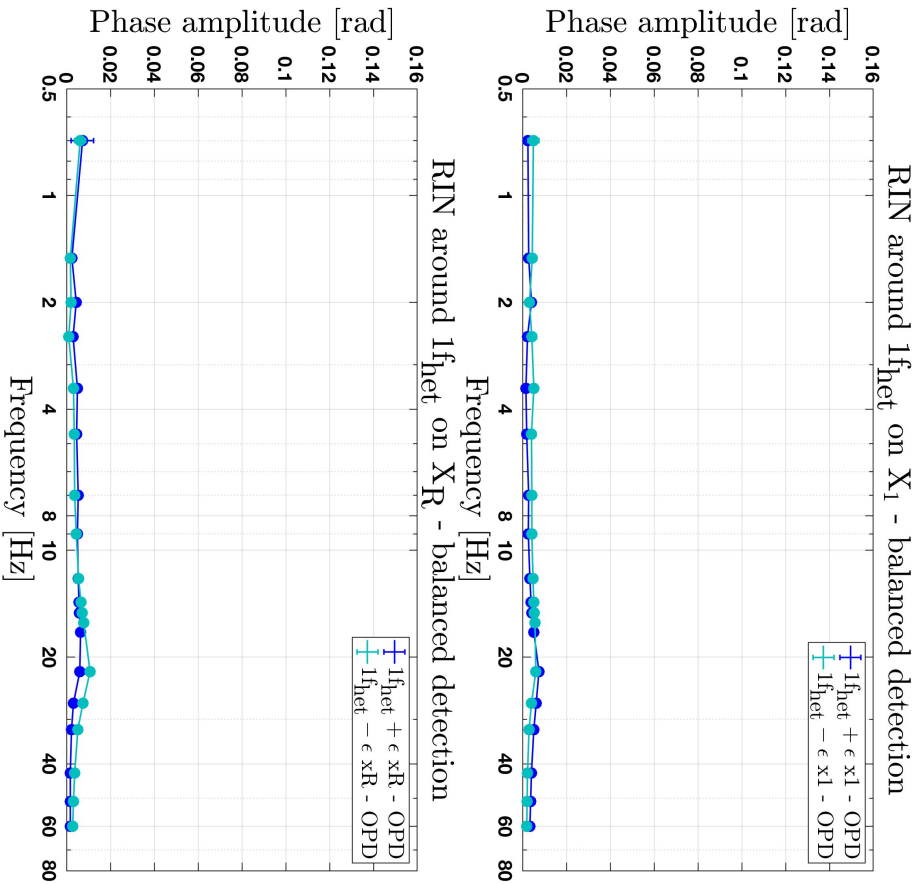
Figure 5.25.: These plots show the RIN injections with balanced detection on the X_1 interferometer on the top, and for the X_R on the bottom. The signals are corrected for the OPD loop. The balanced detection signal is calculated from the A and B side for both $+\epsilon$ and $-\epsilon$ frequency offsets. On the left side RIN near $1f_{het}$ can be reduced over the whole frequency band by $\approx 90\%$, RIN near $2f_{het}$ can not be removed with balanced detection, and has a similar amplitude to the single-diode measurement. To show the difference to the single-diode results the same y-scale as in previous plots is used.

5.3. RIN subtraction

The aim of this experiment is to show the dependency of the RIN subtraction from the measurement signals with the reference signal on the phase difference between the two.

These experiments were initially performed in preparation for the in-flight experiments (2016). TM1 was kept stable with the TM control loops, while TM2 was moved in longitudinal offsets with steps on the setpoint of the TM2 longitudinal control loop. During these experiments the impact of SVN on the RIN injection was not known, but did not influence the development of an analysis pipeline for the flight experiments.

Later experiments (2020), which are shown in this section, move TM1 in steps. A plot of the time series of the TM offsets can be found in Figure 5.26. The design of the experiment is changed to measure with TM1, so that A and B port of X_1 and X_R can both be measured, since the laboratory phasemeter only has 5 channels. The amplitude of the injected RIN is reduced, compared to the first set of subtraction experiments and to the transfer function experiments, to reduce the coupling of small vector noise.

5.3.1. Design and data analysis

For this experiment the subtracted signals are of interest, these are

$$o1\_A = \frac{\lambda}{4\pi\cos(\alpha)}\left(x1\_A - xR\_A\right), \tag{5.17}$$

$$o1\_B = \frac{\lambda}{4\pi\cos(\alpha)}\left(x1\_B - xR\_B\right), \tag{5.18}$$

$$o1 = \frac{\lambda}{4\pi\cos(\alpha)}\left(x1 - xR\right). \tag{5.19}$$

At the start of the experiment the o1_A signal measures a TM offset of 266 nm, or $\frac{\pi}{2}$, while o1_B measures an offset of -266 nm. TM1 is moved in steps up to an offset of -340 nm from the original position, these steps are repeated to a positive offset of 340 nm. A time series plot of the measured phase offset by the o1_A signal can be found in Figure 5.26, the segments selected for analysis are 800 seconds long. The script used to command these offsets can be found in Appendix A.16. For each of the TM offset positions the phase noise is measured. During these experiments the TM1 longitudinal control loop and OPD loop are turned on. Since the frequency range of interest in this experiment is above the corner frequency of the TM control loop the phase noise suppressed by the loop is not restored as shown in Section 4.3.4. The DWS control loops are not used.

RIN is injected as a noise around either $1f_{het}$ or $2f_{het}$. A description of the injection and measurement of RIN with the demodulated power signals can be found in Section 4.5; a spectrum of the injected RIN can be seen in Figure 4.26.

The dependency of the subtraction efficiency of phase noise due to RIN on the phase difference between the two signals used was derived in Section 3.4. The measured phase noise due to the RIN injection can be compared with the predicted noise levels calculated from the measured demodulated RIN.

The error on the mean noise level and the mean test mass position is calculated from the distribution of the data points. The mean error on the test mass position in the laboratory is smaller than in flight because the TM loops take a shorter time to stabilise than the DFACS control. In the step experiments in-flight shown in Chapter 6 the test mass is not yet stable at the desired offset in the segment selected for analysis.

For the x1_A signal the contrast changes with each TM step, a plot of this can be seen in Figure 5.27. The mean contrast over the duration of the $1f_{het}$ RIN injection can be seen in Table 5.5. The reason for the big step in contrast in the reference interferometer during the first big TM step is not clear, there is no step in the phase signal, the beam powers, or the available OPD loop data.

The coupling of $1f_{het}$ RIN for correlated RIN depends on the contrast directly, for uncorrelated RIN indirectly through the heterodyne efficiency. Here, RIN is only injected on one beam, and the calculation uses the individual beam powers. The heterodyne efficiency for this measurement is calculated from the mean contrast and mean beam powers of each step. The mean heterodyne efficiency of the whole experiment duration can also be found in Table 5.5. The resulting phase noise due to the injected RIN is calculated as an average over a bigger frequency range, and not at one particular offset frequency. Small changes in the noise due to changing contrast and measurement beam power over the experiment duration can be expected, with bigger changes due to changing TM position. The subtraction of the measurement and reference signal produces the expected noise pattern. In a setup where the main noise contribution in the phase signal is RIN without SVN the expectation is a near constant phase noise level for all TM offsets in the single-diode measurement.

However, since the injection of RIN also produces small vector noise, an additional component is added to the noise shape. The noise of the x1 signals also changes with changing test mass offset, since the coupling of SVN depends on the phase difference between the two beams. In
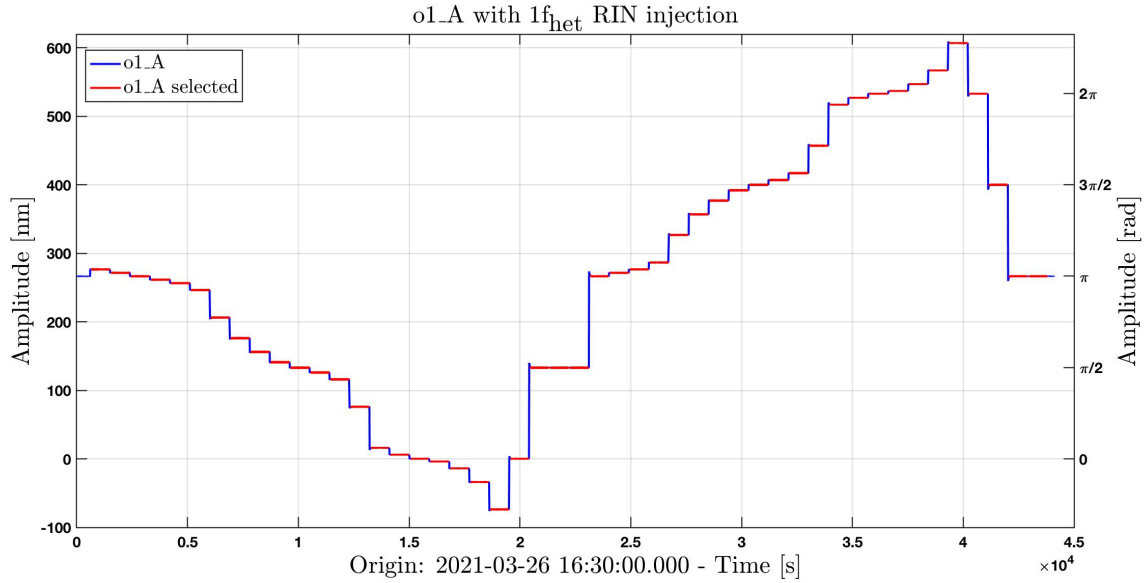
Figure 5.26.: This is the time series of the subtracted signal o12_A (blue) with an injection of $1f_{het}$ RIN. Shown in red are the segments at each TM offset selected for analysis. With this subtraction RIN is removed from the final signal, the efficiency of this subtraction depends on the phase difference between the two signals. TM1 is moved in steps every 15 minutes, with more measurements around a phase offset of π.

the initial experiments the injected RIN had a high noise amplitude, with a high contribution of SVN, since the impact of this additional noise was not yet known.

To prevent a dominant coupling of SVN the injection voltages are lower. This is possible since the subtracted signal shows a significantly lower sensing noise. In the experiments shown here the amplitude of the noise is reduced to 600 Count in CDS units, which is $\approx 97.5\,\mathrm{mVpp}$ after the differential-to-single ended electronics. This injection leads to a RIN level of $\tilde{r}_r^{(1)} \approx 100\,\frac{10^{-6}}{\sqrt{\mathrm{Hz}}}$ for $1f_{het}$ RIN and $\tilde{r}_r^{(2)} \approx 96\,\frac{10^{-6}}{\sqrt{\mathrm{Hz}}}$ for $2f_{het}$ RIN. RIN is measured with the demodulated power signals, a plot of the RIN level over the course of the measurement can be found in Figure 5.29. A description of the measurement of the demodulated power can be found in Section 4.5.3.

To measure the mean phase noise per TM step the mean amplitude spectral density in a specified frequency band is calculated for each TM offset. Two spectral ranges without big features are selected for analysis: a lower band between $2.2\,\mathrm{Hz}$ and $3.2\,\mathrm{Hz}$, and at higher frequencies between $14\,\mathrm{Hz}$ and $15.5\,\mathrm{Hz}$. This mean noise for the frequency band of interest is then plotted over the mean test mass position. Features in the spectrum between the two selected bands are avoided. Due to the $21\,\mathrm{Hz}$ effect shown in Section 5.2.3 the coupling is not calculated for higher frequency bands.

In this experiment the gain of the OPD loop is lowered from -0.02 to -0.008, so that the flat noise at lower frequencies, visible in the spectrum between $2\,\mathrm{Hz}$ and $5\,\mathrm{Hz}$, can also be used. With the original gain the bump of the OPD loop is in this frequency range, see Section 4.1. In theory, the effect of the OPD loop is removed when the two interferometer signals are subtracted, which reduces the noise by a factor ≈ 100. In practice however, the noise pattern of the subtracted signal with the original gain shows a significant difference to the phase noise calculated from the measured RIN. With this reduced gain the OPD loop bump moves to $\approx 1\,\mathrm{Hz}$. The gain of the longitudinal TM control loop is reduced by half in response to the OPD loop gain change. Any corrections of the OPD loop effect in post-processing similar to previous experiments are the same on all interferometers, and would therefore be subtracted in o1.
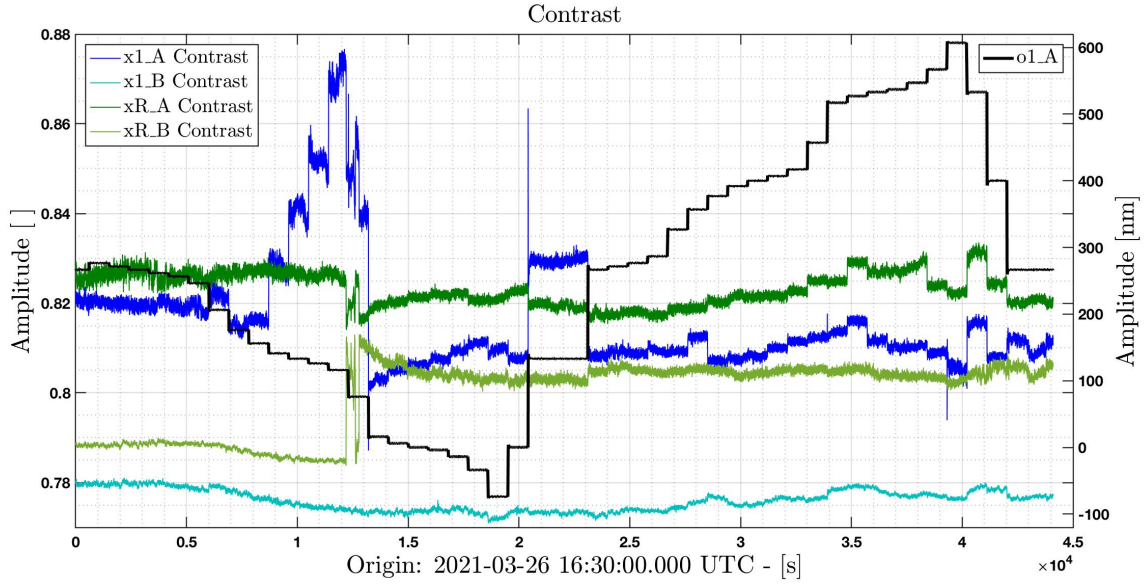
Figure 5.27.: Shown in this plot is the contrast of the individual diodes during the $1f_{het}$ RIN step experiment, also shown is the o1_A signal so that the contrast can be compared with the TM offsets. The o1_A signal was used as input to the longitudinal control loop for TM1. Visible here is the change in contrast due to the TM offset steps.

Diode	PD1_A	PD1_B	PDR_A	PDR_B
P_M	$0.091 \pm 6 \cdot 10^{-7}$	$0.114 \pm 8 \cdot 10^{-7}$	$0.094 \pm 6 \cdot 10^{-7}$	$0.099 \pm 7 \cdot 10^{-7}$
P_R	$0.053 \pm 1 \cdot 10^{-6}$	$0.055 \pm 1 \cdot 10^{-6}$	$0.060 \pm 1 \cdot 10^{-6}$	$0.049 \pm 1 \cdot 10^{-6}$
P_{PM}	$0.139 \pm 2 \cdot 10^{-6}$	$0.161 \pm 2 \cdot 10^{-6}$	$0.150 \pm 2 \cdot 10^{-6}$	$0.144 \pm 2 \cdot 10^{-6}$
Diff. $\frac{P_{calib}}{P_{PM}}$	1.03	1.05	1.03	1.03
Contrast	0.816 ± 0.002	0.776 ± 0.0003	0.815 ± 0.0006	0.800 ± 0.001
η_{het}	0.715 ± 0.01	0.685 ± 0.01	0.697 ± 0.01	0.724 ± 0.01

Table 5.5.: This table shows the individual beam powers P_M and P_R on the relevant diodes calculated from the measurement of the individual beams on the PDA diodes. The combined calibrated power P_{calib} is then compared with the total power P_{PM} as measured by the phasemeter. This difference is smaller in other experiments. The powers are displayed in the power unit of the phasemeter. Since the ratio between the powers is of interest these are not calibrated to mW. Also shown is the mean contrast for each diode. The last row shows the heterodyne efficiency during the $1f_{het}$ RIN injection, calculated from the the contrast and the beam powers.

To calculate the predicted phase noise from the injected $1f_{het}$ RIN, the power of the individual beams is needed. These are calculated from the measured power on the PDA diodes, used are the parameters of Table 4.4 in Section 4.5.5. The calibration parameters to calculate the beam powers on the interferometer diodes are measured before the experiment; a plot of the calculated power of the individual beams together with their combined power can be found in Figure 4.32 for the PDA_1 diode. The powers of the other diodes are similar. As a test of the calibration this calculated combined power can be compared with the total power as measured by the phasemeter. While the small fluctuations are different of the measured and calculated powers, the mean power of the whole experiment is within reasonable agreement, with a difference for 3 of the diodes of $\approx 3\%$, and a difference of $\approx 5\%$ on the PD1_B diode. These power values can be found in Table 5.5.

RIN	1f$_\text{het}$ RIN injection $\left[\frac{10^{-6}}{\sqrt{\text{Hz}}}\right]$	2f$_\text{het}$ RIN injection $\left[\frac{10^{-6}}{\sqrt{\text{Hz}}}\right]$
$\hat{r}_\text{r}^{(1)}$	100.2 ± 10	1.12 ± 0.16
$\hat{r}_\text{m}^{(1)}$	0.96 ± 0.13	0.90 ± 0.12
$\hat{r}_\text{r}^{(2)}$	1.42 ± 0.32	96.2 ± 13
$\hat{r}_\text{m}^{(2)}$	1.27 ± 0.30	1.02 ± 0.16

Table 5.6.: This table shows the mean RIN levels measured with the demodulated power signals. These values are the mean, calculated over the whole experiment duration. In Figure 5.29 the RIN at each TM offset can be seen. This table shows the mean RIN calculated for the higher frequency band. The mean RIN at the lower frequency offset is within 1% of the value shown here.

RIN

The injected RIN is the same for each step. From the demodulated power signals the mean amplitude spectral density of the RIN in the frequency band that couples to the phase signal is calculated. Example amplitude noise spectra, together with the mean RIN calculated, can be seen in Figure 5.28. Shown are both frequency bands selected to calculate the RIN subtraction.

From each TM offset a timespan of 800 seconds is selected. The spectra are calculated with 5000 samples per FFT, with 50% overlap and a BH92 window. At a sampling frequency of 256 Hz, this leads to 80 averages per spectrum. The mean RIN is calculated from the demodulated power signals in the same band which couples to the selected frequency range in the phase signal. The specified range is offset from either 1f$_\text{het, demod}$ ≈ 20.371 Hz or 2f$_\text{het, demod}$ ≈ 20.753 Hz. Since not only the intended RIN couples to this frequency band in the demodulated power measurement, but also the RIN with a negative frequency offset from the demodulation frequency the noise power is divided by 2. More details on the RIN measurement with demodulated powers can be found in Section 4.5.3. The RIN is calculated from the measured demodulated power and mean power for each step individually, and is corrected for the anti-aliasing filter of the ADC and the lowpass filter from the downsampling to 256 Hz. The mean noise power in the selected frequency range is shown with a red marker. Again, visible in the RIN spectra are the peaks at 1f$_\text{het}$ or 2f$_\text{het}$, in this demodulated signal visible at ≈ 20 Hz. These are most likely caused by crosstalk between the AOMs or AOM electronics. The noise increase in the non-injected RIN measured around 2f$_\text{het}$ is present for some of the spectra at different frequencies, the source of this noise is unknown. Since this effect is significantly smaller than the injected RIN the impact on the calculated phase noise is negligible.

The mean RIN over the measurement duration can be found in Table 5.6. A plot of this mean RIN per TM offset can be found in Figure 5.29 for both injections. The fluctuations and drift in the measured RIN was also seen in other longer experiments. This drift is the reason why the RIN can not just be measured at the start of the injection with a high sampling frequency, and then be assumed constant. The fluctuations of the non-injected RIN are due to increases in noise in the selected frequency range only present for a few steps, or due to a more broadband noise increase due to a short spike in the power measurement. These smaller spikes have been observed in different experiments and were caused by vibrations.

This measured RIN level is then used together with the measured TM offset to calculate the prediction for the phase noise. This prediction is shown together with the measured phase noise values in the next section. The phase noise of each step is calculated from the measured RIN of both beams at this TM position, the fluctuations visible in the RIN transfer to the calculated phase noise.
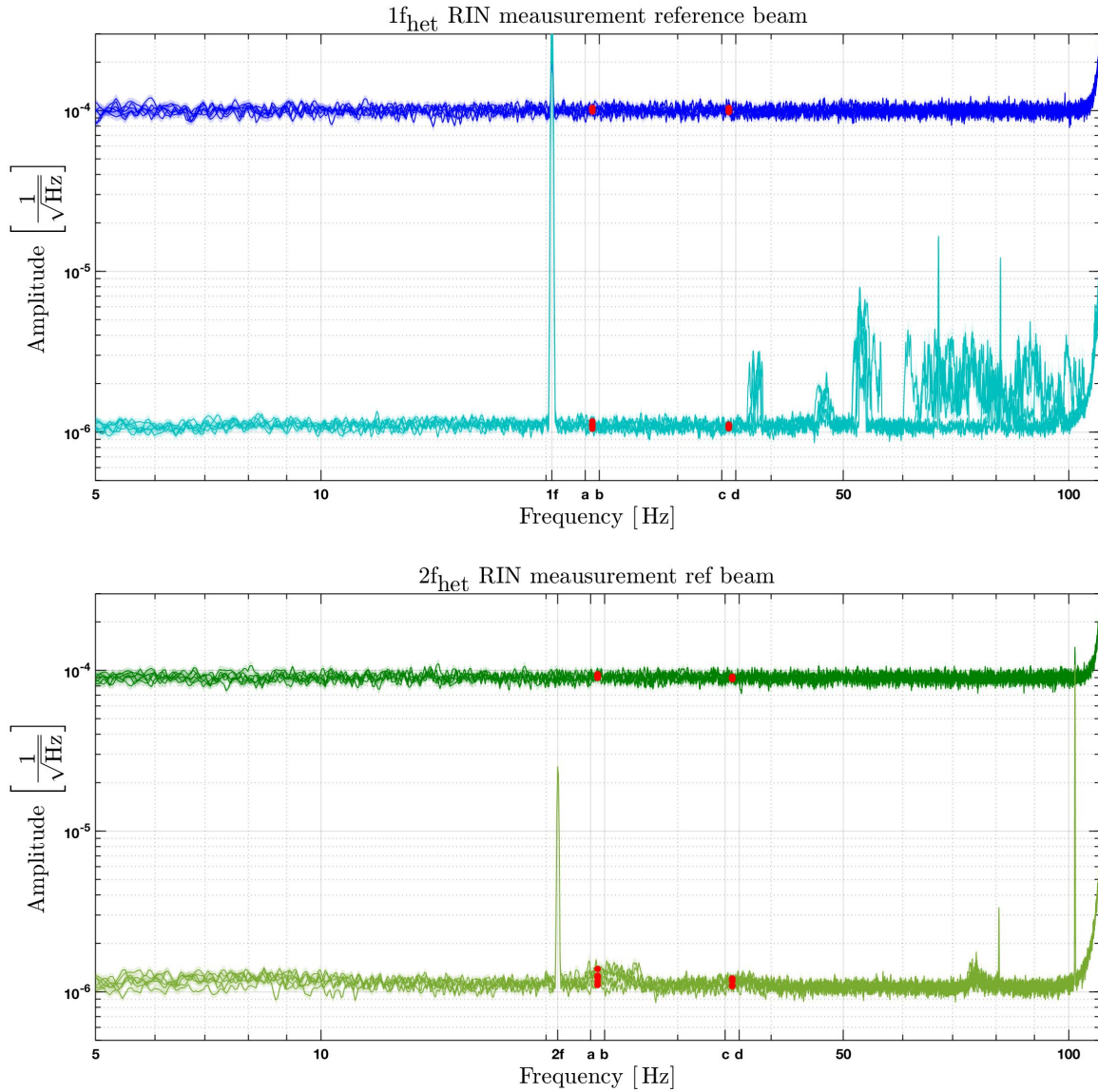
Figure 5.28.: Shown here are example spectra used to calculate the mean noise seen in Figure 5.29, the 1f$_{het}$ RIN (blue) and 2f$_{het}$ RIN (green) are measured with the demodulated power signals. The RIN with the higher noise amplitude is injected, in the spectra with lower noise amplitude the RIN is injected on the other frequency. Each RIN spectrum is from a different TM offset, calculated from 800 seconds of data. Used is a BH92 window with 50% overlap, and 80 averages. A frequency band offset from the either 1f$_{het}$ or 2f$_{het}$ is selected to calculate the mean noise, the offsets are from a=2.2 Hz to b=3.2 Hz and from c=14 Hz to d=15.5 Hz. These frequencies are shown on the x-axis, the mean noise calculated is shown with a red dot; the error bars of the mean noise are not as visible due to the logarithmic y-axis.
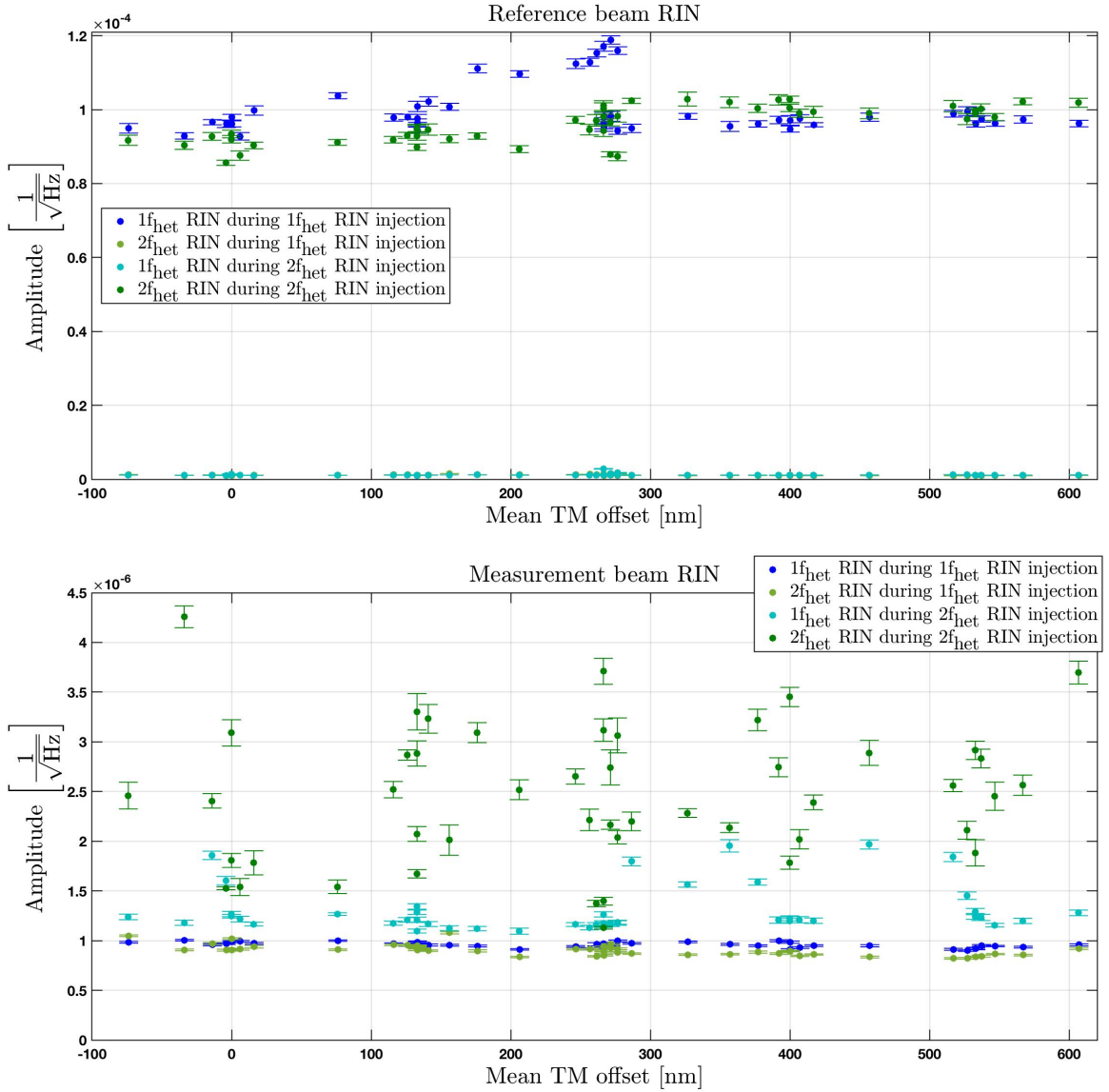
Figure 5.29.: During this measurement the RIN is measured with the demodulated power signals. Shown here are both the RIN level at $1f_{\text{het}}$ (blue) and $2f_{\text{het}}$ (green) for both sets of TM steps. The RIN with the higher amplitude is injected, while the lower amplitude RIN is a measurement of the noise in the other frequency band. The injected RIN amplitude is the same for one set of TM steps. The mean noise is calculated in a frequency band offset from the either $1f_{\text{het}}$ or $2f_{\text{het}}$ of $14\,\text{Hz}$ to $15.5\,\text{Hz}$. A comparison of some spectra with their mean noise level can be found in Figure 5.28. The top plot shows the RIN of the reference beam, in the bottom plot the RIN of the measurement beam is shown.

Phase

The same timespan and FFT settings as for the mean RIN value are used for the mean phase noise. In Figure 5.30 a spectrum of the measured phase noise for all TM offsets is shown. The frequency bands chosen to calculate the mean noise are shown, these are selected to exclude the high-frequency peaks. Avoided are the two broad peaks at 6.5 Hz and 9.5 Hz, as well as a small peak at 16.2 Hz. To higher frequencies the number of these peaks increases, the first of the bigger ones in this spectrum is at 25.5 Hz. The source of these peaks is not known.

In the experiment shown in Section 5.2 the frequencies of the injected sinusoidal RIN are chosen to be in areas between these. There a slightly different coupling for RIN higher than 21 Hz could be seen, which is why higher frequencies are avoided here.

The noise level of the individual signals x1_A and xR_A for different TM positions can be found in Figure 5.31; with an injection of RIN at $1f_{het}$ on the top and with $2f_{het}$ RIN on the bottom. Even though the test mass is not in the beam path of the reference interferometer the phase noise of xR_A is shown with the TM offset on the x-axis, since these two signals are subtracted the same axis is used for both in this visualisation. The noise shape of the subtracted signal o1_A with the predicted noise shape from the measured RIN is shown in the same plot. The noise pattern of the subtracted RIN produces the shape as expected from the injected RIN. Since the subtracted noise level is significantly lower than the noise of the single diode signals the noise amplitude for this plot is increased by a factor 5 for $1f_{het}$ RIN, and a factor 10 for $2f_{het}$ RIN.

The fluctuations in the mean phase noise over the measurement duration are due to environmental impacts on the measurement, most of this noise subtracts in the calculation of the subtracted signals o1_A and o1_B. The residuals of this additional noise can be seen especially well around a TM offset of 266 nm, since more measurements are done at this position.

With a noise injection it is not possible to measure the amplitude of sidebands as in Section 5.1.4.
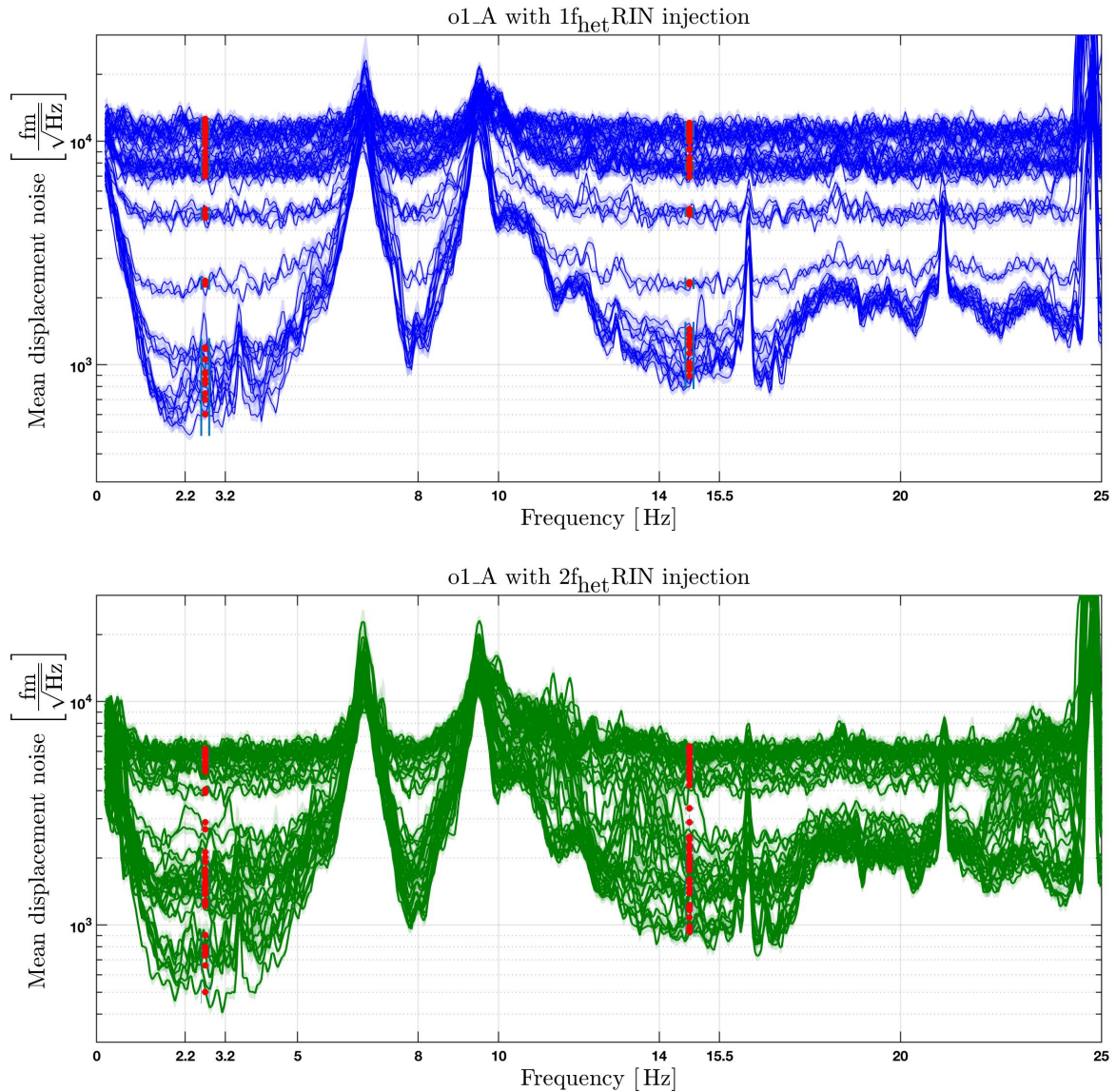
Figure 5.30.: The top plot shows the phase spectrum of o1_A with a RIN injection around $1f_{het}$, the bottom plot shows the $2f_{het}$ RIN injection. In the frequency bands $2.2\,\mathrm{Hz}$ to $3.2\,\mathrm{Hz}$ and $12.5\,\mathrm{Hz}$ to $15.5\,\mathrm{Hz}$ the mean noise value is calculated. This mean noise is then compared to the value calculated from the measured RIN. With these frequency ranges the peaks in the spectrum are avoided. At lower frequencies than are visible here the OPD loop acts on the phase noise from the RIN injection, and its effect could not be completely removed.
The sensing noise floor consisting of ADC noise, electronic noise and shot noise is at $\approx 100\frac{\mathrm{fm}}{\sqrt{\mathrm{Hz}}}$, the lower bound of this plot is at $300\frac{\mathrm{fm}}{\sqrt{\mathrm{Hz}}}$.
The same timespans and window as in the RIN calculation are used for the calculation of the phase spectral densities.
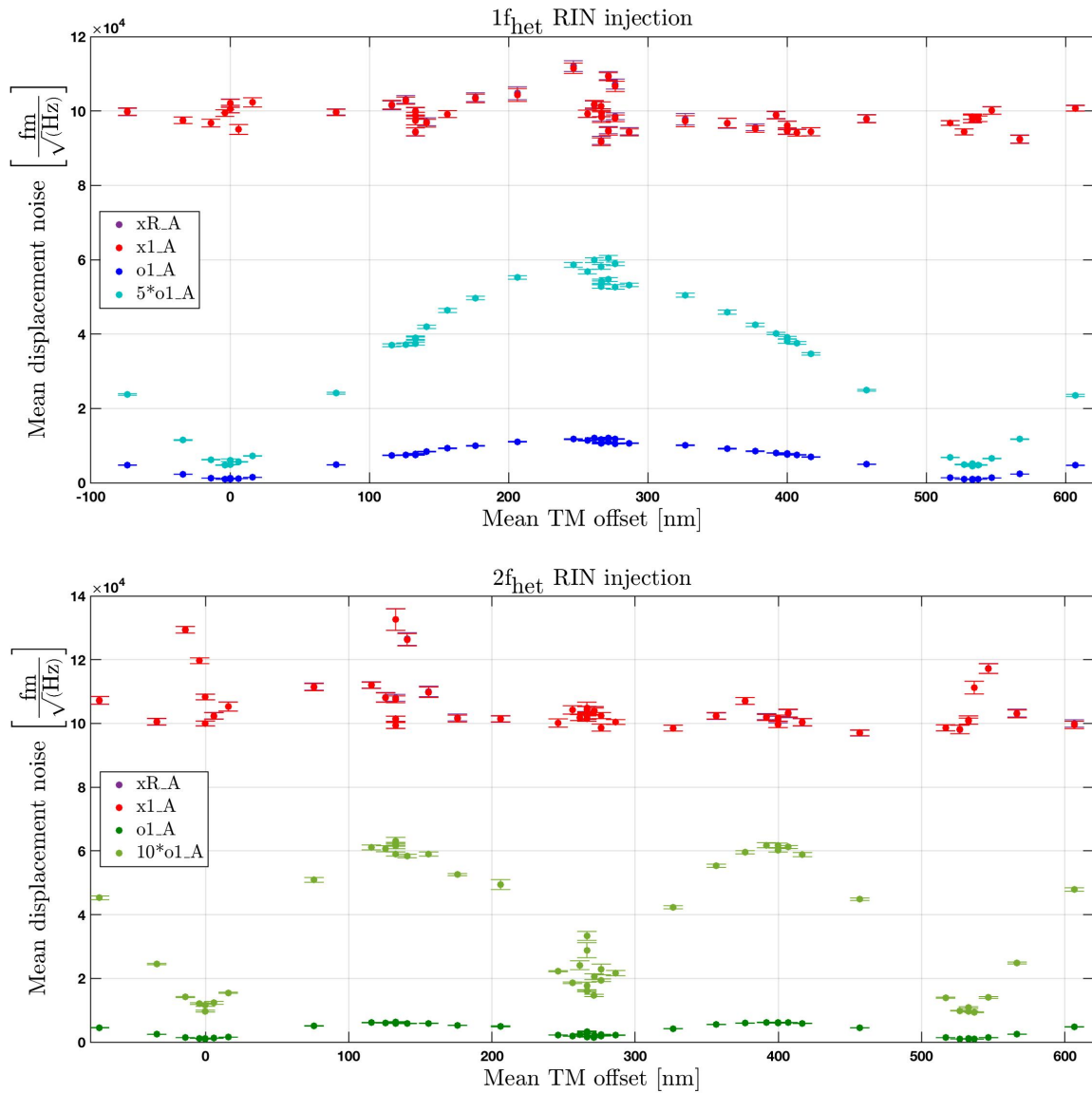
Figure 5.31.: Shown here is the sensing noise between 12.5 Hz and 15.5 Hz. This noise is calculated for the individual interferometer signals x1_A (red) and xR_A (purple), these can be seen at the top of each plot. The time series of these two signals are subtracted to create the final signal o1_A. The top plot shows this noise for changing TM position for the first set of steps with an injection of $1f_\mathrm{het}$ RIN. This subtracted noise shape is too low to see details, the noise amplitude is therefore multiplied with a factor 5. On the bottom the same kind of plot is shown for the set of steps with an $2f_\mathrm{het}$ RIN injection, again the noise amplitude of o1_A is increased. Both noise shapes show the expected subtraction pattern for the RIN injected, they can be seen together with the phase noise calculated from the measured RIN in Figures 5.32 and 5.33. The noise level of the individual interferometers is equivalent to $\approx 1400 \frac{\mu\mathrm{rad}}{\sqrt{\mathrm{Hz}}}$.

Phase response to RIN injection

From the theoretical prediction the noise over TM position (NoP) is calculated from the measured RIN. In these experiments RIN is injected on the reference beam, this RIN is uncorrelated to the RIN of the measurement beam. The phase noise contributions for $1f_{het}$ RIN, $2f_{het}$ RIN and the noise floor are added quadratically. The noise is calculated as $\left[\frac{fm}{\sqrt{Hz}}\right]$, and the TM displacement is measured in nanometre. In Section 3.4.1 the derivation of the fit functions for correlated RIN with $\hat{r}_r \approx \hat{r}_m$ can be found. The derivation of the coupling of uncorrelated RIN is shorter and uses the derived coupling at a single injection frequency from Section 3.4.2.

The equations derived earlier are:

$$\hat{o}1\_A_{1f_{het}}^2 = \left(\frac{\lambda}{4\pi\cos(\alpha)} \cdot \sqrt{\frac{2\left(\tau_r^4 P_r^2 \hat{r}_r^{(1)^2} + \rho_m^4 P_m^2 \hat{r}_m^{(1)^2}\right)}{\eta_{het}\tau_r^2\rho_m^2 P_r P_m}} \sin\left(\frac{4\pi\cos\alpha}{\lambda} \frac{o1\_A}{2}\right)\right)^2, \quad \left[\frac{fm^2}{Hz}\right]$$

(5.20)

$$\hat{o}1\_A_{2f_{het}}^2 = \left(\frac{\lambda}{4\pi\cos(\alpha)} \cdot \sqrt{\frac{\hat{r}_r^{(2)^2} + \hat{r}_m^{(2)^2}}{2}} \sin\left(\frac{4\pi\cos\alpha}{\lambda} o1\_A\right)\right)^2, \quad \left[\frac{fm^2}{Hz}\right]$$

(5.21)

$$\hat{o}1\_A = \sqrt{\hat{o}1\_A_{1f_{het}}^2 + \hat{o}1\_A_{2f_{het}}^2 + \text{noisefloor}^2}, \quad \left[\frac{fm}{\sqrt{Hz}}\right]$$

(5.22)

In this experiment the RIN on the measurement beam is a factor ≈ 40 lower than the injected RIN on the reference beam, the $\hat{r}_r^{(1)}$ and $\hat{r}_r^{(2)}$ contributions are dominant in the calculation of the phase noise for injected RIN.

To calculate the $1f_{het}$ phase noise from the measured RIN the mean beam powers of each step are used. The individual beam powers are calibrated from the measurement of the individual beam powers with the amplitude stabilisation diodes. A plot of these calibrated beam powers on the PD1_A diode, together with the total beam power as measured by the phasemeter, can be found in Figure 4.32. The heterodyne efficiency is calculated from the mean beam powers and the mean contrast for each step.

An overview of the mean beam powers of the whole experiment in phasemeter units during this experiment, and the mean heterodyne efficiency η_{het}, can be found in Table 5.5.

As could be seen in the measurement of the RIN transfer function in Section 5.1, the coupling from $1f_{het}$ RIN to phase in the X_1 and X_R interferometer is slightly different, since it depends on the power ratios between the two beams. In the noise maximum of the subtracted signal the phase noise of the two interferometer adds linearly. The individual contributions can be calculated from the measured RIN as was seen in Section 5.1. Here, this coupling is a factor $\sqrt{2}$ bigger since RIN couples from positive and negative frequency offset ϵ. In the measurement shown the RIN contribution of the two interferometers involved is calculated individually, and then added according to the estimated Equation 3.74 shown in Section 3.4.1.

$$\hat{o}1\_A^{(1)} \approx \left[\frac{\sqrt{P_{1A,r}^2 \hat{r}_r^{(1)^2} + P_{1A,m}^2 \hat{r}_m^{(1)^2}}}{\sqrt{2}\,\eta_{het,1A} P_{1A,r} P_{1A,m}} + \frac{\sqrt{P_{RA,r}^2 \hat{r}_r^{(1)^2} + P_{RA,m}^2 \hat{r}_m^{(1)^2}}}{\sqrt{2}\,\eta_{het,RA} P_{RA,r} P_{RA,m}}\right] \dots$$
$$\cdot \left|\sin\left(\frac{4\pi\cos\alpha}{\lambda} \frac{o1\_A}{2}\right)\right| \cdot \frac{\lambda}{4\pi\cos(\alpha)}, \quad \left[\frac{fm}{\sqrt{Hz}}\right] \quad (5.23)$$

This approximation gives a more accurate peak noise, in comparison to phase noise calculated with Equation 5.20, where the beam powers of the two interferometers are assumed to be

the same. However, this calculation does not include the remaining noise around TM offsets of 0 and 2π. Since the two interferometers are reasonably well matched the true remaining noise level can be calculated by subtraction of the two calculated phase noise levels to $349.2 \pm 15 \left[\frac{\text{fm}}{\sqrt{\text{Hz}}}\right]$ for the A side and $159.3 \pm 6 \left[\frac{\text{fm}}{\sqrt{\text{Hz}}}\right]$ for the B side for the higher frequency measurement.

5.3.2. Results

This Section shows the measurement of the RIN and the phase noise in the corresponding frequency bands, both of these are shown with respect to the TM offset they were measured at. From the measured RIN a phase noise contribution is predicted, which is then compared to the measured phase noise with a fit.

This predicted phase noise for both the $1f_{het}$ and $2f_{het}$ RIN injection can be seen together with the measured phase noise in Figures 5.32 and 5.33. Already it can be seen that the calculated phase noise fits well to the measured phase noise, both in noise amplitude and shape of the noise.

To compare the calculated phase noise with the measured phase noise a fit is constructed, which includes a scale factor on the calculated noise power and the noise floor. This is the most relevant result, since this fit also takes the drift in RIN and the change in contrast into account. The size of this scale factor is used as an estimation of the error of the calculated phase noise; and the residuals of this fit can be used as clues to the source of the discrepancy. In Figures 5.34 and 5.35 the phase noise with the power scale factor is shown together with the residuals of the fit.

An overview of the results can be seen in Table 5.7. The χ^2 of the fit with the scaling factor is shown in the last row, see also Appendix A.11. An example plot of the covariance of the fit parameters can be found in Appendix A.21.

As a sanity check the peak phase noise of the phasemeter measurement and of the calculated phase noise from the RIN measurement is calculated individually. The same fit as in later flight experiments is used to calculate the peak phase noise. The mean phase noise from the RIN injection is calculated from the mean values over the whole measurement duration, due to the change of the contrast, power and RIN over the measurement duration the error on this value is bigger. These calculated mean peak values can also be found in Table 5.7.

$1f_{het}$ RIN	meas. $\left[\frac{fm}{\sqrt{Hz}}\right]$	pred. $\left[\frac{fm}{\sqrt{Hz}}\right]$	power scale	floor $\left[\frac{fm}{\sqrt{Hz}}\right]$	χ^2
A: 2.2 Hz to 3.2 Hz	11037 ± 21	11178 ± 39	0.967 ± 0.004	657.0 ± 6.2	14.8
B: 2.2 Hz to 3.2 Hz	10116 ± 28	9875 ± 36	1.065 ± 0.005	696.1 ± 6.0	17.2
A: 14 Hz to 15.5 Hz	11018 ± 19	11159 ± 46	0.974 ± 0.003	940.5 ± 5.9	9.4
B: 14 Hz to 15.5 Hz	9835 ± 27	9857 ± 39	1.035 ± 0.003	987.8 ± 6.9	8.7
$2f_{het}$ RIN	meas. $\left[\frac{fm}{\sqrt{Hz}}\right]$	pred. $\left[\frac{fm}{\sqrt{Hz}}\right]$	power scale	floor $\left[\frac{fm}{\sqrt{Hz}}\right]$	χ^2
A: 2.2 Hz to 3.2 Hz	5942 ± 16	5263 ± 41	1.092 ± 0.006	749.4 ± 5.1	132.5
B: 2.2 Hz to 3.2 Hz	5883 ± 19	5263 ± 41	1.123 ± 0.007	733.5 ± 6.1	20.4
A: 14 Hz to 15.5 Hz	5898 ± 14	5770 ± 43	1.048 ± 0.005	1009.2 ± 5.4	69.2
B: 14 Hz to 15.5 Hz	5882 ± 19	5770 ± 43	1.047 ± 0.004	1057.3 ± 5.6	39.4

Table 5.7.: This table shows an overview of the results of the measured and calculated phase noise.
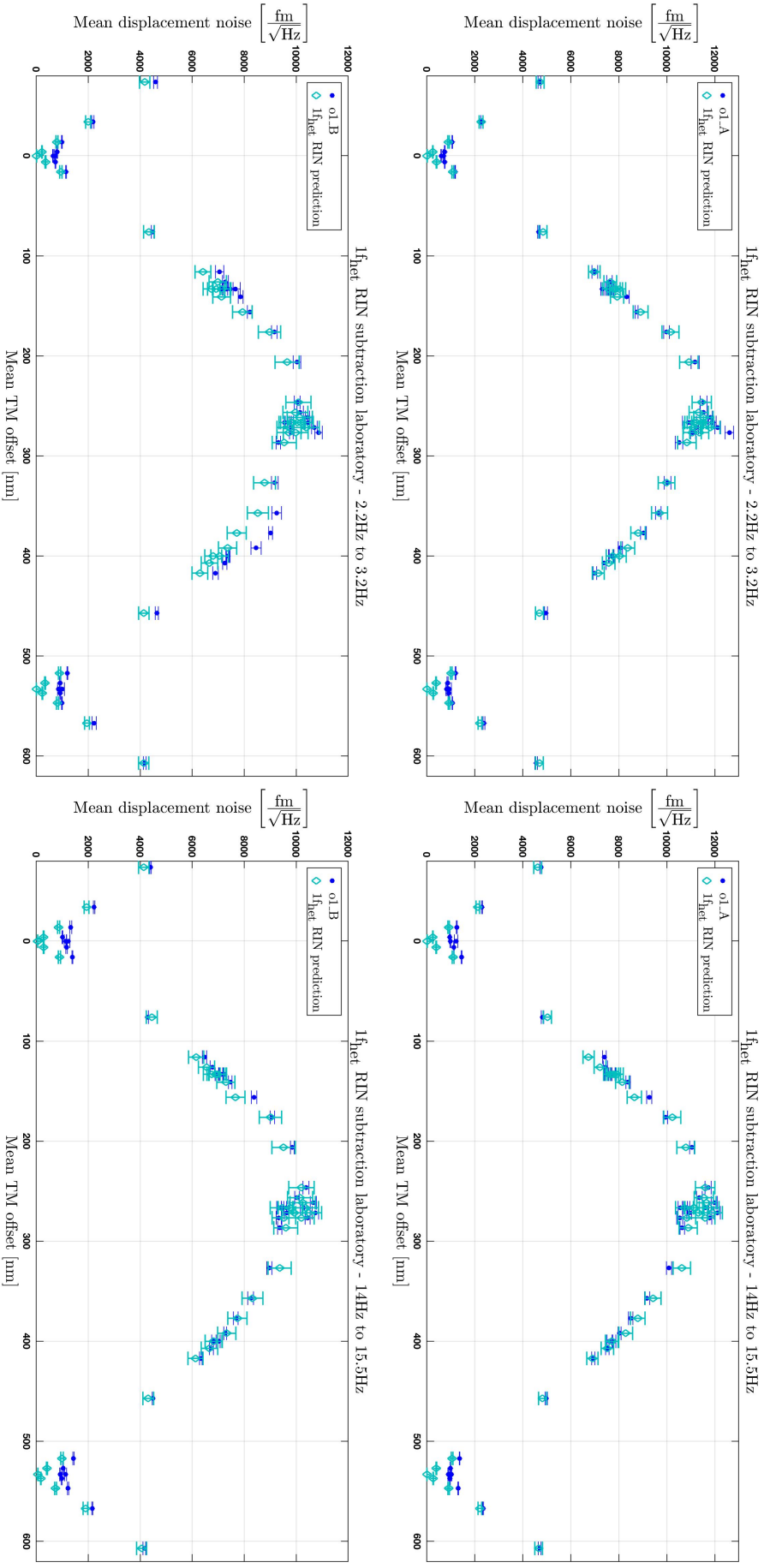
Figure 5.32.: The top plot shows the phase noise for the $1f_{het}$ RIN injection measured on the A side, the bottom for the B side. The left plots show the lower frequency range, and the right plots the higher frequency range selected for analysis. The x-axis shows the mean TM offset at which the mean noise level is measured. From the measured RIN the expected phase noise can be calculated. Since this RIN is injected on only one beam the equations for un-correlated RIN are used. This predicted phase noise is shown in lighter colours.
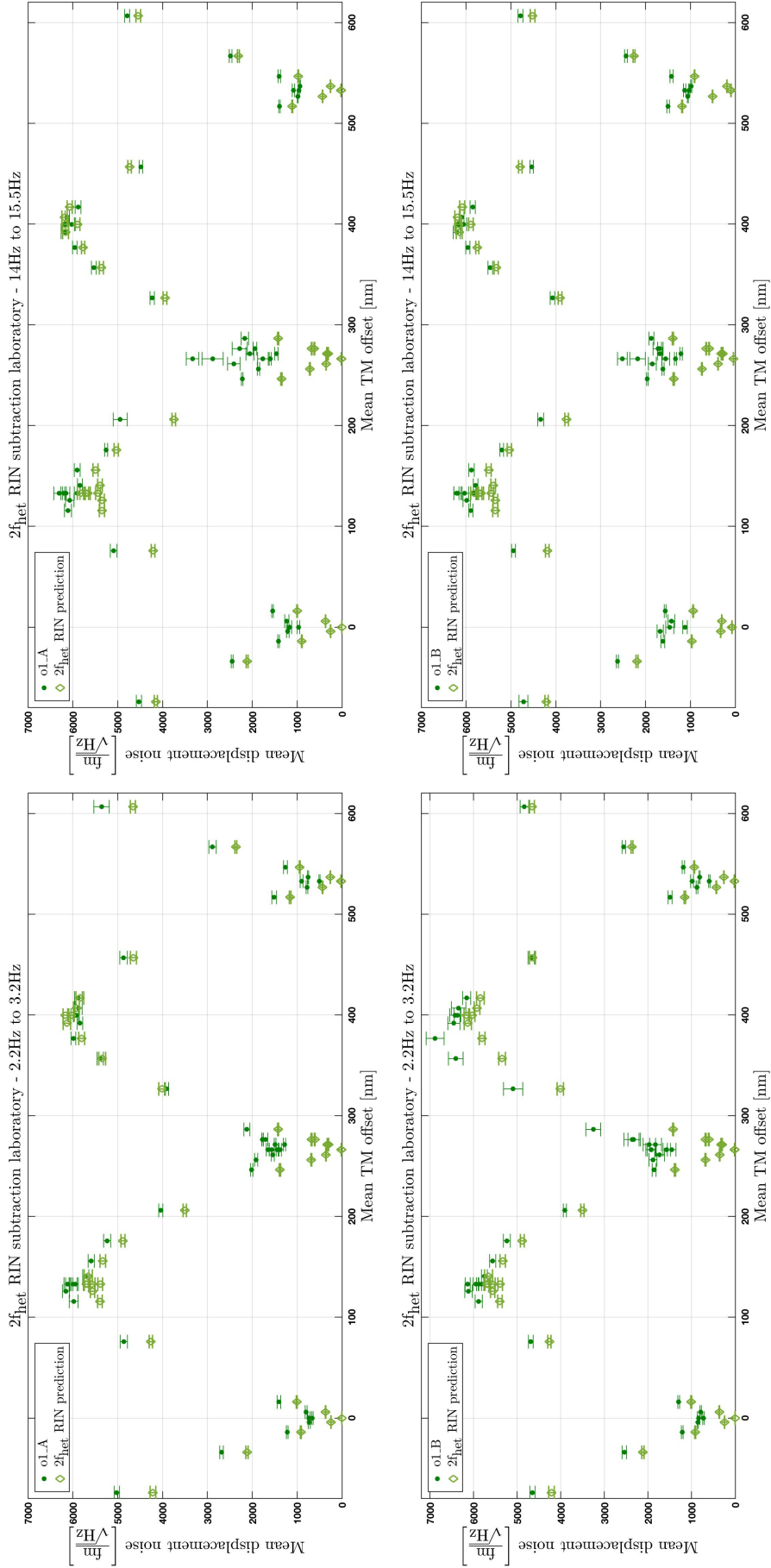
Figure 5.33.:: The top plot shows the phase noise for the 2f$_{het}$ RIN injection measured on the A side, the bottom for the B side. The left plots show the lower frequency range, and the right plots the higher frequency range selected for analysis. The x-axis shows the mean TM offset at which the mean noise level is measured. From the measured RIN the expected phase noise can be calculated. Since this RIN is injected on only one beam the equations for un-correlated RIN are used. This predicted phase noise is shown in lighter colours.
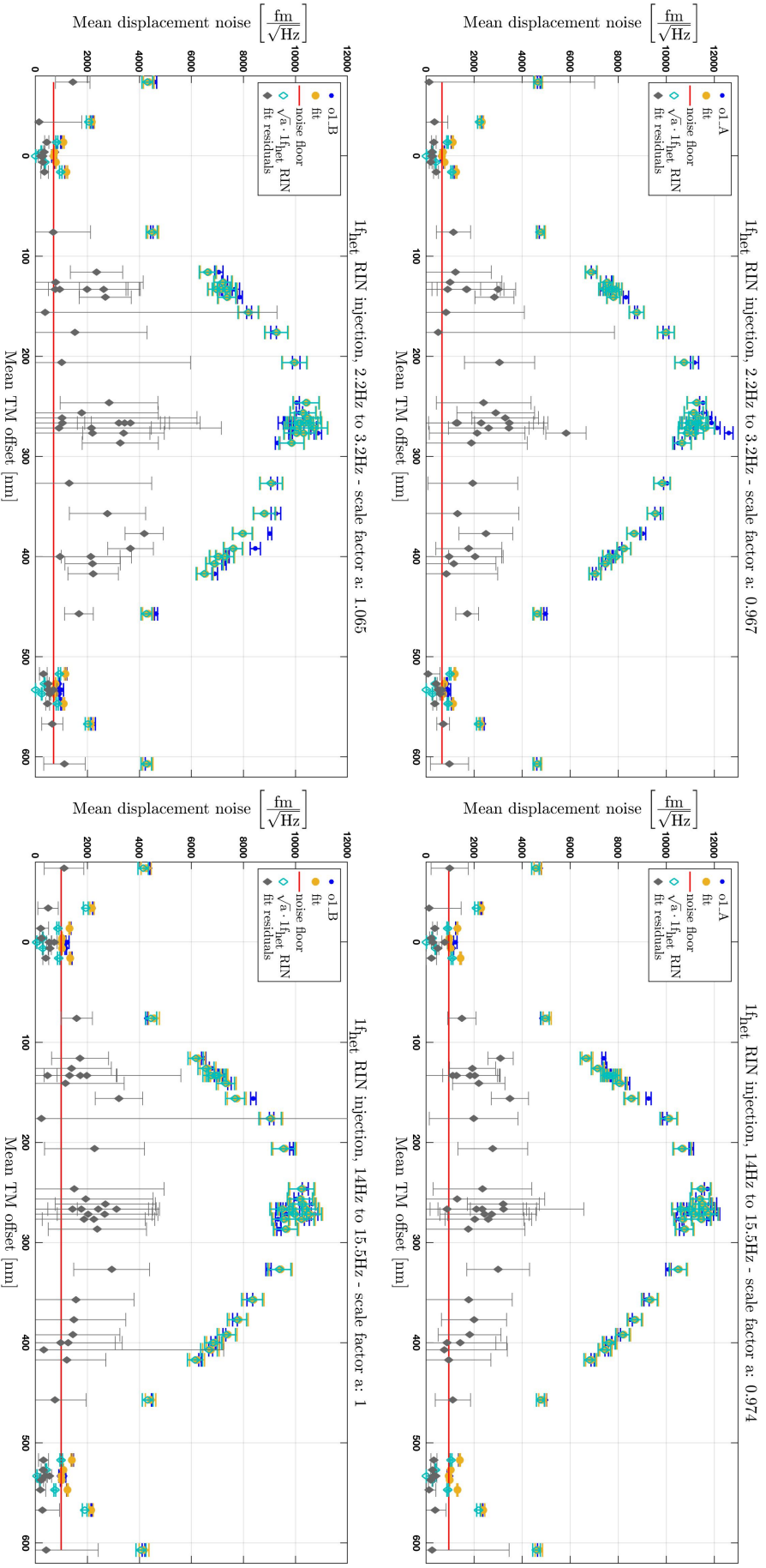
Figure 5.34.: These plots show the phase noise as measured during an $1f_\text{het}$ RIN injection (dark blue), together with the phase noise calculated from the measured RIN multiplied with a scaling factor (light blue). This power scaling factor is the result of a fit of the predicted phase noise with a noise floor to the measured phase noise, this fit result is shown in yellow. The calculated noise floor is shown in red. The residuals of this fit are shown in grey.
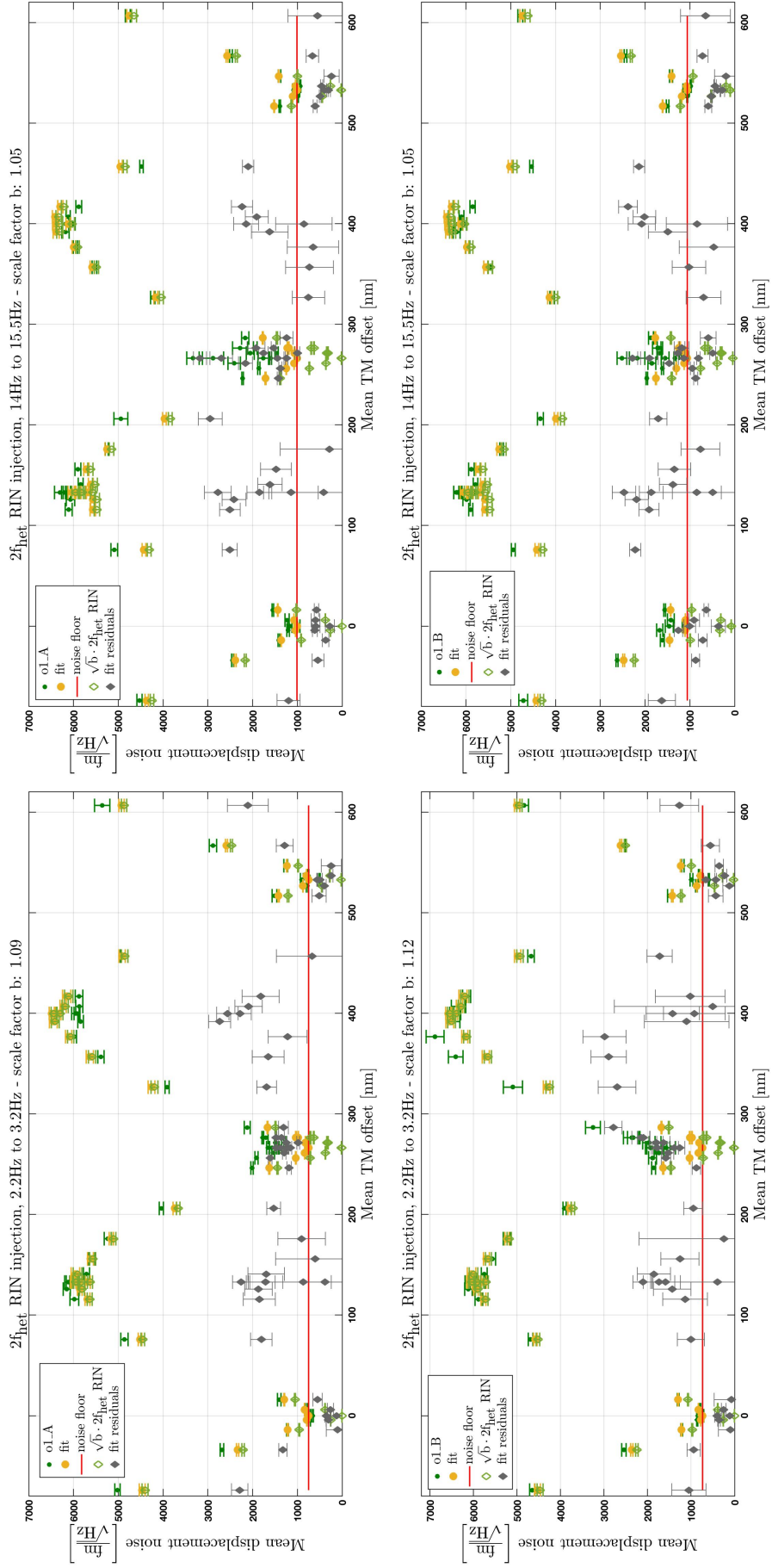
Figure 5.35.: These plots show the phase noise as measured during an $2f_{het}$ RIN injection (dark green), together with the phase noise calculated from the measured RIN multiplied with a scaling factor (light green). This power scaling factor is the result of a fit of the predicted phase noise with a noise floor to the measured phase noise, this fit result is shown in yellow. The calculated noise floor is shown in red. The residuals of this fit are shown in grey.

5.3.3. Error Discussion

Previous estimations of the error of the measurement of the RIN power with the demodulated signals are in the order of $\approx 7\%$, as was explained in Section 4.5.3. This error was estimated from the non-whiteness of the measured RIN power in the relevant frequency ranges. In RIN amplitude this equals an error of $\approx 3.4\%$, which leads to an error of the calculated phase noise.

For the $1f_{het}$ RIN measurement the biggest power scaling factor necessary to explain the measured phase floor with the calculated RIN contribution is ≈ 1.065 in the B-side measurement at the lower frequency range, which is a factor ≈ 1.03 in noise amplitude. This bigger error of the prediction is most likely due to a few points above the TM offset of $-200\,\text{nm}$, where the measured phase noise is higher than the calculated phase noise.

In the measurement of the transfer function shown in Section 5.1.5 the calculated phase amplitude from the injected RIN is bigger than the measured phase amplitude; here the B-side phase noise amplitude is smaller than calculated and the A side phase noise amplitude is bigger by a few percent.

In this RIN subtraction experiment the difference between the total beam powers, as measured by the phasemeter and combined from the individual powers of the calibrated beams, is bigger than in the transfer function experiment. The mean difference over the whole experiment duration for each diode can be seen in Table 5.5; the biggest difference is $\approx 5\%$. This error is included in the error of the mean beam powers, and increases the errors on the calculated phase noise level and the heterodyne efficiency per step. The difference in measured and predicted phase noise is smaller than this error would suggest, since the beam powers appear both in the numerator and denominator. Both beam powers are measured with the same electronics, the error on the ratio between the two is likely smaller. The reason for this difference is not known, a possible effect is the temperature difference between the experiment, which was run over night, and the calibration, which was done the morning after.

The biggest RIN power scaling factor in the $2f_{het}$ RIN measurement is ≈ 1.12. However, this is clearly due to a few bad data points. The next biggest scaling factor is ≈ 1.09, which is a factor ≈ 1.04 in amplitude noise. Both of these are for the lower frequency band. At the higher frequencies the amplitude noise scaling factor is only ≈ 1.02.

In the measurement of the transfer function in Section 5.1.5 the measured phase amplitude was $\approx 14\%$ bigger than the predicted phase amplitude for smaller RIN injections. In the transfer function experiment it could be seen that this effect is not subtracted with balanced detection. In the RIN subtraction experiment in Section 5.3.4 it can be seen that this effect is most likely also not removed with the reference, although this is hard to separate from the SVN component.

In both experiments the residuals of the scaling factor fit are lower near offsets of $0\,\text{nm}$ and $532\,\text{nm}$, or 0 and 2π in phase. These data points are used by the fit to calculate the noise floor. In the area between these TM offsets the residuals increase, most likely due to the different scatter in measured phase noise and measured RIN for the different TM positions. In the $2f_{het}$ RIN measurement the fit is clearly worse around offsets of $266\,\text{nm}$, or π in radian, where a maximum of a contribution of $1f_{het}$ RIN or SVN with this phase dependency would be expected. Due to this the calculated noise floor is probably higher than in an experiment where these contributions are smaller. A lower noise floor would decrease the difference between measured phase noise and calculated phase noise from the measured RIN.

Small Vector Noise

The difference between the measured and calculated mean phase noise for $1f_{\text{het}}$ RIN is about $\approx 140 \frac{\text{fm}}{\sqrt{\text{Hz}}}$ for the A-side. On the B side the measurement between $2.2\,\text{Hz}$ and $3.2\,\text{Hz}$ shows a difference of $\approx 240 \frac{\text{fm}}{\sqrt{\text{Hz}}}$. The difference between the two for the frequency range between $14\,\text{Hz}$ and $15.5\,\text{Hz}$ is $\approx 40 \frac{\text{fm}}{\sqrt{\text{Hz}}}$, which is almost within the error bars.

The difference in peak phase noise from the phasemeter measurement and as calculated from the mean RIN over the whole measurement duration for $2f_{\text{het}}$ RIN for the higher frequency band is $\approx 120 \frac{\text{fm}}{\sqrt{\text{Hz}}}$.

In the experiments shown here the injection voltage is smaller than in the transfer function experiments of Section 5.1. In previous experiments a linear dependency of the SVN amplitude to the injected RIN was seen for bigger injections, see Equation 5.15 in Section 5.1.5. With the assumption that this dependency holds for smaller RIN injections the SVN would change the peak phase amplitude noise with the same dependency on the phase difference with one small difference: since the injected noise is not only at a positive frequency offset $+\epsilon$ from either $1f_{\text{het}}$ or $2f_{\text{het}}$, but also at $-\epsilon$, and both couple to the same frequency band. The RIN amplitude level to calculate the SVN contribution is a factor $\sqrt{2}$ bigger.

Due to the lower injection voltages of the RIN injection the contribution of SVN is not as high as in experiments with sinusoidal RIN injections. With a bigger RIN injection the SVN is visible in the single-interferometer measurement, with changing phase difference similar to the pattern observed in Section 5.1.5.

For $1f_{\text{het}}$ RIN with a noise amplitude of $\hat{r}_{\text{r}}^{(1)} = (100 \pm 0.9)\frac{10^{-6}}{\sqrt{\text{Hz}}}$ the peak phase noise changes for one interferometer by $k_{iab} = \pm(9.05 \pm 0.08)\frac{\mu\text{rad}}{\sqrt{\text{Hz}}}$, or $\pm(768.5 \pm 7)\frac{\text{fm}}{\sqrt{\text{Hz}}}$, due to the combined SVN contribution. For the $2f_{\text{het}}$ RIN measurement the injected RIN has a noise amplitude of $\hat{r}_{\text{r}}^{(2)} = (96 \pm 0.7)\frac{10^{-6}}{\sqrt{\text{Hz}}}$, this would lead to a peak noise amplitude change due to SVN for one interferometer of $k_{icd} = \pm(8 \pm 0.06)\frac{\mu\text{rad}}{\sqrt{\text{Hz}}}$, or $\pm(736.5 \pm 5)\frac{\text{fm}}{\sqrt{\text{Hz}}}$.

In the reference interferometer the phase offset is stable, while the contribution of SVN to the measurement interferometer changes with the TM offset. In this noise injection it is not clear how the creation of SVN depends on the frequency, what the ratios of sine and cosine component and the resulting offset of the SVN pattern from the interferometric zero is, and if this offset is the same for the whole frequency band. The SVN could in principle be removed from the x1 signal with a fit similar to Section 5.1.5, but not from the xR signal, since the phase is stabilised at $0\,\text{rad}$ with the OPD loop.[1] With a SVN fit to the o1 signal, as in Section 5.1.4 equation 5.9, the RIN noise shape would also be fitted as a SVN contribution due to the similar phase dependency.

The calculated contribution of the SVN to the measured phase noise can not be seen in the comparison between the peak phase noise amplitudes. It is likely that the SVN coupling increases above a threshold voltage, and the behaviour at lower injection voltages does not follow the linear behaviour observed previously.

In the first version of the RIN subtraction experiment the RIN injections had a higher voltage, the injections were bigger by a factor 5. In these experiments the coupling of SVN to the measurement interferometer signals x1_A and x1_B was clearly visible in the noise level for different TM offsets. Therefore, the injection of noise is not a special case where SVN does not couple.

Overall, the confidence in the RIN subtraction results is high. The visible contribution of SVN is at a level where the calculated and measured phase noise are within good agreement.

---

[1] Due to the cosine terms SVN also changes the phase amplitude at $0\,\text{rad}$.

5.3.4. RIN subtraction with sinusoidal injection

As an additional test the RIN subtraction with a RIN equivalent sinusoidal intensity modulation is measured. Due to COVID19 this experiment was performed remotely, the OMS was not adjusted before this experiment, and the beam powers on the bench are a factor 3 lower as in other experiments.

For this experiment the same injection frequency offset of $\epsilon = 12\,\mathrm{Hz}$ as in the previous sections is used. With an injection amplitude of $200\,\mathrm{Count}$ the RIN amplitude is a factor 10 smaller than the biggest injection in the RIN transfer function experiment. This amplitude is chosen because the injected signal is still visible in the single diode measurement, and because for this lower injection voltage the SVN contribution is smaller. Here, the injection voltages correspond to a RIN amplitude of $\tilde{r}_r^{(1)} = 0.0088 \pm 7 \cdot 10^{-6}$ for $1f_{\mathrm{het}}$ RIN and $\tilde{r}_r^{(2)} = 0.0085 \pm 1 \cdot 10^{-5}$ for $2f_{\mathrm{het}}$ RIN.

At each TM offset the phase is measured for 15 minutes. As in previous experiments the amplitude is calculated with a DFT. An amplitude spectrum of selected TM offsets for the $1f_{\mathrm{het}} + 12\,\mathrm{Hz}$ RIN injection can be found in Figure 5.36. Shown is the amplitude spectrum of x1_A and o1_A calculated with the lpsd function of LTPDA. At $12\,\mathrm{Hz}$ the phase response to the injected RIN is visible, the peak height in both signals changes with the TM offset. In the x1_A signal this change is due to SVN, since the phase difference between the reference and measurement beam changes, as in the experiments shown in Section 5.1. The amplitude change in the o1_A signal is both due to the SVN contributions of x1_A and xR_A, and the subtraction of the phase amplitude from the injected RIN that both signals have in common. The same processing as in Section 5.1.5 is used to calculate the amplitudes of the injected RIN and the phase response for each step, and the same processing as in Section 5.3 is used to build the measured and predicted data. As in the previous experiments the errors of the measured amplitudes are the result of the error calculation of the DFT, which is low due to the still decent SNR. In the calculation of the predicted phase amplitude from the injected $1f_{\mathrm{het}}$ RIN the average calibrated beam power of each TM step is used, due to the long
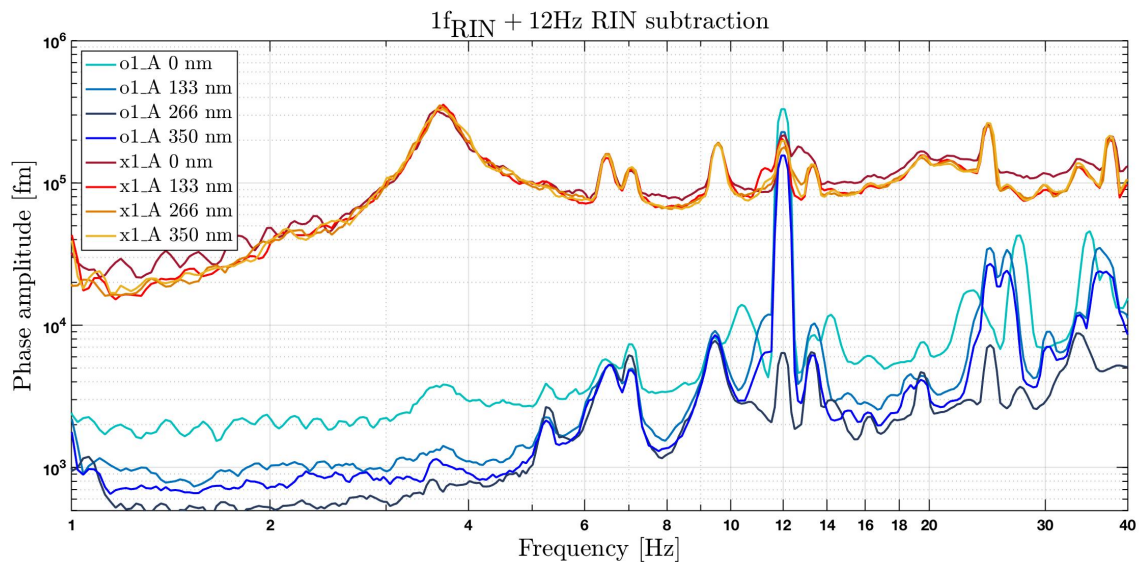
Figure 5.36.: In this plot the amplitude spectra of the x1_A signal (red) are compared with the subtracted signal o1_A (blue) for selected TM offsets. Sinusoidal RIN is injected at $1f_{\mathrm{het}} + 12\,\mathrm{Hz}$ on the reference beam, this injected RIN is visible at $12\,\mathrm{Hz}$ in the phase signal. This data is plotted using the unit [fm] to compare it to the results in this section, it can be calibrated to radian with $1000\,\mathrm{fm} \approx 11.8\,\mu\mathrm{rad}$. These amplitude spectra are calculated with the lpsd function, using a HFT70 window.

measurement duration its error is also low. These error bars do not include any systematic errors, like the expected offset due to SVN.

The measured phase amplitudes for each TM offset are shown in Figure 5.37, together with the predicted phase amplitude calculated from the measured RIN. The predicted phase noise from the measured RIN is calculated using the similar equations as in the noise injection measurement, since this sinusoidal injection is only on the $+\epsilon$ frequency offset the predicted phase noise is smaller by a factor $\frac{1}{\sqrt{2}}$ compared with a noise injection, see equation 5.22. Or, to reach the same coupling equation, the phase amplitudes as calculated for the transfer function measurement in Section 5.1 for x1 and xR can be added together. Since the beam powers on the two diodes are different the phase amplitude due to the $1f_{\text{het}}$ RIN injection are calculated for the x1 and xR signal. These are added linearly and combined with the expected noise subtraction, see also Equation 3.74, where the same was done for a noise injection. The phase amplitude of the subtracted signals are calculated from the measured RIN with

$$
\tilde{o}1\_A^{(1)} \approx \left[\frac{\sqrt{P_{1A,r}^2 \tilde{r}_r^{(1)^2} + P_{1A,m}^2 \tilde{r}_m^{(1)^2}}}{\sqrt{4\,\eta_{\text{het},1A} P_{1A,r} P_{1A,m}}} + \frac{\sqrt{P_{RA,r}^2 \tilde{r}_r^{(1)^2} + P_{RA,m}^2 \tilde{r}_m^{(1)^2}}}{\sqrt{4\,\eta_{\text{het},RA} P_{RA,r} P_{RA,m}}} \right] \cdots
$$
$$
\cdot \left| \sin\left(\frac{4\pi \cos\alpha}{\lambda} \frac{o1\_A}{2} \right) \right| \cdot \frac{\lambda}{4\pi \cos(\alpha)}, \qquad \text{[fm]} \qquad (5.24)
$$

$$
\tilde{o}1\_A,B^{(2)} = \sqrt{\frac{\tilde{r}_r^{(2)^2} + \tilde{r}_m^{(2)^2}}{4}} \left| \sin\left(\frac{4\pi \cos\alpha}{\lambda} o1\_A \right) \right| \cdot \frac{\lambda}{4\pi \cos(\alpha)}. \qquad \text{[fm]} \qquad (5.25)
$$

These predicted phase amplitudes are shown in Figure 5.37, with the same colours as in the main RIN subtraction experiment.

In the x1 signal (red) the SVN contribution is visible as a sinusoidal pattern around its mean value. The xR signal does not change with the TM offset, but is plotted over the same phase difference to make the comparison to the x1 signal easier. From previous experiments a combined SVN amplitude of $k_{iab} \approx 588\mu rad$, or $\approx 5 \cdot 10^4$fm, for $1f_{\text{het}}$ and $k_{iab} \approx 189\mu rad$, or $\approx 1.6 \cdot 10^4$fm, for $2f_{\text{het}}$ RIN can be expected per interferometer. This SVN contribution is a factor 10 smaller than the maximum SVN in the experiment shown in Section 5.1.5. The SVN which can be observed on the x1 diode for $1f_{\text{het}}$ RIN is at a similar amplitude as predicted, the $2f_{\text{het}}$ RIN injection SVN is a factor 3.5 bigger than expected.

The subtraction of the SVN components of x1 and xR was shown in Section 5.1.4 Equation 5.9. Here, the SVN contribution of x1_A and x1_B is calculated with the same fit as in the RIN transfer function experiment, and subtracted from the phase noise of o1_A and o1_B. The phase noise with the SVN contribution subtracted is also shown in Figure 5.37, in yellow. Part of the amplitude measured on xR is due to a static SVN offset of unknown amplitude. It is not clear what the SVN contribution of the reference interferometer signal is, due to the cosine component of SVN it is not necessarily zero with the OPD loop active. However, it seems clear that both are needed for this subtraction to work.
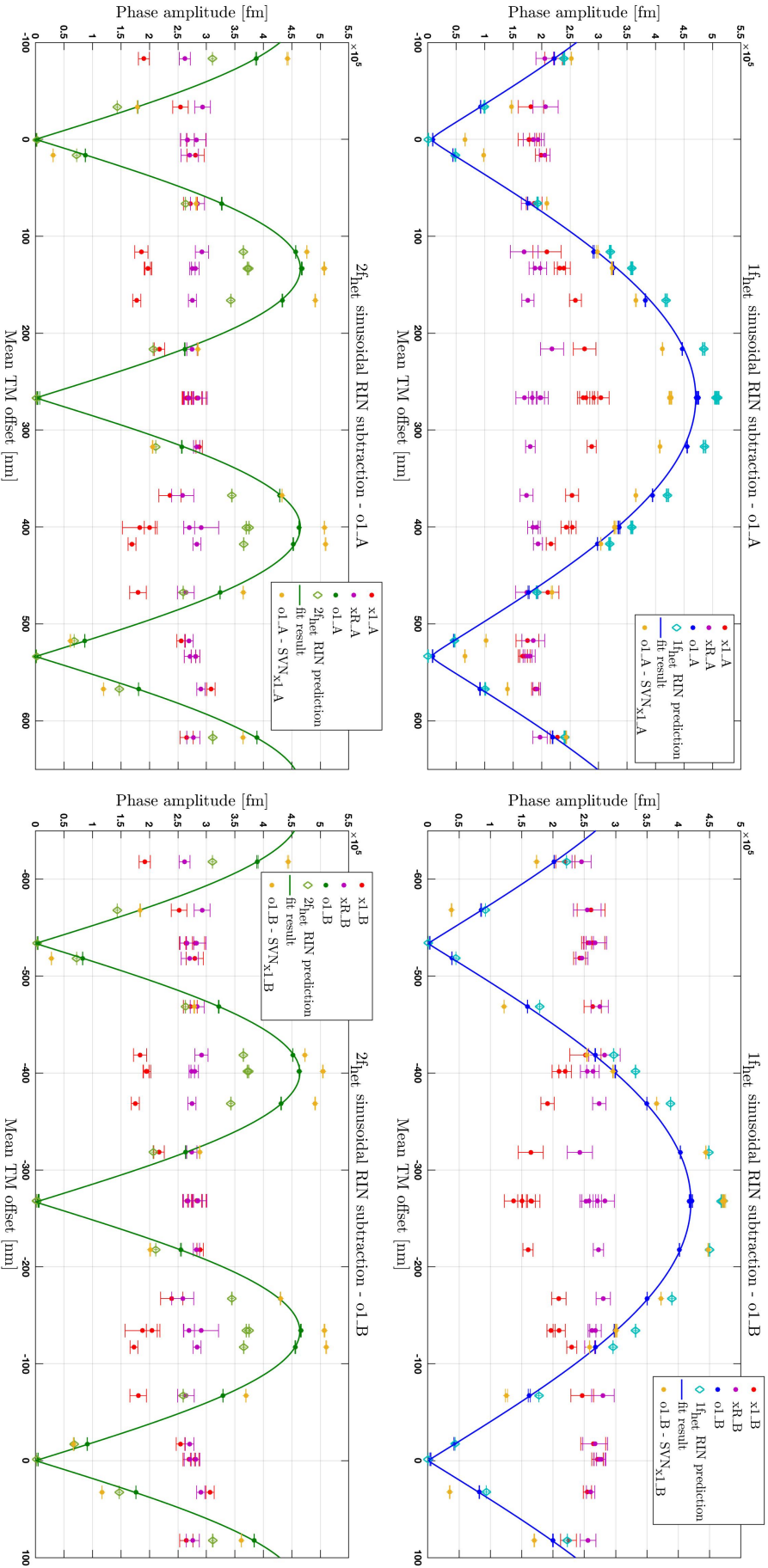
Figure 5.37.: Shown here is the subtraction of a RIN equivalent intensity modulation. TM1 is moved in steps. The phase amplitude due to the injected RIN is measured on x1 (red) and xR (purple), and on the subtracted signal o1. RIN is injected for both 1f_het (top plots, blue) and 2f_het (bottom plots, green). To help the eye on this plot a fit to the measured phase noise of the subtracted signal is shown. During this experiment the injected RIN is measured with the demodulated power signals, the expected phase amplitude due to this injection is also shown for each step for 1f_het RIN (light blue) and 2f_het (light green). The measured phase noise in the o1 signals with the SVN contribution of the x1 signals subtracted is shown in yellow.

170

Error discussion

For both injections the predicted and measured noise shape is similar. The difference between the two is within the possible offset range due to SVN, which can be observed on the x1 signal. Since the SVN contribution on the xR signal is not known the combined SVN contribution can not be calculated. For the $1f_{het}$ RIN injection it seems like the two contributions almost cancel, the phase amplitude calculated from the measured RIN is $\approx 9.5\%$ bigger than the measured phase amplitude. The agreement between calculated and measured phase amplitude is worse than in the transfer function experiment.

For $2f_{het}$ RIN the difference is close to 2 times the observed SVN on the x1 signal, the measured phase amplitude is $\approx 28\%$ bigger than calculated from the measured RIN. The difference between the two values is too big to be confident in the results.

For the $2f_{het}$ RIN it is likely that a similar effect leads to a higher measured phase noise in this experiment and in the RIN transfer function experiment shown in Section 5.1.5. In the transfer function experiment the measured RIN is $\approx 14\%$ bigger for the smaller injections. The RIN injection amplitude of the experiment presented here is smaller than in the transfer function experiment. With the assumption that this additional effect decreases further with the injected RIN amplitude the observed change in this measurement with two diodes might be approximately a factor 2 bigger than with one diode. So, the contribution of the effect which causes the error in the transfer function experiment seems to add when the two interferometer signals are subtracted. This contribution also adds when the balanced signal is calculated, but the factor $\frac{1}{2}$ in the balanced detection equation reduces the offset back to the original value. This behaviour might be an important clue in future investigations of this difference. However, these estimations do not consider the combined SVN contribution of the two signals, the impact of which on the subtracted signal is unknown.

In the $1f_{het}$ RIN injection measurement the phase amplitudes of o1_B, with the SVN contribution of the x1_B signal subtracted, are closer to the predicted phase amplitudes. In the other three measurements the phase amplitude of the subtracted signal is further away from the predicted phase amplitude with the SVN contribution subtracted. From a comparison of the x1 signals with the o1 signals it is clear that the SVN can not be added to o1 instead, even though it would move the measured phase amplitude closer to the predicted one. It seems unlikely that the SVN contribution of the xR signal is big enough to move the measured phase amplitudes to the predictions. The reason for this big discrepancy is not known.

Injection	o1A [fm]	o1A pred. [fm]	o1B [fm]	o1B pred. [fm]
$1f_{het}$ RIN	470470 ± 149	509585 ± 208	419990 ± 155	464450 ± 190
$2f_{het}$ RIN	464850 ± 90	372822 ± 200	463990 ± 91	372822 ± 290

Table 5.8.: Shown in this table is the peak phase amplitude of the injected RIN calculated with a fit to the measured phase amplitude for each TM position. The predicted phase amplitude is calculated from the mean RIN amplitude over the whole timespan, with the coupling as in Equation 5.25. The ratios between measured and predicted phase amplitude are 0.92 on the A side and 0.9 on the B side for the $1f_{het}$ RIN injection, for the $2f_{het}$ RIN injection this ratio is 1.28 for both.

171

6

RIN flight experiments

In this chapter the results of RIN experiments performed during the LPF mission are described. Section 6.1 shows the planning of the RIN in-flight experiments. The commands to execute the in-flight experiments were written by ESA scientists from the input of the experiment scientists. These tele-commands were then uploaded in a packet with the experiments of the whole week to the satellite. In most cases the experiments were performed by the LPF satellite without further input from ground, and the data was downloaded and preprocessed for analysis. A more detailed description of this process can be seen in the report on the initial operations time [83], first results of the OMS experiments are also shown there. More results and a short description of the mission extension can be found in [84]. More details on the planning phase of the OMS experiments can be found in [40].

A few differences in the experiment planning between the laboratory and in-flight OMS have to be taken account, a short overview can be found in Section 6.1.1.

The first flight RIN subtraction experiment was performed on 2016-04-25, on DOY116, the experiment design is shown in Section 6.1.2. The results of this experiment can be found in Section 6.2, together with a description of the analysis method for flight data.

The second RIN subtraction experiment was performed on DOY033, which is 2017-02-02. Due to a scheduling issue this experiment was not performed as planned. This experiment design can be found in Section 6.1.3. The results can be found in Section 6.3. The focus of this section is more on the results and less on the analysis method, as the core of the analysis script is the same as for the first experiment.

In the first experiment it was found that the noise shape between the peaks at higher frequencies is different than in the band between $0.6\,\mathrm{Hz}$ and $0.9\,\mathrm{Hz}$. To investigate this noise shape short timespans of $100\,\mathrm{Hz}$ IDL data for some of the test mass offsets were downloaded for both the balanced detection signal o12 and for the single-diode signal o12_A. The results of these investigations can be found in Section 6.4, where higher frequencies are investigated. For the in-flight experiment higher frequencies concerns everything above $1\,\mathrm{Hz}$, since the sampling frequency for most the phase measurement is only $10\,\mathrm{Hz}$.

In the last few days of the mission the RIN level was measured directly, on DOY192 (2017-07-11), for both the measurement and reference beam with and without the fast amplitude control loop. This measurement was performed for both the nominal $1\,\mathrm{kHz}$ heterodyne frequency and also for $2\,\mathrm{kHz}$. The planning of this experiment is described Section 6.1.4, the analysis of these measurements can be found in Section 6.5.

RIN is not only relevant in the longitudinal measurement, but also in the DWS measurements; these investigations were performed by Lennart Wissel (AEI); with first results in his masters thesis [57]. More details can be found in his upcoming PhD thesis.

The results of these first dedicated experiments inspired an investigation of the contribution of RIN to the phase noise in other experiments. The performance of the OMS was frequently measured in so-called noise runs. During these timespans no experiments were performed, and the phase noise of the OMS was observed. The measured noise is explained by the

different noise contributions, most of which were shown in Chapter 3. An overview of these contributions for the flight OMS can be found in [70][19]. Changing noise levels at higher frequencies were observed during these noise runs, this changing noise level is compared with the previously measured RIN coupling in Section 6.6.

During the free-fall experiment the test mass was also moved over a bigger distance. The aim of this experiment is an exploration of the noise at lower frequencies, which contains actuation noise during the standard operational setting [85][86][87]. In this experiment the test masses were kept in free-fall by short kicks, instead of a continuos actuation, which allows for periods without actuation noise. In Section 6.7 the sensing noise of these experiments is compared with the results of the previous RIN experiments. Using the same method as in the RIN subtraction experiments a fit to the measured noise for changing TM offset is made. In Section 6.8 an overview of the measured RIN levels over the mission duration is shown.

6.1. Experiment design

In the previous chapters it could be seen how the coupling from RIN to the phase measurement depends on the TM position; this knowledge is applied to the operation of the Optical Metrology System (OMS) on-board LISA Pathfinder. The LPF satellite had to perform regular station keeping manoeuvres to keep the orbit around L1. These were scheduled at first over every weekend, and then every other weekend. During these manoeuvres the input to DFACS was switched from the interferometric measurement to capacitive sensing. First designs of the transition back to science mode were focused on a fast switch-back to the optical measurement, the TM was to be kept stable at the position the capacitive sensors measures as zero. This zero measurement however is different than the optical zero, and the TM would have had an offset in the interferometric measurement. This would result in a phase difference between reference and measurement interferometer, which would change from week to week. For most noise sources this phase difference would not have been be a problem. However, since RIN is an important noise source to minimize it was decided to always move the TM to optical zero at the end of station keeping after the properties of RIN subtraction became clear. This change in the transition from station keeping to science mode was made well in advance of the launch, and was easy to implement.

In a sense, the big success of this investigation was to show that the impact of RIN is not mission critical, if the TM is moved to the optical zero position. Instead of regularly moving the TM in search of the noise minimum the very expensive experiment time in orbit could be used for other investigations.
A few differences between the ground setup and the flight setup have to be kept in mind for the design and analysis of the flight experiments, a short overview can be found in Section 6.1.1. Two TM step experiments along the x-axis were performed to measure the RIN subtraction with the reference and understand the impact of RIN on the sensing noise floor, the design of these experiments will be shown in Sections 6.1.2 and 6.1.3. The design of an additional experiment to measure the RIN directly can be found in Section 6.1.4.

6.1.1. Restrictions in flight

For the design of the in-flight RIN experiments the differences to the laboratory setup have to be taken into account. In general, the sampling frequency of the flight setup is limited to 10 Hz. For the RIN experiments Science Data Mode 19 (SDM19) is used. This packet contains 10 Hz data for o12, φ_R and $xF = \frac{c}{2\pi\delta L} \cdot (\varphi_F - \varphi_R)$, namely the LTPDA channels LTPDATelemetry.DMU_OMS_o12,
LTPDATelemetry.DMU_OMS_PSI_R
and LTPDATelemetry.DMU_OMS_PSI_F,
as well as the DWS channels at 10 Hz.

This choice of channels differs from the data packets commonly used for noise measurements, not included here are the commanded forces with a sampling frequency of 10 Hz. The commanded forces are subtracted from the differential acceleration of the TMs oÏ2 to estimate the gravitational imbalance on the satellite Δg; a description of the calculation of Δg can be found in [70]. Since Δg is of lower interest in this analysis, this force data was not downloaded at this higher sampling frequency.

For flight experiments the RIN is investigated between 0.6 Hz and 5 Hz. Due to the lower sample rate of the in-flight data compared with the on-ground measurements the aliasing from higher frequencies is increased in the frequency range under analysis, the RIN level calculated has to be understood as an upper limit. This effect is visible in the flight RIN subtraction experiments for mean noise levels above 1 Hz, in Section 6.4 higher frequencies are investigated. In the laboratory measurement the sampling frequency of the phase signal is no limitation since the phasemeter calculates the phase signals at a sampling frequency of ≈ 162 Hz and the CDS saves these at 256 Hz.

The noise measurement at one TM offset takes longer in flight than it does in the ground setup since movement of the TM is slower than a change of the piezo position. At each step the TM moves past the set-point and needs some time to stabilise. This time is significantly shorter in the laboratory as well.

For the first flight RIN subtraction experiment 45 setpoints of TM2 along the x-axis are implemented, the measurement duration is about 750 seconds, or 12.5 minutes, per TM offset. The step sizes are 30 nm and 10 nm, in both cases it takes about 18 minutes to move the TM. In the second experiment the TM is moved in smaller steps around areas of interest in the RIN subtraction shape, and moved in bigger steps between those. Implemented are 37 TM offsets.

This experiment is easier in the laboratory; in the experiments described in Section 5.3 the TM mirrors are moved every 15 minutes. The description of the system as-is was the goal of the OMS experiments, with the experiments as designed the RIN contribution to the sensing noise floor can be estimated. Coupling parameters and other details can be measured in the laboratory on ground, which is why for the in-flight experiments RIN was not artificially increased by turning off the amplitude stabilisation. In the flight OMS it was not possible to inject RIN or RIN equivalent intensity modulations in the kHz range, these kinds of experiments were therefore not possible in flight.

6.1.2. First RIN subtraction experiment

In the first RIN subtraction experiment TM2 is moved over a relatively long range of 1100 nm to show the predicted RIN subtraction with the reference signal from the measurement signal for phase differences of more than 2π. The experiment design before the launch assumed a duration of 1 hour between steps. However, over the course of the first engineering tests it became clear that the control over the TM is very good, and the time it took to move could be shortened to ≈ 20 minutes to increase the number of offsets. With a desired noise measurement time of 10 minutes the TM is moved every half hour to a new position. To keep the timeline simple the step size is the same for most offsets.

The phase difference between the measurement signal and the reference signal in radian is of bigger interest for this analysis than the step sizes in nanometre. The phase difference can be plotted as a real and imaginary part in a phase diagram. Half a wavelength of TM offsets are covered with a negative offset of the interferometric zero, and one-and-a-half with a positive offset from zero. Around zero and 2π more measurements are performed since these setpoints are very interesting for performance optimisation. The rest of the phase space is more evenly covered with measurement points. Since the TM is moved either 10 nm or 30 nm the same offset in phase space is not measured twice. This is visible in Figure 6.1.2, where measurements in the full wavelength is plotted in blue, the half-wavelength below zero in green, and the half-wavelength above 2π in red.

These offsets in the unit nanometre can be found as a list in Appendix A.18. A code snippet of the commanding of the TM motion to its first offset can be found in Appendix A.19.
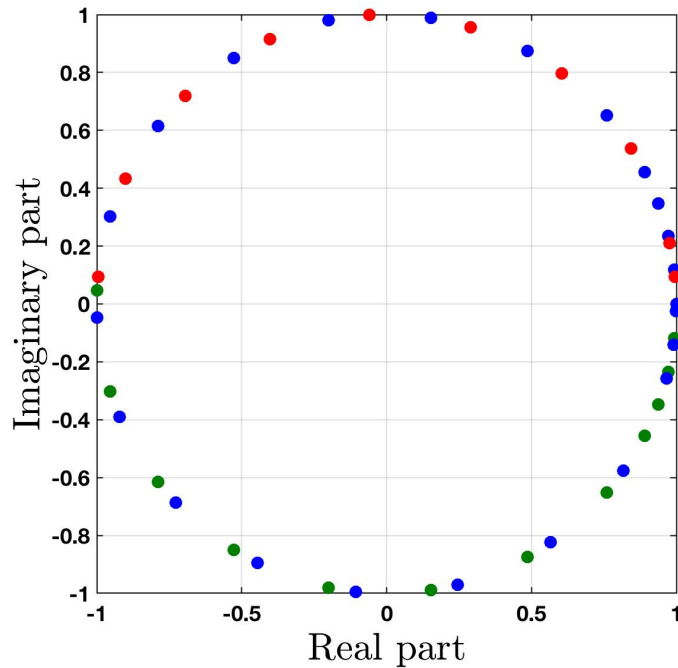

Figure 6.1.

Shown here are the TM offsets of the first step experiment plotted as phase difference between measurement signal and reference signal. TM offsets from $-\pi$ to 0 are shown in green, from 0 to 2π in blue, and from 2π to $\frac{3}{2}\pi$ in red.

6.1.3. Second RIN subtraction experiment
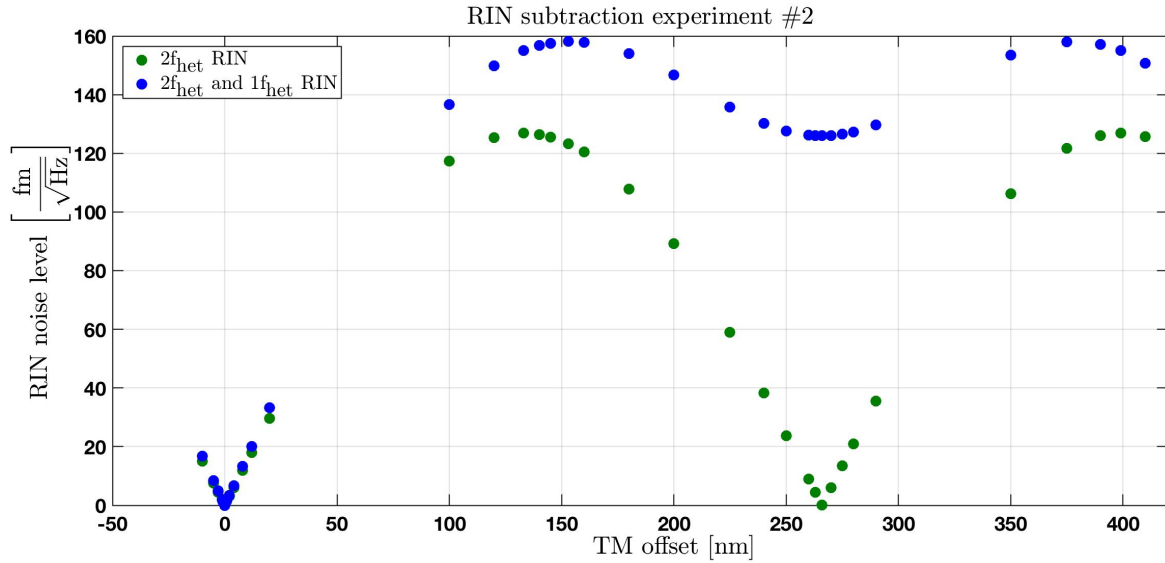
Figure 6.2.: These are the planned TM offsets for the second experiment, and the predicted phase noise level due to RIN. At each TM position the noise is measured with and without balanced detection. In the balanced signal only RIN at $2f_{het}$ is expected, the noise shape is shown in green. To show this RIN contribution here the measured value of the first experiment is used. For each TM offset the noise level without balanced detection is measured too. The expectation for this measurement is a phase noise contribution from both $1f_{het}$ RIN and $2f_{het}$ RIN. As a first estimate for the contribution of RIN at $1f_{het}$ without balanced detection the previously measured $2f_{het}$ RIN value is used as well. The two RIN contributions are added quadratically, and are shown in blue.

The first RIN subtraction experiment was designed to show the dependency of the phase noise level on the TM offset, the second one is optimised for detail questions.

One of the points of interest is the ratio of $1f_{het}$ RIN to $2f_{het}$ RIN in the system. In the first experiment no $1f_{het}$ RIN could be found. In the o12 signal a noise maximum in the coupling of $1f_{het}$ RIN is at a phase difference of π, where the coupling of $2f_{het}$ RIN has a minimum. To make $1f_{het}$ RIN visible, the noise is measured at each step with only one interferometer port, the signal under analysis is o12_A = x1_A − xR_A. Both x1_A and xR_A still contain phase noise from $1f_{het}$ RIN, which is subtracted in the calculation of o12_A in the expected noise shape, and would normally be removed by balanced detection. For each step the noise is measured under standard conditions with both diodes and balanced detection. The noise levels at 0 and π phase difference should differ in the contribution of $1f_{het}$ RIN for the two measurements o12 and o12_A. For a good fit to the $2f_{het}$ RIN contribution additional offsets TM around $\frac{\pi}{2}$ phase difference are included. The planned TM offsets of this experiment can be found in Appendix A.18, a plot of a possible noise shape with these TM offsets can be found in Figure 6.2.

One of the problems with the first experiment is the impossibility to separate the interesting noise contributions from aliasing effects. During this second experiment data at 100 Hz is recorded for some of the TM offsets. The spectrum of these measurements can be compared with spectra from 10 Hz data, and shed some light on the down-conversion of higher frequency noise to the sensing noise floor.

From the first experiment some experience on how much time it takes the TM to settle after steps of different size was gained, the measurement time is adjusted to fit to the changing step size in this experiment.

This experiment had a planning problem; due to an instability in the transition from capacitive readout to optical readout at the end of the station keeping the start of the experiment was pushed back. However, the end of the experiment was not moved, which lead to a part of the intended timeline to be cut off. The last TM offset was at 270 nm, the rest of the experiment did not run as planned.

In addition, the start of the experiment features higher noise in the laser frequency and amplitude. Due to this, a noise comparison between TM offsets around 0 nm and 266 nm for an estimation of the contribution of $1f_{het}$ RIN is not possible. In Section 6.3 the available data is analysed to gain as much knowledge as possible from this experiment.

6.1.4. Direct measurement

During the last days of the mission an experiment was performed to measure the RIN near $1f_{het}$ and $2f_{het}$ directly. The two beams were measured individually;. With only one beam active the fluctuations measured in the bin at the heterodyne frequency are not a measurement of the phase signal, but of the noise of the laser power. This measurement was performed with the nominal heterodyne frequency of $f_{het} = 1\,kHz$; additionally the phasemeter was set to a heterodyne frequency of $2f_{het} = f_{het,\,2} = 2\,kHz$. From this laser power noise measurement and the DC power measurement, the Relative Intensity Noise around the heterodyne frequency can be calculated. This RIN measurement was performed with and without the amplitude stabilisation active.

Under analysis here is the signal on the A quadrant of the PDR_A diode. Recorded was the raw phasemeter output of the single-bin discrete Fourier transform: the sine and cosine components $y_{R,A,A}$ and $z_{R,A,A}$, as well as the dc component $d_{R,A,A}$, were recorded at $100\,Hz$. This data was recorded on IDL channels, the sine component is recorded on LST10139, cosine on LST10140 and the DC value on LST10141. Due to the high sampling frequency not all quadrants are available for analysis.

The nominal processing of these components and the calculation of the phase can be found in Section 2.6. With the same calibration coefficients as used for the normal phase calculation the real and imaginary component are calculated. These are used to calculate RIN in a range of $50\,Hz$ around either $1f_{het}$ or $2f_{het}$. The calculation of RIN and the results of this experiment can be found in Section 6.5.

As an example for the timing of the experiment the measurement for RIN at $1f_{het}$ can be found in Figure 6.3. After this block, the heterodyne frequency of the phasemeter is switched to $2\,kHz$ by changing the Lookup Table (LUT), see Figure 6.4.
Then, to test the system, the heterodyne frequency of the laser module is set to $2\,kHz$, this changes the frequency difference between the two beams. After this, heterodyne frequency of the laser module is changed back to the nominal $1\,kHz$, since the measurement should be performed under standard operating conditions.

		#	Activity	Sequence ref.	Notes	Duration
DOY	Time		SAVED STACK: "191_Part1_IDL_1kHz" (64 commands)			3:32:07
192	0:00:01	1	Set DMU_LA_HK pkt @ 1Hz	LSEF130A	(SID=20)	
192	0:00:10	2	Stop laser control loops	SYEF140A	(LOEF239A)	3min
192	0:02:50	3	Allocate TM(128,4) to Science Store Set TM(128,4) SID=9 "DMU_RawSci_RT_0009_R_PMAB"	SYEF140A LOEF424M	(CHEF912C) LSC90020	
192	0:02:55	4	**Switch REF Beam and REF Pstab OFF**	SYEF140A	(step 4 start)	10sec
		5	WAIT 30 mins			30min
192	0:33:07	6	Record raw phasemeter channel [R,A,A] 100Hz 2 mins in IDL		(Channel ID = 12)	23min
192	0:55:09	7	Set TM(128,4) SID=9 "DMU_RawSci_RT_0009_R_PMAB"			2sec
192	0:55:11	8	**Switch MEAS Pstab OFF**	LLC10901		10sec
192		9	WAIT 30 mins			30min
192	1:25:18	10	Record raw phasemeter channel [R,A,A] 100Hz 2 mins in IDL		(Channel ID = 12)	23min
192	1:47:20	11	Set TM(128,4) SID=9 "DMU_RawSci_RT_0009_R_PMAB"			2sec
192	1:47:22	12	**Switch MEAS Beam OFF; REF Beam and REF Pstab ON**	LLC10901	Vref=2.33V	20sec
192		13	WAIT 30 mins			30min
192	2:17:39	14	Record raw phasemeter channel [R,A,A] 100Hz 2 mins in IDL		(Channel ID = 12)	23min
192	2:39:41	15	Set TM(128,4) SID=9 "DMU_RawSci_RT_0009_R_PMAB"			2sec
192	2:39:43	16	**Switch REF Pstab OFF**	LLC10901		10sec
192		17	WAIT 30 mins			30min
192	3:09:50	18	Record raw phasemeter channel [R,A,A] 100Hz 2 mins in IDL		(Channel ID = 12)	23min
192	3:31:52	19	Deallocate TM(128,4) from Science Store	SYEF140A	(step 9)	
192	3:31:56	20	**Switch REF Beam OFF**	SYEF140A		3min
192	3:32:01	21	Set DMU_LA_HK pkt @ 1/600Hz	LSEF130A	(SID=20)	

Figure 6.3.: This table shows the overview of the commanding for the RIN direct measurement at $1f_{het}$. Recorded were the sine, cosine and dc component of the PDR_AA quadrant. Printed in bold letters are the switches between measurement beam and reference beam and the status of the amplitude stabilisation. After this block the heterodyne frequency was changed to $2\,kHz$; and the measurement was repeated. Then the heterodyne frequency was switched back to the nominal $1\,kHz$.

DOY	Time		SAVED STACK: "191_Part2_Set2kHz" (1110 commands)			1:00:00
192	14:53:56	22	Set PM HK packets @ 1Hz	SYEF140A	(SID=10, SID=11)	1min
192	14:54:56	23	Stop OMS Processing (and Disable OPD)	LOEF209A	(OPD loop already stopped)	
192	15:00:56	-	Set DMU_LA_Ctl_HK_SID packet @ 1/5Hz	LOEF130A	(SID=21)	
192	15:08:55	24	Set DMU to Configuration Mode	LSEF108A		
192	15:09:25	25	Set both Phase Meters to Configuration Mode	LOEF122B		
192	15:10:23	26	**Write LUT to DMU RAM**	**LOEF141A (saved stacks)**	**2x 500 commands PMA_2kHz_LUT_RT PMB_2kHz_LUT_RT**	
192	15:28:17	27	**Transfer LUTs to PMs**	**LOEF126A**		
192	15:30:11	28	**Verify PM LUTs**	**LOEF132A, B**		
192	15:32:58	29	Both PMs to Run Mode	LOEF122C		
192	15:34:38		Set heterodyne frequency to 2kHz	LSEF250A		58mins
192	15:35:42		DMU to Operative Mode	LSEF104A		
192	15:36:15		Start OMS	LOEF200A		
192	15:37:11		Restore LA amplifier and stabiliser	LOEF117A		
192			**Sanity check psi-R/psi-F stability**		**Beams activated = sensible psi-R, psi-F**	
192	15:38:29	-	Set DFACS_HK_OPS packet @ 1Hz	CHEF901A	(SID=200)	
192	15:42:01		Switch off MEAS/REF beams	LLC10901		
192	15:44:37		Stop OMS Processing	LOEF209A		
192	15:46:20		Set DMU to Configuration Mode	LSEF108A		
192	15:46:56		Set heterodyne frequency to 1kHz	LSEF250A		
192	15:49:06	30	DMU to Operative Mode	LSEF104A		
192	15:49:45	31	Start OMS and Enable OPD	LOEF200A		
192	16:06:45	32	Set PM HK packets @ 1/600Hz	SYEF140A	(2xLSEF130A)	1min
192	16:07:37	-	Set DFACS_HK_OPS packet @ 1/30Hz	CHEF901A	(SID=200)	
192	16:07:48	-	Set DMU_LA_Ctl_HK_SID packet @ 1/600Hz	LOEF130A	(SID=21)	

Figure 6.4.: Shown here are the commands to switch the heterodyne frequency of the phasemeter from 1 kHz to 2 kHz to allow a direct RIN measurement at $2f_{het}$. By changing the PM Look-up-table (LUT) the processing of the phasemeter is changed to measure at the new heterodyne frequency. The frequency difference between the two beams is changed back to the original 1 kHz at 15:46:56.

6.2. First RIN subtraction experiment
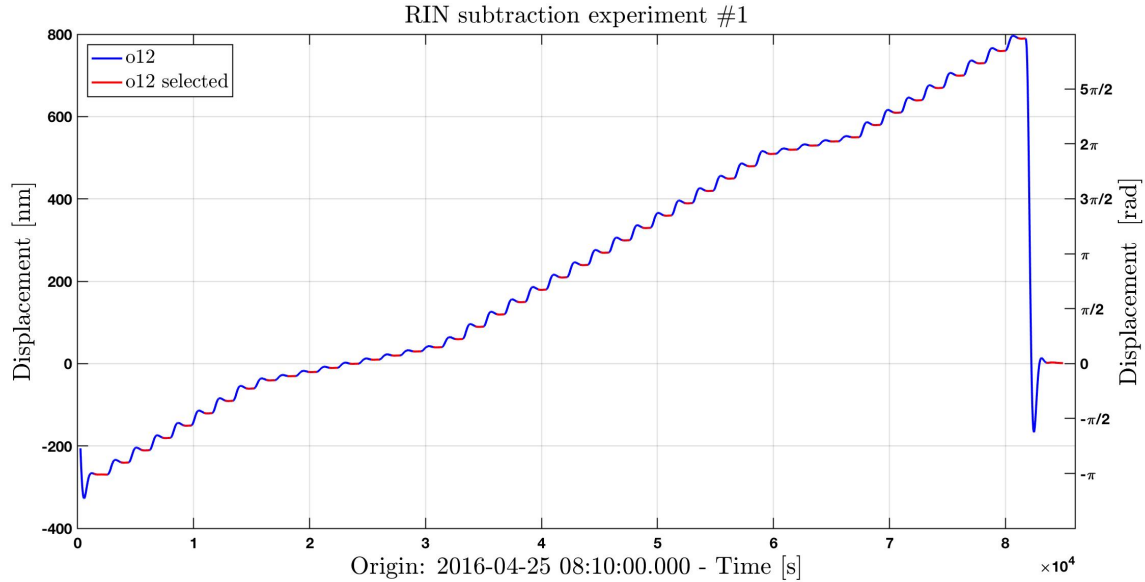
Figure 6.5.: This plot shows the measurement of the TM position with the o12 signal during the first RIN subtraction experiment. Highlighted in red are the segments selected for analysis. At the start of the experiment TM2 is moved to an offset of $-300\,$nm, and is then moved in steps to an offset of $800\,$nm. At the end the TM is moved back to the nominal zero position. A TM offset of $532\,$nm corresponds to a phase difference between the two interferometers of 2π. This plot was already published in [83] and [84].

In this section the results of the first in-flight RIN subtraction experiment are shown. As described in Section 6.1.2 TM2 is moved to an initial offset of $-300\,$nm, and then moved in steps up to a TM offset of $800\,$nm. The o12 time series of this experiment can be seen in Figure 6.5. For each step a timespan is selected where the TM is sufficiently stable, shown here in red.

For each of the steps the mean TM position and the mean phase noise level are calculated. The error on the TM position is calculated from the scatter of the data points. The main contribution of this error is the remaining motion of the TM after it is moved to the new position, and has not yet settled at the desired offset. In the segments selected for analysis the TM moves by less than $2\,$nm.

At each TM position the mean phase noise level of a specific frequency band is calculated. To select the frequency band for analysis a spectrum over the whole measurement duration is made, the initial and final big steps are removed. For this spectrum a BH92 window with an overlap of 50% is used on a data stretch of 10^3 samples, which corresponds to segments of 100 seconds with a sampling frequency of $10\,$Hz. This spectrum can be seen in Figure 6.6, selected for analysis are bands between the peaks, see Table 6.2. The peak at $70\,$mHz and the peaks at multiples of $1\,$Hz are known from other measurements. The most likely source for the peaks at $n\,$Hz is the Puls Per Second timing (PPS), which couples electrically to all interferometers [88].

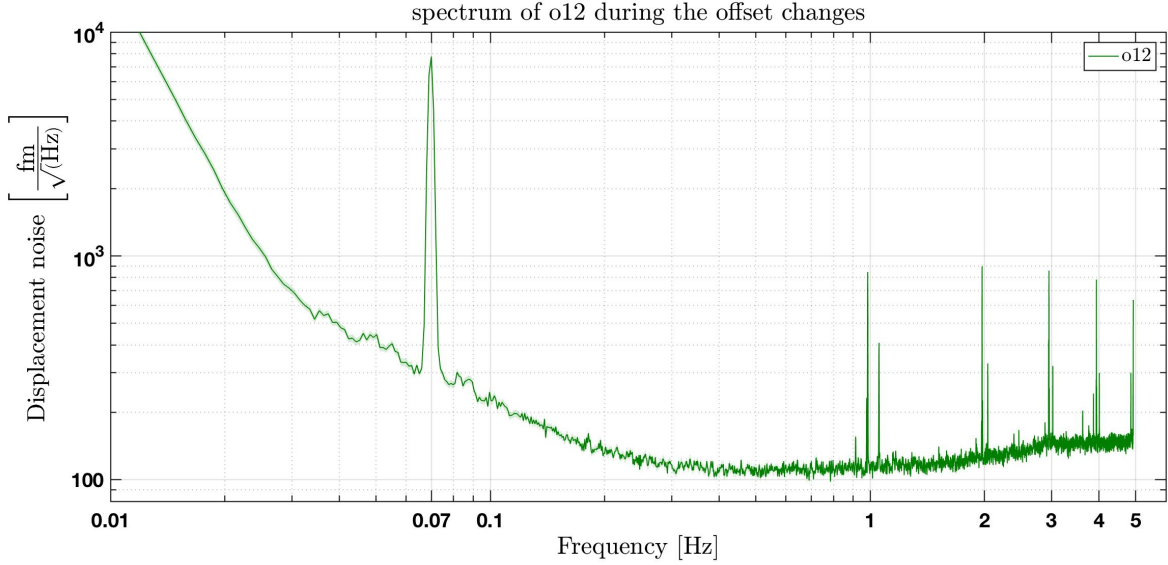**Figure 6.6.:** This is an amplitude noise spectrum over the full measurement duration, without the bigger offsets at the start and end. To calculate this spectrum the measurement is cut into pieces of a length of 1000 samples, with an overlap of 50% and a Blackman-Harris window BH92.

Peak [Hz]	Band [Hz]
0.06991	
0.9846	0.6 to 0.9
1.055	1.1 to 1.8
1.969	2.2 to 2.8
2.954	3.1 to 3.8
3,938	4.1 to 4.7
4.923	

Table 6.1.: Shown here are the frequency bands for which the mean noise at every TM offset is calculated. From these mean noise levels the contribution of RIN to the phase measurement can be calculated with a fit to the measured noise shape.

Frequency noise is a contribution to the noise floor between $0.2\,\mathrm{Hz}$ and $1\,\mathrm{Hz}$ [41][19]. In this experiment the frequency interferometer data was downloaded at a sampling frequency of $10\,\mathrm{Hz}$. This allows the subtraction of frequency noise, as was shown in Section 3.2.1. The mean noise for each step can be compared to the mean noise without subtraction, since RIN is dominant for most of the TM offsets the frequency noise contribution is not significant.

In Figure 6.7 example spectra for some TM offsets are shown, these are the result of averaging of the spectra of the segments of one step. From the spectrum of each segment the frequency band selected is cut, and its mean noise value is calculated.

Due to the lower number of averages in the calculation of the power spectral density the noisePower function of LTPDA is used to calculate the mean noise level at each step. This the first method to calculate the mean noise level as shown in Section 4.5.3 in the description of the measurement of the RIN level. In this function the time series of one step is cut into smaller segments, a spectrum is calculated for each. A segment length of 500 data points is used, with a 50% overlap, as before a Blackman-Harris window BH92 is used. To remove lower frequency effects the drift of each segment is subtracted with a linear fit. The minimum number of segments per step is 27. For some of the steps a longer timespan of data is selected for analysis, which leads to a higher number of measured mean noise levels.

The time series of the mean noise levels can be seen in Figure 6.8, an example step with the mean noise of individual segments is shown in Figure 6.9. The data points further than a set threshold away from the median value of the noise level at its TM position are excluded from the analysis to prevent glitches and random events to influence the noise curve. Here a
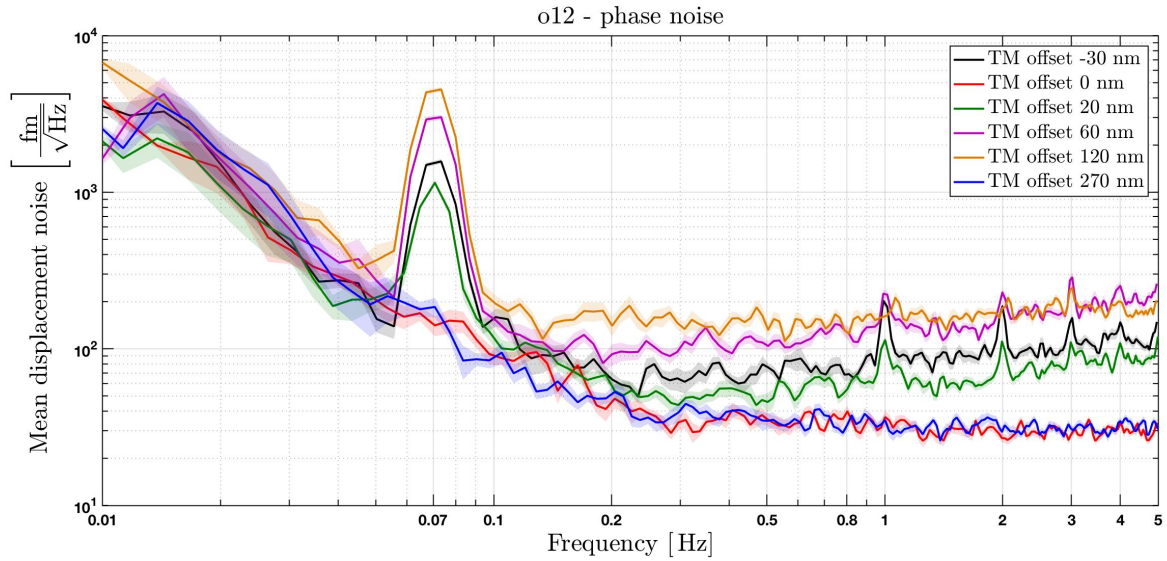
Figure 6.7.: Shown here are the amplitude noise spectra for a selection of TM offsets. The change in noise for the different positions is visible, with a rise in noise to higher frequencies. Used here to calculate the spectrum is the lpsd function, with a BH92 window and an overlap of 50 %. In this section the noise in the frequency band between 0.6Hz and 0.9Hz is analysed, higher frequencies are analysed in Section 6.4.

threshold of 2.5 is chosen. This means that data points which have mean a noise level with a factor of 2.5 higher than the median of this TM offset are removed. In this experiment 3 points are removed from the analysis, one of which is visible in Figure 6.9.

The mean phase noise of each TM offset is calculated by taking the mean of the mean noise of the shorter segments of each step, the error of the mean phase noise level is calculated from the distribution of the individual noise levels, see Appendix A.10.
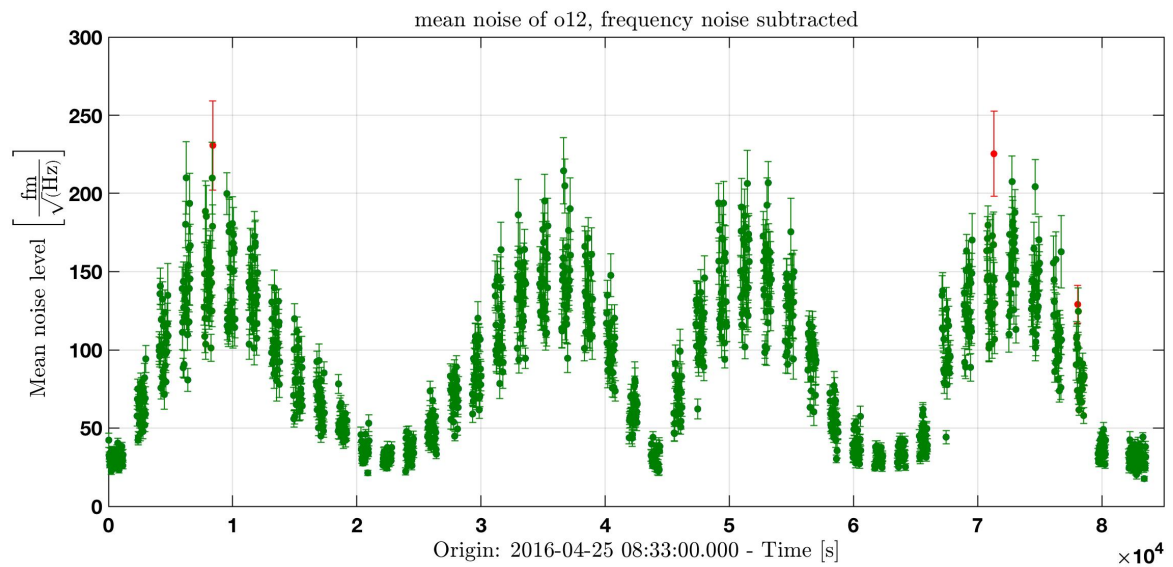
Figure 6.8.: Shown in this plot is the mean phase noise calculated between $0.3\,\mathrm{Hz}$ and $0.9\,\mathrm{Hz}$ over the duration of the experiment. The rise and fall of the noise as the TM offset changes is visible, the shape is irregular since the TM step size is not always the same. Marked in red are the data points removed from the analysis.
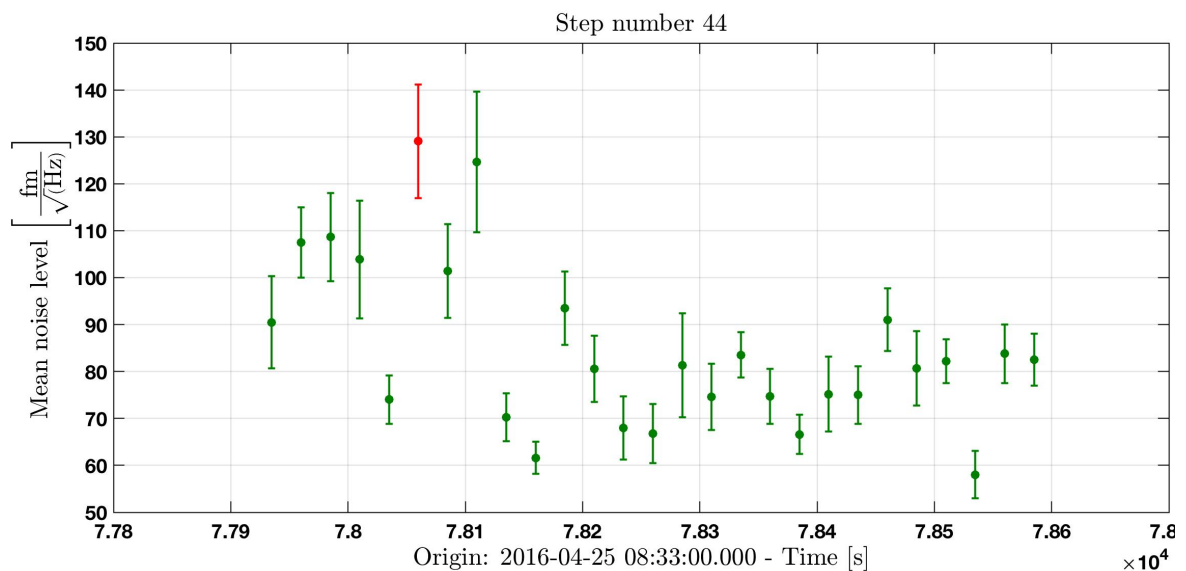
Figure 6.9.: These are the calculated mean noise levels of the individual segments for one step. The error on these values is calculated from the distribution of the points in the selected frequency band. For the final result the mean value of these noise levels is calculated, its error is calculated from the distribution of points. In this step the outlier, in red, is excluded from further analysis. This is step number 44, from 2016-04-26 06:11:30.000 UTC to 2016-04-26 06:23:30.000 UTC, at a TM offset of $760\,\mathrm{nm}$.

6.2.1. Results

From the mean noise of each step and the mean TM position per step the noise over position can be constructed; this is the main subject of investigation of this experiment. The plot of the noise over TM position can be found in Figure 6.10. The contributions of RIN at $1f_{het}$ and $2f_{het}$ can be fitted with the known noise shape. The subtraction of RIN for different TM offsets was calculated in Section 3.4, and already shown for the laboratory setup in Section 5.3.

From the measured noise over position it can immediately be seen that the main contribution must be RIN at $2f_{het}$. This RIN can be described with the function

$$\hat{o}12^{(2)^2} = \left(r2G \cdot \sin\left(\frac{4\pi\cos\alpha}{\lambda}\, o12\right) \right)^2, \qquad \left[\frac{fm^2}{Hz}\right] \qquad (6.1)$$

The function is fitted to the measured noise levels with a Markov-Chain-Monte-Carlo Algorithm (MCMC), which is implemented in LTPDA. The parameter r2G is the result of the fit, from this fitted peak phase noise the RIN level can be calculated for correlated and uncorrelated noise with

$$\hat{r}^{(2)}_{correlated} = \frac{1}{\sqrt{2}} \cdot \frac{4\pi\cos(\alpha)}{\lambda}\, r2G, \qquad \left[\frac{1}{\sqrt{Hz}}\right] \qquad (6.2)$$

$$\hat{r}^{(2)}_{uncorrelated} = \frac{4\pi\cos(\alpha)}{\lambda}\, r2G. \qquad \left[\frac{1}{\sqrt{Hz}}\right] \qquad (6.3)$$

In the flight model the angle of the beam on the TM surface is $\alpha = 4.5°$. Since both beams have the same laser as origin the RIN in the measurement beam and reference beam would be expected to be correlated, however it is not clear how the AOMs and the fibres change the correlation. Therefore, the RIN level for both correlated and uncorrelated RIN will be computed. Likely is a combination of the two.

For a noise measurement between $0.6\,Hz$ and $0.9\,Hz$ the fit produces a result for the $2f_{het}$ RIN contribution of $r2G = (152.35 \pm 1.367)\frac{fm}{\sqrt{Hz}}$, and a sensing noise floor of $nf = (35.312 \pm 0.509)\frac{fm}{\sqrt{Hz}}$. Under the assumption that the RIN amplitude is at the same level in both beams, this phase noise corresponds to a RIN level of one beam of $\hat{r}^{(2)}_{correlated} = (1.27 \pm 0.01)\frac{10^{-6}}{\sqrt{Hz}}$ for correlated RIN and $\hat{r}^{(2)}_{uncorrelated} = (1.79 \pm 0.02)\frac{10^{-6}}{\sqrt{Hz}}$ for uncorrelated RIN.

These results, and additional noise and RIN levels for higher frequencies, can be found in Table 6.2; the covariance of the fit parameters can be found in Appendix A.21. A description of the RIN shape at higher frequencies can be found in Section 6.4.

A first fit ot the measurement included RIN at $1f_{het}$ in the fit function, but the calculated contribution is smaller than its error with $r1G = (2.2 \pm 32.3)\frac{fm}{\sqrt{Hz}}$. Therefore the $1f_{het}$ term is excluded from the final fit function. In the development of this analysis the laser wavelength λ and a possible offset of the point of lowest noise from the optical zero were included, for both the known values were within the errors of the fitted value. In the final fit function these parameters are set to $\lambda = 1064\,nm$ and $x_{offset} = 0\,nm$.

In this measurement no contribution of $1f_{het}$ RIN could be found. One reason might be that this noise is subtracted with balanced detection; the flight model OMS was constructed very carefully, and the A and B port of every interferometer are well matched. In addition, the contribution of $1f_{het}$ RIN depends on the matching of the reference and measurement beam. The contrast in most experiments is very high, which reduces the amount of $1f_{het}$ RIN present. In this experiment the contrast of the X_{12} interferometer is 0.98; the contrast of X_R was not recorded. In comparison contrasts of the ground setup are typically between 0.8 and 0.85.

In the flight OMS $1f_{het}$ RIN is also actively suppressed with the fast amplitude control loop. The two beams are measured individually on the PDA diodes on the optical bench. The noise
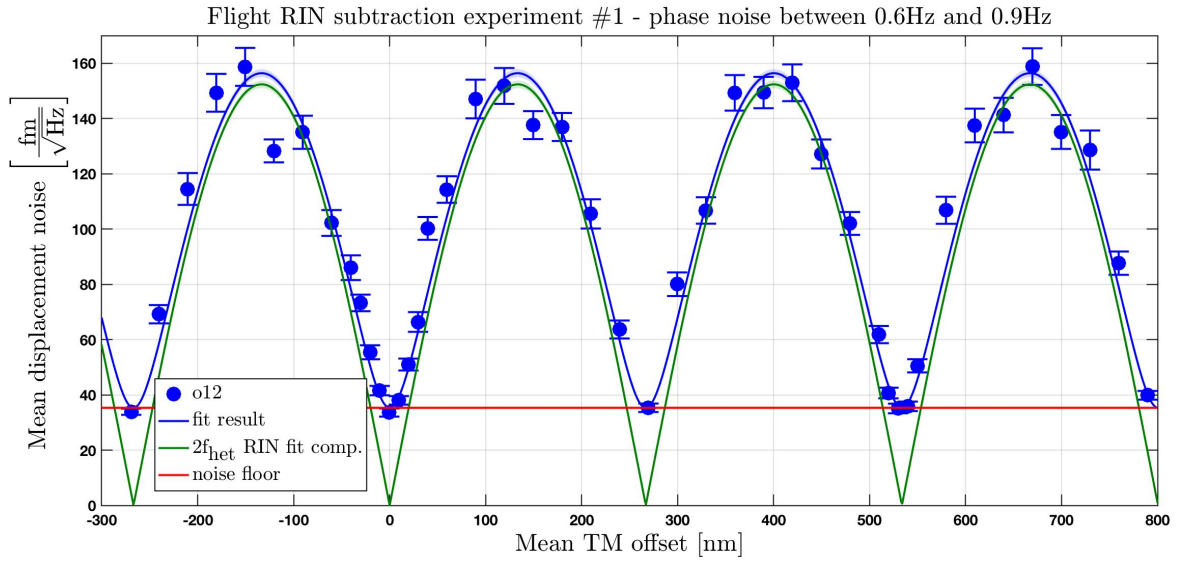
Figure 6.10.: Shown here is the measured displacement noise between 0.6 Hz and 0.9 Hz for each TM position. The noise shape is consistent with the subtraction of phase noise due to $2f_{het}$ RIN. Shown in blue is the fit to the measured data, the $2f_{het}$ RIN fit component is shown in green. The fitted noise floor during this measurement, shown in red, is consistent with other measurements. In Table 6.2 the fitted values can be found.

around $1f_{het}$ is isolated and used as input on the laser amplitude control of the AOM drivers of the flight model. In the laboratory experiments the equivalence of this input is used to inject RIN. While it would have been possible to turn the stabilisation off for an attempt to measure position dependency of the $1f_{het}$ RIN contribution this experiment was not done due to time constraints.

6.3. Second RIN subtraction experiment

The second RIN subtraction experiment was performed on 2017-02-02. TM offsets were selected to investigate around the optical zero, around maximum noise and around the first noise minimum. Between these areas TM2 is moved in bigger steps. In the first RIN subtraction experiment no contribution of RIN at the heterodyne frequency could be found, to find the contribution of $1f_{het}$ RIN balanced detection is turned off for 25 minutes at each offset. A plot of the time series of the o12 signal with the TM offset changes of this experiment can be found in Figure 6.11. At each offset a timespan where the TM position is stable is selected for analysis, shown in red is the timespan with balanced detection on and in green without. The uncertainty on the TM position in later calculations originates from the drift, the measurement error is small compared to the range of TM offsets. A typical TM drift at each offset is below 0.5 nm, while a typical TM step size is between 1 nm and 15 nm, with one big step from an offset of 20 nm to 100 nm. A list of the implemented TM offsets can be found in Appendix A.18.

For the noise level with balanced detection it is expected for TM offsets of 0 nm and 266 nm that the sensing noise level will be similar, whereas for a single diode the noise level of 266 nm offset should be higher than 0 nm due to the $1f_{het}$ RIN contribution.

However, the noise level near zero TM offset is higher than expected due to other noise sources present at the start of the investigation. This experiment was scheduled as first item after station keeping, after the switch from capacitive sensing to the OMS measurement the system appears to be not stable yet. This higher noise is probably caused by instabilities in the laser power and an increase in frequency noise. In Figure 6.12 the TM steps are shown together with the Frequency control loop input and a measurement of the laser power. A description of the laser frequency noise states can be found here [41], and in a paper currently in preparation [59]. It is likely that the RIN at $1f_{het}$ and $2f_{het}$ is also increased when the laser is unstable. Due to this the start time of the experiment was delayed, but the noise is still higher for the steps around 0 nm TM offset. The last steps were cut off due to this higher noise as well, since the experiment start time was moved and the end time was kept the same.
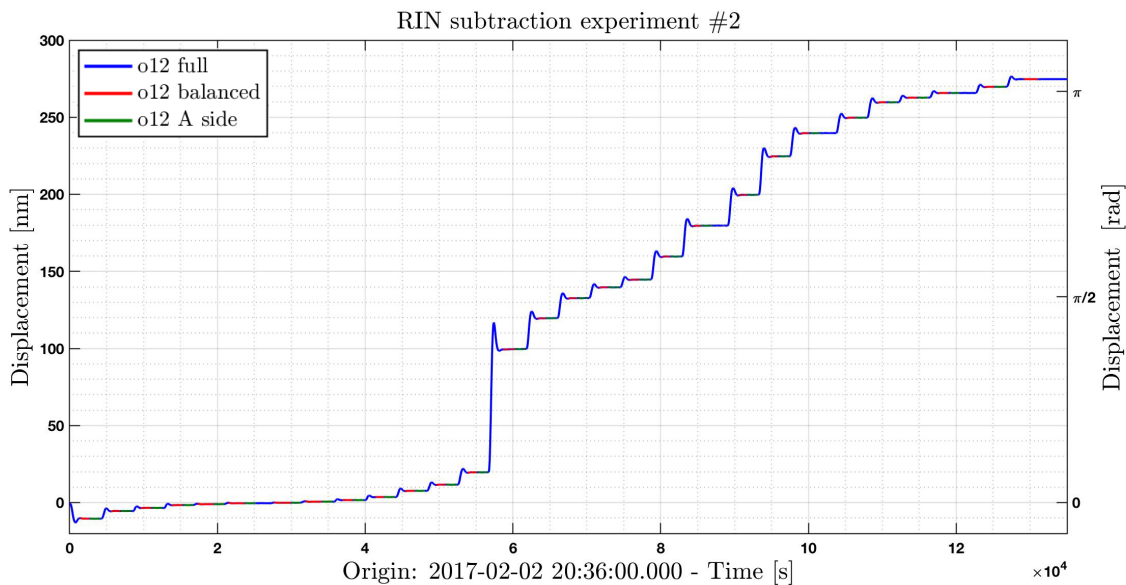
Figure 6.11.: Shown here is the time series of the o12 signal of the second RIN subtraction experiment. At each TM offset position the noise is measured with balanced detection (red) and with only the A side of the interferometers (green). The timespans selected for analysis are highlighted. This plot was already published in [83] and [84].
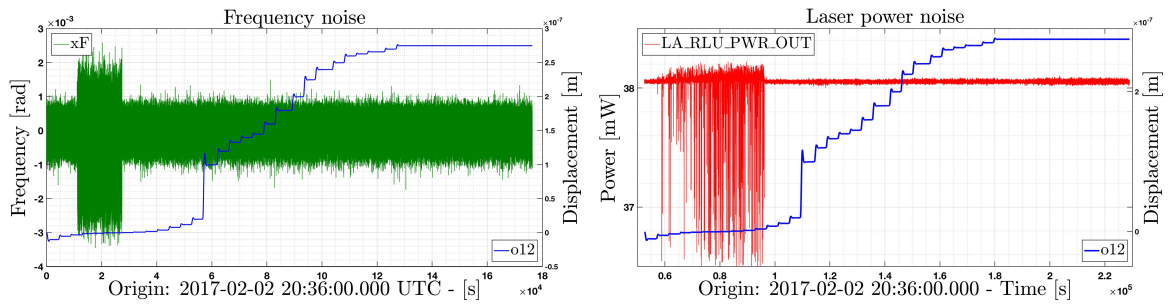
Figure 6.12.: Shown here is the time series of the TM steps measured with the o12 signal (blue). At the start of this experiment the system experienced an increase in frequency noise (green, shown on the left) and laser power noise (red, shown on the right). One part of this experiment is a comparison of the phase noise around 0 nm and 266 nm TM offset for a measurement of the contribution of $1f_{het}$ RIN. Due to these other noise contributions this analysis could not be done.
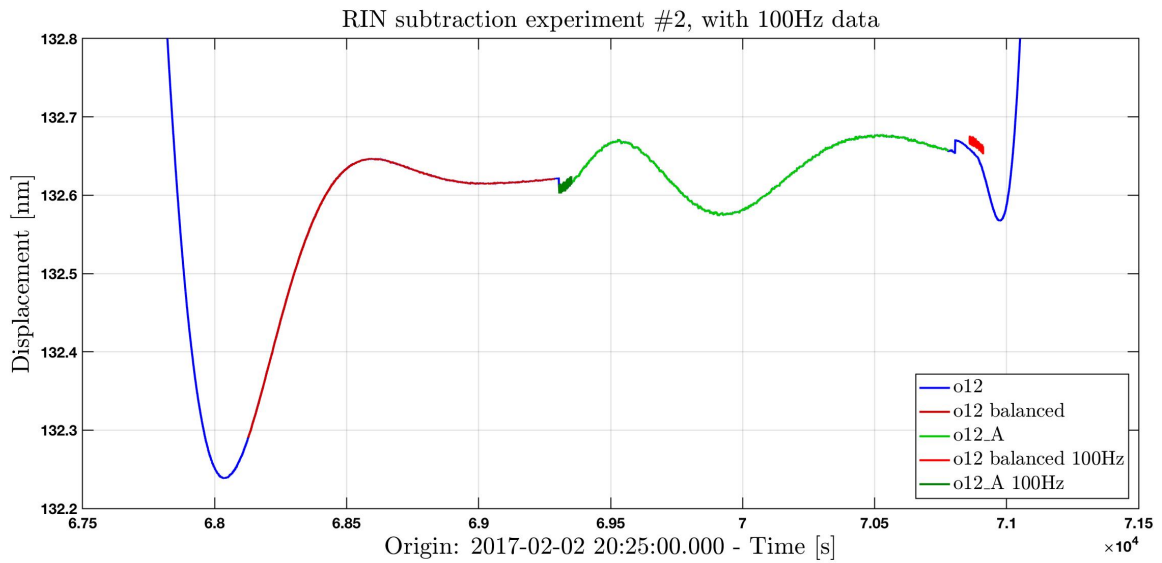
Figure 6.13.: Shown here is the o12 measurement at a TM offset of 133 nm. The TM takes some time to stabilise at the new offset. During TM motion the phasemeter is set to regular balanced detection, the timespan selected for analysis is shown in dark red. Then the phasemeter is switched to the A side, shown in green. The shorter light green timespan shows data recorded at 100 Hz. After the phasemeter is switched back to balanced detection again 100 Hz data is recorded, shown in light red. Then the TM is moved to the next offset. This plot was already published in [83] and [84].
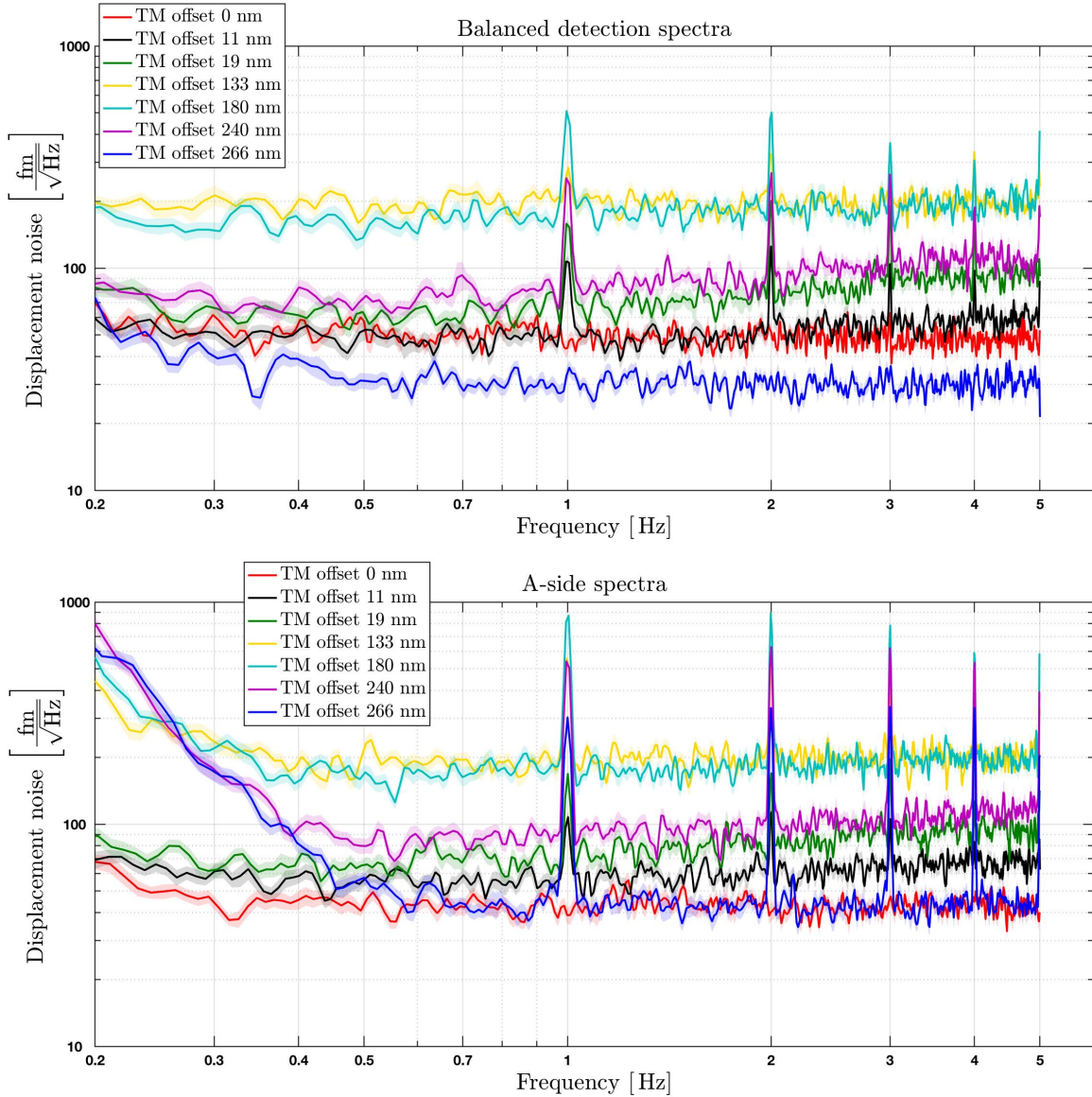
Figure 6.14.: These measurements are taken with balanced detection on (top) and with the A side (bottom); with the frequency noise subtracted. The amplitude noise spectra are calculated with 300 samples in each FFT, with an overlap of 50%, and a Blackman-Harris window. Test mass offsets between 0 nm and 266 nm are chosen as example spectra. These spectra were already published in [83] and [84].

For some TM offsets the o12, φ_R and xF signals are recorded at 100 Hz, for both the balanced detection measurement and the A side measurement. Due to on-board limitations in the handling of the relatively large file sizes the IDL 100 Hz data for balanced detection is not recorded in the same timespan as the 10 Hz data of this step. An example offset where high frequency data was recorded can be found in Figure 6.13. There the TM offset is at 133 nm, which corresponds to a phase difference of $\frac{\pi}{2}$ between measurement and reference signal. An investigation of this data can be found in section 6.4.

The analysis of the noise for each offset is the same as in the first experiment. Example spectra can be found in Figure 6.14.

6.3.1. Results

As in the analysis of the first RIN subtraction experiment the expected contribution of RIN together with the noise floor is fitted to the measured noise shape. In Figure 6.15 the measured phase noise levels for both balanced detection and the single-diode signal measured between 0.6 Hz and 0.9 Hz can be seen, together with the fit results to the measured noise.

The fitted peak phase noise, and the RIN levels calculated from this phase noise, can be found in Table 6.2. Shown there are also the results of the mean noise calculated at higher frequency, these will be discussed in more detail in Section 6.4.

For the frequency band between 0.6 Hz to 0.9 Hz the fit result for the phase noise in the o12 signal is $r2G = (194.24 \pm 2.132)\frac{\text{fm}}{\sqrt{\text{Hz}}}$; this gives a RIN level of one beam of $\hat{r}^{(2)}_{\text{correlated}} = (1.62 \pm 0.02)\frac{10^{-6}}{\sqrt{\text{Hz}}}$ for correlated RIN and $\hat{r}^{(2)}_{\text{uncorrelated}} = (2.29 \pm 0.03)\frac{10^{-6}}{\sqrt{\text{Hz}}}$ for uncorrelated RIN.

In the single-diode signal o12_A the fit result for the peak phase noise is $r2G = (192.53 \pm 2.040)\frac{\text{fm}}{\sqrt{\text{Hz}}}$; from this the RIN levels of $\hat{r}^{(2)}_{\text{correlated}} = (1.60 \pm 0.02)\frac{10^{-6}}{\sqrt{\text{Hz}}}$ for correlated RIN and $\hat{r}^{(2)}_{\text{uncorrelated}} = (2.27 \pm 0.02)\frac{10^{-6}}{\sqrt{\text{Hz}}}$ for uncorrelated RIN can be calculated.

As was already mentioned, the sensing noise at the start of the experiment is increased due to other noise effects; the measurements removed from the fit are coloured in grey. One of the intended purposes of this experiment is a comparison of the noise floor between a TM offset of 0 rad and π rad to calculate the contribution of RIN at $1f_{\text{het}}$ to the phase noise. Due to this noise increase this comparison is not possible.

In theory, a first estimation can be done by a comparison of the noise floor at π rad between the balanced and single diode signal, an increase of $\sqrt{2}$ is expected from the lower SNR ratio in the single-diode signal. When $\sqrt{2} \cdot \text{nf}_{\text{o12}} < \text{nf}_{\text{o12\_A}}$ the assumption can be made that the difference between the two is due to $1f_{\text{het}}$ RIN. Then, this $1f_{\text{het}}$ RIN contribution to the phase noise can be estimated by

$$r1G \approx \sqrt{2 \cdot \text{nf}_{\text{o12}}^2 - \text{nf}_{\text{o12\_A}}^2}. \tag{6.4}$$

From this the RIN level can be calculated using Equation 3.63. However, for the frequency band between 0.6 Hz and 0.9 Hz no such contribution can be found. The noise floor of the single-diode signal is at $\text{nf}_{\text{o12\_A}} = (48.715 \pm 0.646)\frac{\text{fm}}{\sqrt{\text{Hz}}}$, in the balanced signal the noise floor is $\text{nf}_{\text{o12}} = (35.522 \pm 0.487)\frac{\text{fm}}{\sqrt{\text{Hz}}}$. Since $35.522 \cdot \sqrt{2} \approx 50.236$ the assumption made above is not applicable.

The similarity between the balanced and single-diode noise is also reassuring, one of the reasons that both ports of the interferometer are included is redundancy. If one of the phasemeters or one of the diodes were to fail, the sensing noise at higher frequencies would still only increase by a factor $\sqrt{2}$.
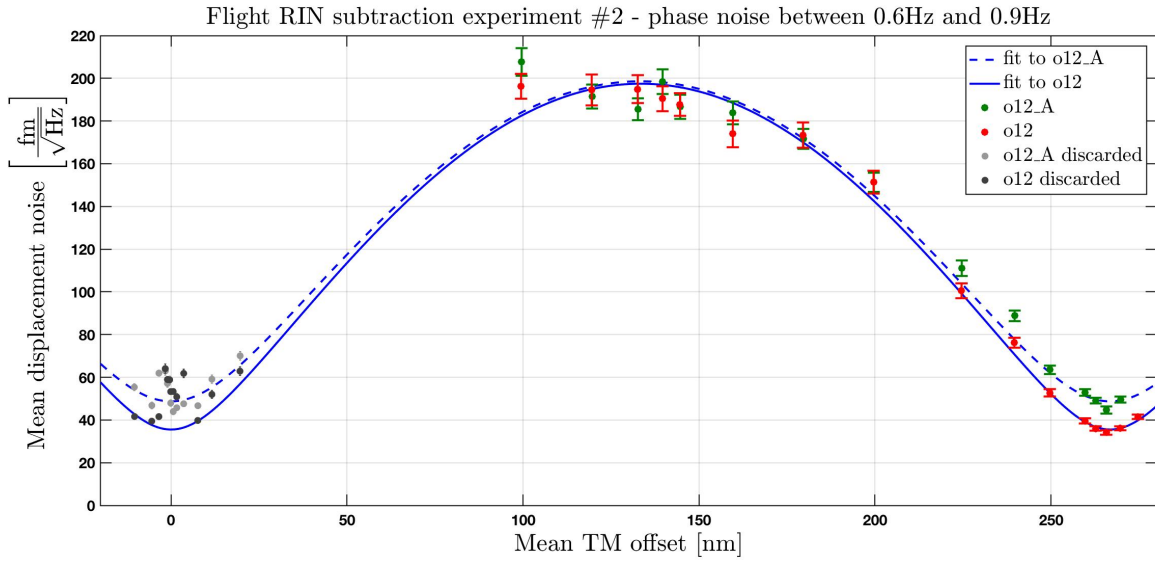
Figure 6.15.: Shown here is the mean noise between $0.6\,\mathrm{Hz}$ to $0.9\,\mathrm{Hz}$ for each step of the second RIN subtraction experiment. Due to the higher noise at the start of the experiment the TM offsets shown in grey are not used for the fit. The noise floor of the single-diode signal is $\sqrt{2}$ is higher than the balanced signal due to the lower SNR in o12_A; the contribution of $2\mathrm{f_{het}}$ is almost the same. The o12 result was already published in [84].

6.4. Higher frequencies in the RIN subtraction experiments

In the previous analysis the sensing noise for different TM positions in a frequency band between $0.6\,\mathrm{Hz}$ and $0.9\,\mathrm{Hz}$ was investigated, this section is concerned with the sensing noise floor at higher frequencies. In the first part of this section the same analysis as before is done for the frequency range between $1\,\mathrm{Hz}$ and $5\,\mathrm{Hz}$. Since the main investigations of other experiments concern the mHz range, this already counts as a high-frequency investigation.

In these investigations an increase in the sensing noise to higher frequencies is visible, from the known noise sources a white noise floor would be expected. To investigate if this increase is due to aliasing of unknown effects from a higher frequency to the sensing noise when the data is downsampled, the OMS interferometer signals were recorded at a higher sampling frequency. Due to on-board limitations data with a higher sampling rate can only be recorded for short periods of time. This data is then saved in a special IDL package and downloaded to earth. When this data arrives it has to be processed differently to the other OMS data. In normal circumstances the $10\,\mathrm{Hz}$ data is adjusted for small sample slips and the individual channels are resampled, so that the timestamps of the data sets are the same. This higher frequency IDL data arrives with a label that displays a sampling frequency of $10\,\mathrm{Hz}$, and a start time which is the time the recorded data was handed over to be saved. Therefore, in the preprocessing of this data the sampling frequency has to be manually changed to $100\,\mathrm{Hz}$, and the start time has to be set to the start of the data recording, which can be found in the telecommand history (TC history). The TC history is a record of the performed actions of the satellite.

6.4.1. RIN subtraction and aliasing
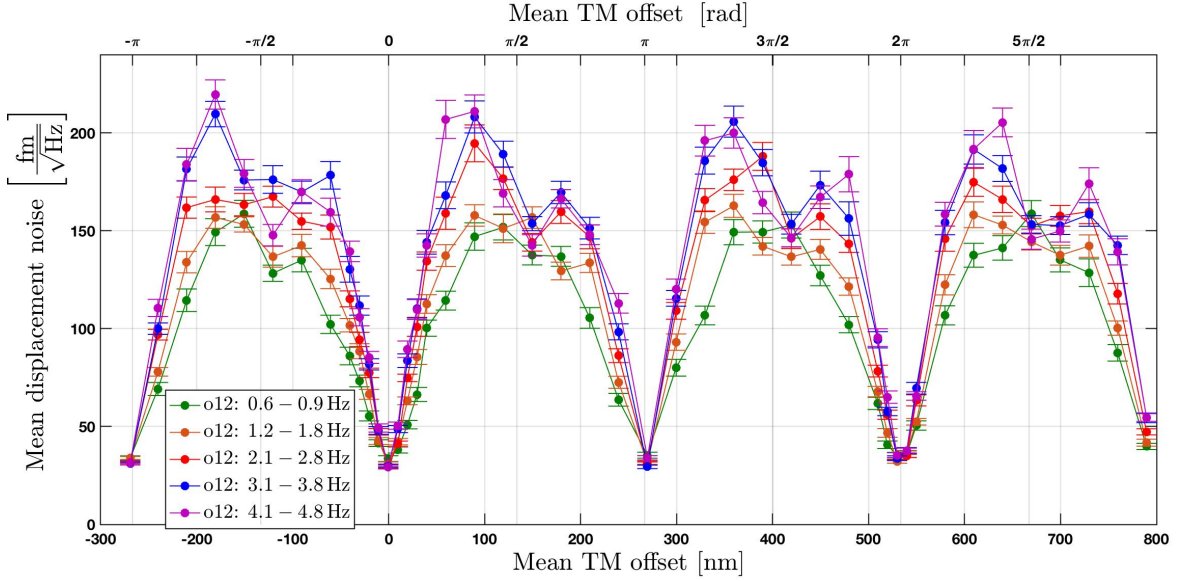
Figure 6.16.: This plot shows the average noise level of o12 in the higher frequency bands over the mean TM offset for the first RIN subtraction experiment. The noise to higher frequencies shows additional structure, in addition to the phase noise shape as expected from the coupling of $2f_{het}$ RIN. The bottom x-axis shows the offset of the TM from its nominal position in the optical zero, the top x-axis shows the phase difference between the measurement and reference signal in radian.

In the initial analysis only the noise between $0.6\,Hz$ and $0.9\,Hz$ was the subject of the analysis. Now, the noise between the peaks at higher frequencies is analysed. The analysis is done in the same way as for previous results for both RIN subtraction experiments. The same timespans where the TM is stable are selected. For these the noise over time and position for the frequency bands shown in Table 6.2 is calculated.

The shape of the noise over TM position for the first experiment can be seen in Figure 6.16. The same analysis was done for noise spectra where the frequency noise was subtracted. The result is the same since frequency noise does not contribute significantly. The phase noise contribution of frequency noise decreases to higher frequencies, while the RIN contribution is increased for most of the TM offsets.

These noise measurements do not follow a clean $|\sin(2\varphi)|$ noise shape as expected from the coupling of $2f_{het}$ RIN, but have regular features. In addition to the expected noise increase a bigger noise increase is to the left of the expected maximum noise, and a smaller increase to the right. This structure is not symmetric around the optical zero. As these features repeat, there must be a regularity to their emergence. One possible cause could be small vector noise. The expected coupling of SVN to a subtracted interferometer signal was shown in Section 5.1.4 in the discussion of laboratory results. Since the phase of the reference interferometer is constant the combined SVN can be described as a constant offset due to the SVN of the X_R interferometer, and a phase dependant SVN contribution of the X_{12} interferometer. A fit to the measured noise shape with a fit function consisting of $2f_{het}$ RIN, SVN and the noise floor did not produce reasonable results.

Another reason could be a phase dependant subtraction of the noise around $10\,Hz$; which can be seen in the next section in Figures 6.18 and 6.20, where the phase is measured with

a sampling frequency of 100 Hz. This noise increase is most likely due to the the OPD loop. The investigation of the cause for these additional noise features is still ongoing, presented here are preliminary results.

In Figure 6.17 the phase noise over TM position is shown for the second step experiment, since the number of successful steps is smaller the same features are not easy to see here. As in the analysis of the mean noise in the lower frequency band the first few TM offsets are removed from the fit to the phase noise.

From the measured phase noise at higher frequencies of both experiments the mean phase noise r2G is calculated by the same fit. From this phase noise the RIN level can be calculated, the results for correlated and uncorrelated RIN for both balanced and single-diode signals can be found in Table 6.2. Due to the additional noise features the fit calculates a higher phase noise level, which subsequently leads to a higher calculated RIN contribution. For the overview of the measured RIN levels in Section 6.8 the value calculated for the phase noise between 0.6 Hz and 0.9 Hz is used.
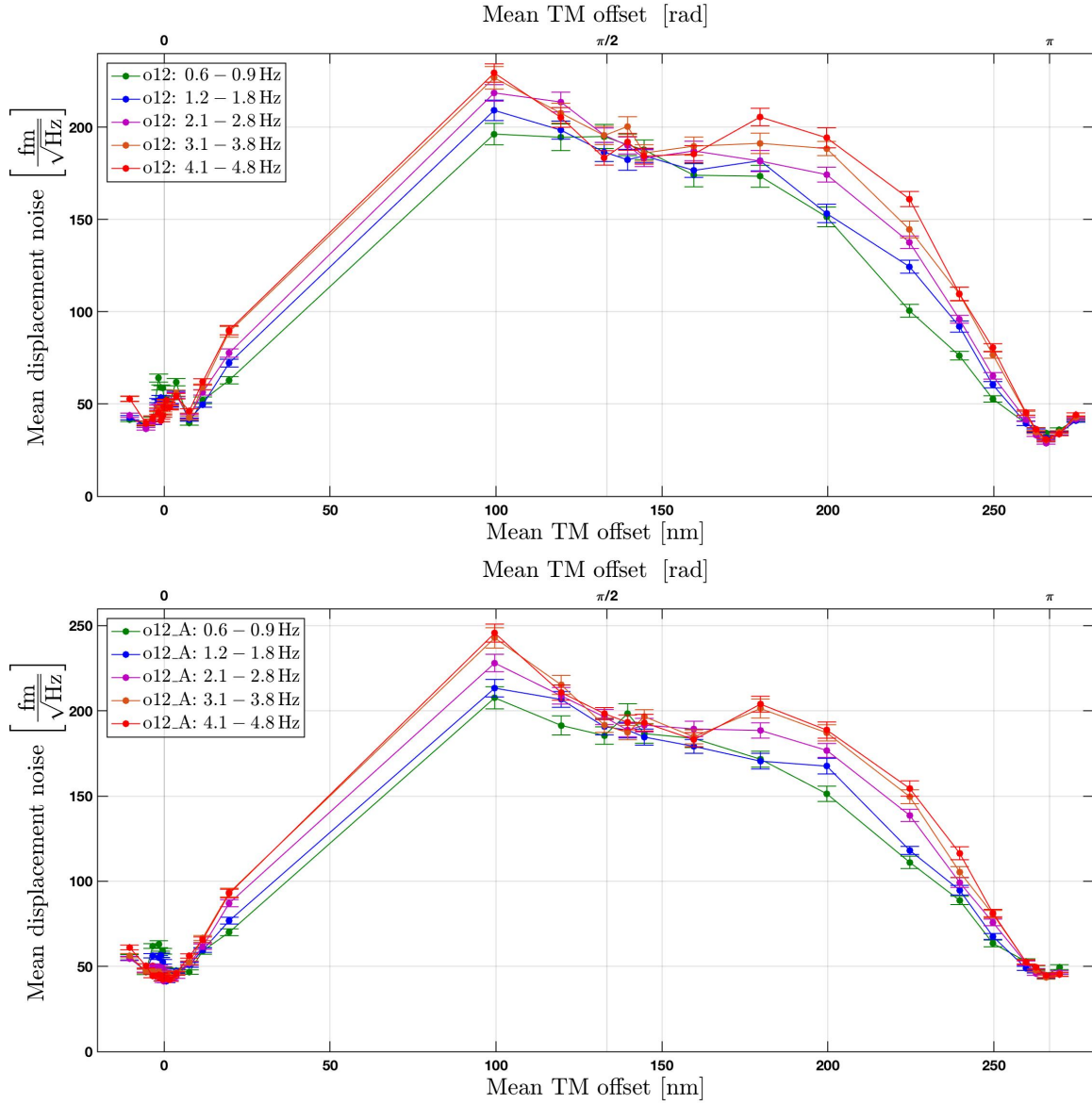
Figure 6.17.: These plots show the phase noise at the higher frequencies from the second RIN subtraction experiment; on the top with the balanced signal and on the bottom on the A side. The noise structures as in the first experiment are not as visible here due to the lower number of steps, however a small dip in the noise around a phase difference of $\frac{\pi}{2}$ is visible, in both the balanced and the single-diode noise with a similar shape.

6.4.2. 100 Hz data

For the TM offsets of 0 nm, 133 nm, 240 nm, 266 nm and 410 nm an additional measurement of the phase noise in o12 and o12__A with a sampling frequency of 100 Hz was implemented in the second RIN subtraction experiment. The noise at 410 nm was not measured. A selection of spectra of these measurements were already published in [83] and [84].

In Figure 6.18 the amplitude spectral density of both the balanced (red) and single-diode phase signal (green), with a sampling frequency of 100 Hz, at the TM offsets of 133 nm and 240 nm can be seen. These are shown together with the 10 Hz data from the same offset. As expected, the measured phase noise at the maximum of the RIN contribution at an offset of 133 nm is higher than the noise at an offset of 240 nm, which is near the minimum.
Visible in the plots of the balanced signal is a noise increase around 10 Hz, this additional noise has a higher amplitude for a TM offset of 240 nm than for 133 nm. This noise aliases down to the 10 Hz data, visible for example in the sensing noise difference between 3 Hz and 5 Hz at the 240 nm TM offset.

This effect is most likely caused by the OPD loop, the precise mechanism is still under investigation.[1] A time series of the reference interferometer measurement when the TM is at an offset of 266 nm can be seen in Figure 6.19. Visible there is an increase in lines for phase offsets further away from 0 nm. In another measurement a decrease in these lines when the phase moves closer to zero could be observed.
These spikes occur with a frequency of ≈ 10 Hz and are the cause for the noise increase around this frequency in the spectrum of the reference signal in Figure 6.18. During the TM offsets discussed before these spikes are present during the whole measurement duration at a similar level. Calibrated to displacement the OPD offset drifts between $2 \cdot 10^{-3}$ nm and $4 \cdot 10^{-3}$ nm.
The reference interferometer data is plotted in blue together with the o12 and o12__A spectra. It can be seen that the noise in xR is at a similar level for the 240 nm and 133 nm TM offset measurements. To show this noise in the same plot with the subtracted measurement the noise amplitude is divided by a factor 200.

Since the cause is the OPD loop this effect is common to all interferometers, and the subtraction of this noise depends on the phase difference between the two signals in complicated ways. With the data available, it can be see that in the 133 nm TM offset measurement this coupling is smaller than with 240 nm, these offsets are $\frac{\pi}{2}$ rad and 2.83 rad. At an offset of 266 nm, or π rad, this OPD noise is again subtracted, see Figure 6.20, in the A side signal. The balanced signal of this TM offset has a problem with the high-frequency data recording and it shows a higher sensing noise, a contribution due to this OPD loop effect is not visible. This noise is currently under investigation for a longer discussion on the changing noise floor over the mission duration [59].
As already mentioned, the lines in the spectra at regular 1 Hz intervals are most likely due to the Puls-Per-Second (PPS) timing, with these high-frequency data it can be seen that this effect extends also to higher frequencies.

---

[1]This effect is part of an ongoing investigation into the changing phase noise over the mission duration. This is a preliminary result from research together with Gerhard Heinzel, Martin Hewitson, David Robertson, Sarah Paczkowski, Brigitte Kaune, Michael Born and Lennart Wissel.
The source of the noise is most likely the noise of the OPD loop actuators. The level and frequency of this noise depends on the state of the loop (rate of phase change, phase offset between the beams), and couples to the phase of all interferometers. This phase noise is subtracted in the o12 signal, under some circumstances dependent on the actuator noise and the phase difference between the interferometers remaining noise is visible, see Figures 6.18 and 6.20. In the 10 Hz phase signals this OPD actuator noise contributes through aliasing, and might be responsible for the rise in the phase noise to higher frequencies.
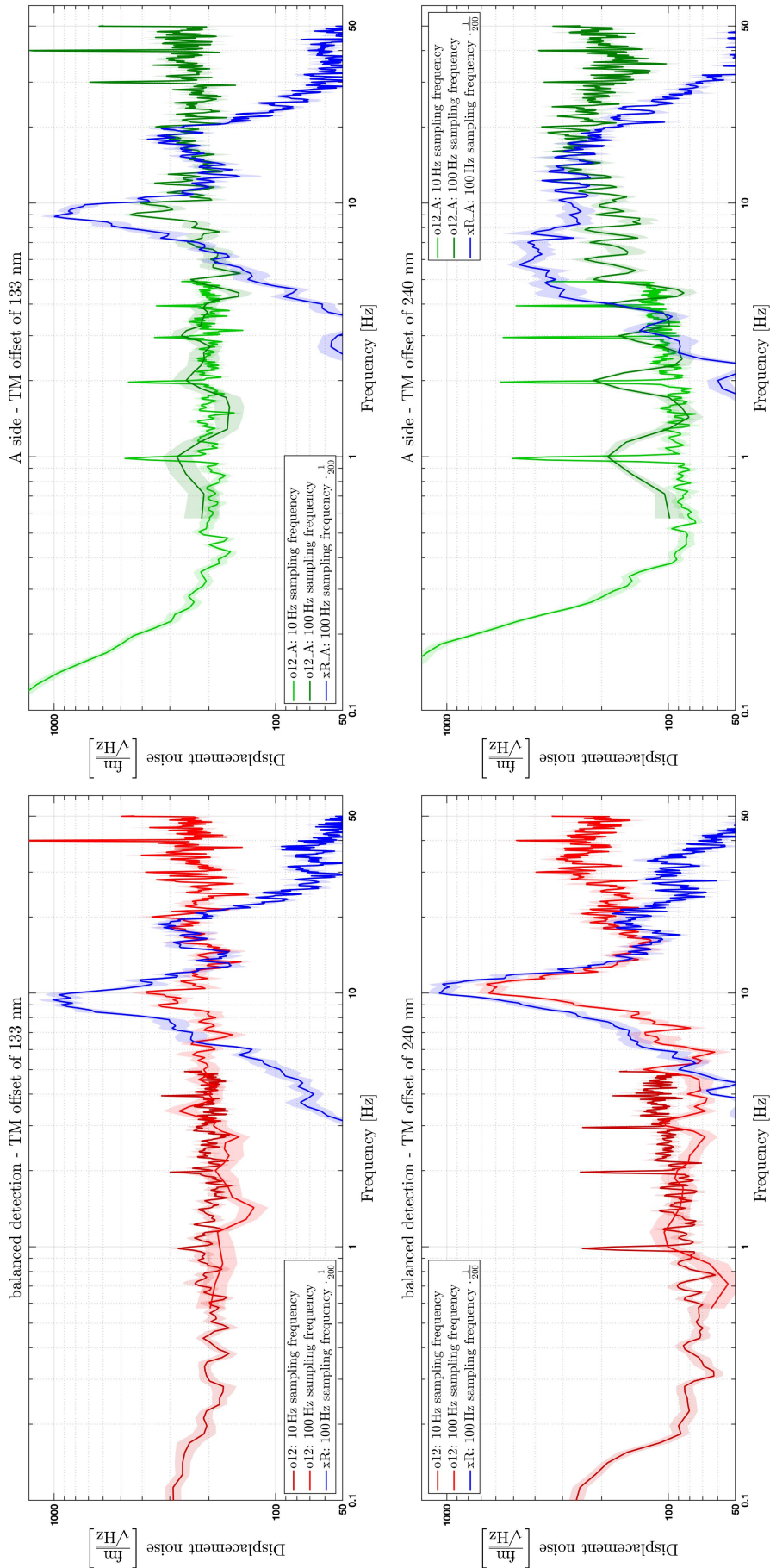
Figure 6.18.: These spectra are measured at a TM offset of 133 nm (top) and 240 nm (bottom). Shown in red is the measurement with balanced detection on, green is the measurement with balanced detection off. The spectra of 100 Hz data are calculated with 700 samples in each FFT, with an overlap of 50% and BH92 window; this leads to 13 averages. At a TM offset of 133 nm the maximum noise level for $2f_{het}$ RIN is expected, while for a TM offset of 240 nm this noise is expected to be near a minimum. Visible in both spectra are additional higher frequency effects, which alias down to the sensing noise in the 10 Hz measurement. Shown in blue is the amplitude noise of the xR signal, its noise amplitude is decreased with a factor 200 to show it in the same plot.
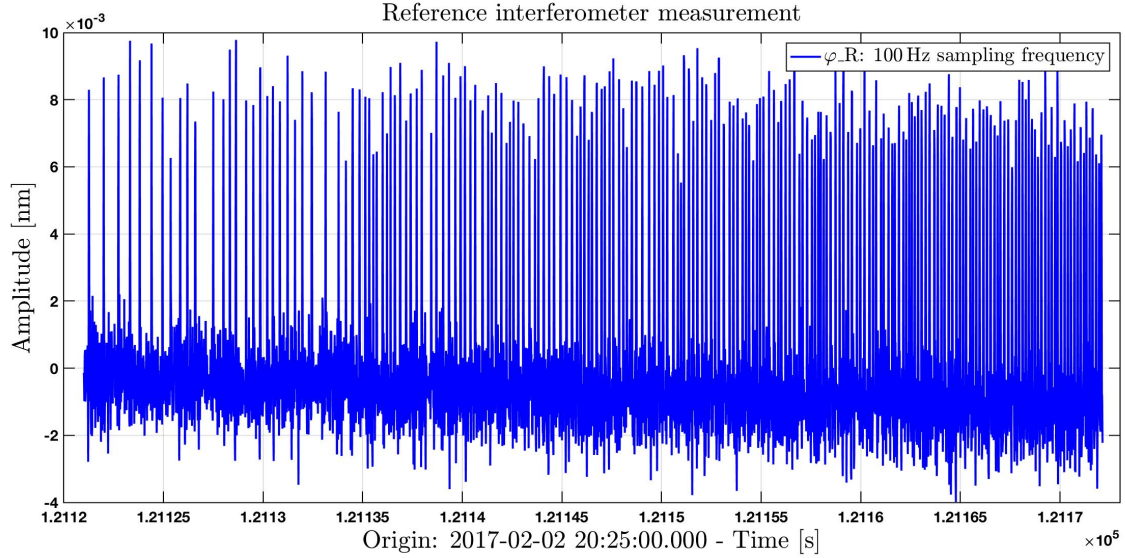
Figure 6.19.: Shown here is the measurement of the reference interferometer signal, recorded at a sampling frequency of $100\,\mathrm{Hz}$. Visible here is an increase in the number of lines in the time series as the phase drifts away from 0. These spikes appear as a noise around $10\,\mathrm{Hz}$ in the φ_R phase signal, and have an amplitude in the same range as the step size of the OPD control loop actuator. This data is recorded during the TM offset of $266\,\mathrm{nm}$. The coupling of this noise to the subtracted signal is visible Figure 6.18 in the balanced detection measurement, and with a lower coupling parameter in other measurements.

In Figure 6.20 the spectra measured at the TM offsets of $0\,\mathrm{nm}$ and $266\,\mathrm{nm}$ can be seen. For both of these TM offsets the coupling of $2\,\mathrm{f}_\mathrm{het}$ RIN is at a minimum, a contribution of $1\,\mathrm{f}_\mathrm{het}$ RIN is not visible. The spectra calculated from $100\,\mathrm{Hz}$ data for the $266\,\mathrm{nm}$ TM offset show a higher phase noise than the $10\,\mathrm{Hz}$ data. In Figure 6.21 example time series of the recorded $100\,\mathrm{Hz}$ data are shown together with the same channel recorded with a standard sampling frequency of $10\,\mathrm{Hz}$.

In the noise model the sensing noise of these two TM offsets only differs in the contribution of $1\mathrm{f}_\mathrm{het}$ RIN. In the experiment presented here the laser power and laser frequency both show a significantly higher noise at the time when the TM is at an offset of $0\,\mathrm{nm}$, than at an offset of $266\,\mathrm{nm}$. These times of higher noise were shown in Figure 6.12. The times of higher frequency noise are one aspect of the changing sensing noise over the measurement duration. More information can be found in [41], and in a paper which is currently in preparation [59].

This increase in frequency noise is visible in Figure 6.20, the frequency noise contribution (purple) is calculated as shown in Section 3.2.1. The coupling from the frequency noise to the length measurement is calculated between $0.2\,\mathrm{Hz}$ and $0.9\,\mathrm{Hz}$ from the transfer function estimation from the xF signal to the o12 signal with a sampling frequency of $10\,\mathrm{Hz}$. When the measurement is switched from the balanced detection measurement to the single diode measurement the frequency interferometer is also switched to the A-side measurement, since for the frequency control loop the subtracted signal is used as input. For the noise subtraction to work both signals need to have balanced detection, or both have to be single diode measurements.

The coupling parameter calculated with the $10\,\mathrm{Hz}$ data is also applied to the $100\,\mathrm{Hz}$ measurement to calculate the high-frequency contribution of the frequency noise. The frequency noise is a factor ≈ 2.5 higher in the measurement at a TM offset of $0\,\mathrm{nm}$ than in the other measurements shown here.

Visible in the measurement with a sampling frequency of 10 Hz at a TM offset of 266 nm is the increase in sensing noise in the single diode signal due to the lower SNR compared with the balanced signal. For the frequency band between 0.6 Hz and 0.9 Hz the noise floor levels calculated from the fit to the whole experiment are $\mathrm{nf_{o12}} = (35.522 \pm 0.487)\frac{\mathrm{fm}}{\sqrt{\mathrm{Hz}}}$ and $\mathrm{nf_{o12\_A}} = (48.715 \pm 0.646)\frac{\mathrm{fm}}{\sqrt{\mathrm{Hz}}}$, see Section 6.3.

The measured 100 Hz of the 266 nm TM offset shows quantisation noise, which increases the calculated phase noise level. The A-side measurement of the same offset shows a similar effect. This effect is not present in the data at the standard sampling frequency of 10 Hz. These spectra do not show an increase in phase noise as would be expected from the phase noise at higher frequencies measured at the higher sampling frequency. Shown together with the data measured by the satellite in Figure 6.21 is the time series of the 100 Hz data downsampled to 10 Hz in post-processing. The same moving-average filter as in the flight processing is used. This data downsampled in post-processing differs from the standard 10 Hz data in the starting point of the moving average, the two time series measure the same TM displacement but show a different noise. The quantisation noise from the 100 Hz data is not visible any more in the time series with the lower sampling frequency. [1]

---

[1]The level difference of this quantisation effect is ≈ 0.0009 nm, which is $\approx 0.01 \,\mu$rad. The step-size of the OPD actuator is ≈ 1.88 nm, or ≈ 0.022 rad [89], a more recent source for this value could not be found. The quantisation in o12 is not remaining actuator noise, there are fewer spikes in the actuator signal than in o12. The quantisation effect is most likely related to the phase readout.
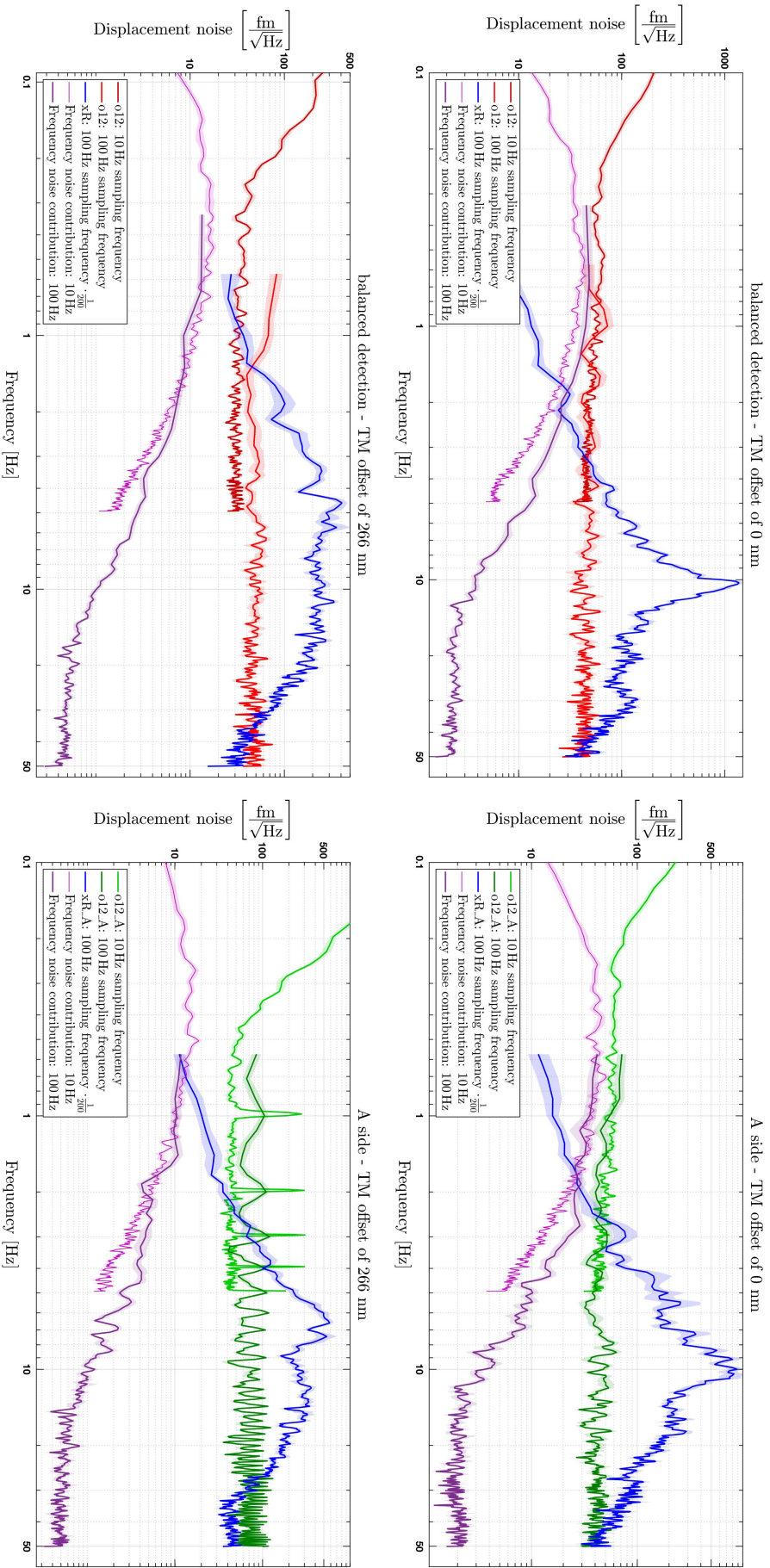
Figure 6.20.: These spectra are measured at TM offsets of 0 nm (top) and 266 nm (bottom). Shown in red is the measurement with balanced detection on, green is the measurement with balanced detection off. From 10 Hz and 100 Hz data the spectra are calculated with 700 samples in each FFT with an overlap of 50% and BH92 windows. With these TM offsets the coupling from the noise around 10 Hz in the reference interferometer signal (blue) to the subtracted signal seems to be below the noise floor. The higher frequency noise contribution at the start of the experiment, at a TM offset of 0 nm, is also visible; this noise contribution is calculated from the 10 Hz data and the 100 Hz data (purple).
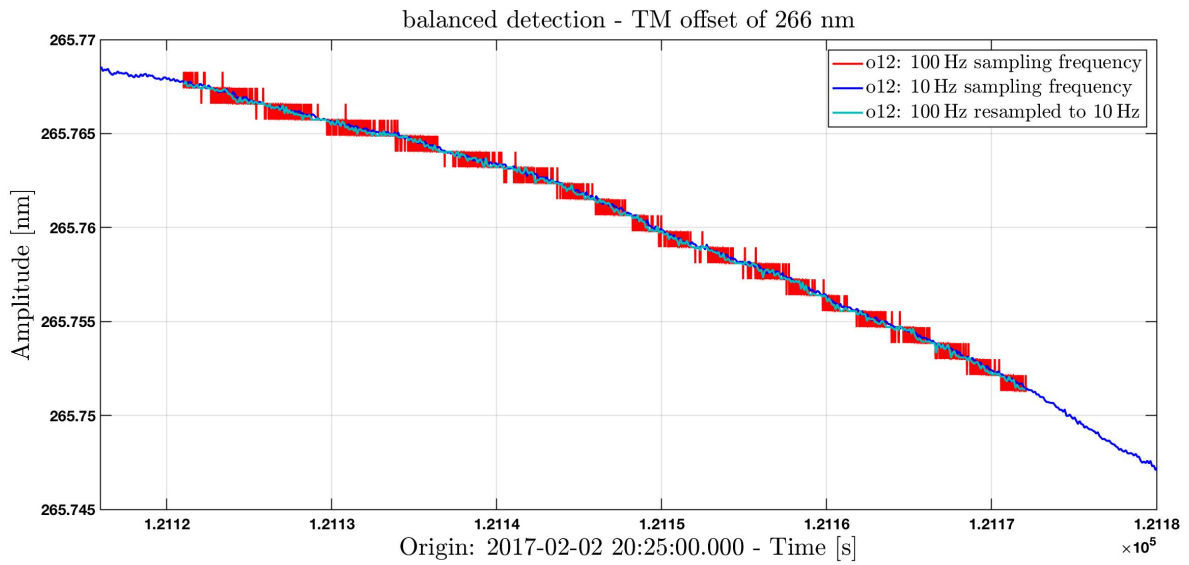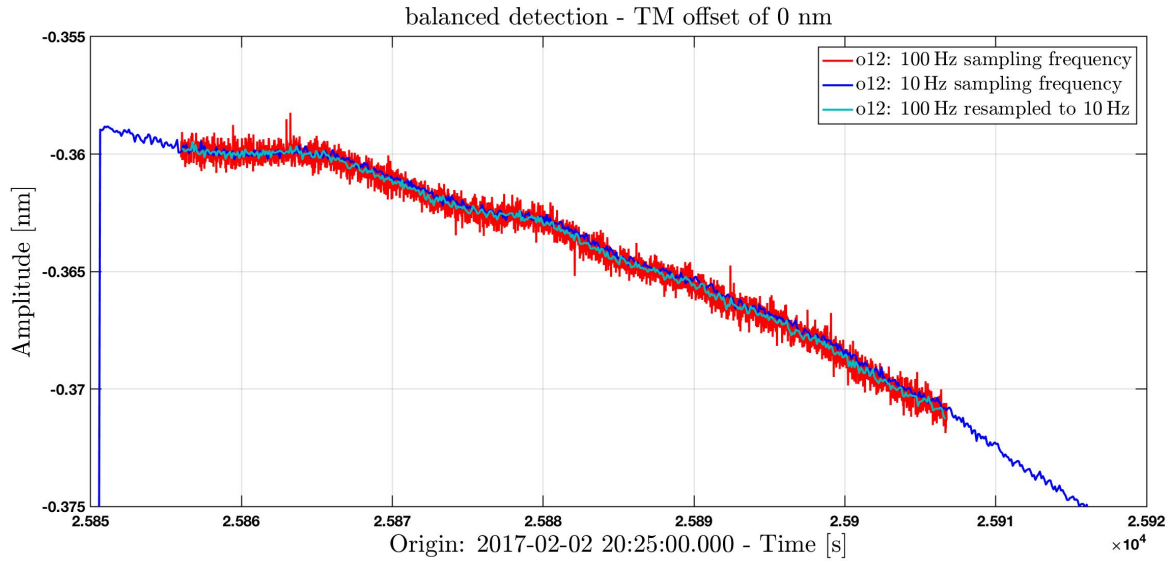
Figure 6.21.: Shown here are two example time series of the 100 Hz (red) data and 10 Hz data (blue), together with the 100 Hz data downsampled to 10 Hz (cyan), of the balanced detection signal o12. Compared with the measurement at a TM offset of 0 nm the phase measured at a TM offset of 266 nm shows significant quantisation. This effect is also visible in the spectra of the two time series, see Figure 6.20.

| Frequency [Hz]	r2G $\left[\frac{\text{fm}}{\sqrt{\text{Hz}}}\right]$	$\hat{r}^{(2)}_{\text{correlated}}$ $\left[\frac{10^{-6}}{\sqrt{\text{Hz}}}\right]$	$\hat{r}^{(2)}_{\text{uncorrelated}}$ $\left[\frac{10^{-6}}{\sqrt{\text{Hz}}}\right]$	noise floor $\left[\frac{\text{fm}}{\sqrt{\text{Hz}}}\right]$	χ^2
First experiment					
0.6 - 0.9	152.35 ± 1.367	1.27 ± 0.01	1.79 ± 0.02	35.312 ± 0.509	4.36
1.2 - 1.8	162.63 ± 1.161	1.35 ± 0.01	1.91 ± 0.01	34.247 ± 0.365	16.50
2.1 - 2.8	181.72 ± 1.259	1.51 ± 0.01	2.14 ± 0.01	33.028 ± 0.330	27.01
3.1 - 3.8	187.63 ± 1.327	1.56 ± 0.01	2.21 ± 0.02	32.607 ± 0.380	33.19
4.1 - 4.8	180.91 ± 1.454	1.51 ± 0.01	2.13 ± 0.02	34.709 ± 0.436	34.32
Second experiment, balanced signal o12					
0.6 - 0.9	194.24 ± 2.132	1.62 ± 0.02	2.29 ± 0.03	35.522 ± 0.487	2.02
1.2 - 1.8	195.43 ± 1.710	1.63 ± 0.01	2.30 ± 0.02	34.254 ± 0.408	13.58
2.1 - 2.8	209.51 ± 1.635	1.74 ± 0.01	2.47 ± 0.02	32.194 ± 0.339	30.97
3.1 - 3.8	211.67 ± 1.797	1.76 ± 0.02	2.49 ± 0.02	34.265 ± 0.377	32.18
4.1 - 4.8	204.68 ± 1.701	1.70 ± 0.01	2.41 ± 0.02	34.236 ± 0.418	43.60
Second experiment, single-diode signal o12_A					
0.6 - 0.9	192.53 ± 2.040	1.60 ± 0.02	2.27 ± 0.02	48.715 ± 0.646	4.29
1.2 - 1.8	196.82 ± 1.703	1.64 ± 0.01	2.32 ± 0.02	46.549 ± 0.566	12.39
2.1 - 2.8	203.46 ± 1.676	1.69 ± 0.01	2.40 ± 0.02	46.899 ± 0.545	21.68
3.1 - 3.8	203.07 ± 1.762	1.69 ± 0.01	2.39 ± 0.02	46.814 ± 0.530	29.84
4.1 - 4.8	205.59 ± 1.667	1.71 ± 0.01	2.42 ± 0.02	47.882 ± 0.581	31.66

Table 6.2.: Shown in this table are the fit results to the measured phase noise. The results of the first RIN subtraction experiment is shown in the top table, and the results of the second experiment in the other two. Fitted to the measured data are the phase noise level r2G and the noise floor. From the phase noise the $2f_{\text{het}}$ RIN level is calculated for both correlated and uncorrelated RIN. The real RIN is probably a combination of the two, its value can be expected between the two results. This data contains unexplained noise contributions, the χ^2 value of the fit is quite high. One such contribution could be small vector noise, another is the coupling of spikes in the OPD loop to the subtracted signal. The first experiment is shown in Section 6.2, the second in 6.3. The analysis of the noise at higher frequencies can be found in Section 6.4.

6.5. RIN direct measurement

Shown in this section are the results of the direct measurement of the RIN level around $1f_{het}$ and $2f_{het}$. The design of this experiment was shown in Section 6.1.4. The measurement beam and reference beam are measured individually. With only one beam active the fluctuations measured by the phasemeter in the FFT bin of the heterodyne frequency are a measurement of the voltage noise at f_{het}. For this experiment the phasemeter is set to its nominal heterodyne frequency $f_{het} = 1\,\text{kHz}$, and also to a new heterodyne frequency $f_{het,\,2} = 2\,\text{kHz}$ to measure RIN around $2f_{het}$. With these PM settings the combined RIN of the positive and negative frequency offset is measured in the same bin, since these two RIN components are uncorrelated the actual RIN level is a factor $\sqrt{2}$ smaller.

The process to calculate the RIN level from the measured voltage fluctuations is the same for both PM settings. The phasemeter measures the sine, cosine and dc component of the heterodyne signal, the components are calculated as:

$$y_{i,\hat{j},k} = \sum_{n=1}^{N-1} V(n) \cdot \sin\left(\frac{2\pi f_{het}}{f_{sampling}}\right) \tag{6.5}$$

$$z_{i,\hat{j},k} = \sum_{n=1}^{N-1} V(n) \cdot \cos\left(\frac{2\pi f_{het}}{f_{sampling}}\right) \tag{6.6}$$

$$d_{i,\hat{j},k} = \sum_{n=1}^{N-1} V(n). \tag{6.7}$$

The variable $y_{i,\hat{j},k}$ is called the sine component and $z_{i,\hat{j},k}$ the cosine component, these are calculated with N samples from the sampled voltage $V(n)$, with sine or cosine values from a look-up-table (LUT), the values in this LUT were pre-computed on ground. N is called the DFT length. The sampling frequency of the phasemeter is $f_{sampling} = 50\,\text{kHz}$ [40][51][90]. These sine, cosine and dc components are recorded with a sampling frequency of $100\,\text{Hz}$. With the same calibration coefficients as used in the regular phase calculation the real and imaginary part I and R of the signal are calculated [52]. This calibration removes the effect of the windowing of the phasemeter and the dark current of the diodes,

$$DC_{i,\hat{j},k} = c_{i,\hat{j},k}^{dc}\, d_{i,\hat{j},k} - c_{i,\hat{j},k}^{offset}, \tag{6.8}$$

$$\text{Re}\{F_{i,\hat{j},k}\} = c_{i,\hat{j},k}^{Ry}\, y_{i,\hat{j},k} + c_{i,\hat{j},k}^{Rz}\, z_{i,\hat{j},k} + c_{i,\hat{j},k}^{Rd}\, d_{i,\hat{j},k}, \tag{6.9}$$

$$\text{Im}\{F_{i,\hat{j},k}\} = c_{i,\hat{j},k}^{Iy}\, y_{i,\hat{j},k} + c_{i,\hat{j},k}^{Iz}\, z_{i,\hat{j},k} + c_{i,\hat{j},k}^{Id}\, d_{i,\hat{j},k}. \tag{6.10}$$

As was shown in Section 2.6, the real and imaginary component are used to calculate the phase $F_{i,\hat{j},k}$, which is normally sampled to $10\,\text{Hz}$ with a moving average filter and transmitted to ground. For this analysis the PDR_AA quadrant is used, the c-coefficients can be found in Table 6.5 [91].

coefficient	value
$c_{R,A,A}^{dc}$	3.0517578125e-08
$c_{R,A,A}^{offset}$	-0.00196966511602325
$c_{R,A,A}^{Ry}$	0
$c_{R,A,A}^{Rz}$	1.90740195827835e-09
$c_{R,A,A}^{Rd}$	-6.10349999676824e-08
$c_{R,A,A}^{Iy}$	1.90741214986779e-09
$c_{R,A,A}^{Iy}$	0
$c_{R,A,A}^{Id}$	-6.10353260885916e-08

Table 6.3.: This table shows the c-coefficients of the A quadrant of the diode PDR_A. These are used to calculate the real and imaginary part of the phase signal from the measured sine and cosine components of the heterodyne signal.

For this experiment the sine, cosine and dc component are recorded on the channels LST10139, LST10140 and LST10141. The $\mathrm{I} = \mathrm{Im}\{\mathrm{F}_{i,\hat{j},k}\}$ and $\mathrm{R} = \mathrm{Re}\{\mathrm{F}_{i,\hat{j},k}\}$ components calibrated from this data are used to calculate the RIN at higher frequencies. Since in this measurement only one beam is active I and R contain only noise. Due to the way they are processed these two noises are orthogonal to each other, and together describe the voltage noise in the FFT bin. A scatter plot of the imaginary and real component can be found in Figures A.21 and A.22 in Appendix A.20. These are shown for both the reference and measurement beam at $1\mathrm{f_{het}}$ and $2\mathrm{f_{het}}$, with and without the amplitude stabilisation.

Visible is the bigger distribution of points for the measurements without the control loop active. The scatter of I and R is not a circle around zero, and the error is different for different measurements, and is therefore probably not due to imperfect calibration in the c-coefficients. A likely cause are the spikes in the time series, also visible in their spectra as peaks, in the time series it can be observed that their contribution is different in the I and R component.

From the two components the voltage noise near either $1\mathrm{f_{het}}$ or $2\mathrm{f_{het}}$ can be calculated with:

$$\mathrm{V}_f(n) = \sqrt{\mathrm{I}_f^2 + \mathrm{R}_f^2}, \qquad\qquad f = \{1\mathrm{f_{het}}, 2\mathrm{f_{het}}\}. \qquad (6.11)$$

The RIN near either $1\mathrm{f_{het}}$ or $2\mathrm{f_{het}}$ is calculated with

$$\sqrt{2}\cdot\hat{r}_{\mathrm{m,r}}^{(f)} = \mathrm{RIN}_f = \frac{\mathrm{V}_f(n)}{\mathrm{DC}} = \frac{\sqrt{\mathrm{I}_f^2 + \mathrm{R}_f^2}}{\mathrm{DC}}, \qquad f = \{1\mathrm{f_{het}}, 2\mathrm{f_{het}}\}. \qquad (6.12)$$

Where the DC value is the laser power as computed in line 6.8 from the dc bin measurement $\mathrm{d_{R,A,A}}$ of the PDR_AA quadrant.

Spectra of the RIN as calculated for the higher frequencies can be found in Figure 6.22. The RIN measured with the amplitude stabilisation clearly shows a lower noise for both $1\mathrm{f_{het}}$ and $2\mathrm{f_{het}}$ and looks like a white noise. Without the stabilisation the RIN is a factor ≈ 20 higher for $1\mathrm{f_{het}}$ and a factor ≈ 10 higher for $2\mathrm{f_{het}}$. The source for the lines at $1\,\mathrm{Hz}$ and multiples in the spectrum without the stabilisation are visible in the time series. Due to the PPS the power spikes to an irregular offset value every second. The Puls Per Second is a $1\,\mathrm{Hz}$ timing signal distributed through the whole satellite [88], and seems to couple through the AOMs to the laser amplitude. These amplitude spikes probably are suppressed with the fast amplitude stabilisation during normal operations, but for many experiments these lines are still visible in the phase signal.

A quick estimate shows that the photocurrent associated with RIN near $1\mathrm{f_{het}}$ and $2\mathrm{f_{het}}$ is in a similar range as ADC noise. The photocurrent for ADC noise in one quadrant was measured on ground to $\mathrm{I_{q,\ ADC}} = 102\,\frac{\mathrm{nA}}{\sqrt{\mathrm{Hz}}}$ [66][19]. The equivalent noise in the RIN spectrum can be calculated with

$$\hat{x}_{\mathrm{ADC}} = \frac{\mathrm{I_{q,\ ADC}}}{\mathrm{R_{PD}}\cdot\mathrm{P_{R,A,A}}}, \qquad\qquad \left[\frac{1}{\sqrt{\mathrm{Hz}}}\right] \qquad (6.13)$$

where $\mathrm{P_{R,A,A}}$ is the mean power on one quadrant. This mean power is calibrated from the standard $10\,\mathrm{Hz}$ sigma measurement as shown in Section 3.5, and divided by 4 since only one quadrant is active. A bigger error has to be assumed on this value since the distribution of power on the four quadrants is not known. The photodiode responsivity was measured in flight to $\mathrm{R_{PD}} = (0.821\pm 0.01)\frac{\mathrm{A}}{\mathrm{W}}$, see Table 3.3 in Section 3.5 and [62]. Since ADC noise depends on the laser power, it will be different for each RIN measurement. For the measurements with the stabilisation on this ADC noise is in the order of $\hat{x}_{\mathrm{ADC}} \approx 1\frac{10^{-6}}{\sqrt{\mathrm{Hz}}}$, without the stabilisation there is less power on the QPD, and the ADC noise is therefore higher at $\hat{x}_{\mathrm{ADC}} \approx 3\frac{10^{-6}}{\sqrt{\mathrm{Hz}}}$. This ADC noise is similar for measurement beam and reference

Figure 6.22.: These plots show the RIN calculated from the I and R component of the phasemeter output of PDR_AA. This data is sampled with $100\,\mathrm{Hz}$. RIN near $1\mathrm{f}_{\mathrm{het}}$ is plotted in blue, near $2\mathrm{f}_{\mathrm{het}}$ in green. Clearly visible is the rise in noise when the amplitude stabilisation is turned off. The lines in these spectra are visible as spikes in the time series in $1\,\mathrm{s}$ intervals.

Measurement	ADC noise	$\hat{r}^{(1,2)}_{\text{r, m; measured}}$	$\hat{r}^{(1,2)}_{\text{m,r}}$	$\hat{r}^{(1,2)}_{\text{correlated}}$	$\hat{r}^{(1,2)}_{\text{uncorrelated}}$
Amplitude stabilisation ON, in $\left[\frac{10^{-6}}{\sqrt{\text{Hz}}}\right]$					
$1f_{\text{het}}$, m beam	1.02 ± 0.01	1.67 ± 0.01	0.93 ± 0.06	1.67 ± 0.09	1.19 ± 0.06
$1f_{\text{het}}$, r beam	0.87 ± 0.01	1.48 ± 0.01	0.75 ± 0.07	-	-
$2f_{\text{het}}$, m beam	1.02 ± 0.01	1.71 ± 0.02	0.96 ± 0.06	1.32 ± 0.15	1.03 ± 0.07
$2f_{\text{het}}$, r beam	0.88 ± 0.01	1.15 ± 0.01	0.36 ± 0.1	-	-
Amplitude stabilisation OFF, in $\left[\frac{10^{-6}}{\sqrt{\text{Hz}}}\right]$					
$1f_{\text{het}}$, m beam	3.79 ± 0.05	28.8 ± 1	20.3 ± 0.8	44.8 ± 1.3	31.8 ± 0.9
$1f_{\text{het}}$, r beam	3.42 ± 0.04	34.6 ± 1	24.4 ± 1	-	-
$2f_{\text{het}}$, m beam	3.68 ± 0.05	12.8 ± 0.5	9.0 ± 0.4	19.4 ± 0.4	13.7 ± 0.3
$2f_{\text{het}}$, r beam	3.34 ± 0.04	14.7 ± 0.3	10.4 ± 0.2	-	-

Table 6.4.: The second column of this table shows the calculated ADC noise level. The error on this ADC noise level is calculated from the fluctuations of the beam power during the measurement, and the uncertainty of R_{PD}. The third column shows the mean RIN level as measured, the next column shows the actual RIN $\hat{r}^{(1,2)}_{\text{m,r}}$ calculated from this value for both beams by subtracting the ADC and electronic noise. From these individual RIN levels the combined RIN is calculated, for RIN which is correlated and uncorrelated between the two beams. These RIN levels are shown in the last two columns.

beam. It is shown together with the RIN spectra calculated. The calculated ADC noise levels can be found in Table 6.4.

During normal operations the power is measured with the dc bin of the phasemeter $d_{i,\hat{j},k}$, the calibrated value $DC_{i,\hat{j},k}$ of this measurement is used to calculate the sigma parameter used in the other analysis. Sigma is calculated as:

$$DC_{i,\hat{j}} = \frac{1}{2}\left(DC_{i,\hat{j},A} + DC_{i,\hat{j},B}\right) \tag{6.14}$$

$$\text{sigma}_i = \frac{4}{N}\sum_{\hat{j}} DC_{i,\hat{j}}. \tag{6.15}$$

The sigma_i parameter is therefore the average DC-bin measurement on one diode of the interferometer X_i. First, the average between both ports of the same quadrant $\hat{j}$ is calculated, the four quadrants are then summed. The parameter N displays the number of quadrants active in the computation of the power. Over the LPF mission timeline there were no observable QPD quadrant failures, therefore N=4. The result can be calibrated to power.

In this experiment the dc-bin of the PDR_AA quadrant $d_{R,A,A}$ is available at $100\,\text{Hz}$ and calibrated to $DC_{R,A,A}$. The amplitude noise spectrum calculated from the RIN of this measurement can be found in Figure 6.23. Without the amplitude stabilisation this measurement too shows a higher noise, the spectra are labelled with $1f_{\text{het}}$ and $2f_{\text{het}}$ to show during which timespan this DC measurement was taken.

In Table 6.4 the mean RIN levels for $1f_{\text{het}}$ and $2f_{\text{het}}$ RIN for both beams are shown. This mean value is calculated between $0.2\,\text{Hz}$ and $50\,\text{Hz}$ for measurement with the amplitude stabilisation on, and between $0.2\,\text{Hz}$ and $0.8\,\text{Hz}$ with the stabilisation off. These RIN levels calculated are the result of the RIN with positive and negative frequency offset added together, the actual RIN level is $\sqrt{2}$ lower. This is true under the assumption that these two components are uncorrelated, and have the same noise level. The measurement with the stabilisation on is limited by ADC noise and electronic noise, the actual RIN levels are difficult to estimate. An estimation of the RIN level is attempted two ways. The first is an estimation of the RIN
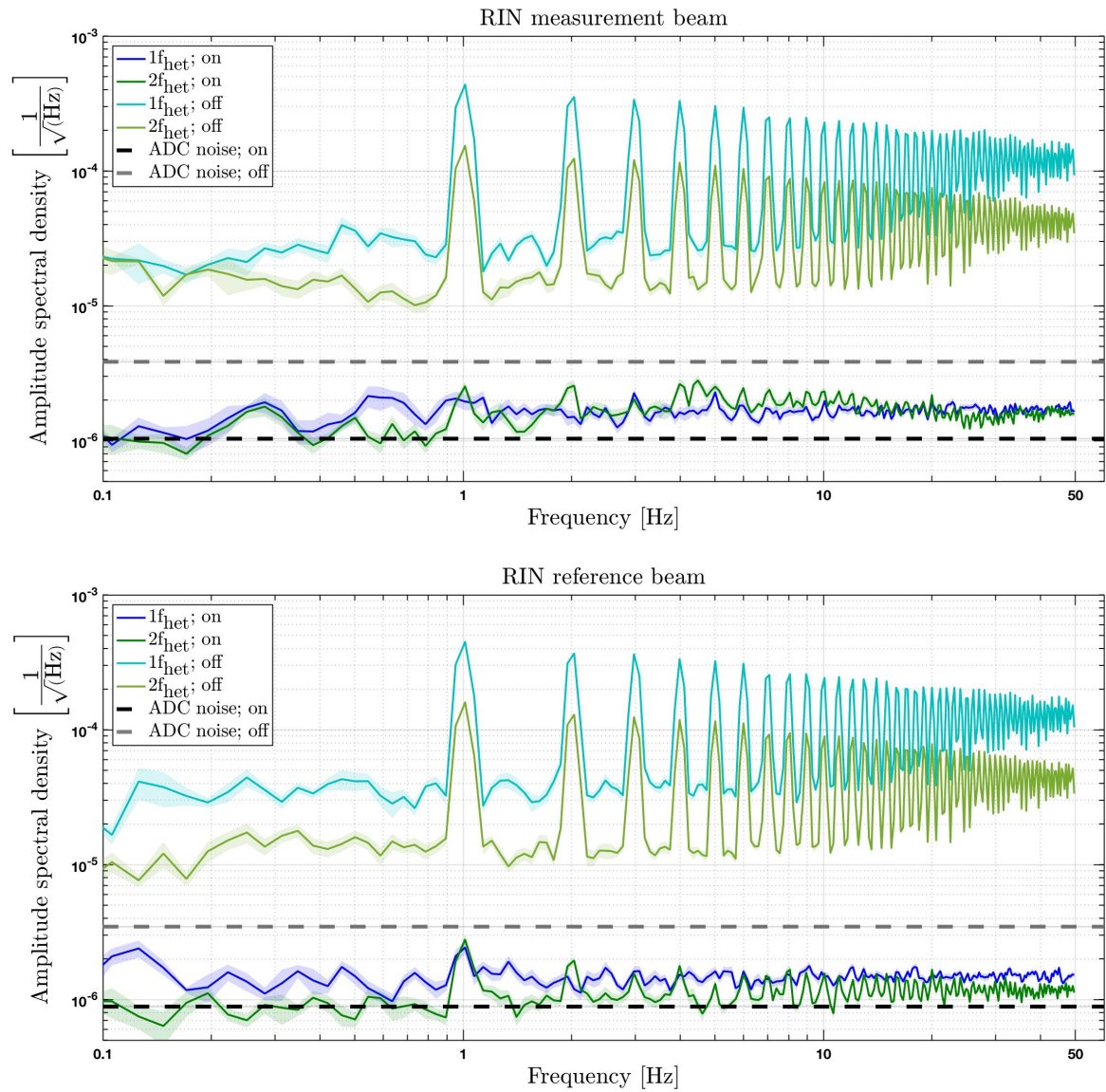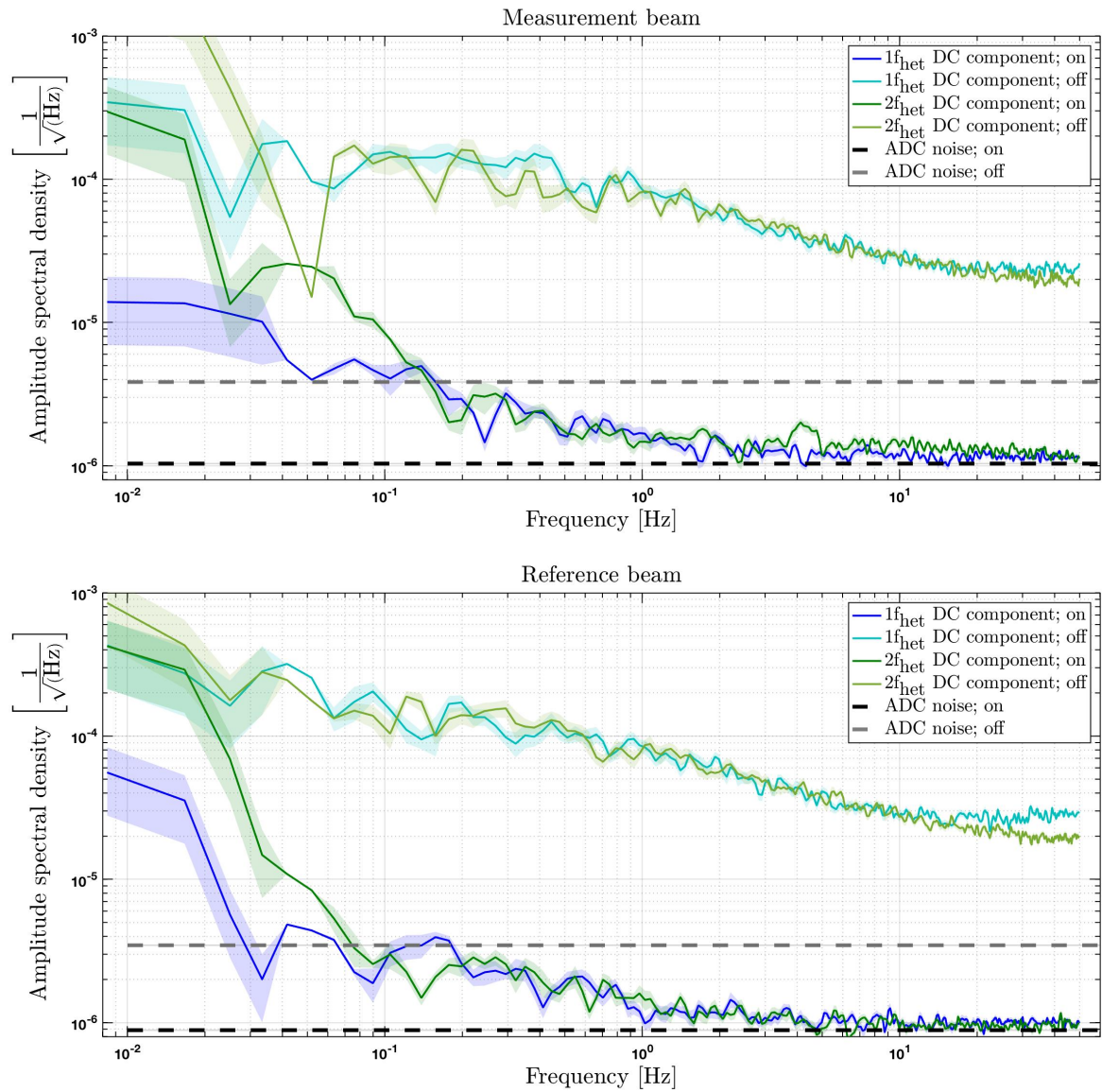
Figure 6.23.: These plots show the RIN calculated from the DC component of the PM output of PDR_AA. This data was sampled with 100 Hz, the plot colours are the same as in Figure 6.22. Again visible is the rise in noise without the amplitude stabilisation on.

by a subtraction of the ADC noise and electronic noise from the measured values, with

$$\hat{r}_{m,r}^{(1,2)} \approx \frac{1}{\sqrt{2}} \sqrt{\hat{r}_{r,\,m;\,measured}^{(1,2)^2} - \hat{x}_{ADC}^2 - \hat{x}_{elec}^2} \cdot \left[\frac{1}{\sqrt{Hz}}\right] \tag{6.16}$$

The electronic noise can be calculated in a similar way to the ADC noise. By using the electric current noise $I_{q,\,elec} = 17.2\,\frac{pA}{\sqrt{Hz}}$, see Section 3.5, the combined noise is increased by $\approx 1\%$, compared to the ADC noise. The RIN levels calculated this way can be found in Table 6.4.

With this calculation a $1f_{het}$ RIN contribution can be found, which is at a higher level as the $2f_{het}$ RIN. This could not be observed in the other RIN experiments. The main source of error on this estimation is the calculation of the ADC noise level, it was assumed that $\frac{1}{4}$ of the power of the diode is in the quadrant under analysis; if the beam is miss-aligned this power could be smaller, and the ADC noise level higher, and the calculated RIN levels smaller. The measured $DC_{R,A,A}$ value is has a different calibration compared to the sigma parameters, the same calibration as before can not be used here.

The RIN level can also be estimated by reducing the RIN without stabilisation by the gain of the amplitude control loop. From measurements on ground the gains can be estimated to $g_{ampstab}(1f_{het}) \approx 16$ and $g_{ampstab}(2f_{het}) \approx 11$ [92]. Dividing the $\hat{r}_{m,r}^{(1,2)}$ RIN without the amplitude stabilisation by these gains yields for the RIN with stabilisation $\hat{r}_m^{(1)} \approx 1.3\,\frac{10^{-6}}{\sqrt{Hz}}$, $\hat{r}_r^{(1)} \approx 1.5\,\frac{10^{-6}}{\sqrt{Hz}}$, $\hat{r}_m^{(2)} \approx 0.8\,\frac{10^{-6}}{\sqrt{Hz}}$ and $\hat{r}_r^{(2)} \approx 0.9\,\frac{10^{-6}}{\sqrt{Hz}}$. These values are at a similar level to other measurements, but since the loop gain was estimated from a plot of measurements made in a ground setup in 2010 these results are less trustworthy than the first method.

From the measurements available an overview of RIN over the different frequency ranges can be created. A plot of RIN with all the data available can be seen in Figure 6.24. Shown in grey is the RIN calculated from the standard power measurement, commonly called sigma since these values are not calibrated to Watt. The sigma parameter of the X_R interferometer is only available at the housekeeping sampling frequency of $0.0333\,Hz$. This measurement is not useful for the analysis, between $0.016\,Hz$ and $0.002\,Hz$ the spectrum is dominated by aliasing, and below this by the window function. However, the sigma measurement of the X_F and the X_{12} interferometer are available at $10\,Hz$. The RIN calculated from these measurements is used for analysis here since the RIN is the same on all diodes.

Since the RIN at $1f_{het}$ and $2f_{het}$ should be symmetric around their centre frequency, these spectra are shifted upwards in frequency, and plotted with both positive and negative frequency offset. In the measurement without stabilisation the RIN is divided by $\sqrt{2}$ to account for this. Since the measurement with stabilisation is limited by ADC noise, the noise is shown as it was measured.

These spectra were already seen in Figure 6.22. Here they look different, since the frequency axis is not logarithmic with respect to either $1f_{het}$ or $2f_{het}$. In the spectrum without the amplitude stabilisation the noise spectra are shown only between $0.1\,Hz$ and $0.8\,Hz$ frequency offset to remove the peaks towards higher frequencies.

Also shown is the RIN calculated from the dc bin of the PD_RAA quadrant, with a sampling frequency of $100\,Hz$.
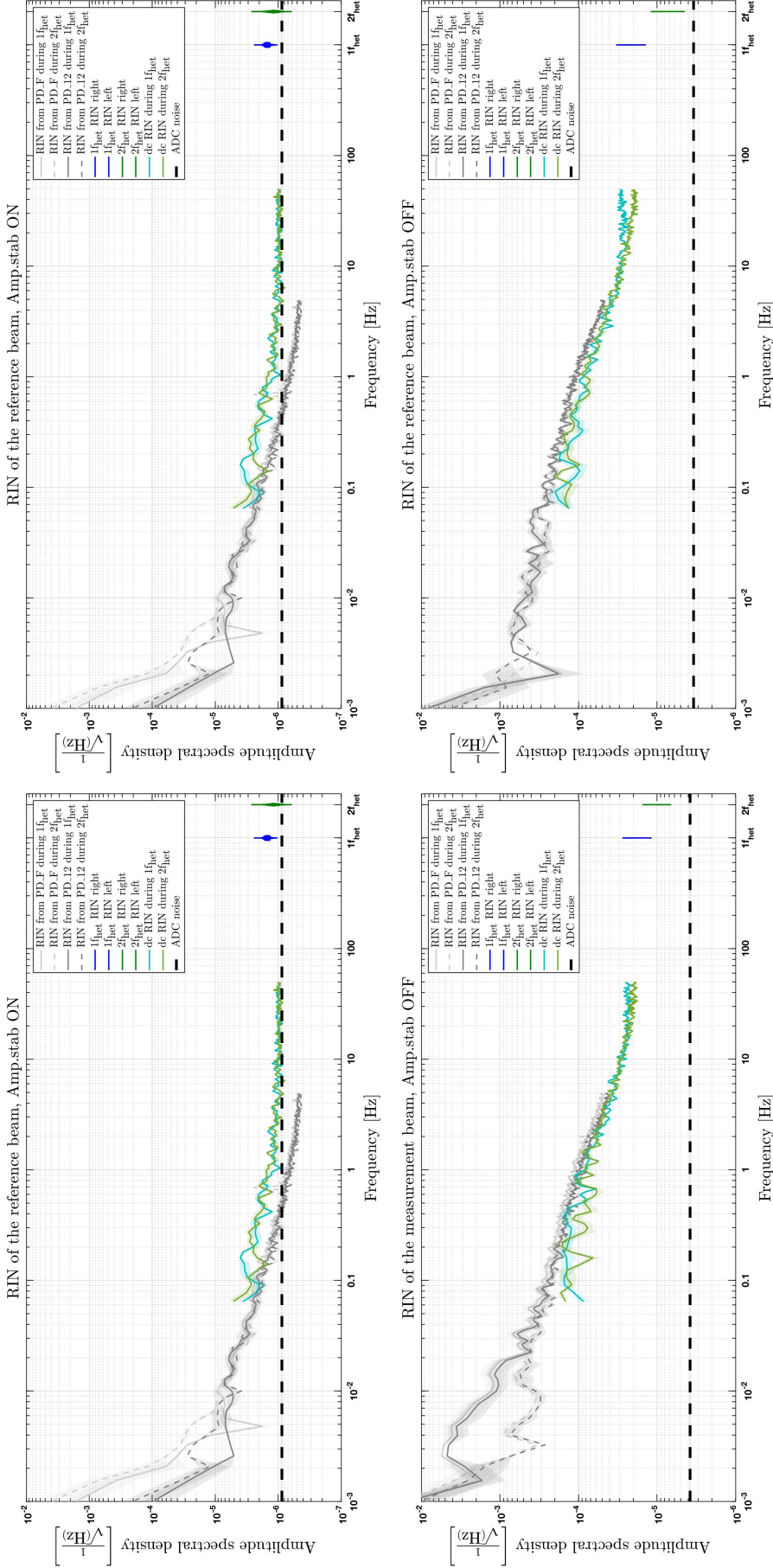
Figure 6.24.: From the combined power measurement through the sigma channel (grey), the 100 Hz phasemeter measurement of the dc component and the RIN data at $1f_{het}$ and $2f_{het}$ a full RIN spectrum can be constructed.

Shown on the left is the measurement beam, on the right the reference beam. The top two show measurements with the amplitude stabilisation on, the bottom two have the stabilisation off. The ADC noise is calculated with the power as measured on one quadrant of the 100 Hz measurement; in the standard power measurement (grey) all 8 quadrants are used. Due to the better SNR the ADC noise is a factor $\sqrt{8}$ lower. These spectra are calculated with the lpsd function of LTPDA, the 4 samples at the lowest frequency are not as trustworthy since the BH92 window correlates these with the DC bin of the FFT; these are removed from the spectrum. To mitigate this effect a detrend of order 1 is applied to the data, this removes a linear fit from the time series. The BH92 window segments have an overlap of 66.1%, to increase the averaging of these shorter timespans.

209

6.5.1. Comparison with ground measurements

In preparation of the mission the RIN level was also measured. The aim of this measurement was the test of the fast amplitude control loop with different setpoints. More information on these experiments can be found in the test report [92]. This report describes the performance tests of the laser setup for the in-flight components. In this report, Beam 1 is the measurement beam, and Beam 2 is the reference beam. This series of experiments is also called "Hannover-Tests". A description of these experiments, which is publicly available, can be found in [40].

RIN at kHz frequencies

The RIN of the individual beams is shown in Figure 6.25, these pictures are copied from the test report, page 87.

In these plots it can be seen that the RIN at $1f_{het} = 1\,\mathrm{kHz}$ is lower than at $2f_{het} = 2\,\mathrm{kHz}$. The RIN levels are estimated from the plot for an amplitude control loop setpoint of 1500. An overview of the estimated values for both beams, together with the combined RIN for both correlated and uncorrelated RIN between the two beams, can be found in Table 6.5.

The RIN level measured in this section, with the amplitude stabilisation on, is not comparable to the ground measurement due to the ADC noise. In the ground measurement the $1f_{het}$ RIN is lower than the $2f_{het}$, in the flight experiment these are the other way round. The reason is not clear, but considering the uncertainties of both measurements, and since there are only two experiments, this was not further investigated.

Without the stabilisation the RIN of the in-flight measurement is higher than $10 \cdot \frac{10^{-6}}{\sqrt{\mathrm{Hz}}}$, see Figure 6.22 and Table 6.4; while the RIN of the ground measurement is below $10 \cdot \frac{10^{-6}}{\sqrt{\mathrm{Hz}}}$. The cause for the higher RIN of the in-flight measurement is not clear.
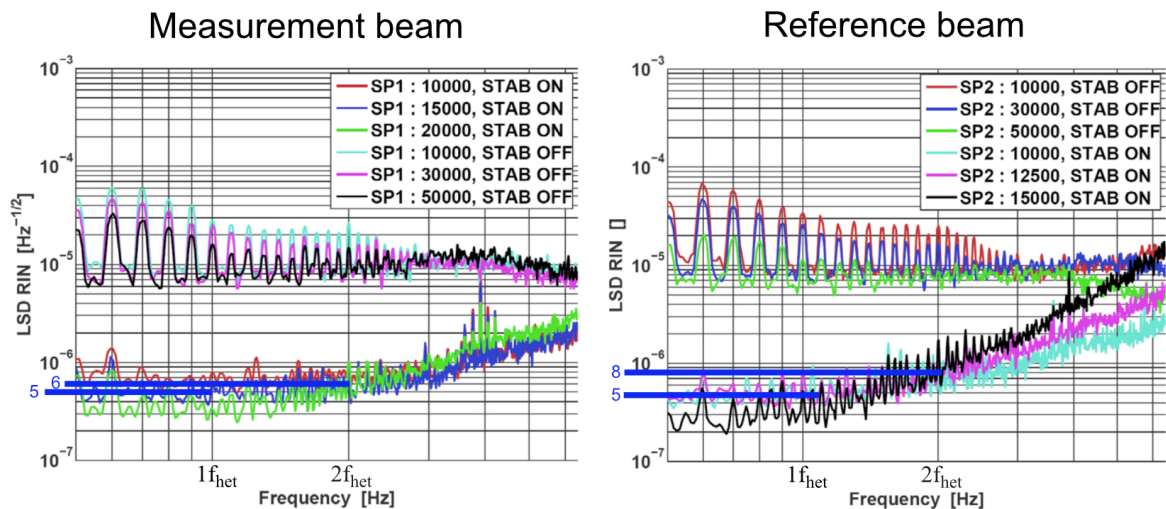

Figure 6.25.: These plots are copied from [92]. Shown on the left is the RIN of the measurement beam, on the right of the reference beam. The RIN was measured for different settings of the fast amplitude stabilisation.

RIN	$\hat{r}_{\mathrm{m}}^{(1,2)}\left[\frac{10^{-6}}{\sqrt{\mathrm{Hz}}}\right]$	$\hat{r}_{\mathrm{r}}^{(1,2)}\left[\frac{10^{-6}}{\sqrt{\mathrm{Hz}}}\right]$	$\hat{r}_{\mathrm{correlated}}^{(1,2)}\left[\frac{10^{-6}}{\sqrt{\mathrm{Hz}}}\right]$	$\hat{r}_{\mathrm{uncorrelated}}^{(1,2)}\left[\frac{10^{-6}}{\sqrt{\mathrm{Hz}}}\right]$
$1\mathrm{f}_{\mathrm{het}}$	0.5 ± 0.1	0.5 ± 0.1	1 ± 0.14	0.7 ± 0.1
$2\mathrm{f}_{\mathrm{het}}$	0.6 ± 0.1	0.8 ± 0.1	1.4 ± 0.14	1 ± 0.1

Table 6.5.: This table shows the RIN level of both beams, estimated from the plot of the ground measurement with the amplitude stabilisation at a setpoint of 1500. See Figure 6.25, which was copied from [92]. From these RIN values the combined RIN is estimated, for correlated and uncorrelated noise between the two beams. For the calculation of the $1\mathrm{f}_{\mathrm{het}}$ combined RIN it is assumed that both beams have the same beam power, and that the beamsplitter is 50/50.

low frequency RIN

Also measured during this test-run was the RIN at lower frequencies, see Figure 6.26. The left plot is also copied from the test report, page 93; the right plot is copied from [40]. Without the fast amplitude stabilisation on, the RIN of the ground measurement at lower frequencies is one order of magnitude bigger than in the in-flight measurement. The in-flight measurement can be seen in Figure 6.24. The RIN at lower frequencies with the stabilisation on is comparable between the two measurements.
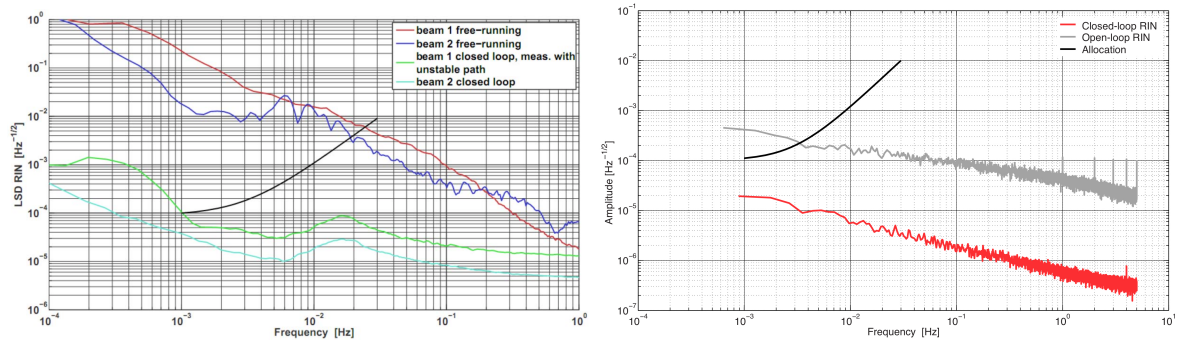

Figure 6.26.: The left plot was copied from [92], it shows the RIN with and without the amplitude stabilisation on for the individual beams. Beam 1 is the measurement beam, Beam 2 is the reference beam. The right plot was copied from [40], it shows the RIN of both beams as measured on either PD1_A or PD1_B.
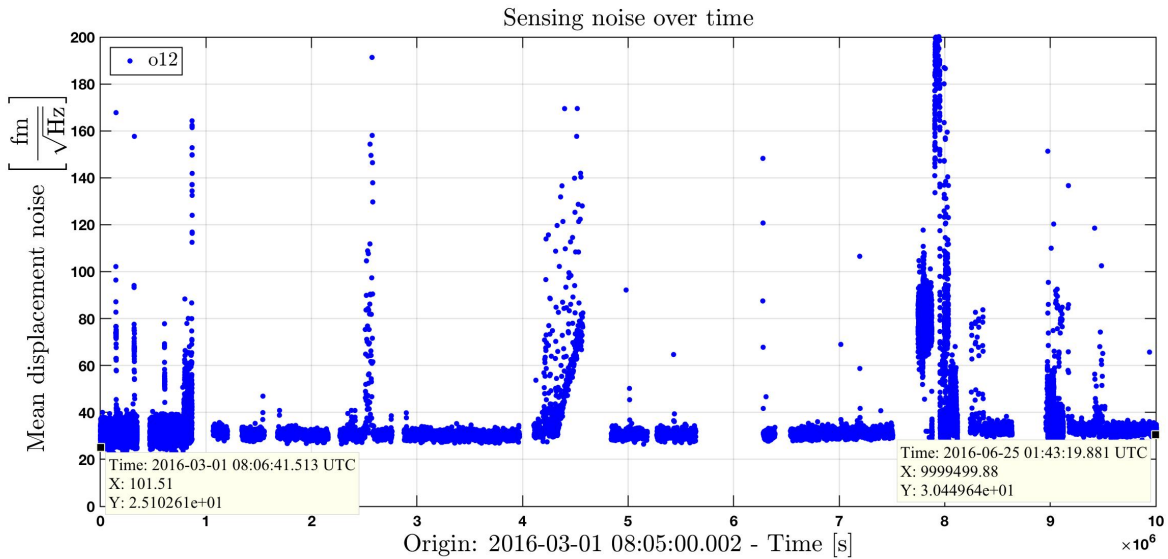
6.6. RIN during noise runs

Figure 6.27.: Shown here is the mean noise over time, the data stretch under analysis is 185 days long. The mean noise is calculated for the band between 0.3 Hz and 0.8 Hz. Used are a segment length of 2000 samples, with an overlap of 50% and a detrend of order 1. As always a Blackman-Harris window BH92 is used. Shown here are not only the mean noise of the noise runs, but also the mean noise during experiments and during the transition after station keeping.

Shown in this section is an analysis of the noise for different TM positions for the noise runs of the initial operations time. The aim of this brief exploration is the noise shape around the nominal TM offset of 0 nm. Shown in Figure 6.27 is a plot of the mean noise over time. This noise is calculated with the same analysis tools as were already used in the RIN subtraction experiments. Following the same procedure each measured noise is paired with its mean TM position. Analysed is the o12 measurement with a sampling frequency of 10 Hz, with the frequency noise subtracted. The mean noise level is calculated in the band between 0.3 Hz and 0.8 Hz.

The segment length used to calculate the spectra are increased from 50 seconds to 200 seconds. This change could be made since the TM moves slower and there is no need to adjust to the limited measurement duration of one TM offset. The analysis is carried out for all segments where the OMS produces a reasonable measurement. This data also includes experiments, transitions from station keeping and glitches.

The noise for each TM position can be seen in Figure 6.28, visible there is the big distribution of noise levels and TM offsets due to experiments and station keeping transitions. Of bigger interest here however is the area around a TM position of 0 nm with lower noise, this can be seen in Figure 6.29. In this noise measurement the fit result of the first RIN subtraction experiment was copied, visible is the same noise shape as was already seen in this experiment. A more detailed analysis of the noise over time, with a more careful selection of the times selected, in not only the longitudinal signal o12 but also the angular signals can be found in an upcoming paper [59].
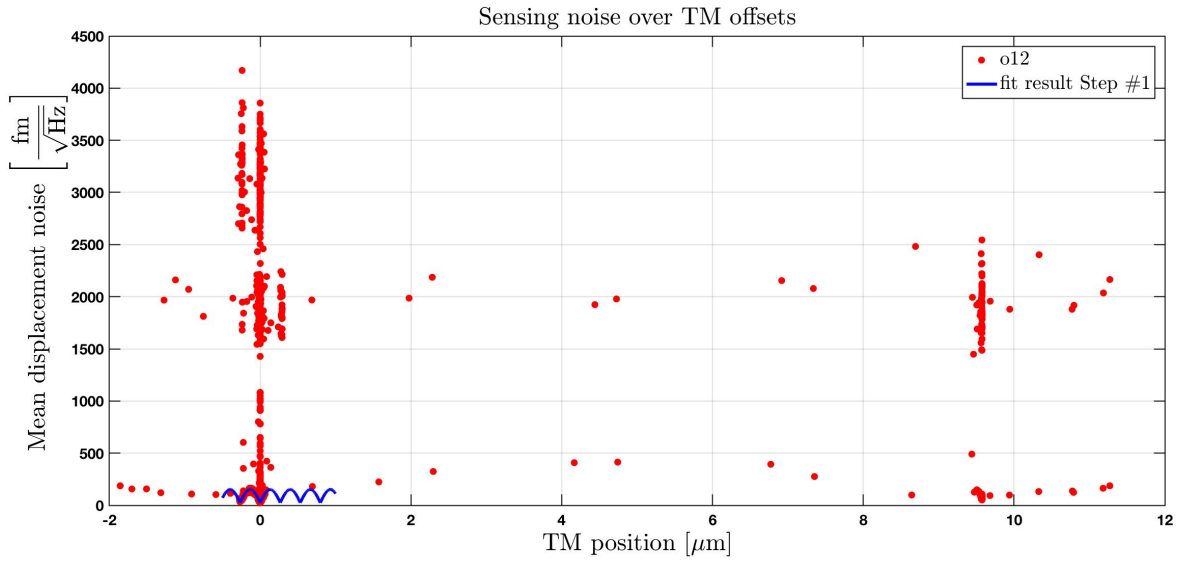
Figure 6.28.: Shown here is the mean sensing noise plotted over the mean TM position. Due to the high number of points the error bars are not shown. Most of the time the TM is positioned near the zero position. The measured noise changes by a factor 100 since the transients after station keeping, glitches and times when experiments were performed are included in this analysis. The fit result of the first RIN subtraction experiment is shown in blue.
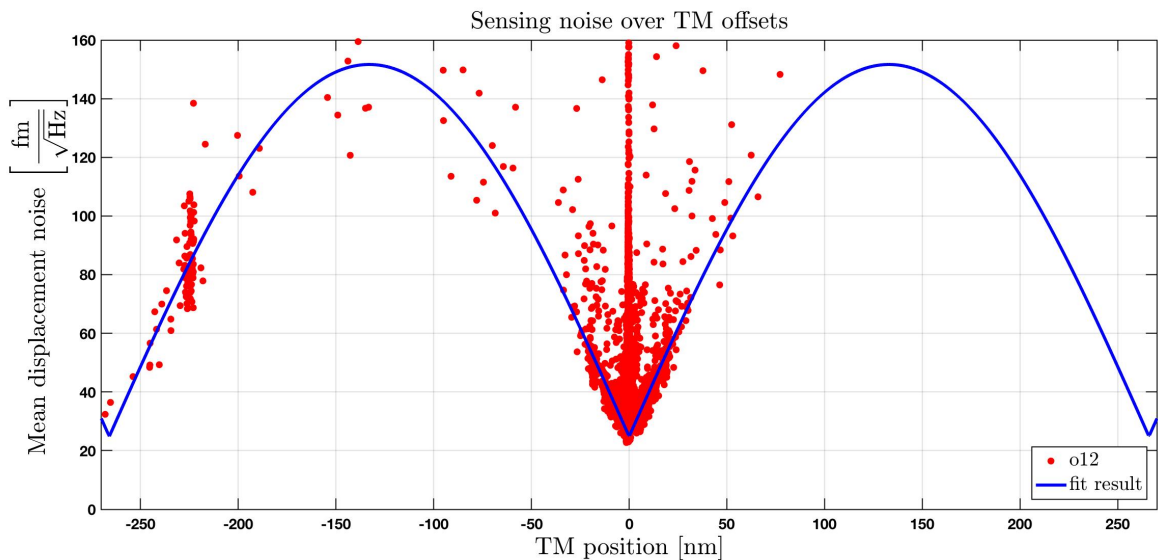
Figure 6.29.: Shown here is the same plot as in Figure 6.28, zoomed in on the nominal TM position. The sensing noise away from zero increases in the noise shape as predicted from the coupling of $2f_{het}$ RIN.

6.6.1. Test mass drift

RIN is only subtracted completely if the phase difference between measurement and reference signal is zero. Small offsets or drifts around zero lead to remaining RIN, which is not subtracted. To find the amount of TM drift during normal science operations the time series of the noise runs is cut into segments of 20 seconds. For each of the segments the mean TM position is calculated. This analysis is performed for segments 20 to 49 from the segment catalogue, which is a list of the timespans with phase measurements from the OMS. Most of the segments still contain the drift to zero after the station keeping and some glitches, which leads points in the histogram far from zero.

For each noise measurement a histogram of the TM positions is calculated. As an example three histograms can be found in Figure 6.30. For most noise runs under analysis the mean TM position is at a small offset from 0 nm, this offset differs between noise runs and is smaller than 1 nm for most. This small offset leads to an insignificant rise in RIN.
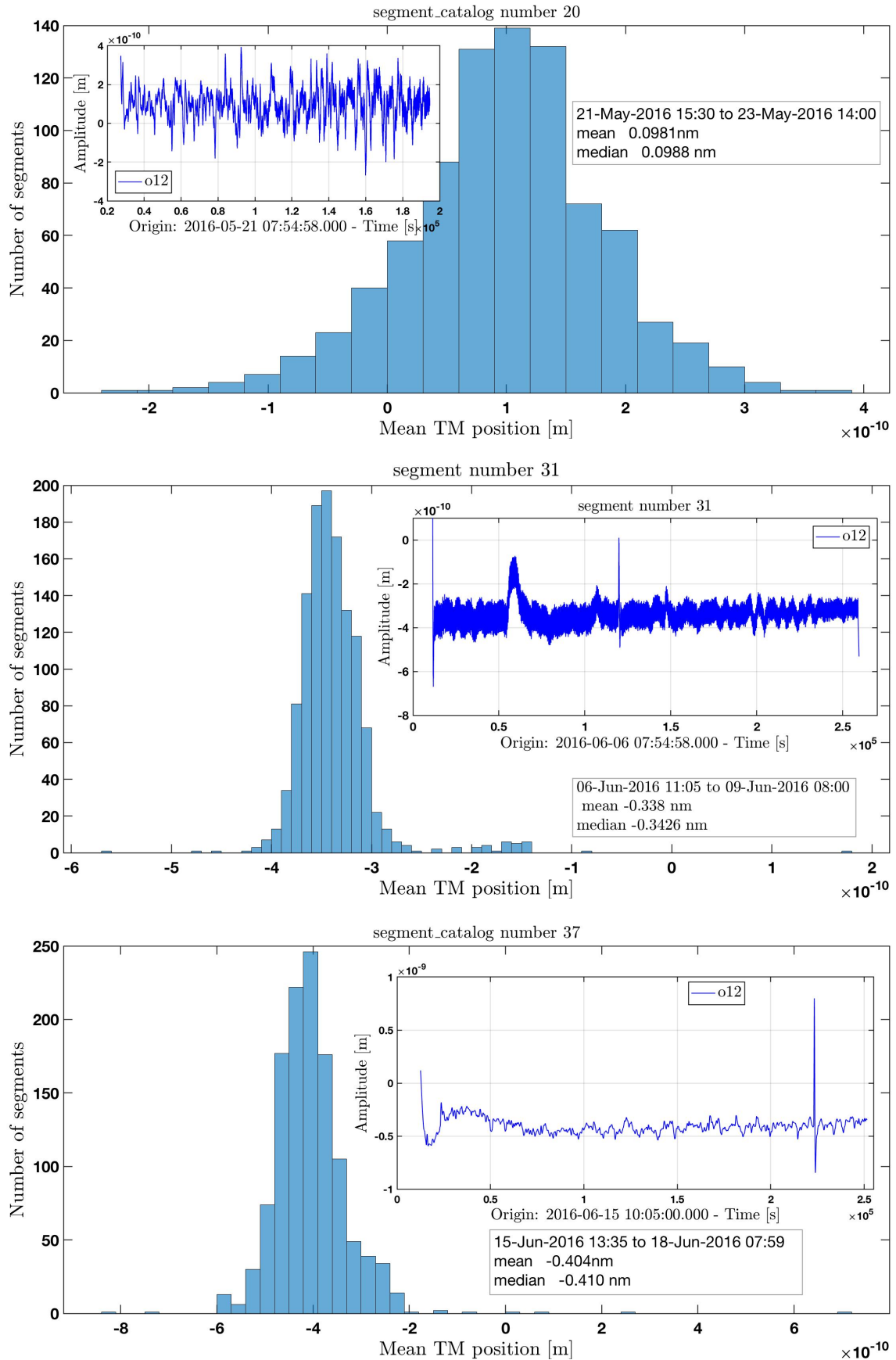
Figure 6.30.: Shown here are three example histograms of the average TM offset during the noise runs. The average TM offset is calculated from segments of 200 samples. The offsets to the optical zero position are small.

6.7. RIN in the free-fall experiment

Before launch one important noise contribution at lower frequencies was expected to be the electrostatic actuation noise [14]. When the satellite was assembled great care was taken to achieve gravitational balance between the two TMs. Due to this the electrostatic force required along the x-axis to keep the difference between the two TMs could be reduced during the mission operations as more about the properties was learned [73]. The electrostatic actuation noise is proportional to the electrostatic force authority. The maximum applicable force on TM2 along the x-axis could be reduced to 50 pN in the ultra-ultra-reduced low acceleration mode (UURLA) configuration. This reduction was a significant improvement to the initial force of 2200 pN in the nominal configuration. To measure the low frequency noise without this noise present an experiment was designed where the actuation is temporarily set to zero. Since TM2 still needs to be acted upon short force kicks are applied [85][86][87]. This actuation moves TM2 away from the optical centre, when the TM falls back due to the gravitational force, another force kick is applied. This actuation mode is also called intermittent control.

In this free-fall experiment the TM is moved over relatively big distances; a byproduct of this huge motion is an increase of noise at higher frequencies. From the previous experiments an increase in sensing noise due to $2f_{het}$ RIN is expected for TM offsets away from the optical zero. The first experiment shown in this section is the second free-fall experiment, which was performed on 2016-06-10, there the TM moved by ≈ 50 nm by force kicks of ≈ 1.6 nN.[2] Also shown is the third free-fall experiment, where the motion was increased to ≈ 300 nm per parabola with force kicks of ≈ 12 nN; it was run on 2016-07-20.

The TM moves over the same position many times over many parabolas. The sensing noise can be measured for one position multiple times for short time periods. First, the time series of the phase measurement is cut into segments which include one parabola. In the second experiment 229 parabolas are used, in the third experiment 753 parabolas. These individual
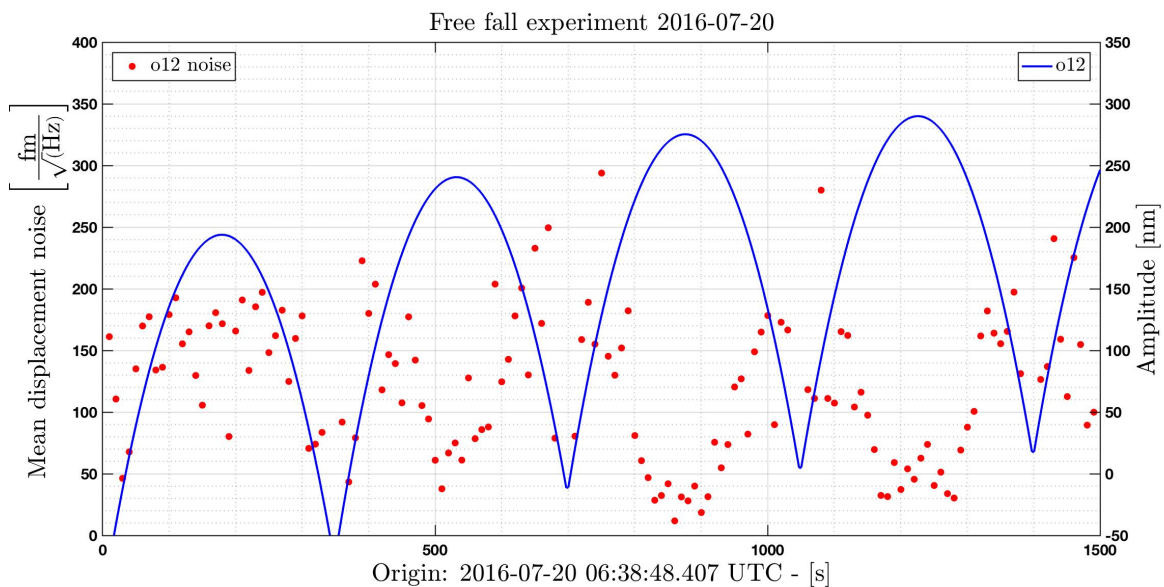

Figure 6.31.: This plot shows the first few parabolas of the third free fall experiment (blue), also shown is the mean noise level calculated between 1.2 Hz and 1.8 Hz (red). This noise level depends on the TM position, a plot of this dependency can be found in Figure 6.33.

---

[2]The first free-fall experiment was on 2016-06-09. In this experiment the phase noise was increased.

Measurement	r2G $\left[\frac{\text{fm}}{\sqrt{\text{Hz}}}\right]$	$\hat{r}^{(2)}_{\text{correlated}}$ $\left[\frac{10^{-6}}{\sqrt{\text{Hz}}}\right]$	noise floor $\left[\frac{\text{fm}}{\sqrt{\text{Hz}}}\right]$	χ^2
Free fall #2	198.52 ± 0.424	1.655 ± 0.004	40.803 ± 0.1397	3.1
Free fall #3	219.34 ± 0.978	1.828 ± 0.008	34.509 ± 0.3824	8.98

Table 6.6.: Shown here are the results of a fit to the mean noise of the two free flight experiments under analysis. The fit consists of a noise floor component, and the contribution of $2f_{\text{het}}$ RIN. From the measured phase noise the RIN level was calculated for correlated RIN, in the same way as was shown in previous Sections. For uncorrelated RIN the noise level calculated from the measured phase noise is a factor $\sqrt{2}$ bigger. The χ^2 value is a measurement of the fit accuracy, due to the larger distribution of points it is not surprising that this value is bigger than 1. See also A.11.

parabolas are then split into segments of 20 seconds, with 50% overlap. Using a BH92 window an amplitude noise spectrum for each is calculated. From the distribution of the measured noise levels for different TM positions mean noise values are calculated. The parabola are split into smaller segments the same way, this causes the structure in the distribution of the TM offsets.

The sensing noise between 1.2 Hz and 1.8 Hz of the second experiment is shown in Figure 6.32, an increase in noise with bigger TM offset is visible. In the third experiment the expected reduction in noise around the TM offset 266 nm, or π rad, for $2f_{\text{het}}$ is visible, see Figure 6.33.

The noise data is split into TM offset segments, from the mean noise data points within these segments a mean noise and mean TM position are calculated. For the second experiment the lower TM offsets are split according to the visible distribution of TM offsets, above 30 Hz the TM offsets are split in 5 nm blocks. The third experiment is split into segments of 10 nm, this happens to fit with the visible distribution. These mean values are shown in red with the error bars as calculated by the mean function of LTPDA from the distribution of points. The same $2f_{\text{het}}$ RIN fit function as in the the other RIN experiments is used to make a fit to the mean noise per TM offset. A plot of the fit results can also be found in Figures 6.32 and 6.33. The results of the fit are shown in Table 6.6. For a visual comparison of the RIN of these experiments the fit result of the first RIN subtraction experiment is also copied into the plots.

The mean RIN in the free fall experiments is higher than in the dedicated experiment. In the third free fall experiment the distribution of points around the noise peak is mainly in an area of $\approx \pm 100 \frac{\text{fm}}{\sqrt{\text{Hz}}}$ around the mean noise value. In the first RIN subtraction experiment most measured noise values at the noise peak are in an area $\approx \pm 50 \frac{\text{fm}}{\sqrt{\text{Hz}}}$ around the mean value. The confidence in the result of the dedicated experiment is higher, since the free fall experiment might contain other sensing noise, which leads to a bigger distribution of measured noise values.
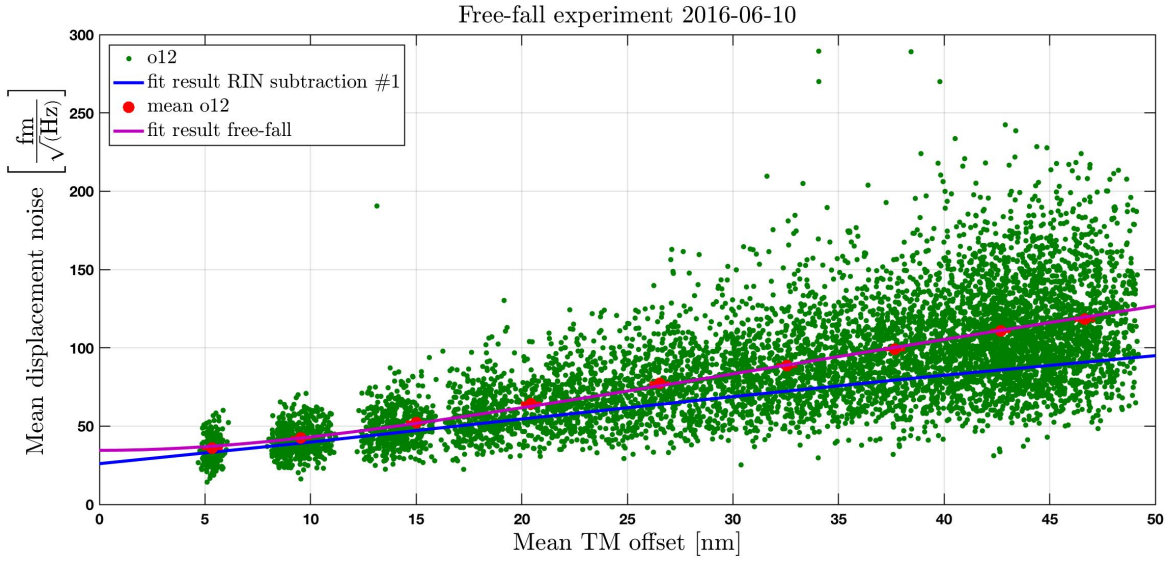
Figure 6.32.: Shown here is the mean noise level calculated between 1.2 Hz and 1.8 Hz for the second free-fall experiment. Shown on the x-axis is the mean TM offset for which the mean noise level is calculated. The y-axis shows the mean noise level; from this measurement it is not clear if the noise increase for bigger offsets is due to an increase in RIN. From the measured data points the mean noise for segments of 5 nm length are calculated, these are shown in red. For smaller TM offsets the segment length is adapted to the distribution of TM offsets.
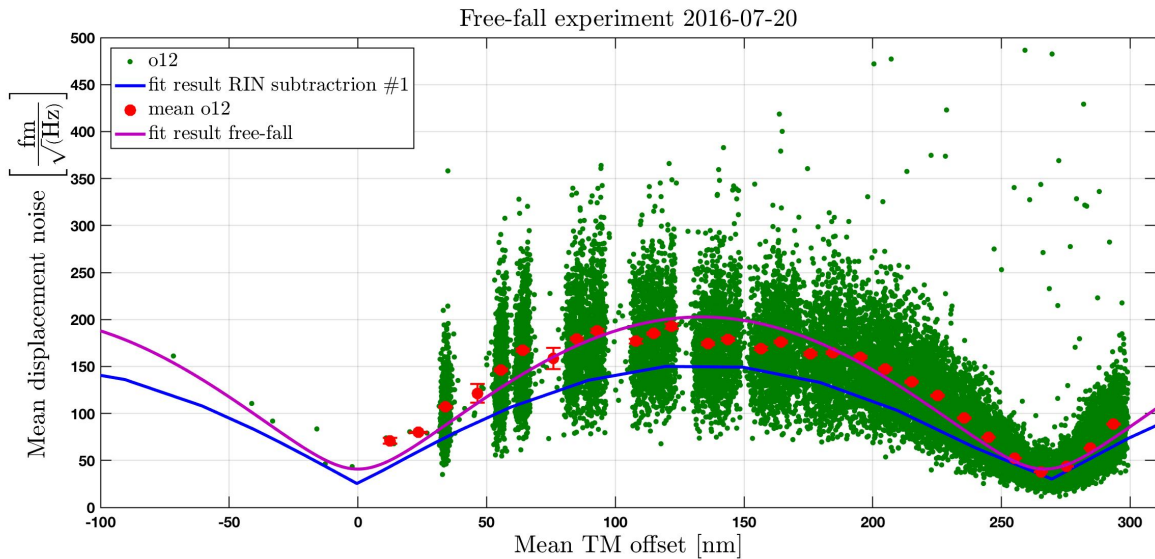
Figure 6.33.: The same analysis is performed for a free-fall experiment with larger TM motion. This flight covers enough range to show the expected decrease in noise around a phase difference of π, which corresponds to a TM offset of 266 nm, as would be expected for the coupling of $2f_{het}$ RIN to the o12 signal. From the measured data points the mean noise for segments of 10 nm length are calculated, these are shown in red. Due to this regular spacing of the intervals for the calculation of the mean values some averages only have a few data points; their error bars are visibly bigger.

Error discussion

The measured phase noise in these experiments shows a bigger distribution than in the RIN subtraction experiments. This increase in noise is probably not due to an increase in crosstalk from the angular degrees of freedom since this noise couples at lower frequencies. In this experiment the TM reached top velocities of $\approx 3\,\frac{\mathrm{nm}}{\mathrm{s}}$ at the start and end of the parabola, at the apex this velocity is obviously zero. Due to the drift in the TM offset of the start and end points of the parabola the same TM position is sampled at different speeds. The big scatter of the measured noise levels might be due to changes in the TM velocity at the time the spectrum is calculated. One noise source which depends on the rate of phase change is the so-called doppler effect. Due to the motion of the TM the heterodyne frequency in the bin of the phasemeter is shifted by small amounts, this shift causes an increase in sensing noise [37][34]. Another noise source due to higher TM velocity arises due to the sampling of the data. With a moving average filter the $100\,\mathrm{Hz}$ is downsampled to $10\,\mathrm{Hz}$. If the first and last sample of the moving average are different an increase in phase noise is visible. During normal operations this is not a consideration since the TM is relatively stationary. The sensing noise was also calculated for some of the transients from the TM offset after station keeping back to the nominal TM position. In these an increase in sensing noise depending on TM velocity could also be observed.

In other experiments a small vector noise component was found, it is not clear how this noise would contribute in these circumstances. The sensing noise measured here has to be understood as an upper limit of the RIN contribution, since the other noise contributions are hard to estimate.

Later free-fall experiments were performed with a lower actuation authority and an out-of-loop force to reduce the amplitude of the parabola by counteracting the force on the TM due to the gravitational imbalance; which decreased the amplitude of the parabola to $\approx 27\,\mathrm{nm}$. With this smaller amplitude an estimate of the RIN level at times when no dedicated RIN experiment was performed is not possible.

6.8. Overview of the RIN flight experiment results

The RIN contribution to the sensing noise was measured during LPF operations with two RIN subtraction measurements, the analysis of these was shown in Sections 6.2 and 6.3. Shown in Table 6.7 are the RIN levels calculated from the phase noise between 0.6 Hz and 0.9 Hz measured during these experiments. The noise floor level observed in these measurements is consistent with the results presented in [19]; in this paper the performance of the LPF sensor noise is shown. For the noise model in this paper an upper $2f_{het}$ RIN limit of $5 \frac{10^{-6}}{\sqrt{Hz}}$ was assumed. Compared to phasemeter readout noise and frequency noise, RIN plays a minor role since the TMs are near the optical zero position. Setting the optical zero as the standard position of the test mass is an important component of the good performance of the OMS. With a RIN contribution as measured in the first RIN subtraction experiment the sensor noise is a factor ≈ 5 higher for TM offsets with maximum RIN coupling.

In these experiments only a phase noise contribution of $2f_{het}$ RIN to the noise floor could be found. While the assumption after the first experiment was that the $1f_{het}$ RIN contribution is removed with balanced detection, in the second RIN subtraction experiment with no balanced detection no $1f_{het}$ RIN contribution could be seen.

At the end of the operations time a direct measurement of the RIN level at $1f_{het}$ and $2f_{het}$ was performed, see Section 6.5. This measurement is limited by ADC noise. By subtracting this noise from the measured noise an estimation of the RIN present was made for the individual beams. Shown in Table 6.7 is the $2f_{het}$ RIN of both beams combined, with the amplitude stabilisation on.

These results also suggest that the RIN level in the two beams can be different; in previous calculations of the RIN from the measured phase noise one of the assumptions is that the RIN in the two beams has the same noise amplitude. It is not clear if this RIN ratio is time-dependent. Since the RIN level is calculated from the phase noise, the value shown can again be used to calculate the phase noise in different circumstances, even if it does not describe the RIN in the two beams accurately.

In this experiment, and in measurements made on the ground in preparation of the mission, an $1f_{het}$ RIN level was measured at a similar level as $2f_{het}$ RIN. Why no phase noise contribution due to this RIN could be found in the second RIN subtraction experiment, where balanced detection was turned off so that this contribution is not removed, is not clear. One reason might be the limits on the analysis of the direct measurement due to the ADC noise contribution. Or the fast amplitude stabilisation suppresses $1f_{het}$ RIN better during in orbit than it did during the measurements made during the test-runs.

While it was not planned as a RIN experiment, an estimation of the RIN contribution from two of the free-fall experiments could be made, see Section 6.7. In this experiment the TM is moved in a parabola, and is not stable at a fixed position at different TM offsets from the optical zero. Due to this motion shorter time segments are used to calculate the mean noise. Here, the mean phase noise is calculated in the frequency range from 1.2 Hz to 1.8 Hz, these mean noise levels are then used to calculate the RIN contribution. The mean sensing noise of these measurements show a bigger distribution. The calculated RIN levels are the result of taking the average of a bigger number of individual noise measurements. With the same fit function as in the dedicated experiments the RIN contribution is calculated from the mean sensing noise over the parabola. Due to noise related to the relatively fast motion of the test mass, like Doppler noise and the moving average filter, this calculated RIN level is an overestimation. Since more data points are used to calculate the average noise level per TM offset the RIN values calculated from this experiment have a smaller error, however due to the aforementioned noise sources of the faster TM motion the systematic errors are

Date	Experiment	$\hat{r}^{(2)}_{\text{correlated}} \left[\frac{10^{-6}}{\sqrt{\text{Hz}}} \right]$	$\hat{r}^{(2)}_{\text{uncorrelated}} \left[\frac{10^{-6}}{\sqrt{\text{Hz}}} \right]$
2010	Ground	1.4 ± 0.14	1 ± 0.1
2016-04-25	RIN subtraction #1	1.27 ± 0.01	1.79 ± 0.02
2016-06-10	Free fall #2	1.655 ± 0.004	2.341 ± 0.006
2016-07-20	Free fall #3	1.828 ± 0.008	2.585 ± 0.011
2017-02-02	RIN subtraction #2	1.62 ± 0.02	2.29 ± 0.03
2017-07-11	direct	1.32 ± 0.15	1.03 ± 0.07

Table 6.7.: Shown in this table is an overview of the $2f_{\text{het}}$ RIN levels for both correlated and uncorrelated RIN between the two beams, measured during in-flight experiments. The RIN value from the ground measurement is estimated from plots in [92].

bigger.

In addition to the longitudinal TM displacement the RIN contribution to the DWS signal was measured by angular offsets to the TMs, see [57]. From the changing noise level for different angular offsets the RIN contribution can be calculated. The analysis of these experiments is still ongoing.

The RIN depends on the temperature of the laser crystal and the pump current, these values were set during the commissioning of the OMS and changed over the course of the mission duration. These changes are one possible source for the changing sensing noise over the mission duration. A paper on this topic is in preparation [59].
The actuator of the slow frequency control loop is the temperature setpoint of the laser crystal, since changing this temperature also changes the RIN the slow frequency control loop was not used.

In the LPF OMS the two interfered beams originate from the same laser source, and have a similar power level when they reach the diodes. For the LISA mission the situation is different; the interfered beams not only originate from different laser sources, but some of these lasers are on different satellites 2.5 million kilometres apart. The coupling of RIN to the phase measurement with different power levels of the beams, low contrast, and the delays due to the light travel time between the different optical metrology systems is the subject of ongoing research.

7

Summary

Chapter 1 briefly introduced black holes and gravitational waves. Which are not only interesting on their own, but research on these topics also furthers the understanding of the universe as a whole. In addition to measurements of gravitational waves from the ground with LIGO, a future observatory in space is motivated. This mission is called LISA, which is currently in development and scheduled to launch in 2034. To demonstrate the feasibility of the technology for this mission the LISA Pathfinder mission (LPF) is introduced, it was in operation from 2016 till 2017. This thesis shows experiments on the ground related to LPF, and results from in-flight experiments. Some of the analysis techniques used in this thesis are introduced as well.

In Chapter 2 the measurement of the phase in the LISA Pathfinder Optical Metrology System (OMS) is shown. First, the concept of heterodyne interferometry is explained. Two laser beams with a frequency difference f_{het} are interfered. Changes in the pathlength between the two beams cause a phase change in the interfered signal, called the heterodyne signal. From this phase change φ the change in pathlength in metre is calculated, from which the displacement of two test masses (TMs) is measured. In the next Section the OMS at the AEI laboratory, with modulation bench (MB) and optical bench (OB) is shown. On the modulation bench a laser beam is split in two. The two resulting beams are frequency shifted with Acousto Optic Modulators (AOMs) to create the frequency difference f_{het}. The OB consists of four interferometers, it is placed between the two TMs. These TMs are in the beampath of one of the beams, called the measurement beam. With two interferometers the displacement of these TMs is measured, the signals of two additional interferometers are used to reduce the noise. Used in the laboratory setup is the engineering model of the OB (EM OB). For the flight model optical bench (FM OB) a few mirrors were moved, and the angle with which the measurement beam hits the test masses was increased. This phase change φ of the heterodyne signal is measured with a phasemeter; the processing of this signal to the desired TM displacement is shown for the laboratory and flight model.

In Chapter 3 the most relevant noise sources related to the OMS are shown. The main focus here lies on Relative Intensity Noise; RIN around the heterodyne frequency f_{het} and around twice the heterodyne frequency $2f_{het}$ couples to the phase measurement. The coupling of this noise is described for a phase measurement with a single diode for RIN correlated and uncorrelated between measurement and reference beam. The subtraction of this noise from the phase signal by using both interferometer output ports in a process called balanced detection, and by subtraction with a reference signal is also shown. To test the calculated coupling from RIN to the phase later experiments use a RIN equivalent sinusoidal intensity modulation on one of the beams, here differences in the beam powers of the measurement and reference beam are taken into account for the calculation of the phase change.

To prepare the laboratory setup as a test-bed for the in-flight operations of the OMS during the LPF mission the previous analog laboratory system was updated to a digital system. This new laboratory setup is explained in Chapter 4. With a system similar to the AdvLigo Control and Data System (CDS) of the advanced Laser Interferometer Gravitational-Wave Observatory (aLIGO) the phasemeter data is recorded and saved. In addition, this system contains the digital versions of the previous analog control loops to stabilise the optical pathlength difference (OPD loop) and laser frequency (Frequency control loop). For the planned experiments to test the subtraction of phase noise due to RIN from the measurement signal with the reference signal an additional control loop on the longitudinal and angular degrees of freedom of both test masses is constructed. This control loop is used to keep the TMs at a fixed position at different offsets.

In preparation of the later RIN experiments the injection and measurement of RIN with the laboratory setup is shown. At first, RIN was measured at the original frequency. Since this necessitates the recording of the beam powers at a sampling frequency of 16 kHz the duration of these measurements is limited. To enable long-term monitoring of the RIN of both beams additional channels to record a demodulated version of these signals is introduced, these signals can be recorded at the lower sampling frequency of 256 Hz.

With this new digital setup the coupling from injected RIN to the phase is measured, and compared with the predicted coupling. These experiments are shown in Chapter 5. To measure the coupling from RIN to the phase from a single diode a RIN equivalent sinusoidal intensity modulation at a fixed frequency and with decreasing amplitude is injected. In the analysis of this experiment a contribution of Small Vector Noise (SVN) to the measured phase amplitude was found. This noise is created during the injection of the RIN in the electronics of the AOMs. To measure this SVN, and subtract it with a fit, a second version of this experiment was designed. In this second experiment the measured coupling from $1f_{\text{het}}$ RIN to the phase is consistent with the previous calculations. The measured amplitude for the $2f_{\text{het}}$ RIN injection is $\approx 20\%$ bigger than predicted; the reason for this difference could not be found.

In a second set of experiments the frequency dependency of the RIN coupling is measured; here the injection amplitude is kept constant, while the frequency of the RIN equivalent sinusoidal intensity modulation is changed. The results show a frequency independent coupling of RIN to the phase, when the measured amplitude is corrected for the OPD control loop, for frequencies below 21 Hz. Above this frequency the coupling of $1f_{\text{het}}$ RIN shows additional features, which were not investigated further, but seem to be related to the OPD loop.

The third set of experiments demonstrates the subtraction of RIN with the signal of the reference interferometer. This interferometer is used as input to the OPD control loop, and to subtract remaining noise from the other interferometers. The efficiency of this subtraction for phase noise due to RIN depends on the phase difference between the two signals, in this case between one port of the interferometer of TM1 and the corresponding port of the reference interferometer. To create the phase difference between the two signals TM1 is moved in steps, for each the phase noise is measured. During this experiment the injected RIN is recorded with the demodulated power signals. These are then used to calculate the predicted phase noise. In two frequency bands, between 2.2 Hz and 3.2 Hz, and between 14 Hz and 15.5 Hz, the measured and calculated phase noise are compared. For the higher frequency band, for both the $1f_{\text{het}}$ RIN and $2f_{\text{het}}$ RIN injection, the predicted and measured phase noise are within 5% of each other. As an additional test, this subtraction is done with a sinusoidal RIN injection. In this experiment SVN again contributes to the measured phase amplitude. Since this contribution can not be removed here the difference between measured and predicted phase amplitude is bigger than in the RIN subtraction with a noise injection.

In Chapter 6 the RIN experiments during the LPF mission are presented. First, the design of the RIN flight experiments is shown; in two experiments TM2 is moved in steps to measure the changing phase noise level and calculate the RIN responsible. In a third experiment the raw phasemeter data of one interferometer quadrant is used to measure the RIN directly.

The focus of the first RIN experiment is the subtraction of RIN over a longer range of phase difference, in this measurement a contribution of $2f_\text{het}$ RIN to the phase noise could be found. In the second RIN subtraction experiment the implemented TM steps cover a shorter range, but in addition to the standard phase measurement with balanced detection at each offset the phase noise with only one interferometer side active is measured. The phase noise contribution of $1f_\text{het}$ RIN can be removed with balanced detection, and should be visible in this additional measurement. However, no significant contribution could be found. This is most likely due to the active suppression of amplitude noise around $1f_\text{het}$ with the fast amplitude stabilisation. In the measured phase noise for changing TM position additional noise features to the expected RIN contribution could be found. With an additional measurement of the phase noise with a sampling frequency of $100\,\text{Hz}$, instead of $10\,\text{Hz}$, these features can be attributed to the imperfect subtraction of noise around $10\,\text{Hz}$ created by the OPD loop actuation.

In the direct measurement the RIN of both beams is measured individually, with and without the amplitude stabilisation active. For $1f_\text{het}$ RIN with the amplitude stabilisation the recorded noise is at a similar level as expected from ADC noise, which is consistent with the results of the second RIN subtraction experiment where no significant $1f_\text{het}$ RIN phase noise contribution could be found. Without the stabilisation the recorded noise is one order of magnitude bigger, suggesting that without active stabilisation of RIN at this frequency this noise would play a significant role in the contributions to the phase noise.

With a second set of experiments $2f_\text{het}$ RIN is measured. With the stabilisation active the measured $2f_\text{het}$ RIN is at a similar level as $1f_\text{het}$ RIN, both measurements are limited by ADC noise. Without the stabilisation the $2f_\text{het}$ RIN level is a factor ≈ 2 lower.

One main part of the LPF operations were the noise-run measurements. There, the noise of the system is measured over a long duration, the measured phase noise is compared with the expected noise contributions. Over time, as more understanding of the system was gained, the measured noise decreased and its contributions can be described with more detail. During these noise runs the TM drifts around its zero position by less than a nanometre. Due to the performed experiments and the transients after station keeping manoeuvres the TM shows a bigger offset distribution. Associated with this is an increase in the coupling of RIN, the shape of the measured phase noise is consistent with the results of the dedicated RIN experiments. Another experiment where the TM is moved over a bigger distance is the free-fall experiment. To remove actuation noise the test masses are not acted upon continuously, but only in brief force kicks. In-between these kicks the TM moves in a parabola. From the mean phase noise for a mean TM offset from its optical zero the RIN level can be calculated, using the same method as in the dedicated experiments. Again, a contribution of $2f_\text{het}$ RIN to the phase noise could be found. Due to other noise related to the motion of the test masses the calculated RIN level is higher than in the dedicated experiments.

A summary of the calculated RIN levels for these experiments can be found in Section 6.8.

8 Conclusion and Outlook

This thesis started with the transition from the LISA Pathfinder OMS ground setup with analog control loops and a simpler data recording setup to a more sophisticated digital setup. With most components of the control loops in software, it is easier to change the gain or the filter of the loop, to monitor the status and to inject signals. In addition to the previous control loops on the optical pathlength difference and the frequency, a set of control loops on the TM longitudinal and angular degrees of freedom was implemented. This digital system also allows the timed injection of noise, sinusoidal signals and steps. At first this was used to run scripted experiments over night, the weekend or the holidays in a more quiet environment. Near the end of my thesis an additional noise contribution in small vector noise was found, and the main laboratory experiments related to RIN were repeated. Here, this digital setup showed its true strength, as many tasks could now be performed remotely, which was a big advantage during the COVID-19 pandemic.

To confirm the calculated coupling from RIN to a phase noise contribution a number of experiments were performed where RIN was injected on the reference beam. For a sinusoidal RIN equivalent intensity modulation near $1f_{het}$ the coupling to the phase could be confirmed, The measured phase for a RIN injection near $2f_{het}$ is $\approx 18\%$ bigger than calculated from the measured RIN, the cause of this discrepancy could not be found. It might be related to the effect of a filter, either in the phase measurement or in the RIN measurement, which acts differently on $1f_{het}$ and $2f_{het}$. The effects of all known filters were considered, and no cause could be found. If the cause is a filter or some other property of the LPF laboratory setup, then one could expect that measured and calculated phase would match in other experiments. In a different optical setup, with a different phasemeter, both $1f_{het}$ and $2f_{het}$ RIN were injected. In this experiment the measured phase noise is close to the value predicted from the injected RIN for both [82]. This increases the confidence in the calculated coupling coefficients.

When phase noise due to RIN is subtracted with a reference signal the efficiency of this subtraction depends on the phase difference between the two signals. This subtraction was successfully shown in the laboratory with a RIN injection for both $1f_{het}$ and $2f_{het}$. Since other sensing noise is subtracted in the calculation of the o1 signals a smaller RIN injection can be used to reach a reasonable signal-to-noise-ratio, therefore the injection voltage on the AOM electronics is lower in these experiments. The lowest voltage in the RIN transfer function experiment is $0.305\,\mathrm{Vpp}$ out of CDS, which is $0.1525\,\mathrm{Vpp}$ after the differential-to-single ended electronics. The voltage after the differential-to-single ended electronics in the RIN subtraction experiment is $\approx 0.0975\,\mathrm{mVpp}$. If the additional effect, which causes the discrepancy in the RIN transfer function experiment, is related to a higher injection voltage it seems to be a smaller effect in the RIN subtraction experiment. And it is also likely that this effect is rising when a threshold voltage is reached, since the voltage difference between the two experiment is only $\approx 50\%$, and a bigger effect would be expected in the RIN subtraction

experiment if it was a linear dependency.

Near the end of the writing phase a new experiment was designed to measure the $2f_{het}$ RIN transfer function with a lower injection voltage. This experiment was run once, but did not produce good results. Due to time constraints this experiment was not repeated. The idea is a combination of the successful RIN subtraction experiment with the SVN subtraction of the second RIN transfer function experiment. This new experiment design is as follows:

- Set the longitudinal TM control loop setpoint to 133 nm. This maximises the $2f_{het}$ RIN coupling to the o1_A, o1_B and o1 signal.

- Inject a $2f_{het}$ RIN equivalent sinusoidal intensity modulation, with a smaller amplitude than in the previous experiment.

- Move the OPD loop setpoint in steps. This changes the phase difference between measurement and reference beam, which changes the SVN amplitude. The phase difference between the two interferometers is kept at $\frac{\pi}{2}$ by the TM control loop.

- The combined SVN contribution should be visible in a plot of the phase amplitude at the injection frequency in the o1 signals, with the OPD loop setpoint as the x-values.

- Subtract SVN with a fit, and calculate the mean of the residuals. Since $2f_{het}$ RIN is correlated between the two interferometers the measured mean amplitude should be twice the predicted value of the previous experiment.

The SVN contribution is the combination of the SVN of the two interferometers, and requires a fit with the equation for the subtracted signal as shown in Section 5.1.4.

Since the properties of RIN subtraction with a reference could successfully be shown in the laboratory, these methods can be used to learn about properties of the sensing noise of the flight OMS. To measure the RIN level the TM is moved from its nominal position in the optical zero. From the increase in phase noise the RIN level can be calculated.
To measure RIN directly the phasemeter can be used, this requires changing phasemeter settings and data at a high sampling frequency. An overview of the measured RIN levels of the flight OMS can be found in Section 6.8.
Experiments to measure the RIN contribution in the flight OMS either take a long time, or are require major changes to the system; this makes a continuos monitoring of the RIN level over the mission duration impractical.

LISA

The research into the coupling of RIN to the phase for the LISA mission currently in development is still ongoing [93][94]. As in the LISA Pathfinder OMS the phase noise contribution of $1f_{het}$ RIN is subtracted with balanced detection in LISA. In the LPF OMS phase noise due to $2f_{het}$ RIN can be subtracted from the measurement with the reference signal, since both signals use the same laser beams. For LISA two lasers per satellite are planned, the local interference signals all use different beams. Additionally, since one main part of the measurement is the interference of the local beam with the beam from the far spacecraft the powers involved are very different. This makes a local subtraction of $2f_{het}$ with an optimised working point more difficult. While the RIN of the individual signals in the different spacecraft has some overlap, due to the separation of 2.5 million kilometres the light travel time is a considerable factor. The analysis method to recover the gravitational wave signals from the measured phase signals of the three satellites is called Time Delayed Interferometry (TDI). To characterise the RIN contribution, the noise has to be traced

through the TDI algorithm.

One main avenue of research so far has been the suppression of frequency noise in this measurement, since it is expected to be one main contribution to the phase noise. Currently in development is the coupling of RIN of all the lasers involved, with the proper delays, to the measured phase. The subsequent tracing of this error through the TDI algorithm is one of the research topics at the AEI.

With TM offset experiments similar to experiments presented here the RIN level could be measured in the LISA mission. The long duration of these experiments is a disadvantage, because this makes the regular monitoring of RIN very expensive.
One possibility to improve the monitoring of RIN in the LISA is the inclusion of demodulated power channels, similar to the ones implemented in the laboratory. Relevant would be the monitoring of RIN at $2f_{het}$, this could be achieved with a demodulation frequency with a small frequency offset to $2f_{het}$. For LISA, the heterodyne frequency is in the MHz range. This heterodyne frequency is created by the relative motion of the spacecraft through the doppler effect. Due to different relative speeds in the orbits of the three satellites this frequency drifts, which makes switches in the phasemeter processing necessary [95]. The planned photodiodes can measure at this higher frequency, However, to record this data an ADC with a sampling frequency in the MHz range on the power measurement diodes would be needed, which is not realistic for LISA.
The LISA phasemeter uses a tracking Phase-Locked Loop (PLL). A method similar to the direct RIN measurement of Section 6.12 can not be implemented, since this phase measurement system does not use a SBDFT. However, an FFT algorithm is implemented as an auxiliary measurement system to acquire the initial laser link between the spacecraft. This FFT could be used to measure the RIN of the interfered beams at a frequency near $2f_{het}$, with a method similar to the direct RIN measurement. The required calculation could be done on-board. And the result could be saved and downloaded at a very low sampling frequency for longterm monitoring purposes, as part of the Housekeeping data.
Since the heterodyne frequency changes over the mission duration this RIN measurement frequency either needs to be adjusted, or a measurement of the spectral shape of RIN has to be done on ground with a high sampling frequency. From this ground measurement estimates of the RIN in flight can then be made with a lower number of dedicated measurements at set frequencies.

A Appendix

A.1. Photodiode connection on the EM OB
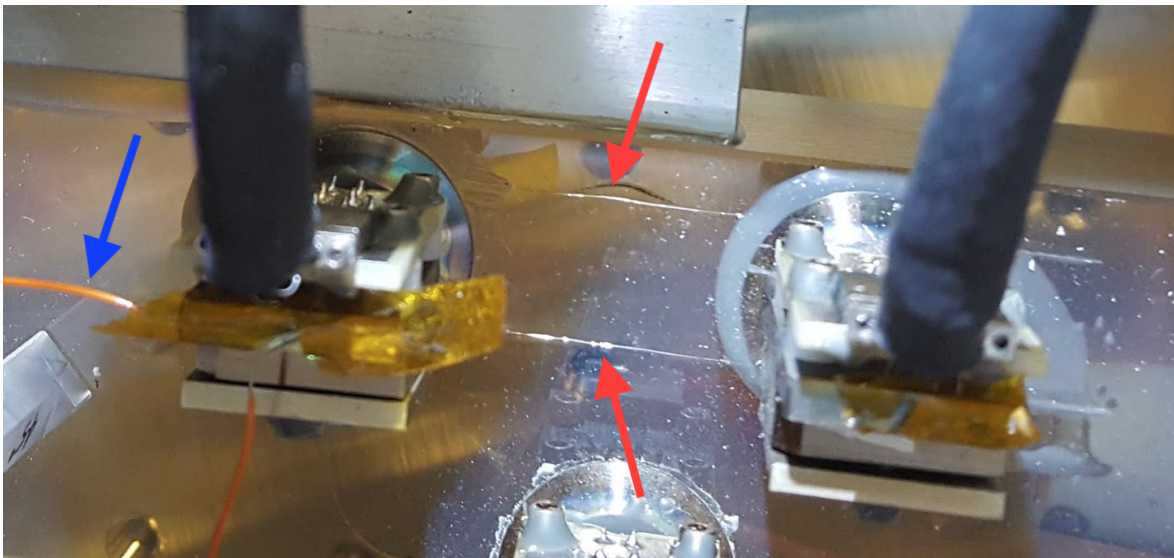
Figure A.1.: The shields of the QPD were connected on the optical bench. Through thin wires the metal base of the diodes were connected, these are marked with a red arrow. Additionally the metal casings are connected with each other, marked here with a blue arrow. Since the diodes are also connected via the phasemeter and the amplitude stabilisation diodes are measured using a separate set of electronics these OB connections created ground loops, and were removed.

A.2. Simulink® implementation of the phasemeter calculation
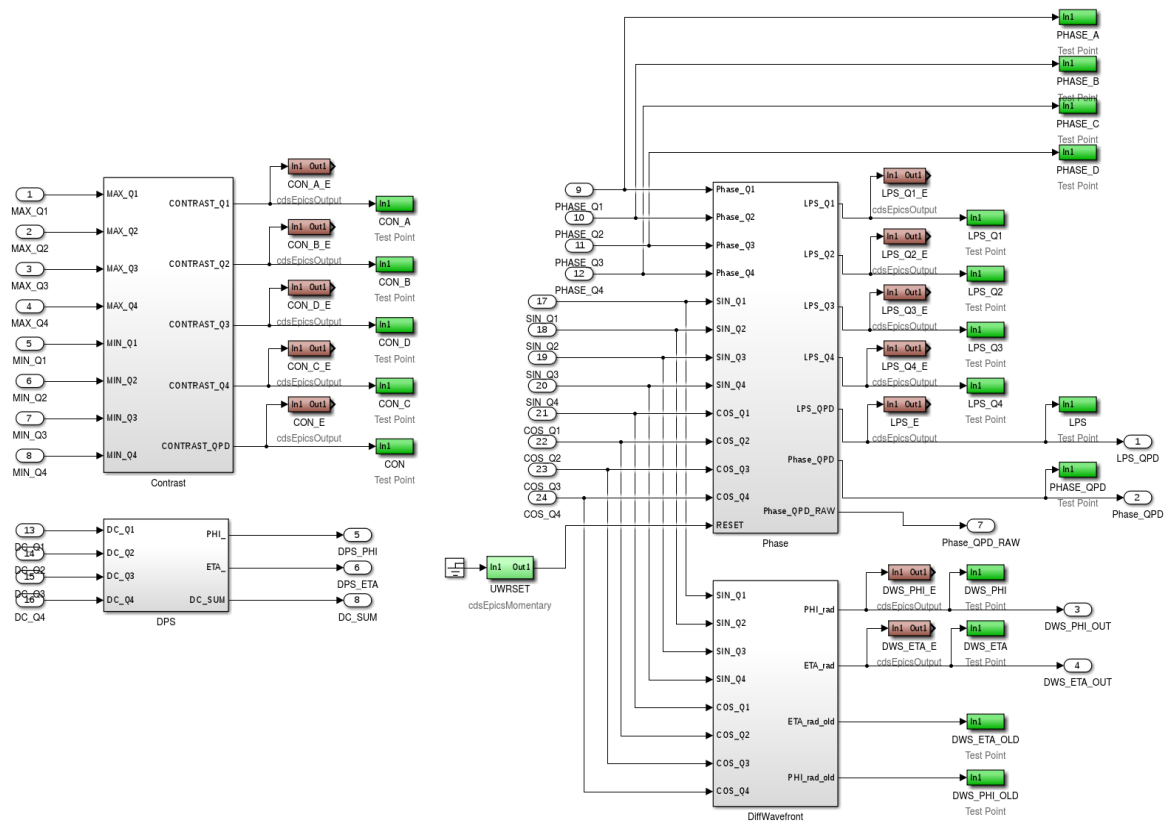
Figure A.2.: From the phase of individual quadrants the longitudinal and angular signals are calculated, shown here exemplary for the x1 signal. The calculation of the phase signal was already shown in A.3, the output of this calculation is re-named for the interferometer at hand and send out for further processing. The calculation within the block with the label DiffWavefront can be found in Figure A.4. The calculation in the block DPS is similar, but uses the power on the individual quadrants instead of the phase. The result are the DWS and DPS signals, before the calibration to test mass orientation.
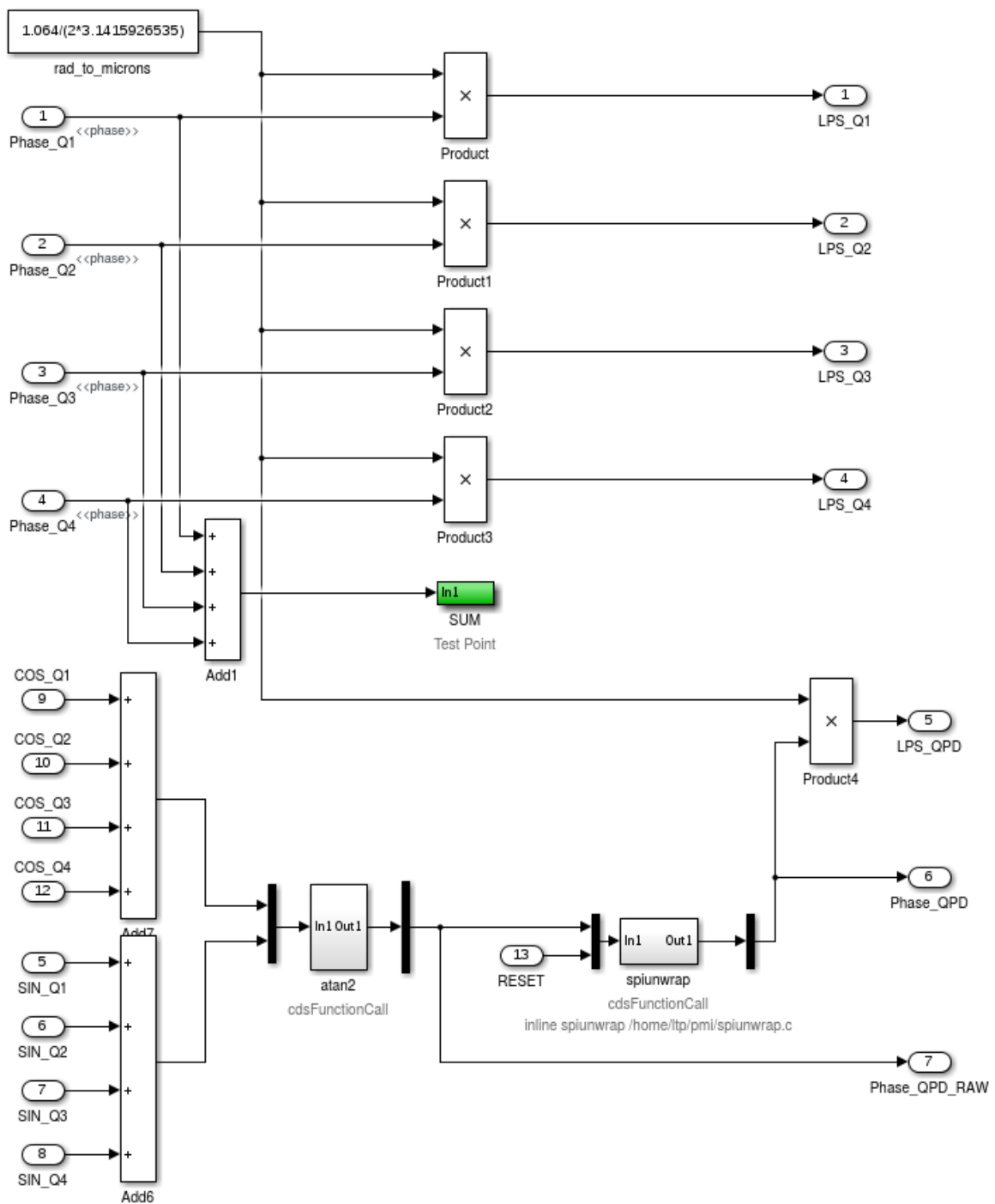
Figure A.3.: This graphic shows the calculation of the phase in Simulink® of one QPD, the input from the phasemeter is on the left. Inputs 1-4 are the phase of four quadrants of one diode, as calculated by the phasemeter. The signal used for the following analysis is calculated from the sine and cosine outputs of the phasemeter, inputs 5-12. These real and imaginary parts of the phase amplitude are summed, and the phase is calculated (atan2 function) and phase-tracked (spiunwrap function). The output used for the longitudinal signal is number 6 PHASE_QPD. The channel PHASE_QPD is used for further analysis of the longitudinal signal. The channels SUM, PHASE_QPD_RAW and LPS_QPD were used for de-bugging purposes.
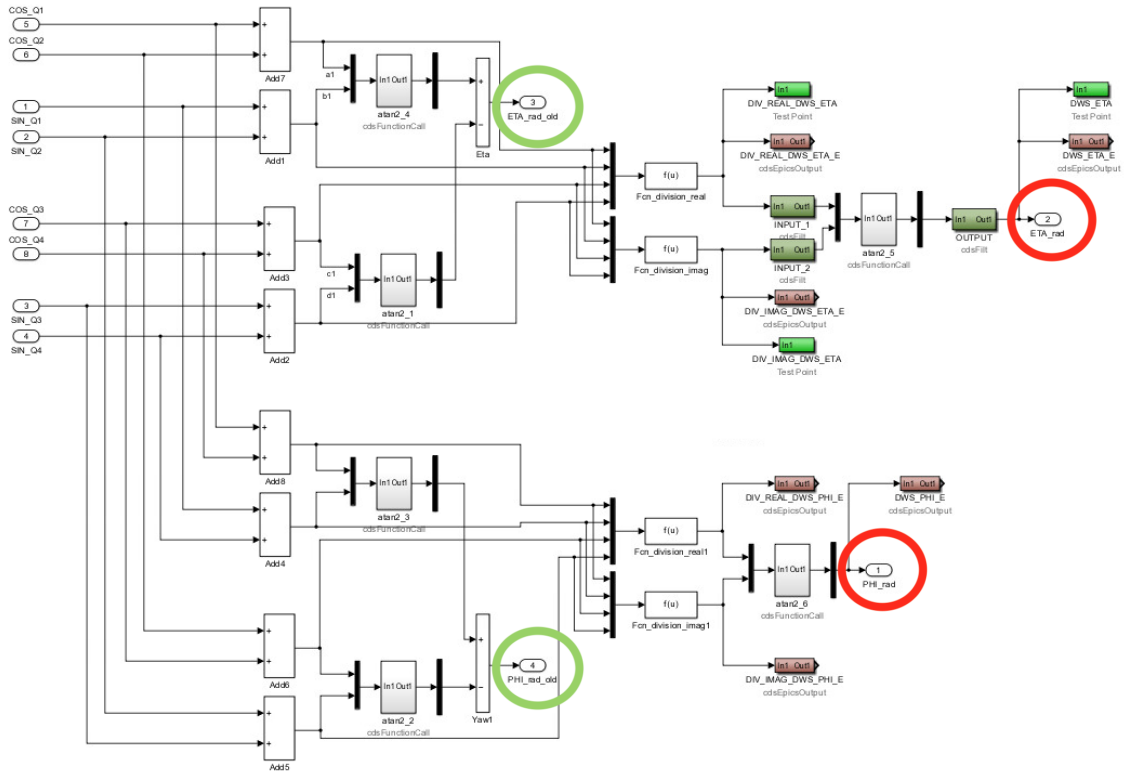
Figure A.4.: This graphic shows the calculation of the DWS signal in Simulink®, the input from the phasemeter is on the left. The signal used for the following analysis is calculated from the sine and cosine outputs of the phasemeter, inputs 1-8. Shown in this graph is the old DWS processing marked in green, and the new DWS processing (red) which is used for the analysis.
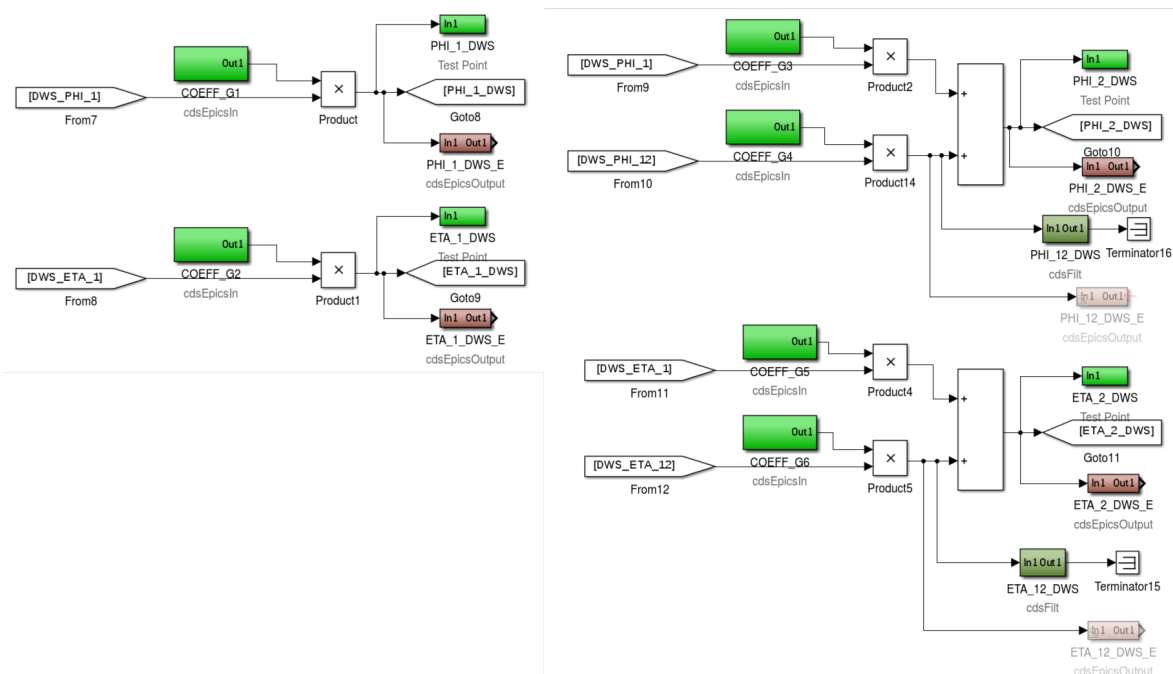
Figure A.5.: This graphic shows the calibration of the test mass orientation from the DWS signal as implemented in Simulink®. The k parameters used here were measured in Glasgow. The angular signal of TM1 can directly be calculated from the DWS signals of the X_1 interferometer, to calculate the motion of TM2 the motion of TM1 has to be removed from the DWS signal as measured by the X_{12} interferometer.
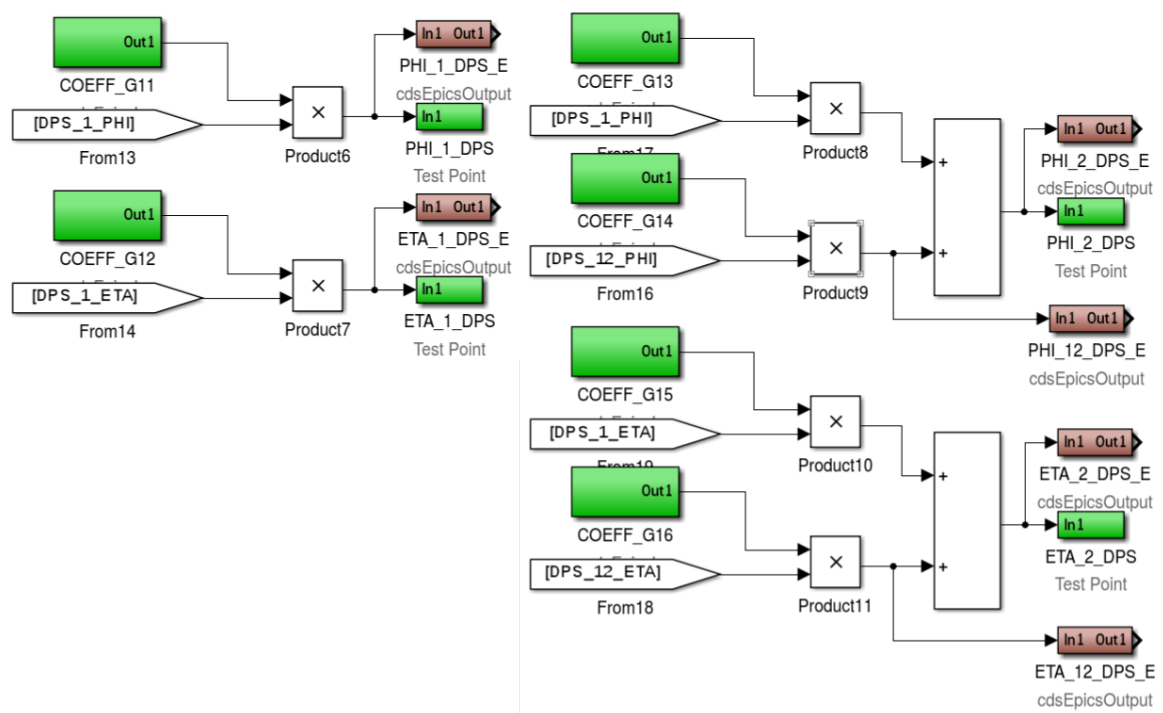
Figure A.6.: This graphic shows the calibration of the DPS signal in Simulink®. This calculation is similar to the DWS calculation. From the power of the individual quadrants the spot position on the diodes can be calculated. This signal can then be calibrated to a measurement of the test mass orientation. The k parameters necessary for this calibration were measured in Glasgow.
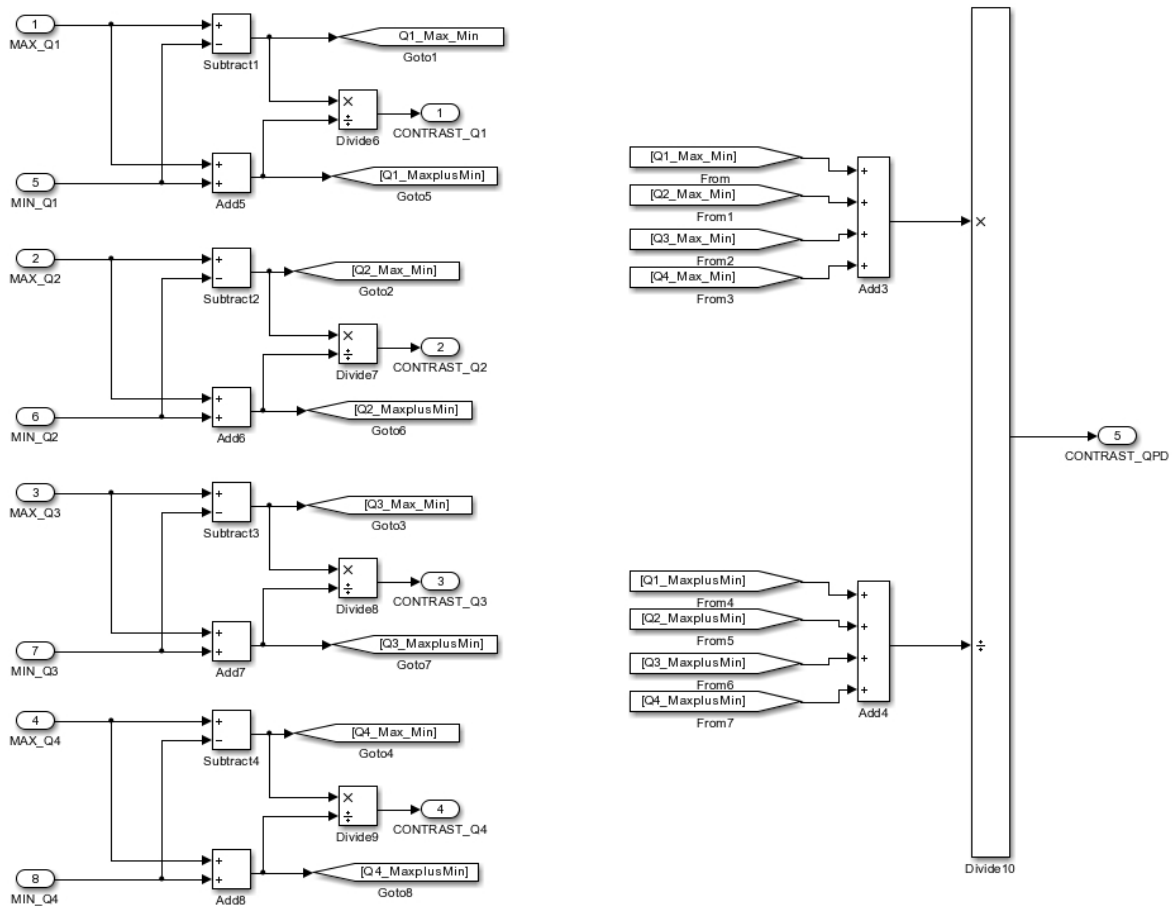
Figure A.7.: This graphic shows the calculation of the contrast in Simulink®. The interferometer contrast is a measurement of the matching between the two interfered beams, it is calculated from the maximal and minimal values of the heterodyne signal. A Contrast of 1 would have the beams interfere so that in one port of the interferometer the power drops to zero while the other port receives all the power. At lower contrast values the two beams are not matched as well, and destructive interference does not remove all of the beam power and the minimum value of the heterodyne signal is bigger than zero.

For the laboratory the contrast of the individual quadrants is calculated, this measurement is commonly used for alignment purposes. For the data analysis the contrast of the full diode is used. This measurement is needed for the calculation of the sensing noise contribution of the ADC and transimpedance amplifier circuits.

A.3. Matlab code for the model of the OPD loop

This is the model of the OPD loop used to correct the measured phase.

```matlab
% Lab Notch filter
% at OPD frequencies gain of 1 and delay of 0

% Lab OPD filter - implemented as CDS model
OPD_filt = pzmodel(-0.02 * 1e9, {1e-2, 1e-2, 0.5, 50}, {1, 5, 15});

% DAC
% AA of the ADC and AI of the DAC are the same
% at OPD frequencies gain of 1 and delay of 0

% lab differential to single ended electronics and piezo driver
diff2single = ao(0.0092);
diff2single.setName('diff 2 single');

Driver = ao(11);
Driver.setName('Piezo Driver');

% lab piezo Actuator
act_gain = 0.06;
act_delay = 0.015;


OPD_act = pzmodel(-act_gain, {}, {}, act_delay).*diff2single.*Driver;

% additional lowpass, reason unknown
OPD_lp = pzmodel(1.1, {20, 40}, {}, 0);

% OLG of the whole chain
OLG = OPD_filt.*OPD_act.*OPD_lp.*0.1;
```

The additional gain of 0.1 in OLG is not necessary in the mfh objects used to develop this model. The individual components are copied from mfh to the pzmodel needed for the fftfilt function, the reason for this gain is not known. For both mfh and pzmodel the transfer function output fits to the measured transfer function.

A.4. Simulink® implementation of the OPD control loop
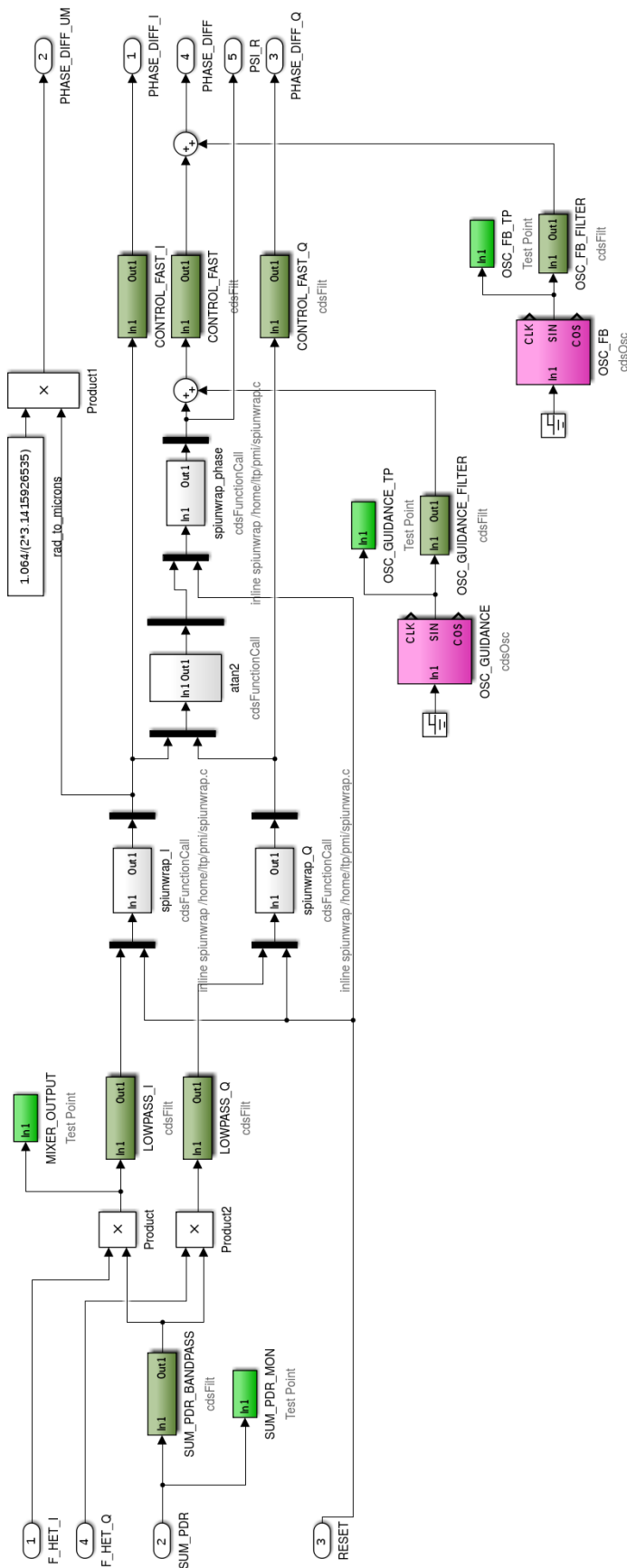
Figure A.8.: Shown here is the Simulink® diagram of the OPD loop, implemented in the LTP FST model. The inputs 1 and 4 are the digitally created heterodyne signal. Input 2 is the sum of the voltage output of all four quadrants of the reference diode, this voltage is bandpassed around the heterodyne frequency. From the beatnote between the bandpassed voltage and the digital heterodyne signal the phase of the reference diode is calculated. This phase is then lowpassed and fed through phase tracking and a filter bank. Output 4 is used to control the OPD piezo. The two oscillator banks, the components shown in pink, are used as guidance and feedback inputs to the OPD loop. Input 3 is used to re-set the phase tracking to zero.

A.5. Matlab code for the model of the frequency control loop

Shown here is the matlab script used to create the model, the modeled filters were implemented in Simulink® via the `foton` tool.

```matlab
f = logspace(-2, log10(40), 1000);

%% Freq IFO
C = 2*pi*0.38/3e8;
Xf = pzmodel(C, {}, {}, 20e-3); % rad/Hz
Xf_r = -1.*resp(Xf, plist('f', f));

%% OSTT Fast (From Loop_Coeff_5p10.txt)
a = [-1.58];
b = [1.0];

fs = 100;
Cfast = miir(-a, [1 -b], fs); % V/rad
Cfast_r = -1.*resp(Cfast, plist('f', f));

%% Slow freq controller
a = [-5.0e-05];
b = [1.0];

fs = 100;
Cslow = miir(-a, [1 -b], fs); % V/rad
Cslow_r = -1.*resp(Cslow, plist('f', f));

%% Fast Actuator
A = 2e6; % Hz/V
Afast = pzmodel(A, {}, {});
Afast_r = resp(Afast, plist('f', f));

%% Slow actuator
p0 = 2/2/pi;

A = 5e8; % Hz/V
Aslow = pzmodel(A, p0, {});
Aslow_r = resp(Aslow, plist('f', f));

%% OLG Fast
OLG_fast = Xf_r.*Cfast_r.*Afast_r;
OLG_fast.setName('OLG fast model');

%% OLG Slow
s = 2*pi*1i*f;
Gs = ao(plist('yvals', 5e8./(0.5*s+1), 'xvals', f, 'type', 'fsdata'));

OLG_slow = Xf_r.*Cfast_r .*(Afast_r - Aslow_r.*Cslow_r);
OLG_slow.setName('OLG slow model');
```

A.6. Simulink® implementation of the frequency control loop
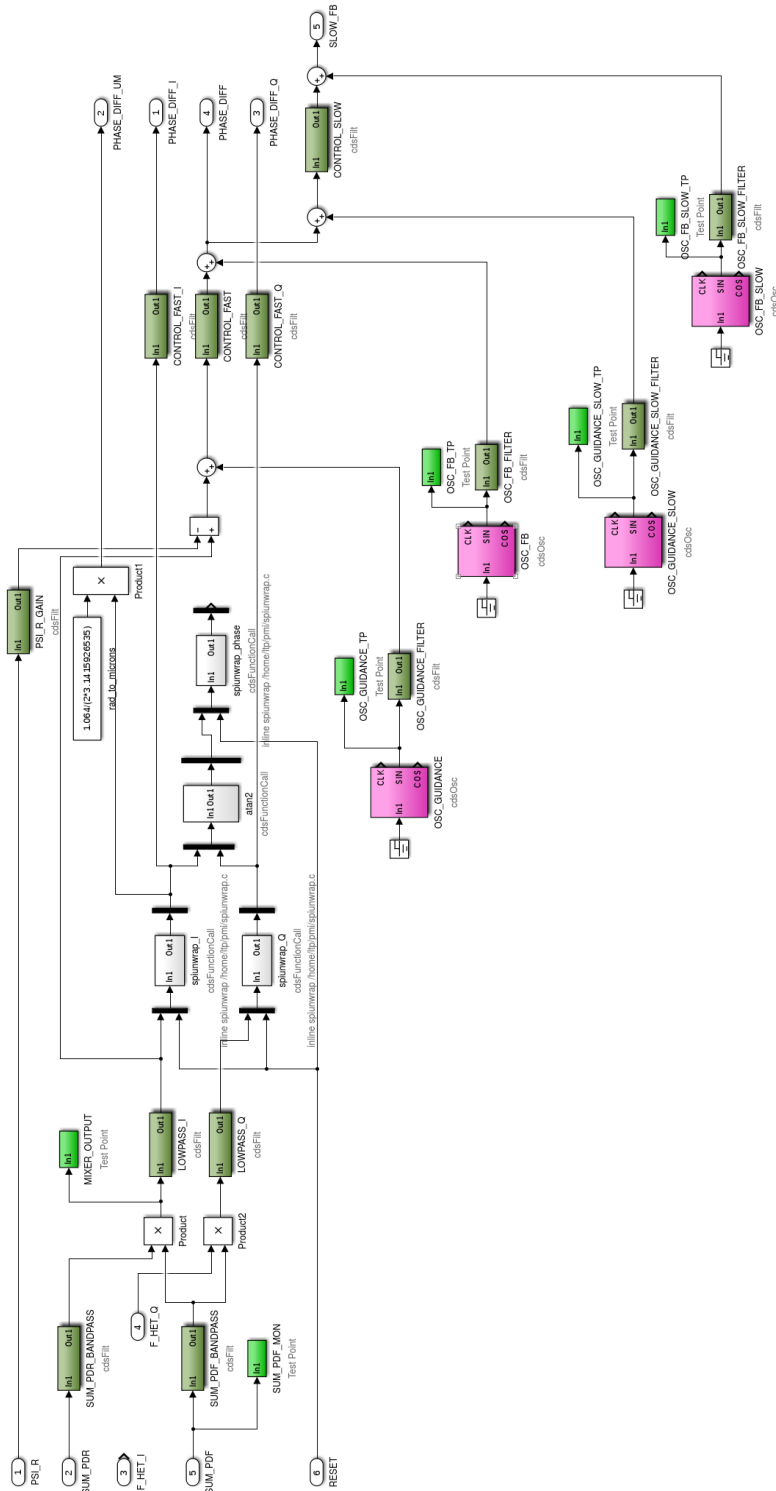
Figure A.9.: Shown here is the Simulink® diagram of the frequency control loop, implemented in the FST model. The voltage outputs of the phasemeter are used as input, SUM_PDR and SUM_PDF. From the digital representation of these voltages the real and imaginary components of the heterodyne signal are calculated. To remove high frequency noise these signals are lowpassed, in LOWPASS_I and LOW-PASS_Q. From the output of LOWPASS_I the reference phase PSI_R is subtracted, which was calculated in the OPD loop model. From this frequency noise signal xF the response of the frequency loop is calculated, the output signal of the fast loop is calculated in the filter CONTROL_FAST. Via the model output PHASE_DIFF the signal is transferred to DAC_10 of the FST model. The fast frequency loop output is also connected to the input of the filter bank CON-TROL_SLOW, where the response of the slow control loop is calculated. This control signal is connected via SLOW_FB output to DAC_14. The differential voltage outputs of the DAC are transferred to single-ended signals and connected to the fast and slow frequency change inputs of the laser system.

A.7. TM1 longitudinal control loop model

Shown here is the model of the longitudinal test mass control loop of TM1. The transfer function of the digital filter and the coupling matrix is known since they are implemented in Simulink®. The transfer function of the DAC which transforms the internal CDS units Count to a voltage is also known. The transfer function of the test mass driver was measured. The phase measurement through the QPD, the TIA, the phasemeter and the initial calculation in CDS takes a signal in metre (test mass motion) and measures it in radian. This signal is then calibrated to nanometre. The delay of this phase measurement was measured for the model of the OPD loop. The unknown component of this loop is the motion per volt of the piezo actuator, which could be calibrated from the measurement.

```matlab
%% model of the TM control loop.
f = logspace(-2, 2.5, 5000);

% x1x digital filter, input in nm and output in Count
linear = pzmodel(30, {6.28e-5, 6.28e-4}, {6.28e-3});
x1_x = 1*linear;

% Coupling Matrix
CM_gain = ao(38307.484, plist('yunits', ''));

% TM driver
d = 5e-4; % delay of the TM driver
x1_TM_driver = 2*pzmodel(-0.5, {[0.95 0.7]}, {}, d);

% known gain
DAC_gain = ao(50/15.3, plist('yunits', 'mV Count^-1'));

% from transfer function, the delay is from both piezo and DAC
Piezo_gain = 0.5*ao(1.2629173e-11, plist('yunits', 'm mV^-1'));
Piezo_gain = pzmodel(Piezo_gain.y, {}, {}, 0.005);
% scaled to other units to help the brain:
% Piezo_gain_test = 0.5*ao(12.629173, plist('yunits', 'nm V^-1'));

% PM measurement
% TM motion in m -> rad -> m in the PM measurement,
% then calibration to nanometre
d = 0.015; % delay of the phase measurement
PM = pzmodel(10^9, {},{}, d);


OLG_x1 = x1_x * CM_gain.y *DAC_gain.y *x1_TM_driver* Piezo_gain *PM;
OLG_x1r = OLG_x1.resp(plist('f', f));
OLG_x1r.setName('OLG x1')

CLG1_x1 = 1./(1-OLG_x1r);
CLG2_x1 = OLG_x1r./(1-OLG_x1r);
```

A.8. Simulink® implementation of the TM control loops and TM driver circuit
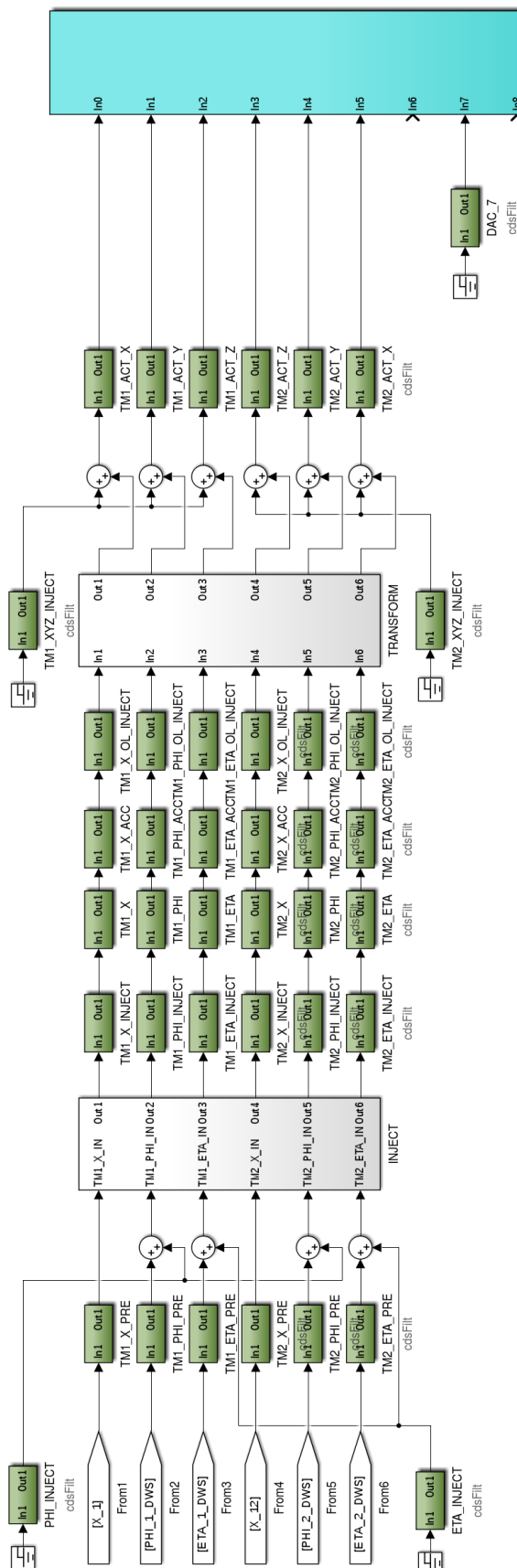
Figure A.10.: This shows the filter chain in Simulink® for the test mass control loops, the digital filters are implemented in the filter boxes without addendum. The additional filters in the chain allow for injections on the control loops before and after the application of the digital filter as well as for open-loop measurements. From the intended actuation on each DOF the desired motion of the three-axis piezos is calculated in the matrix TRANSFORM, the three axis on each piezo are labelled x, y and z. The label x on the piezo does not suggest longitudinal motion for signals injected on it, this instead would be achieved by signals of similar size on all three piezos. X_1 and X_12 are longitudinal channels with the reference signal subtracted. The DWS inputs are calculated as in Figure A.4.
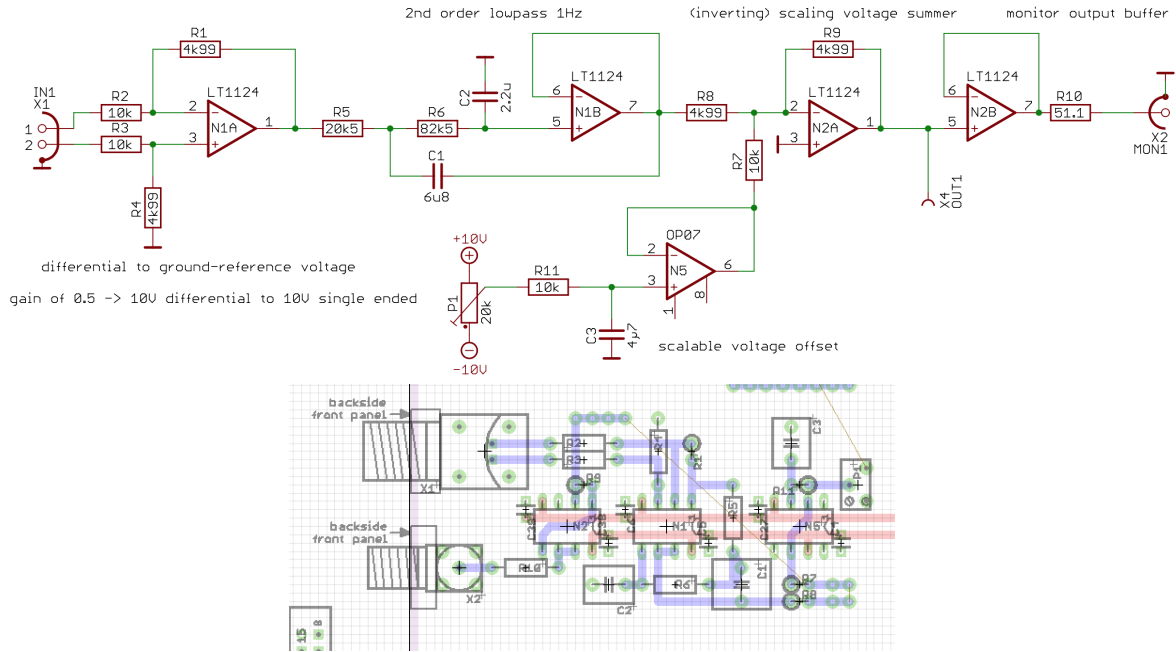
Figure A.11.: Shown here is the circuit board of one channel of the test mass driver, there are 6 channels total who share a the power supply and ground. This circuit has a differential voltage as input and transforms it to a single-ended signal. A lowpass is used to remove quantisation noise of the DAC. With an analog voltage offset on the individual piezo channels the angular offset can be adjusted, the offset voltage is added to the control signals from CDS after the lowpass. This path was chosen to preserve more of the digital range for actuation and not to include digital offsets for angular alignment. The trimmer for the analog voltage offset P1 is mounted on the front of the circuit board.
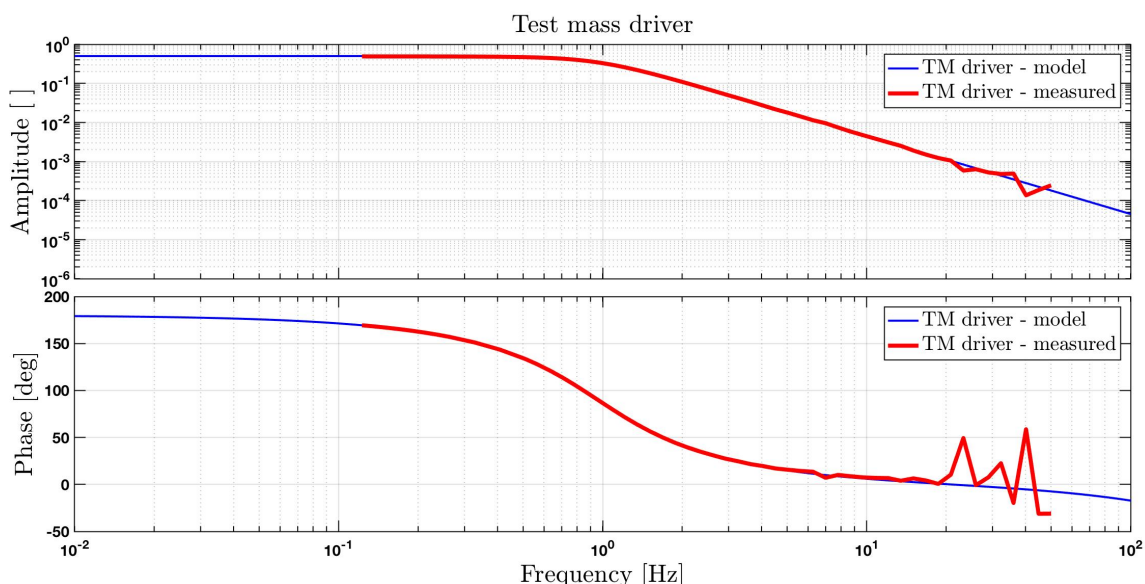
Figure A.12.: Shown here is the measured transfer function of one channel of the test mass driver circuit. The model for the control loop contains poles at $0.95\,\mathrm{Hz}$ and $0.7\,\mathrm{Hz}$ as well as a delay of $0.0004\,\mathrm{s}$. The gain of 0.5 of this measurement is due to a single-ended voltage signal on the differential input of the circuit, this differential voltage is accounted for in the full model with an additional factor 2.

A.9. System Identification Experiments in the laboratory OMS

During the design phase of the system identification experiments of the in-flight system some of the planned experiments were implemented in the lab setup. The ground setup of course produces different results, since the TM mirrors are easier to control with the piezo than the free-falling TMs with capacitive actuation. These experiments were helpful to test the data analysis pipelines with the constraints of limited experiment time.

The in-flight SysID experiments feature a number of short injections at different frequencies with short breaks between them. The same timeline was implemented as a shell script to be run on the CDS.
A short segment of the code can be found in Appendix A.9.
In CDS the sine injections for all channels and frequencies are relative to midnight. This is good for the reproducibility of experiments with injections at more than one frequency, because these will always have the same phase relation to each other and not depend on the order or delay with which they were started. However, this means that most times when a sine injection is started it begins at an arbitrary point in the cycle. Due to this arbitrary start amplitude we have a jump in the system. To prevent this in normal circumstances a ramp-up can be included, so that the sine amplitude gradually gets bigger and there are no sudden voltage changes.
In this case this solution is not applicable because the time where the signal is injected is very short, and if a ramp-down is included at the end of the injection to prevent a sudden drop to zero the result is a very distorted sine wave. This was fixed in the programming of the injections with an uncertainty of the start time of the injections, the system will wait till the signal to be injected is at zero, and only then start.
This is a code snippet of a system identification experiment on board LISA Pathfinder.

```
LPF investigation design
name:   inv01101:V003
duration [s]:   10800 (3.00 h)
description:
Like inv01101_001 with amplitudes/100


design schedule:

500     1500 [1000]
guidance x1    sine_amplitude=1e-08     sine_frequency=0.001
sine_phase=0              sine_bias=NaN

2000    3000 [1000]
guidance x1    sine_amplitude=1e-08     sine_frequency=0.003
sine_phase=0              sine_bias=NaN
```

Shown here is a short segment of the same experiment as implemented in the laboratory.

```bash
#!/bin/bash

# let the shell expand aliases
shopt -s expand_aliases

alias sw="/opt/rtcds/geo/g6/pt-user_apps/scripts/switch.sh"

HOSTNAME=$(hostname)
echo "guidance injection to TM1 x, duration 3 hours"
echo

if [ $HOSTNAME != ltp-fe1 ]; then
echo "run this script on ltp-fe1"
echo
exit 1
fi

echo "wait 500 seconds"
sleep 500 # seconds

echo "starting guidance injection x1 0.001Hz for 1000 seconds"
tdssine 0.001 10 G6:LTP-TM1_X_INJECT_EXC 1000
echo "wait 500 seconds"
sleep 500 # seconds

echo "starting guidance injection x1 0.003Hz for 1000 seconds"
tdssine 0.003 10 G6:LTP-TM1_X_INJECT_EXC 1000
echo "wait 500 seconds"
sleep 500 # seconds
```

A.10. Error of the LTPDA mean function

The mean function of LTPDA is often used to calculate the mean value of a number of measurements for a final result. One such example can be found in Section 5.1.5, in this experiment the transfer function from RIN to phase noise is measured. This measurement is repeated for many OPD loop setpoint offsets to subtract small vector noise with a fit; to calculate the RIN level the mean value of the residuals is used.

For a set of datapoints x_n with length n the mean value is calculated as

$$d = \frac{1}{n}\sum_n x_n. \tag{A.1}$$

The error dy of this mean value is calculated with

$$dy = \frac{\sigma(x_n)}{\sqrt{n}}. \tag{A.2}$$

Due to the high number of measurements the error is often quite small, even though the bigger distribution of measured amplitudes or noise levels would visually suggest a larger error. In this calculation the error of the individual data points does not factor in, the error of the individual data points can be quite different between individual data points.

As a test the mean value x_{mean} and error $x_{mean,\,dy}$ were also calculated with a weighted mean function, the results were the same and the calculated errors only increased by a small amount. Therefore the built-in function of LTPDA was used.

$$w_n = \frac{1}{x_{n,\,dy}}, \tag{A.3}$$

$$x_{mean} = \frac{\sum_n \cdot w_n}{\sum_n w_n}, \tag{A.4}$$

$$x_{mean,\,dy} = \frac{1}{\sum_n w_n}. \tag{A.5}$$

Here the weight w_n is calculated from the error of the individual data points $x_{n,\,dy}$ of the dataset x_n. These errors $x_{n,\,dy}$ are often the result of a DFT or noisePower function; the errors are similar for most data points since the input data is similar.

A.11. χ^2 parameter of a fit

This parameter compares the result of a fit with the input data, a lower value is a sign of a good fit. Here this parameter is computed as

$$\chi^2 = \frac{1}{n-2}\sum_n \frac{(d_n - f_n)^2}{dy_n^2}, \tag{A.6}$$

where d_n are the n data points of the measured data and dy_n is their error, f_n is the value expected from the fit results for data point n. The subtraction of the measured data point with the fit value, adjusted for the measurement error of this point. The sum of these individual mismatches between data and fit is divided by the number of data points n minus 2 to normalise the result.

A.12. DAQ downsampling filter

When the data is saved at a lower sampling frequency than it is recorded at a downsampling filter tf_{DAQ} is applied. For these experiments the relevant downsampling filter is from $64\,\text{kHz}$, or really $2^{16}\,\text{kHz}$, to the sampling frequency of $256\,\text{Hz}$. Implemented are second-order-sections filter (SOS); the first value is a gain and the three rows are the implemented SOS filters [50].

```
1  static  double dCoeff256x[13] = {2.296084727953743e−05,
2  −1.9971538121386385, 0.9971724295485971, −1.9998859428966878, 1.0000000000000002,
3  −1.9990827274780281, 0.9991201182251324, −1.9997348047494339, 0.9999999999999999,
4  −0.9980046339426777, 0.0000000000000000, 1.0000000000000000, 0.0000000000000000};
```
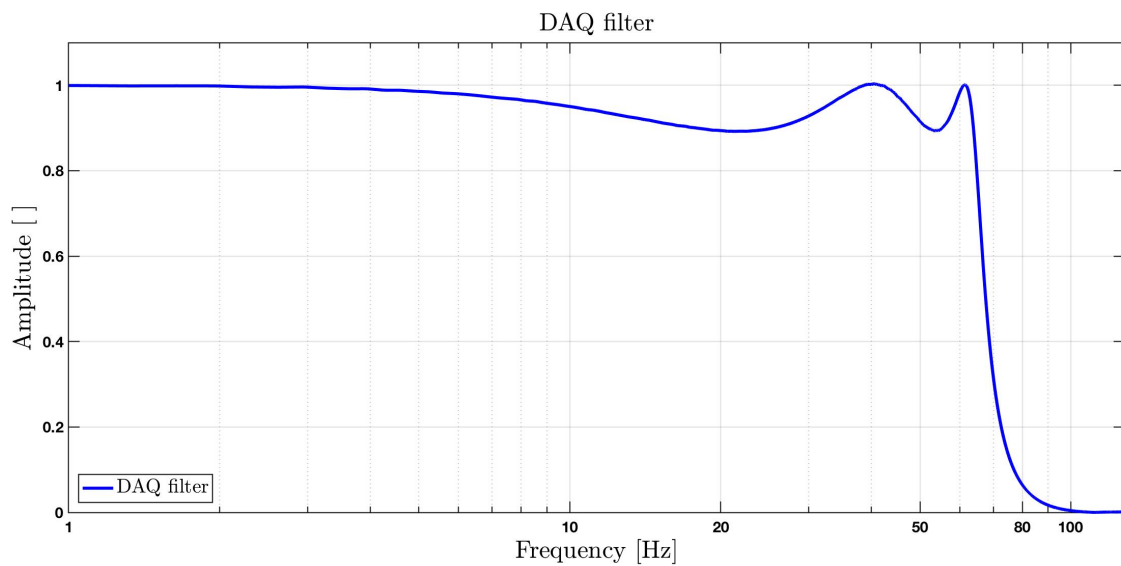

Figure A.13.: This plot shows the downsampling filter from a sampling frequency of $64\,\text{kHz}$ to $256\,\text{Hz}$. This filter is implemented in the data acquisition module of CDS.

A.13. Simulink® implementation of the RIN demodulation signal

To measure the high-frequency RIN the measured power is demodulated to lower frequencies. The power signal is multiplied with a sinusoidal demodulation signal with an amplitude of 1, the frequency chosen for the $1f_{het}$ RIN measurement is $1603\,\text{Hz}$ and $3226\,\text{Hz}$ for $2f_{het}$. The demodulation signals contain the injected RIN at lower frequencies since $\sin(f_{RIN}t) \cdot \sin(f_{demod}t) = \frac{1}{2}(\cos(f_{RIN}t - f_{demod}t) - \cos(f_{RIN}t + f_{demod}t))$. To restore the amplitude of the original signal the time series of the demodulated signal has to be multiplied by a factor 2.
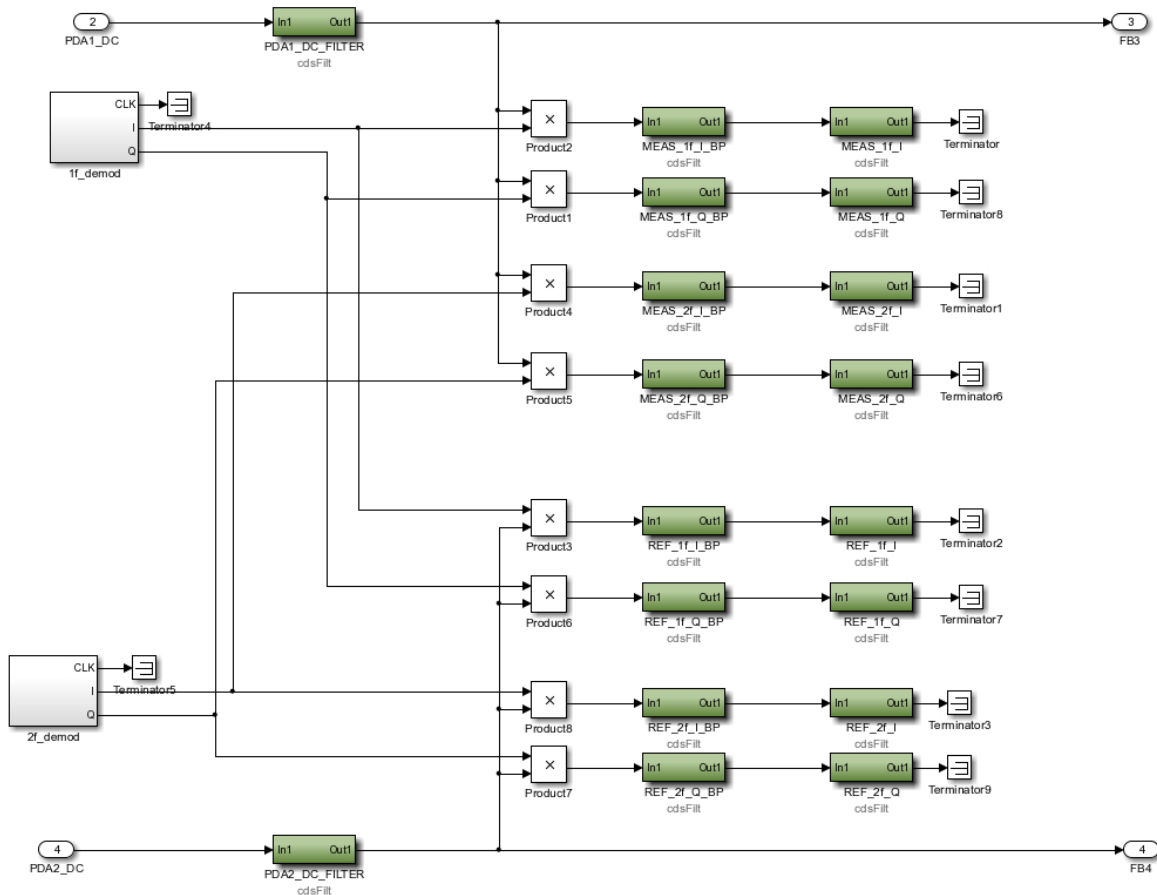
Figure A.14.: Shown here is the Simulink® implementation for the measurement of the demodulated RIN signals. The power is recorded as-is in the PDA1_DC_FILTER and PDA2_DC_FILTER components, either at a sampling frequency of $16\,\text{kHz}$ or $256\,\text{Hz}$. With one oscillator for $1f_{het}$ and one for $2f_{het}$ for both the measurement beam (PDA1) and the reference beam (PDA2) the demodulated signals are created. The I and Q component of the power are recorded at a sampling frequency of $256\,\text{Hz}$. In post-processing the RIN is calculated from the I component. Since the amplitude is of interest only one of the components is needed.

A.14. Code snippet of RIN injection of the laboratory RIN transfer function measurement v1

This small part of code shows the first two $1f_{het} + 12\,Hz$ RIN injections of the RIN transfer function measurement, the amplitude of the injection is in the CDS unit count. The first amplitude is 3500, and then decreases. Shown is the injection for the phase measurement with 10 minutes duration, when this block is finished the experiment is repeated with an injection duration of 1 minute for the $1f_{het} + 12\,Hz$ RIN measurement with the same amplitudes. Then follows the injections for the $2f_{het} + 12\,Hz$ RIN transfer function measurement, first the injections with 1 minute duration for the RIN measurement and then with 10 minutes duration for the phase measurement.

```bash
#!/bin/bash

# let the shell expand aliases
shopt -s expand_aliases
alias sw="/opt/rtcds/geo/g6/pt-user_apps/scripts/switch.sh"

HOSTNAME=$(hostname)
echo "RIN linearity AOM1, 10min version"
echo
if [ $HOSTNAME != ltp-fe1 ]; then
echo "run this script on ltp-fe1"
echo
exit 1
fi

# 1f_het = 1623.37658691

date
echo "noise measurement"
sleep 10 # seconds

echo "starting 1f injection 1635.37658691 Hz -> 12Hz"
tdssine 1635.37658691 3500 G6:FST-DAC_AOM1_EXC 598
echo "wait 2 seconds"
sleep 2 # seconds

tdssine 1635.37658691 3000 G6:FST-DAC_AOM1_EXC 598
echo "wait 2 seconds"
sleep 2 # seconds

tdssine 1635.37658691 2500 G6:FST-DAC_AOM1_EXC 598
echo "wait 2 seconds"
sleep 2 # seconds
```

A.15. Code snippet of the RIN injection of the RIN frequency dependency measurement

This code snippet shows the start of the RIN injections to test the frequency dependency around $1f_{het} + 12\,Hz$. The first injections at lower frequencies have a duration of 20 minutes, at higher injection frequencies the duration is only 10 minutes. Due to the long duration of the measurement no RIN is measured directly.

```bash
#!/bin/bash

# let the shell expand aliases
shopt -s expand_aliases

alias sw="/opt/rtcds/geo/g6/pt-user_apps/scripts/switch.sh"

HOSTNAME=$(hostname)
echo "RIN frequency AOM1, 10min version"
echo

if [ $HOSTNAME != ltp-fe1 ]; then
echo "run this script on ltp-fe1"
echo
exit 1
fi

#1f_het = 1623.37658691
#2f_het = 3246.75317382

date
echo "starting 1f injection  -> +0.7Hz"
tdssine 1624.07658691 1500 G6:FST-DAC_AOM1_EXC 1190
sleep 10

echo "starting 1f injection  -> -0.7Hz"
tdssine 1622.67658691 1500 G6:FST-DAC_AOM1_EXC 1190
sleep 10

echo "starting 1f injection  -> +1.5Hz"
tdssine 1624.87658691 1500 G6:FST-DAC_AOM1_EXC 1190
sleep 10

echo "starting 1f injection  -> -1.5Hz"
tdssine 1621.87658691 1500 G6:FST-DAC_AOM1_EXC 1190
sleep 10

echo "starting 1f injection  -> +2Hz"
tdssine 1625.37658691 1500 G6:FST-DAC_AOM1_EXC 590
sleep 10

echo "starting 1f injection  -> -2Hz"
tdssine 1621.37658691 1500 G6:FST-DAC_AOM1_EXC 590
sleep 10
```

A.16. Code snippet of the RIN subtraction experiment - TM steps

Shown in this code snippet are the commanded offsets on the TM control loop setpoint.
Different versions of this script exist, shown here are the TM offsets as used in Section
5.3. Previous versions had more TM offsets with a shorter measurement duration, and a
higher RIN injection level. The RIN injection is started with the GUI for excitations in CDS
before the TM offset script is executed. With this user interface sinusoidal signals and noise
injections can be defined with the frequency, or frequency range, and their amplitude. For a
RIN injection an additional bandpass filter around either $1\,f_{het}$ or $2\,f_{het}$ is included, these can
also be switched on and off with the user interface.

```bash
#!/bin/bash

# let the shell expand aliases
shopt -s expand_aliases

alias sw="/opt/rtcds/geo/g6/pt-user_apps/scripts/switch.sh"

HOSTNAME=$(hostname)
echo injection test
echo

if [ $HOSTNAME != ltp-fe1 ]; then
echo run this script on ltp-fe1
echo
exit 1
fi

tdswrite -verb -sw G6:LTP-TM1_X OFFSET ON

for n in 0 25 50 75 100 125 150 175 200 225 250 275 300
275 250 225 200 175 150 125 100 75 50 25 0
do
echo switch offset $n
tdswrite -verb G6:LTP-TM1_X_OFFSET $n
echo "wait 3600 seconds"
sleep 3600 # seconds
done


for n in 25 50 75 100 125 150 175 200 225 250 275
300 275 250 225 200 175 150 125 100 75 50 25 0
do
echo switch offset -$n
tdswrite -verb G6:LTP-TM1_X_OFFSET -$n
echo "wait 3600 seconds"
sleep 3600 # seconds
done

echo done
```

Figure A.15.: Shown here is the measured 1f$_{\text{het}}$ RIN amplitude of the x1_B signal, the amplitude of the injected RIN is increased. The injection amplitude in the CDS unit Count can be found in the legend.
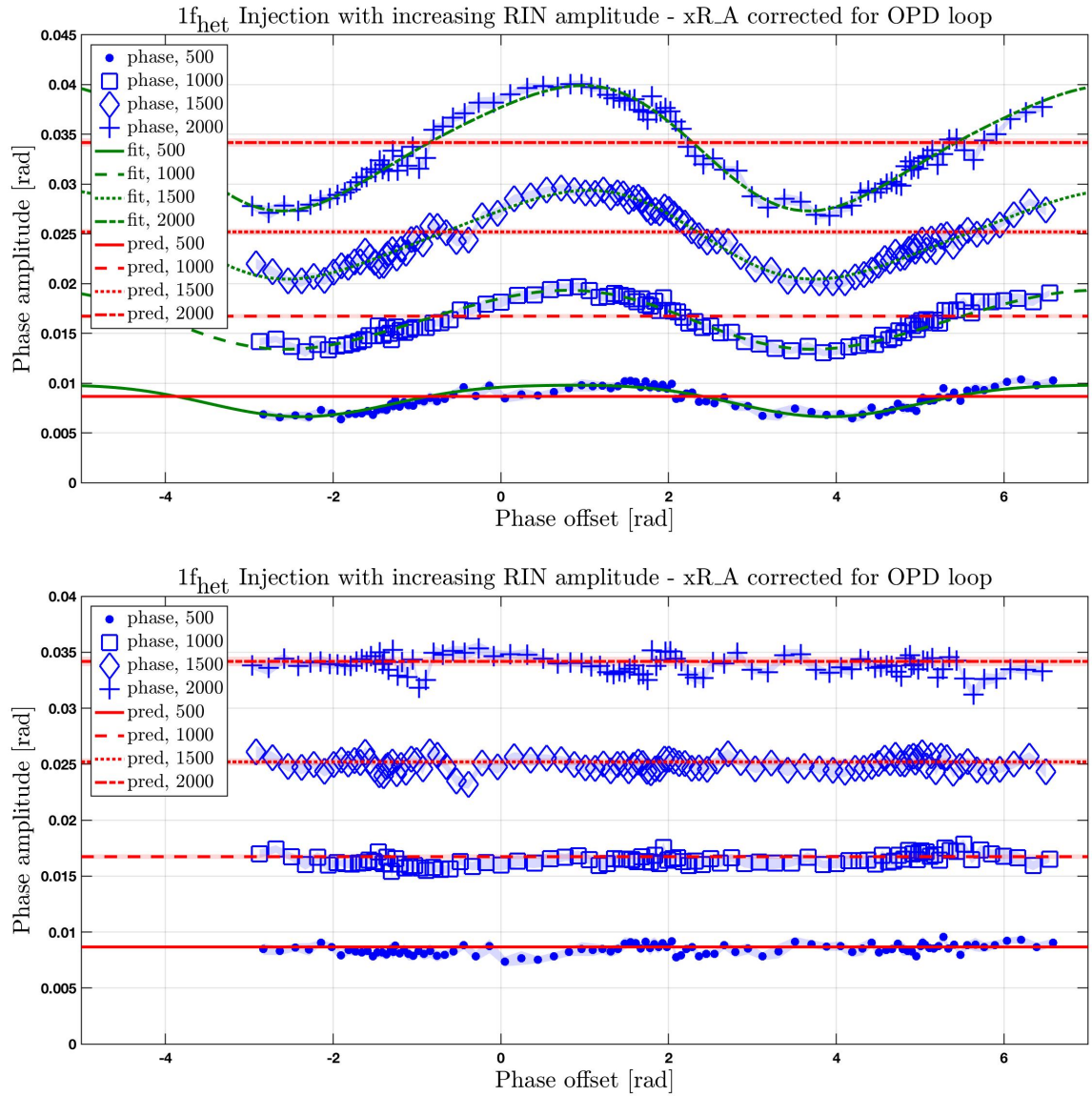
Figure A.16.: Shown here is the measured $1f_{het}$ RIN amplitude of the xR__A signal, the amplitude of the injected RIN is increased. The injection amplitude in the CDS unit Count can be found in the legend.
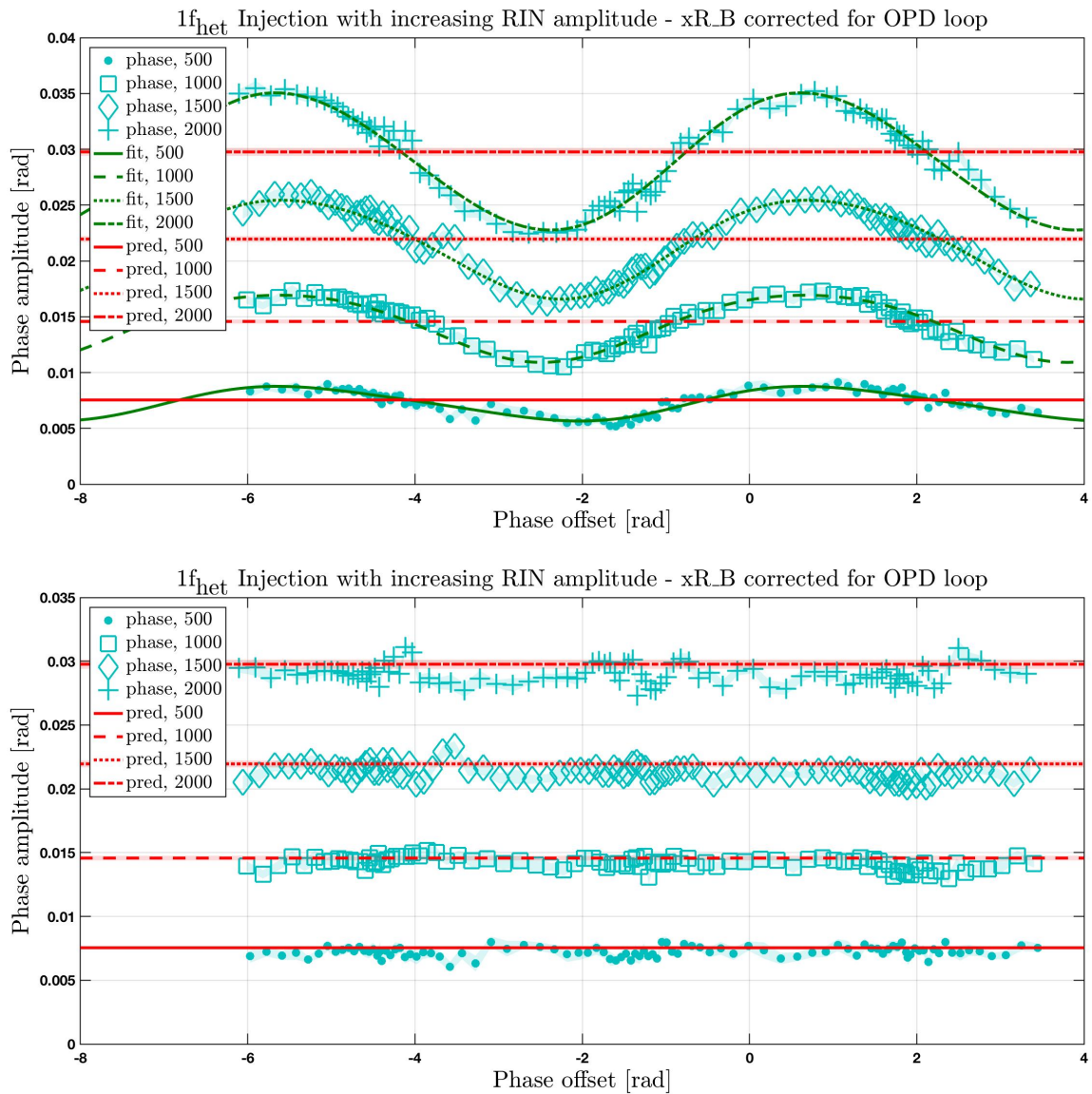
Figure A.17.: Shown here is the measured $1f_{het}$ RIN amplitude of the xR_B signal, the amplitude of the injected RIN is increased. The injection amplitude in the CDS unit Count can be found in the legend.
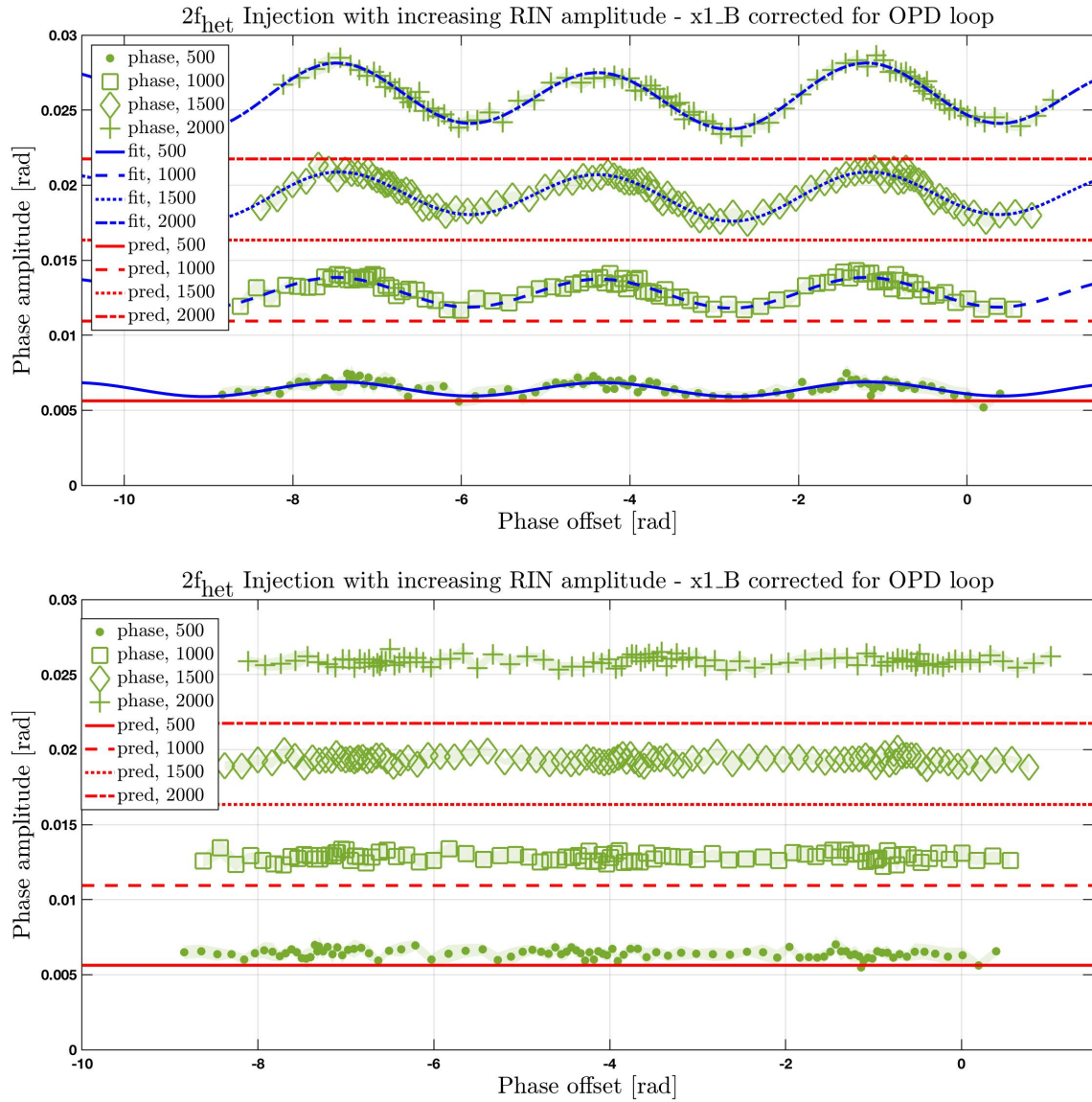
Figure A.18.: Shown here is the measured $2f_{het}$ RIN amplitude of the x1_B signal, the amplitude of the injected RIN is increased. The injection amplitude in the CDS unit Count can be found in the legend.
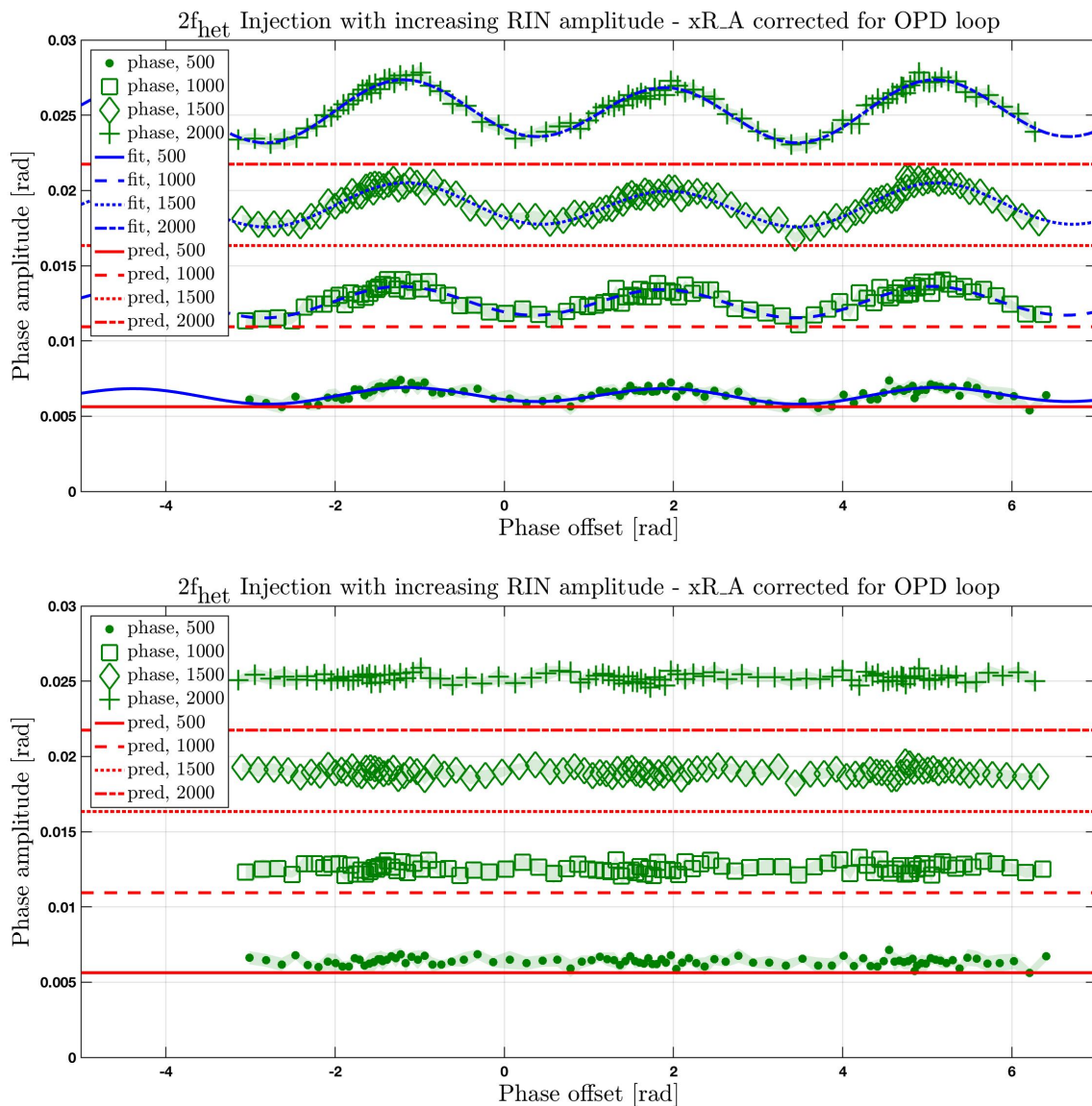
Figure A.19.: Shown here is the measured $2f_{het}$ RIN amplitude of the xR_A signal, the amplitude of the injected RIN is increased. The injection amplitude in the CDS unit Count can be found in the legend.
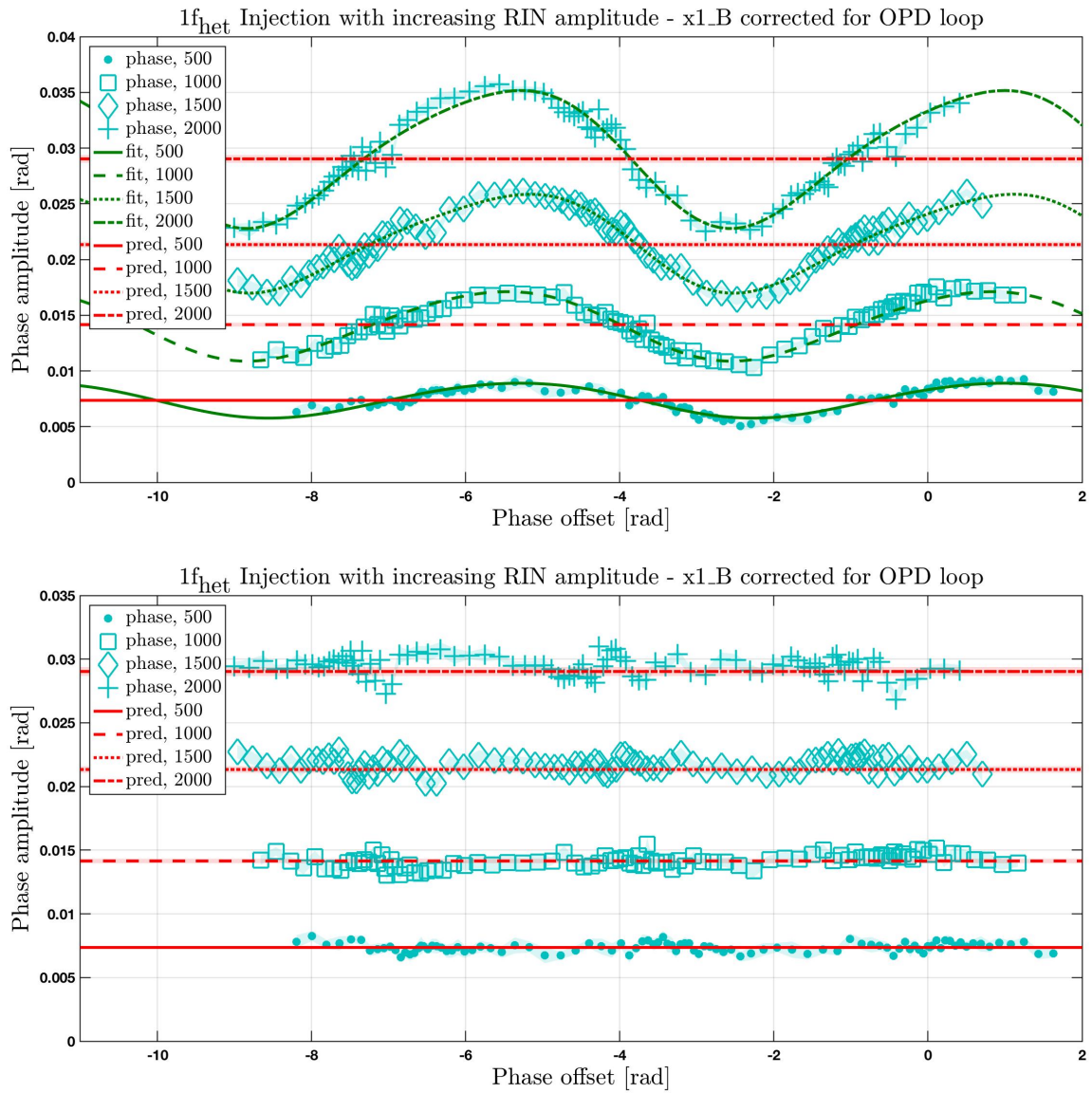
Figure A.20.: Shown here is the measured $2f_{het}$ RIN amplitude of the xR_B signal, the amplitude of the injected RIN is increased. The injection amplitude in the CDS unit Count can be found in the legend.
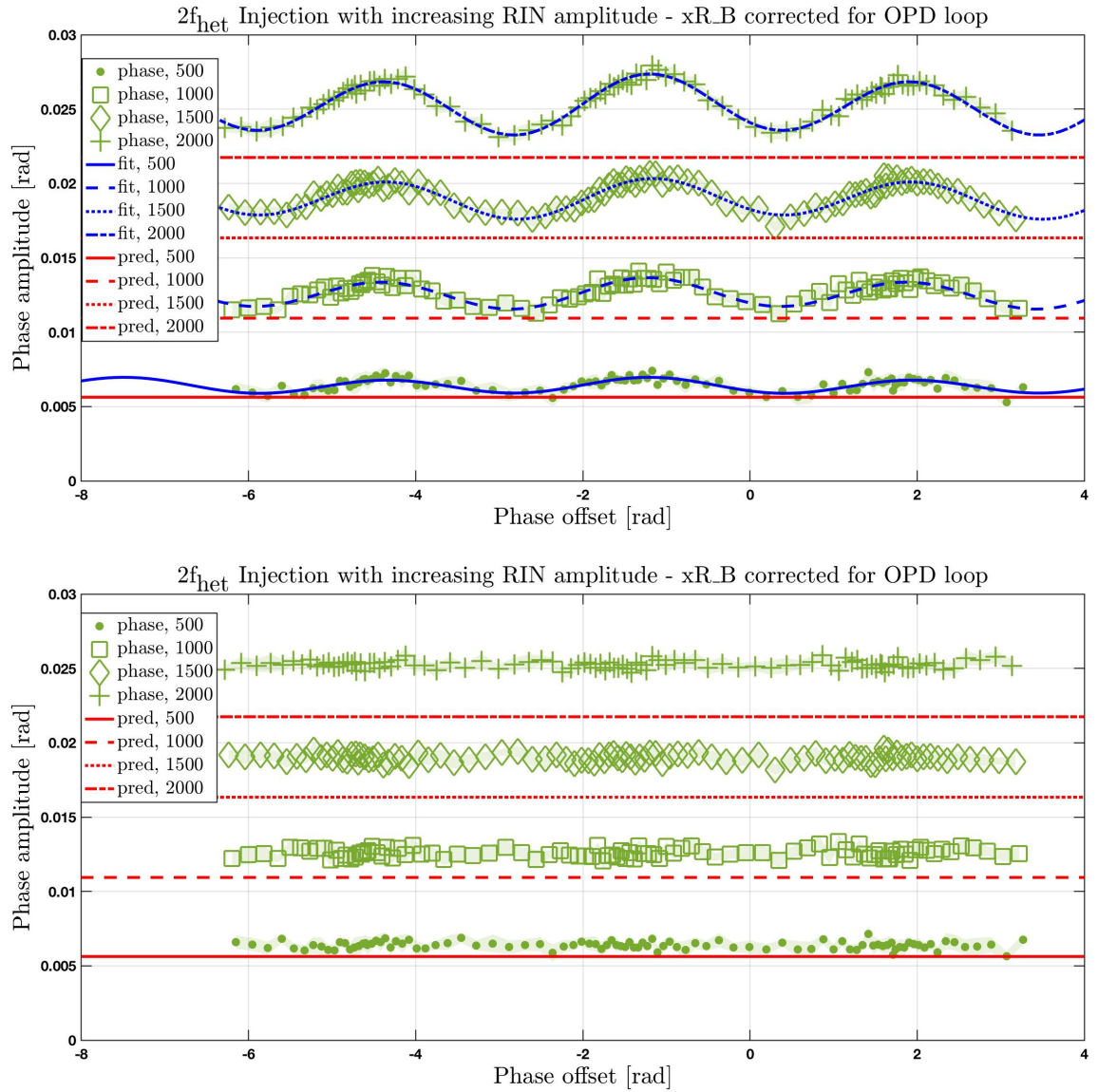
Amp. [Count]	$P_{m,1A}$	$P_{r,1A}$	$P_{m,1B}$	$P_{r,1B}$
500	$0.200 \pm 5 \cdot 10^{-6}$	$0.0802 \pm 2 \cdot 10^{-6}$	$0.252 \pm 6 \cdot 10^{-6}$	$0.083 \pm 2 \cdot 10^{-6}$
1000	$0.200 \pm 5 \cdot 10^{-6}$	$0.0812 \pm 2 \cdot 10^{-6}$	$0.253 \pm 6 \cdot 10^{-6}$	$0.0841 \pm 2 \cdot 10^{-6}$
1500	$0.200 \pm 5 \cdot 10^{-6}$	$0.082 \pm 2 \cdot 10^{-6}$	$0.252 \pm 6 \cdot 10^{-6}$	$0.0849 \pm 2 \cdot 10^{-6}$
2000	$0.200 \pm 5 \cdot 10^{-6}$	$0.0826 \pm 2 \cdot 10^{-6}$	$0.253 \pm 6 \cdot 10^{-6}$	$0.0856 \pm 2 \cdot 10^{-6}$

Amp. [Count]	$P_{m,RA}$	$P_{r,RA}$	$P_{m,RB}$	$P_{r,RB}$
500	$0.207 \pm 5 \cdot 10^{-6}$	$0.0914 \pm 3 \cdot 10^{-6}$	$0.222 \pm 5 \cdot 10^{-6}$	$0.0739 \pm 2 \cdot 10^{-6}$
1000	$0.208 \pm 5 \cdot 10^{-6}$	$0.0926 \pm 3 \cdot 10^{-6}$	$0.222 \pm 5 \cdot 10^{-6}$	$0.0748 \pm 2 \cdot 10^{-6}$
1500	$0.207 \pm 5 \cdot 10^{-6}$	$0.0935 \pm 3 \cdot 10^{-6}$	$0.222 \pm 5 \cdot 10^{-6}$	$0.0755 \pm 2 \cdot 10^{-6}$
2000	$0.208 \pm 5 \cdot 10^{-6}$	$0.0942 \pm 3 \cdot 10^{-6}$	$0.223 \pm 5 \cdot 10^{-6}$	$0.0761 \pm 2 \cdot 10^{-6}$

Diff. $\frac{P_{calib}}{P_{PM}}$	$d_{1A} = 1.001$	$d_{1B} = 1.001$	$d_{RA} = 1.001$	$d_{RB} = 0.992$
Amp. [Count]	c_{1A}	c_{1B}	c_{RA}	C_{RB}
500	$0.705 \pm 4 \cdot 10^{-5}$	$0.754 \pm 7 \cdot 10^{-5}$	$0.775 \pm 7 \cdot 10^{-5}$	$0.723 \pm 5 \cdot 10^{-5}$
1000	$0.702 \pm 3 \cdot 10^{-5}$	$0.752 \pm 4 \cdot 10^{-5}$	$0.774 \pm 5 \cdot 10^{-5}$	$0.719 \pm 3 \cdot 10^{-5}$
1500	$0.706 \pm 2 \cdot 10^{-5}$	$0.756 \pm 5 \cdot 10^{-5}$	$0.778 \pm 5 \cdot 10^{-5}$	$0.723 \pm 3 \cdot 10^{-5}$
2000	$0.706 \pm 3 \cdot 10^{-5}$	$0.754 \pm 5 \cdot 10^{-5}$	$0.788 \pm 5 \cdot 10^{-5}$	$0.725 \pm 3 \cdot 10^{-5}$

Amp. [Count]	$\eta_{het,\,1A}$	$\eta_{het,\,1B}$	$\eta_{het,\,RA}$	$\eta_{het,\,RB}$
500	0.626 ± 0.0132	0.788 ± 0.0168	0.726 ± 0.0151	0.722 ± 0.0154
1000	0.621 ± 0.013	0.786 ± 0.0168	0.724 ± 0.0151	0.715 ± 0.0153
1500	0.623 ± 0.0131	0.785 ± 0.0167	0.726 ± 0.0151	0.715 ± 0.0152
2000	0.625 ± 0.0131	0.780 ± 0.0166	0.726 ± 0.0151	0.715 ± 0.0152

Table A.1.: Shown in the top two tables are the calibrated beam powers during the second version of the transfer function experiment. The errors of the calibration are calculated by a comparison of the summed calibrated beam powers with the power as measured by the phasemeter with $\frac{P_{calib}}{P_{PM}}$. The next table shows the mean contrast over the whole measurement duration In the calculation of the phase amplitude from a $1f_{het}$ RIN injection the mean values in the time of the injected RIN are used. The last table shows the mean heterodyne efficiency over the course of the $1f_{het}$ RIN injection.

Injection amp. [Count]	$\tilde{r}^{(1)}$ [ ]	$\tilde{r}^{(2)}$ [ ]
500	$0.0225 \pm 4 \cdot 10^{-6}$	$0.0217 \pm 1 \cdot 10^{-6}$
1000	$0.0449 \pm 4 \cdot 10^{-6}$	$0.0434 \pm 2 \cdot 10^{-6}$
1500	$0.0674 \pm 4 \cdot 10^{-6}$	$0.0651 \pm 3 \cdot 10^{-6}$
2000	$0.0899 \pm 5 \cdot 10^{-6}$	$0.0868 \pm 5 \cdot 10^{-6}$

Table A.2.: These are the measured RIN amplitudes, injected on the reference beam. The first row shows the injection amplitude in CDS units, the next two rows show the resulting amplitude for $1f_{het}$ RIN and $2f_{het}$ RIN.

Amp. [Count]	x1A [rad]	x1A pred. [rad]	x1B [rad]	x1B pred. [rad]
$1f_{het}$ RIN; 500	$0.0081 \pm 4 \cdot 10^{-5}$	$0.00899 \pm 2 \cdot 10^{-6}$	$0.00731 \pm 3.7 \cdot 10^{-5}$	$0.00744 \pm 1 \cdot 10^{-6}$
$1f_{het}$ RIN; 1000	$0.0159 \pm 5 \cdot 10^{-5}$	$0.0174 \pm 2 \cdot 10^{-6}$	$0.0140 \pm 4.9 \cdot 10^{-5}$	$0.0143 \pm 2 \cdot 10^{-6}$
$1f_{het}$ RIN; 1500	$0.0238 \pm 6 \cdot 10^{-5}$	$0.0263 \pm 2 \cdot 10^{-6}$	$0.0216 \pm 6 \cdot 10^{-5}$	$0.0216 \pm 2 \cdot 10^{-6}$
$1f_{het}$ RIN; 2000	$0.0323 \pm 8 \cdot 10^{-5}$	$0.0355 \pm 3 \cdot 10^{-6}$	$0.0293 \pm 8 \cdot 10^{-5}$	$0.0294 \pm 3 \cdot 10^{-6}$

Amp. [Count]	xRA [rad]	xRA pred. [rad]	xRB [rad]	xRB pred. [rad]
$1f_{het}$ RIN; 500	$0.00843 \pm 4 \cdot 10^{-5}$	$0.00876 \pm 2 \cdot 10^{-6}$	$0.00726 \pm 4 \cdot 10^{-5}$	$0.00767 \pm 1 \cdot 10^{-6}$
$1f_{het}$ RIN; 1000	$0.0164 \pm 5 \cdot 10^{-5}$	$0.0169 \pm 2 \cdot 10^{-6}$	$0.0142 \pm 5 \cdot 10^{-5}$	$0.0148 \pm 2 \cdot 10^{-6}$
$1f_{het}$ RIN; 1500	$0.0249 \pm 6 \cdot 10^{-5}$	$0.0255 \pm 2 \cdot 10^{-6}$	$0.0214 \pm 6 \cdot 10^{-5}$	$0.0223 \pm 2 \cdot 10^{-6}$
$1f_{het}$ RIN; 2000	$0.0337 \pm 8 \cdot 10^{-5}$	$0.0346 \pm 3 \cdot 10^{-6}$	$0.0291 \pm 8 \cdot 10^{-5}$	$0.0303 \pm 2 \cdot 10^{-6}$

Amp. [Count]	x1A [rad]	x1A pred. [rad]	x1B [rad]	x1B pred. [rad]
$2f_{het}$ RIN; 500	$0.00641 \pm 3 \cdot 10^{-5}$	$0.00563 \pm 3 \cdot 10^{-7}$	$0.00641 \pm 3 \cdot 10^{-5}$	$0.00563 \pm 3 \cdot 10^{-7}$
$2f_{het}$ RIN; 1000	$0.0128 \pm 3 \cdot 10^{-5}$	$0.0109 \pm 6 \cdot 10^{-7}$	$0.0128 \pm 3 \cdot 10^{-5}$	$0.0109 \pm 6 \cdot 10^{-7}$
$2f_{het}$ RIN; 1500	$0.0193 \pm 3 \cdot 10^{-5}$	$0.0163 \pm 8 \cdot 10^{-7}$	$0.0193 \pm 3 \cdot 10^{-5}$	$0.0163 \pm 8 \cdot 10^{-7}$
$2f_{het}$ RIN; 2000	$0.0259 \pm 3 \cdot 10^{-5}$	$0.0217 \pm 11 \cdot 10^{-7}$	$0.0259 \pm 3 \cdot 10^{-5}$	$0.0217 \pm 11 \cdot 10^{-7}$

Amp. [Count]	xRA [rad]	xRA pred.[rad]	xRB [rad]	xRB pred. [rad]
$2f_{het}$ RIN; 500	$0.00652 \pm 5 \cdot 10^{-5}$	$0.00563 \pm 3 \cdot 10^{-7}$	$0.00638 \pm 3 \cdot 10^{-5}$	$0.00563 \pm 3 \cdot 10^{-7}$
$2f_{het}$ RIN; 1000	$0.0129 \pm 7 \cdot 10^{-5}$	$0.0109 \pm 6 \cdot 10^{-7}$	$0.0126 \pm 3 \cdot 10^{-5}$	$0.0109 \pm 6 \cdot 10^{-7}$
$2f_{het}$ RIN; 1500	$0.0194 \pm 10 \cdot 10^{-5}$	$0.0163 \pm 8 \cdot 10^{-7}$	$0.0190 \pm 3 \cdot 10^{-5}$	$0.0163 \pm 8 \cdot 10^{-7}$
$2f_{het}$ RIN; 2000	$0.0257 \pm 14 \cdot 10^{-5}$	$0.0217 \pm 11 \cdot 10^{-7}$	$0.0252 \pm 3 \cdot 10^{-5}$	$0.0217 \pm 11 \cdot 10^{-7}$

Table A.3.: These tables show the measured and predicted phase amplitudes due to the injected RIN. The errors of the measured values are the result of the average of the residuals after the subtraction of small vector noise. Due to the high number of data points this error is small. The predictions are calculated from measured RIN, beam powers and contrast. These measured values are the result of an mean value of the timeseries measurement over the duration of one RIN injection amplitude. Due to the long duration of these measurements the calculated error is also small.

Table A.4.: This table shows the fit results for small vector noise contribution to the $1f_{\text{het}}$ RIN transfer function measurement. The fit components for x1_A, x1_B, xR_A and xR_B are listed, in that order, for increasing RIN injection amplitude from 500 to 2000 Count. With the parameters k_{ia}, k_{ib}, k_{ic} and k_{id} the contribution of SVN is characterised. The phase amplitude due to the RIN injection φ_{RIN} is also calculated by the fit, for a better error estimation the mean value of the residuals after the SVN subtraction is used instead. For this $1f_{\text{het}}$ RIN injection the φ-SVN contribution with the parameters k_{ia} and k_{ib} is dominant. The χ^2 parameter for each fit is also shown, in the last row. This parameter is a measurement of the fit quality, a short explanation can be found in Appendix A.11.

Amp. [Count]	k_{ia} [rad]	k_{ib} [rad]	k_{ic} [rad]	k_{id} [rad]	φ_{RIN} [rad]	χ^2
500	$0.00103 \pm 7 \cdot 10^{-5}$	$0.000874 \pm 6 \cdot 10^{-5}$	$0.000172 \pm 7 \cdot 10^{-5}$	$-9.65 \cdot 10^{-5} \pm 6 \cdot 10^{-5}$	$0.00805 \pm 5 \cdot 10^{-5}$	1.17
1000	$0.00196 \pm 7 \cdot 10^{-5}$	$0.00242 \pm 6 \cdot 10^{-5}$	$-0.000215 \pm 6 \cdot 10^{-5}$	$-2.19 \cdot 10^{-5} \pm 6 \cdot 10^{-5}$	$0.0159 \pm 5 \cdot 10^{-5}$	1.32
1500	$0.00312 \pm 6 \cdot 10^{-5}$	$0.00302 \pm 7 \cdot 10^{-5}$	$8.56 \cdot 10^{-7} \pm 6 \cdot 10^{-5}$	$0.000208 \pm 7 \cdot 10^{-5}$	$0.0236 \pm 5 \cdot 10^{-5}$	1.9
2000	$0.00387 \pm 6 \cdot 10^{-5}$	$0.00466 \pm 7 \cdot 10^{-5}$	$0.000129 \pm 6 \cdot 10^{-5}$	$1.88 \cdot 10^{-5} \pm 6 \cdot 10^{-5}$	$0.0321 \pm 5 \cdot 10^{-5}$	3.54
500	$0.000125 \pm 7 \cdot 10^{-5}$	$0.000948 \pm 6 \cdot 10^{-5}$	$-7.66 \cdot 10^{-5} \pm 7 \cdot 10^{-5}$	$-2.78 \cdot 10^{-5} \pm 6 \cdot 10^{-5}$	$0.0074 \pm 5 \cdot 10^{-5}$	0.826
1000	$0.00197 \pm 7 \cdot 10^{-5}$	$0.00239 \pm 6 \cdot 10^{-5}$	$-0.000102 \pm 6 \cdot 10^{-5}$	$-0.000209 \pm 6 \cdot 10^{-5}$	$0.0141 \pm 5 \cdot 10^{-5}$	1.3
1500	$0.00312 \pm 6 \cdot 10^{-5}$	$0.00295 \pm 7 \cdot 10^{-5}$	$-0.000347 \pm 6 \cdot 10^{-5}$	$-0.000555 \pm 7 \cdot 10^{-5}$	$0.0217 \pm 5 \cdot 10^{-5}$	1.78
2000	$0.00402 \pm 6 \cdot 10^{-5}$	$0.00453 \pm 7 \cdot 10^{-5}$	$-0.000468 \pm 6 \cdot 10^{-5}$	$-0.000684 \pm 6 \cdot 10^{-5}$	$0.0295 \pm 5 \cdot 10^{-5}$	3.41
500	$0.00111 \pm 6 \cdot 10^{-5}$	$0.00113 \pm 7 \cdot 10^{-5}$	$-0.000287 \pm 6 \cdot 10^{-5}$	$-2.89 \cdot 10^{-5} \pm 7 \cdot 10^{-5}$	$0.00849 \pm 5 \cdot 10^{-5}$	1.26
1000	$0.00186 \pm 5 \cdot 10^{-5}$	$0.00228 \pm 7 \cdot 10^{-5}$	$-5.76 \cdot 10^{-6} \pm 6 \cdot 10^{-5}$	$-0.000175 \pm 6 \cdot 10^{-5}$	$0.0164 \pm 5 \cdot 10^{-5}$	1.27
1500	$0.00318 \pm 6 \cdot 10^{-5}$	$0.00297 \pm 8 \cdot 10^{-5}$	$-5.07 \cdot 10^{-5} \pm 7 \cdot 10^{-5}$	$-0.000538 \pm 7 \cdot 10^{-5}$	$0.0249 \pm 5 \cdot 10^{-5}$	1.57
2000	$0.00404 \pm 6 \cdot 10^{-5}$	$0.00462 \pm 7 \cdot 10^{-5}$	$-0.000199 \pm 6 \cdot 10^{-5}$	$-0.000774 \pm 6 \cdot 10^{-5}$	$0.0339 \pm 5 \cdot 10^{-5}$	3.31
500	$0.00117 \pm 6 \cdot 10^{-5}$	$0.000949 \pm 7 \cdot 10^{-5}$	$1.03 \cdot 10^{-5} \pm 6 \cdot 10^{-5}$	$0.000199 \pm 7 \cdot 10^{-5}$	$0.00724 \pm 5 \cdot 10^{-5}$	0.892
1000	$0.00184 \pm 6 \cdot 10^{-5}$	$0.00238 \pm 7 \cdot 10^{-5}$	$-0.000278 \pm 6 \cdot 10^{-5}$	$-7.72 \cdot 10^{-5} \pm 6 \cdot 10^{-5}$	$0.0142 \pm 5 \cdot 10^{-5}$	1.15
1500	$0.00321 \pm 6 \cdot 10^{-5}$	$0.00303 \pm 7 \cdot 10^{-5}$	$-0.000264 \pm 7 \cdot 10^{-5}$	$0.000235 \pm 7 \cdot 10^{-5}$	$0.0213 \pm 5 \cdot 10^{-5}$	1.61
2000	$0.0039 \pm 6 \cdot 10^{-5}$	$0.00473 \pm 7 \cdot 10^{-5}$	$-6.6 \cdot 10^{-5} \pm 6 \cdot 10^{-5}$	$0.000223 \pm 6 \cdot 10^{-5}$	$0.0289 \pm 5 \cdot 10^{-5}$	3.05

Amp. [Count]	k_{ia} [rad]	k_{ib} [rad]	k_{ic} [rad]	k_{id} [rad]	φ_{RIN} [rad]	χ^2
500	$-8.27\cdot10^{-5}\pm6\cdot10^{-5}$	$9.55\cdot10^{-5}\pm7\cdot10^{-5}$	$-0.000325\pm6\cdot10^{-5}$	$-0.00033\pm6\cdot10^{-5}$	$0.0064\pm5\cdot10^{-5}$	0.574
1000	$-0.000155\pm6\cdot10^{-5}$	$0.00018\pm7\cdot10^{-5}$	$-0.000644\pm6\cdot10^{-5}$	$-0.000722\pm6\cdot10^{-5}$	$0.0128\pm5\cdot10^{-5}$	0.446
1500	$-0.000257\pm6\cdot10^{-5}$	$0.000105\pm6\cdot10^{-5}$	$-0.00102\pm6\cdot10^{-5}$	$-0.00107\pm6\cdot10^{-5}$	$0.0193\pm4\cdot10^{-5}$	0.507
2000	$-0.000117\pm7\cdot10^{-5}$	$0.000143\pm5\cdot10^{-5}$	$-0.00128\pm6\cdot10^{-5}$	$-0.00146\pm6\cdot10^{-5}$	$0.0258\pm4\cdot10^{-5}$	0.474
500	$-1.51\cdot10^{-5}\pm6\cdot10^{-5}$	$2.5\cdot10^{-5}\pm7\cdot10^{-5}$	$-0.00033\pm6\cdot10^{-5}$	$-0.000335\pm6\cdot10^{-5}$	$0.0064\pm5\cdot10^{-5}$	0.573
1000	$-4.16\cdot10^{-5}\pm6\cdot10^{-5}$	$4.86\cdot10^{-5}\pm6\cdot10^{-5}$	$-0.000645\pm6\cdot10^{-5}$	$-0.000736\pm6\cdot10^{-5}$	$0.0128\pm5\cdot10^{-5}$	0.445
1500	$-3.41\cdot10^{-6}\pm6\cdot10^{-5}$	$0.000238\pm6\cdot10^{-5}$	$-0.001\pm6\cdot10^{-5}$	$-0.0011\pm6\cdot10^{-5}$	$0.0193\pm4\cdot10^{-5}$	0.519
2000	$-0.000235\pm7\cdot10^{-5}$	$0.000293\pm5\cdot10^{-5}$	$-0.00126\pm6\cdot10^{-5}$	$-0.00149\pm6\cdot10^{-5}$	$0.0259\pm4\cdot10^{-5}$	0.516
500	$-4.14e-06\pm5\cdot10^{-5}$	$9.58\cdot10^{-5}\pm7\cdot10^{-5}$	$-0.00033\pm6\cdot10^{-5}$	$-0.000366\pm6\cdot10^{-5}$	$0.00638\pm5\cdot10^{-5}$	0.464
1000	$-6.82\cdot10^{-5}\pm5\cdot10^{-5}$	$0.000115\pm7\cdot10^{-5}$	$-0.000572\pm6\cdot10^{-5}$	$-0.000761\pm6\cdot10^{-5}$	$0.0126\pm4\cdot10^{-5}$	0.616
1500	$-0.000227\pm5\cdot10^{-5}$	$0.000189\pm7\cdot10^{-5}$	$-0.000888\pm6\cdot10^{-5}$	$-0.000927\pm6\cdot10^{-5}$	$0.0189\pm4\cdot10^{-5}$	0.493
2000	$-0.000174\pm5\cdot10^{-5}$	$0.000284\pm7\cdot10^{-5}$	$-0.00121\pm6\cdot10^{-5}$	$-0.00142\pm6\cdot10^{-5}$	$0.0252\pm4\cdot10^{-5}$	0.437
500	$-9.01\cdot10^{-5}\pm5\cdot10^{-5}$	$2.62\cdot10^{-5}\pm7\cdot10^{-5}$	$-0.000325\pm6\cdot10^{-5}$	$-0.000361\pm6\cdot10^{-5}$	$0.00638\pm5\cdot10^{-5}$	0.456
1000	$-0.000112\pm5\cdot10^{-5}$	$0.000132\pm7\cdot10^{-5}$	$-0.000563\pm6\cdot10^{-5}$	$-0.000746\pm6\cdot10^{-5}$	$0.0126\pm5\cdot10^{-5}$	0.628
1500	$-5.55\cdot10^{-5}\pm5\cdot10^{-5}$	$0.000172\pm7\cdot10^{-5}$	$-0.000861\pm6\cdot10^{-5}$	$-0.000894\pm6\cdot10^{-5}$	$0.019\pm4\cdot10^{-5}$	0.45
2000	$-0.000194\pm5\cdot10^{-5}$	$0.000238\pm7\cdot10^{-5}$	$-0.00119\pm6\cdot10^{-5}$	$-0.00141\pm6\cdot10^{-5}$	$0.0253\pm4\cdot10^{-5}$	0.429

Table A.5.: This table shows the fit results for small vector noise contribution to the $2f_{\mathrm{het}}$ RIN transfer function measurement. The fit components for x1_A, x1_B, xR_A and xR_B are listed, in that order, for increasing injection amplitude. With the parameters k_{ia}, k_{ib}, k_{ic} and k_{id} the contribution of SVN is characterised. The phase amplitude due to the RIN injection φ_{RIN} is also calculated by the fit, for a better error estimation the mean value of the residuals after the SVN subtraction is used instead. For this $2f_{\mathrm{het}}$ RIN injection the 2φ-SVN contribution with the parameters k_{ic} and k_{id} is dominant. The χ^2 parameter for each fit is also shown, in the last row. See also Appendix A.11.

A.18. Planned TM offsets of the flight experiments

Here is an overview of the implemented test mass offsets of the first in-flight RIN subtraction experiment. These offsets are in the unit nanometre.

```
tm_offsets = [−270, −240, −210, −180, −150, −120, −90, −60, −40, −30, −20, −10,
0, 10, 20, 30, 40, 60, 90, 120, 150, 180, 210, 240, 270, 300, 330, 360, 390,
420, 450, 480, 510, 520, 530, 540, 550, 580, 610, 640, 670, 700, 730, 760, 790];
```

This is the list of the intended offsets of the second RIN subtraction experiment, the focus is more on the main areas of interest in the RIN subtraction shape. For all of these test mass offsets the o12 noise is measured with balanced detection and with only the A-side of the interferometers. These offsets are:

```
tm_offsets = [−10, −5, −3, −1.2, −0.6, 0, 0.3, 1, 2, 4, 8, 12, 20, 100, 120, 133,
140, 145, 153, 160, 180, 200, 225, 240, 250, 260, 263, 266, 270,
275, 280, 290, 350, 375, 390, 399, 410];
```

Due to a timing problem the end of the experiment was cut off, the last TM offset is at 270 nm.

At the test mass offsets 0 nm, 133 nm, 240 nm, 266 nm and 410 nm the measurement of the noise with a sampling frequency of 100 Hz for 1 minute is implemented.

Shown here is an example timeline for one of steps:

- 30min: move test mass to new offset
- 15min: noise measurement A+B side
- 10min: mask B side
- 15min: noise measurement A side
- 10sec: un-mask B side (immediately after start the slew to the next TM position)

The time to move the test mass is increased for bigger TM offsets, and for the TM positions where 100Hz data is measured this segment is added to both the balanced detection and the A side measurement.

A.19. Code snippet of TM motion of the in-flight RIN subtraction experiment

This code snippet shows the commands to move TM2 to the first offset position of $-270\,\mathrm{nm}$ by a change of the setpoint of the longitudinal control loop, while the set-points of the control loops on the other degrees of freedom remain at 0.0. With similar commands the test mass was moved to the other offsets.

To increase readability additional settings indicated by single letters and command IDs were removed.

```
ADC70114 DFA_Set_SlewConfig_TM2  2016.113.13.52.44.483831 2016.116.08.06.19.000000
ADP73118 TM2_slew_X_set       Raw     Dec           1.0
ADP73119 TM2_slew_X_target  Raw     Dec           −2.7E−7
ADP73120 TM2_slew_X_holdtime Raw     Dec           2.0
ADP73121 TM2_slew_Y_set       Raw     Dec           0.0
ADP73122 TM2_slew_Y_target  Raw     Dec           0.0
ADP73123 TM2_slew_Y_holdtime Raw     Dec           0.0
ADP73124 TM2_slew_Z_set       Raw     Dec           0.0
ADP73125 TM2_slew_Z_target  Raw     Dec           0.0
ADP73126 TM2_slew_Z_holdtime Raw     Dec           0.0
ADP73127 TM2_slew_Theta_set Raw     Dec           0.0
ADP73128 TM2_slew_Theta_target Raw  Dec           0.0
ADP73129 TM2_slew_Theta_holdtime Raw Dec           0.0
ADP73130 TM2_slew_Eta_set    Raw     Dec           0.0
ADP73131 TM2_slew_Eta_target Raw     Dec           0.0
ADP73132 TM2_slew_Eta_holdtime Raw  Dec           0.0
ADP73133 TM2_slew_phi_set    Raw     Dec           0.0
ADP73134 TM2_slew_phi_target Raw     Dec           0.0
ADP73135 TM2_slew_phi_holdtime Raw  Dec           0.0
ADC70204 DFA_Start_Slew_TM2        2016.113.13.52.44.547662 2016.116.08.06.40.000000
ADC00017 DFA_CtrlParamUpdate       2016.113.13.52.44.547664 2016.116.08.06.41.000000
ADP65001 DFA_ControlGrp      Eng     Dec           DfcsConSlew
ADC70207 DFA_Stop_Slew_TM2         2016.113.13.52.44.547666 2016.116.08.06.46.000000
```

A.20. RIN direct measurement - Scatter of real and imaginary component

Figure A.21.: These plots show the scatter between the real and imaginary component of the measurement beam on PDR_AA. The top two plots show distribution of these components around $1f_{het}$ and $2f_{het}$ with the amplitude stabilisation on. The red cross marks the zero point, the noise is not centred around zero for all measurements made, while white noise would show a circle here small protrusions are visible. Out of frame are a few points in the measurements without the stabilisation, these time series contain irregular spikes which are also visible in their complex components.
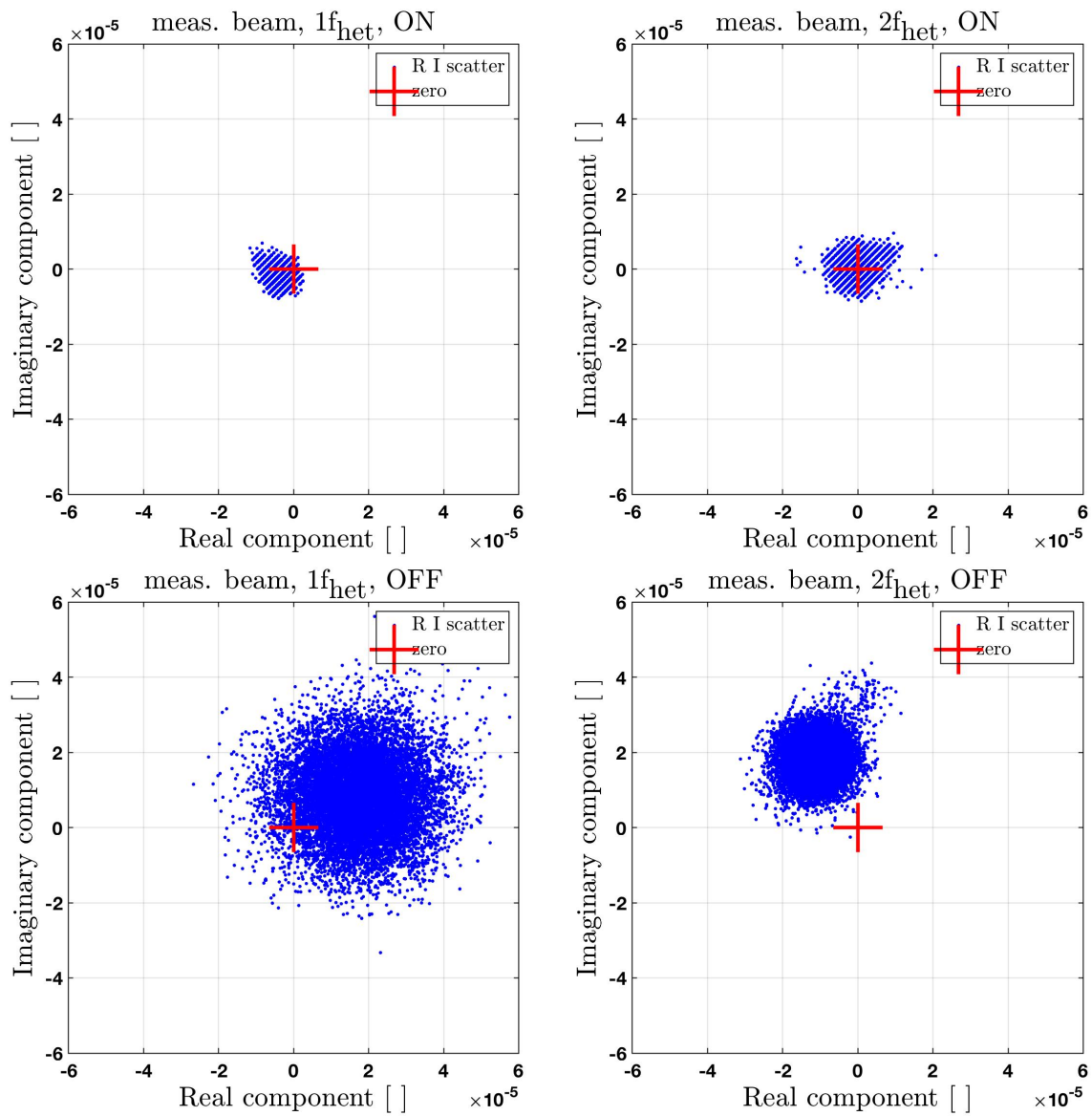
Figure A.22.: These plots show the scatter between the real and imaginary component of the reference beam on PDR_AA. The top two plots show distribution of these components around $1f_{het}$ and $2f_{het}$ with the amplitude stabilisation on. The red cross marks the zero point, the noise is not centred around zero for all measurements made, while white noise would show a circle here small protrusions are visible. Out of frame are a few points in the measurements without the stabilisation, these time series contain irregular spikes which are also visible in their complex components.
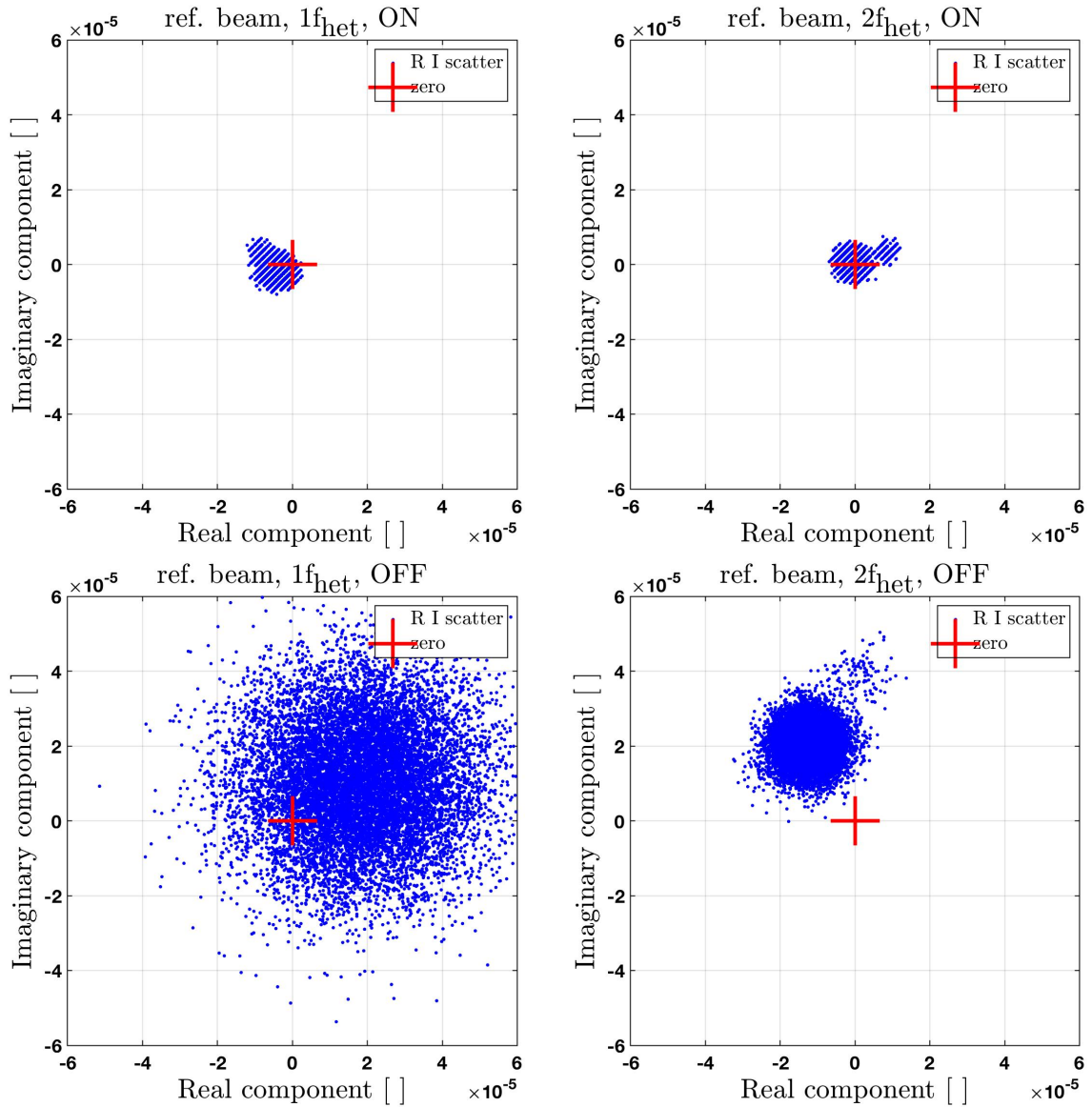
A.21. Fit parameters covariance and histograms

Shown here are the covariance of the fit parameters and histograms. Used as example are the fit to the small vector noise contribution of the RIN transfer function experiment of Section 5.1.5, see Figure A.23. Also shown are the fit properties of one measurement of the RIN subtraction in the laboratory and in space, see Figure A.24. The circles show the distribution of values during the exploration of the parameter space, a circle shows no correlation between the two parameters which are compared. If the shape is more elliptical, or even a line, the two fit parameters are dependant on each other.
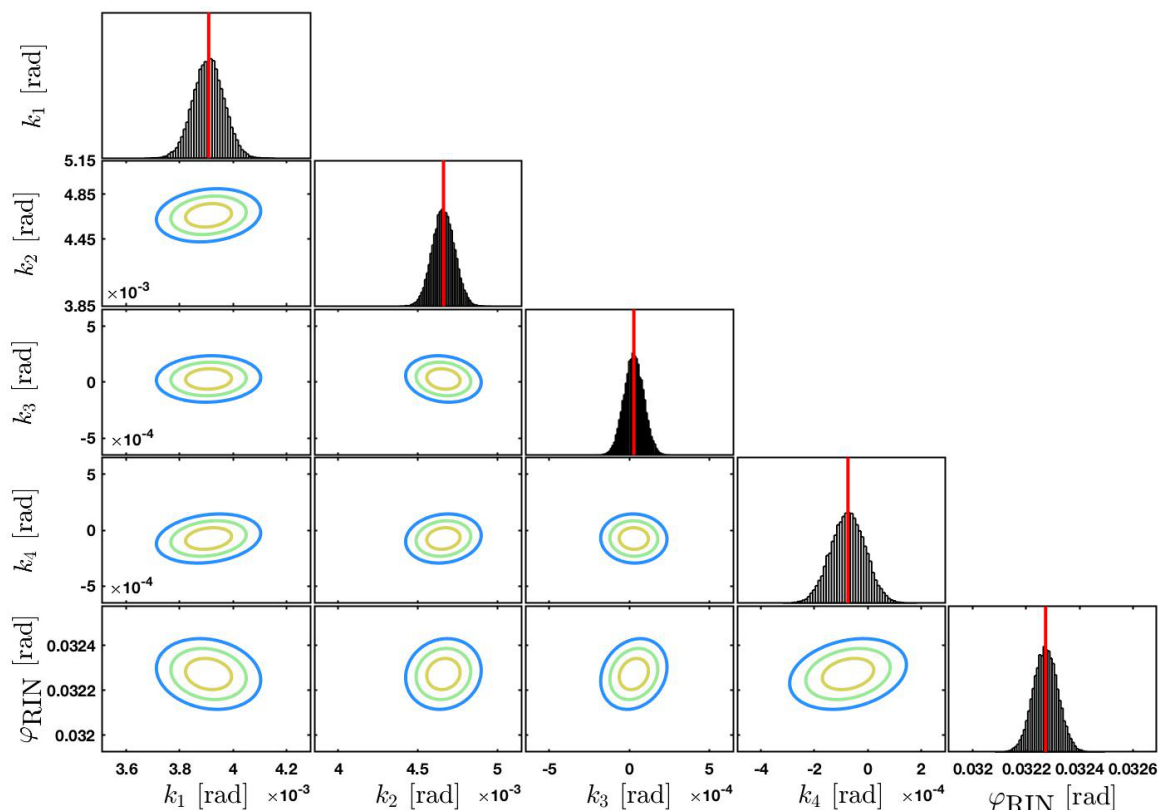
Figure A.23.: Shown here is the covariance and histograms of the fit to the SVN measured with the x1_A signal, with a RIN injection amplitude of 2000 Count.
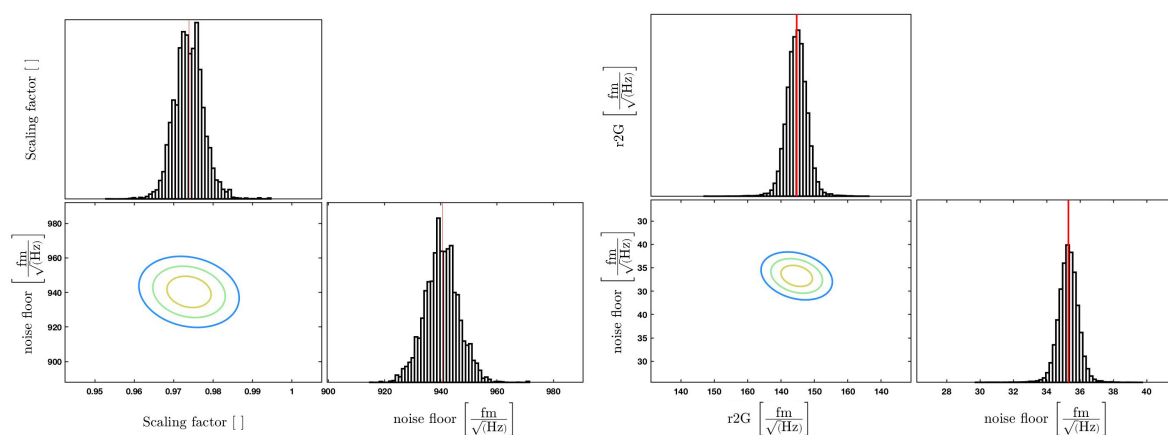
Figure A.24.: Shown here on the left is the covariance and histograms of the scaling factor fit from the calculated to the measured phase noise in the RIN subtraction experiment, with an injection of RIN at $1f_{het}$, measured in the higher frequency band on the A-side. The right plot shows the fit properties of the first in-flight RIN subtraction measurement, with the phase noise measured in the frequency band between $0.6\,\mathrm{Hz}$ to $0.9\,\mathrm{Hz}$.

Bibliography

[1] Albert Einstein. Näherungsweise Integration der Feldgleichungen der Gravitation. *Sitzungsberichte der Königlich Preußischen Akademie der Wissenschaften (Berlin)*, pages 688–696, 1916. 1

[2] Albert Einstein. Über Gravitationswellen. *Sitzungsberichte der Königlich Preußischen Akademie der Wissenschaften (Berlin)*, pages 154–167, 1918. 1

[3] J. H. Taylor, L. A. Fowler, and P. M. McCulloch. Measurements of general relativistic effects in the binary pulsar PSR1913 + 16. *Nature*, 277(5696):437–440, 1979. doi: 10.1038/277437a0. URL https://doi.org/10.1038/277437a0. 1

[4] Joel M. Weisberg, Joseph H. Taylor, and Lee A. Fowler. Gravitational waves from an orbiting pulsar. *Scientific American*, 245(4):74–82, 1981. doi: 10.1038/scientificamerican1081-74. 1

[5] B. P. et al. Abbott. Observation of gravitational waves from a binary black hole merger. *Phys. Rev. Lett.*, 116:061102, Feb 2016. doi: 10.1103/PhysRevLett.116.061102. URL https://link.aps.org/doi/10.1103/PhysRevLett.116.061102. 1

[6] The eLISA Consortium, :, P. Amaro Seoane, S. Aoudia, H. Audley, G. Auger, S. Babak, J. Baker, E. Barausse, S. Barke, M. Bassan, V. Beckmann, M. Benacquista, P. L. Bender, E. Berti, P. Binétruy, J. Bogenstahl, C. Bonvin, D. Bortoluzzi, N. C. Brause, J. Brossard, S. Buchman, I. Bykov, J. Camp, C. Caprini, A. Cavalleri, M. Cerdonio, G. Ciani, M. Colpi, G. Congedo, J. Conklin, N. Cornish, K. Danzmann, G. de Vine, D. DeBra, M. Dewi Freitag, L. Di Fiore, M. Diaz Aguilo, I. Diepholz, R. Dolesi, M. Dotti, G. Fernández Barranco, L. Ferraioli, V. Ferroni, N. Finetti, E. Fitzsimons, J. Gair, F. Galeazzi, A. Garcia, O. Gerberding, L. Gesa, D. Giardini, F. Gibert, C. Grimani, P. Groot, F. Guzman Cervantes, Z. Haiman, H. Halloin, G. Heinzel, M. Hewitson, C. Hogan, D. Holz, A. Hornstrup, D. Hoyland, C. D. Hoyle, M. Hueller, S. Hughes, P. Jetzer, V. Kalogera, N. Karnesis, M. Kilic, C. Killow, W. Klipstein, E. Kochkina, N. Korsakova, A. Krolak, S. Larson, M. Lieser, T. Littenberg, J. Livas, I. Lloro, D. Mance, P. Madau, P. Maghami, C. Mahrdt, T. Marsh, I. Mateos, L. Mayer, D. McClelland, K. McKenzie, S. McWilliams, S. Merkowitz, C. Miller, S. Mitryk, J. Moerschell, S. Mohanty, A. Monsky, G. Mueller, V. Müller, G. Nelemans, D. Nicolodi, S. Nissanke, M. Nofrarias, K. Numata, F. Ohme, M. Otto, M. Perreur-Lloyd, A. Petiteau, E. S. Phinney, E. Plagnol, S. Pollack, E. Porter, P. Prat, A. Preston, T. Prince, J. Reiche, D. Richstone, D. Robertson, E. M. Rossi, S. Rosswog, L. Rubbo, A. Ruiter, J. Sanjuan, B. S. Sathyaprakash, S. Schlamminger, B. Schutz, D. Schütze, A. Sesana, D. Shaddock, S. Shah, B. Sheard, C. F. Sopuerta, A. Spector, R. Spero, R. Stanga, R. Stebbins, G. Stede, F. Steier, T. Sumner, K. X. Sun, A. Sutton, T. Tanaka, D. Tanner, I. Thorpe, M. Tröbs, M. Tinto, H. B. Tu, M. Vallisneri, D. Vetrugno, S. Vitale, M. Volonteri, V. Wand, Y. Wang, G. Wanner, H. Ward,

B. Ware, P. Wass, W. J. Weber, Y. Yu, N. Yunes, and P. Zweifel. The Gravitational Universe, 2013. URL arXiv:1305.5720. 1, 2

[7] B. Abbott, R. Abbott, R. Adhikari, A. Ageev, B. Allen, R. Amin, S.B. Anderson, W.G. Anderson, M. Araya, H. Armandula, and et al. Detector description and performance for the first coincidence observations between LIGO and GEO. *Nuclear Instruments and Methods in Physics Research Section A: Accelerators, Spectrometers, Detectors and Associated Equipment*, 517(1-3):154?179, Jan 2004. ISSN 0168-9002. doi: 10.1016/j. nima.2003.11.124. URL http://dx.doi.org/10.1016/j.nima.2003.11.124. 1

[8] B. P. et al. Abbott. GWTC-1: A Gravitational-Wave Transient Catalog of Compact Binary Mergers Observed by LIGO and Virgo during the First and Second Observing Runs. *Phys. Rev. X*, 9:031040, Sep 2019. doi: 10.1103/PhysRevX.9.031040. URL https://link.aps.org/doi/10.1103/PhysRevX.9.031040. 1

[9] D M Macleod, S Fairhurst, B Hughey, A P Lundgren, L Pekowsky, J Rollins, and J R Smith. Reducing the effect of seismic noise in LIGO searches by targeted veto generation. *Classical and Quantum Gravity*, 29(5):055006, Feb 2012. ISSN 1361-6382. doi: 10.1088/0264-9381/29/5/055006. URL http://dx.doi.org/10.1088/0264-9381/29/5/055006. 1

[10] Athena-LISA Synergy Working Group: Monica Colpi, Andrew C. Fabian, Matteo Guainazzi, Paul McNamara, Luigi Piro, and Nial Tanvir. Athena-LISA synergies. 2019. URL https://www.cosmos.esa.int/documents/678316/1700384/Athena_LISA_Whitepaper_Iss1.0.pdf. 2

[11] Pau Amaro-Seoane, Heather Audley, Stanislav Babak, John Baker, Enrico Barausse, Peter Bender, Emanuele Berti, Pierre Binetruy, Michael Born, Daniele Bortoluzzi, Jordan Camp, Chiara Caprini, Vitor Cardoso, Monica Colpi, John Conklin, Neil Cornish, Curt Cutler, Karsten Danzmann, Rita Dolesi, Luigi Ferraioli, Valerio Ferroni, Ewan Fitzsimons, Jonathan Gair, Lluis Gesa Bote, Domenico Giardini, Ferran Gibert, Catia Grimani, Hubert Halloin, Gerhard Heinzel, Thomas Hertog, Martin Hewitson, Kelly Holley-Bockelmann, Daniel Hollington, Mauro Hueller, Henri Inchauspe, Philippe Jetzer, Nikos Karnesis, Christian Killow, Antoine Klein, Bill Klipstein, Natalia Korsakova, Shane L Larson, Jeffrey Livas, Ivan Lloro, Nary Man, Davor Mance, Joseph Martino, Ignacio Mateos, Kirk McKenzie, Sean T McWilliams, Cole Miller, Guido Mueller, Germano Nardini, Gijs Nelemans, Miquel Nofrarias, Antoine Petiteau, Paolo Pivato, Eric Plagnol, Ed Porter, Jens Reiche, David Robertson, Norna Robertson, Elena Rossi, Giuliana Russano, Bernard Schutz, Alberto Sesana, David Shoemaker, Jacob Slutsky, Carlos F. Sopuerta, Tim Sumner, Nicola Tamanini, Ira Thorpe, Michael Troebs, Michele Vallisneri, Alberto Vecchio, Daniele Vetrugno, Stefano Vitale, Marta Volonteri, Gudrun Wanner, Harry Ward, Peter Wass, William Weber, John Ziemer, and Peter Zweifel. Laser Interferometer Space Antenna, 2017. URL https://www.elisascience.org/articles/lisa-mission/lisa-mission-proposal-l3. 2

[12] S.Vitale for the LPF collaboration. The LTP experiment on the LISA Pathfinder mission. In *Proceedings of the 5th LISA Symposium*, 2005. URL arXiv:gr-qc/0504062. 3

[13] P McNamara, S Vitale, and K Danzmann. LISA Pathfinder. *Classical and Quantum Gravity*, 25(11):114034, may 2008. doi: 10.1088/0264-9381/25/11/114034. URL https://doi.org/10.1088/0264-9381/25/11/114034. 3

[14] F Antonucci, M Armano, H Audley, G Auger, M Benedetti, P Binetruy, J Bogenstahl, D Bortoluzzi, P Bosetti, N Brandt, M Caleno, P Cañizares, A Cavalleri, M Cesa,

M Chmeissani, A Conchillo, G Congedo, I Cristofolini, M Cruise, K Danzmann, F De Marchi, M Diaz-Aguilo, I Diepholz, G Dixon, R Dolesi, N Dunbar, J Fauste, L Ferraioli, V Ferrone, W Fichter, E Fitzsimons, M Freschi, A García Marin, C García Marirrodriga, R Gerndt, L Gesa, F Gilbert, D Giardini, C Grimani, A Grynagier, B Guillaume, F Guzmán, I Harrison, G Heinzel, V Hernández, M Hewitson, D Hollington, J Hough, D Hoyland, M Hueller, J Huesler, O Jennrich, P Jetzer, B Johlander, N Karnesis, C Killow, X Llamas, I Lloro, A Lobo, R Maarschalkerweerd, S Madden, D Mance, I Mateos, P W McNamara, J Mendes, E Mitchell, A Monsky, D Nicolini, D Nicolodi, M Nofrarias, F Pedersen, M Perreur-Lloyd, E Plagnol, P Prat, G D Racca, J Ramos-Castro, J Reiche, J A Romera Perez, D Robertson, H Rozemeijer, J Sanjuan, A Schleicher, M Schulte, D Shaul, L Stagnaro, S Strandmoe, F Steier, T J Sumner, A Taylor, D Texier, C Trenkel, H-B Tu, S Vitale, G Wanner, H Ward, S Waschke, P Wass, W J Weber, T Ziegler, and P Zweifel. The LISA Pathfinder mission. *Classical and Quantum Gravity*, 29(12):124014, jun 2012. doi: 10.1088/0264-9381/29/12/124014. URL https://doi.org/10.1088/0264-9381/29/12/124014. 3, 216

[15] M Armano, H Audley, G Auger, J Baird, P Binetruy, M Born, D Bortoluzzi, N Brandt, A Bursi, M Caleno, A Cavalleri, A Cesarini, M Cruise, K Danzmann, I Diepholz, R Dolesi, N Dunbar, L Ferraioli, V Ferroni, E Fitzsimons, M Freschi, J Gallegos, C García Marirrodriga, R Gerndt, L I Gesa, F Gibert, D Giardini, R Giusteri, C Grimani, I Harrison, G Heinzel, M Hewitson, D Hollington, M Hueller, J Huesler, H Inchauspé, O Jennrich, P Jetzer, B Johlander, N Karnesis, B Kaune, N Korsakova, C Killow, I Lloro, R Maarschalkerweerd, S Madden, D Mance, V Martín, F Martin-Porqueras, I Mateos, P McNamara, J Mendes, L Mendes, A Moroni, M Nofrarias, S Paczkowski, M Perreur-Lloyd, A Petiteau, P Pivato, E Plagnol, P Prat, U Ragnit, J Ramos-Castro, J Reiche, J A Romera Perez, D Robertson, H Rozemeijer, G Russano, P Sarra, A Schleicher, J Slutsky, C F Sopuerta, T Sumner, D Texier, J Thorpe, C Trenkel, H B Tu, D Vetrugno, S Vitale, G Wanner, H Ward, S Waschke, P Wass, D Wealthy, S Wen, W Weber, A Wittchen, C Zanoni, T Ziegler, and P Zweifel. The LISA Pathfinder mission. *Journal of Physics: Conference Series*, 610:012005, may 2015. doi: 10.1088/1742-6596/610/1/012005. URL https://doi.org/10.1088/1742-6596/610/1/012005. 3

[16] ESA BR-323: LISA pathfinder - first steps to observing gravitational waves from space. *ESA Brochure*, 323. URL https://sci.esa.int/s/WX6Gd3A. 3

[17] Michele Armano, Heather Audley, Jonathon Baird, Pierre Binetruy, Michael Born, Daniele Bortoluzzi, Eleanora Castelli, Antonella Cavalleri, Andrea Cesarini, Mike Cruise, Karsten Danzmann, Marcus de Deus Silva, Ingo Diepholz, George Dixon, Rita Dolesi, Luigi Ferraioli, Valerio Ferroni, Ewan Fitzsimons, Mario Freschi, Luis Gesa, Ferran Gibert, Domenico Giardini, Roberta Giusteri, Catia Grimani, Jonathan Grzymisch, Ian Harrison, Gerhard Heinzel, Martin Hewitson, Daniel Hollington, David Hoyland, Mauro Hueller, Henri Inchauspe, Oliver Jennrich, Philippe Jetzer, Nikolaos Karnesis, Brigitte Kaune, Natalia Korsakova, Christian J Killow, Alberto Lobo, Ivan Lloro, Li Liu, Juan-Pedro Lopez-Zaragoza, Rolf Maarschalkerweerd, Davor Mance, Neda Meshksar, V Mart?n, L Martin-Polo, Joseph Martino, Fernando Martin-Porqueras, Ignacio Mateos, Paul McNamara, Jose Mendes, Luis Mendes, Miquel Nofrarias, Sarah Paczkowski, Michael Perreur-Lloyd, Antoine Petiteau, Paolo Pivato, Eric Plagnol, Jose Ramos-Castro, Jens Reiche, David Robertson, Francisco Rivas, Giuliana Russano, Jacob Slutsky, Carlos Sopuerta, Timothy Sumner, Daniel Texier, Ira Thorpe, Daniele Vetrugno, Stefano Vitale, Gudrun Wanner, Harry Ward, Peter Wass, William Weber, Lennart Wissel, Andreas Wittchen, and Peter Zweifel. LISA Pathfinder. 2019. URL arXiv:1903.08924. 3

[18] M. Armano, H. Audley, J. Baird, P. Binetruy, M. Born, D. Bortoluzzi, E. Castelli, A. Cavalleri, A. Cesarini, A. M. Cruise, K. Danzmann, M. de Deus Silva, I. Diepholz, G. Dixon, R. Dolesi, L. Ferraioli, V. Ferroni, E. D. Fitzsimons, M. Freschi, L. Gesa, F. Gibert, D. Giardini, R. Giusteri, C. Grimani, J. Grzymisch, I. Harrison, G. Heinzel, M. Hewitson, D. Hollington, D. Hoyland, M. Hueller, H. Inchauspé, O. Jennrich, P. Jetzer, N. Karnesis, B. Kaune, N. Korsakova, C. J. Killow, J. A. Lobo, I. Lloro, L. Liu, J. P. López-Zaragoza, R. Maarschalkerweerd, D. Mance, N. Meshksar, V. Martín, L. Martin-Polo, J. Martino, F. Martin-Porqueras, I. Mateos, P. W. McNamara, J. Mendes, L. Mendes, M. Nofrarias, S. Paczkowski, M. Perreur-Lloyd, A. Petiteau, P. Pivato, E. Plagnol, J. Ramos-Castro, J. Reiche, D. I. Robertson, F. Rivas, G. Russano, J. Slutsky, C. F. Sopuerta, T. Sumner, D. Texier, J. I. Thorpe, D. Vetrugno, S. Vitale, G. Wanner, H. Ward, P. J. Wass, W. J. Weber, L. Wissel, A. Wittchen, and P. Zweifel. Beyond the required LISA free-fall performance: New LISA Pathfinder results down to 20 μHz. *Phys. Rev. Lett.*, 120:061101, Feb 2018. doi: 10.1103/PhysRevLett.120.061101. URL https://link.aps.org/doi/10.1103/PhysRevLett.120.061101. 3, 37, 58, 60

[19] M. Armano, H. Audley, J. Baird, P. Binetruy, M. Born, D. Bortoluzzi, N. Brandt, E. Castelli, A. Cavalleri, A. Cesarini, A. M. Cruise, K. Danzmann, M. de Deus Silva, I. Diepholz, G. Dixon, R. Dolesi, L. Ferraioli, V. Ferroni, E. D. Fitzsimons, R. Flatscher, M. Freschi, A. García, R. Gerndt, L. Gesa, D. Giardini, F. Gibert, R. Giusteri, C. Grimani, J. Grzymisch, F. Guzman, I. Harrison, M.-S. Hartig, G. Heinzel, M. Hewitson, D. Hollington, D. Hoyland, M. Hueller, H. Inchauspé, O. Jennrich, P. Jetzer, U. Johann, B. Johlander, N. Karnesis, B. Kaune, C. J. Killow, N. Korsakova, J. A. Lobo, L. Liu, J. P. López-Zaragoza, R. Maarschalkerweerd, D. Mance, V. Martín, L. Martin-Polo, F. Martin-Porqueras, J. Martino, P. W. McNamara, J. Mendes, L. Mendes, N. Meshksar, A. Monsky, M. Nofrarias, S. Paczkowski, M. Perreur-Lloyd, A. Petiteau, P. Pivato, E. Plagnol, J. Ramos-Castro, J. Reiche, F. Rivas, D. I. Robertson, G. Russano, J. Sanjuan, J. Slutsky, C. F. Sopuerta, F. Steier, T. Sumner, D. Texier, J. I. Thorpe, D. Vetrugno, S. Vitale, V. Wand, G. Wanner, H. Ward, P. J. Wass, W. J. Weber, L. Wissel, A. Wittchen, and P. Zweifel. Sensor noise in LISA Pathfinder: In-flight performance of the optical test mass readout. *Phys. Rev. Lett.*, 126:131103, Apr 2021. doi: 10.1103/PhysRevLett.126.131103. URL https://link.aps.org/doi/10.1103/PhysRevLett.126.131103. 3, 33, 56, 71, 127, 174, 183, 204, 220

[20] P. Welch. The use of fast fourier transform for the estimation of power spectra: A method based on time averaging over short, modified periodograms. *IEEE Transactions on Audio and Electroacoustics*, 15(2):70–73, 1967. doi: 10.1109/TAU.1967.1161901. 4

[21] Steven W. Smith. *Digital Signal Processing - A Practical Guide for Engineers and Scientists*. Newbes, an imprint of Elsevier, 2003. ISBN 075067444X, 9780750674447. 4, 59

[22] M.; Benedetti M.; Bogenstahl J.; Bortoluzzi D.; Bosetti P.; Brandt N.; Cavalleri A.; Ciani G.; Cristofolini I.; Cruise M.; Danzmann K.; Diepholz I.; Dolesi R.; Fauste J.; Ferraioli L.; Fertin D.; Fichter W.; Garcia A.; Garcia C.; Grynagier A.; Guzman F.; Fitzsimons E.; Heinzel G.; Hollington D.; Hough J.; Hueller M.; Hoyland D.; Jennrich O.; Johlander B.; Killow C.; Lobo A.; Mance D.; Mateos I.; McNamara P. W.; Monsky A.; Nicolini D.; Nicolodi D.; Nofrarias M.; Perreur-Lloyd M.; Plagnol E.; Racca G. D.; Ramos-Castro J.; Robertson D.; Sanjuan J.; Schulte M. O.; Shaul D. N. A.; Smit M.; Stagnaro L.; Steier F.; Sumner T. J.; Tateo N.; Tombolato D.; Vischer G.; Vitale S.; Wanner G.; Ward H.; Waschke S.; Wand V.; Wass P.; Weber W. J.; Ziegler T.; Zweifel P. Hewitson, M.; Armano. Data analysis for the LISA technology package. *Classical and Quantum*

Gravity, 26, 2009. URL http://stacks.iop.org/0264-9381/26/i=9/a=094003. 4, 7, 26

[23] Michael Tröbs and Gerhard Heinzel. Improved spectrum estimation from digitized time series on a logarithmic frequency axis. *Measurement*, 39(2):120–129, 2006. ISSN 0263-2241. doi: 10.1016/j.measurement.2005.10.010. URL https://doi.org/10.1016/j.measurement.2005.10.010. 4, 35, 103

[24] F.J. Harris. On the use of windows for harmonic analysis with the discrete fourier transform. *Proceedings of the IEEE*, 66(1):51–83, 1978. doi: 10.1109/PROC.1978.10837. 4

[25] A. Rüdiger G. Heinzel and R. Schilling. Spectrum and spectral density estimation by the discrete fourier transform (DFT), including a comprehensive list of window functions and some new flat-top windows. Technical report, AEI Hannover, 2002. 4

[26] M. Armano, H. Audley, J. Baird, P. Binetruy, M. Born, D. Bortoluzzi, E. Castelli, A. Cavalleri, A. Cesarini, A.?M. Cruise, and et al. Calibrating the system dynamics of LISA Pathfinder. *Physical Review D*, 97(12), Jun 2018. ISSN 2470-0029. doi: 10.1103/physrevd.97.122002. URL http://dx.doi.org/10.1103/PhysRevD.97.122002. 4

[27] Nikolaos Karnesis. *Bayesian data analysis for LISA Pathfinder - Techniques applied to system identification experiments*. PhD thesis, Departament de Física Universitat Autònoma de Barcelona, 2014. 4

[28] Nikolaos Karnesis, Miquel Nofrarias, Carlos F. Sopuerta, Ferran Gibert, Michele Armano, Heather Audley, Giuseppe Congedo, Ingo Diepholz, Luigi Ferraioli, Martin Hewitson, and et al. Bayesian model selection for LISA Pathfinder. *Physical Review D*, 89(6), Mar 2014. ISSN 1550-2368. doi: 10.1103/physrevd.89.062001. URL http://dx.doi.org/10.1103/PhysRevD.89.062001. 4

[29] Vinzenz Wand. *Interferometry at low frequencies: Optical phase measurment for LISA and LISA Pathfinder*. PhD thesis, Leibniz Universität Hannover, 2007. URL https://doi.org/10.15488/9698. 9, 12, 13, 28, 33, 34, 62

[30] Gerhard Heinzel. *Advanced optical techniques for laser-interferometric gravitational-wave detectors*. PhD thesis, Max Planck Institute for Gravitational Physics (Albert-Einstein-Institute), 1999. URL https://doi.org/10.15488/5622. 9

[31] Andreas Wittchen. Noise investigation on the LISA Pathfinder optical bench ground setup. Master's thesis, Max Planck Institute for Gravitational Physics (Albert-Einstein-Institute), 2013. 9, 15, 109

[32] A. García F. Guzmán F. Steier C. Killow D. Robertson H. Ward C. Braxmaier G. Heinzel, V. Wand. Investigation of noise sources in the LTP interferometer S2-AEI-TN-3028. Technical report, AEI Hannover, University of Glasgow, EADS Astrium Immenstaad, 2005. 10, 33, 34, 35, 36, 62, 70, 125

[33] Harry Ward. Optical bench interferometer detailed design S2-UGL-DDD-3003. Technical report, Institute for Gravitational Research Department of Physics and Astronomy University of Glasgow, 2007. 12

[34] Felipe Guzmán Cervantes. *Gravitational wave observation from space: optical phase measurments for LISA and LISA Pathfinder*. PhD thesis, Max Planck Institute for Gravitational Physics (Albert-Einstein-Institute), 2009. URL https://www.tib.eu/de/suchen/id/TIBKAT:606793232. 12, 13, 18, 22, 25, 26, 29, 33, 34, 60, 111, 125, 219

[35] Frank Steier. *Interferometry techniques for spaceborne gravitational wave detectors*. PhD thesis, Laser Interferometry & Gravitational Wave Astronomy, AEI-Hannover, MPI for Gravitational Physics, Max Planck Society, escidoc:24010, 2008. URL https://doi.org/10.15488/7144. 12

[36] Antonio Francisco Garcia Marin. *Minimisation of optical pathlength noise for the detection of gravitational waves with the spaceborne laser interferometer LISA and LISA Pathfinder*. PhD thesis, Gottfried Wilhelm Leibniz Universität Hannover, Hannover, 2007. URL https://doi.org/10.15488/6868. 12, 33, 34, 35, 62

[37] Anneke Monsky. *Understanding interferometric drag-free sensors in space using intelligent data analysis tools*. PhD thesis, Max Planck Institute for Gravitational Physics (Albert-Einstein-Institute), 2010. URL https://www.tib.eu/de/suchen/id/TIBKAT:629992401/. 12, 33, 34, 62, 111, 219

[38] G Heinzel, V Wand, A Garcia, O Jennrich, C Braxmaier, D Robertson, K Middleton, D Hoyland, A Rudiger, R Schilling, and et al. The LTP interferometer and phasemeter. *Classical and Quantum Gravity*, 21(5):581–587, 2004. URL http://stacks.iop.org/0264-9381/21/S581. 12

[39] Gudrun Wanner. *Complex optical systems in space: numerical modelling of the heterodyne interferometry of LISA Pathfinder and LISA*. PhD thesis, Gottfried Wilhelm Leibniz Universität Hannover, 2010. URL https://doi.org/10.15488/7550. 12

[40] Heather. E. Audley. *Preparing for LISA Pathfinder Operations: characterisation of the optical metrology system*. PhD thesis, Leibniz Universität Hannover, 2014. URL https://www.tib.eu/de/suchen/id/TIBKAT:820514756. 12, 21, 22, 26, 33, 36, 62, 71, 173, 203, 210, 211

[41] Sarah Paczkowski. *Laser Frequency Stabilisation and Interferometer Path Length Differences during the LISA Pathfinder Satellite Mission*. PhD thesis, Max Planck Institute for Gravitational Physics (Albert-Einstein-Institute), 2020. URL https://doi.org/10.15488/11130. 14, 35, 71, 183, 188, 198

[42] Gudrun Wanner and Nikolaos Karnesis. Preliminary results on the suppression of sensing cross-talk in LISA Pathfinder. *Journal of Physics: Conference Series*, 2017. doi: 10.1088/1742-6596/840/1/012043. URL https://doi.org/10.1088/1742-6596/840/1/012043. 14, 58

[43] F Antonucci, M Armano, H Audley, G Auger, M Benedetti, P Binetruy, C Boatella, J Bogenstahl, D Bortoluzzi, P Bosetti, N Brandt, M Caleno, A Cavalleri, M Cesa, M Chmeissani, G Ciani, A Conchillo, G Congedo, I Cristofolini, M Cruise, K Danzmann, F De Marchi, M Diaz-Aguilo, I Diepholz, G Dixon, R Dolesi, N Dunbar, J Fauste, L Ferraioli, D Fertin, W Fichter, E Fitzsimons, M Freschi, A García Marin, C García Marirrodriga, R Gerndt, L Gesa, D Giardini, F Gibert, C Grimani, A Grynagier, B Guillaume, F Guzmán, I Harrison, G Heinzel, M Hewitson, D Hollington, J Hough, D Hoyland, M Hueller, J Huesler, O Jeannin, O Jennrich, P Jetzer, B Johlander, C Killow, X Llamas, I Lloro, A Lobo, R Maarschalkerweerd, S Madden, D Mance, I Mateos, P W McNamara, J Mendes, E Mitchell, A Monsky, D Nicolini, D Nicolodi, M Nofrarias, F Pedersen, M Perreur-Lloyd, A Perreca, E Plagnol, P Prat, G D Racca, B Rais, J Ramos-Castro, J Reiche, J A Romera Perez, D Robertson, H Rozemeijer, J Sanjuan, A Schleicher, M Schulte, D Shaul, L Stagnaro, S Strandmoe, F Steier, T J Sumner, A Taylor, D Texier, C Trenkel, D Tombolato, S Vitale, G Wanner, H Ward, S Waschke, P Wass, W J Weber, and P Zweifel. From laboratory experiments to LISA Pathfinder:

achieving LISA geodesic motion. *Classical and Quantum Gravity*, 28(9):094002, 2011. URL http://stacks.iop.org/0264-9381/28/i=9/a=094002. 14, 72

[44] Rolf Bork. AdvLigo CDS Design Overview. Technical report, LIGO, 2010. URL https://dcc.ligo.org/LIGO-T0900612/public. 16, 18

[45] B P Abbott R Abbott T Abernathy M R Ackley K Adams C Adams T Addesso et al. Aasi, J Abbott. Advanced LIGO. *Classical and Quantum Gravity*, 32(7):074001, Mar 2015. ISSN 1361-6382. doi: 10.1088/0264-9381/32/7/074001. URL http://dx.doi.org/10.1088/0264-9381/32/7/074001. 18

[46] Rolf Bork, Jonathan Hanks, David Barker, Joseph Betzwieser, Jameson Rollins, Keith Thorne, and Erik von Reis. advligorts: The advanced LIGO real-time digital control and data acquisition system. *SoftwareX*, 13:100619, 2021. ISSN 2352-7110. doi: https://doi.org/10.1016/j.softx.2020.100619. URL https://www.sciencedirect.com/science/article/pii/S2352711020303320. 18

[47] Daniel Gering. Diploma thesis, not published; from personal correspondence with Michael Born (AEI). 18

[48] S Goßler, A Bertolini, M Born, Y Chen, K Dahl, D Gering, C Gräf, G Heinzel, S Hild, F Kawazoe, O Kranz, G Kühn, H Lück, K Mossavi, R Schnabel, K Somiya, K A Strain, J R Taylor, A Wanner, T Westphal, B Willke, and K Danzmann. The AEI 10 m prototype interferometer. *Classical and Quantum Gravity*, 27(8):084023, apr 2010. doi: 10.1088/0264-9381/27/8/084023. URL https://doi.org/10.1088/0264-9381/27/8/084023. 18

[49] T. Westphal, G. Bergmann, A. Bertolini, M. Born, Y. Chen, A. V. Cumming, L. Cunningham, K. Dahl, C. Gräf, G. Hammond, G. Heinzel, S. Hild, S. Huttner, R. Jones, F. Kawazoe, S. Köhlenbeck, G. Kühn, H. Lück, K. Mossavi, J. H. Pöld, K. Somiya, A. M. van Veggel, A. Wanner, B. Willke, K. A. Strain, S. Goßler, and K. Danzmann. Design of the 10m AEI prototype facility for interferometry studies. *Applied Physics B*, 106(3):551–557, 2012. doi: 10.1007/s00340-012-4878-z. URL https://doi.org/10.1007/s00340-012-4878-z. 18

[50] Peter Fritschel. A note on the DAQ decimation filters LIGO-T1400719-v1. Technical report, LIGO, 2014. 18, 93, 247

[51] D.M.Hoyland. Phasemeter design description issue 3 S2-UBI-DDD-3012. Technical report, University of Birmingham - Department of Astrophysics and Space Research, 2007. 21, 22, 203

[52] U. Denskat, R. Gerndt, G. Link, and U. Johann. Phasemeter processing and laser control. Technical Report S2-ASD-RS-3018, ASD, September 2009. 22, 25, 26, 28, 55, 62, 203

[53] Gerhard Heinzel. LISA Pathfinder LTP phasemeter. Technical report, Max Planck Institute for Gravitational Physics (Albert-Einstein-Institute), 2004. 22, 23

[54] P.-D. Henchoz H.P. Weber R. Stierlin, R. Bättig. Excess-noise suppression in a fibre-optic balanced heterodyne detection system. *Optical and Quantum Electronics*, 18(6):445–454, 1986. doi: 10.1007/BF02041170. URL https://doi.org/10.1007/BF02041170. 25, 38

[55] Gerald Hechenblaikner. Measurement of the absolute wavefront curvature radius in a heterodyne interferometer. *Journal of the Optical Society of America A*, 27(9):2078, Aug 2010. ISSN 1520-8532. doi: 10.1364/josaa.27.002078. URL http://dx.doi.org/10.1364/JOSAA.27.002078. 28

[56] V Wand, J Bogenstahl, C Braxmaier, K Danzmann, A García, F Guzmán, G Heinzel, J Hough, O Jennrich, C Killow, D Robertson, Z Sodnik, F Steier, and H Ward. Noise sources in the LTP heterodyne interferometer. *Classical and Quantum Gravity*, 23(8): S159–S167, mar 2006. doi: 10.1088/0264-9381/23/8/s21. URL https://doi.org/10.1088/0264-9381/23/8/s21. 33

[57] Lennart Wissel. In-orbit performance and behaviour of the LISA Pathfinder Optical Metrology System. Master's thesis, Max Planck Institute for Gravitational Physics (Albert-Einstein-Institute), 2017. 33, 38, 53, 59, 173, 221

[58] A. Garciaa A. Monsky, F. Steier. OPD noise investigations for LTP S2-AEI-TN-3062. Technical report, AEI Hannover, 2009. 34

[59] M. Armano, H. Audley, J. T. Baird, P. Binetruy, M. Born, D. Bortoluzzi, N. Brandt, A. Bursi, E. Castelli, A. Cavalleri, M. Cruise, K. Danzmann, M. de Deus Silva, I. Diepholz, G. Dixon, R. Dolesi, L. Ferraioli, V. Ferroni, E. D. Fitzsimons, R. Flatscher, M. Freschi, C. García Marirrodriga, R. Gerndt, L. Gesa, F. Gibert, D. Giardini, R. Giusteri, C. Grimani, J. Grzymisch, I. Harrison, G. Heinzel, M-S Hartig, M. Hewitson, D. Hollington, D. Hoyland, M. Hueller, H. Inchauspé, O. Jennrich, P. Jetzer, B. Johlander, N. Karnesis, B. Kaune, C. J. Killow, N. Korsakova, J.A. Lobo, L. Liu, J. P. López-Zaragoza, R. Maarschalkerweerd, S. Madden, D. Mance, V. Martín, L. Martin-Polo, J. Martino, F. Martin-Porqueras, P. W. McNamara, J. Mendes, L. Mendes, N. Meshksar, A. Monsky, M. Nofrarias, S. Paczkowski, M. Perreur-Lloyd, A. Petiteau, P. Pivato, E. Plagnol, J. Ramos-Castro, J. Reiche, F. Rivas, D. I. Robertson, G. Russano, J. Sanjuan, J. Slutsky, C.F. Sopuerta, F. Steier, T. J. Sumner, D. Texier, J. I. Thorpe, D. Vetrugno, S. Vitale, V. Wand, G. Wanner, H. Ward, P. J. Wass, W. J. Weber, L. Wissel, A. Wittchen, and P. Zweifel. Sensor noise in LISA Pathfinder: An extensive in-flight review of the angular and longitudinal interferometric measurement system. *(not published yet)*, 2022. 34, 55, 127, 188, 196, 198, 212, 221

[60] *Mephisto Product Line - User's Manual.* Innolight. 35, 70

[61] Martin Hewitson and Antonio Garcia. Laser amplitude noise characterisation LTP S2-AEI-TN-3055. Technical report, Max Planck Institute for Gravitational Physics (Albert-Einstein-Institute), Università degli studi di trento, January 15, 2009. 36

[62] Brigitte Kaune. *In-orbit Stability Analysis of the LISA Pathfinder Optical Metrology: Photoreceivers and Polarisation.* PhD thesis, Max Planck Institute for Gravitational Physics (Albert-Einstein-Institute), 2021. URL https://doi.org/10.15488/10887. 37, 55, 58, 204

[63] Antonio Garcia, Frank Steier, and Gerhard Heinzel. S2-AEI-TN-30XX coupling of laser amplitude noise into the LTP phase readout noise AEI INTERNAL TN. NOT FOR EXTERNAL DISTRIBUTION. Technical report, Max Planck Institute for Gravitational Physics (Albert-Einstein-Institute), 2009. 38, 109

[64] Gerald Hechenblaikner. Common mode noise rejection properties of amplitude and phase noise in a heterodyne interferometer. *J. Opt. Soc. Am. A 30*, 1:8, 2013. 38

[65] Lennart Wissel, Andreas Wittchen, Thomas S. Schwarze, Martin Hewitson, Gerhard Heinzel, and Hubert Halloin. Relative-intensity-noise coupling in heterodyne interferometers. *(accepted for publication in Phys. Rev. Applied)*, 2021. 38

[66] Gerhard Heinzel. LTP interferometer noise S2-AEI-TN-3076. Technical report, AEI Hannover, 2016. 41, 54, 56, 204

[67] Ewan Fitzsimons and David Robertson. S2-UGL-TN-303. Technical report, LTP Project Institute for Gravitational Research Department of Physics and Astronomy University of Glasgow Glasgow G12 8QQ, Scotland, 2010. 55

[68] G. Heinzel. Electronic Noise in Interferometers. In Seiji Kawamura and Norikatsu Mio, editors, *Gravitational Wave Detection II*, volume 32, page 83, Jan 2000. 56

[69] Tv low temperature function and metrological performance test report for the PFM phasemeter - S2-UBI-TR-3063. Technical report, 2009. 56

[70] M. Armano, H. Audley, G. Auger, J. T. Baird, M. Bassan, P. Binetruy, M. Born, D. Bortoluzzi, N. Brandt, M. Caleno, L. Carbone, A. Cavalleri, A. Cesarini, G. Ciani, G. Congedo, A. M. Cruise, K. Danzmann, M. de Deus Silva, R. De Rosa, M. Diaz-Aguiló, L. Di Fiore, I. Diepholz, G. Dixon, R. Dolesi, N. Dunbar, L. Ferraioli, V. Ferroni, W. Fichter, E. D. Fitzsimons, R. Flatscher, M. Freschi, A. F. García Marín, C. García Marirrodriga, R. Gerndt, L. Gesa, F. Gibert, D. Giardini, R. Giusteri, F. Guzmán, A. Grado, C. Grimani, A. Grynagier, J. Grzymisch, I. Harrison, G. Heinzel, M. Hewitson, D. Hollington, D. Hoyland, M. Hueller, H. Inchauspé, O. Jennrich, P. Jetzer, U. Johann, B. Johlander, N. Karnesis, B. Kaune, N. Korsakova, C. J. Killow, J. A. Lobo, I. Lloro, L. Liu, J. P. López-Zaragoza, R. Maarschalkerweerd, D. Mance, V. Martín, L. Martin-Polo, J. Martino, F. Martin-Porqueras, S. Madden, I. Mateos, P. W. McNamara, J. Mendes, L. Mendes, A. Monsky, D. Nicolodi, M. Nofrarias, S. Paczkowski, M. Perreur-Lloyd, A. Petiteau, P. Pivato, E. Plagnol, P. Prat, U. Ragnit, B. Raïs, J. Ramos-Castro, J. Reiche, D. I. Robertson, H. Rozemeijer, F. Rivas, G. Russano, J. Sanjuán, P. Sarra, A. Schleicher, D. Shaul, J. Slutsky, C. F. Sopuerta, R. Stanga, F. Steier, T. Sumner, D. Texier, J. I. Thorpe, C. Trenkel, M. Tröbs, H. B. Tu, D. Vetrugno, S. Vitale, V. Wand, G. Wanner, H. Ward, C. Warren, P. J. Wass, D. Wealthy, W. J. Weber, L. Wissel, A. Wittchen, A. Zambotti, C. Zanoni, T. Ziegler, and P. Zweifel. Sub-femto-*g* free fall for space-based gravitational wave observatories: LISA Pathfinder results. *Phys. Rev. Lett.*, 116:231101, Jun 2016. doi: 10.1103/PhysRevLett.116.231101. URL https://link.aps.org/doi/10.1103/PhysRevLett.116.231101. 58, 60, 174, 176

[71] Marie-Sophie Hartig, Sönke Schuster, Gerhard Heinzel, and Gudrun Wanner. Non-geometric tilt-to-length coupling in space interferometry: mechanisms and analytical descriptions. *(not published yet)*, 2022. 58

[72] Marie-Sophie Hartig, Sönke Schuster, and Gudrun Wanner. Geometric tilt-to-length coupling in space interferometry: mechanisms and analytical descriptions. *(not published yet)*, 2022. 58

[73] Eleonora Castelli. *LISA Pathfinder noise performance results: disturbances in the sub-mHz frequency band and projection to LISA*. PhD thesis, University of Trento, 2020. 58, 216

[74] Quentin Baghi, Natalia Korsakova, Jacob Slutsky, Eleonora Castelli, Nikolaos Karnesis, and Jean-Baptiste Bayle. Detection and characterization of instrumental transients in LISA Pathfinder and their projection to LISA. *(not published yet)*, 2022. 58

[75] M. Armano, H. Audley, G. Auger, J. T. Baird, P. Binetruy, M. Born, D. Bortoluzzi, N. Brandt, A. Bursi, M. Caleno, A. Cavalleri, A. Cesarini, M. Cruise, K. Danzmann, M. de Deus Silva, I. Diepholz, R. Dolesi, N. Dunbar, L. Ferraioli, V. Ferroni, E. D. Fitzsimons, R. Flatscher, M. Freschi, J. Gallegos, C. García Marirrodriga, R. Gerndt, L. Gesa, F. Gibert, D. Giardini, R. Giusteri, C. Grimani, J. Grzymisch, I. Harrison, G. Heinzel, M. Hewitson, D. Hollington, M. Hueller, J. Huesler, H. Inchauspé,

O. Jennrich, P. Jetzer, B. Johlander, N. Karnesis, B. Kaune, C. J. Killow, N. Korsakova, I. Lloro, L. Liu, J. P. López-Zaragoza, R. Maarschalkerweerd, S. Madden, D. Mance, V. Martín, L. Martin-Polo, J. Martino, F. Martin-Porqueras, I. Mateos, P. W. McNamara, J. Mendes, L. Mendes, A. Moroni, M. Nofrarias, S. Paczkowski, M. Perreur-Lloyd, A. Petiteau, P. Pivato, E. Plagnol, P. Prat, U. Ragnit, J. Ramos-Castro, J. Reiche, J. A. Romera Perez, D. I. Robertson, H. Rozemeijer, F. Rivas, G. Russano, P. Sarra, A. Schleicher, J. Slutsky, C. Sopuerta, T. J. Sumner, D. Texier, J. I. Thorpe, C. Trenkel, D. Vetrugno, S. Vitale, G. Wanner, H. Ward, P. J. Wass, D. Wealthy, W. J. Weber, A. Wittchen, C. Zanoni, T. Ziegler, and P. Zweifel. Charge-induced force noise on free-falling test masses: Results from LISA Pathfinder. *Phys. Rev. Lett.*, 118:171101, Apr 2017. doi: 10.1103/PhysRevLett.118.171101. URL https://link.aps.org/doi/10.1103/PhysRevLett.118.171101. 60

[76] Alexander Schleicher. DFACS user manual S2-ASD-MA-2004. Technical report, Airbus Defence and Space, 2014. 60, 72

[77] Vinzenz Wand and Gerhard Heinzel. Required OPD precision in the LTP interferometer S2-AEI-TN-3031. Technical report, Max Planck Institute for Gravitational Physics (Albert-Einstein-Institute), 2006. 62

[78] V. Wand F. Steier F.Guzmán A. Garciaa, G. Heinzel. Performance analysis of the fast LTP interferometric control loops: OPD and laser frequency S2-AEI-TN-3035. Technical report, AEI Hannover, 2009. 62, 70

[79] Michael Kersten. OMS control loop analysis and filter design S2-AEI-TN-3107. Technical report, Astrium, 2011. 70

[80] R. Flatscher, R. Gerndt, K. Rogalla, N. Gradmann, and D. Kolbe. OMS performance parameter characterization during OSTT S2-ASD-TR-3155-1. Technical report, Astrium, 2012. 71

[81] M Armano, H Audley, J Baird, P Binetruy, M Born, D Bortoluzzi, E Castelli, A Cavalleri, A Cesarini, A M Cruise, and et al. Spacecraft and interplanetary contributions to the magnetic environment on-board LISA Pathfinder. *Monthly Notices of the Royal Astronomical Society*, 494(2):3014?3027, Apr 2020. ISSN 1365-2966. doi: 10.1093/mnras/staa830. URL http://dx.doi.org/10.1093/mnras/staa830. 83

[82] Thomas Schwarze. *Phase extraction for laser interferometry in space: phase readout schemes and optical testing.* PhD thesis, 2018. URL https://doi.org/10.15488/4233. 109, 227

[83] Gerhard Heinzel, Martin Hewitson, Michael Born, Lennart Wissel, Brigitte Kaune, Gudrun Wanner, Karsten Danzmann, Sarah Paczkowski, Michael Tröbs, Andreas Wittchen, Nikos Karnesis, Heather Audley, and Jens Reiche. *LPF Final Report for the German Contribution to the Nominal Mission.* Max Planck Institute for Gravitational Physics (Albert Einstein Institute), 2018. URL https://doi.org/10.2314/GBV:1030758840. 173, 182, 188, 189, 190, 196

[84] Gerhard Heinzel, Martin Hewitson, Michael Born, Lennart Wissel, Brigitte Kaune, Gudrun Wanner, Karsten Danzmann, Sarah Paczkowski, Michael Tröbs, Andreas Wittchen, Nikos Karnesis, Heather Audley, and Jens Reiche. *LISA Pathfinder Mission Extension Report for the German Contribution.* Max Planck Institute for Gravitational Physics (Albert Einstein Institute), 2020. URL https://doi.org/10.2314/KXP:1692401564. 173, 182, 188, 189, 190, 192, 196

276

[85] M Armano, H Audley, G Auger, J Baird, P Binetruy, M Born, D Bortoluzzi, N Brandt, A Bursi, M Caleno, A Cavalleri, A Cesarini, M Cruise, C Cutler, K Danzmann, I Diepholz, R Dolesi, N Dunbar, L Ferraioli, V Ferroni, E Fitzsimons, M Freschi, J Gallegos, C García Marirrodriga, R Gerndt, LI Gesa, F Gibert, D Giardini, R Giusteri, C Grimani, I Harrison, G Heinzel, M Hewitson, D Hollington, M Hueller, J Huesler, H Inchauspé, O Jennrich, P Jetzer, B Johlander, N Karnesis, B Kaune, N Korsakova, C Killow, I Lloro, R Maarschalkerweerd, S Madden, P Maghami, D Mance, V Martín, F Martin-Porqueras, I Mateos, P McNamara, J Mendes, L Mendes, A Moroni, M Nofrarias, S Paczkowski, M Perreur-Lloyd, A Petiteau, P Pivato, E Plagnol, P Prat, U Ragnit, J Ramos-Castro, J Reiche, J A Romera Perez, D Robertson, H Rozemeijer, G Russano, P Sarra, A Schleicher, J Slutsky, C F Sopuerta, T Sumner, D Texier, J Thorpe, C Trenkel, H B Tu, D Vetrugno, S Vitale, G Wanner, H Ward, S Waschke, P Wass, D Wealthy, S Wen, W Weber, A Wittchen, C Zanoni, T Ziegler, and P Zweifel. Free-flight experiments in LISA Pathfinder. *Journal of Physics: Conference Series*, 610: 012006, May 2015. doi: 10.1088/1742-6596/610/1/012006. 174, 216

[86] M. Armano, H. Audley, J. Baird, P. Binetruy, M. Born, D. Bortoluzzi, E. Castelli, A. Cavalleri, A. Cesarini, A. M. Cruise, K. Danzmann, M. de Deus Silva, I. Diepholz, G. Dixon, R. Dolesi, L. Ferraioli, V. Ferroni, E. D. Fitzsimons, M. Freschi, L. Gesa, F. Gibert, D. Giardini, R. Giusteri, C. Grimani, J. Grzymisch, I. Harrison, M-S. Hartig, G. Heinzel, M. Hewitson, D. Hollington, D. Hoyland, M. Hueller, H. Inchauspé, O. Jennrich, P. Jetzer, N. Karnesis, B. Kaune, N. Korsakova, C. J. Killow, J. A. Lobo, L. Liu, J. P. López-Zaragoza, R. Maarschalkerweerd, D. Mance, N. Meshksar, V. Martín, L. Martin-Polo, J. Martino, F. Martin-Porqueras, I. Mateos, P. W. McNamara, J. Mendes, L. Mendes, M. Nofrarias, S. Paczkowski, M. Perreur-Lloyd, A. Petiteau, P. Pivato, E. Plagnol, J. Ramos-Castro, J. Reiche, D. I. Robertson, F. Rivas, G. Russano, J. Slutsky, C. F. Sopuerta, T. Sumner, D. Texier, J. I. Thorpe, D. Vetrugno, S. Vitale, G. Wanner, H. Ward, P. J. Wass, W. J. Weber, L. Wissel, A. Wittchen, and P. Zweifel. LISA Pathfinder performance confirmed in an open-loop configuration: Results from the free-fall actuation mode. *Phys. Rev. Lett.*, 123:111101, Sep 2019. doi: 10.1103/PhysRevLett.123.111101. URL https://link.aps.org/doi/10.1103/PhysRevLett.123.111101. 174, 216

[87] Roberta Giusteri. *Parabolic flights in pico-g for space-based gravitational wave observatory: the free-fall experiment on LISA Pathfinder.* PhD thesis, University of Trento, 2017. 174, 216

[88] R Purvinskis. Electrical ICD S2-ASD-ICD-3002. Technical report, Airbus Defense and Space, 2015. 182, 204

[89] M. Stadler. Ltp laser modulator l21c0 - lme design assembly synthesis report S2-CSZ-RP-3027. Technical report, Contraves Space, 2007. 199

[90] Gerhard Heinzel. LISA Pathfinder LTP phasemeter. Technical report, AEI, 2004. 203

[91] Norm_coeff_5p1_19jan2016.txt. 203

[92] Alexander Hannes. LA PFM function and performance test procedure, "hanover-tests" as-run S2-KTM-TP-3010. Technical report, KAYSER - THREDE, 2010. 208, 210, 211, 221

[93] personal correspondance with Lennart Wissel (AEI), 2021. 228

[94] RIN requirements for LISA LISA-AEI-TN-xxxx (in development). Technical report, AEI Hannover, 2021. 228

[95] Simon Barke. *Inter-spacecraft frequency distribution for future gravitational wave observatories.* PhD thesis, 2015. URL https://www.tib.eu/de/suchen/id/TIBKAT%3A837514436. 229

Danksagung

Eigenständigkeitserklärung

Hiermit versichere ich, die vorliegende Arbeit selbstständig verfasst und keine anderen als die angegebenen Quellen und Hilfsmittel benutzt, sowie die Zitate deutlich kenntlich gemacht zu haben.

Hannover, February 1, 2022   Andreas Wittchen

List of Publications

This is the list of publications related to my thesis. From 2012 to 2013 i did my master thesis at the AEI, in the laboratory setup of the LPF OMS [1]. The same optical setup is used for my PhD thesis.

Part of the contract with the DLR are two reports, one for the initial mission duration and one for the extended mission; these include a Section on the RIN experiments [2][3].

For the LISA Symposium 11, 5 to 9 September 2016 in Zurich, i wrote a short segment for the conference proceedings [4].
The main results of the LPF operations can be found here [5][6]. My focus during the operations was more on the optical metrology system, these results are published in a paper [7]. A longer paper is currently in preparation. A paper with the derivation of the RIN coupling, together with results from a simulator and the laboratory measurement, is also in preparation.

I did not work directly on other experiments, but as part of the LPF collaboration I'm cited as author on other papers and conference proceedings such as [8] [9] [10] [11] [12] [13] [14] [15] [16] [17] [18] [19] [20] [21] [22] [23] [24] [25][26] [27] [28] [29] [30] [31] [32] [33] [34] [35].

Bibliography

[1] Andreas Wittchen. Noise investigation on the LISA pathfinder optical bench ground setup. Master's thesis, Max Planck Institute for Gravitational Physics (Albert-Einstein-Institute), 2013. 1

[2] Gerhard Heinzel, Martin Hewitson, Michael Born, Lennart Wissel, Brigitte Kaune, Gudrun Wanner, Karsten Danzmann, Sarah Paczkowski, Michael Tröbs, Andreas Wittchen, Nikos Karnesis, Heather Audley, and Jens Reiche. *LPF Final Report for the German Contribution to the Nominal Mission.* Max Planck Institute for Gravitational Physics (Albert Einstein Institute), 2018. URL https://doi.org/10.2314/GBV:1030758840. 1

[3] Gerhard Heinzel, Martin Hewitson, Michael Born, Lennart Wissel, Brigitte Kaune, Gudrun Wanner, Karsten Danzmann, Sarah Paczkowski, Michael Tröbs, Andreas Wittchen, Nikos Karnesis, Heather Audley, and Jens Reiche. *LISA Pathfinder Mission Extension Report for the German Contribution.* Max Planck Institute for Gravitational Physics (Albert Einstein Institute), 2020. URL https://doi.org/10.2314/KXP:1692401564. 1

[4] Andreas Wittchen and the LPF Collaboration. Coupling of relative intensity noise and pathlength noise to the length measurement in the optical metrology system of LISA pathfinder. In *10TH INTERNATIONAL LISA SYMPOSIUM*, 2017. doi: https://doi.org/10.1088/1742-6596/840/1/012003. 1

[5] M. Armano, H. Audley, G. Auger, J. T. Baird, M. Bassan, P. Binetruy, M. Born, D. Bortoluzzi, N. Brandt, M. Caleno, L. Carbone, A. Cavalleri, A. Cesarini, G. Ciani, G. Congedo, A. M. Cruise, K. Danzmann, M. de Deus Silva, R. De Rosa, M. Diaz-Aguilo, L. Di Fiore, I. Diepholz, G. Dixon, R. Dolesi, N. Dunbar, L. Ferraioli, V. Ferroni, W. Fichter, E. D. Fitzsimons, R. Flatscher, M. Freschi, A. F. Garcia Marin, C. Garcia Marirrodriga, R. Gerndt, L. Gesa, F. Gibert, D. Giardini, R. Giusteri, F. Guzman, A. Grado, C. Grimani, A. Grynagier, J. Grzymisch, I. Harrison, G. Heinzel, M. Hewitson, D. Hollington, D. Hoyland, M. Hueller, H. Inchauspé, O. Jennrich, P. Jetzer, U. Johann, B. Johlander, N. Karnesis, B. Kaune, N. Korsakova, C. J. Killow, J. A. Lobo, I. Lloro, L. Liu, J. P. López-Zaragoza, R. Maarschalkerweerd, D. Mance, V. Martín, L. Martin-Polo, J. Martino, F. Martin-Porqueras, S. Madden, I. Mateos, P. W. McNamara, J. Mendes, L. Mendes, A. Monsky, D. Nicolodi, M. Nofrarias, S. Paczkowski, M. Perreur-Lloyd, A. Petiteau, P. Pivato,

E. Plagnol, P. Prat, U. Ragnit, B. Rais, J. Ramos-Castro, J. Reiche, D. I. Robertson, H. Rozemeijer, F. Rivas, G. Russano, J. Sanjuan, P. Sarra, A. Schleicher, D. Shaul, J. Slutsky, C. F. Sopuerta, R. Stanga, F. Steier, T. Sumner, D. Texier, J. I. Thorpe, C. Trenkel, M. Troebs, H. B. Tu, D. Vetrugno, S. Vitale, V. Wand, G. Wanner, H. Ward, C. Warren, P. J. Wass, D. Wealthy, W. J. Weber, L. Wissel, A. Wittchen, A. Zambotti, C. Zanoni, T. Ziegler, and P. Zweifel. Sub-Femto-g Free Fall for Space-Based Gravitational Wave Observatories: LISA Pathfinder Results. *PHYSICAL REVIEW LETTERS*, 116(23), JUN 7 2016. ISSN 0031-9007. doi: {10.1103/PhysRevLett.116.231101}. 1

[6] M. Armano, H. Audley, J. Baird, P. Binetruy, M. Born, D. Bortoluzzi, E. Castelli, A. Cavalleri, A. Cesarini, A. M. Cruise, K. Danzmann, M. de Deus Silva, I. Diepholz, G. Dixon, R. Dolesi, L. Ferraioli, V. Ferroni, E. D. Fitzsimons, M. Freschi, L. Gesa, F. Gibert, D. Giardini, R. Giusteri, C. Grimani, J. Grzymisch, I. Harrison, G. Heinzel, M. Hewitson, D. Hollington, D. Hoyland, M. Hueller, H. Inchauspé, O. Jennrich, P. Jetzer, N. Karnesis, B. Kaune, N. Korsakova, C. J. Killow, J. A. Lobo, I. Lloro, L. Liu, J. P. López-Zaragoza, R. Maarschalkerweerd, D. Mance, N. Meshksar, V. Martín, L. Martin-Polo, J. Martino, F. Martin-Porqueras, I. Mateos, P. W. McNamara, J. Mendes, L. Mendes, M. Nofrarias, S. Paczkowski, M. Perreur-Lloyd, A. Petiteau, P. Pivato, E. Plagnol, J. Ramos-Castro, J. Reiche, D. I. Robertson, F. Rivas, G. Russano, J. Slutsky, C. F. Sopuerta, T. Sumner, D. Texier, J. I. Thorpe, D. Vetrugno, S. Vitale, G. Wanner, H. Ward, P. J. Wass, W. J. Weber, L. Wissel, A. Wittchen, and P. Zweifel. Beyond the Required LISA Free-Fall Performance: New LISA Pathfinder Results down to 20 mu Hz. *PHYSICAL REVIEW LETTERS*, 120(6), FEB 5 2018. ISSN 0031-9007. doi: {10.1103/PhysRevLett.120.061101}. 1

[7] M. Armano, H. Audley, J. Baird, P. Binetruy, M. Born, D. Bortoluzzi, N. Brandt, E. Castelli, A. Cavalleri, A. Cesarini, A. M. Cruise, K. Danzmann, M. de Deus Silva, I. Diepholz, G. Dixon, R. Dolesi, L. Ferraioli, V. Ferroni, E. D. Fitzsimons, R. Flatscher, M. Freschi, A. García, R. Gerndt, L. Gesa, D. Giardini, F. Gibert, R. Giusteri, C. Grimani, J. Grzymisch, F. Guzman, I. Harrison, M.-S. Hartig, G. Heinzel, M. Hewitson, D. Hollington, D. Hoyland, M. Hueller, H. Inchauspé, O. Jennrich, P. Jetzer, U. Johann, B. Johlander, N. Karnesis, B. Kaune, C. J. Killow, N. Korsakova, J. A. Lobo, L. Liu, J. P. López-Zaragoza, R. Maarschalkerweerd, D. Mance, V. Martín, L. Martin-Polo, F. Martin-Porqueras, J. Martino, P. W. McNamara, J. Mendes, L. Mendes, N. Meshksar, A. Monsky, M. Nofrarias, S. Paczkowski, M. Perreur-Lloyd, A. Petiteau, P. Pivato, E. Plagnol, J. Ramos-Castro, J. Reiche, F. Rivas, D. I. Robertson, G. Russano, J. Sanjuan, J. Slutsky, C. F. Sopuerta, F. Steier, T. Sumner, D. Texier, J. I. Thorpe, D. Vetrugno, S. Vitale, V. Wand, G. Wanner, H. Ward, P. J. Wass, W. J. Weber, L. Wissel, A. Wittchen, and P. Zweifel. Sensor noise in lisa pathfinder: In-flight performance of the optical test mass readout. *Phys. Rev. Lett.*, 126:131103, Apr 2021. doi: 10.1103/PhysRevLett.126.131103. URL https://link.aps.org/doi/10.1103/PhysRevLett.126.131103. 1

[8] M. Armano, H. Audley, J. Baird, M. Born, D. Bortoluzzi, N. Car-

dines, E. Castelli, A. Cavalleri, A. Cesarini, A. M. Cruise, K. Danzmann, M. de Deus Silva, G. Dixon, R. Dolesi, L. Ferraioli, V. Ferroni, E. D. Fitzsimons, M. Freschi, L. Gesa, D. Giardini, F. Gibert, R. Giusteri, C. Grimani, J. Grzymisch, I Harrison, M-S Hartig, G. Heinzel, M. Hewitson, D. Hollington, D. Hoyland, M. Hueller, H. Inchauspé, O. Jennrich, P. Jetzer, N. Karnesis, B. Kaune, C. J. Killow, N. Korsakova, J. P. López-Zaragoza, R. Maarschalkerweerd, D. Mance, V. Martín, L. Martin-Polo, J. Martino, F. Martin-Porqueras, I. Mateos, P. W. McNamara, J. Mendes, L. Mendes, N. Meshksar, M. Nofrarias, S. Paczkowski, M. Perreur-Lloyd, A. Petiteau, P. Pivato, E. Plagnol, J. Ramos-Castro, J. Reiche, F. Rivas, D. Robertson, I, G. Russano, J. Slutsky, C. F. Sopuerta, T. Sumner, D. Texier, J. ten Pierick, J. I. Thorpe, D. Vetrugno, S. Vitale, G. Wanner, H. Ward, P. J. Wass, W. J. Weber, L. Wissel, A. Wittchen, and P. Zweifel. Analysis of the accuracy of actuation electronics in the laser interferometer space antenna pathfinder. *REVIEW OF SCIENTIFIC INSTRUMENTS*, 91(4), APR 1 2020. ISSN 0034-6748. doi: {10.1063/1.5140406}. 1

[9] M. Armano, H. Audley, J. Baird, P. Binetruy, M. Born, D. Bortoluzzi, E. Castelli, A. Cavalleri, A. Cesarini, A. M. Cruise, K. Danzmann, M. de Deus Silva, I. Diepholz, G. Dixon, R. Dolesi, L. Ferraioli, V. Ferroni, E. D. Fitzsimons, M. Freschi, L. Gesa, F. Gibert, D. Giardini, R. Giusteri, C. Grimani, J. Grzymisch, I Harrison, M-S Hartig, G. Heinzel, M. Hewitson, D. Hollington, D. Hoyland, M. Hueller, H. Inchauspé, O. Jennrich, P. Jetzer, N. Karnesis, B. Kaune, N. Korsakova, C. J. Killow, J. A. Lobo, L. Liu, J. P. López-Zaragoza, R. Maarschalkerweerd, D. Mance, N. Meshksar, V. Martín, L. Martin-Polo, J. Martino, F. Martin-Porqueras, P. W. McNamara, J. Mendes, L. Mendes, M. Nofrarias, S. Paczkowski, M. Perreur-Lloyd, A. Petiteau, P. Pivato, E. Plagnol, J. Ramos-Castro, J. Reiche, D. Robertson, I, F. Rivas, G. Russano, J. Slutsky, C. F. Sopuerta, T. Sumner, D. Texier, J. I. Thorpe, C. Trenkel, D. Vetrugno, S. Vitale, G. Wanner, H. Ward, P. J. Wass, W. J. Weber, L. Wissel, A. Wittchen, P. Zweifel, and Lisa Pathfinder Collaboration. Novel methods to measure the gravitational constant in space. *PHYSICAL REVIEW D*, 100 (6), SEP 20 2019. ISSN 2470-0010. doi: {10.1103/PhysRevD.100.062003}. 1

[10] J. I. Thorpe, J. Slutsky, John G. Baker, Tyson B. Littenberg, Sophie Hourihane, Nicole Pagane, Petr Pokorny, Diego Janches, M. Armano, H. Audley, G. Auger, J. Baird, M. Bassan, P. Binetruy, M. Born, D. Bortoluzzi, N. Brandt, M. Caleno, A. Cavalleri, A. Cesarini, A. M. Cruise, K. Danzmann, M. de Deus Silva, R. De Rosa, L. Di Fiore, I. Diepholz, G. Dixon, R. Dolesi, N. Dunbar, L. Ferraioli, V. Ferroni, E. D. Fitzsimons, R. Flatscher, M. Freschi, C. Garcia Marirrodriga, R. Gerndt, L. Gesa, F. Gibert, D. Giardini, R. Giusteri, A. Grado, C. Grimani, J. Grzymisch, I Harrison, G. Heinzel, M. Hewitson, D. Hollington, D. Hoyland, M. Hueller, H. Inchauspé, O. Jennrich, P. Jetzer, B. Johlander, N. Karnesis, B. Kaune, N. Korsakova, C. J. Killow, J. A. Lobo, I Lloro, L. Liu, J. P. López-Zaragoza, R. Maarschalkerweerd, D. Mance, V. Martín, L. Martin-Polo, J. Martino, F. Martin-Porqueras, S. Madden, I Mateos, P. W. McNamara, J. Mendes, L. Mendes, M. Nofrarias, S. Paczkowski, M. Perreur-Lloyd, A. Petiteau, P. Pivato, E. Plagnol, P. Prat, U. Ragnit, J. Ramos-Castro,

J. Reiche, D. Robertson, I, H. Rozemeijer, F. Rivas, G. Russano, P. Sarra, A. Schleicher, D. Shaul, C. F. Sopuerta, R. Stanga, T. Sumner, D. Texier, C. Trenkel, M. Troebs, D. Vetrugno, S. Vitale, G. Wanner, H. Ward, P. Wass, D. Wealthy, W. J. Weber, L. Wissel, A. Wittchen, A. Zambotti, C. Zanoni, T. Ziegler, P. Zweifel, P. Barela, C. Cutler, N. Demmons, C. Dunn, M. Girard, O. Hsu, S. Javidnia, I Li, P. Maghami, C. Marrese-Reading, J. Mehta, J. O'Donnell, A. Romero-Wolf, J. Ziemer, LISA Pathfinder Collaboration, and ST7-DRS Operations Team. Micrometeoroid Events in LISA Pathfinder. *ASTROPHYSICAL JOURNAL*, 883(1), SEP 20 2019. ISSN 0004-637X. doi: {10.3847/1538-4357/ab3649}. 1

[11] M. Armano, H. Audley, J. Baird, P. Binetruy, M. Born, D. Bortoluzzi, E. Castelli, A. Cavalleri, A. Cesarini, A. M. Cruise, K. Danzmann, M. de Deus Silva, I. Diepholz, G. Dixon, R. Dolesi, L. Ferraioli, V. Ferroni, E. D. Fitzsimons, M. Freschi, L. Gesa, F. Gibert, D. Giardini, R. Giusteri, C. Grimani, J. Grzymisch, I. Harrison, M-S. Hartig, G. Heinzel, M. Hewitson, D. Hollington, D. Hoyland, M. Hueller, H. Inchauspé, O. Jennrich, P. Jetzer, N. Karnesis, B. Kaune, N. Korsakova, C. J. Killow, J. A. Lobo, L. Liu, J. P. López-Zaragoza, R. Maarschalkerweerd, D. Mance, N. Meshksar, V. Martín, L. Martin-Polo, J. Martino, F. Martin-Porqueras, I. Mateos, P. W. McNamara, J. Mendes, L. Mendes, M. Nofrarias, S. Paczkowski, M. Perreur-Lloyd, A. Petiteau, P. Pivato, E. Plagnol, J. Ramos-Castro, J. Reiche, D. I. Robertson, F. Rivas, G. Russano, J. Slutsky, C. F. Sopuerta, T. Sumner, D. Texier, J. I. Thorpe, D. Vetrugno, S. Vitale, G. Wanner, H. Ward, P. J. Wass, W. J. Weber, L. Wissel, A. Wittchen, and P. Zweifel. LISA Pathfinder Performance Confirmed in an Open-Loop Configuration: Results from the Free-Fall Actuation Mode. *PHYSICAL REVIEW LETTERS*, 123(11), SEP 11 2019. ISSN 0031-9007. doi: {10.1103/PhysRevLett.123.111101}. 1

[12] M. Armano, H. Audley, J. Baird, P. Binetruy, M. Born, D. Bortoluzzi, E. Castelli, A. Cavalleri, A. Cesarini, A. M. Cruise, K. Danzmann, M. de Deus Silva, I. Diepholz, G. Dixon, R. Dolesi, L. Ferraioli, V. Ferroni, E. D. Fitzsimons, M. Freschi, L. Gesa, F. Gibert, D. Giardini, R. Giusteri, C. Grimani, J. Grzymisch, I. Harrison, G. Heinzel, M. Hewitson, D. Hollington, D. Hoyland, M. Hueller, H. Inchauspé, O. Jennrich, P. Jetzer, N. Karnesis, B. Kaune, N. Korsakova, C. J. Killow, J. A. Lobo, I. Lloro, L. Liu, J. P. López-Zaragoza, R. Maarschalkerweerd, D. Mance, C. Mansanet, V. Martín, L. Martin-Polo, J. Martino, F. Martin-Porqueras, I. Mateos, P. W. McNamara, J. Mendes, L. Mendes, N. Meshksar, M. Nofrarias, S. Paczkowski, M. Perreur-Lloyd, A. Petiteau, P. Pivato, E. Plagnol, J. Ramos-Castro, J. Reiche, D. I. Robertson, F. Rivas, G. Russano, J. Sanjuan, J. Slutsky, C. F. Sopuerta, T. Sumner, D. Texier, J. I. Thorpe, C. Trenkel, D. Vetrugno, S. Vitale, G. Wanner, H. Ward, P. J. Wass, D. Wealthy, W. J. Weber, L. Wissel, A. Wittchen, and P. Zweifel. Temperature stability in the sub-milliHertz band with LISA Pathfinder. *MONTHLY NOTICES OF THE ROYAL ASTRONOMICAL SOCIETY*, 486(3):3368–3379, JUL 2019. ISSN 0035-8711. doi: {10.1093/mnras/stz1017}. 1

[13] M. Armano, H. Audley, J. Baird, P. Binetruy, M. Born, D. Bortoluzzi, E. Castelli, A. Cavalleri, A. Cesarini, A. M. Cruise, K. Danzmann, M. de Deus Silva, I. Diepholz, G. Dixon, R. Dolesi, L. Ferraioli, V. Ferroni, E. D. Fitzsimons, M. Freschi, L. Gesa, F. Gibert, D. Giardini, R. Giusteri, C. Grimani, J. Grzymisch, I. Harrison, G. Heinzel, M. Hewitson, D. Hollington, D. Hoyland, M. Hueller, H. Inchauspé, O. Jennrich, P. Jetzer, N. Karnesis, B. Kaune, N. Korsakova, C. J. Killow, J. A. Lobo, I. Lloro, L. Liu, J. P. López-Zaragoza, R. Maarschalkerweerd, D. Mance, N. Meshksar, V. Martín, L. Martin-Polo, J. Martino, F. Martin-Porqueras, I. Mateos, P. W. McNamara, J. Mendes, L. Mendes, M. Nofrarias, S. Paczkowski, M. Perreur-Lloyd, A. Petiteau, P. Pivato, E. Plagnol, J. Ramos-Castro, J. Reiche, D. I. Robertson, F. Rivas, G. Russano, J. Slutsky, C. F. Sopuerta, T. Sumner, D. Texier, J. I. Thorpe, D. Vetrugno, S. Vitale, G. Wanner, H. Ward, P. J. Wass, W. J. Weber, L. Wissel, A. Wittchen, P. Zweifel, and LISA Pathfinder Collaboration. LISA Pathfinder micronewton cold gas thrusters: In-flight characterization. *PHYSICAL REVIEW D*, 99(12), JUN 28 2019. ISSN 2470-0010. doi: {10.1103/PhysRevD.99.122003}. 1

[14] M. Armano, H. Audley, J. Baird, P. Binetruy, M. Born, D. Bortoluzzi, E. Castelli, A. Cavalleri, A. Cesarini, A. M. Cruise, K. Danzmann, M. de Deus Silva, I. Diepholz, G. Dixon, R. Dolesi, L. Ferraioli, V. Ferroni, E. D. Fitzsimons, M. Freschi, L. Gesa, F. Gibert, D. Giardini, R. Giusteri, C. Grimani, J. Grzymisch, I. Harrison, G. Heinzel, M. Hewitson, D. Hollington, D. Hoyland, M. Hueller, H. Inchauspé, O. Jennrich, P. Jetzer, N. Karnesis, B. Kaune, N. Korsakova, C. J. Killow, J. A. Lobo, I. Lloro, L. Liu, J. P. López-Zaragoza, R. Maarschalkerweerd, D. Mance, N. Meshksar, V. Martín, L. Martin-Polo, J. Martino, F. Martin-Porqueras, I. Mateos, P. W. McNamara, J. Mendes, L. Mendes, M. Nofrarias, S. Paczkowski, M. Perreur-Lloyd, A. Petiteau, P. Pivato, E. Plagnol, J. Ramos-Castro, J. Reiche, D. I. Robertson, F. Rivas, G. Russano, J. Slutsky, C. F. Sopuerta, T. Sumner, D. Texier, J. I. Thorpe, D. Vetrugno, S. Vitale, G. Wanner, H. Ward, P. J. Wass, W. J. Weber, L. Wissel, A. Wittchen, P. Zweifel, and LISA Pathfinder Collaboration. LISA Pathfinder platform stability and drag-free performance. *PHYSICAL REVIEW D*, 99(8), APR 16 2019. ISSN 2470-0010. doi: {10.1103/PhysRevD.99.082001}. 1

[15] M. Armano, H. Audley, J. Baird, S. Benella, P. Binetruy, M. Born, D. Bortoluzzi, E. Castelli, A. Cavalleri, A. Cesarini, A. M. Cruise, K. Danzmann, M. de Deus Silva, I. Diepholz, G. Dixon, R. Dolesi, M. Fabi, L. Ferraioli, V. Ferroni, N. Finetti, E. D. Fitzsimons, M. Freschi, L. Gesa, F. Gibert, D. Giardini, R. Giusteri, C. Grimani, J. Grzymisch, I Harrison, G. Heinzel, M. Hewitson, D. Hollington, D. Hoyland, M. Hueller, H. Inchauspé, O. Jennrich, P. Jetzer, N. Karnesis, B. Kaune, N. Korsakova, C. J. Killow, K. Kudela, M. Laurenza, J. A. Lobo, I Lloro, L. Liu, J. P. López-Zaragoza, R. Maarschalkerweerd, D. Mance, N. Meshksar, V. Martín, L. Martin-Polo, J. Martino, F. Martin-Porqueras, I Mateos, P. W. McNamara, J. Mendes, L. Mendes, M. Nofrarias, S. Paczkowski, M. Perreur-Lloyd, A. Petiteau, P. Pivato, E. Plagnol, J. Ramos-

Castro, J. Reiche, D. Robertson, I, F. Rivas, G. Russano, J. Slutsky, C. F. Sopuerta, T. Sumner, D. Telloni, D. Texier, J. Thorpe, I, D. Vetrugno, M. Villani, S. Vitale, G. Wanner, H. Ward, P. Wass, W. J. Weber, L. Wissel, A. Wittchen, and P. Zweifel. Forbush Decreases and < 2 Day GCR Flux Non-recurrent Variations Studied with LISA Pathfinder. *ASTROPHYSICAL JOURNAL*, 874(2), APR 1 2019. ISSN 0004-637X. doi: {10.3847/1538-4357/ab0c99}. 1

[16] G. Anderson, J. Anderson, M. Anderson, G. Aveni, D. Bame, P. Barela, K. Blackman, A. Carmain, L. Chen, M. Cherng, S. Clark, M. Connally, W. Connolly, D. Conroy, M. Cooper, C. Cutler, J. D'Agostino, N. Demmons, E. Dorantes, C. Dunn, M. Duran, E. Ehrbar, J. Evans, J. Fernandez, G. Franklin, M. Girard, J. Gorelik, V. Hruby, O. Hsu, D. Jackson, S. Javidnia, D. Kern, M. Knopp, R. Kolasinski, C. Kuo, T. Le, I Li, O. Liepack, A. Littlefield, P. Maghami, S. Malik, L. Markley, R. Martin, C. Marrese-Reading, J. Mehta, J. Mennela, D. Miller, D. Nguyen, J. O'Donnell, R. Parikh, G. Plett, T. Ramsey, T. Randolph, S. Rhodes, A. Romero-Wolf, T. Roy, A. Ruiz, H. Shaw, J. Slutsky, D. Spence, J. Stocky, J. Tallon, J. I. Thorpe, W. Tolman, H. Umfress, R. Valencia, C. Valerio, W. Warner, J. Wellman, P. Willis, J. Ziemer, J. Zwahlen, M. Armano, H. Audley, J. Baird, P. Binetruy, M. Born, D. Bortoluzzi, E. Castelli, A. Cavalleri, A. Cesarini, A. M. Cruise, K. Danzmann, M. de Deus Silva, I. Diepholz, G. Dixon, R. Dolesi, L. Ferraioli, V. Ferroni, E. D. Fitzsimons, M. Freschi, L. Gesai, F. Gibert, D. Giardini, R. Giusteri, C. Grimani, J. Grzymisch, I Harrison, G. Heinzel, M. Hewitson, D. Hollington, D. Hoyland, M. Hueller, H. Inchauspé, O. Jenntich, P. Jetzer, N. Karnesis, B. Kaune, N. Korsakova, C. J. Killow, J. A. Lobo, I Lloro, L. Liu, J. P. López-Zaragoza, R. Maarschalkerweerd, D. Mance, N. Meshksar, V. Martín, L. Martin-Polo, J. Martino, F. Martin-Porqueras, I Mateos, P. W. McNatnara, J. Mendes, L. Mendes, M. Nofrarias, S. Paczkowski, M. Perreur-Lloyd, A. Petiteau, P. Pivato, E. Plagnol, J. Ramos-Castro, J. Reiche, D. Robertson, I, F. Rivas, G. Russano, C. F. Sopuerta, T. Sumner, D. Texier, D. Vetrugno, S. Vitale, G. Wanner, H. Ward, P. J. Wass, W. J. Weber, L. Wissel, A. Wittchen, P. Zweifel, ST7 Team, and LISA Pathfinder Collaboration. Experimental results from the ST7 mission on LISA Pathfinder. *PHYSICAL REVIEW D*, 98 (10), NOV 14 2018. ISSN 2470-0010. doi: {10.1103/PhysRevD.98.102005}. 1

[17] M. Armano, H. Audley, J. Baird, P. Binetruy, M. Born, D. Bortoluzzi, E. Castelli, A. Cavalleri, A. Cesarini, A. M. Cruise, K. Danzmann, M. de Deus Silva, I. Diepholz, G. Dixon, R. Dolesi, L. Ferraioli, V. Ferroni, E. D. Fitzsimons, M. Freschi, L. Gesa, D. Giardini, F. Gibert, R. Giusteri, C. Grimani, J. Grzymisch, I Harrison, G. Heinzel, M. Hewitson, D. Hollington, D. Hoyland, M. Hueller, H. Inchauspé, O. Jennrich, P. Jetzer, N. Karnesis, B. Kaune, N. Korsakova, C. J. Killow, L. Liu, I Lloro, J. A. Lobo, J. P. López-Zaragoza, R. Maarschalkerweerd, F. Mailland, D. Mance, V. Martín, L. Martin-Polo, F. Martin-Porqueras, J. Martino, I Mateos, P. W. McNamara, J. Mendes, L. Mendes, N. Meshskar, M. Nofrarias, S. Paczkowski, M. Perreur-Lloyd, A. Petiteau, M. Pfeil, P. Pivato, E. Plagnol, J. Ramos-Castro, J. Reiche, D. Robertson, I, F. Rivas, G. Russano, G. Santoruvo, P. Sarra, D. Shaul,

J. Slutsky, C. F. Sopuerta, T. Sumner, D. Texier, J. I. Thorpe, C. Trenkel, D. Vetrugno, S. Vitale, G. Wanner, H. Ward, S. Waschke, P. J. Wass, W. J. Weber, L. Wissel, A. Wittchen, P. Zweifel, and LISA Pathfinder Collaboration. Precision charge control for isolated free-falling test masses: LISA pathfinder results. *PHYSICAL REVIEW D*, 98(6), SEP 11 2018. ISSN 2470-0010. doi: {10.1103/PhysRevD.98.062001}. 1

[18] M. Armano, H. Audley, J. Baird, P. Binetruy, M. Born, D. Bortoluzzi, E. Castelli, A. Cavalleri, A. Cesarini, A. M. Cruise, K. Danzmann, M. de Deus Silva, I. Diepholz, G. Dixon, R. Dolesi, L. Ferraioli, V. Ferroni, E. D. Fitzsimons, M. Freschi, L. Gesa, F. Gibert, D. Giardini, R. Giusteri, C. Grimani, J. Grzymisch, I Harrison, G. Heinzel, M. Hewitson, D. Hollington, D. Hoyland, M. Hueller, H. Inchauspé, O. Jennrich, P. Jetzer, N. Karnesis, B. Kaune, N. Korsakova, C. J. Killow, J. A. Lobo, I Lloro, L. Liu, J. P. López-Zaragoza, R. Maarschalkerweerd, D. Mance, N. Meshksar, V. Martín, L. Martin-Polo, J. Martino, F. Martin-Porqueras, I Mateos, P. W. McNamara, J. Mendes, L. Mendes, M. Nofrarias, S. Paczkowski, M. Perreur-Lloyd, A. Petiteau, P. Pivato, E. Plagnol, J. Ramos-Castro, J. Reiche, D. Robertson, I, F. Rivas, G. Russano, J. Slutsky, C. F. Sopuerta, T. Sumner, D. Texier, J. I. Thorpe, D. Vetrugno, S. Vitale, G. Wanner, H. Ward, P. Wass, W. J. Weber, L. Wissel, A. Wittchen, and P. Zweifel. Calibrating the system dynamics of LISA Pathfinder. *PHYSICAL REVIEW D*, 97(12), JUN 12 2018. ISSN 2470-0010. doi: {10.1103/PhysRevD.97.122002}. 1

[19] M. Armano, H. Audley, J. Baird, P. Binetruy, M. Born, D. Bortoluzzi, E. Castelli, A. Cavalleri, A. Cesarini, A. M. Cruise, K. Danzmann, M. de Deus Silva, I. Diepholz, G. Dixon, R. Dolesi, L. Ferraioli, V. Ferroni, N. Finetti, E. D. Fitzsimons, M. Freschi, L. Gesa, F. Gibert, D. Giardini, R. Giusteri, C. Grimani, J. Grzymisch, I. Harrison, G. Heinzel, M. Hewitson, D. Hollington, D. Hoyland, M. Hueller, H. Inchauspé, O. Jennrich, P. Jetzer, N. Karnesis, B. Kaune, N. Korsakova, C. J. Killow, J. A. Lobo, I. Lloro, L. Liu, J. P. López-Zaragoza, R. Maarschalkerweerd, D. Mance, N. Meshskar, V. Martín, L. Martin-Polo, J. Martino, F. Martin-Porqueras, I. Mateos, P. W. McNamara, J. Mendes, L. Mendes, M. Nofrarias, S. Paczkowski, M. Perreur-Lloyd, A. Petiteau, P. Pivato, E. Plagnol, J. Ramos-Castro, J. Reiche, D. I. Robertson, F. Rivas, G. Russano, J. Slutsky, C. F. Sopuerta, T. Sumner, D. Texier, J. I. Thorpe, D. Vetrugno, S. Vitale, G. Wanner, H. Ward, P. Wass, W. J. Weber, L. Wissel, A. Wittchen, and P. Zweifel. Measuring the Galactic Cosmic Ray flux with the LISA Pathfinder radiation monitor. *ASTROPARTICLE PHYSICS*, 98:28–37, MAR 2018. ISSN 0927-6505. doi: {10.1016/j.astropartphys.2018.01.006}. 1

[20] M. Armano, H. Audley, J. Baird, M. Bassan, S. Benella, P. Binetruy, M. Born, D. Bortoluzzi, A. Cavalleri, A. Cesarini, A. M. Cruise, K. Danzmann, M. de Deus Silva, I. Diepholz, G. Dixon, R. Dolesi, M. Fabi, L. Ferraioli, V. Ferroni, N. Finetti, E. D. Fitzsimons, M. Freschi, L. Gesa, F. Gibert, D. Giardini, R. Giusteri, C. Grimani, J. Grzymisch, I. Harrison, G. Heinzel, M. Hewitson,

D. Hollington, D. Hoyland, M. Hueller, H. Inchauspé, O. Jennrich, P. Jetzer, N. Karnesis, B. Kaune, N. Korsakova, C. J. Killow, M. Laurenza, J. A. Lobo, I. Lloro, L. Liu, J. P. López-Zaragoza, R. Maarschalkerweerd, D. Mance, V. Martín, L. Martin-Polo, J. Martino, F. Martin-Porqueras, I. Mateos, P. W. McNamara, J. Mendes, L. Mendes, M. Nofrarias, S. Paczkowski, M. Perreur-Lloyd, A. Petiteau, P. Pivato, E. Plagnol, J. Ramos-Castro, J. Reiche, D. I. Robertson, F. Rivas, G. Russano, F. Sabbatini, J. Slutsky, C. F. Sopuerta, T. Sumner, D. Telloni, D. Texier, J. I. Thorpe, D. Vetrugno, S. Vitale, G. Wanner, H. Ward, P. Wass, W. J. Weber, L. Wissel, A. Wittchen, A. Zambotti, C. Zanoni, and P. Zweifel. Characteristics and Energy Dependence of Recurrent Galactic Cosmic-Ray Flux Depressions and of a Forbush Decrease with LISA Pathfinder. *ASTROPHYSICAL JOURNAL*, 854(2), FEB 20 2018. ISSN 0004-637X. doi: {10.3847/1538-4357/aaa774}. 1

[21] M. Armano, H. Audley, G. Auger, J. Baird, M. Bassan, P. Binetruy, M. Born, D. Bortoluzzi, N. Brandt, M. Caleno, A. Cavalleri, A. Cesarini, A. M. Cruise, K. Danzmann, M. de Deus Silva, R. De Rosa, L. Di Fiore, I. Diepholz, G. Dixon, R. Dolesi, N. Dunbar, L. Ferraioli, V. Ferroni, E. D. Fitzsimons, R. Flatscher, M. Freschi, C. Garcia Marirrodriga, R. Gerndt, L. Gesa, F. Gibert, D. Giardini, R. Giusteri, A. Grado, C. Grimani, J. Grzymisch, I. Harrison, G. Heinzel, M. Hewitson, D. Hollington, D. Hoyland, M. Hueller, H. Inchauspé, O. Jennrich, P. Jetzer, B. Johlander, N. Karnesis, B. Kaune, N. Korsakova, C. J. Killow, J. A. Lobo, I. Lloro, L. Liu, J. P. López-Zaragoza, R. Maarschalkerweerd, D. Mance, V. Martín, L. Martin-Polo, J. Martino, F. Martin-Porqueras, S. Madden, I. Mateos, P. W. McNamara, J. Mendes, L. Mendes, N. Meshksar, M. Nofrarias, S. Paczkowski, M. Perreur-Lloyd, A. Petiteau, P. Pivato, E. Plagnol, P. Prat, U. Ragnit, J. Ramos-Castro, J. Reiche, D. I. Robertson, H. Rozemeijer, F. Rivas, G. Russano, P. Sarra, A. Schleicher, J. Slutsky, C. F. Sopuerta, R. Stanga, T. J. Sumner, D. Texier, J. I. Thorpe, C. Trenkel, M. Troebs, D. Vetrugno, S. Vitale, G. Wanner, H. Ward, P. J. Wass, D. Wealthy, W. J. Weber, L. Wissel, A. Wittchen, A. Zambotti, C. Zanoni, T. Ziegler, P. Zweifel, LISA Pathfinder Collaboration, and LISA Pathfinder Collaboration. Capacitive sensing of test mass motion with nanometer precision over millimeter-wide sensing gaps for space-borne gravitational reference sensors. *PHYSICAL REVIEW D*, 96(6), SEP 26 2017. ISSN 2470-0010. doi: {10.1103/PhysRevD.96.062004}. 1

[22] M. Armano, H. Audley, G. Auger, J. T. Baird, P. Binetruy, M. Born, D. Bortoluzzi, N. Brandt, A. Bursi, M. Caleno, A. Cavalleri, A. Cesarini, M. Cruise, K. Danzmann, M. de Deus Silva, I. Diepholz, R. Dolesi, N. Dunbar, L. Ferraioli, V. Ferroni, E. D. Fitzsimons, R. Flatscher, M. Freschi, J. Gallegos, C. Garcia Marirrodriga, R. Gerndt, L. Gesa, F. Gibert, D. Giardini, R. Giusteri, C. Grimani, J. Grzymisch, I. Harrison, G. Heinzel, M. Hewitson, D. Hollington, M. Hueller, J. Huesler, H. Inchauspé, O. Jennrich, P. Jetzer, B. Johlander, N. Karnesis, B. Kaune, C. J. Killow, N. Korsakova, I. Lloro, L. Liu, J. P. López-Zaragoza, R. Maarschalkerweerd, S. Madden, D. Mance, V. Martín, L. Martin-Polo, J. Martino, F. Martin-Porqueras, I. Mateos, P. W. McNamara, J. Mendes, L. Mendes, A. Moroni, M. Nofrarias, S. Paczkowski, M. Perreur-Lloyd, A. Pe-

titeau, P. Pivato, E. Plagnol, P. Prat, U. Ragnit, J. Ramos-Castro, J. Reiche, J. A. Romera Perez, D. I. Robertson, H. Rozemeijer, F. Rivas, G. Russano, P. Sarra, A. Schleicher, J. Slutsky, C. Sopuerta, T. J. Sumner, D. Texier, J. I. Thorpe, C. Trenkel, D. Vetrugno, S. Vitale, G. Wanner, H. Ward, P. J. Wass, D. Wealthy, W. J. Weber, A. Wittchen, C. Zanoni, T. Ziegler, and P. Zweifel. Charge-Induced Force Noise on Free-Falling Test Masses: Results from LISA Pathfinder. *PHYSICAL REVIEW LETTERS*, 118(17), APR 26 2017. ISSN 0031-9007. doi: {10.1103/PhysRevLett.118.171101}. 1

[23] M. Armano, H. Audley, G. Auger, J. Baird, M. Bassan, P. Binetruy, M. Born, D. Bortoluzzi, N. Brandt, M. Caleno, A. Cavalleri, A. Cesarini, M. Cruise, K. Danzmann, M. de Deus Silva, R. De Rosa, L. Di Fiore, I. Diepholz, R. Dolesi, N. Dunbar, L. Ferraioli, V. Ferroni, E. Fitzsimons, R. Flatscher, M. Freschi, C. Garca Marrirodriga, R. Gerndt, L. Gesa, F. Gibert, D. Giardini, R. Giusteri, A. Grado, C. Grimani, J. Grzymisch, I. Harrison, G. Heinzel, M. Hewitson, D. Hollington, D. Hoyland, M. Hueller, H. Inchauspé, O. Jennrich, P. Jetzer, B. Johlander, N. Karnesis, B. Kaune, N. Korsakova, C. Killow, A. Lobo, I. Lloro, L. Liu, J. P. López-Zaragoza, R. Maarschalkerweerd, D. Mance, V. Martín, L. Martin-Polo, J. Martino, F. Martin-Porqueras, S. Madden, I. Mateos, P. W. McNamara, J. Mendes, L. Mendes, M. Nofrarias, S. Paczkowski, M. Perreur-Lloyd, A. Petiteau, P. Pivato, E. Plagnol, P. Prat, U. Ragnit, J. Ramos-Castro, J. Reiche, D. I. Robertson, H. Rozemeijer, F. Rivas, G. Russano, P. Sarra, A. Schleicher, D. Shaul, J. Slutsky, C. F. Sopuerta, R. Stanga, T. Sumner, D. Texier, J. I. Thorpe, C. Trenkel, M. Troebs, D. Vetrugno, S. Vitale, G. Wanner, H. Ward, P. Wass, D. Wealthy, W. J. Weber, L. Wissel, A. Wittchen, A. Zambotti, C. Zanoni, T. Ziegler, P. Zweifel, and LISA Pathfinder Collaboration. LISA Pathfinder: First steps to observing gravitational waves from space. In *11TH INTERNATIONAL LISA SYMPO-SIUM*, volume 840 of *Journal of Physics Conference Series*. LISA, 2017. doi: {10.1088/1742-6596/840/1/012001}. 1

[24] M. Armano, H. Audley, G. Auger, J. Baird, M. Bassan, P. Binetruy, M. Born, D. Bortoluzzi, N. Brandt, M. Caleno, A. Cavalleri, A. Cesarini, M. Cruise, K. Danzmann, M. de Deus Silva, R. De Rosa, L. Di Fiore, I. Diepholz, R. Dolesi, N. Dunbar, L. Ferraioli, V. Ferroni, E. Fitzsimons, R. Flatscher, M. Freschi, C. Garcia Marrirodriga, R. Gerndt, L. Gesa, F. Gibert, D. Giardini, R. Giusteri, A. Grado, C. Grimani, J. Grzymisch, I. Harrison, G. Heinzel, M. Hewitson, D. Hollington, D. Hoyland, M. Hueller, H. Inchauspé, O. Jennrich, P. Jetzer, B. Johlander, N. Karnesis, B. Kaune, N. Korsakova, C. Killow, A. Lobo, I. Lloro, L. Liu, J. P. López-Zaragoza, R. Maarschalkerweerd, D. Mance, V. Martín, L. Martin-Polo, J. Martino, F. Martin-Porqueras, S. Madden, I. Mateos, P. W. McNamara, J. Mendes, L. Mendel, M. Nofrarias, S. Paczkowski, M. Perreur-Lloyd, A. Petiteau, P. Pivato, E. Plagnol, P. Prat, U. Ragnit, J. Ramos-Castro, J. Reiche, D. I. Robertson, H. Rozemeijer, F. Rivas, G. Russano, P. Sarra, A. Schleicher, D. Shaul, J. Slutsky, C. F. Sopuerta, R. Stanga, T. Sumner, D. Texier, J. I. Thorpe, C. Trenke, M. Troebs, D. Vetrugno, S. Vitale, G. Wanner, H. Ward, P. Wass, D. Wealthy, W. J. We-

ber, L. Wissel, A. Wittchen, A. Zambotti, C. Zanoni, T. Ziegler, P. Zweifel, and LISA Pathfinder Collaboration. LISA Pathfinder closed-loop analysis: a model breakdown of the in-loop observables. In *11TH INTERNATIONAL LISA SYMPOSIUM*, volume 840 of *Journal of Physics Conference Series*. LISA, 2017. doi: {10.1088/1742-6596/840/1/012038}. 1

[25] M. Armano, H. Audley, G. Auger, J. Baird, M. Bassan, P. Binetruy, M. Born, D. Bortoluzzi, N. Brandt, M. Caleno, A. Cavalleri, A. Cesarini, M. Cruise, K. Danzmann, M. de Deus Silva, R. De Rosa, L. Di Fiore, I. Diepholz, R. Dolesi, N. Dunbar, L. Ferraioli, V. Ferroni, E. Fitzsimons, R. Flatscher, M. Freschi, C. Garca Marrirodriga, R. Gerndt, L. Gesa, F. Gibert, D. Giardini, R. Giusteri, A. Grado, C. Grimani, J. Grzymisch, I. Harrison, G. Heinzel, M. Hewitson, D. Hollington, D. Hoyland, M. Hueller, H. Inchauspé, O. Jennrich, P. Jetzer, B. Johlander, N. Karnesis, B. Kaune, N. Korsakova, C. Killow, A. Lobo, I. Lloro, L. Liu, J. P. López-Zaragoza, R. Maarschalkerweerd, D. Mance, V. Martín, L. Martin-Polo, J. Martino, F. Martin-Porqueras, S. Madden, I. Mateos, P. W. McNamara, J. Mendes, L. Mendes, M. Nofrarias, S. Paczkowski, M. Perreur-Lloyd, A. Petiteau, P. Pivato, E. Plagnol, P. Prat, U. Ragnit, J. Ramos-Castro, J. Reiche, D. I. Robertson, H. Rozemeijer, F. Rivas, G. Russano, P. Sarra, A. Schleicher, D. Shaul, J. Slutsky, C. F. Sopuerta, R. Stanga, T. Sumner, D. Texier, J. I. Thorpe, C. Trenkel, M. Troebs, D. Vetrugno, S. Vitale, G. Wanner, H. Ward, P. Wass, D. Wealthy, W. J. Weber, L. Wissel, A. Wittchen, A. Zambotti, C. Zanoni, T. Ziegler, P. Zweifel, and LISA Pathfinder Collaboration. Laser Frequency Noise Stabilisation and Interferometer Path Length Differences on LISA Pathfinder. In *11TH INTERNATIONAL LISA SYMPOSIUM*, volume 840 of *Journal of Physics Conference Series*. LISA, 2017. doi: {10.1088/1742-6596/840/1/012004}. 1

[26] M. Armano, H. Audley, G. Auger, J. Baird, P. Binetruy, M. Born, D. Bortoluzzi, N. Brandt, A. Bursi, M. Caleno, A. Cavalleri, A. Cesarini, M. Cruise, K. Danzmann, M. de Deus Silva, D. Desiderio, E. Piersanti, I. Diepholz, R. Dolesi, N. Dunbar, L. Ferraioli, V. Ferroni, E. Fitzsimons, R. Flatscher, M. Freschi, J. Gallegos, C. Garcia Marirrodriga, R. Gerndt, L. Gesa, F. Gibert, D. Giardini, R. Giusteri, C. Grimani, J. Grzymisch, I. Harrison, G. Heinzel, M. Hewitson, D. Hollington, M. Hueller, J. Huesler, H. Inchauspé, O. Jennrich, P. Jetzer, B. Johlander, N. Karnesis, B. Kaune, N. Korsakova, C. Killow, I. Lloro, L. Liu, J. P. López-Zaragoza, R. Maarschalkerweerd, S. Madden, D. Mance, V. Martín, L. Martin-Polo, J. Martino, F. Martin-Porqueras, I. Mateos, P. W. McNamara, J. Mendes, L. Mendes, A. Moroni, M. Nofrarias, S. Paczkowski, M. Perreur-Lloyd, A. Petiteau, P. Pivato, E. Plagnol, P. Prat, U. Ragnit, J. Ramos-Castro, J. Reiche, J. A. Romera Perez, D. Robertson, H. Rozemeijer, F. Rivas, G. Russano, P. Sarra, A. Schleicher, J. Slutsky, C. F. Sopuerta, T. Sumner, D. Texier, J. I. Thorpe, R. Tomlinson, C. Trenkel, D. Vetrugno, S. Vitale, G. Wanner, H. Ward, C. Warren, P. J. Wass, D. Wealthy, W. J. Weber, A. Wittchen, C. Zanoni, T. Ziegler, and P. Zweifel. Constraints on LISA Pathfinder's self-gravity: design requirements, estimates and testing procedures. *CLASSICAL*

AND QUANTUM GRAVITY, 33(23), DEC 8 2016. ISSN 0264-9381. doi: {10.1088/0264-9381/33/23/235015}. 1

[27] M. Armano, H. Audley, G. Auger, J. Baird, P. Binetruy, M. Born, D. Bortoluzzi, N. Brandt, A. Bursi, M. Caleno, A. Cavalleri, A. Cesarini, M. Cruise, K. Danzmann, I. Diepholz, R. Dolesi, N. Dunbar, L. Ferraioli, V. Ferroni, E. Fitzsimons, M. Freschi, J. Gallegos, C. Garcia Marirrodriga, R. Gerndt, L. I. Gesa, F. Gibert, D. Giardini, R. Giusteri, C. Grimani, I. Harrison, G. Heinzel, M. Hewitson, D. Hollington, M. Hueller, J. Huesler, H. Inchauspé, O. Jennrich, P. Jetzer, B. Johlander, N. Karnesis, B. Kaune, N. Korsakova, C. Killow, I. Lloro, R. Maarschalkerweerd, S. Madden, D. Mance, V. Martín, F. Martin-Porqueras, I. Mateos, P. McNamara, J. Mendes, L. Mendes, A. Moroni, M. Nofrarias, S. Paczkowski, M. Perreur-Lloyd, A. Petiteau, P. Pivato, E. Plagnol, P. Prat, U. Ragnit, J. Ramos-Castro, J. Reiche, J. A. Romera Perez, D. Robertson, H. Rozemeijer, G. Russano, P. Sarra, A. Schleicher, J. Slutsky, C. F. Sopuerta, T. Sumner, D. Texier, J. I. Thorpe, C. Trenkel, H. B. Tu, D. Vetrugno, S. Vitale, G. Wanner, H. Ward, S. Waschke, P. Wass, D. Wealthy, S. Wen, W. Weber, A. Wittchen, C. Zanoni, T. Ziegler, and P. Zweifel. A noise simulator for eLISA: Migrating LISA Pathfinder knowledge to the eLISA mission. In *10TH INTERNATIONAL LISA SYMPOSIUM*, volume 610 of *Journal of Physics Conference Series*, 2015. doi: {10.1088/1742-6596/610/1/012036}. 1

[28] M. Armano, H. Audley, G. Auger, J. Baird, P. Binetruy, M. Born, D. Bortoluzzi, N. Brandt, A. Bursi, M. Caleno, A. Cavalleri, A. Cesarini, M. Cruise, K. Danzmann, I. Diepholz, R. Dolesi, N. Dunbar, L. Ferraioli, V. Ferroni, E. Fitzsimons, M. Freschi, J. Gallegos, C. Garcia Marirrodriga, R. Gerndt, L. I. Gesa, F. Gibert, D. Giardini, R. Giusteri, C. Grimani, I. Harrison, G. Heinzel, M. Hewitson, D. Hollington, M. Hueller, J. Huesler, H. Inchauspé, O. Jennrich, P. Jetzer, B. Johlander, N. Karnesis, B. Kaune, N. Korsakova, C. Killow, I. Lloro, R. Maarschalkerweerd, S. Madden, D. Mance, V. Martín, F. Martin-Porqueras, I. Mateos, P. McNamara, J. Mendes, L. Mendes, A. Moroni, M. Nofrarias, S. Paczkowski, M. Perreur-Lloyd, A. Petiteau, P. Pivato, E. Plagnol, P. Prat, U. Ragnit, J. Ramos-Castro, J. Reiche, J. A. Romera Perez, D. Robertson, H. Rozemeijer, G. Russano, P. Sarra, A. Schleicher, J. Slutsky, C. F. Sopuerta, T. Sumner, D. Texier, J. I. Thorpe, C. Trenkel, H. B. Tu, S. Vitale, G. Wanner, H. Ward, S. Waschke, P. Wass, D. Wealthy, S. Wen, W. Weber, A. Wittchen, C. Zanoni, T. Ziegler, and P. Zweifel. Disentangling the magnetic force noise contribution in LISA Pathfinder. In *10TH INTERNATIONAL LISA SYMPOSIUM*, volume 610 of *Journal of Physics Conference Series*, 2015. doi: {10.1088/1742-6596/610/1/012024}. 1

[29] M. Armano, H. Audley, G. Auger, J. Baird, P. Binetruy, M. Born, D. Bortoluzzi, N. Brandt, A. Bursi, M. Caleno, A. Cavalleri, A. Cesarini, M. Cruise, K. Danzmann, I. Diepholz, R. Dolesi, N. Dunbar, L. Ferraioli, V. Ferroni, E. Fitzsimons, M. Freschi, J. Gallegos, C. Garcia Marirrodriga, R. Gerndt, L. I. Gesa, F. Gibert, D. Giardini, R. Giusteri, C. Grimani, I. Harrison, G. Heinzel, M. Hewitson, D. Hollington, M. Hueller, J. Huesler, H. Inchauspé, O. Jennrich, P. Jetzer, B. Johlander, N. Karnesis, B. Kaune, N. Korsakova, C. Killow, I. Lloro,

R. Maarschalkerweerd, S. Madden, D. Mance, V. Martín, F. Martin-Porqueras, I. Mateos, P. McNamara, J. Mendes, L. Mendes, A. Moroni, M. Nofrarias, S. Paczkowski, M. Perreur-Lloyd, A. Petiteau, P. Pivato, E. Plagnol, P. Prat, U. Ragnit, J. Ramos-Castro, J. Reiche, J. A. Romera Perez, D. Robertson, H. Rozemeijer, G. Russano, P. Sarra, A. Schleicher, J. Slutsky, C. F. Sopuerta, T. Sumner, D. Texier, J. I. Thorpe, C. Trenkel, H. B. Tu, D. Vetrugno, S. Vitale, G. Wanner, H. Ward, S. Waschke, P. Wass, D. Wealthy, S. Wen, W. Weber, A. Wittchen, C. Zanoni, T. Ziegler, and P. Zweifel. The LISA Pathfinder Mission. In *10TH INTERNATIONAL LISA SYMPOSIUM*, volume 610 of *Journal of Physics Conference Series*, 2015. doi: {10.1088/1742-6596/610/1/012005}. 1

[30] M. Armano, H. Audley, G. Auger, J. Baird, P. Binetruy, M. Born, D. Bortoluzzi, N. Brandt, A. Bursi, M. Caleno, A. Cavalleri, A. Cesarini, M. Cruise, C. Cutler, K. Danzmann, I. Diepholz, R. Dolesi, N. Dunbar, L. Ferraioli, V. Ferroni, E. Fitzsimons, M. Freschi, J. Gallegos, C. Garcia Marirrodriga, R. Gerndt, L. I. Gesa, F. Gibert, D. Giardini, R. Giusteri, C. Grimani, I. Harrison, G. Heinzel, M. Hewitson, D. Hollington, M. Hueller, J. Huesler, H. Inchauspé, O. Jennrich, P. Jetzer, B. Johlander, N. Karnesis, B. Kaune, N. Korsakova, C. Killow, I. Lloro, R. Maarschalkerweerd, S. Madden, P. Maghami, D. Mance, V. Martín, F. Martin-Porqueras, I. Mateos, P. McNamara, J. Mendes, L. Mendes, A. Moroni, M. Nofrarias, S. Paczkowski, M. Perreur-Lloyd, A. Petiteau, P. Pivato, E. Plagnol, P. Prat, U. Ragnit, J. Ramos-Castro, J. Reiche, J. A. Romera Perez, D. Robertson, H. Rozemeijer, G. Russano, P. Sarra, A. Schleicher, J. Slutsky, C. F. Sopuerta, T. Sumner, D. Texier, J. I. Thorpe, C. Trenkel, H. B. Tu, D. Vetrugno, S. Vitale, G. Wanner, H. Ward, S. Waschke, P. Wass, D. Wealthy, S. Wen, W. Weber, A. Wittchen, C. Zanoni, T. Ziegler, and P. Zweifel. Free-flight experiments in LISA Pathfinder. In *10TH INTERNATIONAL LISA SYMPOSIUM*, volume 610 of *Journal of Physics Conference Series*, 2015. doi: {10.1088/1742-6596/610/1/012006}. 1

[31] M. Armano, H. Audley, G. Auger, J. Baird, P. Binetruy, M. Born, D. Bortoluzzi, N. Brandt, A. Bursi, M. Caleno, A. Cavalleri, A. Cesarini, M. Cruise, K. Danzmann, I. Diepholz, R. Dolesi, N. Dunbar, L. Ferraioli, V. Ferroni, E. Fitzsimons, M. Freschi, J. Gallegos, C. Garcia Marirrodriga, R. Gerndt, L. I. Gesa, F. Gibert, D. Giardini, R. Giusteri, C. Grimani, I. Harrison, G. Heinzel, M. Hewitson, D. Hollington, M. Hueller, J. Huesler, H. Inchauspé, O. Jennrich, P. Jetzer, B. Johlander, N. Karnesis, B. Kaune, N. Korsakova, C. Killow, I. Lloro, R. Maarschalkerweerd, S. Madden, D. Mance, V. Martín, F. Martin-Porqueras, I. Mateos, P. McNamara, J. Mendes, L. Mendes, A. Moroni, M. Nofrarias, S. Paczkowski, M. Perreur-Lloyd, A. Petiteau, P. Pivato, E. Plagnol, P. Prat, U. Ragnit, J. Ramos-Castro, J. Reiche, J. A. Romera Perez, D. Robertson, H. Rozemeijer, G. Russano, P. Sarra, A. Schleicher, J. Slutsky, C. F. Sopuerta, T. Sumner, D. Texier, J. I. Thorpe, C. Trenkel, H. B. Tu, S. Vitale, G. Wanner, H. Ward, S. Waschke, P. Wass, D. Wealthy, S. Wen, W. Weber, A. Wittchen, C. Zanoni, T. Ziegler, and P. Zweifel. A Strategy to Characterize the LISA-Pathfinder Cold Gas Thruster System. In *10TH INTERNATIONAL LISA*

SYMPOSIUM, volume 610 of *Journal of Physics Conference Series*, 2015. doi: {10.1088/1742-6596/610/1/012026}. 1

[32] M. Armano, H. Audley, G. Auger, P. Binetruy, M. Born, D. Bortoluzzi, N. Brandt, A. Bursi, M. Caleno, A. Cavalleri, A. Cesarini, M. Cruise, K. Danzmann, I. Diepholz, R. Dolesi, N. Dunbar, L. Ferraioli, V. Ferroni, E. Fitzsimons, M. Freschi, C. Garcia Marirrodriga, R. Gerndt, L. I. Gesa, F. Gibert, D. Giardini, R. Giusteri, C. Grimani, I. Harrison, G. Heinzel, M. Hewitson, D. Hollington, M. Hueller, J. Huesler, H. Inchauspé, O. Jennrich, P. Jetzer, B. Johlander, N. Karnesis, B. Kaune, N. Korsakova, C. Killow, I. Lloro, R. Maarschalkerweerd, S. Madden, D. Mance, V. Martín, F. Martin-Porqueras, I. Mateos, P. McNamara, J. Mendes, E. Mitchell, A. Moroni, M. Nofrarias, S. Paczkowski, M. Perreur-Lloyd, P. Pivato, E. Plagnol, P. Prat, U. Ragnit, J. Ramos-Castro, J. Reiche, J. A. Romera Perez, D. Robertson, H. Rozemeijer, G. Russano, P. Sarra, A. Schleicher, J. Slutsky, C. F. Sopuerta, T. Sumner, D. Texier, J. I. Thorpe, C. Trenkel, H. B. Tu, S. Vitale, G. Wanner, H. Ward, S. Waschke, P. Wass, D. Wealthy, S. Wen, W. Weber, A. Wittchen, C. Zanoni, T. Ziegler, and P. Zweifel. Bayesian statistics for the calibration of the LISA Pathfinder experiment. In *10TH INTERNATIONAL LISA SYMPOSIUM*, volume 610 of *Journal of Physics Conference Series*, 2015. doi: {10.1088/1742-6596/610/1/012027}. 1

[33] F. Gibert, M. Nofrarias, M. Armano, H. Audley, G. Auger, J. Baird, P. Binetruy, M. Born, D. Bortoluzzi, N. Brandt, A. Bursi, M. Caleno, A. Cavalleri, A. Cesarini, M. Cruise, K. Danzmann, I. Diepholz, R. Dolesi, N. Dunbar, L. Ferraioli, V. Ferroni, E. Fitzsimons, M. Freschi, J. Gallegos, C. Garcia Marirrodriga, R. Gerndt, L. I. Gesa, D. Giardini, R. Giusteri, C. Grimani, I. Harrison, G. Heinzel, M. Hewitson, D. Hollington, M. Hueller, J. Huesler, H. Inchauspé, O. Jennrich, P. Jetzer, B. Johlander, N. Karnesis, B. Kaune, N. Korsakova, C. Killow, I. Lloro, R. Maarschalkerweerd, S. Madden, P. Maghami, D. Mance, V. Martín, F. Martin-Porqueras, I. Mateos, P. McNamara, J. Mendes, L. Mendes, A. Moroni, S. Paczkowski, M. Perreur-Lloyd, A. Petiteau, P. Pivato, E. Plagnol, P. Prat, U. Ragnit, J. Ramos-Castro, J. Reiche, J. A. Romera Perez, D. Robertson, H. Rozemeijer, G. Russano, P. Sarra, A. Schleicher, J. Slutsky, C. F. Sopuerta, T. Sumner, D. Texier, J. I. Thorpe, C. Trenkel, H. B. Tu, D. Vetrugno, S. Vitale, G. Wanner, H. Ward, S. Waschke, P. Wass, D. Wealthy, S. Wen, W. Weber, A. Wittchen, C. Zanoni, T. Ziegler, and P. Zweifel. In-flight thermal experiments for LISA Pathfinder: Simulating temperature noise at the Inertial Sensors. In *10TH INTERNATIONAL LISA SYMPOSIUM*, volume 610 of *Journal of Physics Conference Series*, 2015. doi: {10.1088/1742-6596/610/1/012023}. 1

[34] M. Armano, H. Audley, J. Baird, P. Binetruy, M. Born, D. Bortoluzzi, E. Castelli, A. Cavalleri, A. Cesarini, M. Cruise, K. Danzmann, M. de Deus Silva, I. Diepholz, G. Dixon, R. Dolesi, L. Ferraioli, V. Ferroni, E. Fitzsimons, M. Freschi, L. Gesa, F. Gibert, D. Giardini, R. Giusteri, C. Grimani, J. Grzymisch, I. Harrison, G. Heinzel, M. Hewitson, D. Holling-

ton, D. Hoyland, M. Hueller, H. Inchauspé, O. Jennrich, P. Jetzer, N. Karnesis, B. Kaune, N. Korsakova, C. J. Killow, A. Lobo, I. Lloro, L. Liu, J.-P. López-Zaragoza, R. Maarschalkerweerd, D. Mance, N. Meshksar, V. Martín, L. Martin-Polo, J. Martino, F. Martin-Porqueras, I. Mateos, P. McNamara, J. Mendes, L. Mendes, M. Nofrarias, S. Paczkowski, M. Perreur-Lloyd, A. Petiteau, P. Pivato, E. Plagnol, J. Ramos-Castro, J. Reiche, D. Robertson, F. Rivas, G. Russano, J. Slutsky, C. Sopuerta, T. Sumner, D. Texier, J. I. Thorpe, D. Vetrugno, S. Vitale, G. Wanner, H. Ward, P. Wass, W. Weber, L. Wissel, A. Wittchen, and P. Zweifel. LISA Pathfinder. *arXiv e-prints*, page arXiv:1903.08924, 2019. 1

[35] M. Armano, H. Audley, J. Baird, P. Binetruy, M. Born, D. Bortoluzzi, E. Castelli, A. Cavalleri, A. Cesarini, A. M. Cruise, K. Danzmann, M. de Deus Silva, I. Diepholz, G. Dixon, R. Dolesi, L. Ferraioli, V. Ferroni, E. D. Fitzsimons, M. Freschi, L. Gesa, F. Gibert, D. Giardini, R. Giusteri, C. Grimani, J. Grzymisch, I Harrison, M-S Hartig, G. Heinzel, M. Hewitson, D. Hollington, D. Hoyland, M. Hueller, H. Inchauspé, O. Jennrich, P. Jetzer, N. Karnesis, B. Kaune, N. Korsakova, C. J. Killow, J. A. Lobo, L. Liu, J. P. López-Zaragoza, R. Maarschalkerweerd, D. Mance, V. Martín, L. Martin-Polo, J. Martino, F. Martin-Porqueras, I Mateos, P. W. McNamara, J. Mendes, L. Mendes, N. Meshksar, M. Nofrarias, S. Paczkowski, M. Perreur-Lloyd, A. Petiteau, P. Pivato, E. Plagnol, J. Ramos-Castro, J. Reiche, F. Rivas, D. Robertson, I, D. Roma-Dollase, G. Russano, J. Slutsky, C. F. Sopuerta, T. Sumner, D. Telloni, D. Texier, J. I. Thorpe, C. Trenkel, D. Vetrugno, S. Vitale, G. Wanner, H. Ward, P. J. Wass, D. Wealthy, W. J. Weber, L. Wissel, A. Wittchen, and P. Zweifel. Spacecraft and interplanetary contributions to the magnetic environment on-board LISA Pathfinder. *MONTHLY NOTICES OF THE ROYAL ASTRONOMICAL SOCIETY*, 494(2):3014–3027, MAY 2020. ISSN 0035-8711. doi: {10.1093/mnras/staa830}. 1

ANDREAS WITTCHEN

PERSONAL INFORMATION

M.Sc. Andreas Michael Wittchen
andreas.wittchen@aei.mpg.de

born 21.08.1988 at Braunschweig, Germany

EDUCATION

MAX-PLANCK INSTITUT FÜR GRAVITATIONSPHYSIK (ALBERT EINSTEIN INSTITUT)
Hannover, Germany — Ph.D. in Physics *since 28.01.2014*
Thesis title: Relative Intensity Noise in the LISA Pathfinder Interferometer - Experiments on ground and in space

LEIBNIZ UNIVERSITÄT HANNOVER
Hannover, Germany — Master of Science Physics, *13.11.2013*
Minor Subject: Mathematics
Thesis title: Noise Investigation on the LISA Pathfinder Optical Bench Ground Setup
at the Albert-Einstein-Institut Hannover/Max-Planck Institut für Gravitationsphysik

TECHNISCHE UNIVERSITÄT CAROLO-WILHELMINA ZU BRAUNSCHWEIG
Braunschweig, Germany — Bachelor of Science Physics, *30.09.2011*
Minor Subject: Mathematics
Thesis title: Photolumineszenzmessungen an GaInN-Quantenfilmstrukturen auf nicht- und semipolaren Oberflächen
at the Institut für Angewandte Physik

GYMNASIUM IM SCHLOSS
Wolfenbüttel, Germany — Abitur *05.2008*
Major Subjects: Physics, Mathematics, English

AWARDS

ESA CORPORATE TEAM ACHIEVEMENT AWARD 2016
FOR VALUABLE CONTRIBUTION TO THE SUCCESS OF THE LISA PATHFINDER MISSION

ADDITIONAL INFORMATION

PRESENTATIONS

DPG-spring conference 2013: Atomic, Molecular, Plasma Physics and Quantum Optics
 Leibniz Universität Hannover
 Title: Ground-based characterisation of the LISA-Pathfinder optical measurement
 system
DPG-spring conference 2014: Atomic, Molecular, Plasma Physics and Quantum Optics
 Humbold Universität zu Berlin
 Title: LISA Pathfinder: A mission status
LISA Symposium 2014
 University of Florida
 Title: Optimising Test Mass Position for the LISA Pathfinder Optical Metrology System
November der Wissenschaft 2014
 Albert-Einstein Institut Hannover
 Title: LISA Pathfinder − Technologiedemonstration für das Gravitationswellen-
 observatorium eLISA
11th Edoardo Amaldi Conference on Gravitational Waves
 Gravitational Wave International Committee
 Title: Optimising Test Mass Position for the LISA-Pathfinder Optical Metrology System
Einstein weiterdenken 2015
 Albert-Einstein Institut Hannover
 Title: LISA Pathfinder startet ins All − Technologiedemonstration für das Gravitationswellen-
 Observatorium eLISA
LISA Symposium 2016
 Irchel Campus, University of Zurich, Switzerland
 Title: Coupling of relative intensity noise and pathlength noise to the length measurement in the
 optical metrology system of LISA Pathfinder
Die Nacht, die Wissen schafft 2016
 Albert-Einstein Institut Hannover
 Title: LISA Pathfinder − Technologie für ein Gravitationswellen-Observatorium im All

ANDREAS WITTCHEN

CONFERENCES

eLISA meeting 2013; Albert-Einstein Institut, Hannover, Germany
DPG-spring conference 2013: Atomic, Molecular, Plasma Physics and Quantum Optics; Leibniz Universität Hannover, Hannover, Germany
LPF STOC Simulation4; ESAC, Madrid, Spain
DPG-spring conference 2014: Atomic, Molecular, Plasma Physics and Quantum Optics; Humbold Universität zu Berlin, Berlin, Germany
LISA Symposium 2014; University of Florida, Gainesville, FL
preSOVT1.13; APC, Paris, France
SOVT1 DryRun; Albert-Einstein Institut, Hannover, Germany
SOVT1; Albert-Einstein Institut, Hannover, Germany
11th Edoardo Amaldi Conference on Gravitational Waves 2015; GWIC, Gwangju, South Korea
LPF STOC Simulation5; Albert-Einstein Institut, Hannover, Germany
LISA Symposium 2016: Irchel Campus, University of Zurich, Switzerland
LISA Symposium 2020: online